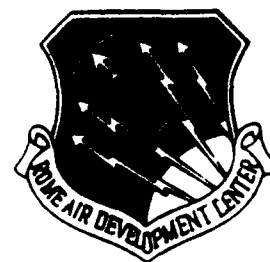


DTIC FILE COPY

2

RADC-TR-88-308
Final Technical Report
November 1988



AD-A226 244

MSW TRANSDUCERS

James C. Sethares, I. Jacob Weinberg, and Edward Cohen

APPROVED FOR PUBLIC RELEASE; DISTRIBUTION UNLIMITED.

DTIC
ELECTE
SEP 06 1990
S B D

ROME AIR DEVELOPMENT CENTER
Air Force Systems Command
Griffiss Air Force Base , NY 13441-5700

00 09 06 039

This report has been reviewed by the RADC Public Affairs Division (PA) and is releasable to the National Technical Information Service (NTIS). At NTIS it will be releasable to the general public, including foreign nations.

RADC-TR-88-308 has been reviewed and approved for publication.

APPROVED:



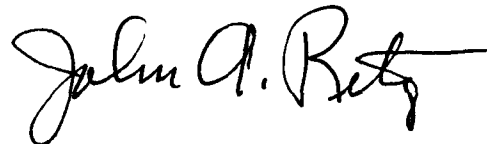
R. J. MAILLOUX
Chief, Antennas & Components Division
Directorate of Electromagnetics

APPROVED:



JOHN K. SCHINDLER
Director of Electromagnetics

FOR THE COMMANDER:



JOHN A. RITZ
Directorate of Plans & Programs

If your address has changed or if you wish to be removed from the RADC mailing list, or if the addressee is no longer employed by your organization, please notify RADC (EEAC) Hanscom AFB MA 01731-5000. This will assist us in maintaining a current mailing list.

Do not return copies of this report unless contractual obligations or notices on a specific document require that it be returned.

REPORT DOCUMENTATION PAGE

Form Approved
OMB No. 0704-0188

1a. REPORT SECURITY CLASSIFICATION UNCLASSIFIED			1b. RESTRICTIVE MARKINGS N/A			
2a. SECURITY CLASSIFICATION AUTHORITY N/A			3. DISTRIBUTION / AVAILABILITY OF REPORT Approved for public release; distribution unlimited			
2b. DECLASSIFICATION / DOWNGRADING SCHEDULE N/A						
4. PERFORMING ORGANIZATION REPORT NUMBER(S) RADC-TR-88-308			5. MONITORING ORGANIZATION REPORT NUMBER(S)			
6a. NAME OF PERFORMING ORGANIZATION Rome Air Development Center		6b. OFFICE SYMBOL (If applicable) EEAC	7a. NAME OF MONITORING ORGANIZATION			
6c. ADDRESS (City, State, and ZIP Code) Hanscom Air Force Base Massachusetts 01731-5000			7b. ADDRESS (City, State, and ZIP Code)			
8a. NAME OF FUNDING / SPONSORING ORGANIZATION AFOSR		8b. OFFICE SYMBOL (If applicable) NE	9. PROCUREMENT INSTRUMENT IDENTIFICATION NUMBER			
8c. ADDRESS (City, State, and ZIP Code) Bolling Air Force Base; DC 20332-6448			10. SOURCE OF FUNDING NUMBERS			
			PROGRAM ELEMENT NO. 61102F	PROJECT NO. 2305	TASK NO. J5	WORK UNIT ACCESSION NO. 02
11. TITLE (Include Security Classification) MSW Transducers						
12. PERSONAL AUTHOR(S) Sethares, J.C., Weinberg, I.J.*, and Cohen, E.**						
13a. TYPE OF REPORT In-House		13b. TIME COVERED FROM Sep 87 to Sep 88		14. DATE OF REPORT (Year, Month, Day) 1988 November		
15. PAGE COUNT 332						
16. SUPPLEMENTARY NOTATION * University of Lowell ** Arcon Corporation						
17. COSATI CODES			18. SUBJECT TERMS (Continue on reverse if necessary and identify by block number)			
FIELD	GROUP	SUB-GROUP	Magnetostatic Waves, Microwaves, Delay Lines, Ferrites			
20	14					
09	01					
19. ABSTRACT (Continue on reverse if necessary and identify by block number)						
<p>This report summarizes research performed at RADC/EEA on magnetostatic wave transducers. Using the theory presented here, MSW delay line characteristics such as insertion loss, phase, time delay, and input impedance may be computed as a function of frequency. The delay line is made up of identical input and output transducers with a ferrite delay medium. Input parameters are: magnetic biasing field, transducer geometry, YIG parameters, and ground plane spacings.</p> <p>The theory developed accurately predicts the behavior of single element MSW transducers on YIG. It predicts the behavior of multielement transducers that are weakly coupled to the YIG when individual transducer elements are narrow compared to interelement spacing, and when maximum transducer dimensions are small compared to electromagnetic wavelengths.</p> <p>The report also includes the following: A review of basic MSW phenomena; a detailed MSW transducer analysis; a description of MSW computer programs with examples; a summary and review of all MSW experiments and publications by RADC relevant to the development of transducer models; a transducer apodization equation that agrees well with experiment; and, a detailed analysis of the back reaction of a strongly coupled MSW onto the generating</p>						
20. DISTRIBUTION/AVAILABILITY OF ABSTRACT <input checked="" type="checkbox"/> UNCLASSIFIED/UNLIMITED <input type="checkbox"/> SAME AS RPT. <input type="checkbox"/> DTIC USERS			21. ABSTRACT SECURITY CLASSIFICATION Unclassified			
22a. NAME OF RESPONSIBLE INDIVIDUAL James C. Sethares			22b. TELEPHONE (Include Area Code) (617) 377-4663		22c. OFFICE SYMBOL RADC/EEAC	

UNCLASSIFIED

SECURITY CLASSIFICATION OF THIS PAGE

Block 19 Continued

current distribution, in a single strip.

Finally, a new generalized transducer model is briefly described, which takes advantage of the best features of the previous models. The new model can be adapted to describe the coupling between MSW and any microwave or millimeter strip line structure.

UNCLASSIFIED

SECURITY CLASSIFICATION OF THIS PAGE

Accession For	
NTIS GRA&I	<input checked="checked" type="checkbox"/>
DTIC TAB	<input type="checkbox"/>
Unannounced	<input type="checkbox"/>
Justification	
By	
Distribution/	
Availability Codes	
Dist	Avail and/or Special
A-1	



Preface

This report represents the combined results of the authors' individual investigations. James Sethares, RADC/EEA, formulated the basic theory and developed the MSW transducer models. He wrote the report, except for Chapters 2 and 8, and part of Chapter 3. I. Jacob Weinberg, University of Lowell, performed the mathematical analysis in Chapter 2, and developed the MSW Fortran programs described in Chapter 3. Edward Cohen, Arcon Corp., developed the analysis in Chapter 8 for strongly coupled transducers and adapted the MSW Fortran programs to obtain the numerical results for the transducer current distribution presented in Chapter 8.

Prof. I. Jacob Weinberg performed his research while at RADC under the 1987 USAF-UES Summer Faculty Research Program sponsored by AFOSR. Edward Cohen performed his research under an Air Force EM Analysis Contract, AF 86-C-0104, with Arcon Corp.

James Sethares expresses his sincere gratitude to his colleagues and co-authors, I. Jacob Weinberg and Edward Cohen for their continued interest in MSW over many years. Contributions of many other individuals are gratefully acknowledged, with special thanks to the following: Alan J. Budreau, Paul H. Carr, Roger Colvin, John S. Derov, Robert E. Floyd, Harold M. Frost, William Kearns, Ilya Koltunov, Kenneth Laker, Frank Olson, John Owens, Tom G. Purnhagen, J. Bradford Merry, Frederick R. Morgenthaler, Peter J. Rainville, George A. Roberts, Marden H. Seavey, Janet C. Sethares, William A. Sethares, Jose H. Silva, Andrew J. Slobodnik, Charles Smith, Jr., Martin R. Stiglitz, Thomas L. Szabo, V. Lawrence Taylor, J. Bruce Thaxler, Li Jun Tsai, and Tung Lin Tsai.

Contents

1. INTRODUCTION AND MSW BASICS	1
1.1 Propagating MSW Modes	2
1.2 Rf Magnetization	3
1.3 MSW Propagation Media	6
1.4 MSW Delay Lines	9
1.4.1 Two Terminal (TT) Model	9
1.4.2 Transmission Line (TL) Model	9
1.5 Transducer and Delay Line Geometry	9
1.6 Device Fabrication	12
1.6.1 Flipped (FC) and Wire Over (WO) Configuration	12
1.6.2 Prototype Delay Lines	15
REFERENCES FOR SECTION 1	20
2. MSW TRANSDUCER ANALYSIS	21
2.1 Polder Permeability Tensor	21
2.2 Basic Equations	24
2.3 Surface Waves (SW)	25
2.3.1 SW Dispersion Relation	25
2.3.2 SW Field Equations	27
2.3.3 SW Power	30
2.4 Forward Volume Waves (FVW)	33
2.4.1 FVW Dispersion Relation	33
2.4.2 FVW Field Equations	35
2.4.3 FVW Power	38
2.5 Backward Volume Waves (BVW)	44
2.5.1 BVW Dispersion Relation	44
2.5.2 BVW Field Equations	45
2.5.3 BVW Power	49
2.6 Radiation Resistance, Reactance and Insertion Loss	52
2.6.1 Two Terminal (Truncated Array) Model	53
2.6.2 Transmission Line Model	53
REFERENCES FOR SECTION 2	55

**BEST
AVAILABLE COPY**

Contents

3. MSW PROGRAM DESCRIPTIONS	57
3.1 SUR and VOL Program Input Descriptions	57
3.1.1 Surface Waves (SUR)	57
3.1.1.1 TT Model (TTOP=1) SUR	58
3.1.1.2 TL Model (TTOP=0) SUR	59
3.1.2 Volume Waves (VOL)	60
3.1.2.1 TT Model (TTOP=1) VOL	61
3.1.2.2 TL Model (TTOP=0) VOL	61
3.2 Interactive Programs, Inputs, and Procedures	61
3.2.1 Surface Waves (ISUR)	62
3.2.2 Volume Waves (IVOL)	62
3.2.3 Interactive Programs	62
3.2.4 Program Execution Procedures	63
3.2.4.1 ISUR	63
3.2.4.2 ISURN	63
3.2.4.3 ISURP	64
3.3 Input Data Batch Files for SUR and VOL	65
3.4 Complete List of MSW Program Files	68
3.5 Combined TT/TL Program	72
4. COMPUTER GENERATED DATA	73
4.1 Independent Conductors and Normal Mode Models	73
4.2 TT and TL Models	73
4.3 MSSW with No Ground Planes	73
4.4 Narrow Band Transducers: Meander Line	77
4.4.1 Independent Conductor Model	77
4.4.2 Normal Mode Model	77
4.4.3 Radiation Resistance and Generation Efficiency	77
4.5 Liftoff	81
4.6 Insertion Loss and Linewidth	81
4.7 Insertion Loss and Strip Width	81
4.8 Microstrip (Transmission Line) Model	89
4.9 Two Element Grating Transducer	89
4.10 Dispersion Relations and Group Velocity	89
4.10.1 MSSW Normalized Dispersion Relations	89
4.10.2 MSSW Normalized Group Velocity	96
4.10.3 Dispersion Curves for Mixed Modes	96
4.11 Apodization	103
4.11.1 MSSW Apodization	106
4.11.2 Normal Mode and Independent Conductors	108
4.11.3 Insertion Loss	115
REFERENCES FOR SECTION 4	120
5. EXPERIMENTAL DATA	121
5.1 IL and Time Delay from S21	121
5.2 Dispersion Relation from CW Experiments	124
5.3 IL: Theory and Experiment	124
5.3.1 Single Element Transducers	124
5.3.2 Multielement Transducer Delay Lines	127
5.3.3 Limits of Theory	127

Contents

5.4	Pulse Experiments	131
5.4.1	Short Pulses and Echoes	131
5.4.2	Pulse Spreading for Long Delays	133
5.4.3	Propagation Loss and Linewidth	135
5.5	MSW Oscillators	135
5.5.1	Wideband Delay Line	140
5.5.2	Narrowband Transducers (N=15)	141
5.5.3	Oscillator Tuning	141
5.6	MSW Device Characteristics	143
5.6.1	Amplitude Ripple	143
5.6.2	Phase Shift Ripple	143
5.6.3	Magnetic Field Tuning	147
5.6.4	Magnetic Field Switching Speed	147
5.6.5	Temperature Sensitivity	147
5.6.6	Crystalline Anisotropy	153
5.7	MSW Diffraction and Pulse Separation	153
5.7.1	MSW Diffraction	153
5.7.2	Spatial Separation of Simultaneous Pulses	158
REFERENCES FOR SECTION 5		160
6.	ADVANCED ANALYSIS AND DESIGN	161
6.1	Transducer Currents and Fields	161
6.1.1	Hyperbolic Current Distribution	161
6.1.2	Hyperbolic Current Distribution Transform	163
6.1.3	Hyperbolic Current Distribution Insertion Loss	165
6.1.4	Transducer Fields	168
6.2	Equivalent Circuit Models	171
6.2.1	Radiation Resistance for TT Model	173
6.2.2	EM and MSW Power	175
6.3	MSW Delay Line Band Pass Filters	176
6.3.1	Long Wavelength Filtering	176
6.3.2	Spatial Harmonic Filtering	176
6.4	Generalized MSW Transducer Model (TT/TL)	181
6.4.1	MSW Power with Spatially Varying Current	181
6.4.2	General Transmission Line for TT/TL	182
6.4.3	Generalized Radiation Resistance	183
REFERENCES FOR SECTION 6		185
7.	SUMMARY AND REVIEW OF SELECTED MSW PUBLICATIONS	187
7.1	Low Loss MSWs	187
7.2	Electromagnetic Transducers for Ultrasonic Waves	188
7.3	MSW Transducers	193
7.3.1	Independent Conductor Model	195
7.3.2	Normal Mode Analysis	195
7.3.3	Generalized Radiation Resistance for Uniform Current Model	197
7.3.4	Generalized Radiation Resistance for Normal Mode Model	197
7.3.5	Space Harmonics for Uniform Current Distribution	198
7.3.6	Nonuniform Current Distribution for Meander Line	198
7.3.7	Generalized Apodization for Radiation Resistance for Flat Field Theory	199
7.3.8	Variable Coupling	201
7.3.9	Assumptions and Physical Basis for Multielement Transducers	201
7.3.10	Insertion Loss	203

Contents

7.3.11 Generalized MSW Analysis	207
7.3.12 Model Limitations and Range of Validity	208
7.3.13 Strongly Coupled MSW	211
7.3.14 Magnetostatic Volume Waves	217
7.4 Review of MSW Transducer Theory	230
REFERENCES FOR SECTION 7	233
8. TRANSDUCER CURRENT DENSITY AND RESPONSE	237
8.1 Introduction and Overview	237
8.2 Statement of the Problem	237
8.3 Field Equations	237
8.4 Boundary Conditions	241
8.5 Fourier Integral Solutions	243
8.6 Determination of $B_1(k)$	243
8.7 Evaluation of Green's Function	245
8.7.1 Introduction	245
8.7.2 Calculation of $G(+/-)$	246
8.7.3 Real Axis Integration	248
8.7.4 Evaluation of $B(q(+/-))$	249
8.7.4.1 Finite Range Integration	250
8.7.4.2 Semi Infinite Range Integration	251
8.8 Numerical Inversion of Integral Equation	254
8.9 Comparison with Emtage's Results	256
8.10 Calculation of $J(k)$	259
8.11 Discussion of Results	261
REFERENCES FOR SECTION 8	292
9. DISCUSSION AND CONCLUSION	295
APPENDIX A: MSW AND MICROWAVE MAGNETICS PUBLICATIONS	297
A1. Review Papers and Related Publications	297
A2. Microwave Magnetism Bibliography	298
A3. AFCRL and RADC Reports	299
APPENDIX B: HYPERBOLIC CURRENT DISTRIBUTION	301
APPENDIX C: LIST OF SYMBOLS AND NOTATION	305
APPENDIX D: BANDPASS FILTER USING LPE/YIG FILMS (UNPUBLISHED PAPER)	307
D1. Introduction	307
D2. Single Pole Narrow Band Filter	308
D3. Discussion	308
REFERENCES FOR APPENDIX D	311
APPENDIX E: TRANSMISSION LINE ANALYSIS FOR TT MODEL EXTENSION	313

Illustrations

1-1.	Three Pure MSW Propagating Modes	3
1-2a.	Rayleigh Type Magnetic Surface Wave Representation	5
1-2b.	MSSW Amplitude Distribution Throughout Thickness of YIG Film Sample for Small and Large Wavelengths	5
1-3a.	Gallium and Lanthanum doped LPE/YIG Films are Useful from 500 MHz to 20 GHz. Above 20 GHz, biasing field requirements are excessive, greater than 2 Teslas. High quality Lithium Ferrite films, when available, will be useful above 20 GHz due to their larger saturation magnetization; and therefore, their lower biasing field requirement	7
1-3b.	Reference Flats for Commercial GGG Wafers from Allied Corporation	8
1-4a.	Narrow Band MSW Delay Line. At 3 GHz center frequency, internal field is about 375 oersteds. MSSW are nonreciprocal, MSFVW and MSBVWs are reciprocal	10
1-4b.	Geometry for MSW Transducer Analysis	10
1-5a.	Wire Over Configuration	11
1-5b.	Flipped Configuration	11
1-6.	Delay Characteristics for Flipped Configuration	13
	(a) Minus Wave Delay Time (b) Plus Wave Delay Time	
	(c) Minus Wave IL (d) Plus Wave IL	
1-7.	Delay Characteristics for Wire Over Configuration	14
	(a) Minus Wave Delay Time (b) Plus Wave Delay Time	
	(c) Minus Wave IL (d) Plus Wave IL	
1-8.	Early MSW Prototype Delay Lines Fabricated at University of Texas, Arlington	16
	(a) Microstrip Transducers (b) YIG Flipped onto Microstrip Circuit	
	(c) Permanent Magnet Biasing Field	

Illustrations

1-9a.	Early MSW Delay Line in Tek Wave Microstrip Package	17
1-9b.	Tuning Coil for MSW Delay Line	17
1-9c.	Compact MSW Delay Line	18
1-10.	Slotline and Coplanar MSW Transducers	19
2-1.	Geometry and Coordinate System Used Throughout Report Except for Chapter 8	22
4-1.	Insertion Loss versus Frequency. Response of a pair of 15-Element grating transducers in a delay line configuration.	74
	a. Independent conductor analysis, top figure	
	b. Normal mode analysis, bottom figure	
4-2.	Comparison of Two Terminal, TT, Model with Transmission Line, TL, Model	75
	a. 8-element grating transducer, top figure	
	b. 2-element grating transducer, bottom figure	
4-3.	Radiation Resistance for Single Strip Transducer with No Ground Planes. MSW wavelength at 3.7 GHz is 282 μm	76
4-4.	Comparison of Independent Conducting Strip Analysis with Normal Mode Analysis	78
	a. Independent Conducting Strips	
	b. Normal Modes. Two normal mode responses superimposed on the same set of axes.	
4-5.	Spatial Harmonic Responses. Meander line 8-Element Transducers. MSW wavelengths are given in terms of center to center strip spacing	79
4-6.	Radiation Resistance and Reactance of 8-Element Transducers. For the particular set of parameters chosen, radiation resistance increases with increasing mode number	80
4-7.	Radiation Resistance Per Unit Transducer Aperture Length versus Frequency, for a 4-Element Grating Transducer with Liftoff "g" as a Parameter	82
4-8.	Insertion Loss for Zero, and 15 μm Liftoff, G. Lower portion of figure shows geometry	83
4-9.	MSSW Insertion Loss versus Frequency for an 8-Element Grating Transducer Pair. $G = 150 \mu\text{m}$ and $G = 10 \mu\text{m}$	84
4-10.	Insertion Loss of MSW Delay Line for Parametric Values of Linewidth. Propagation loss increases with increasing linewidth. Delay line uses single-element transducers at input and output ports	85
4-11.	MSSW Passband, IL, for Parametric Values of Strip Width, Using TT Model	86
4-12.	MSSW Radiation Resistance for Parametric Values of Strip Width, Using TT Model	87
4-13.	MSSW Radiation Reactance for Parametric Values of Strip Width, Using TT Model	88
4-14.	Transmission Line Model Insertion Loss and Input Resistance and Reactance for Single Strip Transducers	90
4-15.	Transmission Line Propagation Constant and Group Delay	91
4-16.	Insertion Loss versus Frequency for Two Bar Grating, for Three Values of Transducer Aperture	92

Illustrations

4-17.	Insertion Loss versus Frequency for Two Bar Gratings for Four Values of Liftoff	93
4-18.	Normalized Dispersion Relations. $S = 1$ corresponds to wave whose energy is concentrated on the YIG surface nearest transducer	94
	a. Two ground planes, left figure	
	b. One ground plane on transducer side of YIG, right figure. Transducer is between ground plane and YIG surface where MSSW energy is concentrated	
4-19.	Generalized Group Velocity Curves for One Closely Spaced Ground Plane	95
	a. Weakly coupled MSSW on YIG surface opposite transducer side of YIG, $s = -1$	
	b. Strongly coupled MSSW on YIG surface near transducer side, $s = +1$	
4-20.	Dispersion Relations for H in yz Plane, FVW/SW Hybrid Mode, See Figure 2-1	97
4-21.	Dispersion Relations for H in xz Plane, BVW/SW Hybrid Mode, See Figure 2-1	98
4-22.	Dispersion Relations for H in xz Plane, SW/BVW Hybrid Mode, See Figure 2-1	99
4-23.	Dispersion Relations for H in xy Plane, FVW/BVW Hybrid Mode, See Figure 2-1	100
4-24.	Dispersion Relation for H in xy Plane, Where Hybrid Modes Have Zero Wavenumber at the Same Frequency, See Figure 4-21	102
4-25.	Group Delay for a Pair of Cascaded Delay Lines with Dispersion Relations Like the Ones Shown in Figure 4-24	103
4-26.	Apodized Transducers	
	a. A length apodized transducer. Radiation resistance can be described by Eq. (4-2)	104
	b. A width apodized transducer. Radiation resistance described by Eq. (4-2), using Table 4-1 Column C	105
4-27.	Apodization of Fundamental Normal Model for an 8-Element Meander Line	
	a. No apodization	109
	b. Width weighted	110
	c. Nonuniform spacing	111
4-28.	Apodization of Independent Conductors for an 8-Element Meander Line	
	a. No apodization	112
	b. Width weighted	113
	c. Nonuniform spacing	114
4-29.	Normal Mode Apodization of a 32-Element Meander Line for Both Plus and Minus Surface Wave	
	a. Minus wave, $s = -1$	116
	b. Plus wave, $s = +1$	117
4-30.	Width Apodization of a 15-Element Grating Transducer Using Independent Conductor Analysis	118
	a. No apodization, top figure, Table 4-1, Column A	
	b. Apodized, narrow strips in center, middle figure, see Table 4-1, Column B	
	c. Apodized, Wide strips in center, lower figure, see Table 4-1, Column C	

Illustrations

5-1.	Network Analyzer Displays of Insertion Loss and Transmission Phase as Function of Frequency, for Unmatched Delay Line.	122
a.	IL versus f. Horizontal scale, 2500-3500 MHz. Vertical scale, 10 dB/div, minimum IL = 12 dB	
b.	Transmission phase versus f. Horizontal scale 2500-3500 MHz. Vertical scale, 90 deg/div	
5-2.	Phase versus f for MSBVW Delay Line, Top Figure; and MSSW, Lower Figure	123
5-3.	Theory versus Experiment Using Data Obtained from Phase of S ₂₁ , a Transmission Scattering Coefficient	125
5-4.	Theory versus Experiment for Single Element Transducers, and FVW Delay Line. Theory: two terminal model. TT. Experiment: data supplied by N. Vlannes, MIT, 1984	126
5-5.	MSSW Passbands for Various Values of Liftoff; Theory and Experiment. Experimental data provided by J. Parekh, NYSU at Stonybrook	128
5-6.	Comparison of Two Terminal TT, Model with Experiment, for 2-Bar Transducer, and for 8-Bar Transducer, Delay Lines	129
5-7.	Width Apodized 15-Element Grating Transducer MSSW Delay Lines, Theory and Experiment	130
5-8.	MSW Pulse Propagation and Reflections on a YIG Slab	131
5-9.	Oscilloscope Traces of Received MSW Pulses Following Paths Indicated in Figure 5-8	132
5-10.	Oscilloscope Traces of MSSW Pulse Spreading as a Function of Delay Time	134
5-11.	Pulse Width as a Function of Delay Time	136
5-12.	YIG Linewidth as a Function of Frequency, Theory and Experiment	137
5-13.	Experimental Arrangement for Investigating MSW Pulse Experiments	138
5-14.	Block Diagram of MSW Oscillator	139
5-15.	Spectrum Analyzer Display of a Wideband MSW Delay Line Oscillator, N=1	140
5-16.	Spectrum Analyzer Display of a Narrow Band MSW Delay Line Oscillator, N=15	141
5-17.	MSSW Delay Line Oscillator Frequency versus Bias Field, Theory and Experiment	142
5-18.	MSW Passband Ripple Reduction with Nonuniform Fields	144
5-19.	MSW Phase Ripple Compared with Coaxial Cable	145
5-20.	Phase Ripple in a 3-Bit Diode Switched Line Phase Shifter	146
5-21.	Figure Showing Construction of a Tunable Planar LPE/YIG Bandstop Filter Implemented in Microstrip	148
5-22.	Oscilloscope Trace of the Output of a Tunable Planar LPE/YIG Bandpass Filter Implemented in Microstrip	149
5-23.	Tuning Sensitivity of Planar LPE/YIG Filters Implemented in Microstrip	150
5-24.	Rapid Switching Speed of Planar LPE/YIG Filter Implemented in Microstrip	151

Illustrations

5-25.	Phase Shift versus Frequency of an Uncompensated MSW Delay Line	152
5-26.	In-Plane Magnetocrystalline Anisotropy of a (III) LPE/YIG Film	154
5-27.	MSW Propagation Along a Curved LPE/YIG Film.	
a.	LPE/YIG film grown on a cylindrical surface. Ring has 3/4 inch outer diameter. YIG is on outer surface of ring.	155
b.	Pulse delay versus bias field, propagation constant and wavelength, on the curved YIG surface.	156
5-28.	Device for Investigating MSW Refraction	157
5-29.	Separation of Simultaneously Received Pulses Using the Device Shown in Figure 5-28	159
6-1.	Hyperbolic Current Distribution	
a.	Current distribution for grating, $\eta = 1$; and for meander line, $\eta = -1$	163
b.	Current distribution for parametric values of skin depth	164
6-2.	Insertion Loss with Hyperbolic Current Distribution	
a.	IL versus f for parametric values of skin depth, $N = 1$	166
b.	IL versus f for parametric values of skin depth, $N = 15$	167
6-3.	Limiting Cases for Hyperbolic Current Distribution. Uniform current; skin depth approaches infinity, favors generation of fundamental response. Doublet current; skin depth approaches zero, favors generation of first space harmonic response.	169
6-4.	RF Magnetic Field Component Using a Truncated Infinite Array Analysis	
a.	Horizontal RF magnetic field for parametric values of G	170
b.	Horizontal RF magnetic field for parametric values of a	170
6-5.	RF Magnetic Field Component Using Superposition for a Finite Array of Conducting Strips. Vertical RF magnetic field component. Top: Four element grating transducer. Bottom: Four element meander line transducer	172
6-6.	Passband Responses for a Pair of Narrow, Intermediate and Wide Single Element Transducers. $G/D = 1/10$ for all three cases.	177
a.	Narrow strips, $A/D = 1$	
b.	Intermediate strips, $A/D = 10$	
c.	Wide strips, $A/D = 50$	
6-7.	Sidelobe Suppression for Bandpass Filtering Using One Wide Strip and Large G	
a.	IL versus f with $G = 180 \mu\text{m}$	178
b.	IL versus f with $G = 250 \mu\text{m}$	179
6-8.	Sidelobe Suppression for Bandpass Filtering Using a Large Number of Narrow Strips and Large G . $H = 650$ oersteds, $D = 6.25 \mu\text{m}$, $T1 = L = 254 \mu\text{m}$, $L1 = 1$ cm $P = 356 \mu\text{m}$, $a = 0.1P$, $\eta = 1$, and $N = 8$	180
6-9.	Equivalent Circuit for Combined TT/TL Model	182

Illustrations

7-1.	Equivalent Circuit Model for Two Terminal MSW Transducer Model	205
7-2.	Width Weighting for a Pair of Identical MSSW Transducers in a Delay Line Configuration, Theoretical	206
7-3.	Comparison of Insertion Loss for Single Strip Transducers as Predicted by the Two Terminal, TT, and the Transmission Line, TL, Model	210
7-4.	Comparison of Insertion Loss for a Uniform Current Distribution Analysis with That of a Mutual Coupling Analysis. $H = 375$ Oe, $D = 30\ \mu\text{m}$, $L_1 = 2$ mm, $a = 150\ \mu\text{m}$, $N = 15$	214
7-5.	Normalized Inductance for Mutual Coupling Analysis Compared with a Uniform Current Analysis	
	a. Meander Line	215
	b. Grating	216
7-6.	Green's Function in the Far Field, at Three Frequencies	218
7-7.	Complex Current Distribution Across a Wide Strip	
	a. Magnitude of Current	219
	b. Phase of Current	220
7-8.	Complex Current Distribution Across a Narrow Strip	
	a. Magnitude of Current	221
	b. Phase of Current	222
7-9.	Volume Wave Insertion Loss, $N = 1$	
	a. FVW with and without Gap	226
	b. BVW Using TT and TL	227
7-10.	BVW Insertion Loss for 4-Element Grating	228
	a. Two Terminal Model	
	b. Transmission Line Model	
7-11.	FVW Width Mode	
	a. Radiation Resistance	231
	b. Insertion Loss	232
8-1.	Transducer Geometry	238
8-2.	Effective Integration Paths in the Quasimagnetostatic Limit, Neglecting Uniform Potential Contributions	247
8-3.	Magnitude of Current Density versus Normalized Position on Strip. $s/h = 10$; $d/h = 10$	263
8-4.	Phase of Current Density versus Normalized Position on Strip. $s/h = 10$; $d/h = 10$	264
8-5.	Magnitude of Current Density versus Normalized Position on Strip. $s/h = 10$; $d/h = 1.0$	265
8-6.	Phase of Current Density versus Normalized Position on Strip. $s/h = 10$; $d/h = 1.0$	266
8-7.	Magnitude of Current Density versus Normalized Position on Strip. $s/h = 10$; $d/h = 0.1$	267
8-8.	Phase of Current Density versus Normalized Position on Strip. $s/h = 10$; $d/h = 0.1$	268
8-9.	Magnitude of Current Density versus Normalized Position on Strip. $s/h = 10$; $d/h = 0.01$	269

Illustrations

8-10.	Phase of Current Density versus Normalized Position on Strip. MSSW Wavelength of 3.4 GHz Wave is 179 μm . $s/h = 10$; $d/h = 0.01$	270
8-11.	Magnitude of Current Density versus Normalized Position on Strip. $s/h = 1.0$; $d/h = 0.01$	271
8-12.	Phase of Current Density versus Normalized Position on Strip. $s/h = 1.0$; $d/h = 0.01$	272
8-13.	Magnitude of Current Density versus Normalized Position on Strip. $s/h = 1.0$; $d/h = 10^{-9}$	273
8-14.	Phase of Current Density versus Normalized Position on Strip. $s/h = 1.0$; $d/h = 10^{-9}$	274
8-15.	Magnitude of Current Density versus Normalized Position on Strip. $s/h = 0.1$; $d/h = 1.0$	275
8-16.	Phase of Current Density versus Normalized Position on Strip. $s/h = 0.1$; $d/h = 1.0$	276
8-17.	Magnitude of Current Density versus Normalized Position on Strip. $s/h = 0.1$; $d/h = 0.1$	277
8-18.	Phase of Current Density versus Normalized Position on Strip. $s/h = 0.1$; $d/h = 0.1$	278
8-19.	Magnitude of Current Density versus Normalized Position on Strip. $s/h = 0.1$; $d/h = 0.01$	279
8-20.	Phase of Current Density versus Normalized Position on Strip. $s/h = 0.1$; $d/h = 0.01$	280
8-21.	Magnitude of Current Density versus Normalized Position on Strip. $s/h = 0.01$; $d/h = 0.01$	281
8-22.	Phase of Current Density versus Normalized Position on Strip. $s/h = 0.01$; $d/h = 0.01$	282
8-23.	Magnitude of Current Density versus Normalized Position on Strip. $s/h = 0.001$; $d/h = 10^{-9}$	283
8-24.	Phase of Current Density versus Normalized Position on Strip. $s/h = 0.001$; $d/h = 10^{-9}$	284
8-25.	Insertion Loss versus Frequency. $s/h = 0.5$; $d/h = 1.0$	285
8-26.	Radiation Impedance versus Frequency. $s/h = 0.5$; $d/h = 1.0$	286
8-27.	Insertion Loss versus Frequency. $s/h = 1.0$; $d/h = 1.0$	287
8-28.	Radiation Impedance versus Frequency. $s/h = 1.0$; $d/h = 1.0$	288
8-29.	Insertion Loss versus Frequency. $s/h = 10.0$; $d/h = 0.01$	289
8-30.	Radiation Impedance versus Frequency. $s/h = 10.0$; $d/h = 0.01$	290
8-31.	Insertion Loss Comparison: Flat Current versus Calculated Current Distribution $H = 375.0$ $T1 = .1000E+01$ $G = .300E-06$ $D = .300E-04$ $L = .100E+01$ $L1 = .300E-02$ $A = .500E-04$ $P = .300E-03$ $DIST = .010$ $DH = 0.0$ $\eta = 1.$ $N = 1$ $RL = 0$	291
D-1.	Single Pole Filter with $H = 600$ Oe, with MSSW	309
D-2.	Two Pole Filter: Solid Line Represents Two Individual Resonant Spikes Before Current Injection. Dashed line shows the result of current injection through flat ribbon strips.	309

Tables

3-1.	Card 1 for TT and TL, SUR	57
3-2.	Input Data for SUR TT	59
3-3.	Input Data for SUR TL	60
3-4.	VOL for TT and TL	60
3-5.	Input Data for VOL TT	61
3-6.	Input Data for VOL TL	61
3-7.	SURTTC - Surface Wave, TT, Composite, Input Data Batch File	65
3-8.	SURMMC - Surface Wave, TT, Composite, Input Data Batch File	66
3-9.	VOLTTC - Volume Wave, TT, Composite, Input Data Batch File	67
3-10.	VOLMMC - Volume Wave, TL, Composite, Input Data Batch File	68
3-11.	Files on CC1159	69
3-12.	File Description for Tape CC1159	70
3-13.	File Description for Tape CC1159, Continued	71
3-14.	DSURN - Combined TT/TL Input Data Batch File	72
4-1.	Strip Widths for Figure 4-30	119
8-1.	Frequency versus $1/b$	242
8-2.	Comparison with Emtage's Results	260

MSW Transducers

1. INTRODUCTION

This report describes research on magnetostatic wave transducers performed at RADC over the past several years. Using the theory presented here, terminal characteristics of MSW delay lines, made up of a pair of transducers and a ferrite delay medium can be computed for cases of practical interest. Insertion loss, phase, time delay, and input impedance versus frequency may be computed. Input parameters are: magnetic biasing field, transducer geometry, YIG parameters and geometry, and ground plane spacing. The theory accurately predicts the behavior of wide band single element MSW transducers on YIG, and the behavior of multielement transducers weakly coupled to the YIG when individual transducer elements are narrow compared to interelement spacing and when maximum transducer dimensions are small compared to electromagnetic wavelengths. Under identical conditions a transducer apodization equation is developed.

Nine chapters and five appendices make up the report. A table of contents is useful in locating specific topics. Organization of the report is as follows: Gyromagnetic wave propagation basics, transducer geometries, and MSW delay line fabrication are discussed in Chapter 1. MSW analysis, starting with Maxwell's equations coupled with the Gyromagnetic equation, is developed in Chapter 2, to the point where transducer radiation resistance, reactance and delay line insertion loss are determined. Chapter 3 provides a description of MSW computer programs and procedures for using them. Examples of computer generated data, in the form of plots, are provided in Chapter 4. A description of MSW experiments and their results, performed at RADC/EEA, are given in Chapter 5. Chapter 6 discusses specialized topics that may be useful for further improvement of transducer

(Received for publication 13 December 1988)

models, and a new generalized model that adapts to any stripline waveguide. Chapter 7 provides a description and evaluation of all MSW related publications produced by EEA. Chapter 8 is a detailed analysis of the back reaction of nonreciprocal magnetostatic surface waves onto the current which generated them. Chapter 9 provides a short discussion.

Appendix A provides a reasonably complete list of publications related to the work of this report. Appendixes B and E provide analytical details related to current distribution and a combined TT/TL model, respectively. A list of symbols and notation is provided in Appendix C. Appendix D describes a prototype band pass filter fabricated at RADC/EEA that has not been previously published.

1.1 Propagating MSW Modes

Figure 1-1 shows the three basic pure propagating magnetostatic wave modes in a magnetic film of yttrium iron garnet, or in other low loss ferrites. At the present time virtually all MSW devices are characterized without regard to magnetocrystalline anisotropy because this effect is small. On the other hand, magnetic anisotropy due to the presence of a DC magnetic biasing field is large and cannot be neglected. This bias field induced anisotropy gives rise to the three distinct propagating modes. They are known as MSSW, MSBVW and MSFVW, for magnetostatic surface waves, backward volume waves, and forward volume waves, respectively.

With present devices, MSWs typically propagate on the order of fifty wavelengths before losing an appreciable amount of energy through scattering and beam spreading. These waves, or modes, are potentially useful for analog signal processing directly at microwave frequencies, and for tunable nanosecond delay lines.

A physical mechanism for propagating MSW modes is the energy transfer between neighboring magnetic dipoles. Minimum loss occurs when the magnetic medium is magnetically saturated; all magnetic domains are removed leaving one large domain with all dipoles having the same amplitude and orientation. When waves are present, the dipoles coherently waver with varying orientation.

Magnetostatic waves can be viewed as ordinary electromagnetic waves propagating in a ferrimagnetic medium with most of the energy carried by the magnetic field component of the EM wave. Ferromagnets, on the other hand, have large conducting losses, and consequently are not used for MSW. The waves are slow, about three orders of magnitude slower than light. Although the electric field can be neglected when calculating magnetic field, using the magnetostatic approximation $\text{curl } \mathbf{H} = 0$; the electric field cannot be neglected when calculating power flow because Poynting's vector, $\mathbf{E} \times \mathbf{H}$, may be large. The RF magnetic field may be calculated from Maxwell's equations along with the gyromagnetic equation which characterizes the magnetic medium. RF magnetic fields are found from the gradient of a scalar potential, ψ . Then, the associated RF electric field follows from the calculated magnetic field. These two calculated RF field components, \mathbf{E} and \mathbf{H} , define the Poynting vector. This is the essence of slow magnetically dominated electromagnetic waves. Unfortunately, they have not been given a useful descriptive name; and this leads to some confusion. They are not magnetostatic in the usual sense of the word; that is to say, non-propagating. Actually, magnetic energy propagates in well defined modes at a velocity midway between the velocity of acoustic waves in solids and electromagnetic waves in space.

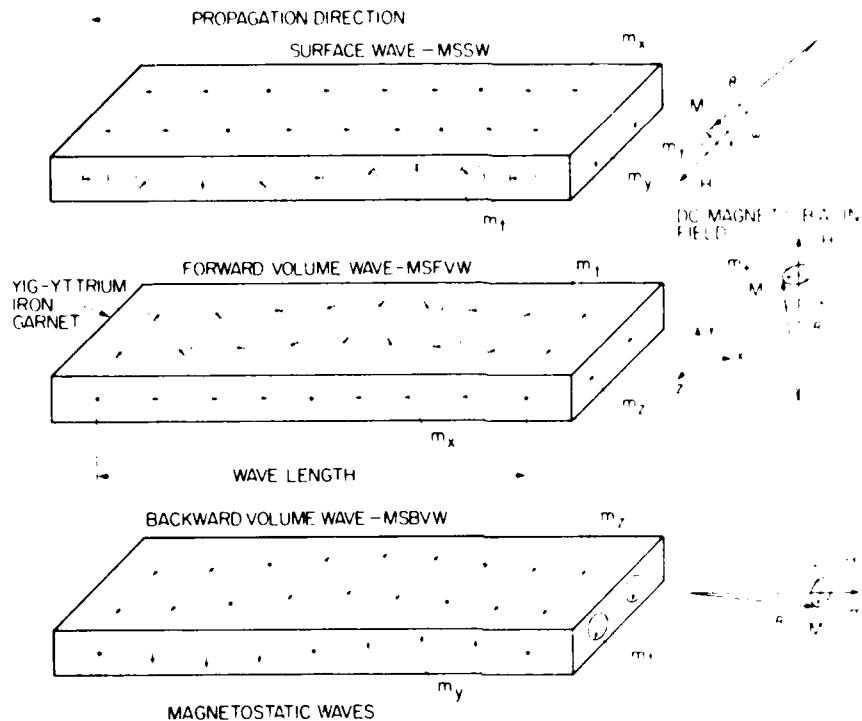


Figure 1-1. Three Pure MSW Propagating Modes

1.2 RF Magnetization

Figure 1-1 also provides a good understanding of wave motion in ferrites. Here are depicted the three pure propagating MSW modes. The basic feature distinguishing one mode from the other is the orientation of the magnetic biasing field, \mathbf{H} , and the direction of propagation relative to the film normal. In all three cases, as depicted, energy propagation is from right to left. The magnetic biasing field is spatially uniform and constant with time. The strength of this applied field is large enough to saturate the magnetic medium; that is, all magnetic domains are removed. For YIG, the saturation magnetization at room temperature is about 1760 gauss everywhere within the medium. In addition, the vector \mathbf{M} is exactly aligned with \mathbf{H} when the magnetic system is undisturbed. When an RF magnetic field is applied perpendicular to \mathbf{H} , a precession of \mathbf{M} takes place about \mathbf{H} at frequency ω and some small angle θ . The transverse component of magnetization, \mathbf{m}_t , rotates counter-clockwise when viewed in the direction opposite to the orientation of \mathbf{H} , as shown.

Consider, for example, the magnetostatic forward volume wave, MSFVW, shown in the center of Figure 1-1. Here \mathbf{H} is pointed in the positive y direction. When a wave is present, the magnitude of \mathbf{M} is unchanged but its orientation changes with wave motion. If we picture the group of circles depicted on the YIG's top surface as moving to the left in the direction of propagation, then it may be seen that \mathbf{m}_t which traces out these circles, rotates in a CCW direction when viewed along the negative y direction, at a fixed position in space. Components m_x and m_z are projections of \mathbf{m}_t onto the sides of the YIG bars; and a wavelength is the distance between two circles along the propagation direction having parallel \mathbf{m}_t , as indicated in the figure. The other two modes behave in a similar manner.

The three modes depicted here are the only pure MSW modes that can exist in a ferrite slab. They are pure in the sense that phase and group velocity vectors are colinear; either parallel or anti-parallel. They are parallel for MSFVW and MSSW and anti-parallel for MSBVW. All other modes have non-colinear phase and group velocity vectors. Actually, the three pure modes exist only in a medium whose magnetocrystalline anisotropy is negligible. Magnetocrystalline anisotropy is neglected in present day MSW devices. Moreover, low linewidth polycrystalline YIG, which has no anisotropy, has successfully been used to demonstrate MSW device operation.¹ It may be possible to propagate MSW over much longer distances than the present limit of about three centimeters, by taking advantage of crystalline orientations that focus MSW. This is not presently done because it is difficult to grow YIG films of high enough quality and large enough area in any plane other than the (111) plane. In this plane magnetocrystalline anisotropy is weak.

As a further example of magnetization dynamics, refer to Figure 1-2a. Depicted here for an MSSW is the movement of the RF magnetization component perpendicular to a DC magnetic field. The RF component, \mathbf{m}_t , is depicted by an arrow whose tip traces out an ellipse. The vector \mathbf{m}_t rotates counter-clockwise when the magnetic biasing field points out of the plane of the figure, as shown. The energy propagation direction is given by $\mathbf{H} \times \hat{\mathbf{n}}$ where $\hat{\mathbf{n}}$ is a unit vector pointing upwards. This elliptical motion resembles particle motion in a Rayleigh surface wave, SAW, hence the name "Rayleigh type magnetic surface wave" is sometimes used. There is however, a subtle difference between magnetic and acoustic surface wave dynamics, in addition to the obvious difference that one is a wave of magnetization and the other a wave of physical displacement. A SAW can be supported by a single solid/free space interface; an MSSW requires two interfaces such as in a thin film.

We can see why MSSWs require two surfaces to support them, by referring to Figure 1-2b and Eqs. (1) and (2). Figure 1-2b shows MSSW amplitude distribution throughout the thickness of the propagation medium; Eq. (1) gives the MSSW amplitude ratio between top and bottom surfaces; and Eq. (2) is the dispersion relation for MSSW on ferrite samples in free space. Note that as YIG thickness, d , approaches zero, the ratio of surface amplitudes approaches unity; and when the thickness approaches infinity, the amplitude ratio approaches zero. This means that energy density is highly concentrated on one surface. However, as the thickness approaches infinity, MSSW wavelength must also approach infinity in order to have a finite frequency [See Eq. (2)]. On the other hand, when thickness approaches zero, MSSW wavelength also approaches zero for a finite frequency. Thus, very thick films only support long wavelengths, and very thin films only support short wavelengths. In the limit, d approaches infinity, wavelengths that satisfy the dispersion relation, but are much larger than sample dimensions are not physically realizable. In the d approaches zero limit, wavelengths of less than one micron are extremely lossy; and, so films less than one micron thick may not be useful for MSW.

$$\text{Amplitude Ratio} = \frac{[\coth(kd/2) - \tanh(kd/2)](1 + K)}{[\coth(kd/2) + \tanh(kd/2)](1 + K) - 2\nu + 2} \quad (1-1)$$

-
1. Zhang, X. and Lin, H. (1982) The present status of microwave ferrite materials and devices in China, presented at the Third Joint Intermag/Magnetism and Magnetic Materials Conference, Montreal, Canada, Paper EC-01.

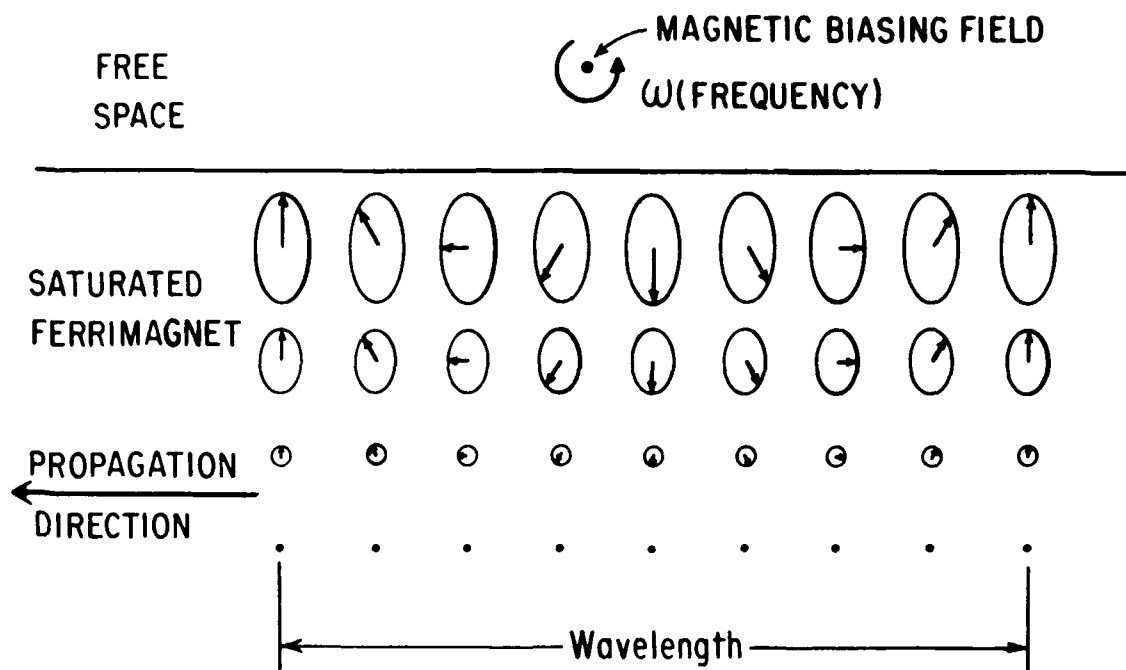


Figure 1-2a. Rayleigh Type Magnetic Surface Wave Representation

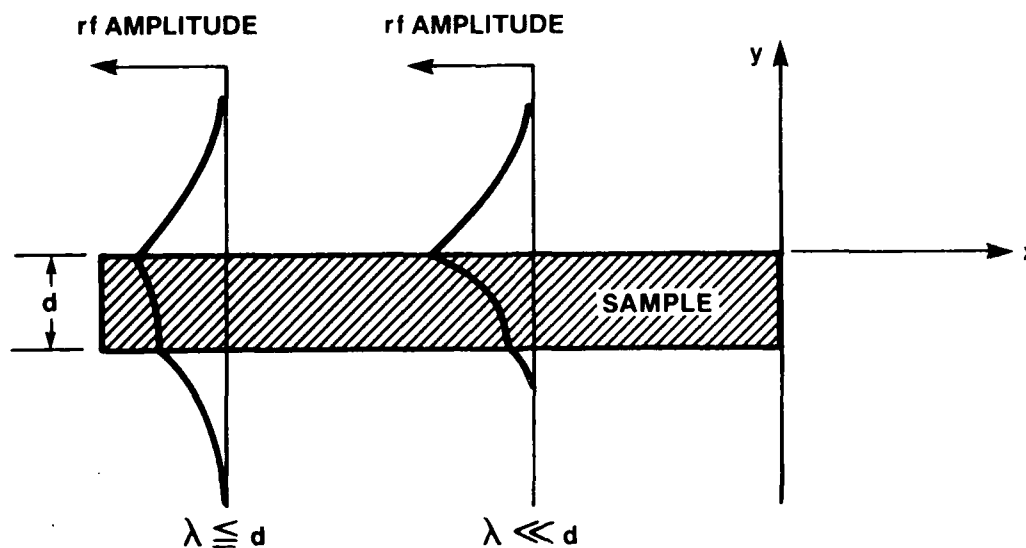


Figure 1-2b. MSSW Amplitude Distribution Throughout Thickness of YIG Film Sample for Small and Large Wavelengths

$$\text{where} \quad K = [H(4\pi M)]/[H^2 - (\omega/\gamma)^2]$$

$$\text{and} \quad v = [4\pi M(\omega/\gamma)]/[H^2 - (\omega/\gamma)^2]$$

$$(\omega/\gamma)^2 = H^2 + 4\pi MH + (2\pi M)^2[1 - \exp(-4\pi d/\lambda)] \quad (1-2)$$

Volume MSWs, on the other hand, resemble plate modes. They, too, require two surfaces; however, in contrast to magnetic surface waves, both surfaces support equal energy densities, and the energy density is not highly concentrated as are MSSW. This means that volume waves should be capable of handling larger power levels before non-linearities or saturation set in, and that, indeed, is borne out by experiment. The preceding statements rigorously apply only when there are no conducting ground planes near the surfaces. Ground planes can significantly modify spatial energy densities. Such effects are beyond the scope of the present discussion.

1.3 MSW Propagation Media

Virtually all MSW investigations are presently done on liquid phase epitaxy yttrium iron garnet, LPE/YIG, films. This is because large, high quality films are commercially available. Refer to Figure 1-3. The material is available from several sources in the United States, Europe, and Japan. Quality of the single crystal films is high. The linewidth at 9 Gz is often better than 0.5 oersteds, by far the lowest linewidth ferrimagnetic material known. Saturation magnetization of the films is the same as for bulk YIG, namely 1750 - 1780 Gauss, depending on purity, at room temperature. Lower saturation magnetization is available. Lower magnetization is obtained with gallium dopants that reduce saturation magnetization without appreciably increasing loss, that is, linewidth.

Crystallographic orientation of commercially available YIG is, generally, as shown in Figure 1-3. The (111) crystallographic plane is used because YIG grows very well in this plane. Its quality is equal to that of the best flux grown single crystal YIG. No significant differences have yet been reported for MSW propagation characteristics along the two crystallographic directions $[\bar{1}10]$ and $[\bar{1}\bar{1}2]$. However, small differences in the two directions can be observed under resonance conditions. Ferromagnetic resonance, FMR, experiments in the (111) plane have shown magneto-crystalline effects. The resonant frequency obtained for a given magnetic field is different along the two orientations. The effect was shown to be small. See Figure 5-26 and Section 5.6.6 for a quantitative estimate of the size of the effect.

Progress has been made in developing other materials for MSW including lithium ferrite, hexagonal ferrites, and low loss polycrystalline YIG¹, although the material loss and size still need improvement. Lithium ferrite is attractive because it has a high saturation magnetization. Hexagonal ferrites are attractive because they possess a large magneto-crystalline anisotropy which reduces biasing field requirements. In this way, with some hexagonal ferrites and for a relatively small applied field, less than a kilogauss, frequencies greater than 50 GHz are feasible. Polycrystalline YIG, as opposed to single crystal, is attractive because it can be more easily deposited on semiconductors, at the present time at least. However, it is doubtful that large amounts of delay will be possible with polycrystalline YIG.

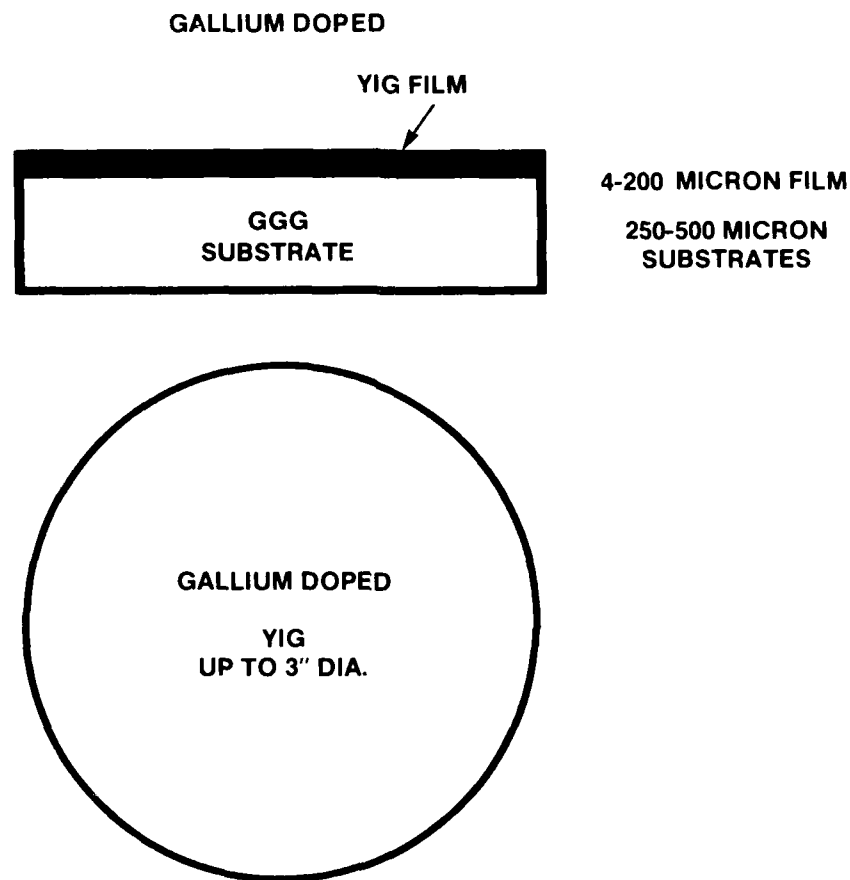


Figure 1-3a. Gallium and Lanthanum doped LPE/YIG Films are Useful from 500 MHz to 20 GHz. Above 20 GHz, biasing field requirements are excessive, greater than 2 Teslas. High quality Lithium Ferrite films, when available, will be useful above 20 GHz due to their larger saturation magnetization; and therefore, their lower biasing field requirement.

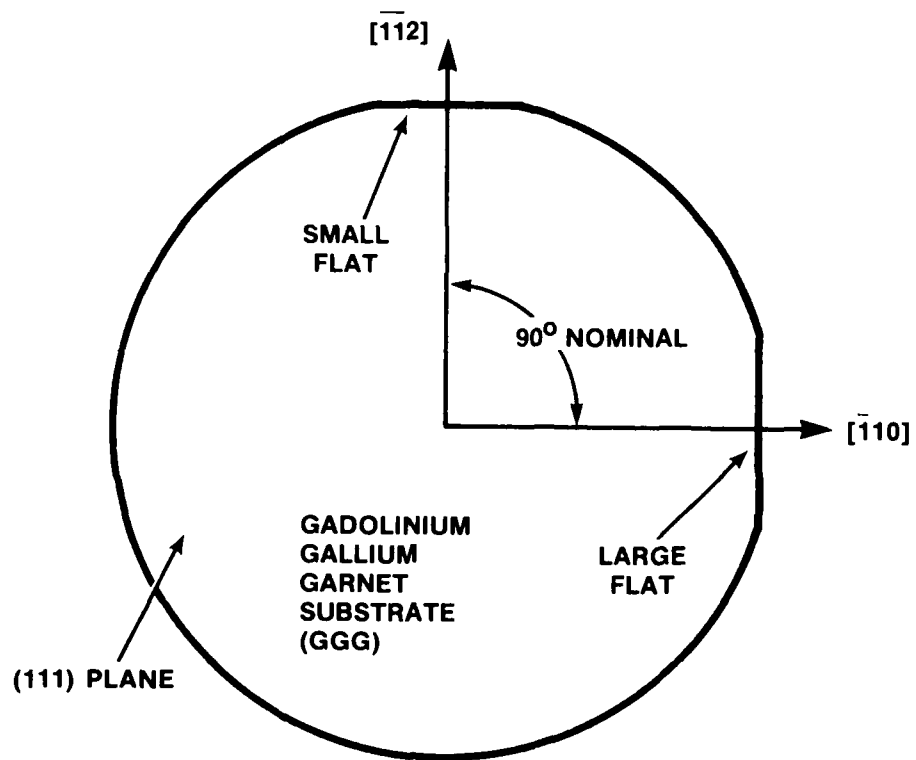


Figure 1-3b. Reference Flats for Commercial GGG Wafers from Allied Corporation

More recently, bismuth doped LPE/YIG films have been shown to have interesting magneto-optical properties. Thin magnetic LPE/YIG films constitute an area of interest for microwave, millimeter wave, and optical signal processing. High performance microwave MSW devices have already been demonstrated.

1.4 MSW Delay Lines

1.4.1 TWO TERMINAL (TT) MODEL

Many of the analytical and graphical results presented in this report are based on the configuration shown in Figure 1-4a. This configuration is defined as a TT, two terminal, model. A microwave signal generator is connected to terminals A and C of a transducer made up of one or more flat ribbon conductors. The conductors are connected in parallel as shown in the figure, or in series, or a combination of both. A basic assumption, in this model, is that any current entering terminal A leaves terminal C. There are no current variations along the transducer conductor length. Conductor length is in the z direction in Figure 1-4b. Current variations across the width, x direction, of the transducer, or across the width of any single conductor, however, are allowed. An MSW is launched at the input transducer and received by an identical transducer at the output, thus forming a delay line. Delay time at a given frequency is dependent on the value of a biasing field. Ground planes above and below the YIG are allowed. MSW power levels are limited to milliwatts; otherwise non-linearities set in. Typically, for MSSW and for 0 dbm input, -3 dbm to -50 dbm appears at the output, depending on frequency and other parameters.

1.4.2 TRANSMISSION LINE (TL) MODEL

Figure 1-5a depicts a transmission line model configuration. The TL model treats each transducer element; there are five per transducer in this figure, as a microstrip line. The lines are assumed to be non-interacting. Here, they are connected in parallel so the characteristic impedance of the entire transducer is one fifth the characteristic impedance of any one microstrip line. If the strips are connected in series, the transducer characteristic impedance would be five times as large as the characteristic impedance of any one microstrip line. The RADIC/MSW computer programs handle either the TT or TL models. The correct one to use in any given case is dictated by the way in which transducers are fed.

1.5 Transducer and Delay Line Geometry

Typical MSW delay line dimensions are 0.3 - 3.0 cm path length between a pair of transducers, 2 - 10 mm transducer aperture and YIG width, 5 - 10 μm thick transducer strips, 5 - 500 μm transducer strip widths, and 5 - 100 μm YIG thickness. At the present time the most useful frequency range is from 1 - 15 GHz. Magnetic bias fields are between 100 and 5000 Gauss, and practical MSW wavelengths are 10 - 1000 μm . Except where specifically stated, all of the analysis presented in this report is based on a two dimensional geometry. In particular, uniformity of all quantities is assumed in the direction parallel to the YIG surface and perpendicular to the propagation direction; that is, parallel to the strip

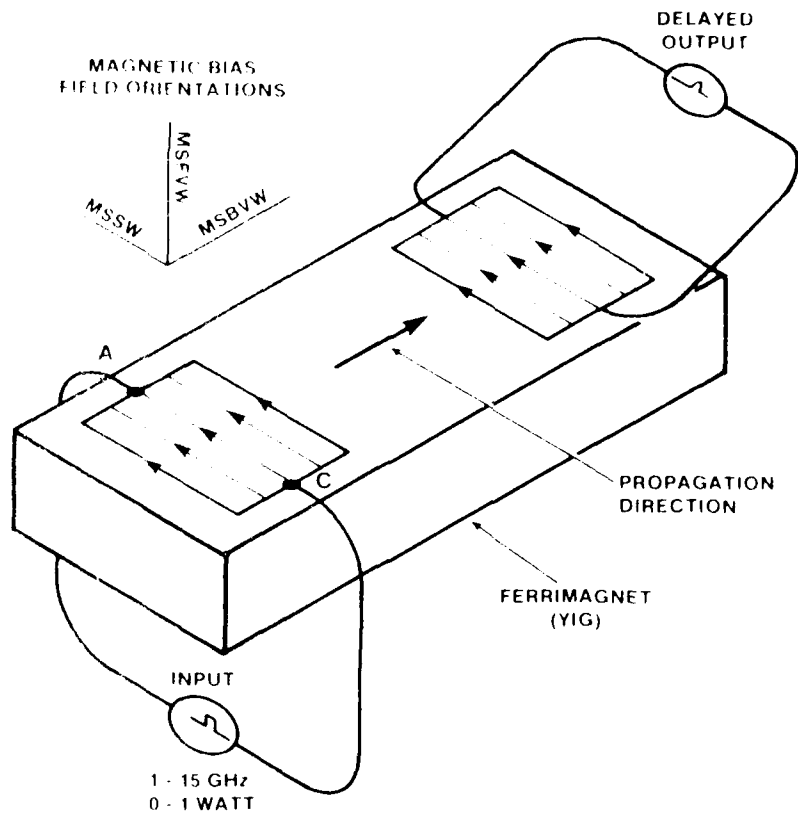


Figure 1-4a. Narrow Band MSW Delay Line. At 3 GHz center frequency, internal field is about 375 oersteds. MSSW are nonreciprocal, MSFVW and MSBVWs are reciprocal.

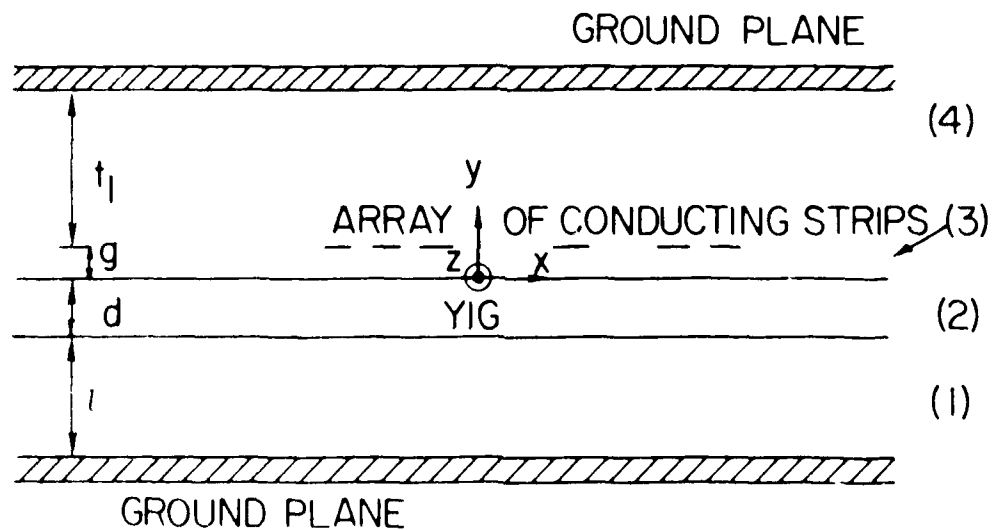


Figure 1-4b. Geometry for MSW Transducer Analysis

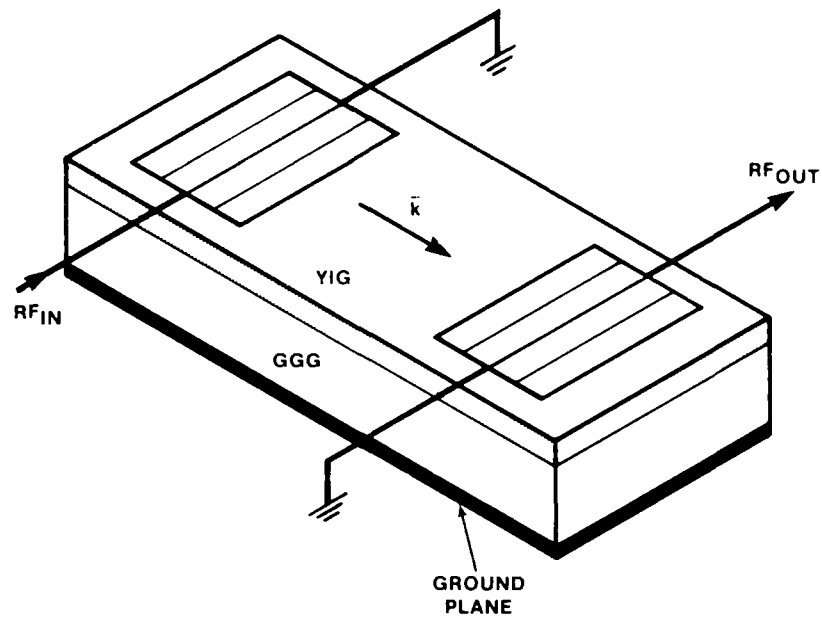


Figure 1-5a. Wire Over Configuration

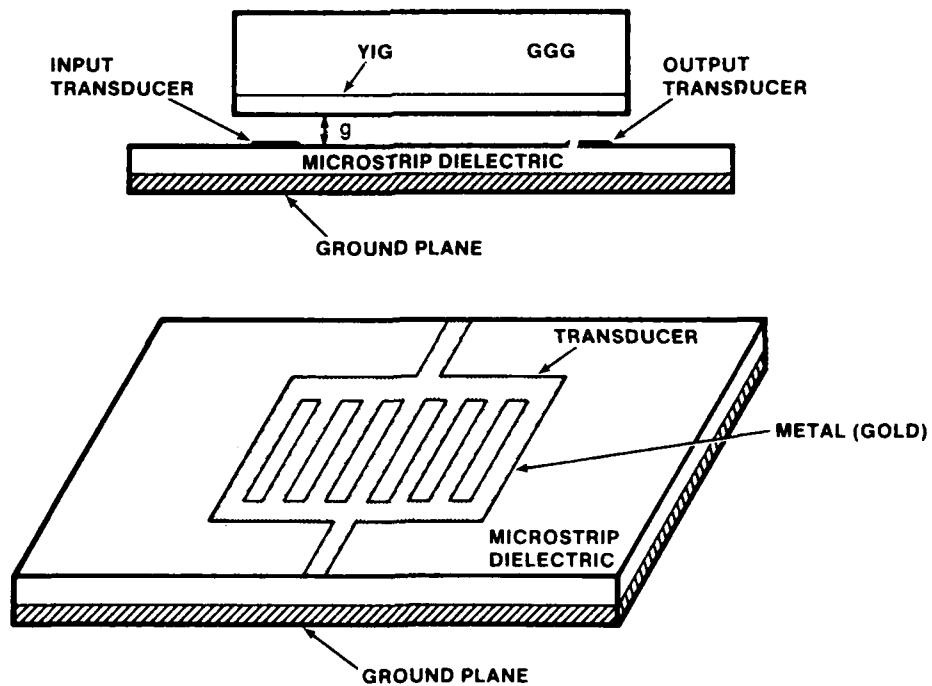


Figure 1-5b. Flipped Configuration

length. With respect to Figure 1-4b, this means that derivatives with respect to z are identically zero for all quantities. Gradual current variations in the z direction are allowed in the transmission line model, and in the combined model presented in Chapter 6.

1.6 Device Fabrication

Two basic configurations are used for the fabrication of MSW devices. In one configuration, metal transducers are deposited directly onto a ferrite. In the other configuration, metal transducers are fabricated on microstrip, and the ferrite film is flipped onto the microstrip circuit. The ferrite may contact the metal transducer. For best performance, dimensional tolerances are controlled to within an accuracy of $5\text{ }\mu\text{m}$ or better. Figure 1-5a shows the configuration in which transducers are deposited directly onto the ferrite. Here, a ground plane is shown deposited on the underside of the GGG. Figure 1-5b shows the flipped configuration. Transducers are fabricated on the microstrip, and YIG is flipped onto the transducers. The YIG film is between the GGG and transducer.

Dielectric constants of GGG and YIG are approximately equal, about 13. Because MSWs satisfy the magnetostatic approximation $\text{curl } \mathbf{H} = 0$ very well, dielectric discontinuities at material interfaces are not important in MSW; and, they can generally be ignored. This assertion is well borne out by experiment, and it can also be shown to follow from the basic equations of motion; that is, Maxwell's equations and the gyromagnetic equation characterizing the magnetic medium, and $\text{curl } \mathbf{H} = 0$.

1.6.1 FLIPPED (FC) AND WIRE OVER (WO) CONFIGURATION

Here we discuss RF energy distribution and time delay characteristics for two basic, FC and WO, configurations. When MSSW are generated on a YIG slab in free space, most of the energy concentrates on the side of the slab nearest the transducer. We define a plus (+) wave as the one most strongly coupled, and a minus (-) wave as the one most weakly coupled. That is, the plus wave is concentrated on the YIG surface closest to the transducer and the minus wave is concentrated on the surface furthest from the transducer. The minus wave is weakly coupled because transducer RF fields must reach through the YIG slab.

Energy concentration is then modified by a ground plane, if one is present. For configuration FC the transducer is between ground plane and YIG surface where MSW energy is concentrated (Figure 1-6). In this figure, plus waves hug the top surface of the YIG. The ground plane strongly perturbs MSW velocity of the plus wave. On the other hand, minus waves hug the bottom YIG surface so the ground plane does not strongly perturb MSW velocity because the wave is shielded from the ground plane by the presence of the YIG itself. This is reflected in the plots shown in Figure 1-6.

For configuration WO, the YIG slab is between transducer and ground plane, as shown in Figure 1-7. Energy in the plus wave is concentrated on the YIG surface furthest from the ground plane so plus waves are not strongly perturbed by this ground plane. The YIG slab shields plus waves from the ground plane. On the other hand, energy in the minus wave is concentrated on the YIG surface closest to the ground plane so that minus waves are strongly perturbed. These effects are evident in the plots of Figure 1-7.

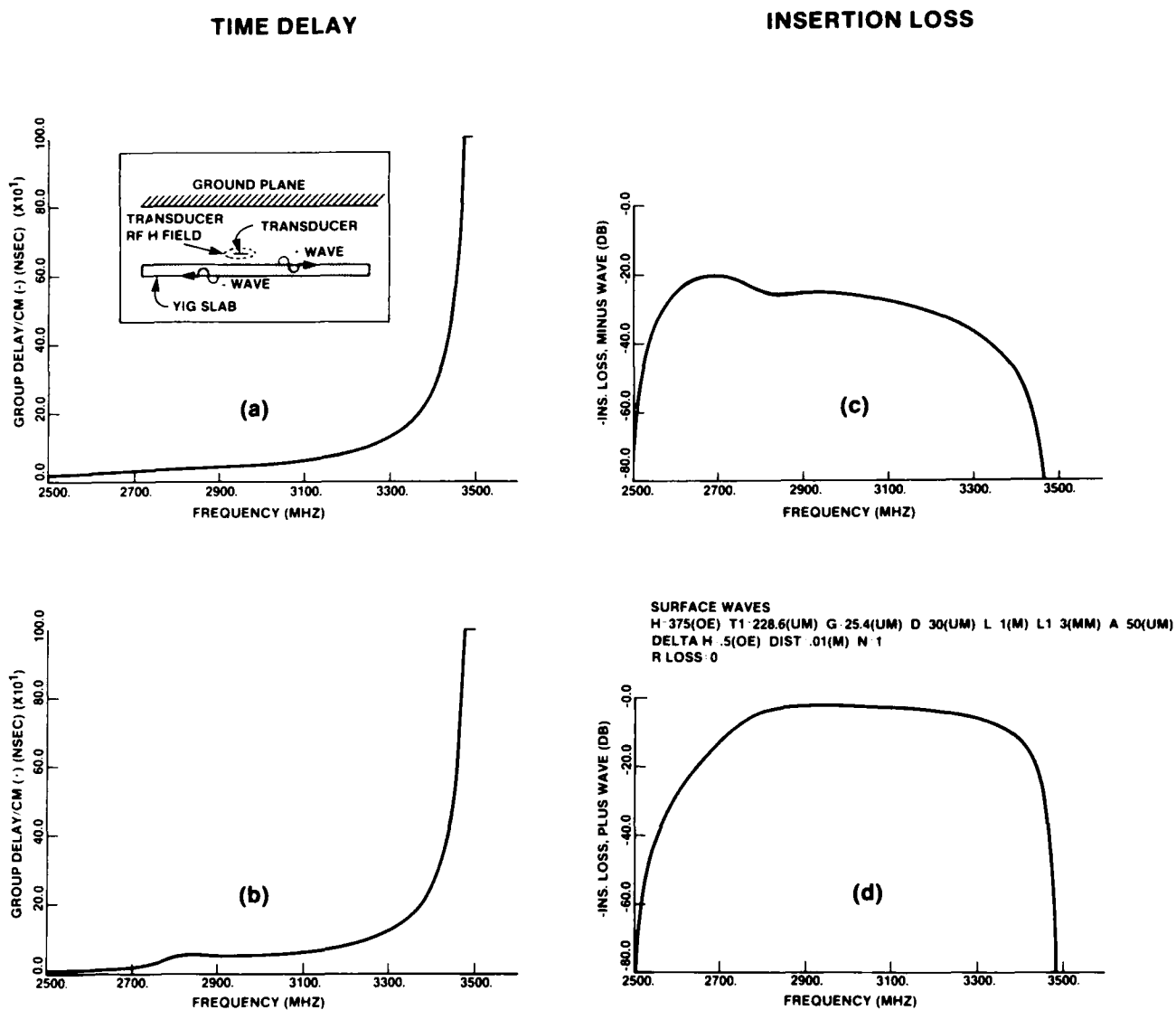


Figure 1-6. Delay Characteristics for Flipped Configuration

- | | |
|---------------------------|-------------------|
| (a) Minus Wave Delay Time | (c) Minus Wave IL |
| (b) Plus Wave Delay Time | (d) Plus Wave IL |

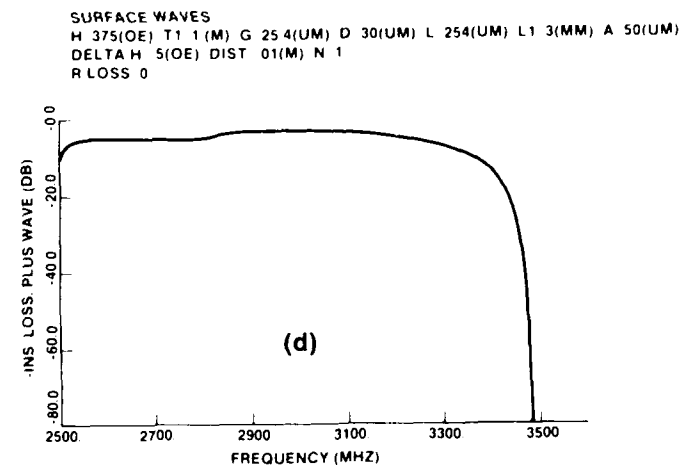
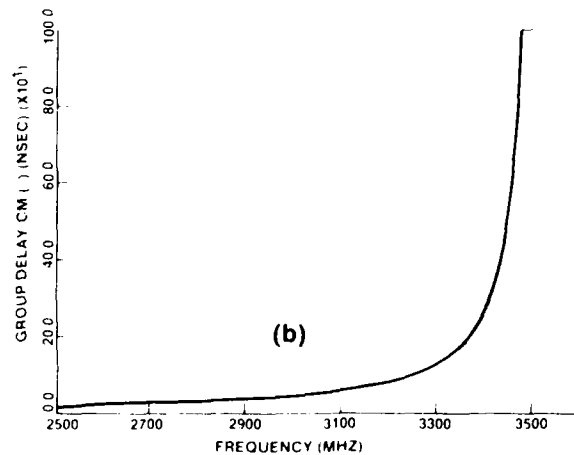
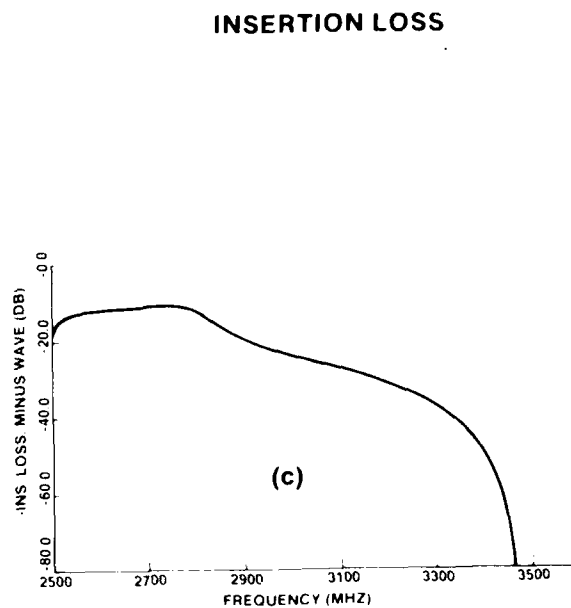
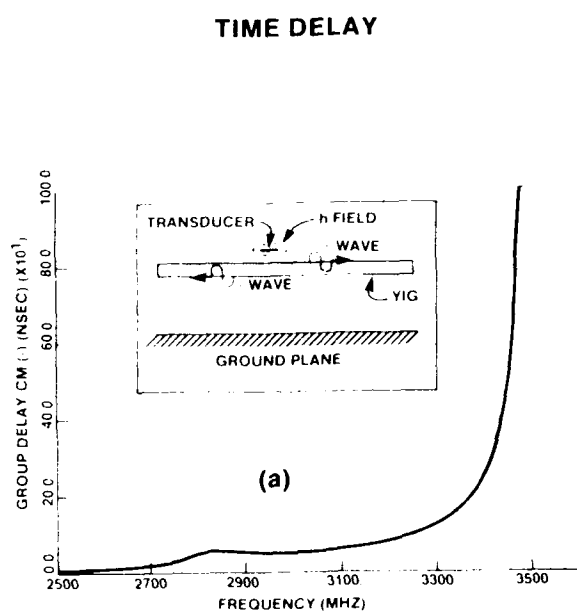


Figure 1-7. Delay Characteristics for Wire Over Configuration

(a) Minus Wave Delay Time

(c) Minus Wave IL

(b) Plus Wave Delay Time

(d) Plus Wave IL

1.6.2 PROTOTYPE DELAY LINES

Figure 1-8 shows parts of a 3 GHz narrow band, multi-element, MSSW delay line. An oversize aluminum block is used here for mechanical support of RF connectors, microstrip and magnet. In this figure, a 1- by 1-inch dielectric alumina microstrip substrate with ground plane is mounted on the aluminum block with silver epoxy. A metal ground plane is deposited on the underside of the alumina. SMA connectors are attached to 50 ohm feed lines. The feed lines terminate at the multielement grating transducer like the one shown in the lower part of Figure 1-5b. The other grating terminal is electrically connected to ground. A hole is drilled through the dielectric to ground, which is then filled with conductive epoxy. Coating metal surfaces with a thin gold layer of 5 μm may reduce losses in MSW devices by as much as 6 dB. Gold coating is highly recommended.

In the center portion of Figure 1-8, a YIG film is shown flipped onto microstrip circuitry. On the right is an alnico horseshoe magnet whose fringing fields are sufficient to saturate the YIG film. The film is biased for MSSW, that is parallel to the film's surface and perpendicular to the propagation direction. Magnetic field biasing using these inexpensive alnico magnets is useful for prototype device development.

Figure 1-9 shows further packaging details. In Figure 1-9a, a microstrip circuit and YIG film are housed in a standard commercial RF package. Again, fringing fields from a U-shaped alnico permanent magnet, placed outside of the package, provide sufficient fields for MSSW. Figure 1-9b shows a tuning coil wrapped around the completely enclosed package. With the coil shown in the figure, an electrical current of 1 ampere is sufficient to tune the delay line center frequency by 3 percent. Figure 1-9c shows a more compact unit in which biasing magnets are placed inside the package. Small alnico magnets are contained inside the package cover as shown on the left. The complete package without tuning coils, is shown on the right. Further order of magnitude size reductions should be possible with thin film rare earth permanent magnets.²

Figure 1-10 shows other, slot and coplanar, electromagnetic waveguiding structures that couple well to YIG delay lines. The dashed rectangles in the figure represent LPE/YIG films. As shown here, coplanar sections provide transduction between electromagnetic signals and magnetostatic waves, and make up a delay line. The two microstrip sections on the left can also form a delay line, if the YIG spans them, as can the slot line section on the right. MSW models are readily adaptable to handle slot and coplanar guides, as will be evident.

In Figure 1-10, the 0.254 mm (10 mils) alumina slabs are standard size commercially available substrates. Thicker substrates are generally less effective because of reduced coupling efficiency between RF magnetic fields, of the EM waveguide structure, and RF magnetization in the YIG. Thinner substrates, 5 mils, are recommended to improve coupling efficiency and to reduce RF leakage. In addition, replacing aluminum with gold results in a significant reduction in insertion loss, from 2 to 6 dB depending on frequency and geometry.

2. Cadieu, F.J. (1987) High coercive force and large remanent moment magnetic films with special anisotropies (INVITED), *J. of Appl. Phys.* **61**(8):4105-4110.

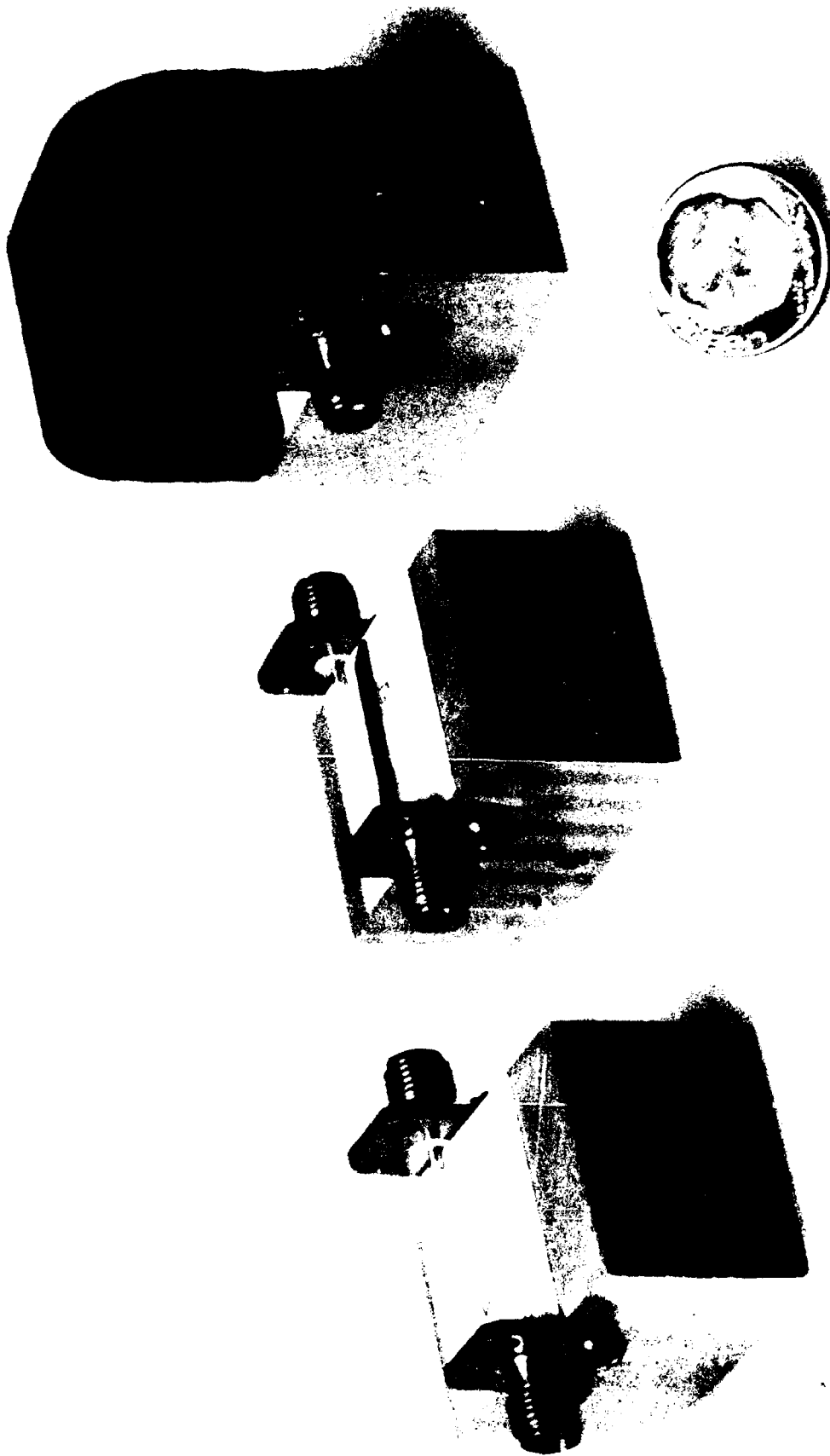


Figure 1-8. Early MSW Prototype Delay Lines Fabricated at University of Texas, Arlington
 (a) Microstrip Transducers (b) YIG Flipped onto Microstrip Circuit (c) Permanent Magnet Biasing Field Illustrations

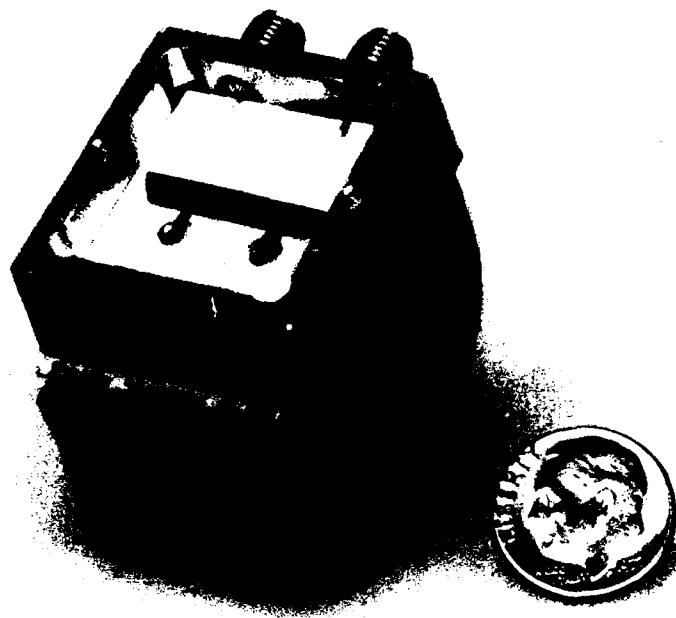


Figure 1-9a. Early MSW Delay Line in Tek Wave Microstrip Package

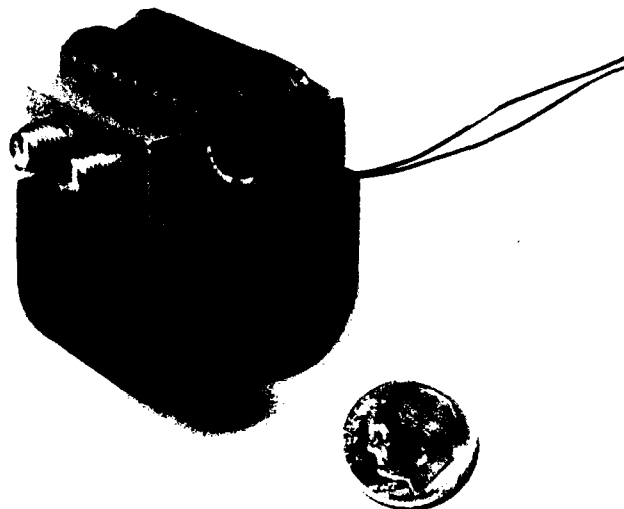


Figure 1-9b. Tuning Coil for MSW Delay Line



Figure 1-9c. Compact MSW Delay Line

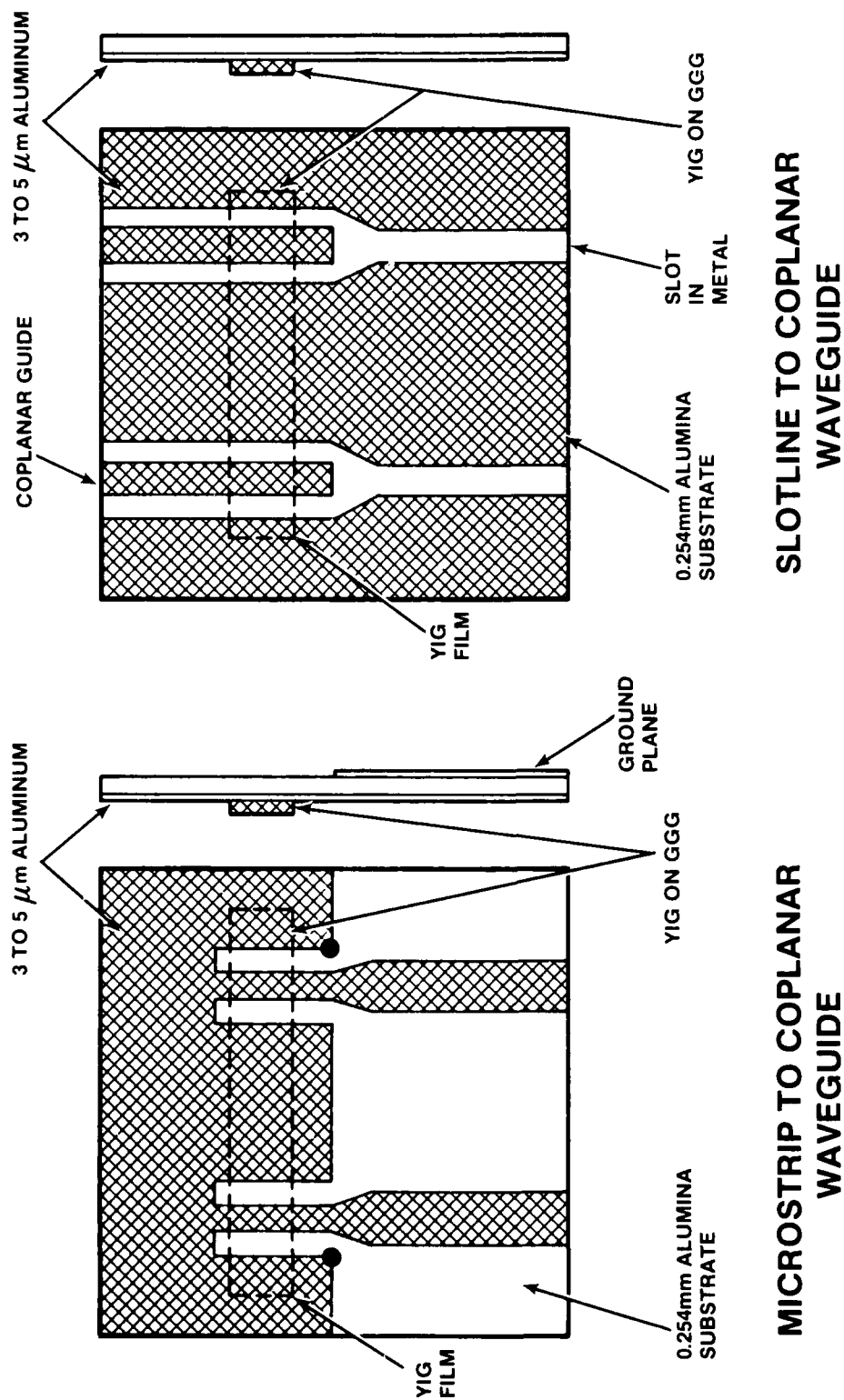


Figure 1-10. Slotline and Coplanar MSW Transducers

References

1. Zhang, X. and Lin, H. (1982) The present status of microwave ferrite materials and devices in China, presented at the Third Joint Intermag/Magnetism and Magnetic Materials Conference, Montreal, Canada, Paper EC-01.
2. Cadieu, F.J. (1987) High coercive force and large remnant moment magnetic films with special anisotropies (INVITED), *J. of Appl. Phys.* **61**(8):4105-4110.

2. MSW TRANSDUCER ANALYSIS

We consider here a magnetostatic wave transducer with a thin YIG film sandwiched between two dielectric layers which may be of finite thickness and a gap between the YIG layer and the transducer (see Figure 2-1). We are interested in obtaining the dispersion relation, wave power, radiation resistance, reactance, and insertion loss. We analyze surface waves, forward volume waves and backward volume waves for a periodic array of conducting strips in a parallel grating or meander line. We consider apodization in the strip dimensions and independent conductors as well as normal modes. The truncated array model and the transmission line model are described. The computer programs developed for the CDC computer, and the description of their use are given. In the analysis, a basic assumption is made of infinite width in the z direction for conducting strips.

The motivation for presenting the analysis in this chapter in terms of h_x and h_y components only, for the three pure MSW propagating modes, MSSW, MSFVW, and MSBVW, is predicated on the fact that $h_z = 0$ for all three modes. Further, for calculating power flow the only components needed are b_y and h_y . This does not mean that z components of \mathbf{m} and \mathbf{b} are necessarily zero; in general, they are not zero.

2.1 Polder Permeability Tensor

We first obtain the permeability tensor for a general configuration as in Figure 2-1, where θ is the angle made by \mathbf{H} with the y axis and ϕ is the angle made by the projection of \mathbf{H} on the (x,y) plane with the x axis. The surface wave direction ($\theta = 90^\circ$, $\phi = 90^\circ$), forward volume wave direction ($\theta = 0^\circ$) and backward volume wave direction ($\theta = 90^\circ$, $\phi = 0^\circ$), are indicated in the figure.

We write the total internal magnetic field vector \mathbf{H}_T and magnetization vector \mathbf{M}_T consisting of d.c. and a.c. components as

$$\mathbf{H}_T = \mathbf{H} + \mathbf{h} e^{i\omega t} \quad (2-1)$$

$$\mathbf{M}_T = \mathbf{M} + \mathbf{m} e^{i\omega t}$$

where the magnitude for \mathbf{M} is

$$|\mathbf{M}| = 1750 \text{ Oe} \quad (2-2)$$

We now utilize the gyromagnetic equation for the YIG region

$$\frac{\partial \mathbf{M}_T}{\partial t} = \gamma \mathbf{H}_T \times \mathbf{M}_T \quad (2-3)$$

where

$$\gamma = 2.8 \text{ MHz/Oe} \quad (2-4)$$

Employing Eq. (2-1) in Eq. (2-3) and assuming linearization, in which terms containing products of components of \mathbf{m} and \mathbf{h} are neglected, we obtain a matrix equation of the form

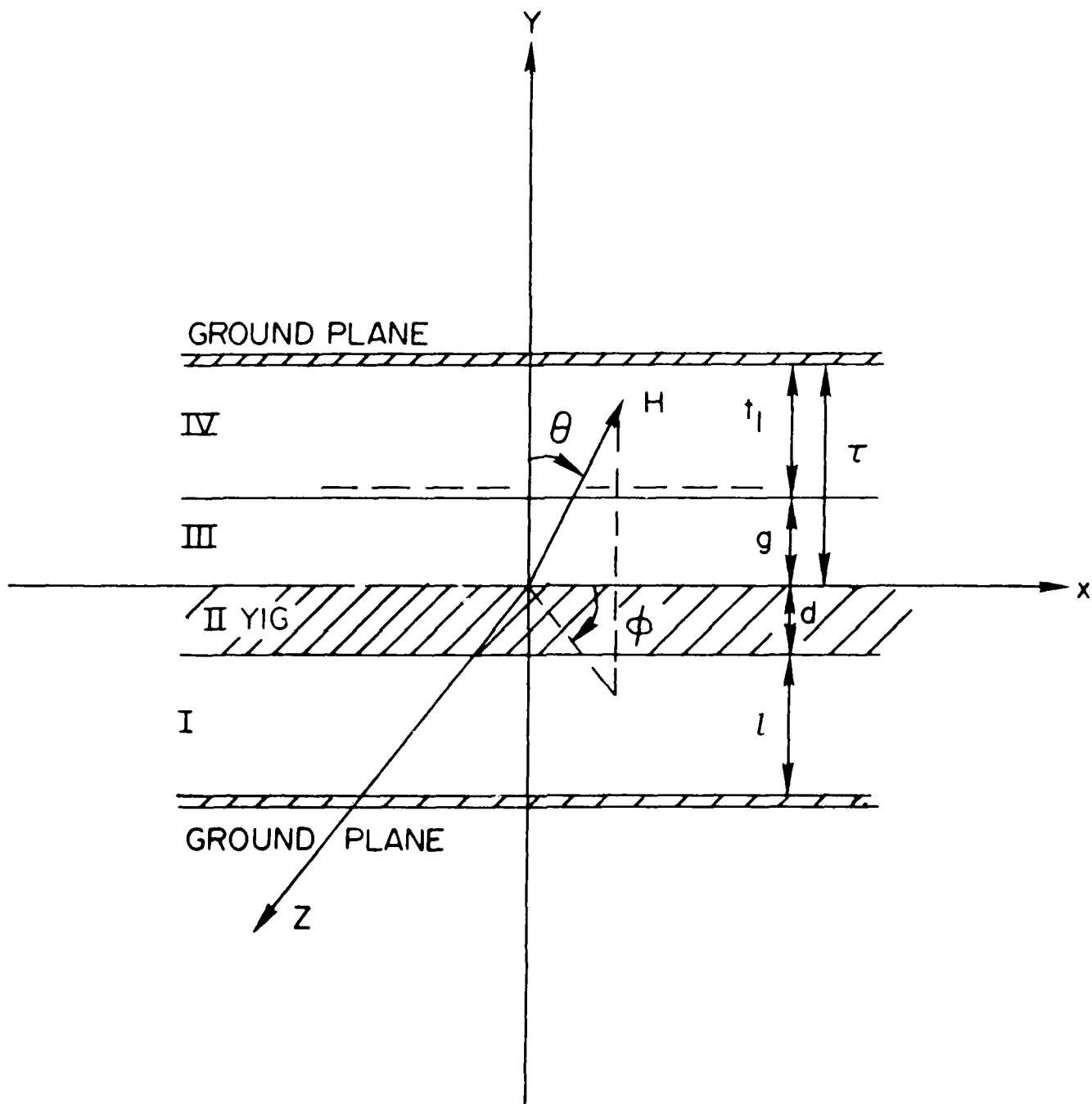


Figure 2-1. Geometry and Coordinate System Used Throughout Report Except for Chapter 8

$$\mathbf{m} = [\chi] \mathbf{h} \quad (2-5)$$

Applying the constitutive relations in the YIG region

$$\mathbf{b} = \mu_0 (\mathbf{h} + \mathbf{m}) \quad (2-6)$$

we obtain, after introducing Eq. (2-5) into Eq. (2-6)

$$\mathbf{b} = \mu_0 [\mu] \mathbf{h} \quad (2-7)$$

or,

$$\begin{pmatrix} b_x \\ b_y \\ b_z \end{pmatrix} = \mu_0 \begin{pmatrix} \mu_{xx} & \mu_{xy} & \mu_{xz} \\ \mu_{yx} & \mu_{yy} & \mu_{yz} \\ \mu_{zx} & \mu_{zy} & \mu_{zz} \end{pmatrix} \begin{pmatrix} h_x \\ h_y \\ h_z \end{pmatrix} \quad (2-8)$$

where, with $f = \omega/2\pi$ and H equal to the magnitude of \mathbf{H} , we obtain

$$\begin{aligned} \mu_{xx} &= 1 + \frac{\gamma^2 H M}{\gamma^2 H^2 - f^2} (\sin^2 \theta \sin^2 \phi + \cos^2 \theta) \\ \mu_{xy} &= \frac{i \gamma M}{\gamma^2 H^2 - f^2} \sin \theta (f \sin \phi + i \gamma H \cos \phi \cos \theta) \\ \mu_{xz} &= \frac{-i \gamma M}{\gamma^2 H^2 - f^2} (f \cos \theta - i \gamma H \sin^2 \theta \sin \phi \cos \phi) \\ \mu_{yx} &= \frac{-i \gamma M}{\gamma^2 H^2 - f^2} \sin \theta (f \sin \phi - i \gamma H \cos \phi \cos \theta) \\ \mu_{yy} &= 1 + \frac{\gamma^2 H M}{\gamma^2 H^2 - f^2} \sin^2 \theta \\ \mu_{yz} &= \frac{i \gamma M}{\gamma^2 H^2 - f^2} \sin \theta (f \cos \phi + i \gamma H \sin \phi \cos \theta) \\ \mu_{zx} &= \frac{i \gamma M}{\gamma^2 H^2 - f^2} (f \cos \phi + i \gamma H \cos \phi \sin \phi \sin^2 \theta) \\ \mu_{zy} &= \frac{-i \gamma M}{\gamma^2 H^2 - f^2} \sin \theta (f \cos \phi - i \gamma H \cos \theta \sin \phi) \\ \mu_{zz} &= 1 + \frac{\gamma^2 H M}{\gamma^2 H^2 - f^2} (\cos^2 \theta + \sin^2 \theta \cos^2 \phi) \end{aligned} \quad (2-9)$$

In the non YIG regions the constitutive relations are simply

$$\begin{pmatrix} b_x \\ b_y \\ b_z \end{pmatrix} = \mu_0 \begin{pmatrix} h_x \\ h_y \\ h_z \end{pmatrix} \quad (2-10)$$

2.2 Basic Equations

In addition to satisfying the gyromagnetic equation we seek to satisfy Maxwell's equations in each region along with appropriate boundary and continuity conditions. Maxwell's equations are written as

$$\nabla \times \mathbf{h} = \frac{\partial \mathbf{D}}{\partial t} \quad , \quad \nabla \cdot \mathbf{b} = 0 \quad (2-11)$$

$$\nabla \times \mathbf{E} = -\frac{\partial \mathbf{B}}{\partial t} \quad , \quad \nabla \cdot \mathbf{D} = 0$$

along with

$$\mathbf{D} = \epsilon_0 [\epsilon] \mathbf{E} \quad (2-12)$$

The following important assumptions are made in the analysis. TE modes are considered in which all variations in the z-direction are neglected and waves propagate only in the x-direction. All time dependence is $e^{i\omega t}$ as in Eq. (2-1). We also have the magnetostatic approximation in which

$$h_z = 0 \quad (2-13)$$

and

$$\omega \epsilon_1 E_x = \omega \epsilon_2 E_y = \omega \epsilon_3 E_z \approx 0 \quad (2-14)$$

Maxwell's equations thus become

$$\begin{aligned} \nabla \times \mathbf{h} = 0 \quad \text{or} \quad \frac{\partial h_x}{\partial y} - \frac{\partial h_y}{\partial x} = 0 \\ \frac{\partial b_x}{\partial x} + \frac{\partial b_y}{\partial y} = 0 \end{aligned} \quad (2-15)$$

and

$$\frac{\partial E_z}{\partial y} = -i\omega b_x \quad (2-16)$$

$$\frac{\partial E_z}{\partial x} = i\omega b_y$$

The remaining equations are also to be satisfied. For surface waves we have additionally $E_x = E_y = 0$.

Since $\nabla \times \mathbf{h} = 0$ we seek a function $\psi(x, y, z, t)$ such that

$$\mathbf{h} = \nabla \psi \quad (2-17)$$

Ignoring the time dependence, the function ψ will satisfy Eqs. (2-10) and (2-15) in the non YIG regions if it is of the form, (omitting time dependence),

$$\psi_j = \int_{-\infty}^{\infty} (A_j e^{iK|y|} + B_j e^{-iK|y|}) e^{-iKx} dK \quad j = 1, 3, 4 \quad (2-18)$$

where j refers to the region number. The boundary and continuity conditions to be satisfied by the solution are, $b_y = 0$ at the ground planes, $y = -(l+d)$ and $y = (t_1 + g)$, h_x and h_y are continuous at the region junctions $y = -d$ and $y = 0$, b_y is continuous at the region junction $y = g$ and

$$h_{x4} - h_{x3} = J(x) \quad (2-19)$$

at the junction $y = g$. The electric current density function $J(x)$ will be discussed later. Note that although the solution Eq. (2-18) is taken as an integral over all K , we will omit the integration temporarily in the analysis, at times. The continuation of the analysis differs for the three cases so we will continue the discussion for each case separately for a while.

2.3 Surface Waves

2.3.1 SW DISPERSION RELATION

For surface waves, ($\theta = \phi = 90^\circ$), the constitutive relations (2-6) through (2-9) in the YIG region become, for b_x and b_y

$$\begin{pmatrix} b_x \\ b_y \end{pmatrix} = \mu_0 \begin{pmatrix} \mu_{11} & -i\mu_{12} \\ i\mu_{12} & \mu_{11} \end{pmatrix} \begin{pmatrix} h_x \\ h_y \end{pmatrix} \quad (2-20)$$

where

$$\mu_{11} = 1 + \frac{\gamma^2 H M}{\gamma^2 H^2 - f^2} \quad , \quad \mu_{12} = -\frac{f \gamma M}{\gamma^2 H^2 - f^2} \quad (2-21)$$

The solution in the YIG region satisfying Eqs. (2-15) and (2-20) is then of the form

$$\psi_2 = \int_{-\infty}^{\infty} (A_2 e^{iK|y|} + B_2 e^{-iK|y|}) e^{-iKx} dK \quad , \quad (2-22)$$

similar to the solutions Eq. (2-18) in the non YIG regions.

Writing

$$\alpha_1 = \mu_{11} + s\mu_{12} \quad , \quad \alpha_2 = \mu_{11} - s\mu_{12} \quad , \quad s = K/|K| \quad (s = -1, 1) \quad (2-23)$$

we have from Eqs. (2-20) and (2-22)

$$b_{y_1} = \mu_0 |K| (\alpha_1 A_2 e^{iKly} - \alpha_2 B_2 e^{-iKly}) e^{-iKx} \quad (2-24)$$

(omitting integration in K) while in the other regions

$$b_{y_j} = \mu_0 |K| (A_j e^{iKly} - B_j e^{-iKly}) e^{-iKx}, \quad j = 1, 3, 4. \quad (2-25)$$

We attempt to find the eight constants $A_j, B_j, j = 1, 2, 3, 4$ in Eqs. (2-18) and (2-22) by solving the eight boundary and continuity conditions described above.

We write

$$T = \frac{\alpha_2 + \tanh |K|l}{\alpha_1 + \tanh |K|l}$$

$$U = (1 - \alpha_2) e^{-iKld} + (1 + \alpha_1) T e^{iKld} \quad (2-26)$$

$$V = (1 + \alpha_2) e^{-iKld} + (1 - \alpha_1) T e^{iKld}$$

The boundary condition, Eq. (2-19), which is

$$-i \int_{-\infty}^{\infty} K e^{-iKx} [A_4 e^{iKlg} + B_4 e^{-iKlg} - A_3 e^{iKlg} - B_3 e^{-iKlg}] dK = J(x) \quad (2-27)$$

becomes, after employing all the other conditions and integrating¹ in x , then multiplying by e^{iKx} and integrating in K ,

$$B_2 = \frac{i\tilde{J}(K)}{2\pi K F(K)} \quad (2-28)$$

where

$$\tilde{J}(K) = \int_{-\infty}^{\infty} J(x) e^{iKx} dx \quad (2-29)$$

is the Fourier transform of $J(x)$ and²

$$F(K) = \frac{e^{iKld}}{2} [V e^{-iKlg} (\coth |K|l_1 - 1) - U e^{iKlg} (\coth |K|l_1 + 1)]. \quad (2-30)$$

The dispersion relation is defined if we set

$$F(K) = 0 \quad (2-31)$$

-
1. Weinberg, I.J. (1980) Dispersion Relations for Magnetostatic Waves, *Ultrasonics Symposium Proceedings*.
 2. Weinberg, I.J. and Sethares, J.C. (1978) *Magnetostatic Wave Transducers with Variable Coupling*, RADC-TR-78-205, ADA063880.

and solve Eq. (2-30) for K as a function of f.

The other constants are then found to be, using Eq. (2-28),

$$\begin{aligned}
 B_1 &= \frac{(1 + T) B_2}{1 + e^{2|K|l}} \quad , \quad A_1 = \frac{e^{2|K|d} (1 + T)}{1 + e^{-2|K|l}} B_2 \\
 A_3 &= \frac{U e^{|K|d} B_2}{2} \\
 B_3 &= \frac{V e^{|K|d} B_2}{2} \\
 A_4 &= \frac{(V e^{-2|K|g} - U) e^{|K|d} B_2}{2(e^{2|K|l} - 1)} \\
 B_4 &= \frac{(V - e^{2|K|g} U) e^{|K|d} B_2}{2(1 - e^{-2|K|l})} \\
 A_2 &= B_2 T e^{2|K|d}
 \end{aligned} \tag{2-32}$$

2.3.2 SW FIELD EQUATIONS

The time-suppressed field equations are, using Eqs. (2-17), (2-24), (2-25), (2-28) and (2-32)

$$\begin{aligned}
 h_{x_1} &= \frac{1}{2\pi} \int_{-\infty}^{\infty} \frac{e^{|K|d}}{F(K)} (T + 1) \tilde{J}(K) \frac{\cosh[|K|(l + d + y)]}{\cosh |K|l} e^{-iKx} dk \\
 b_{y_1} &= \frac{i\mu_0}{2\pi} \int_{-\infty}^{\infty} \frac{se^{|K|d}}{F(K)} (T + 1) \tilde{J}(K) \frac{\sinh[|K|(l + d + y)]}{\cosh |K|l} e^{-iKx} dk \\
 h_{x_2} &= \frac{1}{2\pi} \int_{-\infty}^{\infty} \frac{e^{|K|d}}{F(K)} \tilde{J}(K) [T e^{|K|(d+y)} + e^{-|K|(d+y)}] e^{-iKx} dK \\
 b_{y_2} &= \frac{i\mu_0}{2\pi} \int_{-\infty}^{\infty} \frac{se^{|K|d}}{F(K)} \tilde{J}(K) [\alpha_1 T e^{|K|(d+y)} - \alpha_2 e^{-|K|(d+y)}] e^{-iKx} dK \\
 h_{x_3} &= \frac{1}{2\pi} \int_{-\infty}^{\infty} \frac{e^{|K|d}}{2F(K)} \tilde{J}(K) [U e^{|K|y} + V e^{-|K|y}] e^{-iKx} dK
 \end{aligned} \tag{2-33}$$

$$b_{y_3} = \frac{i\mu_0}{2\pi} \int_{-\infty}^{\infty} \frac{se^{iK|d|}}{2F(K)} \tilde{J}(K) [Ue^{iK|y|} - Ve^{-iK|y|}] e^{-iKx} dK$$

$$h_{x_4} = \frac{1}{2\pi} \int_{-\infty}^{\infty} \frac{e^{iK|d|}}{2F(K)} \tilde{J}(K) [Ue^{iK|g|} - Ve^{-iK|g|}] \frac{\cosh[|K|(g + t_1 - y)]}{\sinh |K| t_1} e^{-iKx} dK$$

$$b_{y_4} = \frac{i\mu_0}{2\pi} \int_{-\infty}^{\infty} \frac{se^{iK|d|}}{2F(K)} \tilde{J}(K) [Ue^{iK|g|} - Ve^{-iK|g|}] \frac{\sinh[|K|(g + t_1 - y)]}{\sinh |K| t_1} e^{-iKx} dK$$

We write

$$F_T(K) = e^{-2|K|d} F(K) \quad \text{or} \quad F(K) = e^{2|K|d} F_T(K) \quad (2-34)$$

which by Eqs. (2-26) and (2-30) can be written as

$$\begin{aligned} 2F_T(K) = & (\coth |K| t_1 - 1) [(1 + \alpha_2) e^{-2|K|d} + (1 - \alpha_1)T] e^{-iK|g|} \\ & - (\coth |K| t_1 + 1) [(1 - \alpha_2) e^{-2|K|d} + (1 + \alpha_1)T] e^{iK|g|} \end{aligned} \quad (2-35)$$

The integrals in Eqs. (2-33) are computed by contour integration as in Ganguly and Webb.³ The integrals on the outer contour are assumed to vanish because of the behavior of $\tilde{J}(K)$. We still need to compute the residue at the simple poles, which are the zeros of $F(K)$ or $F_T(K)$ in Eqs. (2-34). Denote K_s for $s = -1, 1$ as the roots of

$$F_T(K_s) = 0 \quad s = -1, 1 \quad (2-36)$$

Each integral is the residue at each pole which is $2\pi i$ times the integrand with

$$F'_T(K_s) = \left| \frac{\partial}{\partial K} F_T(K) \right|_{K=K_s} \quad (2-37)$$

replacing $F_T(K)$. Defining

$$G(K) = \frac{\tilde{J}(K) e^{-iK|d|}}{F'_T(K)}, \quad (2-38)$$

with K_s the solution of $F_T(K, s) = 0$, and

$$\begin{aligned} G_s = G(K_s), \quad T_s = T(K_s), \quad U_s = U(K_s), \quad V_s = V(K_s) \\ \alpha_1^{(s)} = \alpha_1(s), \quad \alpha_2^{(s)} = \alpha_2(s) \end{aligned} \quad s = -1, 1 \quad (2-38a)$$

3. Ganguly, A.K. and Webb, D. (1975) Microstrip Excitation of MSSW, *IEEE Trans MTT*, **MTT-23**:998.

we obtain the integrals of Eqs. (2-33) as

$$\begin{aligned}
 h_{x_1}^{(s)} &= i G_s (T_s + 1) \frac{\cosh[|K_s|(l + d + y)]}{\cosh |K_s| l} e^{-i K_s x} \\
 b_{y_1}^{(s)} &= -\mu_0 s G_s (T_s + 1) \frac{\sinh[|K_s|(l + d + y)]}{\cosh |K_s| l} e^{-i K_s x} \\
 h_{x_2}^{(s)} &= i G_s [T_s e^{|K_s|(d + y)} + e^{-|K_s|(d + y)}] e^{-i K_s x} \quad s = -1, 1 \\
 b_{y_2}^{(s)} &= -\mu_0 s G_s [\alpha_1^{(s)} T_s e^{|K_s|(d + y)} - \alpha_2^{(s)} e^{-|K_s|(d + y)}] e^{-i K_s x} \quad (2-39) \\
 h_{x_3}^{(s)} &= \frac{i G_s}{2} [U_s e^{|K_s| y} + V_s e^{-|K_s| y}] e^{-i K_s x} \\
 b_{y_3}^{(s)} &= \frac{-\mu_0 s G_s}{2} [U_s e^{|K_s| y} - V_s e^{-|K_s| y}] e^{-i K_s x} \\
 h_{x_4}^{(s)} &= \frac{i G_s}{2} [U_s e^{|K_s| g} - V_s e^{-|K_s| g}] \frac{\cosh[|K_s|(g + t_1 - y)]}{\sinh |K_s| t_1} e^{-i K_s x} \\
 b_{y_4}^{(s)} &= \frac{-\mu_0 s G_s}{2} [U_s e^{|K_s| g} - V_s e^{-|K_s| g}] \frac{\sinh[|K_s|(g + t_1 - y)]}{\sinh |K_s| t_1} e^{-i K_s x} .
 \end{aligned}$$

Eq. (2-31) is the dispersion relation. We find the K_s as a function of frequency f for the two values of s by solving for the roots of Eq. (2-31). For each of the two K_s values we find the field equations using Eq. (2-39).

To find G_s we need $F_T'(K)$ Defining

$$\begin{aligned}
 C_1 &= U e^{|K| g} - V e^{-|K| g} \\
 C_2 &= (\coth |K| t_1 + 1) U e^{|K| g} + (\coth |K| t_1 - 1) V e^{-|K| g} \\
 C_3 &= (\coth |K| t_1 + 1)(1 - \alpha_2) e^{|K| g} - (\coth |K| t_1 - 1)(1 + \alpha_2) e^{-|K| g} \\
 C_4 &= (\coth |K| t_1 - 1)(1 - \alpha_1) e^{-|K| g} - (\coth |K| t_1 + 1)(1 + \alpha_1) e^{|K| g}
 \end{aligned} \quad (2-39a)$$

then

$$\begin{aligned}
 2F_T'(K) &= C_1 e^{-|K| d} \operatorname{st}_1 \operatorname{csch}^2 |K| t_1 - C_2 s g e^{-|K| d} \\
 &\quad + C_3 2s d e^{-2|K| d} + C_4 \frac{s l (\alpha_1 + \alpha_2) \operatorname{sech}^2 |K| l}{(\alpha_1 - \tanh |K| l)^2}
 \end{aligned} \quad (2-40)$$

This completes the determination of the field equations (2-39). Note that for surface waves there exist two solutions for the dispersion relation (2-36): one for $s = -1$ and the other for $s = 1$. Thus there are two sets of field equations (2-39).

2.3.3 SW POWER

The magnetostatic wave power for each of the two solutions is taken as²

$$P(s) = -\frac{l_1}{2} \int_{-(l+d)}^{l_1+g} E_z^{(s)} \overline{h_y^{(s)}} dy \quad s = -1, 1 \quad (2-41)$$

By integration of Eq. (2-16) we have

$$E_z = -\frac{\omega}{K} b_y = -\frac{s\omega}{|K|} b_y. \quad (2-42)$$

Thus

$$P(s) = \frac{s\omega l_1}{2|K_s|} \left[\int_{-(l+d)}^{-d} b_{y_1}^{(s)} \overline{h_{y_1}^{(s)}} dy + \int_{-d}^0 b_{y_2}^{(s)} \overline{h_{y_2}^{(s)}} dy + \int_0^g b_{y_3}^{(s)} \overline{h_{y_3}^{(s)}} dy + \int_g^{g+l_1} b_{y_4}^{(s)} \overline{h_{y_4}^{(s)}} dy \right] \quad s = -1, 1 \quad (2-43)$$

For region 1, utilizing Eqs. (2-10) and (2-39)

$$\int_{-(l+d)}^{-d} b_{y_1}^{(s)} \overline{h_{y_1}^{(s)}} dy = \frac{\mu_0 G_s^2 (T_s + 1)^2}{\cosh^2 |K_s| l} \int_{-(l+d)}^{-d} \sinh^2 [|K_s| (l + d + y)] dy. \quad (2-44)$$

In the above and in what follows $|\tilde{J}(K)|$ is used in computing G_s^2 from Eq. (2-38).

Using

$$\sinh^2 u = \frac{1}{2} (\cosh 2u - 1) \quad (2-45)$$

we have

$$\int_{-(l+d)}^{-d} b_{y_1}^{(s)} \overline{h_{y_1}^{(s)}} dy = \frac{\mu_0 G_s^2 (T_s + 1)^2}{2 \cosh^2 |K_s| l} \left(\frac{\sinh 2|K_s| l}{2|K_s|} - l \right). \quad (2-46)$$

For region 4, we have, similarly,

$$\int_g^{g+t_1} b_{y_4}^{(s)} \overline{h_{y_4}^{(s)}} dy = \frac{\mu_0 G_s^2 (U_s e^{K_s |g|} - V_s e^{-K_s |g|})^2}{8 \sinh^2 K_s |t_1|} \left(\frac{\sinh 2 K_s |t_1|}{2 K_s |t_1|} - t_1 \right). \quad (2-47)$$

For region 3,

$$\int_0^g b_{y_3}^{(s)} \overline{h_{y_3}^{(s)}} dy = \frac{\mu_0 G_s^2}{4} \int_0^g (U_s e^{K_s |y|} - V_s e^{-K_s |y|})^2 dy. \quad (2-48)$$

Thus

$$\int_0^g b_{y_3}^{(s)} \overline{h_{y_3}^{(s)}} dy = \frac{\mu_0 G_s^2}{4 |K_s|} \left[\frac{U_s^2}{2} (e^{2|K_s|g} - 1) - \frac{V_s^2}{2} (e^{-2|K_s|g} - 1) - 2 U_s V_s |K_s| g \right] \quad (2-49)$$

For region 2, we first have, from Eq. (2-20)

$$h_{y_2} = \frac{1}{\mu_{11}} \left(\frac{b_{y_2}}{\mu_0} - i \mu_{12} h_{x_2} \right) \quad (2-50)$$

then

$$\int_{-d}^0 b_{y_2}^{(s)} \overline{h_{y_2}^{(s)}} dy = \frac{1}{\mu_{11}} \left[\frac{1}{\mu_0} \int_{-d}^0 b_{y_2}^{(s)} \overline{h_{y_2}^{(s)}} dy - i \mu_{12} \int_{-d}^0 b_{y_2}^{(s)} \overline{h_{x_2}^{(s)}} dy \right] \quad (2-51)$$

or, using Eq. (2-39) and defining

$$C_5 = \int_{-d}^0 \left[\alpha_1^{(s)2} T_s^2 e^{2|K_s|(d+y)} + \alpha_2^{(s)2} e^{-2|K_s|(d+y)} - 2 \alpha_1^{(s)} \alpha_2^{(s)} T_s \right] dy \quad (2-51a)$$

$$C_6 = \int_{-d}^0 \left[\alpha_1^{(s)} T_s^2 e^{2|K_s|(d+y)} - \alpha_2^{(s)} e^{-2|K_s|(d+y)} + (\alpha_1^{(s)} - \alpha_2^{(s)}) T_s \right] dy$$

we get

$$\int_{-d}^0 b_{y_2}^{(s)} \overline{h_{y_2}^{(s)}} dy = \frac{1}{\mu_{11}} \left[\mu_0 G_s^2 C_5 - \mu_0 s \mu_{12} G_s^2 C_6 \right]. \quad (2-52)$$

Thus, with

$$C_7 = \alpha_1^{(s)} T_s^2 (e^{2|K_s|d} - 1) + \alpha_2^{(s)} (e^{-2|K_s|d} - 1) + 2|K_s|d T_s (\alpha_1^{(s)} - \alpha_2^{(s)}) \quad (2-52a)$$

we get

$$\int_{-d}^0 b_{y_2}^{(s)} \overline{h_{y_2}^{(s)}} dy = \frac{\mu_0 G_s^2}{\mu_{11} 2 |K_s|} \left[\alpha_1^{(s)2} T_s^2 (e^{2|K_s|d} - 1) - \alpha_2^{(s)2} (e^{-2|K_s|d} - 1) - 4\alpha_1^{(s)} \alpha_2^{(s)} T_s |K_s| d - s\mu_{12} C_7 \right]. \quad (2-53)$$

Utilizing the definitions of Eqs. (2-23) we obtain

$$\int_{-d}^0 b_{y_2}^{(s)} \overline{h_{y_2}^{(s)}} dy = \frac{\mu_0 G_s^2}{2 |K_s|} \left[\alpha_1^{(s)} T_s^2 (e^{2|K_s|d} - 1) - \alpha_2^{(s)} (e^{-2|K_s|d} - 1) - 4 |K_s| d T_s \mu_{11} \right] \quad (2-54)$$

thus, with

$$P_1 = \frac{(T_s + 1)^2}{\cosh^2 |K_s| l} \left(\frac{\sinh 2 |K_s| l}{2} - |K_s| l \right)$$

$$P_2 = \alpha_1^{(s)} T_s^2 (e^{2|K_s|d} - 1) - \alpha_2^{(s)} (e^{-2|K_s|d} - 1) - 4 |K_s| d T_s \mu_{11} \quad (2-54a)$$

$$P_3 = \frac{U_s^2}{4} (e^{2|K_s|g} - 1) - \frac{V_s^2}{4} (e^{-2|K_s|g} - 1) - U_s V_s |K_s| g$$

$$P_4 = \frac{(U_s e^{|K_s|g} - V_s e^{-|K_s|g})^2}{4 \sinh^2 |K_s| t_1} \left(\frac{\sinh 2 |K_s| t_1}{2} - |K_s| t_1 \right)$$

we get

$$\frac{P^{(s)}}{l_1} = \frac{s\mu_0 \omega G_s^2}{4 |K_s|^2} (P_1 + P_2 + P_3 + P_4) \quad s = -1, 1 \quad (2-55)$$

which gives the surface wave power for the two s values.

It is seen that the frequency bandwidth for the existence of surface waves is

$$\gamma \sqrt{H(H+M)} < f < \gamma \left(H + \frac{M}{2} \right) \quad (2-56)$$

2.4 Forward Volume Waves

2.4.1 FW DISPERSION RELATION

For forward volume waves, $\theta = 0$, the constitutive relations (2-8) and (2-9) in the YIG region become, for b_x and b_y

$$\begin{pmatrix} b_x \\ b_y \end{pmatrix} = \mu_0 \begin{pmatrix} \mu_{11} & 0 \\ 0 & 1 \end{pmatrix} \begin{pmatrix} h_x \\ h_y \end{pmatrix} \quad (2-57)$$

where μ_{11} has been defined in Eq. (2-21). Here μ_{11} is always negative, unlike surface waves where μ_{11} is always positive. We define^{4,5}

$$\alpha^2 = -\mu_{xx}/\mu_{yy} = -\mu_{11} \quad (2-58)$$

and see that the solution in the YIG satisfying Eqs. (2-15) and (2-57) is of the form

$$\psi_2 = \int_{-\infty}^{\infty} (A_2 \cos \alpha |K| y + B_2 \sin \alpha |K| y) e^{-i K x} dK \quad (2-59)$$

Here, we have for all regions (omitting integration in K)

$$b_{y_j} = \mu_0 |K| (A_j e^{i K y} - B_j e^{-i K y}) e^{-i K x} \quad j = 1, 3, 4 \quad (2-60)$$

$$b_{y_2} = \mu_0 \alpha |K| (-A_2 \sin \alpha |K| y + B_2 \cos \alpha |K| y) e^{-i K x}$$

The eight constants A_i, B_i ($i = 1, 2, 3, 4$) in Eqs. (2-18) and (2-59) are found by solving the eight boundary and continuity conditions.

Proceeding as for surface waves and defining

$$D_1 = (\coth |K| t_1 + 1) - e^{-2|K|l} e^{-2|K|g} (\coth |K| t_1 - 1)$$

$$D_2 = \frac{(\alpha^2 - 1)}{2} (\coth |K| t_1 + 1) + e^{-2|K|g} \frac{(\alpha^2 + 1)}{2} (\coth |K| t_1 - 1) \quad (2-60a)$$

$$D_3 = \frac{(\alpha^2 + 1)}{2} (\coth |K| t_1 + 1) + e^{-2|K|g} \frac{(\alpha^2 - 1)}{2} (\coth |K| t_1 - 1)$$

and

-
4. Weinberg, I.J. (1982) Insertion Loss for Magnetostatic Volume Waves, *IEEE Transactions on Magnetics*.
 5. Weinberg, I.J. and Sethares, J.C. (1983) Magnetostatic Volume Waves, *IEEE MTT-S Digest*.

$$F(K) = F_T(K) = e^{-|K|d} e^{|K|g} \frac{\sin \alpha |K|d}{\alpha} (-D_1 \alpha \cot \alpha |K|d + D_2 + D_3 e^{-2|K|l}) \quad (2-61)$$

with

$$D_4 = \frac{(\alpha^2 + 1)}{2\alpha} \sin \alpha |K|d + e^{-|K|g} \left[\frac{(\alpha^2 - 1)}{2\alpha} \sin \alpha |K|d + \cos \alpha |K|d \right] \quad (2-61a)$$

$$D_5 = \frac{(\alpha^2 - 1)}{2\alpha} \sin \alpha |K|d + \cos \alpha |K|d + e^{2|K|g} \frac{(\alpha^2 + 1)}{2\alpha} \sin \alpha |K|d$$

we obtain the constants as

$$A_1 = \frac{i\tilde{J}(K)}{2\pi KF(K)}$$

$$B_1 = \frac{i\tilde{J}(K)}{2\pi KF(K)} e^{-2|K|(d+l)}$$

$$A_2 = \frac{i\tilde{J}(K)}{2\pi KF(K)} e^{-|K|d} \left[\cos \alpha |K|d + \frac{1}{\alpha} \sin \alpha |K|d + e^{-2|K|l} \left(\cos \alpha |K|d - \frac{1}{\alpha} \sin \alpha |K|d \right) \right]$$

$$B_2 = \frac{i\tilde{J}(K)}{2\pi KF(K)} e^{-|K|d} \left[\frac{1}{\alpha} \cos \alpha |K|d - \sin \alpha |K|d - e^{-2|K|l} \left(\frac{1}{\alpha} \cos \alpha |K|d + \sin \alpha |K|d \right) \right]$$

$$A_3 = \frac{i\tilde{J}(K)}{2\pi KF(K)} e^{-|K|d} \left[\cos \alpha |K|d + \frac{(1 - \alpha^2)}{2\alpha} \sin \alpha |K|d - e^{-2|K|l} \frac{(1 + \alpha^2)}{2\alpha} \sin \alpha |K|d \right] \quad (2-62)$$

$$B_3 = \frac{i\tilde{J}(K)}{2\pi KF(K)} e^{-|K|d} \left\{ \frac{(1 + \alpha^2)}{2\alpha} \sin \alpha |K|d + e^{-2|K|l} \left[\cos \alpha |K|d + \frac{(\alpha^2 - 1)}{2\alpha} \sin \alpha |K|d \right] \right\}$$

$$A_4 = \frac{i\tilde{J}(K)}{2\pi KF(K)} \frac{e^{-|K|l_1}}{2 \sinh |K|l_1} e^{-|K|d} \left[-\cos \alpha |K|d + \frac{(\alpha^2 - 1)}{2\alpha} \sin \alpha |K|d \right. \\ \left. + e^{-2|K|g} \frac{(\alpha^2 + 1)}{2\alpha} \sin \alpha |K|d + e^{-2|K|l} D_4 \right]$$

$$B_4 = \frac{i\tilde{J}(K)}{2\pi KF(K)} \frac{e^{|K|l_1}}{2 \sinh |K|l_1} e^{-|K|d} \left\{ \frac{(\alpha^2 + 1)}{2\alpha} \sin \alpha |K|d \right. \\ \left. - e^{2|K|g} \left[\cos \alpha |K|d + \frac{(1 - \alpha^2)}{2\alpha} \sin \alpha |K|d \right] + e^{-2|K|l} D_5 \right\}$$

where $\tilde{J}(K)$ has been defined in Eq. (2-29).

The dispersion relation is defined as before by setting $F_T(K) = 0$ and solving for K as a function of f . Note that $s = \frac{|K|}{k}$ does not enter into Eq. (2-61) or (2-62) so that the two solutions for $|K|$ are identical for forward volume waves.

2.4.2 FVW FIELD EQUATIONS

Defining

$$\begin{aligned}
 D_6 &= \cos \alpha |K| d + \frac{\sin \alpha |K| d}{\alpha} + e^{-2|K|l} \left(\cos \alpha |K| d - \frac{\sin \alpha |K| d}{\alpha} \right) \\
 D_7 &= \frac{\cos \alpha |K| d}{\alpha} - \sin \alpha |K| d - e^{-2|K|l} \left(\frac{\cos \alpha |K| d}{\alpha} + \sin \alpha |K| d \right) \\
 D_8 &= \cos \alpha |K| d - \alpha \sin \alpha |K| d - e^{-2|K|l} (\cos \alpha |K| d + \alpha \sin \alpha |K| d) \\
 D_9 &= \alpha \cos \alpha |K| d + \sin \alpha |K| d + e^{-2|K|l} (\alpha \cos \alpha |K| d - \sin \alpha |K| d) \\
 D_{10} &= \cos \alpha |K| d + \frac{(1 - \alpha^2)}{2\alpha} \sin \alpha |K| d - e^{-2|K|l} \frac{(1 + \alpha^2)}{2\alpha} \sin \alpha |K| d \\
 D_{11} &= \frac{(1 + \alpha^2)}{2\alpha} \sin \alpha |K| d + e^{-2|K|l} \left(\cos \alpha |K| d + \frac{\alpha^2 - 1}{2\alpha} \sin \alpha |K| d \right) \\
 D_{12} &= -\cos \alpha |K| d + \frac{(\alpha^2 - 1)}{2\alpha} \sin \alpha |K| d + e^{-2|K|l} \frac{(\alpha^2 + 1)}{2\alpha} \sin \alpha |K| d \\
 D_{13} &= \frac{(\alpha^2 + 1)}{2\alpha} \sin \alpha |K| d + e^{-2|K|l} \left(\frac{\alpha^2 - 1}{2\alpha} \sin \alpha |K| d + \cos \alpha |K| d \right) \\
 D_{14} &= \frac{(\alpha^2 + 1)}{2\alpha} \sin \alpha |K| d - e^{-2|K|l} \left(\cos \alpha |K| d + \frac{1 - \alpha^2}{2\alpha} \sin \alpha |K| d \right) \\
 D_{15} &= \frac{(\alpha^2 - 1)}{2\alpha} \sin \alpha |K| d + \cos \alpha |K| d + e^{-2|K|l} \frac{\alpha^2 + 1}{2\alpha} \sin \alpha |K| d
 \end{aligned} \tag{2-62a}$$

the time suppressed field equations are, using Eqs. (2-17), (2-60) and (2-62)

$$\begin{aligned}
 h_{x1} &= \frac{1}{2\pi} \int_{-\infty}^{\infty} \frac{\tilde{J}(K)}{F_T(K)} e^{-|K|d} e^{-|K|l} (e^{|K|l(l+d)} e^{|K|y} + e^{-|K|l(l+d)} e^{-|K|y}) e^{-iKx} dK \\
 b_{y1} &= \frac{i\mu_0}{2\pi} \int_{-\infty}^{\infty} \frac{\tilde{J}(K)S}{F_T(K)} e^{-|K|d} e^{-|K|l} (e^{|K|l(l+d)} e^{|K|y} - e^{-|K|l(l+d)} e^{-|K|y}) e^{-iKx} dK
 \end{aligned} \tag{2-63}$$

$$h_{x2} = \frac{1}{2\pi} \int_{-\infty}^{\infty} \frac{\tilde{J}(K)}{F_T(K)} e^{-|K|d} (D_6 \cos \alpha |K|y + D_7 \sin \alpha |K|y) e^{-iKx} dK$$

$$b_{y2} = \frac{i\mu_0}{2\pi} \int_{-\infty}^{\infty} \frac{\tilde{J}(K)S}{F_T(K)} e^{-|K|d} (D_8 \cos \alpha |K|y - D_9 \sin \alpha |K|y) e^{-iKx} dK$$

$$h_{x3} = \frac{1}{2\pi} \int_{-\infty}^{\infty} \frac{\tilde{J}(K)}{F_T(K)} e^{-|K|d} (D_{10} e^{|K|y} + D_{11} e^{-|K|y}) e^{-iKx} dK$$

$$b_{y3} = \frac{i\mu_0}{2\pi} \int_{-\infty}^{\infty} \frac{\tilde{J}(K)S}{F_T(K)} e^{-|K|d} (D_{10} e^{|K|y} - D_{11} e^{-|K|y}) e^{-iKx} dK$$

$$h_{x4} = \frac{1}{2\pi} \int_{-\infty}^{\infty} \frac{\tilde{J}(K)}{F_T(K)} \frac{e^{-|K|d}}{2 \sinh |K|t_1} [e^{-|K|t_1} (D_{12} + e^{-2|K|t_1} D_{13}) e^{|K|y} \\ + e^{|K|t_1} (D_{14} + e^{-2|K|t_1} D_{15}) e^{-|K|y}] e^{-iKx} dK$$

$$b_{y4} = \frac{i\mu_0}{2\pi} \int_{-\infty}^{\infty} \frac{\tilde{J}(K)S}{F_T(K)} \frac{e^{-|K|d}}{2 \sinh |K|t_1} [e^{-|K|t_1} (D_{12} + e^{-2|K|t_1} D_{13}) e^{|K|y} \\ - e^{|K|t_1} (D_{14} + e^{-2|K|t_1} D_{15}) e^{-|K|y}] e^{-iKx} dK. \quad (2-63)$$

We again evaluate these integrals by contour integration and assume the integrals vanish on the outer contour. Thus the residues are $2\pi i$ times the integrand with $F_T(K_s)$ replacing $F_T(K)$ where $K_s = \pm |K_s|$ are the roots of the dispersion relation $F_T(K_s) = 0$.

Defining

$$D_{16} = \left(\cos \alpha |K_s|d + \frac{1 - \alpha^2}{2\alpha} \sin \alpha |K_s|d \right) e^{|K_s|y} + \frac{1 + \alpha^2}{2\alpha} \sin \alpha |K_s|d e^{-|K_s|y}$$

$$D_{17} = -\frac{(1 + \alpha^2)}{2\alpha} \sin \alpha |K_s|d e^{|K_s|y} + \left(\cos \alpha |K_s|d + \frac{\alpha^2 - 1}{2\alpha} \sin \alpha |K_s|d \right) e^{-|K_s|y}$$

$$D_{18} = \left(\cos \alpha |K_s| d + \frac{1 - \alpha^2}{2\alpha} \sin \alpha |K_s| d \right) e^{|K_s| y} - \frac{(1 + \alpha^2)}{2\alpha} \sin \alpha |K_s| d e^{-|K_s| y} \quad (2-63a)$$

$$D_{19} = -\frac{(1 + \alpha^2)}{2\alpha} \sin \alpha |K_s| d e^{|K_s| y} - \left(\cos \alpha |K_s| d + \frac{\alpha^2 - 1}{2\alpha} \sin \alpha |K_s| d \right) e^{-|K_s| y}$$

$$D_{20} = \frac{\alpha^2 + 1}{2\alpha} \sin \alpha |K_s| d e^{-|K_s| g} + \left(-\cos \alpha |K_s| d + \frac{\alpha^2 - 1}{2\alpha} \sin \alpha |K_s| d \right) e^{|K_s| g}$$

$$D_{21} = \left(\frac{\alpha^2 - 1}{2\alpha} \sin \alpha |K_s| d + \cos \alpha |K_s| d \right) e^{-|K_s| g} + \frac{\alpha^2 + 1}{2\alpha} \sin \alpha |K_s| d e^{|K_s| g}$$

and with $G(K)$ defined in Eq. (2-38) and $G_s = G(K_s)$ we have, after simplifying,

$$h_{x_1}^{(s)} = i G_s 2 \cosh[|K_s|(d + l + y)] e^{-|K_s| l} e^{-i K_s x}$$

$$b_{y_1}^{(s)} = -s \mu_0 G_s 2 \sinh[|K_s|(d + l + y)] e^{-|K_s| l} e^{-i K_s x}$$

$$h_{x_2}^{(s)} = i G_s \left\{ \left[\cos \alpha |K_s|(d + y) + \frac{1}{\alpha} \sin \alpha |K_s|(d + y) \right] \right. \\ \left. + e^{-2|K_s| l} \left[\cos \alpha |K_s|(d + y) - \frac{1}{\alpha} \sin \alpha |K_s|(d + y) \right] \right\} e^{-i |K_s| x}$$

$$b_{y_2}^{(s)} = -s \mu_0 G_s \left\{ \left[\cos \alpha |K_s|(d + y) - \alpha \sin \alpha |K_s|(d + y) \right] \right. \\ \left. - e^{-2|K_s| l} \left[\cos \alpha |K_s|(d + y) + \alpha \sin \alpha |K_s|(d + y) \right] \right\} e^{-i |K_s| x} \quad (2-64)$$

$$h_{x_3}^{(s)} = i G_s (D_{16} + e^{-2|K_s| l} D_{17}) e^{-i K_s x} \quad s = -1, 1$$

$$b_{y_3}^{(s)} = -s \mu_0 G_s (D_{18} + e^{-2|K_s| l} D_{19}) e^{-i K_s x}$$

$$h_{x_4}^{(s)} = i G_s \frac{\cosh |K_s|(t_1 + g - y)}{\sinh |K_s| t_1} (D_{20} + e^{-2|K_s| l} D_{21}) e^{-i K_s x}$$

$$b_{y_4}^{(s)} = s \mu_0 G_s \frac{\sinh |K_s|(t_1 + g - y)}{\sinh |K_s| t_1} (D_{20} + e^{-2|K_s| l} D_{21}) e^{-i K_s x}$$

Defining

$$\begin{aligned}
D_{22} &= (\coth |K|t_1 + 1) \left[d - g + \frac{d(\alpha^2 - 1)}{2} \right] \\
&\quad + t_1 \operatorname{csch}^2 |K|t_1 + e^{-2|K|g} \frac{d}{2} (\alpha^2 + 1) (\coth |K|t_1 - 1) \\
D_{23} &= (\coth |K|t_1 + 1) \left[(g - d) \frac{(\alpha^2 - 1)}{2\alpha} + \alpha d \right] - \frac{(\alpha^2 - 1)}{2\alpha} t_1 \operatorname{csch}^2 |K|t_1 \\
&\quad + e^{-2|K|g} \left[-(\coth |K|t_1 - 1) \frac{(\alpha^2 + 1)}{2\alpha} (d + g) - t_1 \frac{(\alpha^2 + 1)}{2\alpha} \operatorname{csch}^2 |K|t_1 \right] \\
D_{24} &= (\coth |K|t_1 + 1) \frac{d(\alpha^2 + 1)}{2} \\
&\quad + e^{-2|K|g} \left[-(\coth |K|t_1 - 1) \left(g + d + 2l - \frac{d\alpha^2 - d}{2} \right) - t_1 \operatorname{csch}^2 |K|t_1 \right] \\
D_{25} &= \frac{(\alpha^2 + 1)}{2\alpha} (\coth |K|t_1 + 1) (g - d - 2l) - t_1 \frac{(\alpha^2 + 1)}{2\alpha} \operatorname{csch}^2 |K|t_1 \\
D_{26} &= e^{-2|K|g} \left[(\coth |K|t_1 - 1) (-g - d - 2l) \frac{(\alpha^2 - 1)}{2\alpha} - \alpha d (\coth |K|t_1 - 1) \right. \\
&\quad \left. - t_1 \frac{(\alpha^2 - 1)}{2\alpha} \operatorname{csch}^2 |K|t_1 \right]
\end{aligned} \tag{2-64a}$$

we obtain $F_T^+(K)$ as

$$\begin{aligned}
F_T^+(K) &= se^{-|K|l(d-g)} \{ D_{22} \cos \alpha |K|d + D_{23} \sin \alpha |K|d \\
&\quad + e^{-|K|l} [D_{24} \cos \alpha |K|d + (D_{23} + D_{26}) \sin \alpha |K|d] \}
\end{aligned} \tag{2-65}$$

completing the determination of the field equations (2-64). Note that the magnitudes of the two solutions for Eq. (2-64), $s = -1, 1$, are the same.

2.4.3 FVW POWER

As for surface waves, the magnetostatic wave power for each solution is

$$p^{(s)} = \frac{s\omega l_1}{2|K_s|} \left[\int_{-(l+d)}^{-d} b_{y_1}^{(s)} \overline{h_{y_1}^{(s)}} dy + \int_{-d}^0 b_{y_2}^{(s)} \overline{h_{y_2}^{(s)}} dy + \int_0^g b_{y_3}^{(s)} \overline{h_{y_3}^{(s)}} dy + \int_g^{g+l_1} b_{y_4}^{(s)} \overline{h_{y_4}^{(s)}} dy \right] \quad s = -1, 1 \quad (2-66)$$

For region 1, using Eqs. (2-64) and (2-10)

$$\int_{-(l+d)}^{-d} b_{y_1}^{(s)} \overline{h_{y_1}^{(s)}} dy = \mu_0 G_s^2 e^{-2|K_s|l} 4 \int_{-(l+d)}^{-d} \sinh^2 |K_s|(d+l+y) dy \quad (2-67)$$

which, as in Eq. (2-46) is

$$\int_{-(l+d)}^{-d} b_{y_1}^{(s)} \overline{h_{y_1}^{(s)}} dy = \frac{\mu_0 G_s^2 e^{-2|K_s|l}}{|K_s|} (\sinh 2|K_s|l - 2|K_s|l) \quad (2-68)$$

Defining

$$\begin{aligned} D_{27} &= \cos\alpha |K_s|(d+y) - \alpha \sin\alpha |K_s|(d+y) \\ D_{28} &= \cos^2\alpha |K_s|(d+y) - \alpha^2 \sin^2\alpha |K_s|(d+y) \\ D_{29} &= \cos\alpha |K_s|(d+y) + \alpha \sin\alpha |K_s|(d+y) \end{aligned} \quad (2-68a)$$

we have for region 2, from Eqs. (2-64) and (2-57)

$$\int_{-d}^0 b_{y_2}^{(s)} \overline{h_{y_2}^{(s)}} dy = \mu_0 G_s^2 \int_{-d}^0 (D_{27}^2 - 2e^{-2|K_s|l} D_{28} + e^{-4|K_s|l} D_{29}^2) dy \quad (2-69)$$

or, defining

$$\begin{aligned} D_{30} &= (\alpha^2 + 1) |K_s|d - \frac{(\alpha^2 - 1)}{2\alpha} \sin 2\alpha |K_s|d + \cos 2\alpha |K_s|d - 1 \\ D_{31} &= (\alpha^2 - 1) |K_s|d - \frac{(\alpha^2 + 1)}{2\alpha} \sin 2\alpha |K_s|d \\ D_{32} &= (\alpha^2 + 1) |K_s|d - \frac{(\alpha^2 - 1)}{2\alpha} \sin 2\alpha |K_s|d - \cos 2\alpha |K_s|d + 1 \end{aligned} \quad (2-69a)$$

we get

$$\int_{-d}^0 b_{y_2}^{(s)} \overline{h_{y_2}^{(s)}} dy = \frac{\mu_0 G_s^2}{2|K_s|} (D_{30} + 2e^{-2|K_s|l} D_{31} + e^{-4|K_s|l} D_{32}). \quad (2-70)$$

Defining

$$D_{33} = \cos^2 \alpha |K_s| d + \frac{(1 - \alpha^2)^2}{4\alpha^2} \sin^2 \alpha |K_s| d + \frac{(1 - \alpha^2)}{2\alpha} \sin 2\alpha |K_s| d$$

$$D_{34} = \frac{(1 + \alpha^2)^2}{4\alpha^2} \sin^2 \alpha |K_s| d$$

$$D_{35} = -\frac{(1 + \alpha^2)}{2\alpha} \sin 2\alpha |K_s| d - \frac{(1 - \alpha^4)}{2\alpha^2} \sin^2 \alpha |K_s| d$$

$$D_{36} = \frac{(1 + \alpha^2)}{2\alpha} \sin 2\alpha |K_s| d - \frac{(1 - \alpha^4)}{2\alpha^2} \sin^2 \alpha |K_s| d$$

$$D_{37} = -2\cos^2 \alpha |K_s| d + \frac{[(1 + \alpha^2)^2 + (1 - \alpha^2)^2]}{2\alpha^2} \sin^2 \alpha |K_s| d$$

$$D_{38} = \cos^2 \alpha |K_s| d + \frac{(\alpha^2 - 1)^2}{4\alpha^2} \sin^2 \alpha |K_s| d + \frac{(\alpha^2 - 1)}{2\alpha} \sin 2\alpha |K_s| d$$

$$D_{39} = \frac{(\alpha^2 + 1)}{2\alpha} \sin 2\alpha |K_s| d + \frac{(\alpha^4 - 1)}{2\alpha^2} \sin^2 \alpha |K_s| d \quad (2-70a)$$

$$D_{40} = D_{33} e^{2|K_s|y} + D_{34} e^{-2|K_s|y} + D_{35}$$

$$D_{41} = D_{35} e^{2|K_s|y} + D_{36} e^{-2|K_s|y} + D_{37}$$

$$D_{42} = D_{34} e^{2|K_s|y} + D_{38} e^{-2|K_s|y} + D_{39}$$

we get for region 3, from Eqs. (2-64) and (2-10)

$$\int_0^g b_{y_3}^{(s)} \overline{h_{y_3}^{(s)}} dy = \mu_0 G_s^2 \int_0^g (D_{40} + e^{-2|K_s|l} D_{41} + e^{-4|K_s|l} D_{42}) dy. \quad (2-71)$$

Defining

$$D_{43} = \left\{ \frac{(1 + \alpha^2)^2}{4\alpha^2} + \frac{[4\alpha^2 - (1 - \alpha^2)^2]}{4\alpha^2} \cos 2\alpha |K_s| d + \frac{(1 - \alpha^2)}{\alpha} \sin 2\alpha |K_s| d \right\} e^{2|K_s|g}$$

$$D_{44} = \left[\frac{(1 + \alpha^2)^2}{4\alpha^2} (\cos 2\alpha |K_s| d - 1) \right]$$

$$\begin{aligned}
D_{45} &= 2 \cos 2\alpha |K_s| d + \frac{(1 - \alpha^2)}{\alpha} \sin 2\alpha |K_s| d \\
&\quad + \left[\frac{(1 + \alpha^2)}{\alpha} \sin 2\alpha |K_s| d + \frac{(1 - \alpha^4)}{2\alpha^2} (1 - \cos 2\alpha |K_s| d) \right] 2 |K_s| g \\
D_{46} &= \left[-\frac{(1 + \alpha^2)}{2\alpha} \sin 2\alpha |K_s| d + \frac{(1 - \alpha^4)}{4\alpha^2} (\cos 2\alpha |K_s| d - 1) \right] e^{2|K_s|g} \\
D_{47} &= \left[\frac{(1 + \alpha^2)}{2\alpha} \sin 2\alpha |K_s| d + \frac{(1 - \alpha^4)}{4\alpha^2} (\cos 2\alpha |K_s| d - 1) \right] e^{-2|K_s|g} \quad (2-71a) \\
D_{48} &= \frac{(1 + \alpha^2)}{\alpha} \sin 2\alpha |K_s| d + \left[\frac{(1 - \alpha^2)^2}{2\alpha^2} - \frac{(1 + \alpha^2)^2}{2\alpha^2} \cos 2\alpha |K_s| d \right] 2 |K_s| g \\
D_{49} &= \left\{ \frac{(1 + \alpha^2)^2}{4\alpha^2} + \frac{[4\alpha^2 - (1 - \alpha^2)^2]}{4\alpha^2} \cos 2\alpha |K_s| d - \frac{(1 - \alpha^2)}{\alpha} \sin 2\alpha |K_s| d \right\} e^{-2|K_s|g} \\
D_{50} &= 2 \cos 2\alpha |K_s| d - \frac{(1 - \alpha^2)}{\alpha} \sin 2\alpha |K_s| d \\
&\quad + \left[\frac{(1 + \alpha^2)}{\alpha} \sin 2\alpha |K_s| d + \frac{(1 - \alpha^4)}{2\alpha^2} (\cos 2\alpha |K_s| d - 1) \right] 2 |K_s| g
\end{aligned}$$

we get

$$\begin{aligned}
\int_0^g b_{y_3}^{(s)} \overline{h_{y_3}^{(s)}} dy &= \frac{\mu_0 G_s^2}{4 |K_s|} [D_{43} + D_{44} e^{-2|K_s|g} - D_{45} + 2e^{-2|K_s|l} \\
&\quad \times (D_{46} - D_{47} + D_{48}) + e^{-4|K_s|l} (-D_{44} e^{2|K_s|g} - D_{49} + D_{50})]. \quad (2-72)
\end{aligned}$$

Defining

$$\begin{aligned}
D_{51} &= \left[\cos 2\alpha |K_s| d + \frac{(\alpha^2 - 1)^2}{4\alpha^2} \sin 2\alpha |K_s| d - \frac{(\alpha^2 - 1)}{2\alpha} \sin 2\alpha |K_s| d \right] e^{2|K_s|g} \\
D_{52} &= \left[\frac{(\alpha^2 + 1)^2}{4\alpha^2} \sin 2\alpha |K_s| d \right] e^{-2|K_s|g} \\
D_{53} &= -\frac{(\alpha^2 + 1)}{2\alpha} \sin 2\alpha |K_s| d + \frac{(\alpha^4 - 1)}{2\alpha^2} \sin 2\alpha |K_s| d
\end{aligned}$$

$$D_{54} = \left[\frac{(\alpha^4 - 1)}{4\alpha^2} \sin^2 \alpha |K_s| d - \frac{(\alpha^2 + 1)}{4\alpha} \sin 2\alpha |K_s| d \right] e^{2|K_s|g}$$

$$D_{55} = \left[\frac{(\alpha^4 - 1)}{4\alpha^2} \sin^2 \alpha |K_s| d + \frac{(\alpha^2 + 1)}{4\alpha} \sin 2\alpha |K_s| d \right] e^{-2|K_s|g} \quad (2-72a)$$

$$D_{56} = \frac{(\alpha^4 + 1)}{2\alpha^2} \sin^2 \alpha |K_s| d - \cos^2 \alpha |K_s| d$$

$$D_{57} = \left[\cos^2 \alpha |K_s| d + \frac{(\alpha^2 - 1)^2}{4\alpha^2} \sin^2 \alpha |K_s| d + \frac{(\alpha^2 - 1)}{2\alpha} \sin 2\alpha |K_s| d \right] e^{-2|K_s|g}$$

$$D_{58} = \left[\frac{(\alpha^2 + 1)^2}{4\alpha^2} \sin^2 \alpha |K_s| d \right] e^{2|K_s|g}$$

$$D_{59} = \frac{(\alpha^4 - 1)}{2\alpha^2} \sin^2 \alpha |K_s| d + \frac{(\alpha^2 + 1)}{2\alpha} \sin 2\alpha |K_s| d$$

we get for region 4, from Eqs. (2-64) and (2-10)

$$\int_g^{g+t_1} b_{y_4}^{(s)} \overline{h_{y_4}^{(s)}} dy = \frac{\mu_0 G_s^2 (\sinh 2|K_s|t_1 - 2|K_s|t_1)}{4|K_s| \sinh^2 |K_s|t_1} [D_{51} + D_{52} + D_{53} + 2e^{-2|K_s|l} \quad (2-73)$$

$$\times (D_{54} + D_{55} + D_{56}) + e^{-4|K_s|l} (D_{57} + D_{58} + D_{59})].$$

Defining

$$D_{60} = \frac{(\sinh 2|K_s|t_1 - 2|K_s|t_1)}{2 \sinh^2 |K_s|t_1}$$

$$D_{61} = 2e^{-2|K_s|l} (\sinh 2|K_s|l - 2|K_s|l) + (\alpha^2 + 1)|K_s|d - 1$$

$$D_{62} = |K_s|g \left[\frac{(1 + \alpha^2)}{\alpha} \sin 2\alpha |K_s|d + \frac{(1 - \alpha^4)}{2\alpha^2} (1 - \cos 2\alpha |K_s|d) \right]$$

$$D_{63} = \left[\frac{(\alpha^4 - 1)}{4\alpha^2} (1 - \cos 2\alpha |K_s|d) - \frac{(\alpha^2 + 1)}{2\alpha} \sin 2\alpha |K_s|d \right] D_{60}$$

$$D_{64} = \left\{ \frac{(1 + \alpha^2)^2}{8\alpha^2} + \frac{[4\alpha^2 - (1 - \alpha^2)^2]}{8\alpha^2} \cos 2\alpha |K_s|d + \frac{(1 - \alpha^2)}{2\alpha} \sin 2\alpha |K_s|d \right\}$$

$$\times (D_{60} + 1) e^{2|K_s|g}$$

$$\begin{aligned}
D_{65} &= \frac{(1 + \alpha^2)^2}{8\alpha^2} (\cos 2\alpha |K_s| d - 1) (1 - D_{60}) e^{-2|K_s|g} \\
D_{66} &= (\alpha^2 - 1) 2|K_s| d + |K_s| g \left[\frac{(1 - \alpha^2)^2}{\alpha^2} - \frac{(1 + \alpha^2)^2}{\alpha^2} \cos 2\alpha |K_s| d \right] \\
&\quad + \left[\frac{(1 - \alpha^2)^2}{2\alpha^2} - \frac{(1 + \alpha^2)^2}{2\alpha^2} \cos 2\alpha |K_s| d \right] D_{60} \\
D_{67} &= \left[\frac{(\alpha^4 - 1)}{4\alpha^2} (1 - \cos 2\alpha |K_s| d) - \frac{(\alpha^2 + 1)}{2\alpha} \sin 2\alpha |K_s| d \right] (1 + D_{60}) e^{2|K_s|g} \\
D_{68} &= \left[\frac{(1 - \alpha^4)}{4\alpha^2} (1 - \cos 2\alpha |K_s| d) - \frac{(\alpha^2 + 1)}{2\alpha} \sin 2\alpha |K_s| d \right] (1 - D_{60}) e^{-2|K_s|g} \\
D_{69} &= (\alpha^2 + 1) |K_s| d + 1 + \left[\frac{(\alpha^2 + 1)}{2\alpha} \sin 2\alpha |K_s| d + \frac{(\alpha^4 - 1)}{4\alpha^2} (1 - \cos 2\alpha |K_s| d) \right] D_{60} \\
D_{70} &= |K_s| g \left[\frac{(1 + \alpha^2)}{\alpha} \sin 2\alpha |K_s| d + \frac{(\alpha^4 - 1)}{2\alpha^2} (1 - \cos 2\alpha |K_s| d) \right] \\
D_{71} &= \frac{(1 + \alpha^2)^2}{8\alpha^2} (1 - \cos 2\alpha |K_s| d) (1 + D_{60}) e^{2|K_s|g} \\
D_{72} &= \left\{ -\frac{(1 + \alpha^2)^2}{8\alpha^2} - \frac{[4\alpha^2 - (1 - \alpha^2)^2]}{8\alpha^2} \cos 2\alpha |K_s| d - \frac{(\alpha^2 - 1)}{2\alpha} \sin 2\alpha |K_s| d \right\} \\
&\quad \times (1 - D_{60}) e^{-2|K_s|g}
\end{aligned} \tag{2-73a}$$

and employing Eqs. (2-73), (2-72), (2-70) and (2-68) in Eq. (2-66) we get⁵

$$\begin{aligned}
\frac{p^{(s)}}{l_1} &= \frac{s\omega\mu_0 G_s^2}{4|K_s|^2} [D_{61} - D_{62} + D_{63} + D_{64} + D_{65} + e^{-2|K_s|l} \\
&\quad \times (D_{66} + D_{67} + D_{68}) + e^{-4|K_s|l} (D_{69} + D_{70} + D_{71} + D_{72})] \quad s = -1, 1
\end{aligned} \tag{2-74}$$

for the forward volume wave magnetostatic wave power. The magnitudes are identical for the two waves, $s = -1, 1$.

Here the bandwidth for the existence of forward volume waves is

$$\gamma H < f < \gamma \sqrt{H(H + M)}. \tag{2-75}$$

2.5 Backward Volume Waves

2.5.1 BVW DISPERSION RELATION

For backward volume waves, ($\theta = 90^\circ$, $\phi = 0^\circ$), the constitutive relations (2-8) and (2-9) in the YIG region become, for b_x and b_y

$$\begin{pmatrix} b_x \\ b_y \end{pmatrix} = \mu_0 \begin{pmatrix} 1 & 0 \\ 0 & \mu_{11} \end{pmatrix} \begin{pmatrix} h_x \\ h_y \end{pmatrix} \quad (2-76)$$

where μ_{11} has been defined in Eq. (2-21). Here, too, μ_{11} is always negative. We define^{4,5}

$$\alpha^2 = -\frac{\mu_{xx}}{\mu_{yy}} = -\frac{1}{\mu_{11}} \quad (2-77)$$

and see that the solution in the YIG region satisfying Eqs. (2-76) and (2-15) is of the form

$$\psi_2 = \int_{-\infty}^{\infty} (A_2 \cos \alpha |K| y + B_2 \sin \alpha |K| y) e^{-iKx} dK \quad (2-78)$$

Here we have for all regions, omitting the integration in K ,

$$b_{y_j} = \mu_0 |K| (A_j e^{iK|y|} - B_j e^{-iK|y|}) e^{-iKx} \quad j = 1, 3, 4 \quad (2-79)$$

$$b_{y_2} = -\frac{\mu_0}{\alpha^2} |K| (-A_2 \sin \alpha |K| y + B_2 \cos \alpha |K| y) e^{-iKx}$$

The eight constants A_i, B_i , $i = 1, 2, 3, 4$ in Eqs. (2-78) and (2-18) are found by solving the eight boundary and continuity conditions.

Proceeding as for forward volume waves and defining^{4,5}

$$F_1 = \frac{(\alpha^2 - 1)}{2} (\coth |K| t_1 + 1) - e^{-2|K|g} \frac{(\alpha^2 + 1)}{2} (\coth |K| t_1 - 1) \quad (2-79a)$$

$$F_2 = -\frac{(\alpha^2 + 1)}{2} (\coth |K| t_1 + 1) + e^{-2|K|g} \frac{(\alpha^2 - 1)}{2} (\coth |K| t_1 - 1)$$

and

$$F(K) = F_T(K) = e^{-iK|d|} e^{iK|g|} \frac{\sin \alpha |K| d}{\alpha} (-D_1 \alpha \cot \alpha |K| d + F_1 + F_2 e^{-2|K|l}) \quad (2-80)$$

where D_1 was defined in Eq. (2-60a).

With

$$F_3 = -\frac{(\alpha^2 + 1)}{2\alpha} \sin \alpha |K| d + e^{-2|K|g} \left[\frac{(\alpha^2 - 1)}{2\alpha} \sin \alpha |K| d + \cos \alpha |K| d \right] \quad (2-80a)$$

$$F_4 = \frac{(\alpha^2 - 1)}{2\alpha} \sin \alpha |K|d + \cos \alpha |K|d - e^{2|K|g} \frac{(\alpha^2 + 1)}{2\alpha} \sin \alpha |K|d$$

we obtain the constants as

$$A_1 = \frac{i\tilde{J}(K)}{2\pi KF(K)}$$

$$B_1 = \frac{i\tilde{J}(K)}{2\pi KF(K)} e^{-2|K|(d+l)}$$

$$A_2 = \frac{i\tilde{J}(K)}{2\pi KF(K)} e^{-|K|d} [\cos \alpha |K|d - \alpha \sin \alpha |K|d + e^{-2|K|l} (\cos \alpha |K|d + \alpha \sin \alpha |K|d)]$$

$$B_2 = \frac{i\tilde{J}(K)}{2\pi KF(K)} e^{-|K|d} [-\alpha \cos \alpha |K|d - \sin \alpha |K|d + e^{-2|K|l} (\alpha \cos \alpha |K|d - \sin \alpha |K|d)]$$

$$A_3 = \frac{i\tilde{J}(K)}{2\pi KF(K)} e^{-|K|d} \left[\cos \alpha |K|d + \frac{(1 - \alpha^2)}{2\alpha} \sin \alpha |K|d + e^{-2|K|l} \frac{(\alpha^2 + 1)}{2\alpha} \sin \alpha |K|d \right]$$

(2-81)

$$B_3 = \frac{i\tilde{J}(K)}{2\pi KF(K)} e^{-|K|d} \left\{ -\frac{(\alpha^2 + 1)}{2\alpha} \sin \alpha |K|d + e^{-2|K|l} \left[\cos \alpha |K|d - \frac{(1 - \alpha^2)}{2\alpha} \sin \alpha |K|d \right] \right\}$$

$$A_4 = \frac{i\tilde{J}(K)}{2\pi KF(K)} \frac{e^{-|K|t_1}}{2 \sinh |K|t_1} e^{-|K|d}$$

$$\times \left[-\cos \alpha |K|d + \frac{(\alpha^2 - 1)}{2\alpha} \sin \alpha |K|d - e^{2|K|g} \frac{(\alpha^2 + 1)}{2\alpha} \sin \alpha |K|d + e^{-2|K|l} F_3 \right]$$

$$B_4 = \frac{i\tilde{J}(K)}{2\pi KF(K)} \frac{e^{-|K|t_1}}{2 \sinh |K|t_1} e^{-|K|d}$$

$$\times \left\{ -\frac{(\alpha^2 + 1)}{2\alpha} \sin \alpha |K|d - e^{2|K|g} \left[\cos \alpha |K|d + \frac{(1 - \alpha^2)}{2\alpha} \sin \alpha |K|d \right] + e^{-2|K|l} F_4 \right\}$$

where $\tilde{J}(K)$ is as defined earlier. By setting $F_T(K) = 0$ we get the dispersion relation, to be solved for K as a function of f . Here, too, s does not enter Eqs. (2-81) and (2-80) so that the two solutions are identical.

2.5.2 W FIELD EQUATIONS

Defining

$$F_5 = \cos \alpha |K|d - \alpha \sin \alpha |K|d + e^{-2|K|l} (\cos \alpha |K|d + \alpha \sin \alpha |K|d)$$

$$\begin{aligned}
F_6 &= -\alpha \cos \alpha |K|d - \sin \alpha |K|d + e^{-2|K|l} (\alpha \cos \alpha |K|d - \sin \alpha |K|d) \\
F_7 &= -\cos \alpha |K|d + \sin \alpha |K|d - e^{-2|K|l} (\cos \alpha |K|d + \alpha \sin \alpha |K|d) \\
F_8 &= -\alpha \cos \alpha |K|d - \sin \alpha |K|d + e^{-2|K|l} (\alpha \cos \alpha |K|d - \sin \alpha |K|d) \quad (2-81a) \\
F_9 &= \cos \alpha |K|d + \frac{(1 - \alpha^2)}{2\alpha} \sin \alpha |K|d + e^{-2|K|l} \frac{(1 + \alpha^2)}{2\alpha} \sin \alpha |K|d \\
F_{10} &= -\frac{(1 + \alpha^2)}{2\alpha} \sin \alpha |K|d + e^{-2|K|l} \left[\cos \alpha |K|d - \frac{(1 - \alpha^2)}{2\alpha} \sin \alpha |K|d \right] \\
F_{11} &= -\cos \alpha |K|d + \frac{(\alpha^2 - 1)}{2\alpha} \sin \alpha |K|d - e^{-2|K|l} \frac{(1 + \alpha^2)}{2\alpha} \sin \alpha |K|d \\
F_{12} &= -\frac{(1 + \alpha^2)}{2\alpha} \sin \alpha |K|d + e^{-2|K|l} \left[\cos \alpha |K|d + \frac{(\alpha^2 - 1)}{2\alpha} \sin \alpha |K|d \right] \\
F_{13} &= -\frac{(1 + \alpha^2)}{2\alpha} \sin \alpha |K|d - e^{-2|K|l} \left[\cos \alpha |K|d + \frac{(1 - \alpha^2)}{2\alpha} \sin \alpha |K|d \right] \\
F_{14} &= \cos \alpha |K|d + \frac{(\alpha^2 - 1)}{2\alpha} \sin \alpha |K|d - e^{-2|K|l} \frac{(1 + \alpha^2)}{2\alpha} \sin \alpha |K|d
\end{aligned}$$

the time suppressed field equations are, using Eqs. (2-81), (2-79) and (2-17)

$$\begin{aligned}
h_{x_1} &= \frac{1}{2\pi} \int_{-\infty}^{\infty} \frac{\tilde{J}(K)}{F(K)} e^{-|K|d} e^{-|K|l} (e^{|K|l(d+l)} e^{|K|y} + e^{-|K|l(d+l)} e^{-|K|y}) e^{-iKx} dK \\
b_{y_1} &= \frac{i\mu_0}{2\pi} \int_{-\infty}^{\infty} \frac{s\tilde{J}(K)}{F(K)} e^{-|K|d} e^{-|K|l} (e^{|K|l(d+l)} e^{|K|y} - e^{-|K|l(d+l)} e^{-|K|y}) e^{-iKx} dK \\
h_{x_2} &= \frac{1}{2\pi} \int_{-\infty}^{\infty} \frac{\tilde{J}(K)}{F(K)} e^{-|K|d} (F_5 \cos \alpha |K|y + F_6 \sin \alpha |K|y) e^{-iKx} dK \\
b_{y_2} &= -\frac{i\mu_0}{2\pi} \int_{-\infty}^{\infty} \frac{s\tilde{J}(K)}{F(K)} \frac{e^{-|K|d}}{\alpha} (F_8 \cos \alpha |K|y + F_7 \sin \alpha |K|y) e^{-iKx} dK \quad (2-82)
\end{aligned}$$

$$h_{x_3} = \frac{1}{2\pi} \int_{-\infty}^{\infty} \frac{\tilde{J}(K)}{F(K)} e^{-|K|d} (F_9 e^{|K|y} + F_{10} e^{-|K|y}) e^{-iKx} dK$$

$$b_{y_3} = \frac{i\mu_0}{2\pi} \int_{-\infty}^{\infty} \frac{S\tilde{J}(K)}{F(K)} e^{-|K|d} (F_9 e^{|K|y} - F_{10} e^{-|K|y}) e^{-iKx} dK$$

$$h_{x_4} = \frac{1}{2\pi} \int_{-\infty}^{\infty} \frac{\tilde{J}(K)}{F(K)} \frac{e^{-|K|d}}{2\sinh|K|t_1} \\ \times [e^{-|K|t_1}(F_{11} + e^{-2|K|l} F_{12}) e^{|K|y} + e^{|K|t_1}(F_{13} + e^{-2|K|l} F_{14}) e^{-|K|y}] e^{-iKx} dK$$

$$b_{y_4} = \frac{i\mu_0}{2\pi} \int_{-\infty}^{\infty} \frac{s\tilde{J}(K)}{F(K)} \frac{e^{-|K|d}}{2\sinh|K|t_1} \\ \times [e^{-|K|t_1}(F_{11} + e^{-2|K|l} F_{12}) e^{|K|y} - e^{|K|t_1}(F_{13} + e^{-2|K|l} F_{14}) e^{-|K|y}] e^{-iKx} dK$$

Proceeding with contour integration as before, with K_s ($s = -1, 1$) being the roots of $F_T(K_s) = 0$ and $G(K)$ defined in Eq. (2-38), we first define

$$\begin{aligned} F_{15} &= \left(\cos\alpha |K_s|d + \frac{1 - \alpha^2}{2\alpha} \sin\alpha |K_s|d \right) e^{|K_s|y} - \frac{(1 + \alpha^2)}{2\alpha} \sin\alpha |K_s|d e^{-|K_s|y} \\ F_{16} &= \frac{1 + \alpha^2}{2\alpha} \sin\alpha |K_s|d e^{|K_s|y} + \left(\cos\alpha |K_s|d + \frac{(\alpha^2 - 1)}{2\alpha} \sin\alpha |K_s|d \right) e^{-|K_s|y} \\ F_{17} &= \left(\cos\alpha |K_s|d + \frac{1 - \alpha^2}{2\alpha} \sin\alpha |K_s|d \right) e^{|K_s|y} + \frac{(1 + \alpha^2)}{2\alpha} \sin\alpha |K_s|d e^{-|K_s|y} \\ F_{18} &= \frac{1 + \alpha^2}{2\alpha} \sin\alpha |K_s|d e^{|K_s|y} - \left(\cos\alpha |K_s|d + \frac{(\alpha^2 - 1)}{2\alpha} \sin\alpha |K_s|d \right) e^{-|K_s|y} \\ F_{19} &= \frac{\alpha^2 + 1}{2\alpha} e^{-|K_s|g} \sin\alpha |K_s|d - e^{|K_s|g} \left(\cos\alpha |K_s|d + \frac{(1 - \alpha^2)}{2\alpha} \sin\alpha |K_s|d \right) \\ F_{20} &= \left(\cos\alpha |K_s|d + \frac{\alpha^2 - 1}{2\alpha} \sin\alpha |K_s|d \right) e^{-|K_s|g} - e^{|K_s|g} \frac{\alpha^2 + 1}{2\alpha} \sin\alpha |K_s|d \end{aligned} \quad (2-82a)$$

$$F_{21} = \frac{\alpha^2 + 1}{2\alpha} e^{-|K_s|g} \sin \alpha |K_s|d + e^{|K_s|g} \left(\cos \alpha |K_s|d + \frac{(1 - \alpha^2)}{2\alpha} \sin \alpha |K_s|d \right)$$

we obtain

$$h_{x_1}^{(s)} = i G_s 2 \cosh |K_s|(d + l + y) e^{-|K_s|l} e^{-i K_s x}$$

$$b_{y_1}^{(s)} = -s \mu_0 G_s 2 \sinh |K_s|(d + l + y) e^{-|K_s|l} e^{-i K_s x}$$

$$h_{x_2}^{(s)} = i G_s \left\{ \cos \alpha |K_s|(d + y) - \alpha \sin \alpha |K_s|(d + y) + e^{-2|K_s|l} \right. \\ \left. \times [\cos \alpha |K_s|(d + y) + \alpha \sin \alpha |K_s|(d + y)] \right\} e^{-i K_s x}$$

$$b_{y_2}^{(s)} = -s \mu_0 G_s \left\{ \cos \alpha |K_s|(d + y) + \frac{1}{\alpha} \sin \alpha |K_s|(d + y) + e^{-2|K_s|l} \right. \\ \left. \times \left[-\cos \alpha |K_s|(d + y) + \frac{1}{\alpha} \sin \alpha |K_s|(d + y) \right] \right\} e^{-i K_s x}$$

$$h_{x_3}^{(s)} = i G_s (F_{15} + e^{-2|K_s|l} F_{16}) e^{-i K_s x} \quad (2-83)$$

$$b_{y_3}^{(s)} = -s \mu_0 G_s (F_{17} + e^{-2|K_s|l} F_{18}) e^{-i K_s x} \quad s = -1, 1$$

$$h_{x_4}^{(s)} = i G_s \frac{\cosh |K_s|(t_1 + g - y)}{\sinh |K_s|t_1} (F_{19} + e^{-2|K_s|l} F_{20}) e^{-i K_s x}$$

$$b_{y_4}^{(s)} = -s \mu_0 G_s \frac{\sinh |K_s|(t_1 + g - y)}{\sinh |K_s|t_1} (F_{21} - e^{-2|K_s|l} F_{20}) e^{-i K_s x}.$$

Defining

$$F_{22} = (\coth |K|t_1 + 1) \left[d - g + \frac{d(\alpha^2 - 1)}{2} \right] + t_1 \operatorname{csch}^2 |K|t_1 \\ - e^{-2|K|g} \frac{d}{2} (\alpha^2 + 1) (\coth |K|t_1 - 1)$$

$$F_{23} = (\coth |K|t_1 + 1) \left[(g - d) \frac{(\alpha^2 - 1)}{2\alpha} + \alpha d \right] - \frac{(\alpha^2 - 1)}{2\alpha} t_1 \operatorname{csch}^2 |K|t_1 \quad (2-83a) \\ + e^{-2|K|g} \left[(\coth |K|t_1 - 1) \frac{(\alpha^2 + 1)}{2\alpha} (g + d) + t_1 \frac{(\alpha^2 + 1)}{2\alpha} \operatorname{csch}^2 |K|t_1 \right]$$

$$F_{24} = -(\coth |K|t_1 + 1) \frac{d(\alpha^2 + 1)}{2} + e^{-2|K|g}$$

$$\times \left[-(\coth |K|t_1 - 1) \left(g + d + 2l - \frac{d\alpha^2 - d}{2} \right) - t_1 \operatorname{csch}^2 |K|t_1 \right]$$

and using Eq. (2-64a) we obtain $F_T(K)$ as

$$F_T(K) = se^{-|K|(d-g)} \quad (2-84)$$

$$\times \{F_{22} \cos \alpha |K|d + F_{23} \sin \alpha |K|d + e^{-2|K|l} [F_{24} \cos \alpha |K|d - (D_{25} - D_{26}) \sin \alpha |K|d]\}$$

completing the field equations. Here, too, the magnitudes of the two solutions are equal, as for forward volume waves.

2.5.3 BVW POWER

The magnetostatic wave power for each solution, as in Eq. (2-66), is

$$P^{(s)} = \frac{s\omega l_1}{2|k_s|} \left[\int_{-(l+d)}^{-d} b_{y_1}^{(s)} \overline{h_{y_1}^{(s)}} dy + \int_{-d}^0 b_{y_2}^{(s)} \overline{h_{y_2}^{(s)}} dy \right. \\ \left. + \int_0^g b_{y_3}^{(s)} \overline{h_{y_3}^{(s)}} dy + \int_g^{g+t_1} b_{y_4}^{(s)} \overline{h_{y_4}^{(s)}} dy \right] \quad s = -1, 1 \quad (2-85)$$

For region 1, using Eqs. (2-83) and (2-10)

$$\int_{-(l+d)}^{-d} b_{y_1}^{(s)} \overline{h_{y_1}^{(s)}} dy = \mu_0 G_s^2 e^{-2|K_s|l} 4 \int_{-(l+d)}^{-d} \sinh^2 |K_s|(d+l+y) dy \quad (2-86)$$

which, as in Eq. (2-68), is

$$\int_{-(l+d)}^{-d} b_{y_1}^{(s)} \overline{h_{y_1}^{(s)}} dy = \frac{\mu_0 G_s^2 e^{-2|K_s|l}}{|K_s|} (\sinh 2|K_s|l - 2|K_s|l) \quad (2-87)$$

Defining

$$F_{25} = \cos \alpha |K_s|(d+y) + \frac{1}{\alpha} \sin \alpha |K_s|(d+y)$$

$$F_{26} = \frac{1}{\alpha^2} \sin^2 \alpha |K_s|(d+y) - \cos^2 \alpha |K_s|(d+y) \quad (2-87a)$$

$$F_{27} = -\cos \alpha |K_s|(d+y) + \frac{1}{\alpha} \sin \alpha |K_s|(d+y)$$

we obtain for region 2, using Eqs. (2-83) and (2-76)

$$\int_{-d}^0 b_{y_2}^{(s)} \overline{h_{y_2}^{(s)}} dy = -\alpha^2 \mu_0 G_s^2 \int_{-d}^0 (F_{25}^2 + 2e^{-2|K_s|l} F_{26} + e^{-4|K_s|l} F_{27}^2) dy \quad (2-88)$$

or, defining

$$\begin{aligned} F_{28} &= -(\alpha^2 + 1)|K_s|d - \frac{(\alpha^2 - 1)}{2\alpha} \sin 2\alpha |K_s|d + \cos 2\alpha |K_s|d - 1 \\ F_{29} &= (\alpha^2 - 1)|K_s|d + \frac{(\alpha^2 + 1)}{2\alpha} \sin 2\alpha |K_s|d \\ F_{30} &= -(\alpha^2 + 1)|K_s|d - \frac{(\alpha^2 - 1)}{2\alpha} \sin 2\alpha |K_s|d - \cos 2\alpha |K_s|d + 1 \end{aligned} \quad (2-88a)$$

we get

$$\int_{-d}^0 b_{y_2}^{(s)} \overline{h_{y_2}^{(s)}} dy = \frac{\mu_0 G_s^2}{2|K_s|} (F_{28} + 2e^{-2|K_s|l} F_{29} + e^{-4|K_s|l} F_{30}) \quad (2-89)$$

Defining, referring to Eq. (2-70a),

$$\begin{aligned} F_{31} &= D_{33} e^{2|K_s|y} + D_{34} e^{-2|K_s|y} - D_{35} \\ F_{32} &= -D_{35} e^{2|K_s|y} - D_{36} e^{-2|K_s|y} + D_{37} \\ F_{33} &= D_{34} e^{2|K_s|y} - D_{38} e^{-2|K_s|y} - D_{39} \end{aligned} \quad (2-89a)$$

we obtain for region 3, using Eqs. (2-83) and (2-10)

$$\int_0^g b_{y_3}^{(s)} \overline{h_{y_3}^{(s)}} dy = \mu_0 G_s^2 \int_0^g (F_{31} + e^{-2|K_s|l} F_{32} + e^{-4|K_s|l} F_{33}) dy \quad (2-90)$$

Defining

$$\begin{aligned} F_{34} &= -2 \cos 2\alpha |K_s|d - \frac{(1 - \alpha^2)}{\alpha} \sin 2\alpha |K_s|d \\ &+ \left[\frac{(1 + \alpha^2)}{\alpha} \sin 2\alpha |K_s|d + \frac{(1 - \alpha^4)}{2\alpha^2} (1 - \cos 2\alpha |K_s|d) \right] 2|K_s|g \end{aligned}$$

$$F_{35} = -\frac{(1 + \alpha^2)}{\alpha} \sin 2\alpha |K_s| d + \left[\frac{(1 - \alpha^2)^2}{2\alpha^2} - \frac{(1 + \alpha^2)^2}{2\alpha^2} \cos 2\alpha |K_s| d \right] 2 |K_s| g \quad (2-90a)$$

$$F_{36} = 2 \cos 2\alpha |K_s| d - \frac{(1 - \alpha^2)}{\alpha} \sin 2\alpha |K_s| d - \left[\frac{(1 + \alpha^2)}{\alpha} \sin 2\alpha |K_s| d + \frac{(1 - \alpha^4)}{2\alpha^2} (\cos 2\alpha |K_s| d - 1) \right] 2 |K_s| g$$

and referring to Eq. (2-71a)

$$\int_0^g b_{y_3} \overline{h_{y_3}^{(s)}} dy = \frac{\mu_0 G_s^2}{4 |K_s|} [D_{43} + D_{44} e^{-2 |K_s| g} + F_{34} + 2 e^{-2 |K_s| l} (-D_{46} + D_{47} + F_{35}) + e^{-4 |K_s| l} (-D_{44} e^{2 |K_s| g} - D_{49} + F_{36})]. \quad (2-91)$$

For region 4, referring to Eq. (2-72a) and using Eqs. (2-83) and (2-10)

$$\int_g^{g+t_1} b_{y_4} \overline{h_{y_4}^{(s)}} dy = \frac{\mu_0 G_s^2 (\sinh 2 |K_s| t_1 - 2 |K_s| t_1)}{4 |K_s| \sinh^2 |K_s| t_1} \times [D_{51} + D_{52} - D_{53} + 2 e^{-2 |K_s| l} (-D_{54} - D_{55} + D_{56}) + e^{-4 |K_s| l} (D_{57} + D_{58} - D_{59})]. \quad (2-92)$$

Defining as follows and referring to Eq. (2-73a)

$$F_{37} = 2 e^{-2 |K_s| l} (\sinh 2 |K_s| l - 2 |K_s| l) - (\alpha^2 + 1) |K_s| d - 1 \quad (2-92a)$$

$$F_{38} = -(\alpha^2 + 1) |K_s| d + 1 - \left[\frac{(\alpha^2 + 1)}{2\alpha} \sin 2\alpha |K_s| d + \frac{(\alpha^4 - 1)}{4\alpha^2} (1 - \cos 2\alpha |K_s| d) \right] D_{60}$$

and employing Eqs. (2-92), (2-91), (2-89), and (2-87) in Eq. (2-85), we finally get⁵

$$\frac{P^{(s)}}{l_1} = \frac{s \omega \mu_0 G_s^2}{4 |K_s|^2} [F_{37} + D_{62} - D_{63} + D_{64} + D_{65} + e^{-2 |K_s| l} \times (D_{66} - D_{67} - D_{68}) + e^{-4 |K_s| l} (F_{38} - D_{70} + D_{71} + D_{72})] \quad s = -1, 1 \quad (2-93)$$

for the backward volume wave magnetostatic wave power. Here, too, the magnitudes for the two waves, $s = -1, 1$, are identical. The bandwidth for the existence of backward volume waves is

$$\gamma H < f < \gamma \sqrt{H(H + M)}. \quad (2-94)$$

At this point we have obtained expressions for the dispersion relation and magnetostatic wave power for the three cases; surface waves, forward volume waves, and backward volume waves.

2.6 Radiation Resistance, Reactance and Insertion Loss

To find the radiation resistance we need the expression for the transform of the current distribution appearing in Eq. (2-38). For a flat current distribution, for the independent conductors without apodization, the expression employed in the computer programs is,⁶ with $I_0 = 1$

$$|\tilde{J}(K_s)| = \left| I_0 \operatorname{sinc} \frac{aK_s}{2\pi} \frac{1 - \eta^N e^{jK_s p N}}{1 - \eta e^{jK_s p}} \right| \sqrt{l_1} \quad (2-95)$$

where N is the number of conducting strips, a is the strip width and p is the center-to-center spacing, and we define

$$\operatorname{sinc} x = \frac{\sin \pi x}{\pi x}. \quad (2-96)$$

If apodization is included we use

$$|\tilde{J}(K_s)| = \left| \sum_{i=1}^N \operatorname{sinc} \frac{a_i K_s}{2\pi} \eta^i \sqrt{l_{1i}} e^{-jK_s p_{1i}} \right| \quad (2-97)$$

where $\eta = -1$ for a meander line and $\eta = 1$ for a parallel grating.

For a truncated array of normal modes we have, for the fundamental mode

$$|\tilde{J}(K_s)| = \left| \sum_{i=1}^N \operatorname{sinc} \frac{2a_i}{p_i(3 - \eta)} \operatorname{sinc} \left(\frac{K_s p_i}{2\pi} - \frac{3 + \eta}{4} \right) \eta^i \sqrt{l_{1i}} e^{-jK_s p_{1i}} \right| \quad (2-98)$$

The radiation resistance is given by

$$R^{(s)} = \frac{4 |P^{(s)}|}{(1 - \eta) + (1 + \eta)N^2}, \quad s = -1, 1 \quad (2-99)$$

The total radiation resistance is

$$R_m = R^{(1)} + R^{(-1)}. \quad (2-100)$$

6. Weinberg, I. J. (1981) *Analysis and Computer Studies for Magnetostatic Surface Wave Transducers*, RADC-TR-81-96, ADA102207.

The radiation reactance is obtained by numerically evaluating the Hilbert transform⁶

$$x_m = \frac{1}{\pi} \int_{-\infty}^{\infty} \frac{R_m(f')}{f' - f} df' \quad (2-101)$$

2.6.1 TRUNCATED ARRAY (TWO TERMINAL) MODEL

For the truncated array model, the insertion loss is obtained as⁶

$$IL^{(s)} = 20 \log_{10} \frac{4R^{(s)} R_g}{(R_g + R_m + R_L)^2 + (x_m + x_L)^2} - \frac{76.4 \Delta H \Delta r 10^6}{\left| \frac{\partial \omega}{\partial K} \right|} \quad (2-102)$$

where R_g is the source resistance, R_L is the conduction loss and x_L is a series matching reactance. ΔH is a linewidth representing material loss and Δr is a propagation distance. The quantity $\frac{\partial \omega}{\partial K}$ is obtained by numerically differentiating the dispersion relation.

2.6.2 TRANSMISSION LINE MODEL

In the transmission line model we calculate insertion loss from input resistance and reactance of a lossy shorted section of microstrip line and microstrip propagation constants. For one conducting strip we can write, for non-apodization, from Eq. (2-95)

$$\left| \tilde{J}(K_s) \right| = \left| \text{sinc} \frac{aK_s}{2\pi} \right| \sqrt{l_1} \quad (2-103)$$

For N conducting strips we employ array factors to obtain⁶

$$R^{(s)} = \frac{4 \left| P^{(s)} \right|}{(1 - \eta) + (1 + \eta)} \left(\frac{\sin \frac{NK_s p}{2}}{\sin \frac{K_s p}{2}} \right)^2 \quad (2-104)$$

for $\eta = 1$, and

$$R^{(s)} = \frac{4 \left| P^{(s)} \right|}{(1 - \eta) + (1 + \eta)} \left(\frac{\sin \frac{NK_s p}{2}}{\cos \frac{K_s p}{2}} \right)^2 \quad (2-105)$$

for $\eta = -1$ and N even. $\tilde{J}(K_s)$ from Eq. (2-103) is employed in these relations.

Having $R^{(s)}$, $s = -1, 1$, from Eq. (2-104) or (2-105) we obtain R_m and X_m from Eqs. (2-100) and (2-101). Then write

$$\overline{R^{(s)}} = \frac{R^{(s)}}{l_1}, \quad \overline{R_m} = \frac{R_m}{l_1}, \quad \overline{X_m} = \frac{X_m}{l_1} \quad (2-106)$$

Given characteristic Z_0 , propagation constant β_0 , conduction loss constant α_0 and conductivity σ , we have, for one conducting strip, $N = 1$

$$\bar{\beta}_R = \frac{\bar{X}_m}{2Z_0} \quad , \quad \bar{\beta}_c = \beta_0 f$$

$$\bar{\alpha}_R = \frac{\bar{R}_m}{2Z_0} \quad , \quad \bar{\alpha}_c = \frac{c}{a} \alpha_0 \sqrt{f/\sigma} \quad . \quad (2-107)$$

Then, for N strips and $\eta = 1$

$$Z_c = \frac{Z_0}{N} \quad , \quad \alpha_R = \frac{\bar{\alpha}_R}{N} \quad , \quad \alpha_c = \bar{\alpha}_c \quad , \quad \beta_R = \frac{\bar{\beta}_R}{N} \quad , \quad \beta_c = \bar{\beta}_c \quad (2-108)$$

while for $\eta = -1$ and N even

$$Z_c = Z_0 \quad , \quad \alpha_R = \frac{\bar{\alpha}_R}{N} \quad , \quad \alpha_c = \bar{\alpha}_c N \quad , \quad \beta_R = \frac{\bar{\beta}_R}{N} \quad , \quad \beta_c = \bar{\beta}_c N. \quad (2-109)$$

Total attenuation loss is then

$$\alpha = \alpha_R + \alpha_c \quad , \quad \bar{\beta} = \beta_R + \beta_c. \quad (2-110)$$

The input resistance and reactance are then

$$R_{in} = \frac{Z_c \tanh 2\alpha l_1}{1 + \cos 2\bar{\beta} l_1 \operatorname{sech} 2\alpha l_1} \quad (2-111)$$

$$X_{in} = \frac{Z_c \sin 2\bar{\beta} l_1 \operatorname{sech} 2\alpha l_1}{1 + \cos 2\bar{\beta} l_1 \operatorname{sech} 2\alpha l_1} \quad (2-112)$$

and

$$R_{i,m}^{(s)} = R_{in} \frac{\bar{R}_s/2Z_c}{\alpha_c + \bar{R}_m/2Z_c} \quad s = -1, 1 \quad (2-113)$$

$$R_{i,m} = R_{i,m}^{(1)} + R_{i,m}^{(-1)}. \quad (2-114)$$

The insertion loss is then given by⁶

$$IL^{(s)} = 20 \log_{10} \frac{4R_i R_{i,m}^{(s)}}{(R_i + R_{in})^2 + x_{in}^2} - \frac{76.4 \Delta H \Delta r 10^6}{\left| \frac{\partial \omega}{\partial K} \right|} \quad (2-115)$$

where R_i is the source impedance.

References

1. Weinberg, I.J. (1980) Dispersion Relations for Magnetostatic Waves, *Ultrasonics Symposium Proceedings*.
2. Weinberg, I.J. and Sethares, J.C. (1978) *Magnetostatic Wave Transducers with Variable Coupling*, RADC-TR-78-205, ADA063880.
3. Ganguly, A.K. and Webb, D. (1975) Microstrip Excitation of MSSW, *IEEE Trans MTT*, **MTT-23**:998.
4. Weinberg, I.J. (1982) Insertion Loss for Magnetostatic Volume Waves, *IEEE Transactions on Magnetics*.
5. Weinberg, I.J. and Sethares, J.C. (1983) Magnetostatic Volume Waves, *IEEE MTT-S Digest*.
6. Weinberg, I. J. (1981) *Analysis and Computer Studies for Magnetostatic Surface Wave Transducers*, RADC-TR-81-96, ADA102207.

3. MSW PROGRAM DESCRIPTIONS

This chapter provides a description of the Two Terminal, TT, (also known as a Truncated Array, TA) and the Transmission Line, TL, MSW computer program. Programs are written in FORTRAN for the CDC6600 computer with plot routines for the CALCOMP plotter.

There are two main programs: SUR and VOL. The MSSW program utilizes SUR; and MSFVW and MSBVW programs utilize VOL. Input descriptions for SUR and VOL are described in Section 3.1. Updated interactive versions, ISUR and IVOL, are described in Section 3.2. Section 3.3 defines batch files for SUR and VOL. These batch files provide input data and call main programs.

A complete list and brief description of all MSW programs, available on tape, are described in Section 3.4. A combined TT/TL program, for the generalized model described in Chapter 6, Section 6.4, is given in Section 3.5.

3.1 SUR and VOL Program Input Descriptions

In this section we define input variables for the main SUR and VOL programs, and provide sample input variables. The TT (or TA) program requires 7 lines of input variables, denoted as Card 1 through Card 7. The TL program requires 5 lines of input variables, denoted as Card 1 through Card 5.

SUR, as well as VOL, has an option parameter, TTOP, which selects either the TT or TL model. When TTOP=1, the TT model is selected; and, when TTOP=0, the TL model is selected. TTOP appears as the last entry in Card 1. The other 7 entries in Card 1 apply to both TA and TL models.

3.1.1 SURFACE WAVES (SUR)

The TT model has provisions for a linear form of transducer apodization; for strip width, length, and center to center spacing. That is, individual strips in a transducer may have different widths and lengths, and adjacent strips may be separated by different amounts. Weighting between strips in this program must progress in a linear fashion, starting at one end or in the center of the transducer. A more general form of apodization would require program modification. No provisions are made for apodization of the TL model.

Table 3-1 describes input parameters for Card 1. This card is the same for both TT and TL models. Remaining cards for TT (TTOP=1) and TL (TTOP=0) models are treated separately in Sections 3.1.1.1 and 3.1.1.2, respectively.

Table 3-1. Card 1 for TT and TL, SUR

Card 1:	H, T1, D, G, EL, EN, ETA, TTOP
H	Internal, demagnetized, magnetic bias field (oersteds)
T1	Distance between transducer and top ground plane (meters)
D	Thickness of YIG (meters)
G	Gap between transducer and YIG surface (meters)
EL	Distance from bottom ground plane to YIG surface (meters)
EN	Number of transducer strips
ETA=1	for parallel grating, ETA=-1 for meander line
TTOP=0	for TL model, TTOP=1 for TT model

3.1.1.1 TT Model (TTOP=1) SUR

Cards 2, 3, and 4 for the SUR TT model relate to apodization. These apodization cards are not used in the TL model because apodization was not programmed into the TL program. A description of Cards 2 through 7 for TT follows.

Card 2: ELBEGN, ELDEL, ELOPT

- ELBEGN - First strip length, L1 (meters)
- ELDEL - Increment for the remaining strips
- ELOPT - 0 = ELDEL is applied successively to all strips
1 = one half the strips are incremented by ELDEL, then the latter half are decremented by ELDEL

Card 3: ABEGIN, ADEL, AOPT

- ABEGIN - First strip width, 'a', (meters)
- ADEL, AOPT - Serve the same function for strip width 'a', as do ELDEL and ELOPT for strip length, L1

Card 4: PBEGIN, PDEL, POPT

- PBEGIN - Center to center spacing, P, for the first two strips. (If N=1, P is irrelevant)
- PDEL, POPT - Serve same function as stated for L1 and 'a'

Card 5: DELH, DIST, FOPT

- DELH - Linewidth, delta H (oersteds)
- DIST - Distance between transducers, deltaR (meters)
- FOPT - 0 = Normal surface wave bandwidth for both waves
1 = Enlarged bandwidth for one wave (when t1+G and/or L are extremely small)

Card 6: RL, LMODE

- RL - Conduction loss, resistor in series with Rg+Rm
- LMODE - 1 = Truncated infinite array, TT
2 = Normal modes

Card 7: PROGID

- PROGID - Three alphanumeric quantities used for ID plots. First quantity in first 8 columns, second in next 4, and third quantity in next 10 columns.

Motivation for including the FOPT option, see Card 5 above, in the program is that for some combination of input parameters, the dispersion relation is double valued. That is, for a given frequency, there are two values of k satisfying the dispersion relation. This occurs when at least one ground plane is very close to a YIG surface. See, for example, the dispersion curves in Figure 4-18 in Section 4.10.1

Normally, FOPT is set to zero. However, when FOPT=0, and the dispersion relation becomes double valued as frequency is incremented through the MSW bandwidth, a discontinuity occurs in

insertion loss versus frequency plots at the transition frequency where the dispersion relation just becomes double valued. This discontinuity occurs because there is a routine in the program that truncates insertion loss to a constant when the dispersion relation is double valued.

However, experimentally, the passband sometimes continues on past the frequency where the dispersion relation becomes double valued. This is because coupling efficiency to the two modes, defined by their respective K values, is strongly dependent on MSW wavelength. When the wavelength is very small, (large K number) coupling efficiency is very low. Little energy goes into the higher order mode when K is too large. In that case, only the lower K mode is excited. This is reflected in the insertion loss plots.

The FOPT=1 routine allows the calculations to continue as if only the lower K mode is present, and this generally shows up as a much wider bandwidth, sometimes almost a factor of 2 wider.

Table 3-2 provides a set of sample input data for the SUR, TT model.

Table 3-2. Input Data for SUR TT

<u>Card 1</u>	890., .254E-3, .2E-4, 0., 1., 1., 1., 1.
<u>Card 2</u>	.004, 0., 0.
<u>Card 3</u>	25.4E-6, 0., 0.
<u>Card 4</u>	300.E-6, 0., 0.
<u>Card 5</u>	.2, .01, 0.
<u>Card 6</u>	35., 1
<u>Card 7</u>	USERNAME1836SURFACEWAVE

3.1.1.2 TL Model (TTOP=0) SUR

Card 1 is described in Table 3-1, as it is identical to Card 1 in the TT model. Cards 2 through 5 are described separately below.

Card 2: ELBEGN, ABEGIN, PBEGIN

- ELBEGN - Strip length, L1, in meters
- ABEGIN - Strip width, A, in meters
- PBEGIN - Center to center spacing, P, in meters

Card 3: DELH, DIST, FOPT

- DELH - Linewidth, deltaH (oersteds)
- DIST - Distance between transducers, deltaR (meters)
- FOPT - 0 = Normal surface wave bandwidth for both waves
1 = Enlarged bandwidth for one wave (when t1+G and/or L are extremely small)

Card 4: ZC, BTC, SIG, ACC

- Four parameters for the unperturbed transmission line
- ZC - Characteristic impedance in ohms

- BTC - Propagation constant parameter
The propagation constant, BT, in inverse meters is defined by:
 $BT = BTC \times FMHZ$
- SIG - Conductivity in mhos/m
- ACC - Attenuation constant parameter
The attenuation constant, AC, in inverse meters is defined by:
 $AC = [8.68ACC \times \sqrt{PI \times MUO \times FCPS / SIG}] / T1$, where FCPS=frequency
in cycles per second

Card 5: PROGID

- PROGID - Three alphanumeric quantities used for ID plots. First quantity in first 8 columns, second in next 4, and third quantity in next 10 columns.

Table 3-3 provides a set of sample input data for the SUR TL model.

Table 3-3. Input Data for SUR TL

<u>Card 1</u>	890., 254.E-6, .2E-4, 0., 1., 1., 1., 0.
<u>Card 2</u>	.004, 25.4E-6, 300.E-6
<u>Card 3</u>	.2, .01, 0.
<u>Card 4</u>	96., .045, 3.72E3, .093
<u>Card 5</u>	USERNAME 1836 SURFACEWAVE

3.1.2 VOLUME WAVES (VOL)

The VOL program handles both MSFVW and MSBVW. There is a built in option to select forward or backward volume waves. The TT option of VOL requires seven lines of input variables, and the TL option requires 5 lines of input variables. Table 3-4 describes input parameters for Card 1 and Card 2. Cards 1 and 2 apply to both TT and TL for VOL.

Table 3-4. VOL for TT and TL

Card 1:	H, T1, D, EL, ENM, OPN, G, TTOP
	ENM - Thickness mode number
	ENM=0 for fundamental mode
	OPN - 0.=MSFVW, 1.=MSBVW
	All other parameters as in SUR
Card 2:	DELH, DIST, EN, ETA
	All quantities as in SUR

The remaining cards for TT (TTOP=1) and TL (TTOP=0) are each treated separately in Sections 3.1.2.1 and 3.1.2.2, respectively.

3.1.2.1 TT Model (TTOP=1) VOL

All quantities in Cards 3 through 7, below, are as defined in the TT SUR program.

Card 3: ELBEGN, ELDEL, ELOPT

Card 4: ABEGIN, ADEL, AOPT

Card 5: PBEGIN, PDEL, POPT

Card 6: RL

Card 7: PROGID

Table 3-5 provides sample input data for TT VOL

Table 3-5. Input Data for VOL TT

<u>Card 1</u>	1250., 254.E-6, .2E-4, 1., 0., 0., 0., 1.
<u>Card 2</u>	.2, .01, 1., 1.
<u>Card 3</u>	.004, 0., 0.
<u>Card 4</u>	25.4E-6, 0., 0.
<u>Card 5</u>	300.E-6, 0., 0.
<u>Card 6</u>	35.
<u>Card 7</u>	USERNAME 1836 FOWARDVOLM

3.1.2.2 TL Model (TTOP=0) VOL

All quantities in Cards 3, 4, and 5 are as in SUR TL.

Card 3: ELBEGN, ABEGIN, PBEGIN

Card 4: ZC, BTC, SIG, ACC

Card 5: PROGID

Table 3-6 provides sample input data for VOL TL.

Table 3-6. Input Data for VOL TL

<u>Card 1</u>	1250., 254E-6, .2E-4, 1., 0., 1., 0., 0.
<u>Card 2</u>	.2, .01, 1., 1.
<u>Card 3</u>	.0004, 25.4E-6, 300.E-6
<u>Card 4</u>	96., .045, 3.72E3, .093
<u>Card 5</u>	USERNAME 1836 BACWADWAVE

3.2 Interactive Programs, Inputs and Procedures

The SUR and VOL programs have been updated to include saturation magnetization as an input parameter, and to make the programs more interactive. The updated programs are designated ISUR and IVOL.

In SUR and VOL the saturation magnetization is a fixed constant. In addition, when SUR and VOL are run, all calculated data are stored in tables. Plots are obtained from the tables at a later time.

In ISUR and IVOL, saturation magnetization is an input parameter. In addition, when programs are run, plots are obtained immediately while the program is executing. This allows parameters to be changed and their effects seen, interactively.

During a break in program execution, type in one or zero at the prompt, to select TT or TL programs.

3.2.1 SURFACE WAVES (ISUR)

Input data for ISUR is identical with SUR except for Card 1. Replace Card 1 with Line 1 as given below.

Line 1: H, T1, D, G, EL, EN, ETA, PI4M

All quantities except for PI4M are as described in SUR. PI4M is the saturation magnetization in Gauss.

3.2.2 VOLUME WAVES (IVOL)

Input data for IVOL is identical with VOL except for Card 1. Replace Card 1 with Line 1 as given below.

Line 1: H, T1, D, EL, ENM, OPN, G, PI4M

All quantities except for PI4M are as described in VOL. PI4M is the saturation magnetization in Gauss.

3.2.3 INTERACTIVE PROGRAMS

There are five interactive programs as listed below.

1. ISUR - Main Surface Wave Program
 TAPE1 for TT
 TAPE2 for TL
2. ISURN - Surface Waves, combined model, TAPE3 for TT/TL
3. IVOL - Main Volume Wave Program
 TAPE4 for TT
 TAPE5 for TL
4. ISURP - Surface Wave Dispersion, TAPE7
5. ISUWM - Surface Wave Dispersion with Width Modes, TAPE8

Output data for all of these programs is stored on TAPE6. When a program is run, the following three options are possible.

1. Interactive or pen plots
2. Line printer output
3. Terminal output

3.2.4 PROGRAM EXECUTION PROCEDURES

Example procedures for executing three of the interactive programs, ISUR, ISURN, and ISURP, are given below in Sections 3.2.4.1, 3.2.4.2, and 3.2.4.3, respectively. The procedures are for NOS, the present network operating system for the CYBER.

3.2.4.1 ISUR

The following procedure is used for running the interactive surface wave program, ISUR, which uses TAPE1 for input data to TT, and TAPE2 for input data to TL.

PROCEDURE:

/GET, ISUR

/GET, TAPE1 or TAPE2

For printer output and/or pen plots, use

/GET, PEN=OFFPEN4/UN=PLIB

/LIBRARY, PEN

or, for interactive plots with or without printed output, use

/ATTACH, TEK=TEKSIM/UN=PLIB

/LIBRARY, TEK

/FTN, I=ISUR

/LGO

? 1 for TT

0 for TL

Interactive plots are automatic.

After program runs, replace tape.

/REPLACE, TAPE6 'also provides for printed output

/XEDIT, TAPE6 'for terminal output

/ROUTE, TAPE6, DC=LP, UJN=name 'for line printer

/ROUTE, TAPE39, DC=PL, ID=62, TID=C 'for penplots

/RETURN, TAPE39 'if plots not needed

/REWIND, LGO 'when more cases are to be run

3.2.4.2 ISURN

The following procedure is used for running the interactive combined TT/TL surface wave program, ISURN, which uses TAPE3 for input data to TT/TL.

PROCEDURE:

/GET, ISURN

/GET, TAPE3

For printer output and/or penplots, use

```
/GET, PEN=OFFPEN4/UN=PLIB  
/LIBRARY, PEN
```

or, for interactive plots with or without printed output, use

```
/ATTACH, TEK=TEKSIM/UN=PLIB  
/LIBRARY, TEK  
/FTN, ISURN  
/LGO 'interactive plots are automatic  
/REPLACE, TAPE6 'also provides for printed output  
/XEDIT, TAPE6 'for printed output on terminal  
/ROUTE, TAPE6, DC=LP, ID=62, UJN=name 'for line printer  
/ROUTE, TAPE39, DC=PL, ID=62, TID=C 'for penplots  
/RETURN, TAPE39 'if plots not needed  
/REWIND, LGO 'when more cases are to be run.
```

3.2.4.3 ISURP

The following procedure is used for running the interactive surface wave dispersion program, ISURP, which uses TAPE7 for input data.

PROCEDURE:

```
/GET, ISURP  
/GET, TAPE7
```

For printer output and/or pen plots, use

```
/GET, PEN=OFFPEN4/UN=PLIB  
/LIBRARY, PEN
```

or, for interactive plots with or without printed output, use

```
/ATTACH, TEK=TEKSIM/UN=PLIB  
/LIBRARY, TEK  
/FTN, ISURP  
/LGO 'interactive plots are automatic  
/REPLACE, TAPE6 'also provides for printed output  
/XEDIT, TAPE6 'for printed output on terminal  
/ROUTE, TAPE6, DC=LP, ID=62, UJN=name 'for line printer  
/ROUTE, TAPE39, DC=PL, ID=62, TID=C 'for penplots  
/RETURN, TAPE39 'if plots not needed  
/REWIND, LGO 'when more cases are to be run
```

3.3 Input Data Batch Files for SUR and VOL

When it is required to change input data frequently, it is convenient to use Input Data Batch Files which contain the input data, and execute main programs, SUR or VOL.

Tables 3-7 through 3-10 provide four such programs for the CYBER NOS system. The four Input Data Batch Files are identified as SURTTC, SURMMC, VOLTTC, and VOLMMC. The last letter in these names, C, designates a composite file. TT designates the two terminal model, and MM the microstrip (transmission line) model.

Table 3-7. SURTTC - Surface Wave, TT, Composite, Input Data Batch File

```
SETH, T40, CM142000.
USER, SETHARE, SETHARE.
CHARGE, 3282, 2305.
GET, X=SUR.
FTN, I=X, R=0.
GET, PEN=OFFPEN4/UN=PLIB.
LIBRARY, PEN.
LGO.
ROUTE, TAPE39, DC=PL, ID=62, TID=C.
--EOR--
0375.0, .2286E-3, .300E-4, .254E-4, .100E1, 1., 1., 1.
.300E-2, 0., 0.
.500E-4, 0., 0.
.300E-3, 0., 0.
.50E0, .01, 0.
0., 1
SETHARES1836SURFACE TT

COMMENTS FOLLOW
DATA CARDS FOR 2 TERMINAL MODEL:
CARD 1 -- H, T1, D, G, L, N, ETA, TTOP
CARD 2 -- L1 1ST, DEL L1, L1 OPT
CARD 3 -- A 1ST, DEL A, A OPT
CARD 4 -- P 1ST, DEL P, P OPT
CARD 5 -- DEL H, DEL R, F OPT
CARD 6 -- RLOSS, LMODE
CARD 7 -- PLOT ID CARD

TTOP=1.    2 TERMINAL MODEL    TTOP=0.    MICROSTRIP MODEL
FOPT=0.    NORMAL BANDWIDTH    FOPT=1.    LARGER BANDWIDTH
LMODE=1    UNIFORM CONDUCTORS   LMODE=2    NORMAL MODES
--EOR--
```

Table 3-8. SURMMC - Surface Wave, TT, Composite, Input Data Batch File

```

SETH, T040, CM142000.
USER, SETHARE, SETHARE.
CHARGE, 3282, 2305.
GET, X=SUR
FTN, I=X, R=0.
GET, PEN=OFFPEN4/UN=PLIB.
LIBRARY, PEN.
LGO.
ROUTE, TAPE39, DC=PL, ID=62, TID=C.
--EOR--
0375.0, .2286E-3, .3E-4, .254E-4, 1., 1., 1., 0.
.003, .5E-4, .3E-3
.5, .01, 0.
86., .045, 3.72E7, .053
SETHARES1836SURFACE MS

COMMENTS FOLLOW
TTOP=1.    2 TERMINAL MODEL    TTOP=0.    MICROSTRIP MODEL
FOPT=0.    NORMAL BANDWIDTH    FOPT=1.    LARGER BANDWIDTH

DATA CARDS FOR MICROSTRIP MODEL:
CARD 1 -- H, T1, D, G, L, N, ETA, TTOP
CARD 2 -- L1, A, P
CARD 3 -- DEL H, DEL R, F OPT
CARD 4 -- ZC, BTC, SIGMA, ALPHA C
CARD 5 -- PLOT ID CARD
--EOR--

```

Table 3-9. VOLTTC - Volume Wave, TT, Composite, Input Data Batch File

```

SETH, T040, CM142000.
USER, SETHARE, SETHARE.
CHARGE, 3282, 2305.
GET, X=VOL.
FTN, I=X, R=0.
GET, PEN=OFFPEN4/UN=PLIB.
LIBRARY, PEN.
LGO.
ROUTE, TAPE39, DC=PL, ID=62, TID=C.
--EOR--
893., 250.E-6, 25.E-6, 1., 0., 1., 25.E-6, 1.
.5, .01, 4., 1.
.300E-2, 0., 0.
.500E-4, 0., 0.
.300E-3, 0., 0.
0.
SETHARES1836 VOLUME TT

COMMENTS FOLLOW
DATA CARDS FOR 2 TERMINAL MODEL:
CARD 1 -- H, T1, D, L, MODE NO., OPTION, G, TTOP
CARD 2 -- DEL H, DEL R, N, ETA
CARD 3 -- L1 1ST, DEL L1, L1 OPT
CARD 4 -- A 1ST, DEL A, A OPT
CARD 5 -- P 1ST, DEL P, P OPT
CARD 6 -- RLOSS
CARD 7 -- PLOT ID CARD

TTOP=1.    2 TERMINAL MODEL          TTOP=0. MICROSTRIP MODEL
OPTION=0.  FORWARD WAVES             OPTION=1.  BACKWARD WAVES
MODE NO. (EX: MODE NO.=0. FIRST MODE)
--EOR--
--EOR--
END OF FILE

```

Table 3-10. VOLMMC - Volume Wave, TL, Composite, Input Data Batch File

```

SETH, T040, CM142000.
USER, SETHARE, SETHARE.
CHARGE, 3282, 2305.
GET, X=VOL.
FTN, I=X, R=0
GET, PEN=OFFPEN4/UN=PLIB.
LIBRARY, PEN.
LGO.
ROUTE, TAPE39, DC=PL, ID=62, TID=C.
--EOR--
893., 250.E-6, 25.E-6, 1., 0., 1., 25.E-6, 0.
.5, .01, 4., 1.
.003, 50.E-6, 300.E-6
80., .05, 1.E30, .055
SETHARES1836 VOLUME MM

COMMENTS FOLLOW
DATA CARDS FOR MICROSTRIP MODEL:
CARD 1 -- H, T1, D, L, MODE NO., OPTION, G, TTOP
CARD 2 -- DEL H, DEL R, N, ETA
CARD 3 -- L1, A, P
CARD 4 -- ZC, BTC, SIGMA, ALPHA C
CARD 5 -- PLOT IDCARD

(TTOP=1. 2 TERMINAL MODEL)          TTOP=0.    MICROSTRIP MODEL
OPTION=0. FORWARD WAVES             OPTION=1.  BACKWARD WAVES
MODE NO. (EX: MODE NO.=0. FIRST MODE)

--EOR--
--EOR--
END OF FILE

```

3.4 Complete List of MSW Program Files

There are about forty MSW computer programs. All of them are stored on Tape CC1159, which is maintained at AFGL's CYBER Input/Output Section. Tape CC1159 is backed up by Tape M7503 which is maintained at RADC/EEAC.

Table 3-11 lists all MSW programs filed on Tape CC1159. Included in the list is other relevant information about files stored on the tape. Tape CC1159 is catalogued in RECLAIM system memory. This means that files can be listed, without loading the tape on a drive, by using the following NOS system command: /RECLAIM,Z./LIST, TN=CC1159.

Table 3-11. Files on CC1159

RECLAIM, Z./LIST, TN=CC1159			UN=SETHARE 88/09/07.		09.36.49.
RECLAM V4.2		OP=LIST	USERNAME: SETHARE		TAPE: CC1159
PFN	TYPE	LAST MOD	LENGTH	FI	REC
COPY80	I	85/11/27	1	4	1
DISURC	I	84/10/02	4	1	6
DISURP	I	84/10/02	11	1	2
DSURC	I	84/10/02	4	1	7
DSURN	I	86/04/18	5	7	1
DSURP	I	84/10/02	16	1	10
DUM	I	84/10/02	1	1	11
DVOLC	I	84/10/02	4	1	9
DVOLP	I	84/10/02	17	1	1
IFVDSP	I	87/09/15	18	11	6
ILGVC	I	84/10/02	4	1	22
IFGVP	I	84/10/02	37	1	23
ISUR	I	87/09/15	46	11	1
ISURN	I	87/09/15	45	11	2
ISURP	I	87/09/15	16	11	4
ISUWM	I	87/09/15	17	11	5
IVOL	I	87/09/15	47	11	3
LIST	I	84/10/02	1	1	12
LOAD	I	84/10/02	1	1	4
LOAD1	I	84/10/02	1	1	5
MS5	I	85/12/05	85	3	1
NMSW	I	85/12/04	5	3	2
NSSN	I	86/04/18	45	8	1
PLT5	I	86/04/18	4	6	2
SETLOAD	I	84/10/02	3	1	21
SPJ	I	86/04/18	5	8	2
SSN	I	85/12/04	45	2	1
SUDN	I	86/04/08	5	6	1
SUR	I	84/10/02	45	1	15
SURJ	I	86/04/18	44	8	3
SURMMC	I	84/10/02	4	1	13
SURN	I	86/04/08	44	5	1
SURTTC	I	84/10/02	5	1	8
TAPE1	I	87/09/15	5	9	1
TAPE2	I	87/09/15	4	9	2
TAPE3	I	87/09/15	5	9	3
TAPE4	I	87/09/15	4	10	1
TAPE5	I	87/09/15	4	10	2
TAPE7	I	87/09/15	4	10	3
TAPE8	I	87/09/15	4	10	4
TAPE9	I	87/09/15	4	10	5
VOL	I	84/10/02	46	1	16
VOLMMC	I	84/10/02	4	1	17
VOLTTC	I	84/10/02	5	1	14
VSC	I	84/10/02	4	1	3
VSP	I	84/10/02	26	1	19
WMFVC	I	84/10/02	4	1	18
WMFVP	I	84/10/02	32	1	20
XX	I	85/11/27	95	4	2

49 FILES PROCESSED.
RECLAIM COMPLETE.

Tables 3-12 and 3-13 provide a brief description of all files on Tape CC1159.

Table 3-12. File Description for Tape CC1159

<u>MAIN SURFACE WAVE PROGRAMS</u>	
SUR	Main MSSW program
SURTTTC	Batch file, contains input data and calls SUR TT
SURMMC	Batch file, contains input data and calls SUR TL
<u>MAIN VOLUME WAVE PROGRAMS</u>	
VOL	Main MSFVW and MSBVW programs
VOLTTTC	Batch file, contains input data and calls VOL TT
VOLMMC	Batch file, contains input data and calls VOL TL
<u>MAIN INTERACTIVE SURFACE WAVE PROGRAMS</u>	
ISUR	Main interactive MSSW program
Tape1	Input data for ISUR TT
Tape2	Input data for ISUR TL
ISURP	Interactive MSSW dispersion relation
Tape7	Input data for ISURP
ISUWM	MSSW dispersion for width modes
Tape8	Input data for ISUWM
<u>MAIN INTERACTIVE VOLUME WAVE PROGRAMS</u>	
IVOL	Main interactive MSBVW and MSFVW programs
Tape4	Input data for IVOL TT
Tape5	Input data for IVOL TL
IFVDSP	Interactive MSFVW with 4PIM and width modes
Tape9	Input data for FVW with width modes
<u>GENERALIZED COMBINED TT/TL SURFACE WAVE PROGRAMS</u>	
SURN	Main combined TT/TL MSSW program
DSURN	Input data and calling program for SURN
ISURN	Main interactive combined TT/TL MSSW program
Tape3	Input data for ISURN

Table 3-13. File Description for Tape CC1159 (Continued).
Modified and Extended Programs

SURJ	SUR with J(k) a circular Bessel Function
SPJ	Input data and calling program for SURJ
MS5	SUR with J(k) and k using Chapter 8 analysis
PLT5	Input data and calling program for MS5
NSSN	Signal/Noise, S/N, enhancer configuration program
SSN	S/N enhancer configuration working program
NMSW	Input data and calling program for NSSN
ILGVP	Generalized volume wave working program
ILGVC	Input data and calling program for ILGVP
DSURP	Dispersion for nonpure surface waves
DSURC	Calls DSURP
DVOLP	Dispersion for nonpure volume waves
DVLOC	Calls DVOLP
VSP	Nonpure modes, VOL + SUR
VSC	Calls VSP
WMFVP	Width modes for MSFVW
WMFVC	Calls WMFVP
DISURP	MSSW dispersion for pure modes
DISURC	Input data and calling program for DISURP
<u>Miscellaneous Programs Listed</u>	
COPY80	Used for data handling during program execution
SETLOAD	Calling program for other files
DUM	RECLAIM dump batch file
SUDN	Replaced by DSURN
LOAD	Empty file
LOAD1	Empty file
LIST	Empty file
XX	System working file

3.5 Combined TT/TL Program

The main combined TT/TL surface wave program is SURN. Its calling program and input data batch file is DSURN. A listing of DSURN is given in Table 3-14.

Table 3-14. DSURN - Combined TT/TL Input Data Batch File

```
WEIN, T50.
USER, WEINB, WEINB.
CHARGE, 0387, 2305.
GET, X=SURN.
FTN, I=X, R=0, SL.
GET, PEN=OFFPEN4/UN=PLIB.
LIBRARY, PEN.
LGO.
ROUTE, TAPE39, DC=PL, ID=62, TID=C.
--EOR--
0375.0, .2286E-3, .300E-4, .254E-4, .100E1, 1., 1., 1.
.300E-2, 0., 0.
.500E-4, 0., 0.
.300E-3, 0., 0.
.50E0, .01, 0.
0., 1
86., .045, 3.72E7, .053, 0.
WEINBERGSURNNEW OPT SU

COMMENTS FOLLOW
DATA CARDS FOR COMBINED OPTION MODEL:
CARD 1 -- H, T1, D, G, L, N, ETA, TTOP
CARD 2 -- L1 1ST, DEL L1, L1 OPT
CARD 3 -- A 1ST, DEL A, A OPT
CARD 4 -- P 1ST, DEL P, P OPT
CARD 5 -- DEL H, DEL R, F OPT
CARD 6 -- RLOSS, LMODE
CARD 7 -- ZC BTC, SIG, ACC, RLOAD
CARD 8 -- PLOT ID CARD

TTOP=1.    2 TERMINAL MODEL    TTOP=0.    MICROSTRIP MODEL
FOPT=0.    NORMAL BANDWIDTH    FOPT=1.    LARGER BANDWIDTH
LMODE=1    UNIFORM CONDUCTORS  LMODE=2    NORMAL MODES
--EOR--
--EOR--
END OF FILE
```

4. COMPUTER GENERATED DATA

This chapter contains computer generated plots based on the analysis and computer programs presented in this report. A range of input parameters is chosen to illustrate results.

4.1 Independent Conductors and Normal Mode Models

Figure 4-1 illustrates a fundamental difference between the independent conductor model and the normal mode model. Both models give essentially identical results at frequencies close to the fundamental response of the transducer, known as synchronism. At synchronism, the MSW wavelength is equal to the fundamental spatial period, p , of the transducer, 300 μm in this case.

For this case synchronism occurs at 3245 MHz as can be seen in Figure 4-1. There is a slight difference in sidelobe levels, in the predictions of the two models, at the first near-in sidelobe. At frequencies far from synchronism the normal mode analysis is not useful. The normal mode model is accurate for narrow band responses. The sharp response near 3480 MHz in the independent conductor response is the second spatial harmonic; that is, the MSW wavelength there is 150 μm . The normal mode analysis will produce the 3450 MHz response when the mode index value, n , is incremented by 2. (This is illustrated later in Figure 4-4.)

4.2 TT and TL Models

Figure 4-2 compares insertion loss response of the two terminal independent conductor model, TT, with the transmission line, TL, model, for multibar grating transducers. The solid line is for TT and the dashed line for TL models. Note that the position of zeros in insertion loss are in very close agreement. Differences in absolute insertion loss, IL values, are not significant here. The absolute IL values are in agreement when the same loss is included in each model. The important point here is that the position of zeros is a result of employing superposition principles. Superposition of independent conductor responses is assumed in both models.

4.3 MSSW with No Ground Planes

For magnetostatic surface waves (MSSW) with no ground planes it is possible to solve for the radiation resistance in closed form. This serves as a check point for computer generated data, and it is useful for acquiring general insights into magnetostatic wave characteristics. We have been unsuccessful, however, in solving for radiation reactance in closed form even with no ground planes. Figure 4-3 shows plots of the closed form solutions for radiation resistance for single element MSSW transducers for both plus and minus waves. Plus waves are the ones most strongly excited and have most of their energy concentrated at the YIG surface nearest the transducer. They propagate in the $\mathbf{H} \times \hat{\mathbf{n}}$ direction, where $\hat{\mathbf{n}}$ is a unit vector pointing out of the YIG on the transducer side.

There are several important features illustrated in this figure. First, there is a large difference in radiation resistance for the plus and minus waves. Plotted in the figure is radiation resistance per unit transducer length or aperture, ohms/cm. This means that the transducer efficiency can be controlled by adjusting transducer aperture, L_1 . If we make $L_1 = 1$ cm, then $R_{mp} = 50$ ohms at about

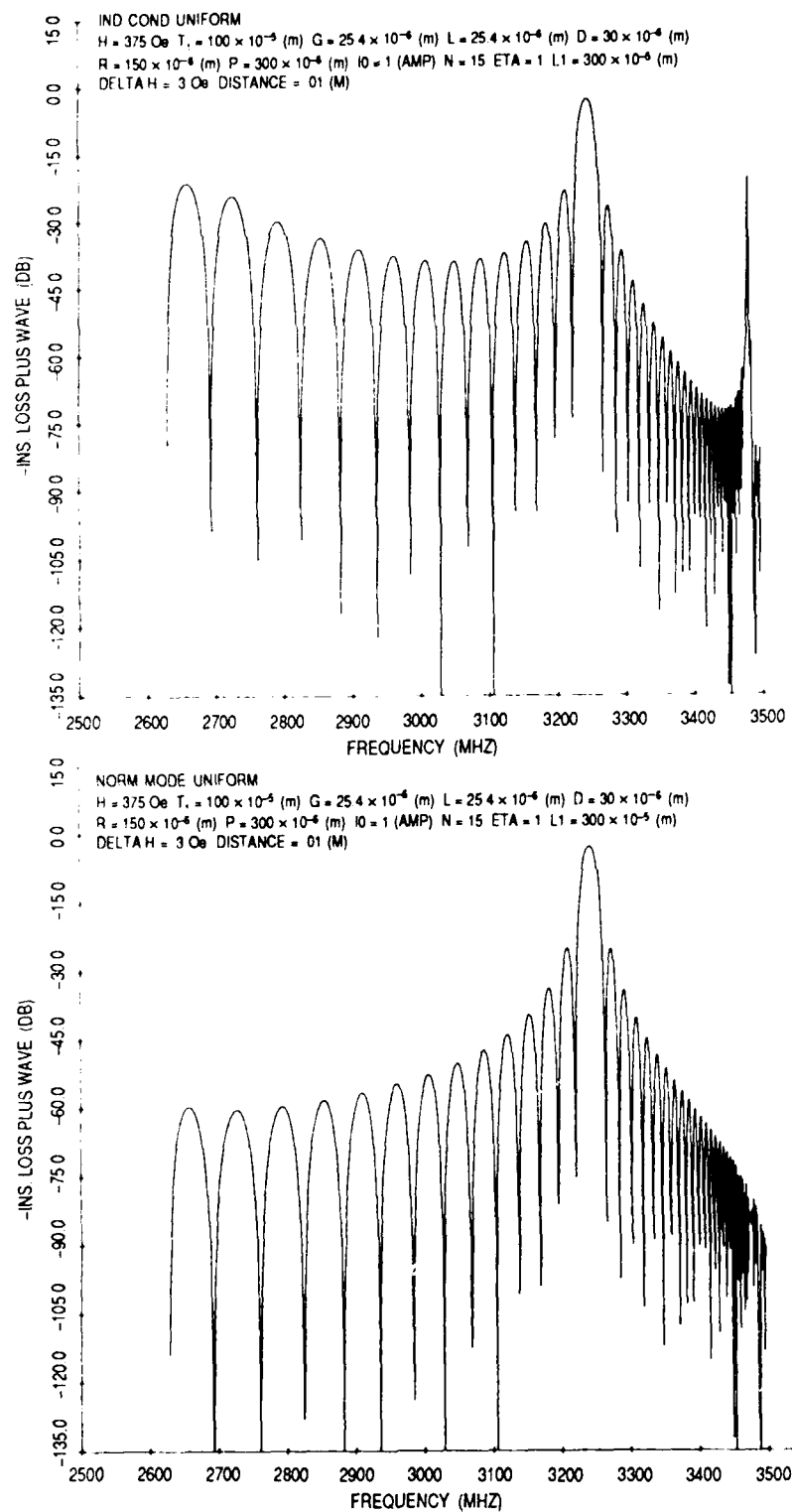


Figure 4-1. Insertion Loss versus Frequency. Response of a pair of 15-element grating transducers in a delay line configuration.

a. Independent conductor analysis, top figure

b. Normal mode analysis, bottom figure

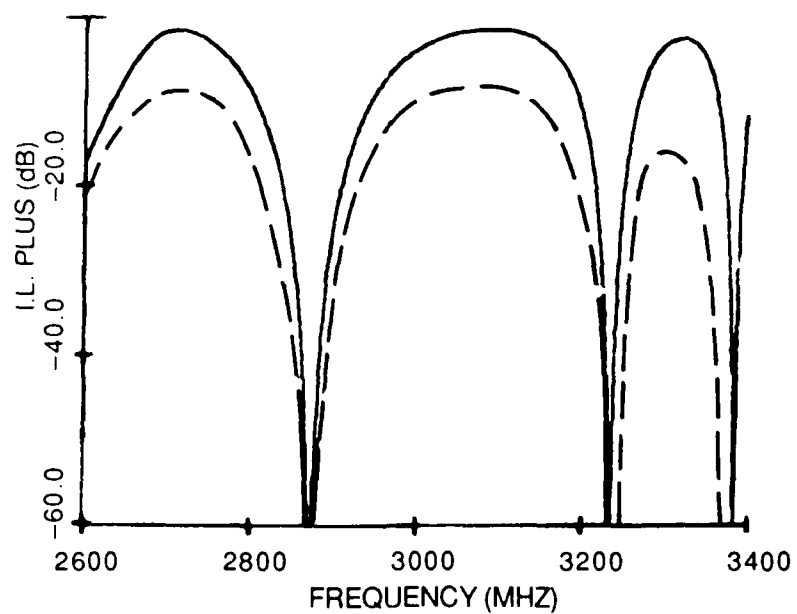
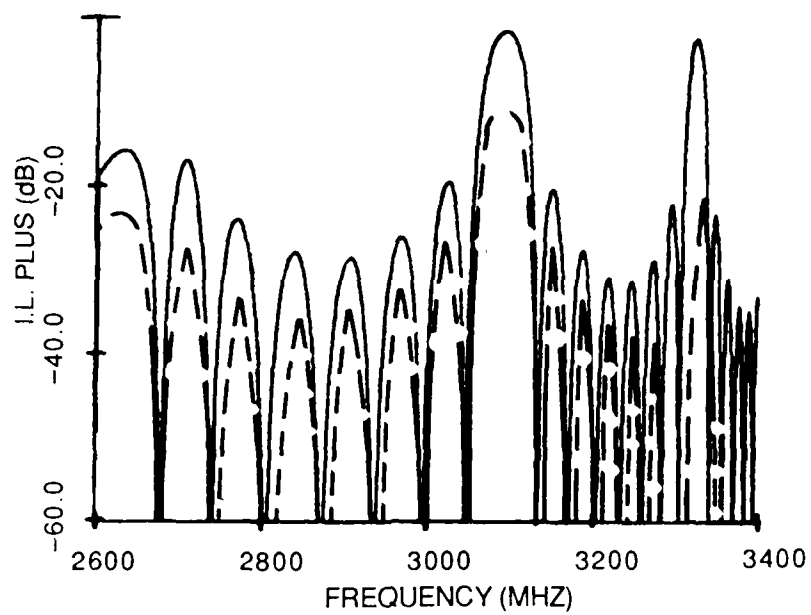


Figure 4-2. Comparison of Two Terminal, TT, Model with Transmission Line, TL, Model

a. 8-element grating transducer, top figure

b. 2-element grating transducer, bottom figure

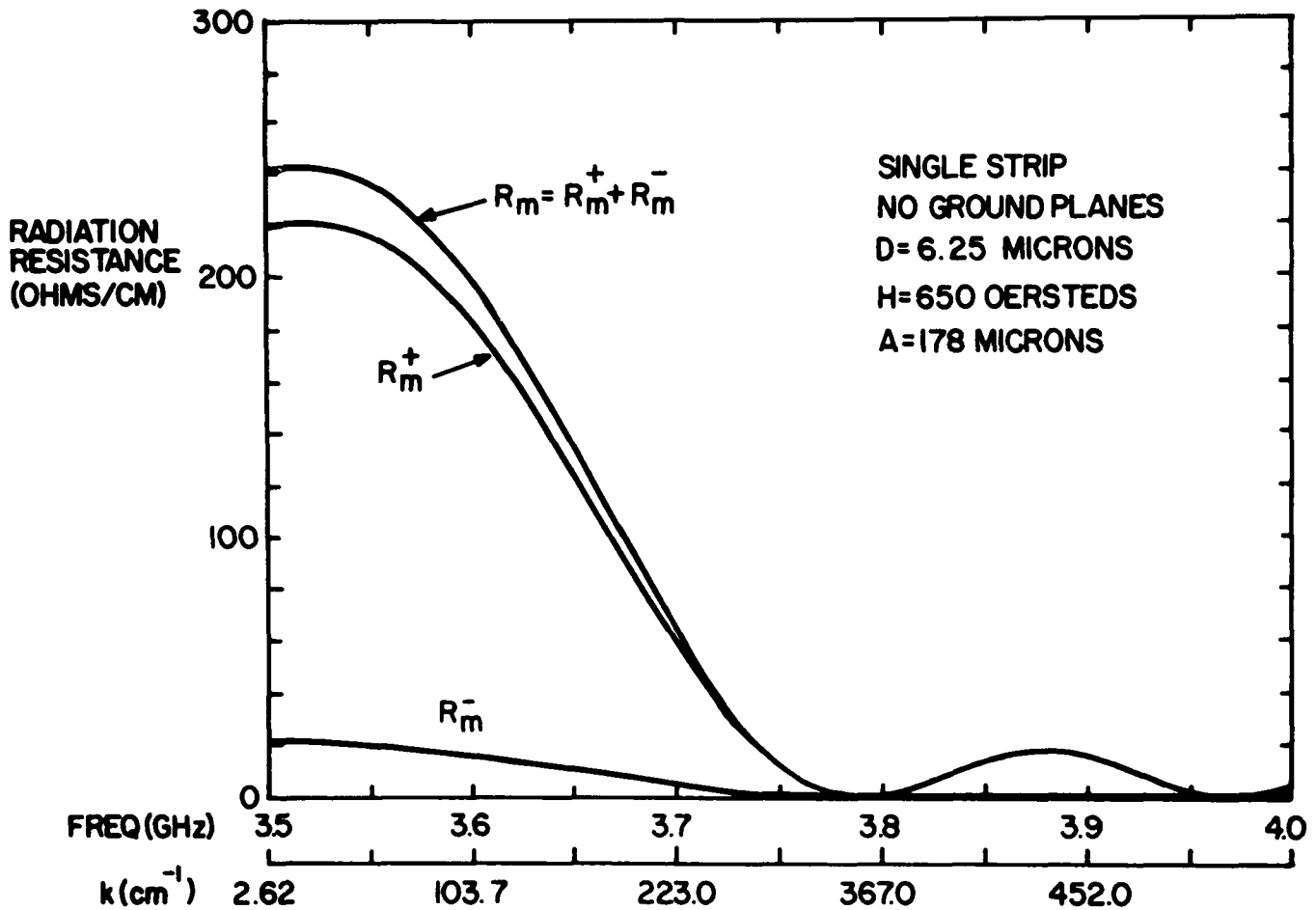


Figure 4-3. Radiation Resistance for Single Strip Transducer with No Ground Planes. MSW wavelength at 3.7 GHz is 282 μm

3.7 GHz. This frequency is efficiently excited in a 50 ohm system. Actually, we need to take into account radiation reactance in order to be accurate. However, we neglect that here for purposes of illustration.

Secondly, the wavelength at 3.7 GHz is 282 μm (wavelength = $2\pi/k$) which is of the same order of magnitude as the strip width A, equal to 178 μm . This result makes physical sense; that is, transducer widths favor the generation of MSW with wavelengths comparable to transducer width. Finally, note that MSW wavelengths are in general large compared to YIG thickness D, equal to 6.25 μm in this case.

Third, the two peaks in radiation resistance occur at k numbers of about 30 and 430 inverse cm. Since $k = 2\pi/\text{wavelength}$, the two wavelengths differ by a factor greater than 10. The shortest wavelength is about 0.15 mm and the longest wavelength is over 2 mm. We expect therefore, that the passband will contain a wide range of wavelengths when using single element transducers.

4.4 Narrow Band Transducers: Meander Line

We now turn to narrow band multielement transducers. Figure 4-4 is a plot of radiation resistance vs frequency for an eight-element meander line transducer. Again, the plus and minus waves are indicated by solid and dashed curves, respectively. Impedance levels of meander line transducers are larger than they are for grating transducers primarily because individual elements in meander lines are connected in series rather than in parallel as they are in grating line transducers.

The analysis presented in this report for meander line transducers breaks down if N , the number of elements, is large. This is because the analysis does not allow large current variations along the meander line length. The criteria for large N is dependent on electromagnetic wavelength compared to meander line length. EM wavelength must be large compared to the stretched out meander line length, NL_1 , in order for the analysis to be valid.

4.4.1 INDEPENDENT CONDUCTOR MODEL

Here in Figure 4-4a, we clearly see five spatial harmonics for the plus wave. These responses were generated with the TT independent conductor strip model. In Figure 4-4b we have plotted two normal mode responses on the same scale. The fundamental and first space harmonic are generated by setting the mode index parameter n equal to 1 and then 3. A comparison of Figures 4-4a and 4-4b again shows the close agreement between the independent conductor model and normal mode model near synchronism.

4.4.2 NORMAL MODE MODEL

In Figure 4-5 peak values of radiation resistance have been labelled with appropriate MSW wavelengths in terms of multiples of periodicity $2P$. The largest radiation resistance occurs at MSW wavelength equal to $2P$. P is the center to center spacing between strips. In a meander line, currents in adjacent strips are oppositely directed. Thus, two strips that are spaced by $2P$ have currents in the same direction. Waves generated by strips $2P$ apart add constructively; waves generated by strips P units apart add destructively, and cancel. This explains the absence of a response at $2P = 2$ wavelengths. Subsequent wavelengths that add constructively are given by $2P = 3, 5, 7, \dots$ wavelengths, as indicated in the figure.

4.4.3 RADIATION RESISTANCE AND GENERATION EFFICIENCY

Radiation resistance does not necessarily decrease as mode index number increases. In Figure 4-6 radiation resistance increases as mode index number increases. An increasing mode index simply defines higher order spatial harmonics.

As radiation resistance increases, it is more difficult to drive current through the strips, so that a large radiation resistance does not imply maximum generation efficiency. Overall efficiency will be determined by the combined effect of radiation resistance, reactance and generator impedance. Figure 4-6 gives radiation resistance and reactance for a multielement transducer, for the TT model. Radiation reactance is actually a Hilbert transform of radiation resistance so it does not constitute fundamental new information. It is needed, however, in the calculation of insertion loss. It is a

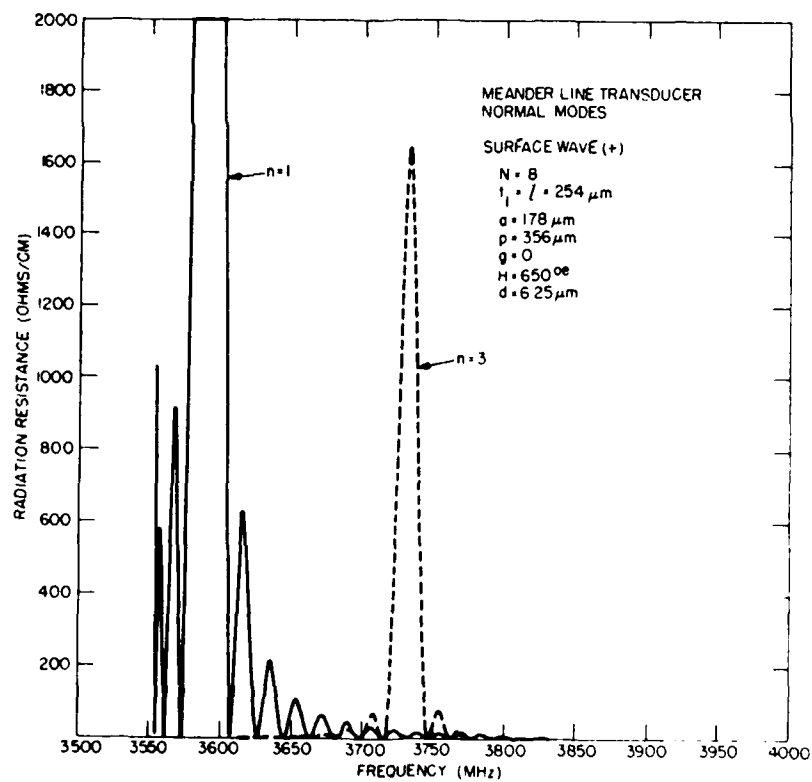
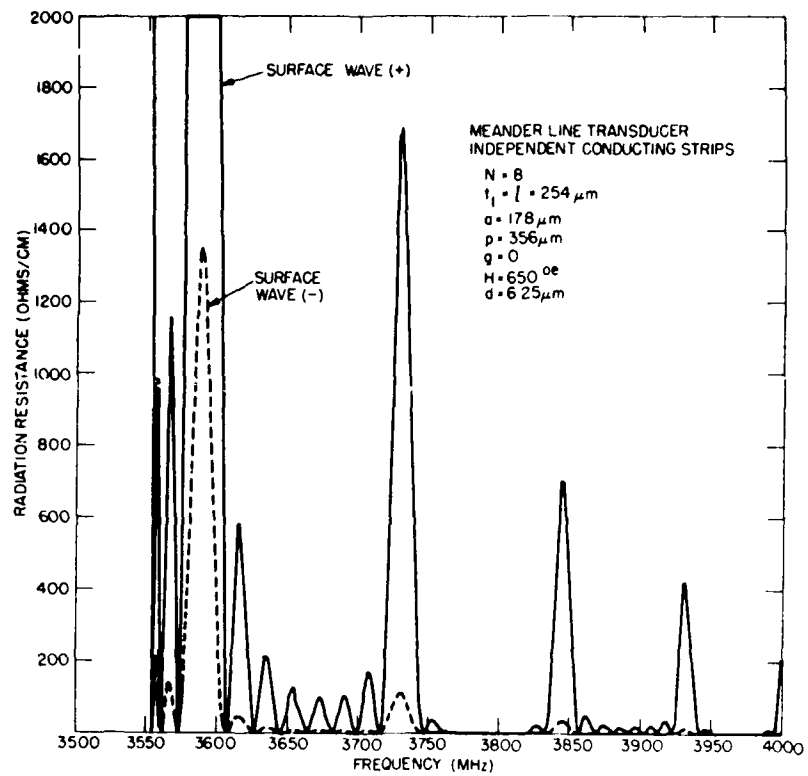


Figure 4-4. Comparison of Independent Conducting Strip Analysis with Normal Mode Analysis
a. Independent Conducting Strips; b. Normal Modes. Two normal mode responses superimposed on the same set of axes.

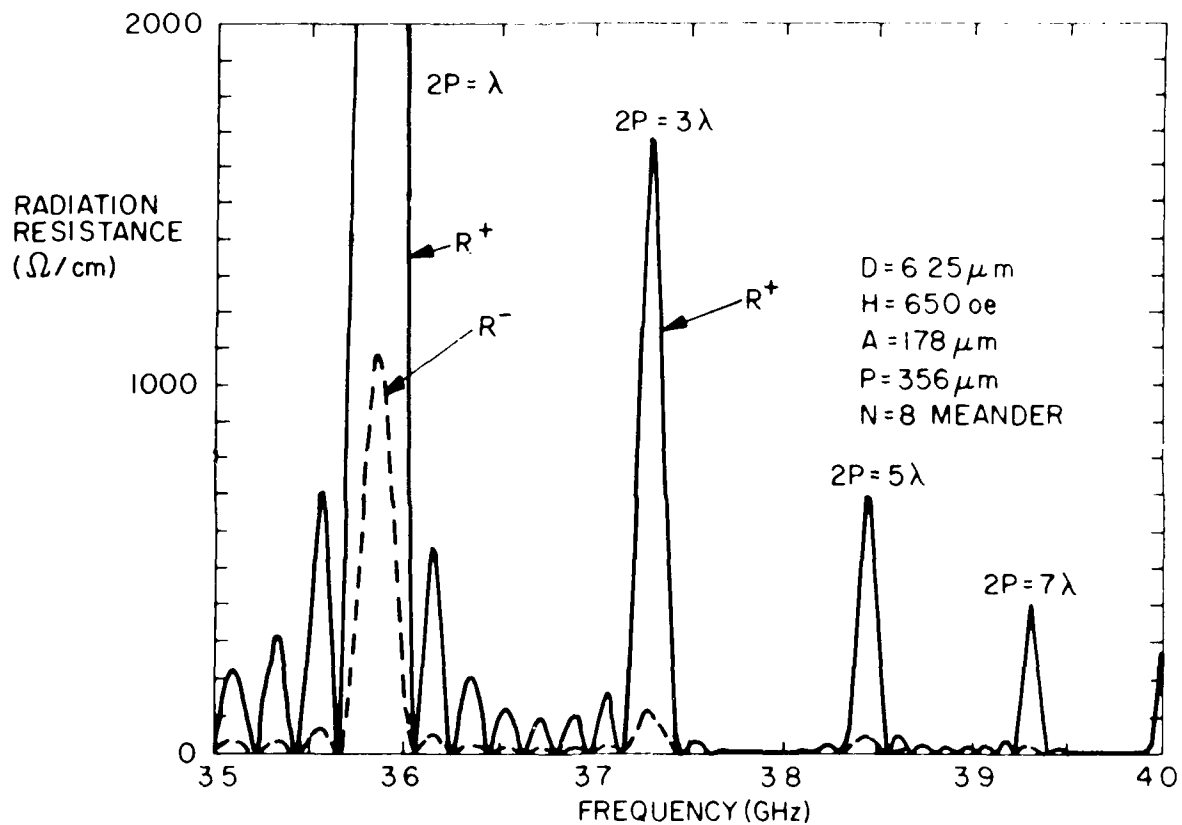


Figure 4-5. Spatial Harmonic Responses. Meander line 8-element transducers. MSW wavelengths are given in terms of center to center strip spacing

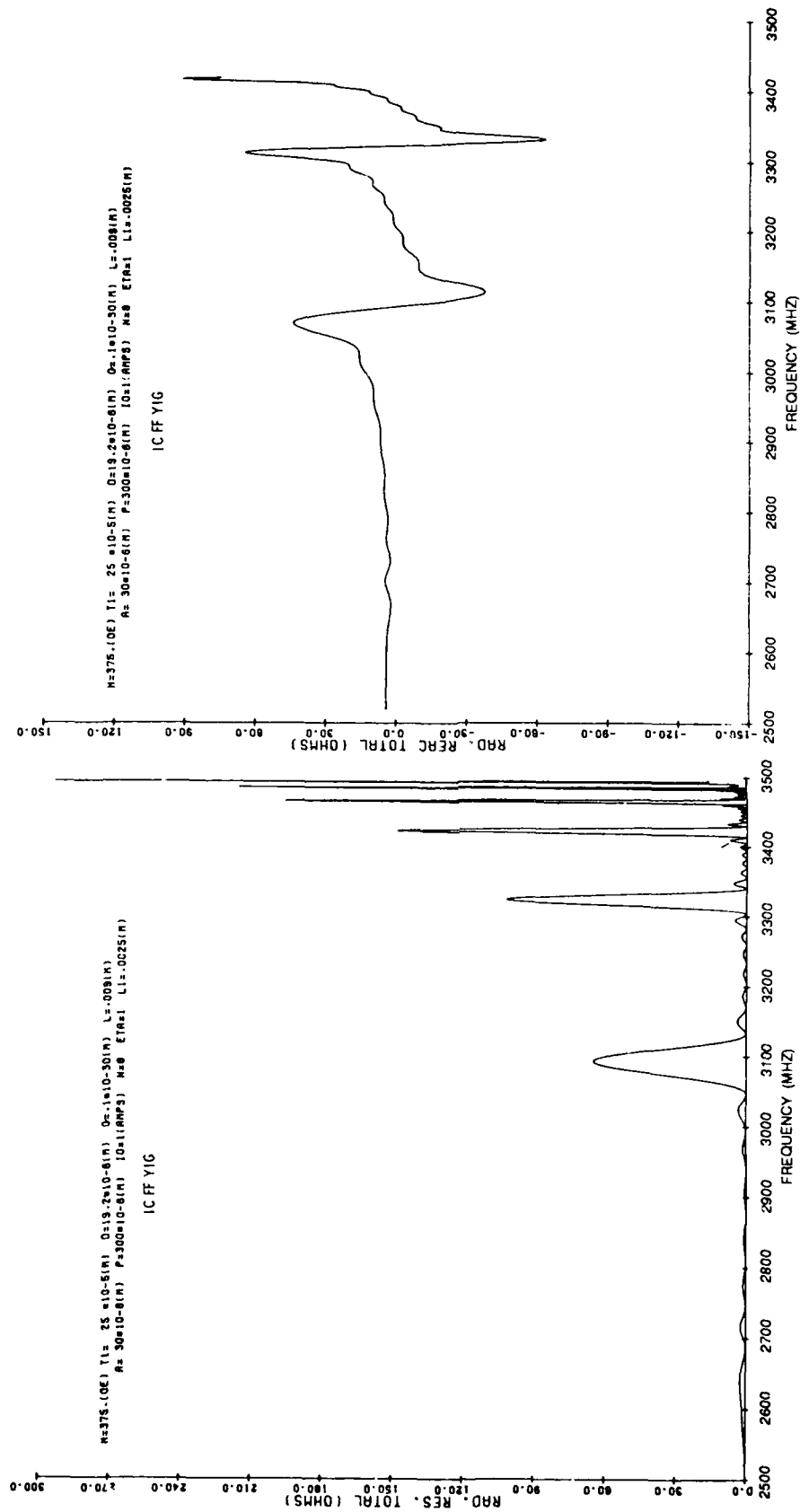


Figure 4-6. Radiation Resistance and Reactance of 8-Element Transducers. For the particular set of parameters chosen, radiation resistance increases with increasing mode number.

measure of transducer electrical reactance and, therefore, affects the amount of current flowing in the conducting strip, for a given applied voltage.

4.5 Liftoff

Figure 4-7 is a plot of radiation resistance versus frequency for different liftoff values, g . Liftoff, g , is the distance between YIG surface and transducer.

Effects of liftoff on insertion loss are shown in Figures 4-8 and 4-9. Figure 4-8 shows how liftoff parameter, G in this case, is defined for these two figures. The figure also shows MSSW wavelength at synchronism (wavelength equals P) and at the first spatial harmonic, where P is twice the wavelength. For small values of liftoff, sidelobe levels decrease faster than the main response, as liftoff is increased. This effect can be used to reduce sidelobe levels in resonator type filters.

Figure 4-9 shows another effect that occurs with large values of liftoff. Large liftoff means large with respect to MSW wavelength. Recall that within the MSSW passband, 2600 to 3400 MHz in this case, the wavelength is largest at the low frequency end of the passband. At synchronism near 3080 MHz the wavelength is equal to the center to center spacing between transducer elements ($P = 300 \mu\text{m}$). Liftoff $g = 150 \mu\text{m}$ for the solid curve. Therefore, the liftoff at synchronism for this case is one half wavelength. This is seen to produce over 30 dB of insertion loss. Near 2600 MHz on the other hand, liftoff is small compared to wavelength so the insertion loss does not increase appreciably with liftoff. This effect can be used to design bandpass filters with very low sidelobes using long wavelength MSWs. This is demonstrated in Section 6.3 of this report.

4.6 Insertion Loss and Linewidth

Figure 4-10 depicts insertion loss versus frequency for MSSW with ferromagnetic resonance linewidth as a parameter. The top curve, $\Delta H = 0$, is for a loss-free system. This is the best that can be done. The bottom curve, $\Delta H = 10$ oersteds, represents a material that is too lossy for potential applications. Losses for the best available material, YIG at the present time, are between $\Delta H = 0$ and $\Delta H = 0.2$ oersteds. This range of linewidths results in insertion losses very close to the ideal lossless case.

There have been reports, see reference 1 in Chapter 1, of polycrystal YIG with linewidths of about one oersted, and that MSW have been observed in polycrystal YIG.

4.7 Insertion Loss and Strip Width

Figures 4-11 to 4-13 show the effects of changing transducer strip width on insertion loss, radiation resistance, and radiation reactance. Results are for a pair of single element transducers 2 mm in length and 10 mm apart with a YIG film $30 \mu\text{m}$ thick flipped onto transducers which are $254 \mu\text{m}$ from a ground plane. The other ground plane is essentially at infinity, $L = \text{one meter}$. A linewidth of 0.5 oersteds is assumed; and conduction loss in the transducers is neglected, that is, resistive loss is assumed to be zero. The parameter $p = 300 \mu\text{m}$, representing transducer element spacing, is arbitrarily set at $300 \mu\text{m}$. Actually, the results are independent of this parameter since there is only one element per transducer, $n = 1$. These results are for the independent conductor two

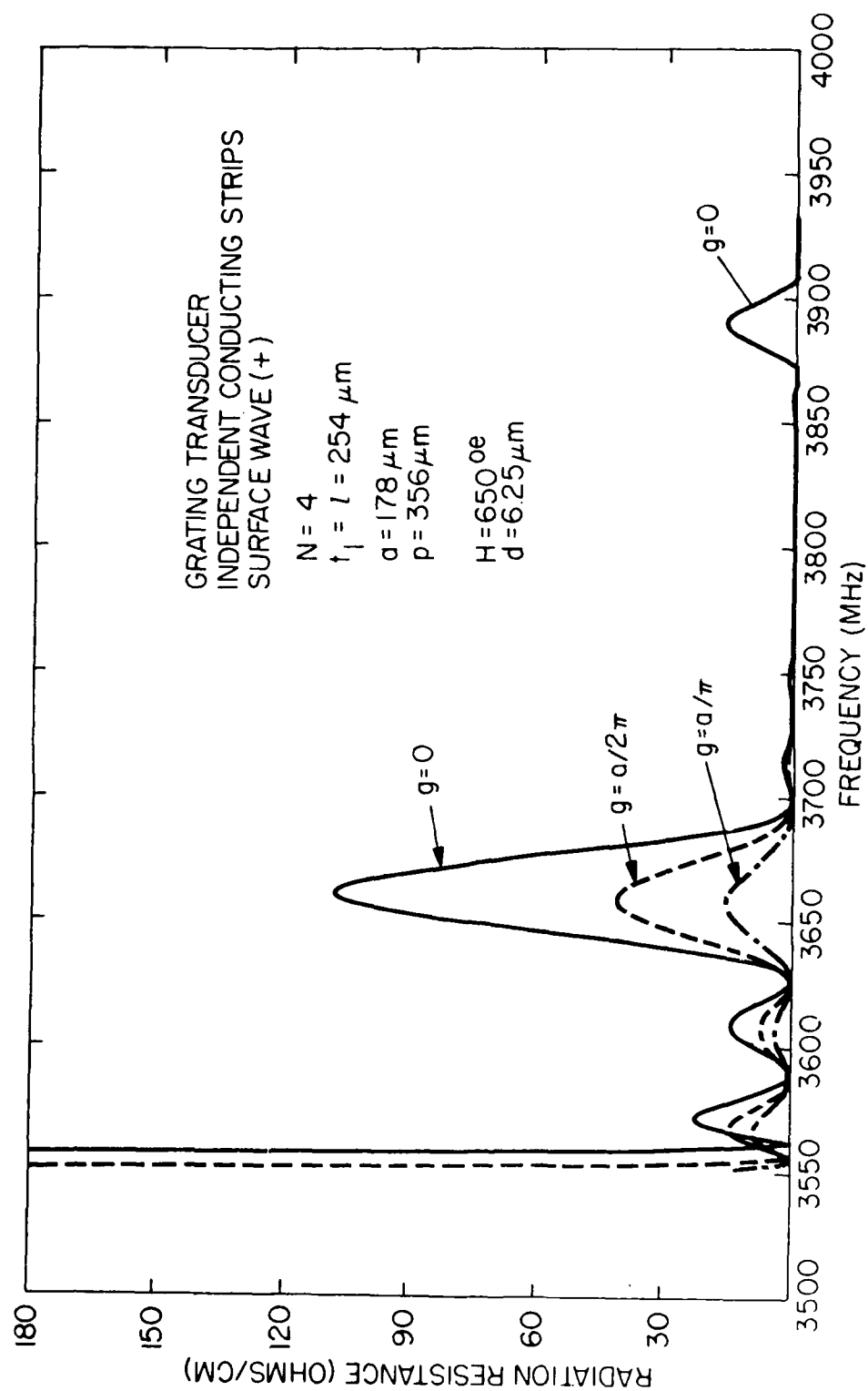


Figure 4-7. Radiation Resistance Per Unit Transducer Aperture Length versus Frequency, for a 4-Element Grating Transducer With Lift-off "g" as a Parameter

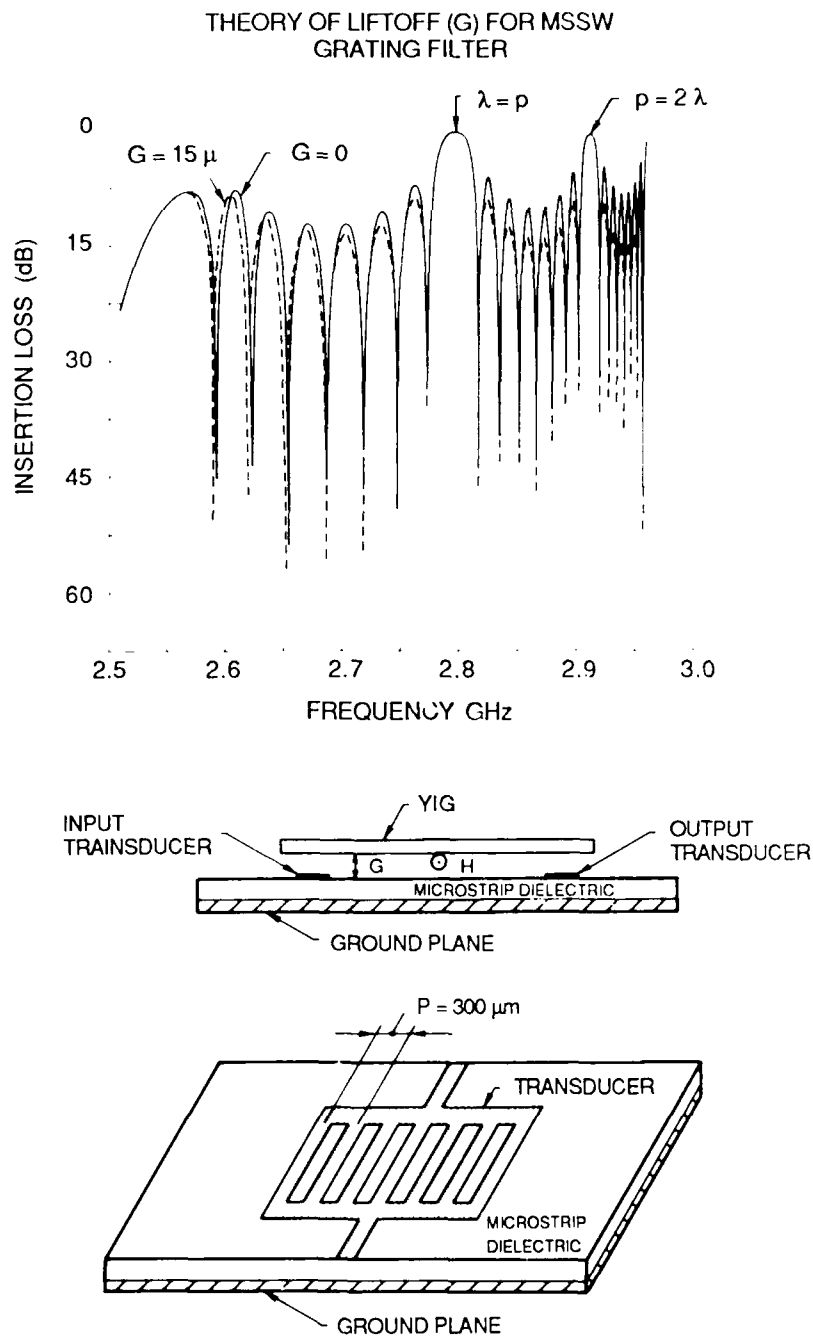


Figure 4-8. Insertion Loss for Zero, and 15 μm Liftoff, G. Lower portion of figure shows geometry.

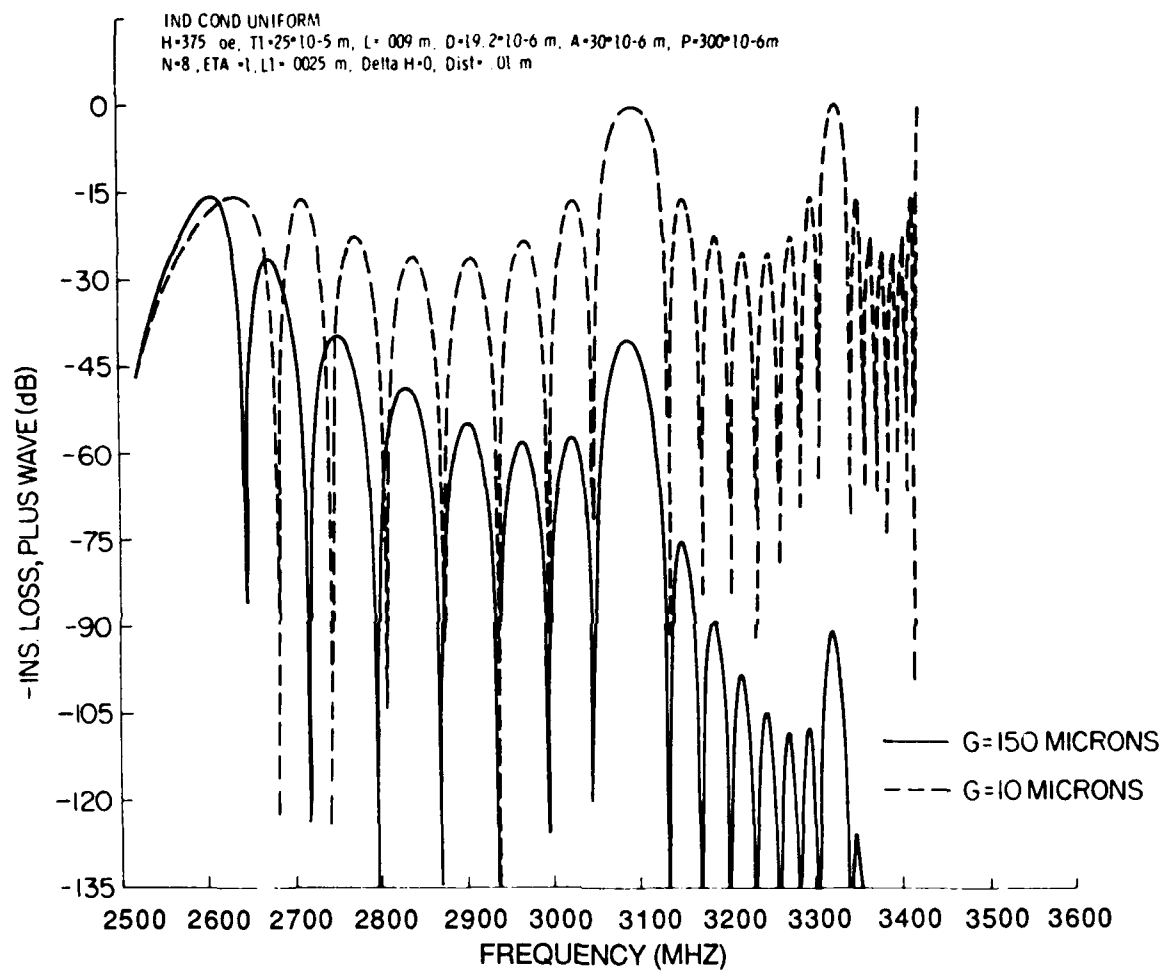


Figure 4-9. MSSW Insertion Loss versus Frequency for an 8-Element Grating Transducer Pair.
 $G = 150 \mu\text{m}$ and $G = 10 \mu\text{m}$

IND COND UNIFORM
H=375 (OE), T1=228 UM, G=25.4 UM, L=1 (M), D=30*10-6(M)
L1=.003(M), A=50*10-6(M), N=1
DIST=.01(M), R LOSS=0

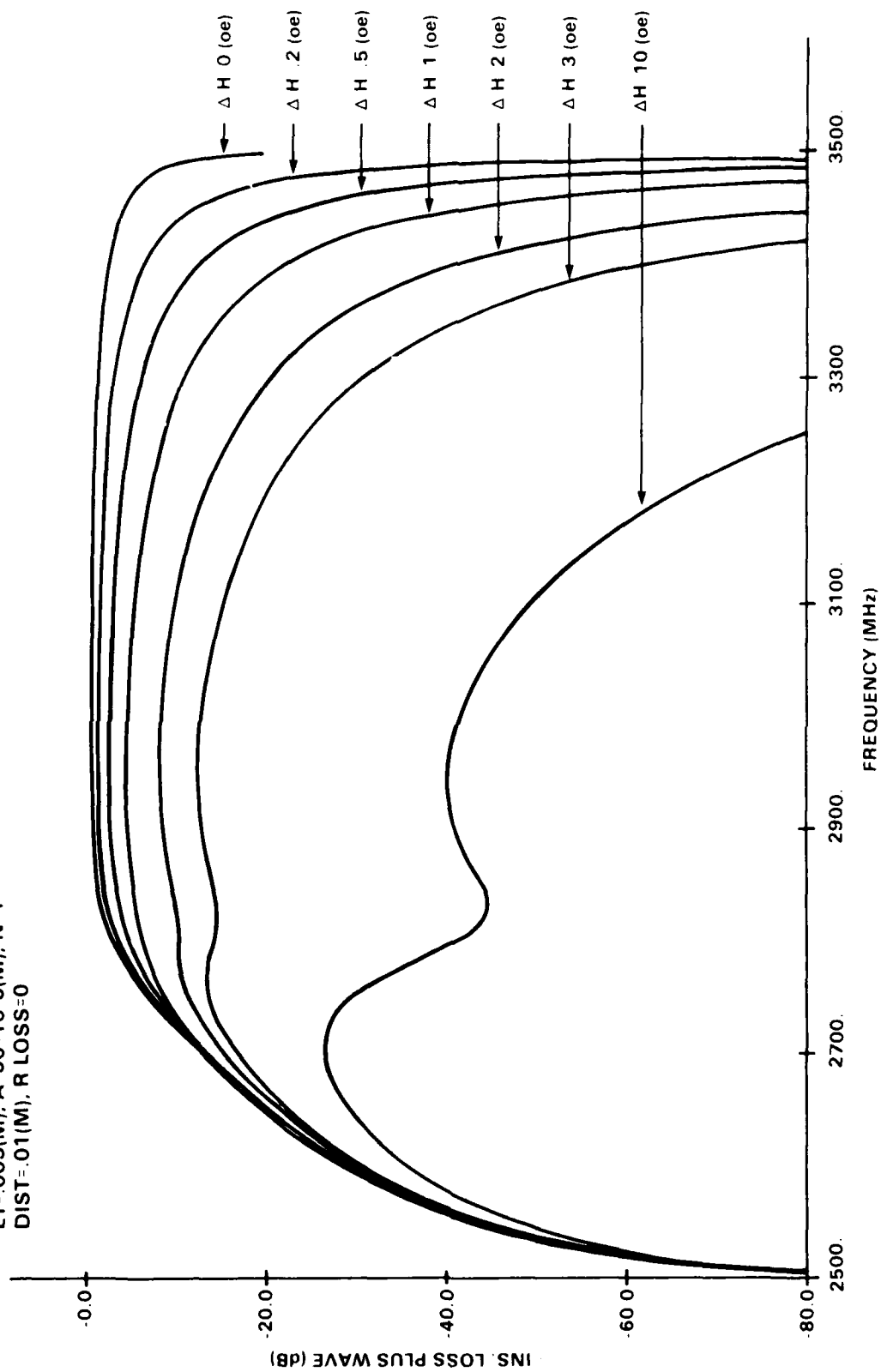


Figure 4-10. Insertion Loss of MSW Delay Line for Parametric Values of Linewidth. Propagation loss increases with increasing linewidth. Delay line uses single-element transducers at input and output ports

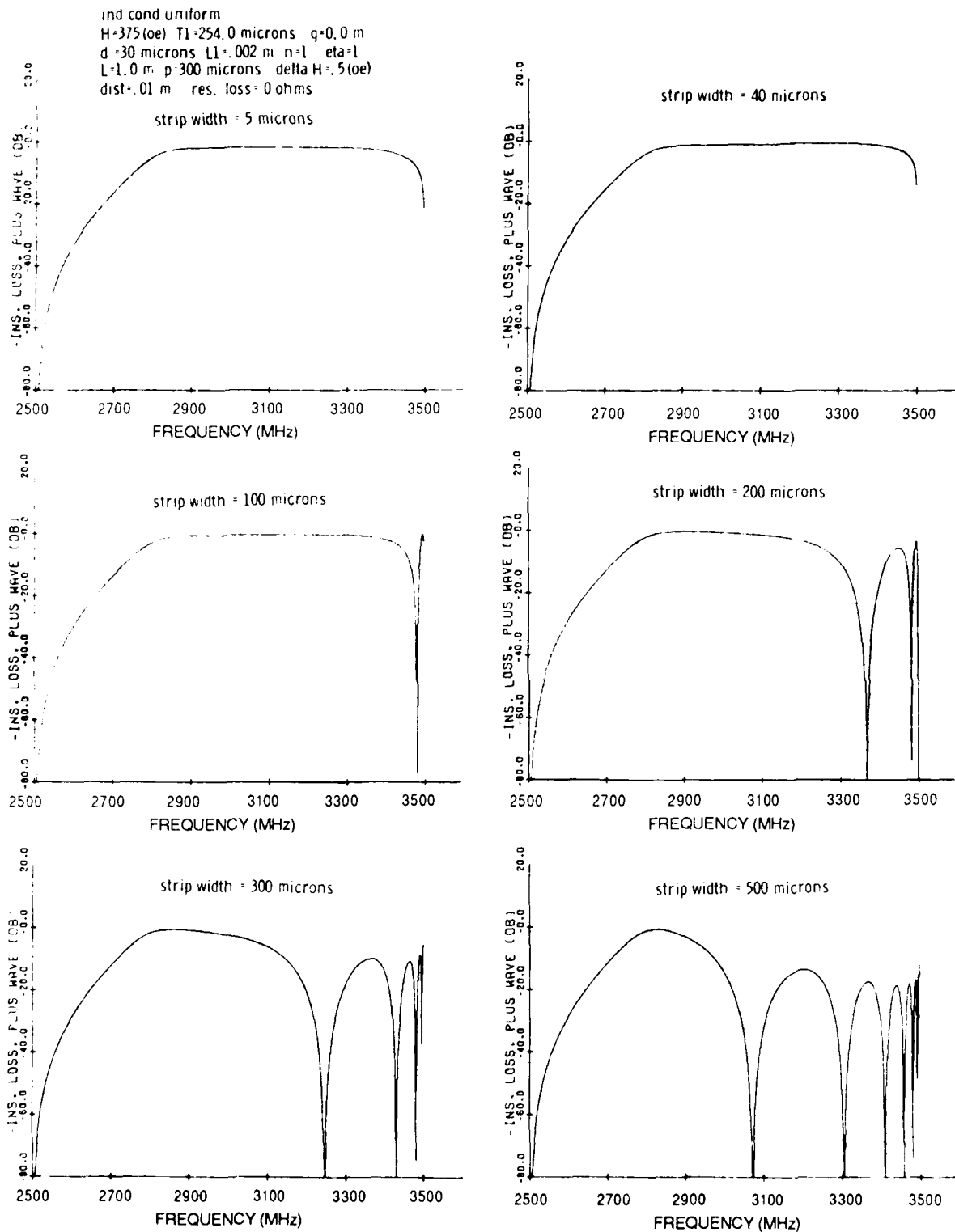


Figure 4-11. MSSW Passband, IL, for Parametric Values of Strip Width, Using TT Model

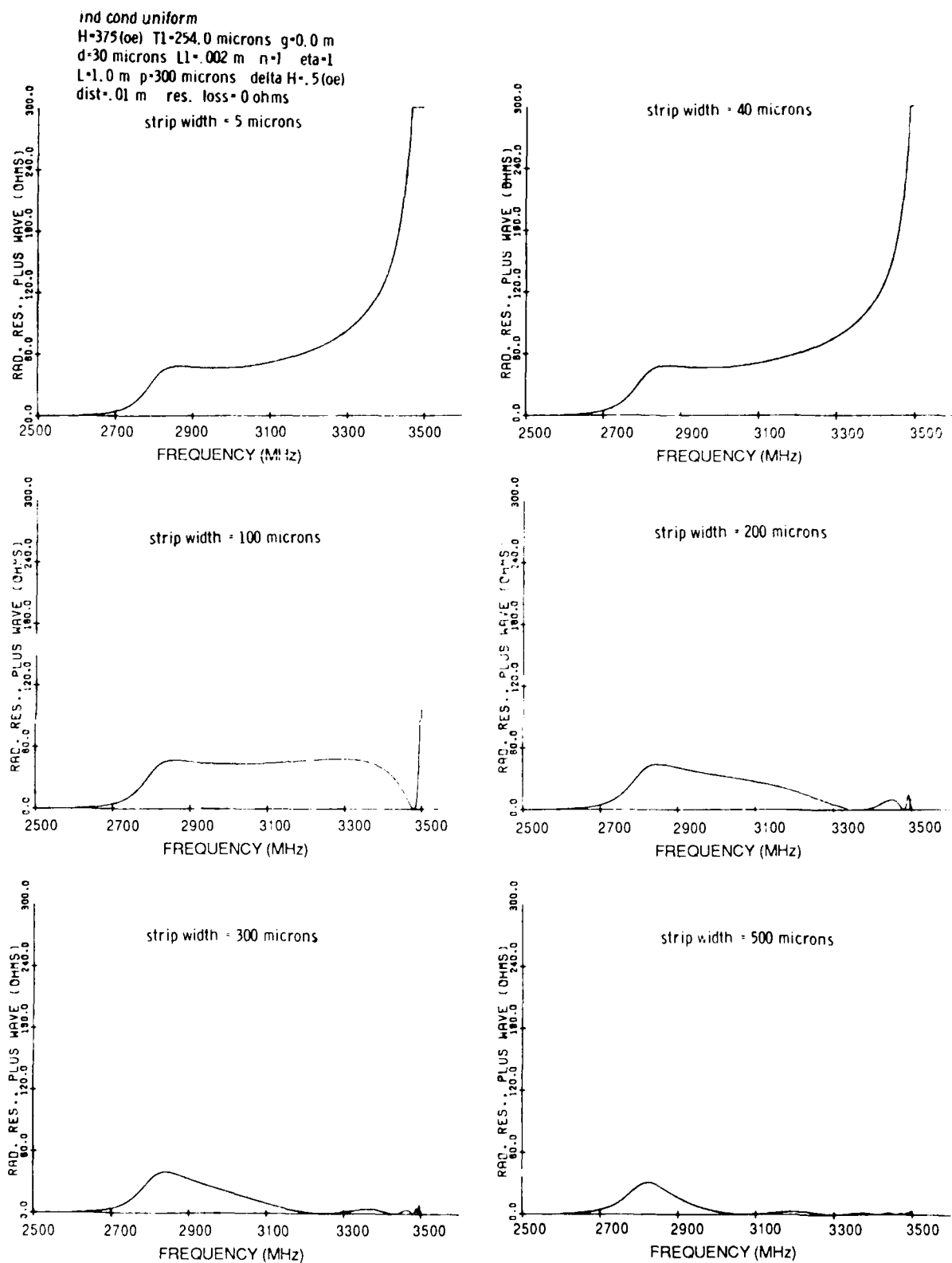


Figure 4-12. MSSW Radiation Resistance for Parametric Values of Strip Width, Using TT Model

ind cond uniform
 $H=375(\text{oe})$ $T1=254.0$ microns $g=0.0$ m
 $d=30$ microns $L1=.002$ m $n=1$ $\eta=1$
 $L=1.0$ m $p=300$ microns $\Delta H=.5(\text{oe})$
 $\text{dist}=.01$ m $\text{res. loss}=0$ ohms

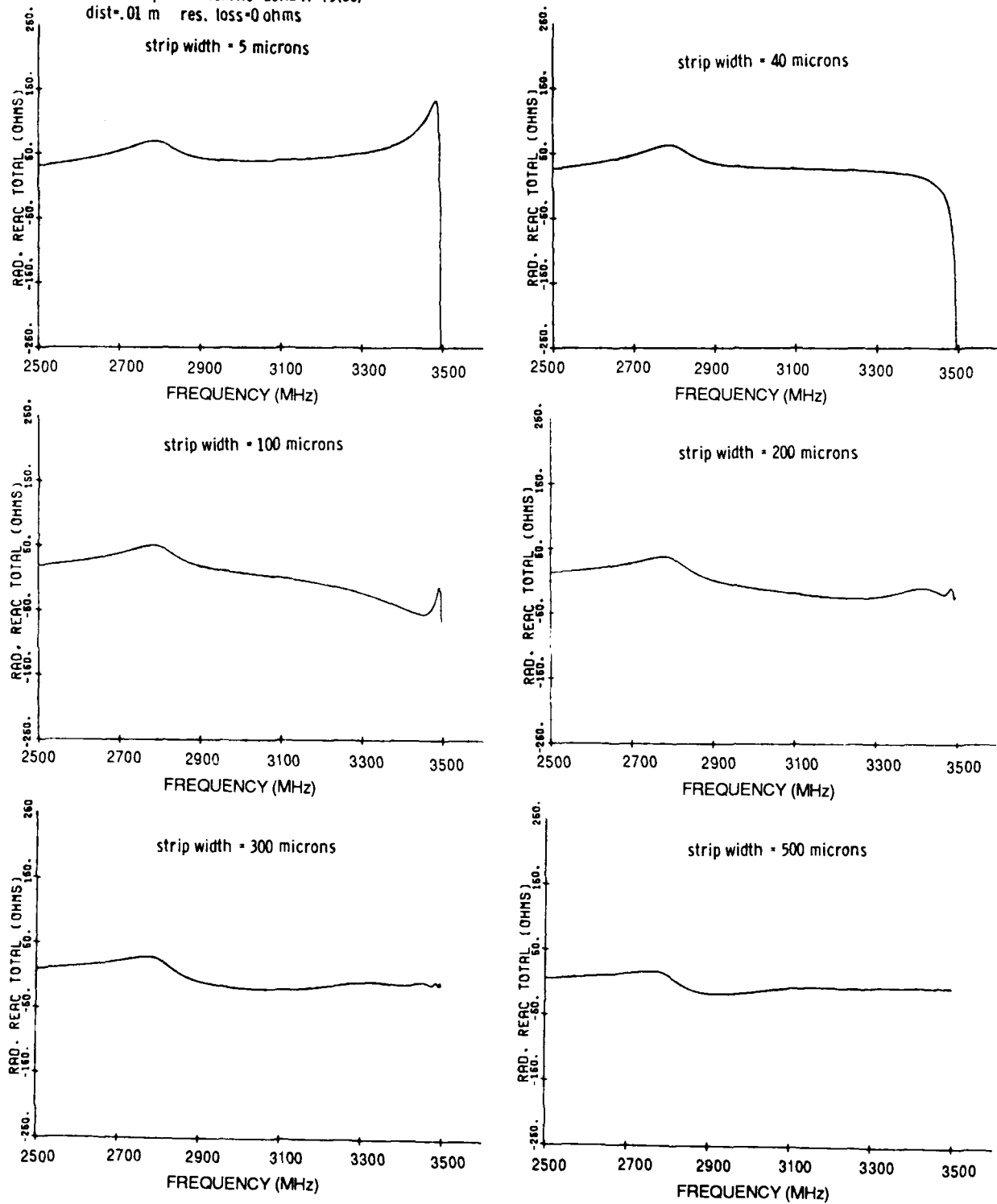


Figure 4-13. MSSW Radiation Reactance for Parametric Values of Strip Width, Using TT Model

terminal model with flat current distribution across the strip width and uniformity along the transducer length L_1 .

An important result here is the multiple insertion loss responses for wide strips. The lowest frequency response minimum insertion loss is insensitive to strip width. Higher frequency responses are severely attenuated with increasing strip width. This effect can be used to design bandpass filters of about 8 percent bandwidth. Note that the value of radiation resistance is close to 50 ohms at some frequency within the passband for all strip widths, and radiation reactance is positive over most of the passband for narrow strips, while for wider strips radiation reactance passes through zero.

4.8 Microstrip or Transmission Line Model

Figures 4-14 and 4-15 show results for the microstrip model, which is also referred to as a transmission line model in this report. Dispersion relations, Figure 4-15, are identical for TL and TT models.

4.9 Two Element Grating Transducer

Figure 4-16 illustrates the effect of changing transducer aperture L_1 on insertion loss, for a two element grating transducer. Results are for the TT model. The three values of L_1 , corresponding to the plots in Figure 4-16 from top to bottom, respectively, are 0.625 mm, 1.25 mm, and 2.5 mm. This figure indicates L_1 is not a critical design parameter with respect to insertion loss. Although radiation resistance is critically dependent on L_1 , the insertion loss is only weakly dependent on L_1 . On the other hand, transducer aperture, L_1 , is important for beam profile control and higher order mode suppression.

Figure 4-17 illustrates the effect of changing the liftoff parameter g . Four insertion loss plots are shown for $g = 0, 20, 50$, and $100 \mu\text{m}$. The main effect of increasing g is to increase insertion loss at the high frequency, or short wavelength end of the passband. Insertion loss at the low frequency end of the passband, where wavelengths are large, are essentially independent of liftoff for all practical g values. Liftoff is an important design parameter.

4.10 Dispersion Relation and Group Velocity

Selected dispersion relations (frequency versus wavenumber) and group velocity characteristics are shown in Figures 4-18 through 4-25.

4.10.1 NORMALIZED DISPERSION RELATIONS

Figure 4-18 shows generalized MSSW dispersion curves for a fixed DC magnetic field. The curves are normalized with respect to film thickness and saturation magnetization. Figure 4-19 shows generalized MSSW group velocity curves for the case where ground planes are on, or close to, a YIG surface. The dispersion relation equation, from which the curves in Figure 4-18 and 4-19 are generated, can be derived from Eqs. (2-30) and (2-31), and can be put in the form:

$$\exp(-2LL\tau) = \frac{(1-\alpha_2)\exp(-2L) + (1+\alpha_1)T}{(1+\alpha_2)\exp(-2L) + (1-\alpha_1)T} \quad (4-1)$$

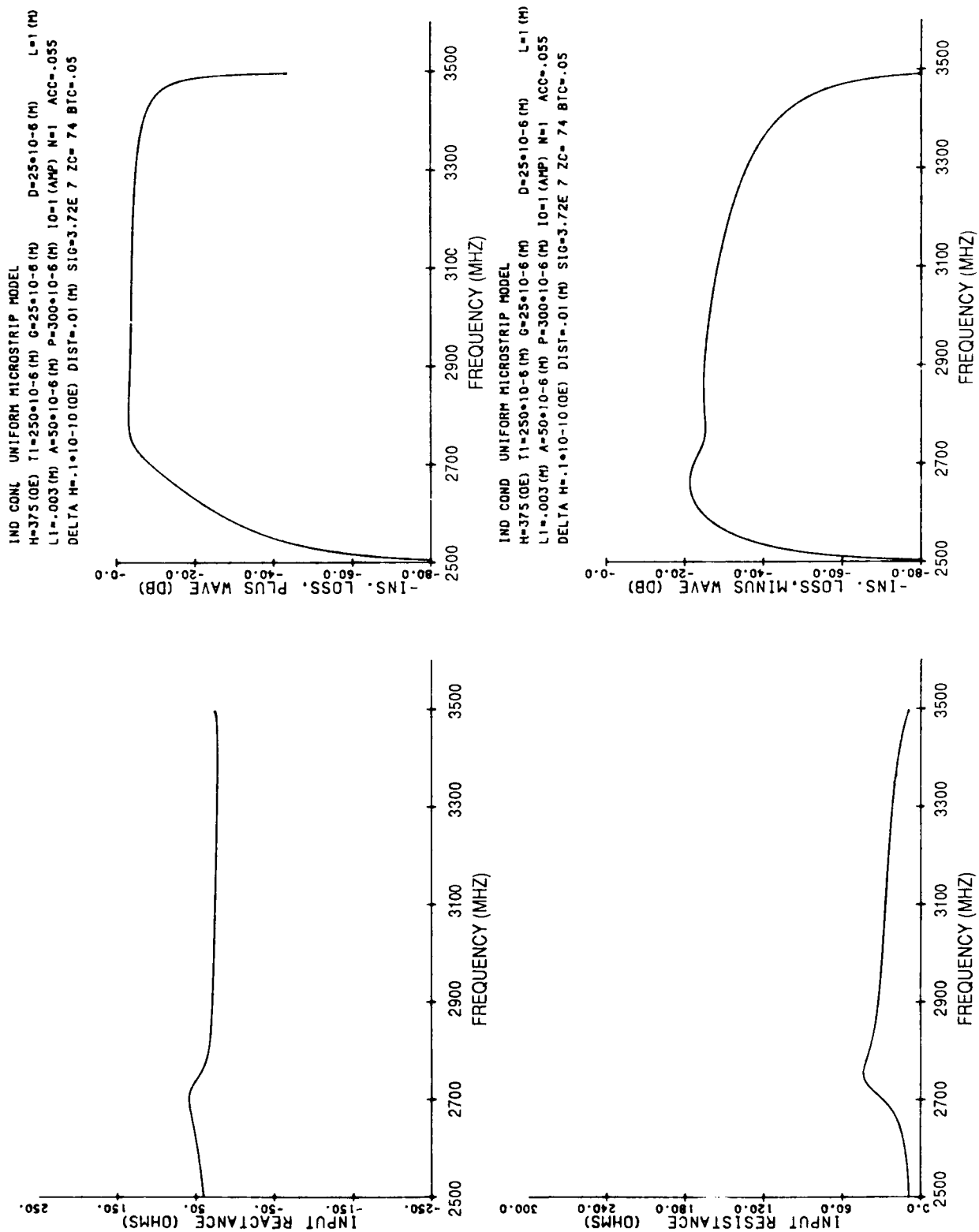


Figure 4-14. Transmission Line Model Insertion Loss and Input Resistance and Reactance for Single Strip Transducers

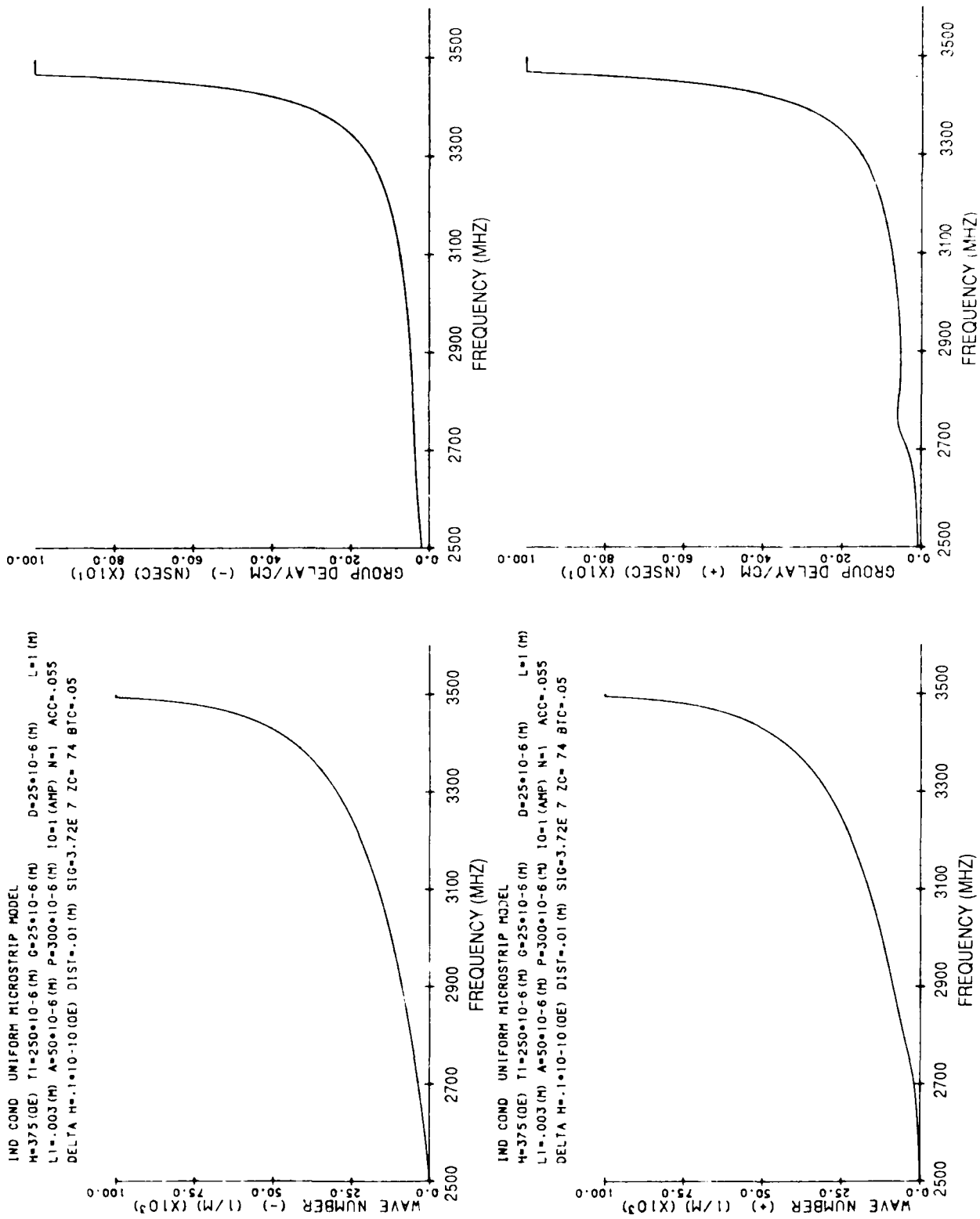


Figure 4-15. Transmission Line Propagation Constance and Group Delay

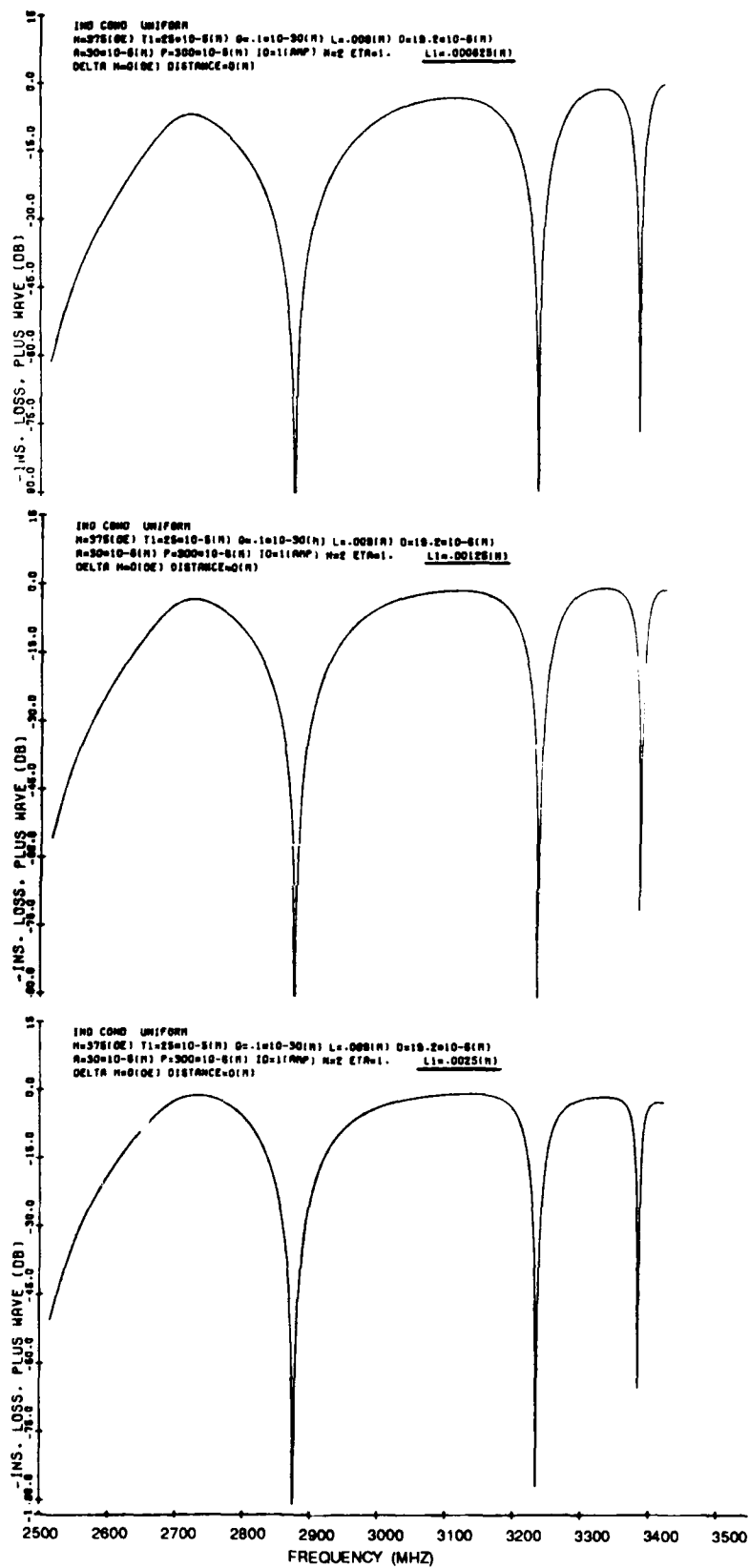


Figure 4-16. Insertion Loss versus Frequency for Two Bar Grating, for Three Values of Transducer Aperture Illustrations

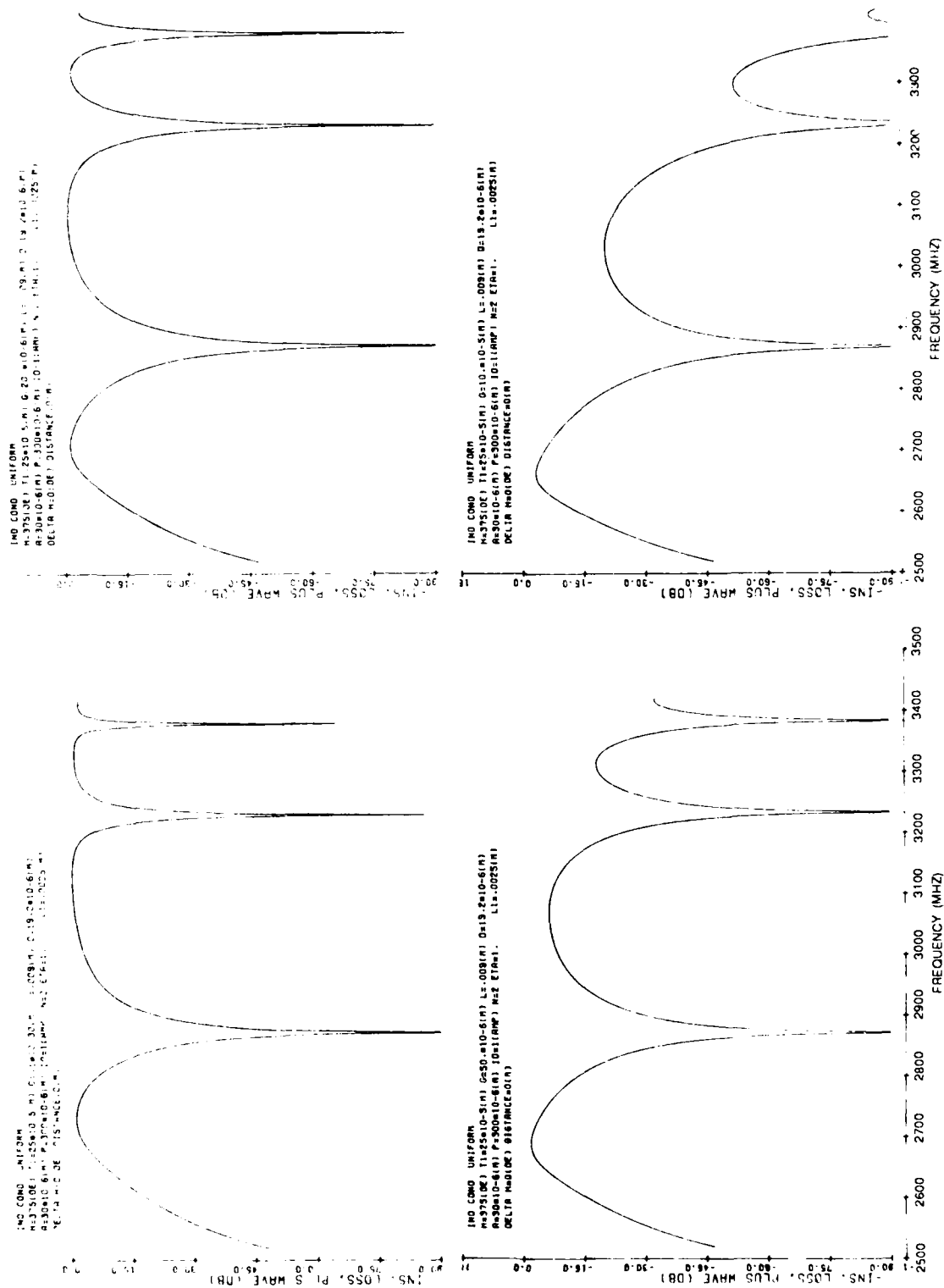


Figure 4-17. Insertion Loss versus Frequency for Two Bar Gratings for Four Values of Lift-off

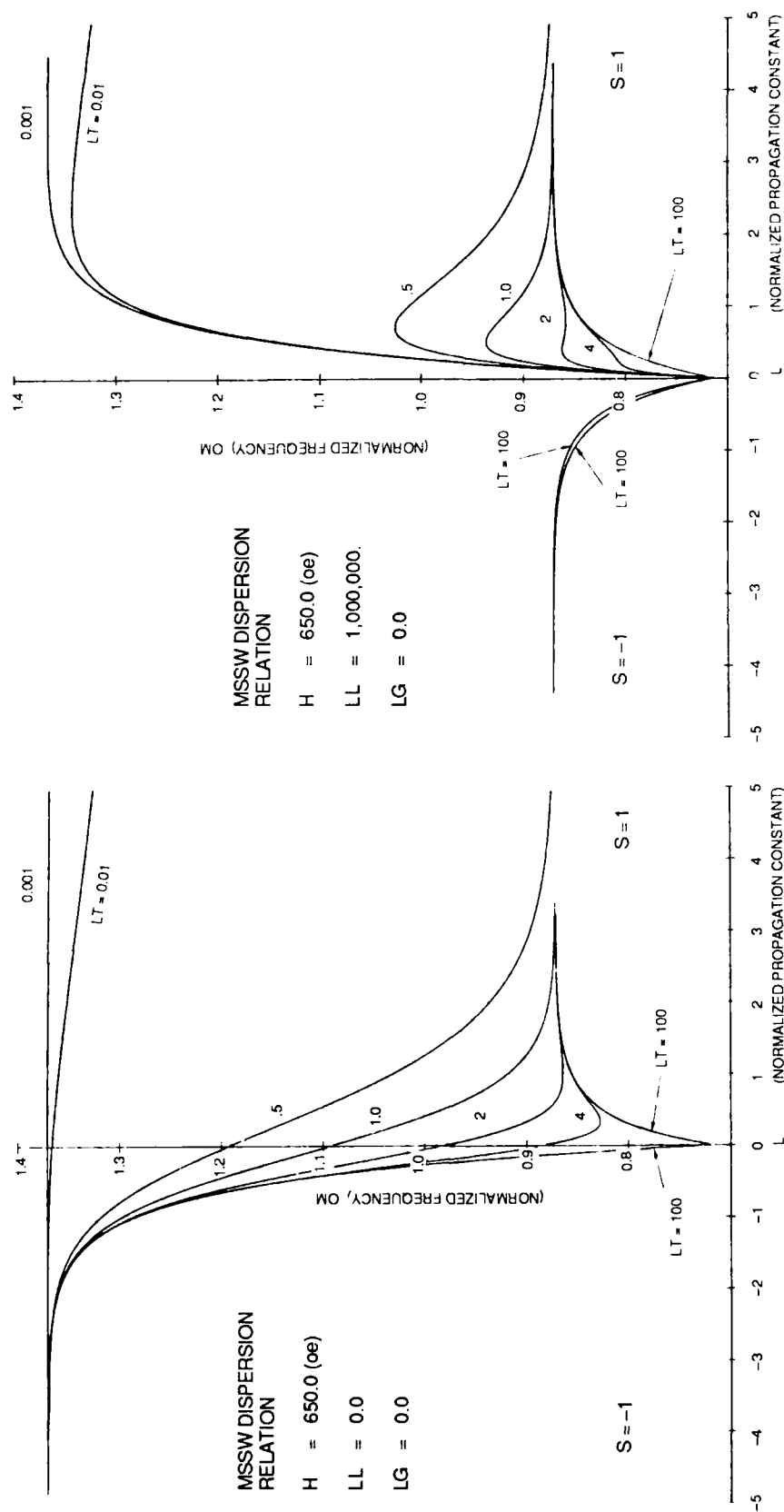


Figure 4-18. Normalized Dispersion Relations, with $S = 1$ corresponding to wave whose energy is concentrated on the YIG surface nearest transducer

a. Two ground planes, left figure

b. One ground plane on transducer side of YIG, right figure. Transducer is between ground plane and YIG surface where MSSW energy is concentrated

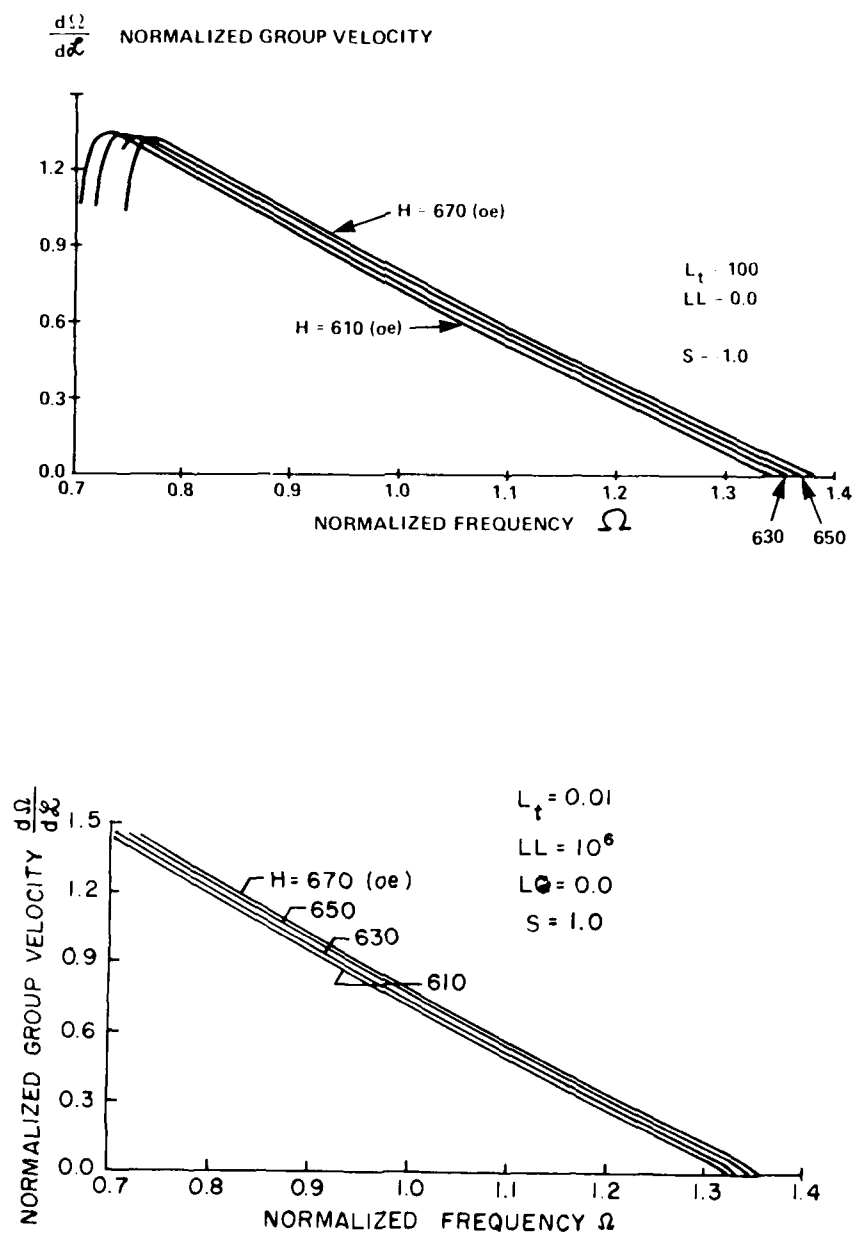


Figure 4-19. Generalized Group Velocity Curves for One Closely Spaced Ground Plane
a. Weakly coupled MSSW on YIG surface opposite transducer side of YIG, $s = -1$
b. Strongly coupled MSSW on YIG surface near transducer side, $s = +1$

where

$$T = \frac{[\alpha_2 + \tanh(LL_1)]}{[\alpha_1 - \tanh(LL_1)]}$$

and α_1 and α_2 are defined by Eqs. (2-21) and (2-23). The normalization for Figures 4-18 and 4-19 is:

$$L_1 = l/d, L = Kd, L_\tau = \tau/d, \text{ where } \tau = t_1 + g, \text{ and } \Omega = \omega / (\gamma 4\pi M).$$

In addition, here, normalized frequency is $OM = \Omega$, $LT = L_\tau$, $LL = L_1$. The normalized propagation constant is L . The parameter s is ± 1 ; and it denotes propagation direction in the expression $\exp[i(\omega t - sKx)]$.

In Figure 4-18a, one of the ground planes is on the YIG surface, $LL = 0$. The other ground plane is spaced by an amount LT from the other YIG surface. Since $LT = \tau/d$, the curve $LT = 100$ corresponds closely to the case of a single ground plane on one surface, the other ground plane being very far away; while the curve $LT = 0.001$ corresponds to the case of a YIG slab sandwiched between two closely spaced ground planes. This latter curve implies that MSSW bandwidth approaches zero when two closely spaced ground planes are used, and relatively wide bandwidths are obtained with only a single ground plane. The curve $LT = 100$ for positive L , $s = +1$, corresponds to MSSW closely bound to a free YIG surface with no ground planes.

In Figure 4-18b one of the ground planes is moved far from the YIG, $LL = 1,000,000 \mu\text{m}$, while the other is spaced LT units from a surface. Again, for $LT = 100$ there are essentially no ground planes while for $LT = 0.001$ there is one closely spaced ground plane.

Figure 4-18 also shows that for some ground plane spacings there are two values of propagation constant, for $s = +1$, at a fixed frequency. See, for instance, the curve labeled $LT = 1.0$ in Figure 4-18b, at $OM = 0.9$. This corresponds to an undesirable choice of ground plane spacings when single mode operation over a passband is desirable. A particularly useful choice of ground plane spacings appears to be that of a single closely spaced ground plane. This will result in single mode wide bandwidth operation. The disadvantage of a closely spaced ground plane is the introduction RF conduction loss. Therefore, some tradeoff will apply between the choice of ground plane spacing and the amount of loss that can be tolerated.

4.10.2 MSSW NORMALIZED GROUP VELOCITY

Figure 4-19 shows a particularly attractive feature of having one closely spaced ground plane for MSSWs. Group velocity is nearly linearly related to frequency, a useful signal processing characteristic. In the figure, plots are shown for four biasing field values. There is excellent tuning via the biasing magnetic field H . This feature is presently useful up to about 6 GHz. Above that frequency, ground plane losses are troublesome. At 3 GHz, gold ground planes introduce negligible loss. When superconducting ground planes become practical, their use with MSW should prove attractive.

4.10.3 DISPERSION CURVES FOR MIXED MODES

Figures 4-20 through 4-23 show dispersion relations; that is, propagation constant, K , versus frequency for MSW propagating at arbitrary angles with respect to the bias field. For all of these

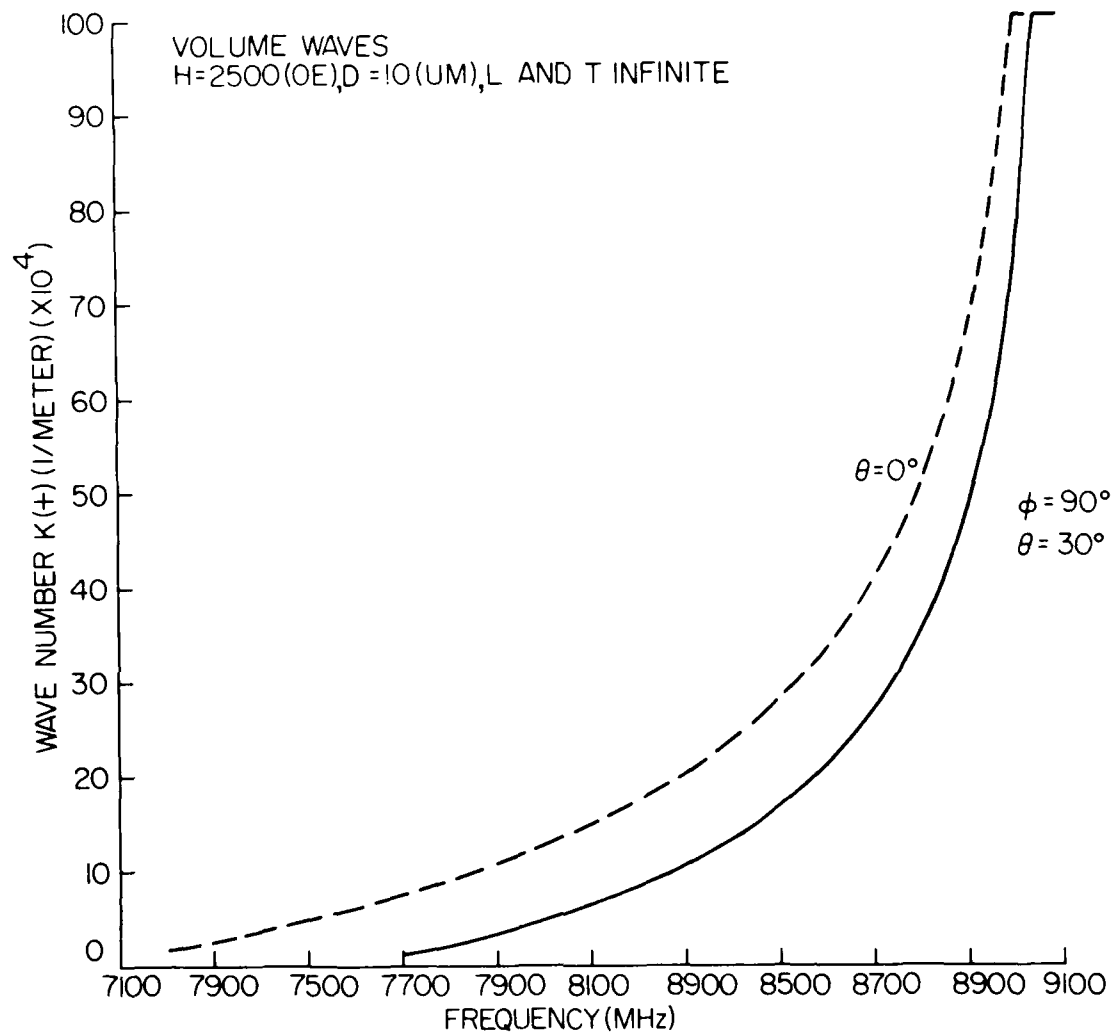


Figure 4-20. Dispersion Relations for H in yz Plane, FVW/SW Hybrid Mode, See Figure 2-1

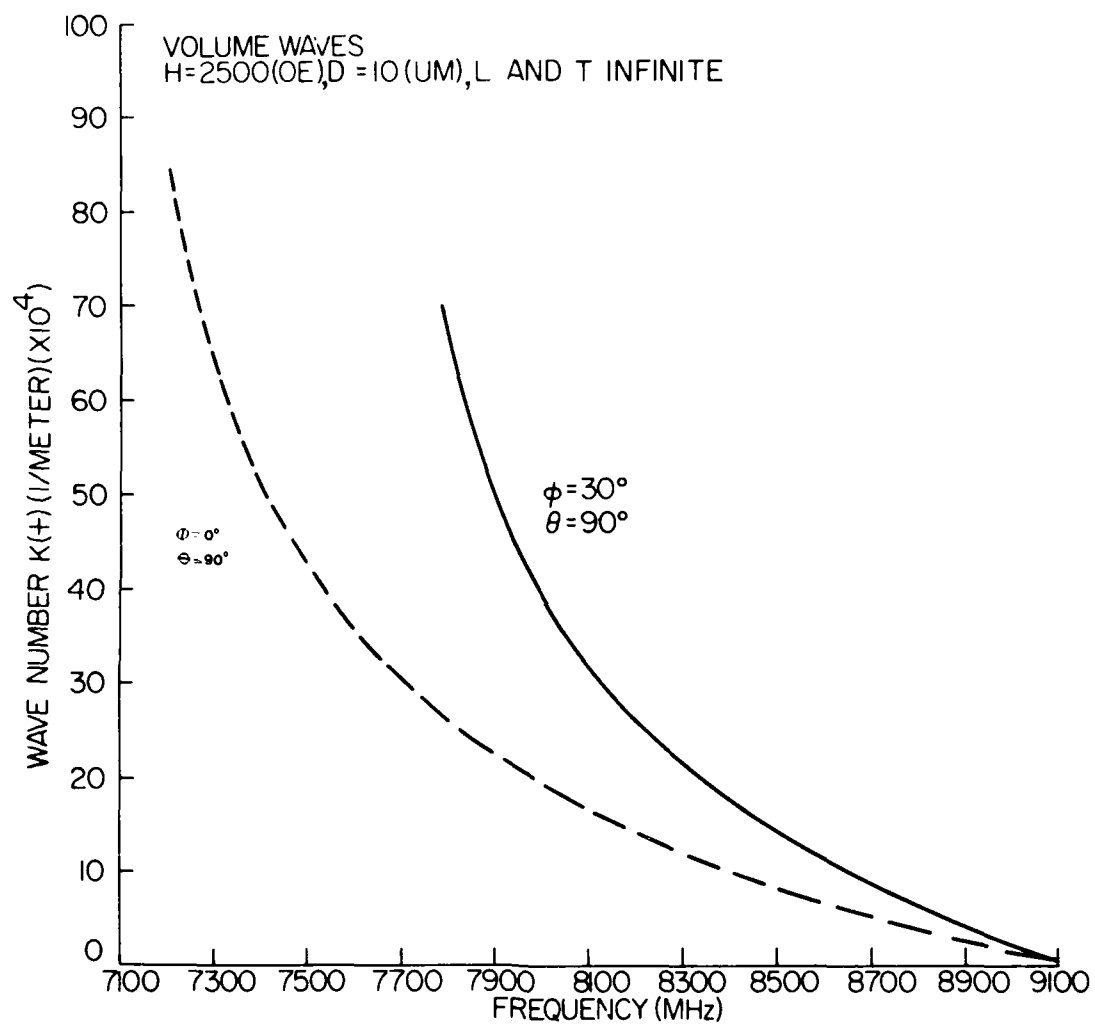


Figure 4-21. Dispersion Relations for H in xz Plane, BVW/SW Hybrid Mode, See Figure 2-1

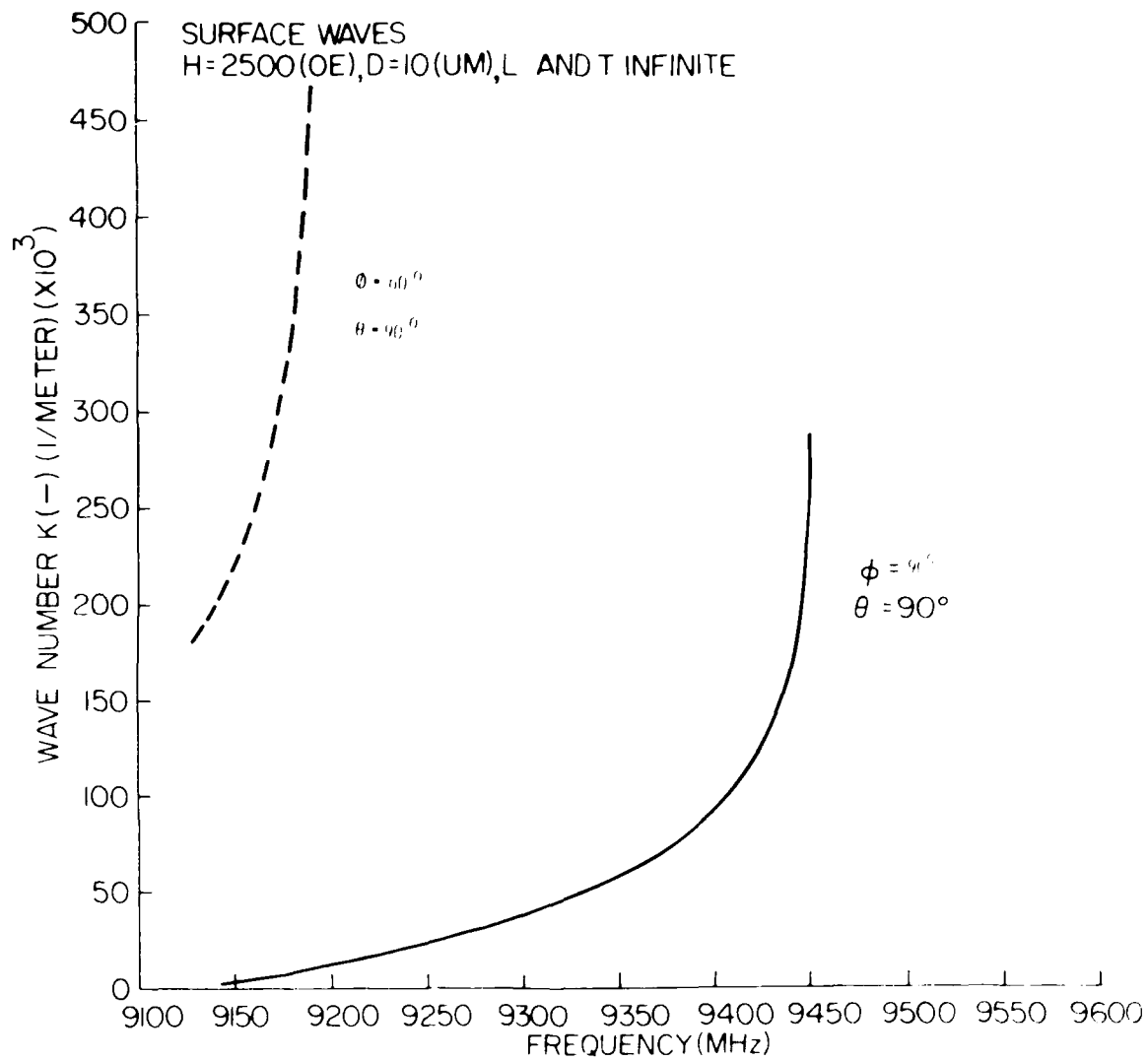


Figure 4-22. Dispersion Relations for H in xz Plane, SW/BVW Hybrid Mode. See Figure 2-1

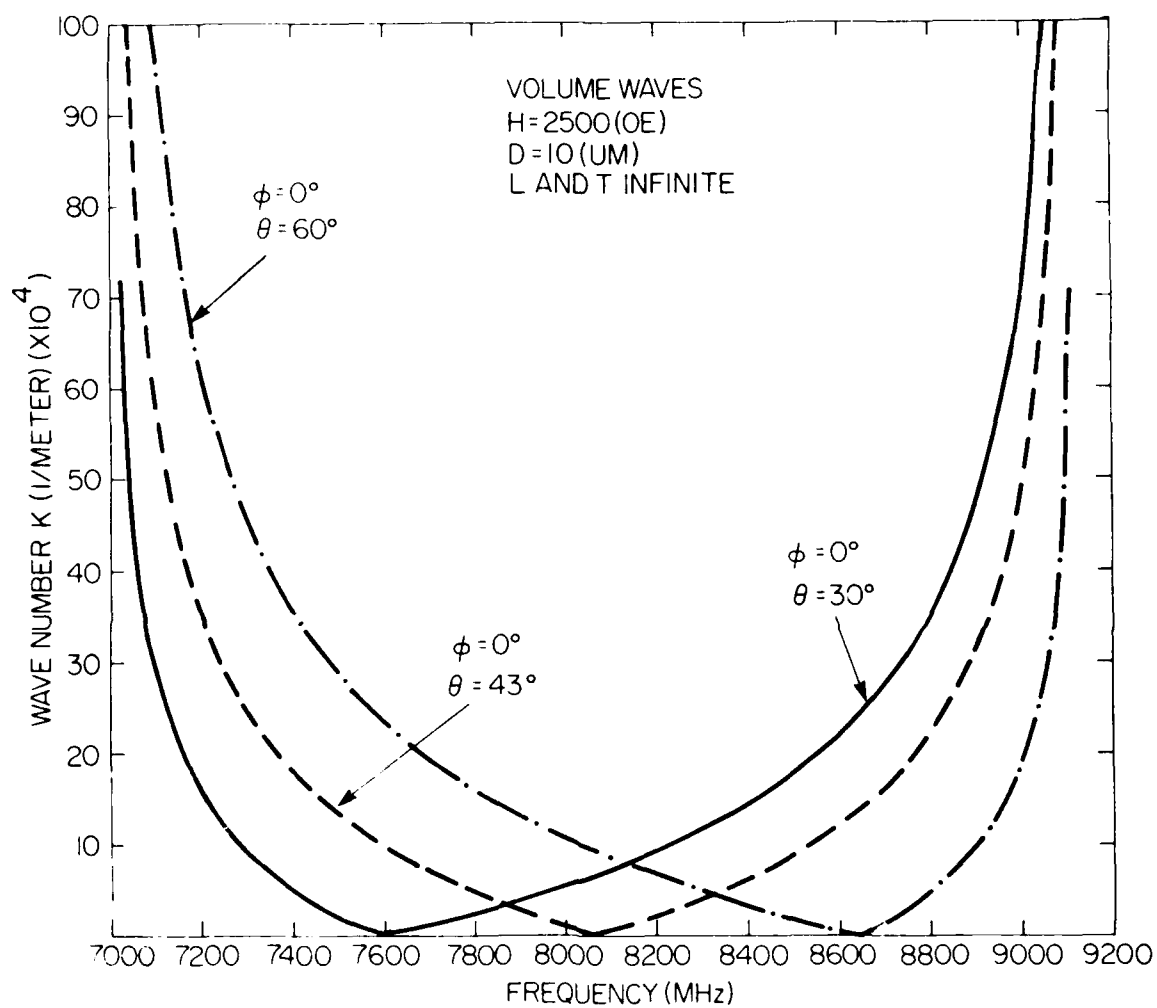


Figure 4-23. Dispersion Relations for H in xy Plane, FVW/BVW Hybrid Mode, See Figure 2-1

figures, 4-20 through 4-23, there are no ground planes (L and T are infinite); biasing fields are 2500 oersteds (internal field); and the YIG thickness is 10 μm . These MSWs are not pure modes, except for the three limiting cases where all angles are either 0 or 90 degrees. Angles are defined in Figures 2-1 and 4-24. These figures define biasing field directions. Wave propagation is always in the x direction. The dashed curve in Figure 4-20, $\theta = 0$, is for a MSFVW pure mode with phase and group velocity collinear. The solid curve is for a hybrid mode. This is a mixture of MSFVW and MSSW. The biasing field for Figure 4-20 is in the transverse yz plane and out of the plane of the film. Phase and group velocities are not in the same direction, or collinear. In Figure 4-21, the biasing field is in the xz plane; that is, in the plane of the film. The dashed curve represents a pure MSBVW and the solid curve a hybrid mode. It is a mixture of MSSW and MSBVW. Figures 4-20 and 4-21 are for positive waves. Figure 4-22 is for biasing fields also in the plane of the film, but for the negatively going waves. A limiting pure MSSW is represented here by a solid curve and a hybrid mode by the dashed curve. It is a combination of MSSW and MSBVW.

Figure 4-23 depicts dispersion relations when the biasing field is in the yx plane, and $\phi = 0$ for three values of θ : 30, 43, and 60 degrees. These hybrid modes are combinations of MSFVWs and MSBVWs. Note the $K = 0$, cutoff condition, for all three curves. This is a general result; that is, within each of the three bandwidths there is a transition from MSBVW-like modes to MSFVW-like modes separated by a frequency which corresponds to a K number of zero. At this frequency there is no propagation. This effect is described in detail by Parekh and Tuan.¹ It means that a delay line with a spatially varying orientation of the biasing field along the direction of propagation, and out of the plane, will have a notch at some frequency within its passband. This effect is believed to be quite general and a similar result obtains for spatially varying biasing fields in the film plane, along the propagation direction, for MSSW to MSBVW conversion. Again, a notch is expected to appear in the frequency band; however, this has not been proven.

Figure 4-24 shows the results of a search for a biasing field orientation that will produce a symmetrical dispersion relation over the bandwidth of a hybrid mode. The purpose was to design a composite nondispersive delay line. The search was successful. A biasing field in the xy plane with $\theta = 43$ degrees produces the desired dispersion as shown in Figure 4-24. Cascading two delay lines, each with a different biasing field magnitude but the same orientation, $\theta = 43$ degrees, results in the group delay versus frequency curve shown in Figure 4-25. There is a flat nondispersive region within the passband of the cascaded hybrid modes. The total group delay is the sum of the two individual delay lines at any given frequency. This configuration, two cascaded separate delay lines using hybrid modes, has not been pursued further because of the large ripples and reflection present in the passband. These occur because the band contains long wavelengths which suffer from large diffraction loss. The concept, however, seems to have merit for obtaining tunable nondispersive delays over restricted bands.

1. Parekh, J.P. and Tuan, H.S. (1987) *Studies of MSFVW to MSBVW Mode Conversion at a Region of Bias Field Discontinuity and of the Dispersion of an MSFVW Pulse*, RADC-TR-87-201, ADA189343.

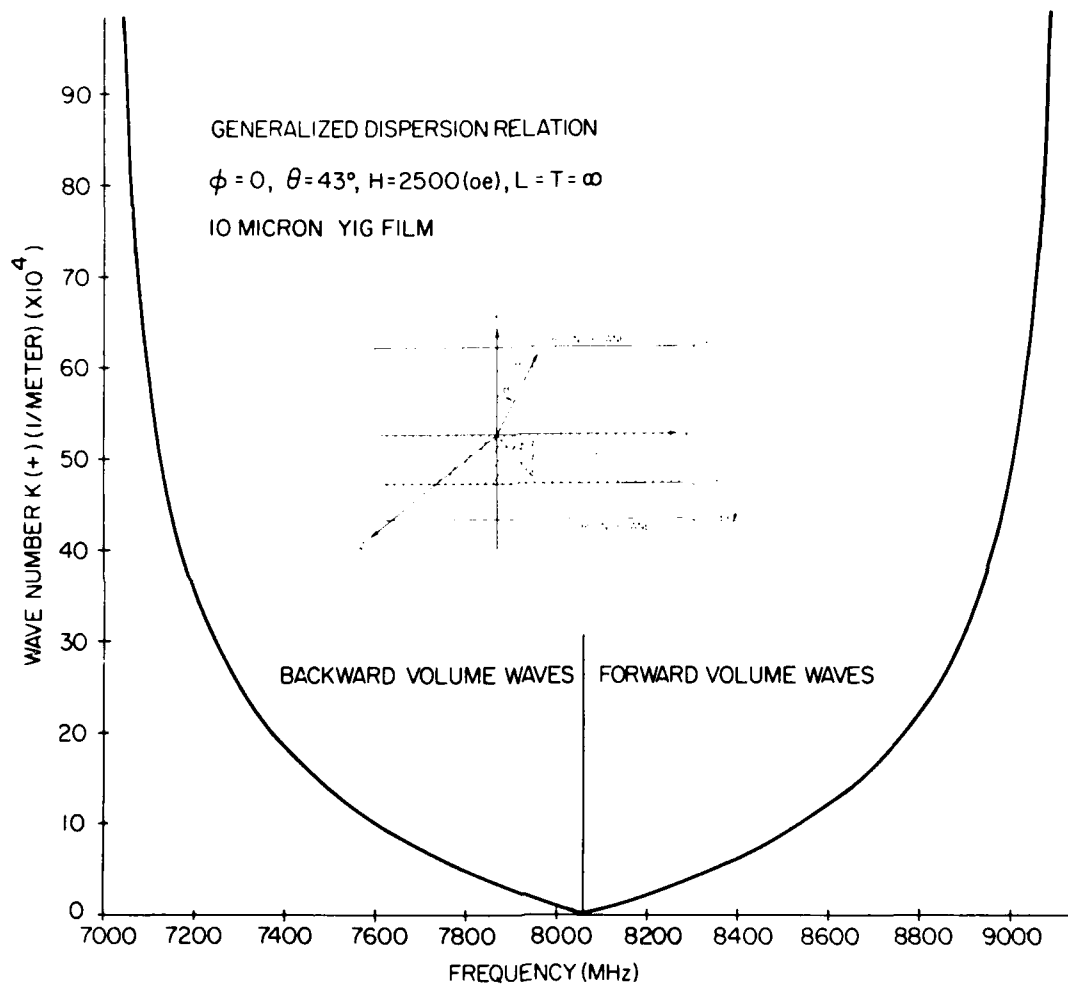


Figure 4-24. Dispersion Relation for H in xy Plane, Where Hybrid Modes Have Zero Wavenumber at the Same Frequency, See Figure 4-21

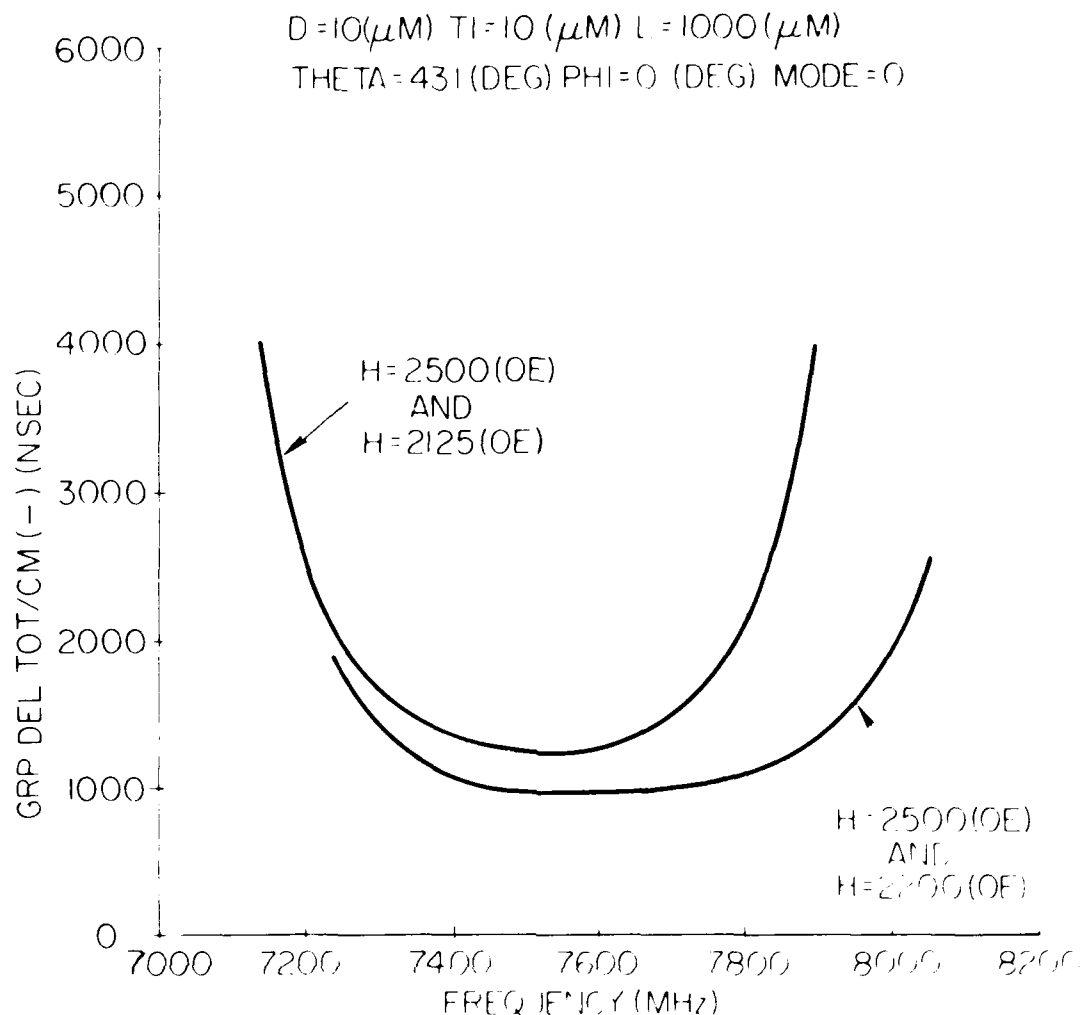
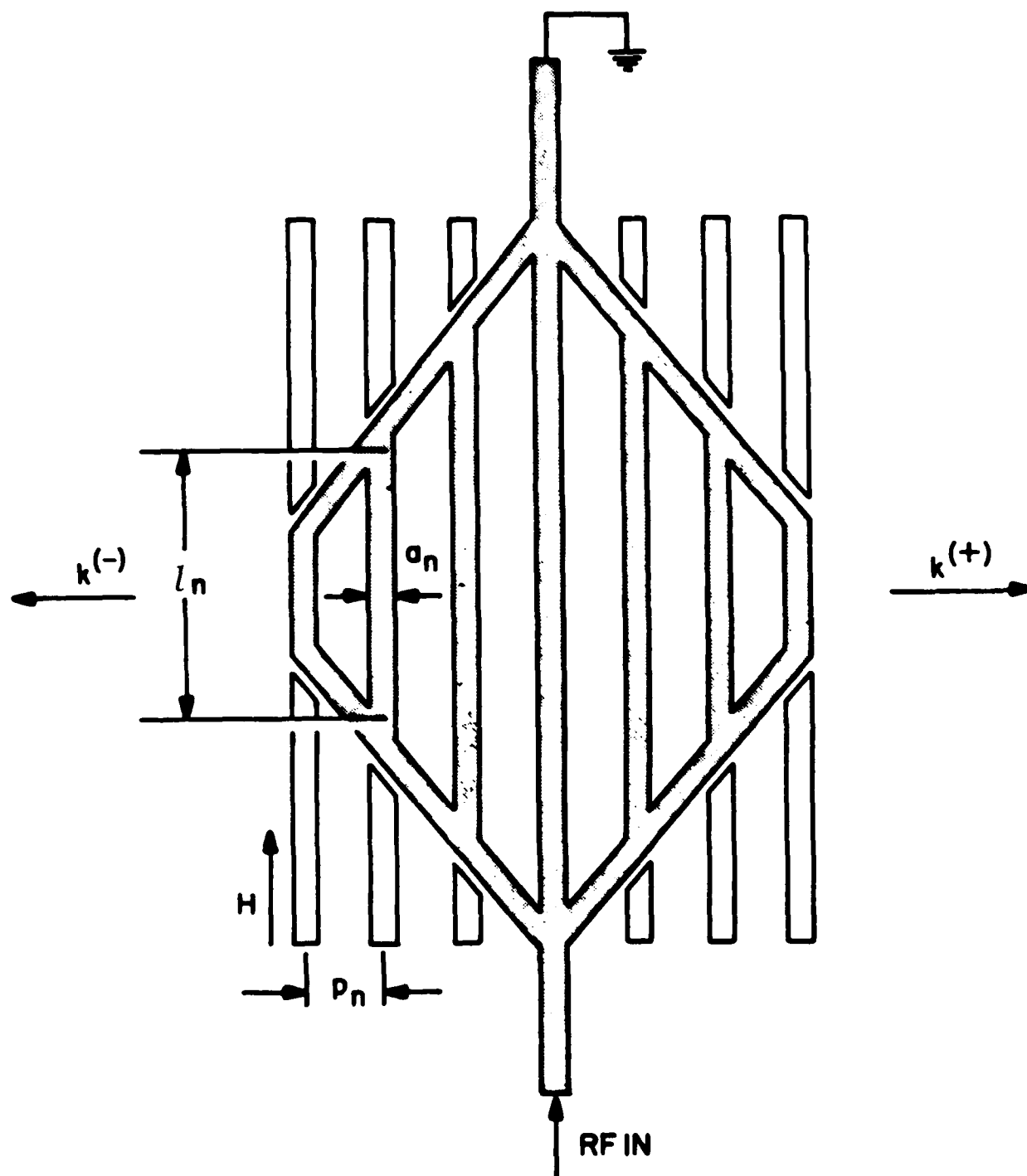


Figure 4-25. Group Delay for a Pair of Cascaded Delay Lines with Dispersion Relations Like the Ones Shown in Figure 4-24

4.11 Apodization

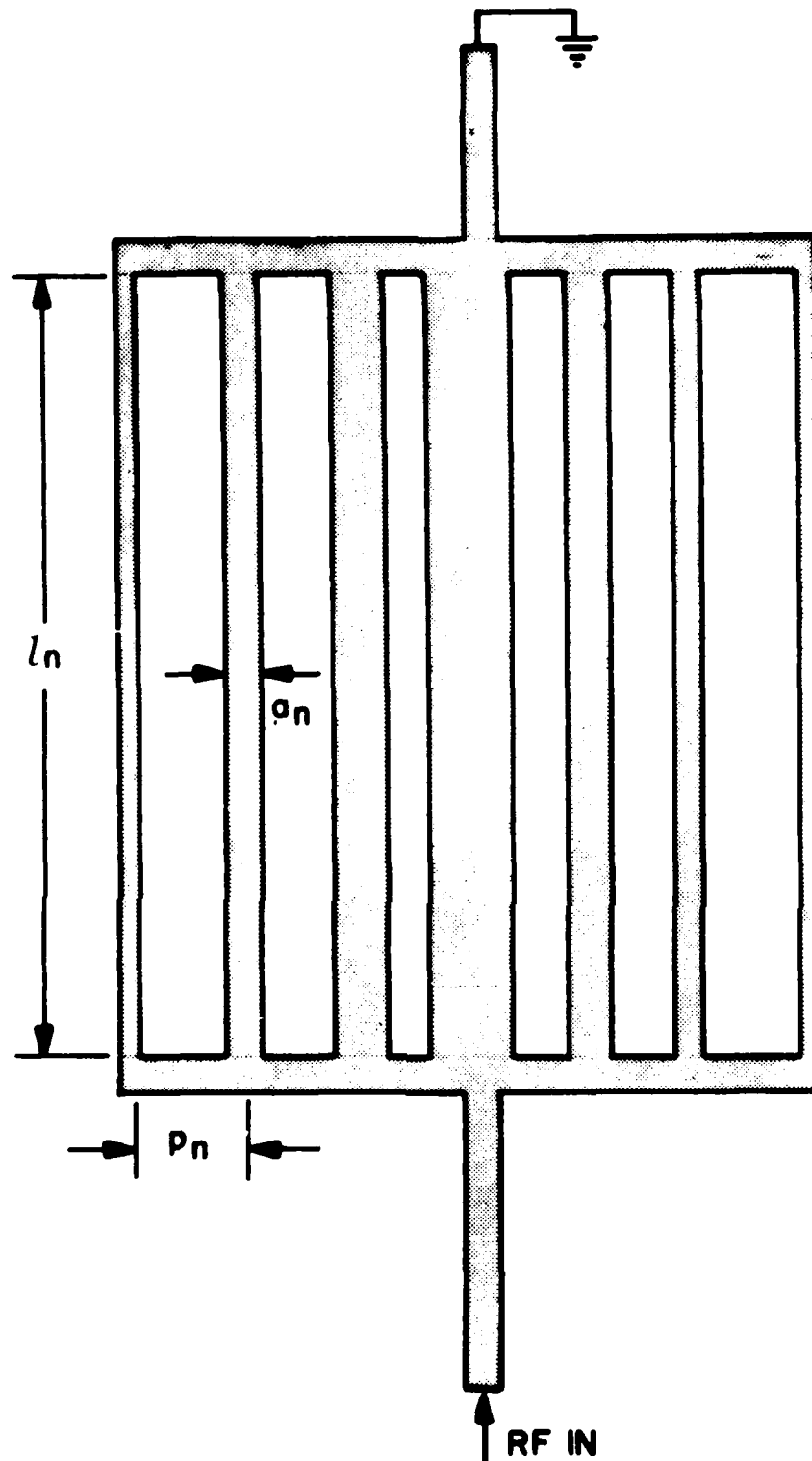
The term apodization is used to indicate any of three forms of weighted transducer elements. Thus; length, width, and spacing apodization refers, respectively, to transducers whose electrodes have weighted length, width and interelectrode spacing. Individual conducting strips, or electrodes, may be connected in parallel to form a grating, in series to form a meander line, or in some combination of series and parallel connections. Length and width apodized grating transducers are shown in Figure 4-26. Each strip has width " a_n ", length " l_n " and center to center spacing of adjacent strips, " p_n ". Another form of apodization that has been demonstrated to work well is that of current weighting.² The current in each individual strip may also be controlled with external circuitry.

2. Attaiyan, Y.J., Owens, J.M., Reed, K.W., and Carter, R.L. (1986) MSSW Transversal Filters Based on Current Weighting in Narrow ($10\mu\text{m}$) Transducers, *IEEE MTT-S Digest*, Paper U 5, 575-578.



LENGTH APODIZATION a_n AND p_n CONSTANT

Figure 4-26a. A length apodized transducer. Radiation resistance can be described by Eq. (4-2)



WIDTH APODIZATION l_n AND p_n CONSTANT

Figure 4-26b. A width apodized transducer. Radiation resistance described by Eq. (4-2), using Table 4-1 Column C. See also, Figure 4-30c, lower figure

Theoretical results given here assume current uniformity along the strip length and strip width. Mutual coupling between current elements and the reaction of the YIG back onto the flat current distribution are not taken into account. Consequently, the theory is most accurate for narrow strips and weak coupling between transducer and ferrite.

Figure 4-26a shows a grating transducer that is length apodized. Unconnected electrode pieces are left in place to reduce diffraction. Orientation of the H field shown in the figure is for coupling to MSSW, although the apodization adapts to forward and backward volume waves. Figure 4-26b shows a grating transducer with width apodization. Center-to-center spacing of electrodes is uniform.

All results in this section are obtainable from Eq. (1) of Reference 3 which is reproduced here as Eq. (4-2):

$$R_m(s) = \frac{R_1(s)}{C(\eta, N)} \times \left| \sum_{n=1}^N U_n V_n \right|^2 \quad (4-2)$$

where $C(\eta, N) = [(1 - \eta) + (1 + \eta)N^2] / 2$

and $U_n = (\eta)^n \text{SQR}(l_{1n}) \exp(-iknp_n)$

The parameter $\eta = +1$ for a grating and -1 for a meander line. Summation is from 1 to N, the number of individual conducting strips; $K (=2\pi/\text{wavelength})$ is the magnetostatic wavenumber; l_{1n} is the length of the nth strip and p_n is the center-to-center spacing between conductors. For a transducer made up of noninteracting strips

$$V_n = \text{sinc}[a_n K / (2\pi)] \quad (4-3)$$

with a_n the width of the nth conducting strip and $\text{sinc}(x)$ is defined as $[\sin(\pi x)]/(\pi x)$.

For a truncated infinite array transducer model

$$V_n = \text{sinc}\{2a_n/[p_n(3 - \eta)]\} \text{sinc}[Kp_n/(2\pi) - (3 + \eta)/4] \quad (4-4)$$

Equation (4-4) applies to apodization of the fundamental normal mode.^{4,5} For a given K the quantities U_n and V_n are functions of transducer dimensions while $C(\eta, N)$ defines how individual strips are connected together.

4.11.1 MSSW APODIZATION

The term $R_1(s)$, defined by Eq. (4-5) below, is a function of liftoff gap g , YIG parameters, and ground plane spacing t_1 and l . Its derivation is published in Reference 6.

3. Sethares, J.C. and Weinberg, I.J. (1979) Apodization of Variable Coupling MSSW Transducers, *J. Appl. Phys.* **50**(3):2458-2460.
4. Sethares, J.C. (1978) Magnetostatic Surface Wave Transducer Design, IEEE Cat. No. 78CH1355-7, MTT, *International Microwave Symposium Digest*, pp 443-446.
5. Sethares, J.C. (1979) Magnetostatic Surface Wave Transducers, *IEEE Trans. MTT* **27**:902-909.
6. Weinberg, I.J. and Sethares, J.C. (1978) *Magnetostatic Wave Transducers With Variable Coupling*, RADC-TR-78-205, ADA063880.

$$R_1(s) = \frac{\omega \mu_0 \exp(-2\beta Kd)}{(K^2) |F'_T(K)|^2} |A_S| \quad (4-5)$$

where A_S and $F'_T(k)$ are defined as follows. The quantity $\omega = 2\pi f$ is the frequency in radians per second, μ_0 the permeability of free space, and d the YIG thickness.

$$\begin{aligned} A_S = & \frac{(T+1)^2}{4 \cosh^2(Kl)} (\sinh(2Kl) - 2Kl) \\ & + \frac{(R_1 e^{Kg} - R_2 e^{-Kg})^2}{16 \sinh^2(Kt_1)} (\sinh(2Kt_1) - 2Kt_1) \\ & + 1/8 (R_1^2 (e^{2Kg} - 1) - R_2^2 (e^{-2Kg} - 1) - 4R_1 R_2 Kg) \\ & + \frac{\alpha_1}{2} T^2 (e^{2\beta Kd} - 1) - \frac{\alpha_2}{2} (e^{-2\beta Kd} - 1) - 2\mu_{11} K T d. \end{aligned} \quad (4-6)$$

$$\begin{aligned} 2sF'_T(K) = & t_1 e^{-\beta Kd} (R_1 e^{Kg} - R_2 e^{-Kg}) \operatorname{csch}^2(Kt_1) \\ & - g e^{-\beta Kd} [(C+1)R_1 e^{Kg} + (C-1)R_2 e^{-Kg}] \\ & + 2\beta d e^{-2\beta Kd} [(C+1)(1-\alpha_2)e^{Kg} - (C-1)(1+\alpha_2)e^{-Kg}] \\ & + [(C-1)(1-\alpha_1)e^{-Kg} - (C+1)(1+\alpha_1)e^{Kg}] \frac{l(\alpha_1 + \alpha_2) \operatorname{sech}^2(Kl)}{[\alpha_1 - \tanh(Kl)]^2} \end{aligned} \quad (4-7)$$

where

$$\begin{aligned} R_1 &= (1 - \alpha_2) e^{-\beta Kd} + (1 + \alpha_1) T e^{\beta Kd} \\ R_2 &= (1 + \alpha_2) e^{-\beta Kd} + (1 - \alpha_1) T e^{\beta Kd} \\ C &= \coth(Kt_1) \\ T &= [\alpha_2 + \tanh(Kl)] / [\alpha_1 - \tanh(Kl)] \end{aligned} \quad (4-8)$$

For a given frequency, magnetic field, and set of dimensions, the magnetostatic wavenumber is obtained from the dispersion relation, Eq. (4-9).

$$\exp(-2\beta Kd) = \frac{[\alpha_2 + \tanh(Kl)] [\alpha_1 + \tanh(K\tau)]}{[\alpha_1 - \tanh(Kl)] [\alpha_2 - \tanh(K\tau)]} \quad (4-9)$$

$$\text{where } \beta = \sqrt{\mu_{11}/\mu_{22}}$$

$$\alpha_1 = \mu_{22} \beta + s\mu_{12}$$

$$\alpha_2 = \mu_{22} \beta - s\mu_{12}$$

and

$$\tau = g + t_1 \quad (4-10)$$

The parameter $s = (+/-)1$ defines propagation direction through the factor

$$\exp[i(\omega t - sKx)] .$$

β and K are real and positive. The μ_{ij} are components of the relative permeability tensor for YIG. For magnetostatic surface waves in an isotropic ferrite,

$$\mu_{11} = \mu_{22} = 1 - \Omega_H / (\Omega^2 - \Omega_H^2)$$

$$\mu_{12} = \Omega / (\Omega^2 - \Omega_H^2)$$

where

$$\Omega_H = H / (4\pi M)$$

$$\Omega = (\omega / \gamma) / (4\pi M) \quad (4-11)$$

with γ the gyromagnetic ratio, $4\pi M$ the saturation magnetization and H the internal biasing field.

When there are no ground planes, $R_1(s)$ takes on a simple form, and an exponential liftoff dependence becomes evident. Substitution of A_g and F'_T into Eq. (4-5) and letting l and t_1 approach infinity yields the liftoff dependence when there are no ground planes.

$$R_1(s) = |R_{10}(s)| \exp(-2Kg) \quad (4-12)$$

where

$$R_{10}(s) = \frac{\omega \mu_0 \mu_{22} T \exp(2\beta Kd)}{2Kd(\alpha_2 - 1)^2} \quad (4-13)$$

$R_{10}(s)$ is independent of liftoff, g . When $g = 0$, the radiation resistance reduces to that of Ganguly and Webb's⁷ Eq. (45).

4.11.2 NORMAL MODE AND INDEPENDENT CONDUCTORS

Figures 4-27a, b, and c show apodization of the lowest order normal mode, $n=1$, of an eight element meander line. Figures 4-28a, b, and c are similar to Figures 4-27a, b, and c, respectively, except that the independent conductor model is used for apodization in place of the normal mode model.

These figures show that if the frequency range of interest is narrow and centered about the fundamental mode, $n=1$, then either the normal mode or independent conductor model can be used for apodization. For wide bandwidth operation, encompassing several normal modes, the independent conductor model must be used.

7. Ganguly, A.K. and Webb, D. (1975) Microstrip Excitation of MSSW, *IEEE Trans MTT* **23**:998.

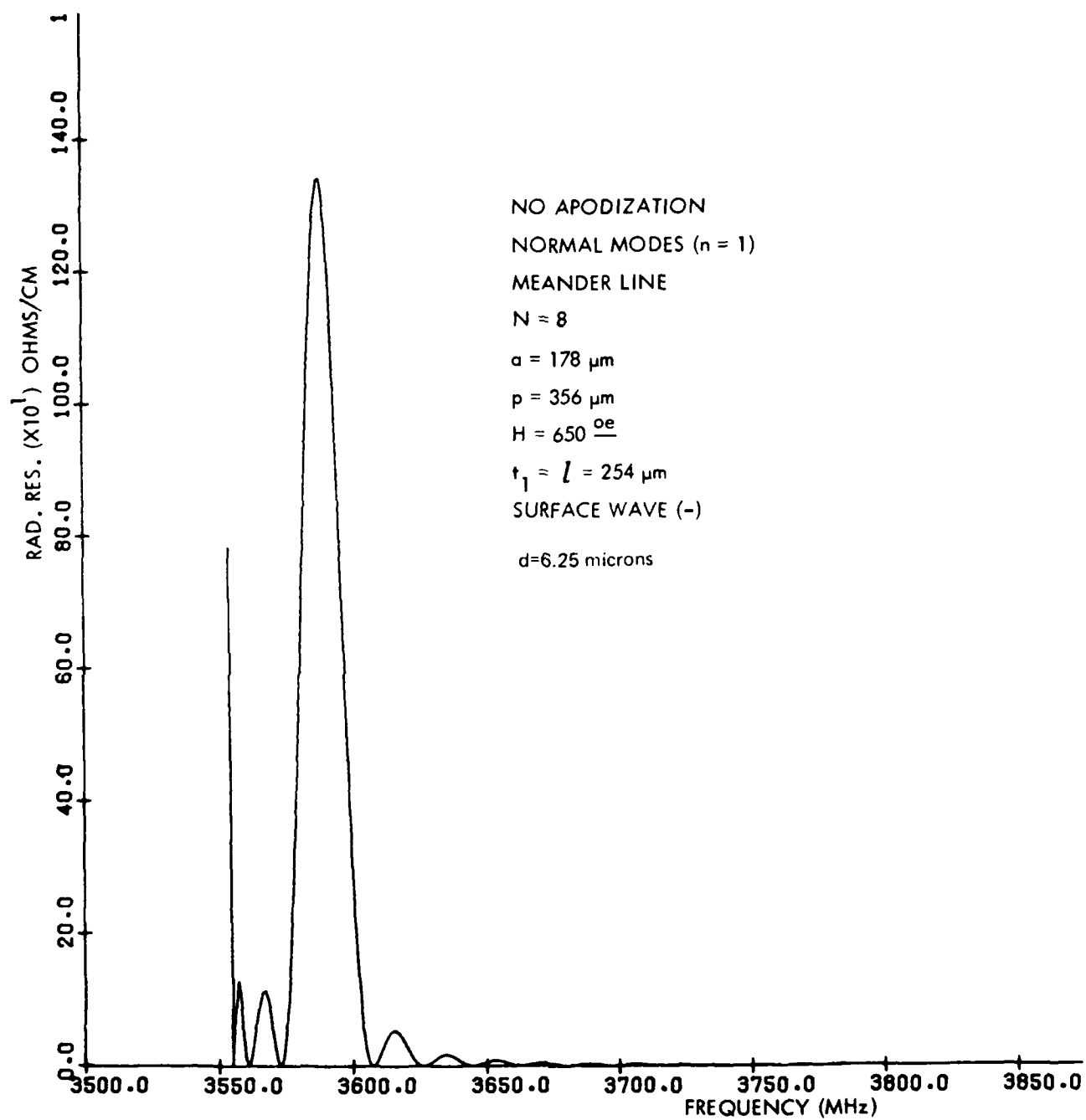


Figure 4-27a. Apodization of Fundamental Normal Mode for an 8-Element Meander Line (No Apodization)

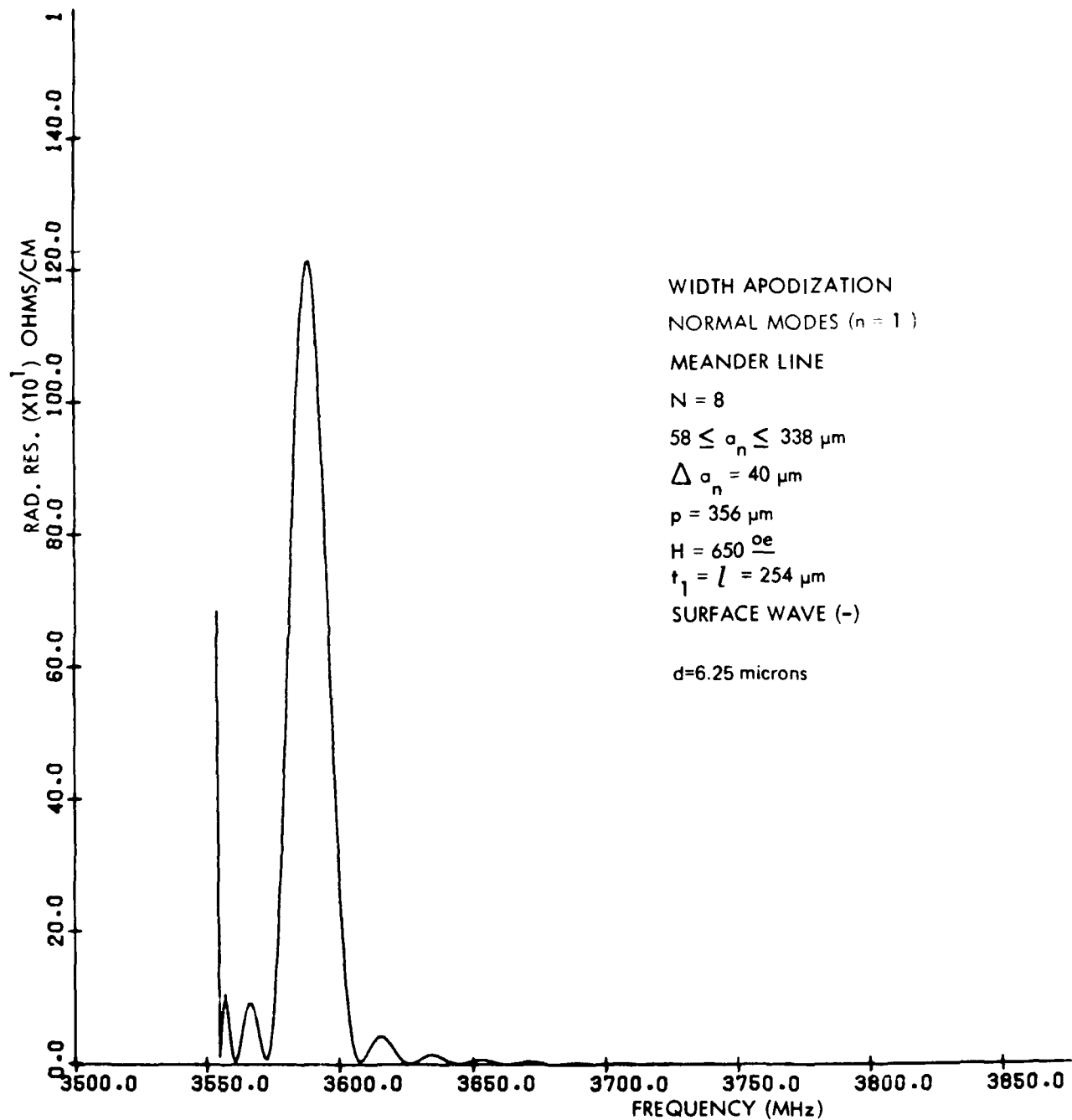


Figure 4-27b. Apodization of Fundamental Normal Mode for an 8-Element Meander Line (Width Weighted)

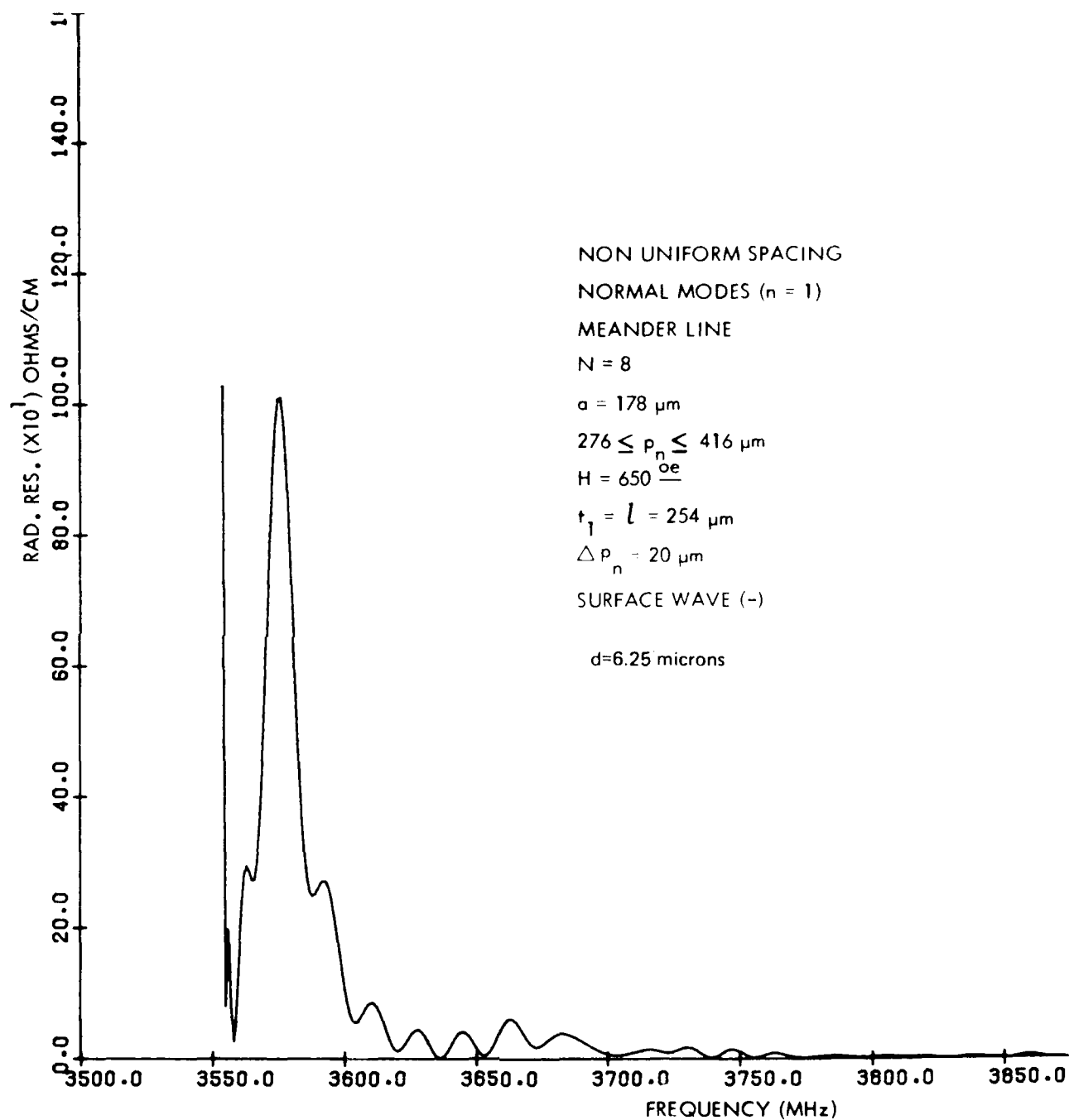


Figure 4-27c. Apodization of Fundamental Normal Mode for an 8-Element Meander Line (Nonuniform Spacing)

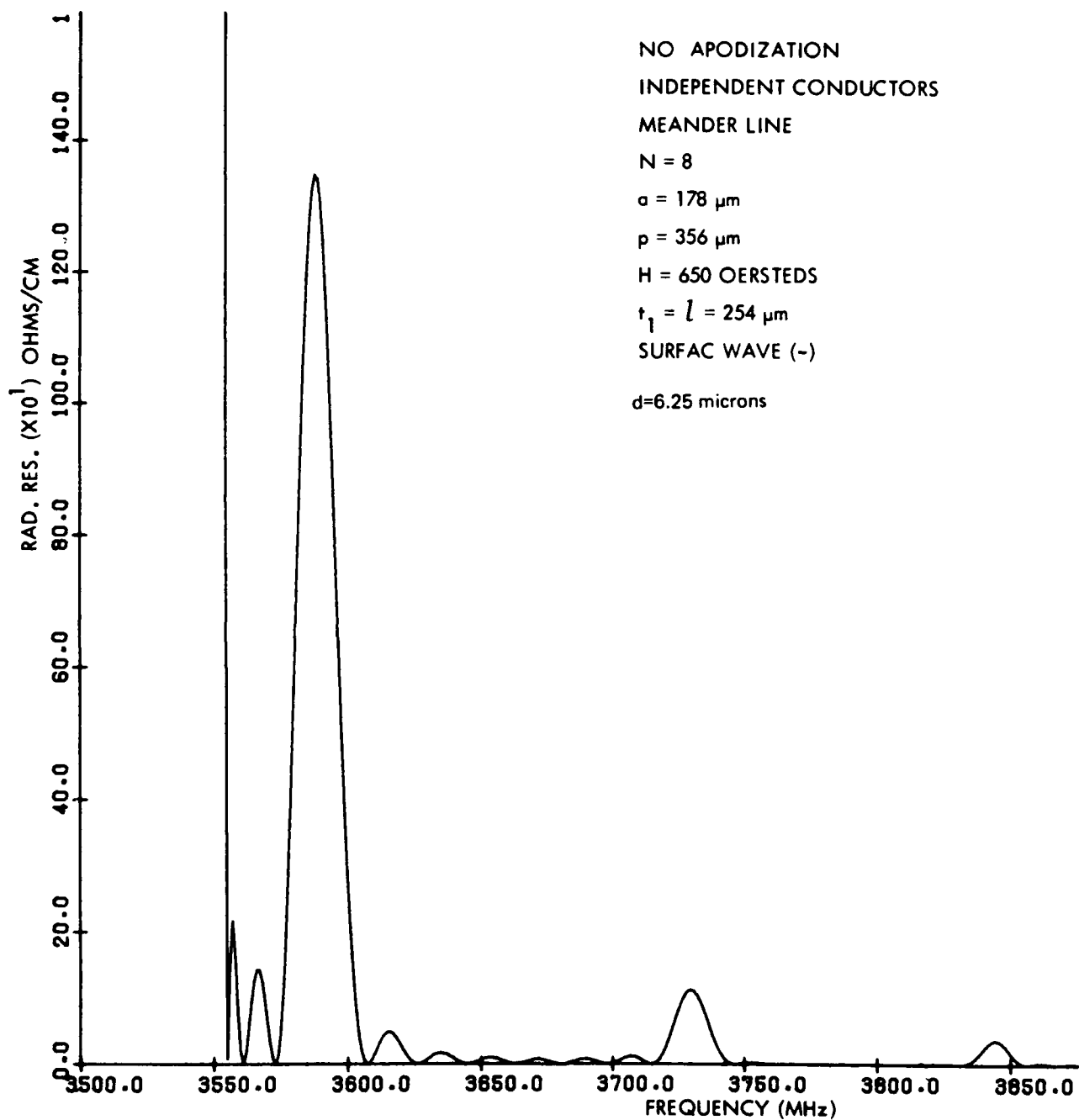


Figure 4-28a. Apodization of Independent Conductors for an 8-Element Meander Line (No Apodization)

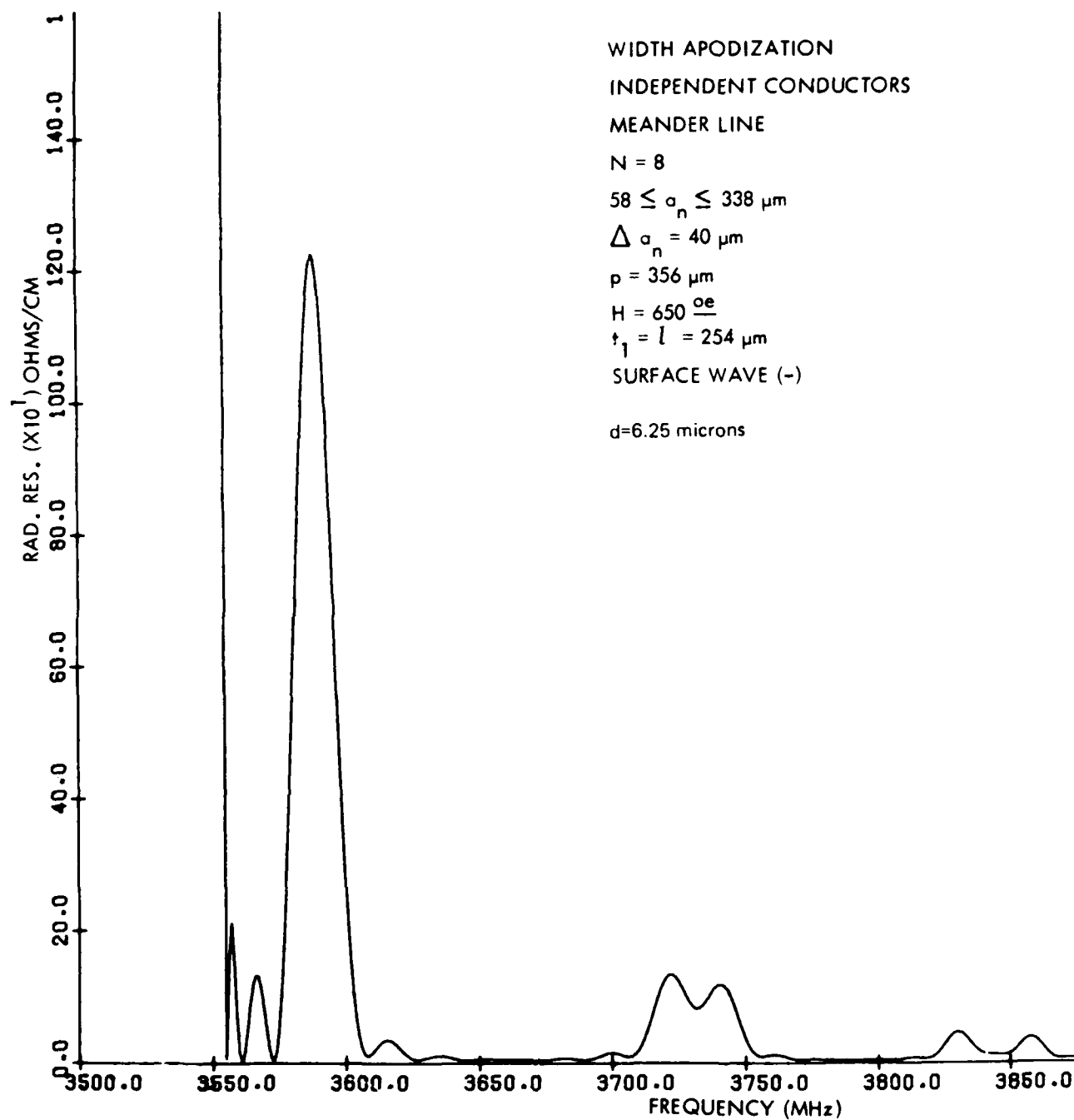


Figure 4-28b. Apodization of Independent Conductors for an 8-Element Meander Line (Width Weighted)

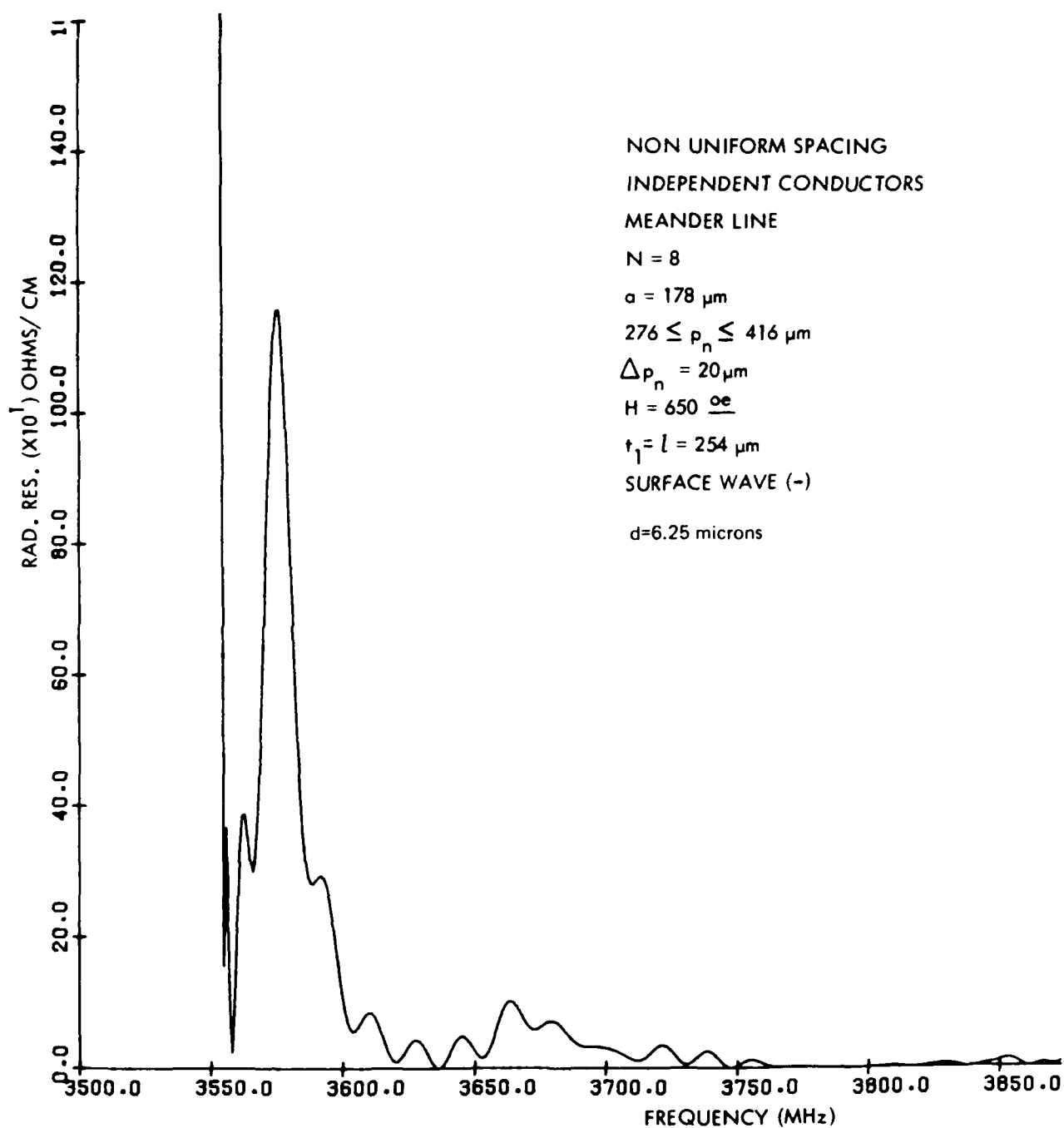


Figure 4-28c. Apodization of Independent Conductors for an 8-Element Meander Line (Nonuniform Spacing)

Width and nonuniform spacing apodization, for the parameters chosen here, do not significantly affect frequency response below 3700 MHz. Above 3700 MHz the effects are pronounced as evidenced by the double response peak near 3725 MHz in Figure 4-28b.

The magnetic biasing field is 650 oersteds and YIG thickness is 6.25 μm for all figures. Ground planes are spaced 254 μm from the YIG surfaces. The minus surface wave is the one most weakly excited with most of its energy on the YIG surface furthest from the transducer. The plus wave has most of its energy on the YIG surface closest to the transducer. The plus wave propagates in the $\mathbf{H} \times \hat{\mathbf{n}}$ direction, where $\hat{\mathbf{n}}$ points outward from the same surface.

Apodization parameters for Figures 4-27 and 4-28 are as follows. For width apodization, in Figures 4-27b and 4-28b, a linear weighting is used; that is, the eight element widths are 58, 98, 138, 178, 218, 258, 298, and 338 μm . Adjacent electrodes differ in width by 40 μm . Center-to-center spacing is 356 μm for all adjacent electrodes.

For the electrode spacing apodization, all eight elements are 178 μm wide. The eight electrodes are centered within the following eight adjacent spaces whose widths are 276, 296, 316, 336, 356, 376, 396, and 416 μm .

Figures 4-29a and 4-29b compare apodization of plus and minus waves. The only significant difference between the two waves is the magnitude of the radiation resistance at a given frequency. This does not necessarily imply that one of the waves is more efficiently generated than the other for all frequencies. For example, neglecting reactances for the moment, the excitation efficiency is dependent on the relative value of radiation resistance to driving source resistance. Assuming a one centimeter transducer aperture and a 100 ohm source resistance, then at 3675 MHz the minus wave is more efficiently excited than the plus wave. This is because the radiation resistance of the minus wave (see Figure 4-29b) is closer to 100 ohms than the radiation resistance of the plus wave (Figure 4-29a) at the same frequency.

4.11.3 INSERTION LOSS

In Sections 4.11.1 and 4.11.2 we discussed the effects of apodization on the radiation resistance. In this section we discuss the effects of apodization on insertion loss. For illustration, we chose a width-weighted 15-element grating transducer. For width apodization and with $N = 15$, $\eta = 1$ for a grating, $C(\eta = 1, N) = N^2$ and; $\eta^n = 1$ for all n , $L1_n = L1$ and $p_n = p$, then Eq. (4-2) with the help of Eqs. (4-3) and (4-4), becomes:

$$R_m(s) = \frac{R_1(s)l_1}{N^2} \left| \sum_{n=1}^{15} e^{-iKnp} \frac{\sin(a_n K/2)}{(a_n K/2)Knp} \right|^2 \quad (4-14)$$

For weighted transducers the delay line insertion loss is given by

$$\text{I.L.}(s) = 20 \log \left[\frac{(R_g + R_m)^2 + X_m^2}{4R_g R_m(s)} \right] \quad (4-15)$$

for the independent conductor model. $R_m(s)$ is now given by Eq. (4-14) with $R_m(s)$ a function of N and a_n .

The computer programs first calculate $R_m(s)$ for a given biasing field, frequency and transducer dimensions. Then X_m is obtained by taking the Hilbert Transform of $R_m = R_m(+) + R_m(-)$. Figure 4-30

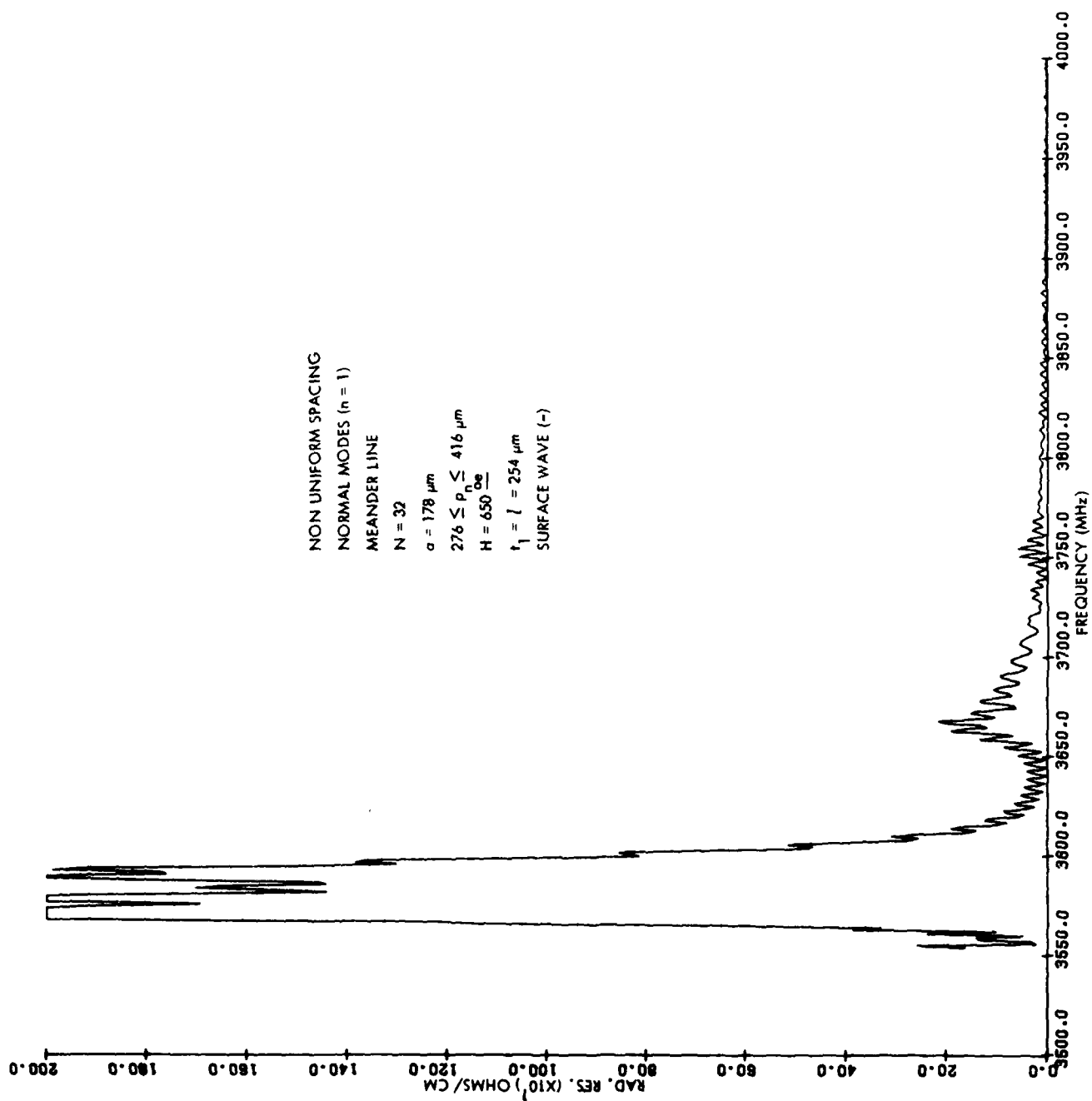


Figure 4-29a. Normal Mode Apodization of a 32-Element Meander Line for Minus Surface Wave, $s = -1$

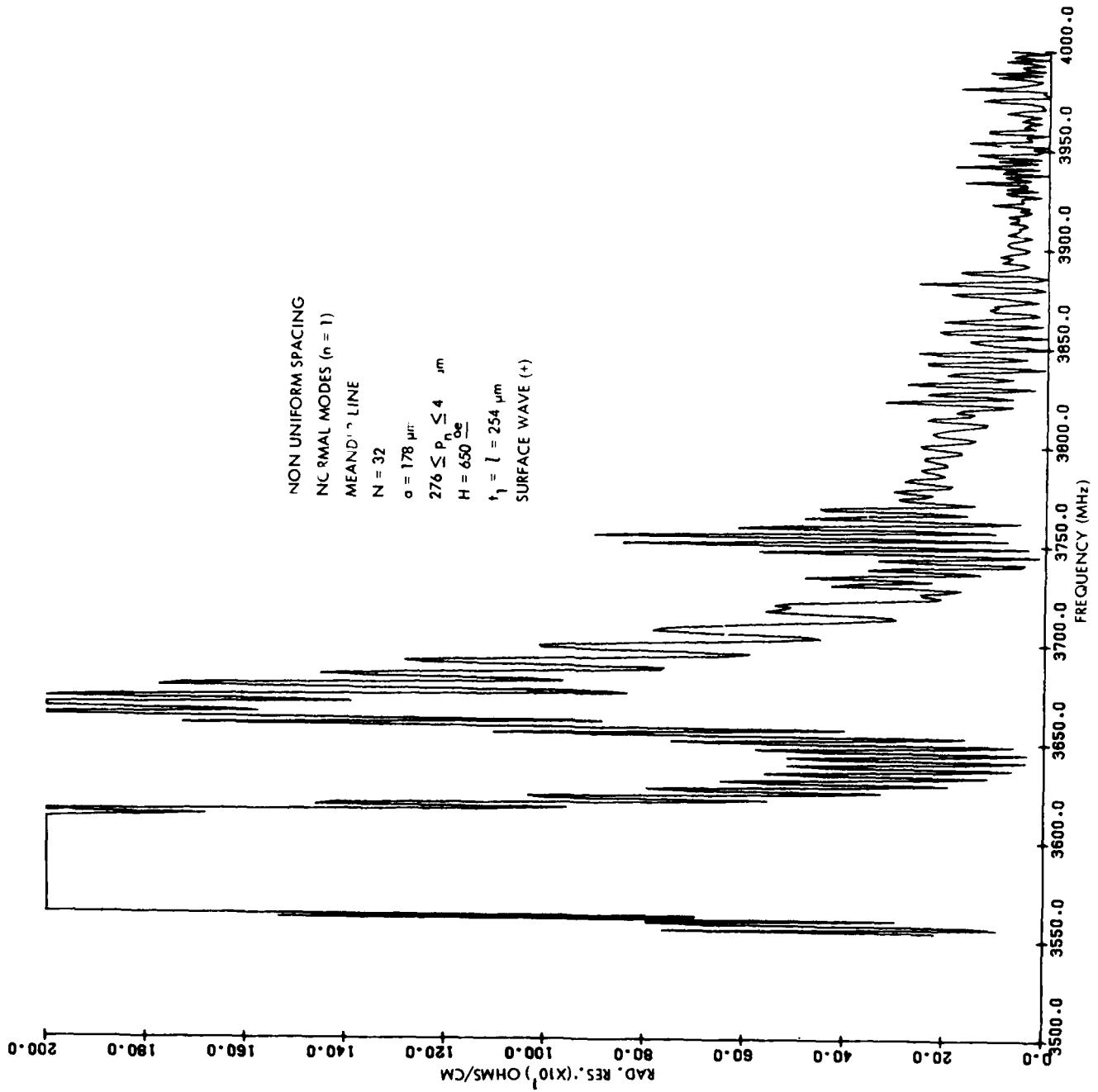


Figure 4-29b. Normal Mode Apodization of a 32-Element Meander Line for Plus Surface Wave, $s = +1$

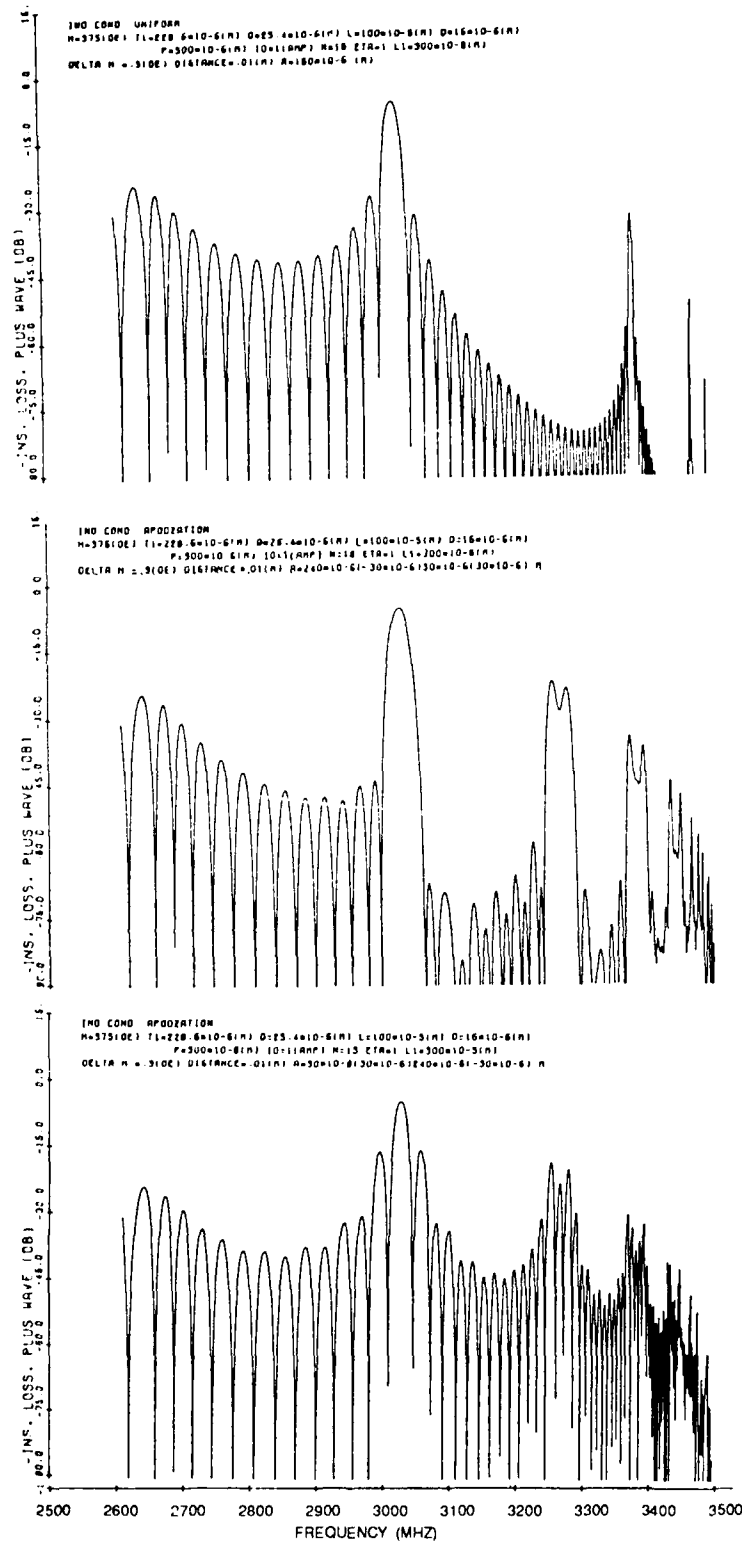


Figure 4-30. Width Apodization of a 15-Element Grating Transducer Using Independent Conductor Analysis

- No apodization, top figure, Table 4-1, Column A
- Apodized, narrow strips in center, middle figure, see Table 4-1, Column B
- Apodized, Wide strips in center, lower figure, see Table 4-1, Column C

shows insertion loss versus frequency. Figure 4-30a is the insertion loss of a uniform, nonapodized transducer. For all three curves in Figure 4-30, biasing field $H = 375$ oersteds, ground plane spacing $T_1 = 228.6 \mu\text{m}$, transducer liftoff $g = 25.4 \mu\text{m}$, ground plane spacing $L = 10$ meters, which is effectively infinite, YIG thickness $d = 16 \mu\text{m}$, center to center spacing of individual transducer strips $p = 300 \mu\text{m}$, number of strips $N = 15$, $\eta = 1$ for the parallel grating connection, transducer aperture $L_1 = 5$ mm, YIG linewidth $\Delta H = 0.3$ oersteds, and propagation distance = 1 cm. For the uniform transducers (Figure 4-30a) all strips are $150 \mu\text{m}$ wide. Strip widths for Figure 4-30 are given in Table 4-1.

Table 4-1. Strip Widths for Figure 4-30

n	$a_n (\mu\text{m})$		
	(a)	(b)	(c)
1	150	240	30
2	150	210	60
3	150	180	90
4	150	150	120
5	150	120	150
6	150	90	180
7	150	60	210
8	150	30	240
9	150	60	210
10	150	90	180
11	150	120	150
12	150	150	120
13	150	180	90
14	150	210	60
15	150	240	30

The fundamental transducer response, synchronism, for all three cases occurs just above 3000 MHz. The fundamental spatial periodicity and the MSW wavelength are the same, $300 \mu\text{m}$, for all responses. For the uniform grating, (Figure 4-30a) the first spatial harmonic occurs just below 3400 MHz where the MSW wavelength is $150 \mu\text{m}$. In the other two apodized responses, the first spatial harmonic occurs just above 3250 MHz where the wavelength is close to $225 \mu\text{m}$. The theoretical apodization formula, Eq. (4-2), has been independently verified by Ishak⁸. It is most accurate when strips are narrow compared to interelectrode spacings.

8. Ishak, W., Hewlett Packard, Palo Alto, CA, private communication.

References

1. Parekh, J.P. and Tuan, H.S. (1987) *Studies of MSFVW to MSBVW Mode Conversion at a Region of Bias Field Discontinuity and of the Dispersion of an MSFVW Pulse*, RADC-TR-87-201, ADA189343.
2. Attaliyan, Y.J., Owens, J.M., Reed, K.W., and Carter, R.L. (1986) MSSW Transversal Filters Based on Current Weighting in Narrow (10 μm) Transducers, *IEEE MTT-S Digest*, Paper U 5, 575-578.
3. Sethares, J.C. and Weinberg, I.J. (1979) Apodization of Variable Coupling MSSW Transducers, *J. Appl. Phys.* **50**(3):2458-2460.
4. Sethares, J.C. (1978) Magnetostatic Surface Wave Transducer Design, IEEE Cat. No. 78CH1355-7, MTT, *International Microwave Symposium Digest*, pp 443-446.
5. Sethares, J.C. (1979) Magnetostatic Surface Wave Transducers, *IEEE Trans. MTT* **27**:902-909.
6. Weinberg, I.J. and Sethares, J.C. (1978) *Magnetostatic Wave Transducers With Variable Coupling*, RADC-TR-78-205, ADA063880.
7. Ganguly, A.K. and Webb, D. (1975) Microstrip Excitation of MSSW, *IEEE Trans MTT* **23**:998.
8. Ishak, W., Hewlett Packard, Palo Alto, CA, private communication.

5. EXPERIMENTAL DATA

Chapter 5 describes the results of MSW experiments performed at RADC. Many of the results have not previously been published. In those instances where they have been published, the more important results are highlighted, and references to the original literature are provided for further details.

Three types of experiments were performed. In one type, CW experiments on delay lines using a network analyzer were performed to measure scattering parameters. From scattering parameter measurements, insertion loss and phase delay are obtained. In a second type of experiment, a spectrum analyzer is used to measure oscillator frequency spectra. The third type uses RF pulses containing many RF periods. The shortest pulse length used was 20 nsec because of equipment limitations. Pulse propagation times are measured directly with an oscilloscope. Sections 5.1, 5.2, and 5.3 describe insertion loss measurements using CW experiments. Section 5.4 describes pulse propagation experiments and Section 5.5 describes oscillator experiments. The remaining sections in Chapter 5 describe various aspects of MSW characteristics or devices.

5.1 Insertion Loss and Time Delay from Scattering Parameters

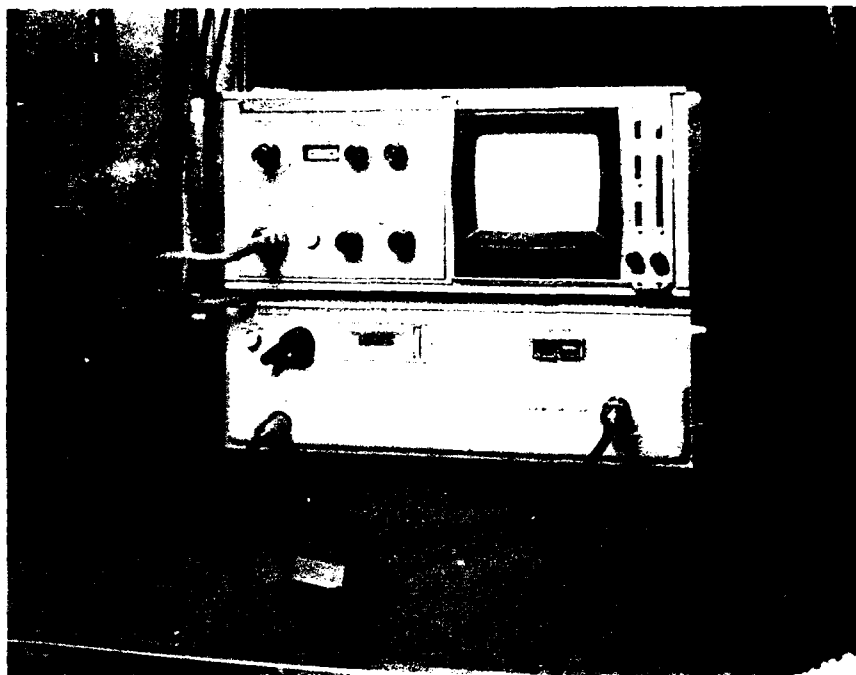
Insertion loss versus frequency, and phase versus frequency for a delay line were measured with the network analyzer shown in Figure 5-1. The analyzer actually measures scattering parameters from which insertion loss and time delay are derived. Figure 5-1a shows an MSW delay line under test. Insertion loss versus frequency is displayed on the screen. Figure 5-1b shows insertion phase versus frequency for the same device over the same frequency range. Experimental IL data can be compared directly with computer generated IL data. Group time delay is derived from the slope of the phase versus frequency network analyzer output data.

The magnitude of the scattering parameter S_{21} , in dB, is the same as the IL from computer generated output. The zero dB reference level in Figure 5-1a is at the top of the scope screen. Increasing IL is downward on the vertical scale. The horizontal scale is frequency. Essentially, Figure 5-1a displays the frequency passband of a delay line. The phase ϕ , of S_{21} , is equal to $\phi_0 + \phi_K$ where $\phi_K = K\Delta R$, $K = 2\pi/\lambda$ is the MSW propagation constant and ΔR the distance between input and output transducer, thus

$$\phi = \phi_0 + \phi_K. \quad (5-1)$$

The EM phase shift in connecting cables and connectors external to the delay line reference planes is ϕ_0 . Over the bandwidth of an MSW delay line, ϕ_K is generally much larger than ϕ_0 , except in the very long MSW wavelength region where all MSW theories break down anyway. The network analyzer displays phase shift modulo 360 degrees. In Figure 5-1b the vertical scale extends from -180 to +180 degrees. The absolute phase value is determined by adding an appropriate integral number of 360 degrees of phase shift. Long MSW wavelengths, for which K approaches zero, occur at the low frequency end of the passband for MSSW and MSFVWs; and at the high frequency end of the passband for MSBVWs. This latter point is further discussed in connection with Figure 5-2. Figure 5-2 depicts phase shift versus frequency of a MSBVW delay line (see Figure 5-2a) and a MSSW delay line, (see Figure 5-2b). First, we note that the phase versus frequency line segments change slope as a function of

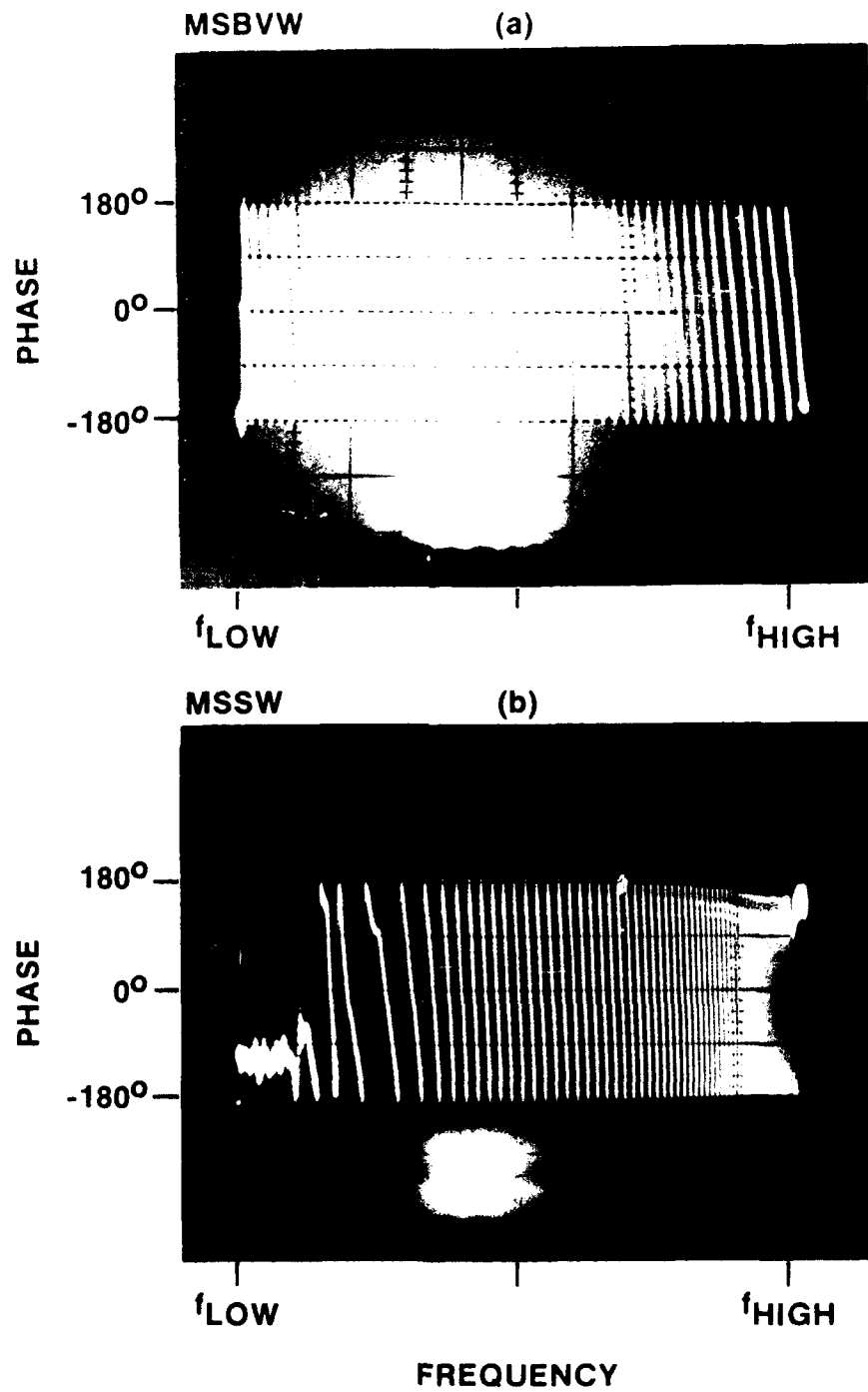
- a. "IL" versus f . Horizontal scale, 2500-3500 MHz. Vertical scale, 10 dB/div, minimum, IL = 12 dB.



- b. Transmission phase versus f . Horizontal scale 2500-3500 MHz. Vertical scale, 90 deg/div.



Figure 5-1. Network Analyzer Displays of Insertion Loss and Transmission Phase as Function of Frequency, for Unmatched Delay Line.



5-2. Phase versus f for MSBVW Delay Line, Top Figure; and MSSW, Lower Figure

frequency. This is due to the dispersive nature of MSW. That is, different frequencies travel with different velocities. Secondly, we note that larger slopes occur at opposite ends of the frequency band for MSBVWs and MSSWs. This means that over a finite bandwidth, two delay lines can be connected in series to produce a cascaded device in which total group time delay is constant, that is, independent of frequency.

The relationship between group time delay and phase of S21 can be obtained as follows. Group velocity is given by Eq. (5-2).

$$v_g = \frac{\partial \omega}{\partial K} \quad (5-2)$$

and group time delay is given by,

$$\tau_g = \Delta R / v_g \quad (5-3)$$

where ΔR is the distance between input and output transducers. For a small change in frequency; $\Delta \phi$, a small change in ϕ , is very nearly equal to $\Delta \phi_K = \Delta R \Delta K$, because ϕ_O is much less sensitive to frequency changes than is ϕ_K . With $\Delta \phi \cong \Delta R \Delta K$ and the use of Eqs. 5-2 and 5-3, we have for well behaved functions, that is no discontinuities in ϕ versus ω ,

$$\tau_g = \lim_{\Delta f \rightarrow 0} \left[\frac{\Delta \phi}{\Delta \omega} \right] \quad (5-4)$$

From Figure 5-2 we can see the variation of group delay across the passband. Further, a large (small) slope, $\Delta \phi / \Delta \omega$, means a long (short) time delay.

5.2 Dispersion Relation from CW Experiments

At a fixed frequency, the propagation constant K may be determined from Eq. (5-1) using the approximation that $\phi_O \ll \phi_K$. This is an excellent approximation over most of the passband. It breaks down near the end of the passband where $K \rightarrow 0$. The close agreement between theory and experiment is shown in Figure 5-3. The solid line is a theoretical curve from the computer programs and the dashed line represents experiment. Experimental data were taken from 2380 to 3250 MHz which corresponds to an observable bandwidth of 870 MHz. Outside this band insertion loss was excessive.

5.3 Insertion Loss: Theory and Experiment

Agreement between theory and experiment of the insertion loss of single element transducers, and of a small number of narrow multielement transducers, is excellent, especially considering the assumptions made. This is shown in Sections 5.3.1 and 5.3.2. For a small number of thin conducting strips, no significant differences have yet been found between the predictions of the two models described in this report, the TT and TL models. When the number of transducer elements is large and strips are wide both theories break down catastrophically. This is demonstrated in Section 5.3.3.

5.3.1 SINGLE ELEMENT TRANSDUCERS

Figure 5-4 shows the excellent agreement between theory and experiment for single element transducers. The figure is for a FVW delay line having a pair of single element transducers. The delay

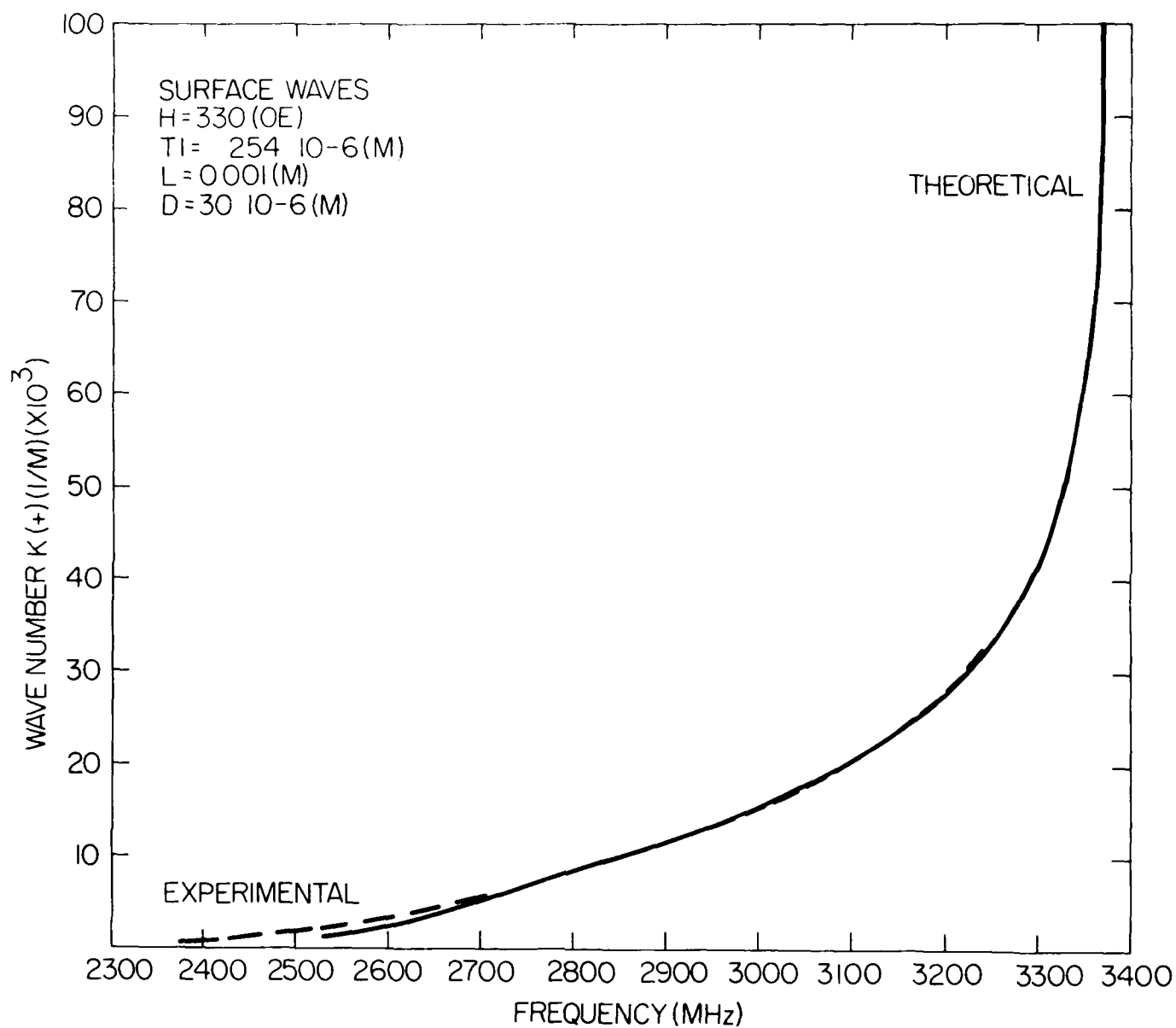
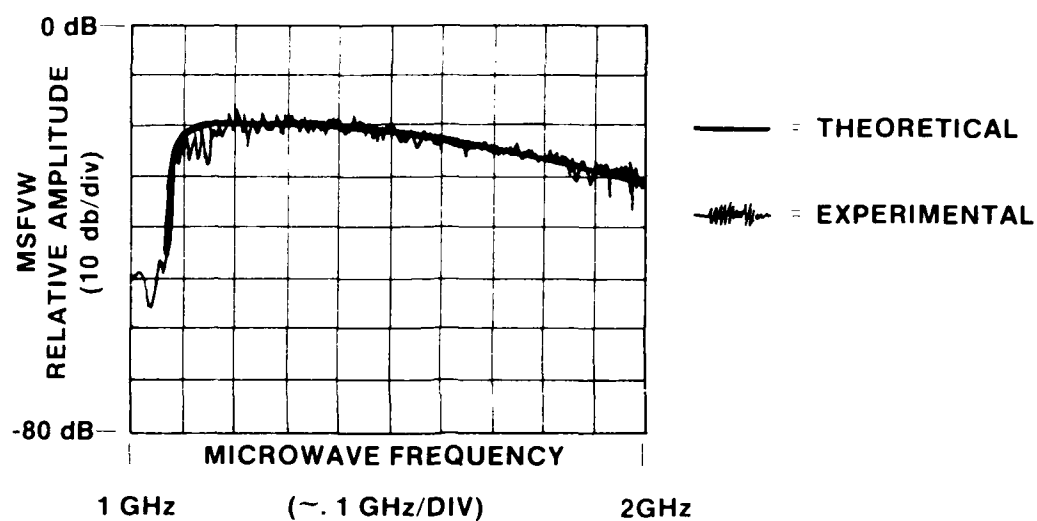


Figure 5-3. Theory versus Experiment Using Data Obtained from Phase of S21, a Transmission Scattering Coefficient

RELATIVE AMPLITUDE OF MSFVW
1 INCH YIG DISK

EXPERIMENTAL FIELD
 $H_0 = 1900\text{G.}$



THEORETICAL MODEL PARAMETERS

FORWARD VOLUME WAVES

H 400.0 TI .100 E-01 G .169 E-04 D .474 E-04 L .100 E-01 L_1 .300 E-02
A .500 E-04 P .300 E-03 DIST .008 DH .50 E-00 ETA 1. N 1
RL 45
1st (M=0) MODE

Figure 5-4. Theory versus Experiment for Single Element Transducers and FVW Delay Line.

Theory: two terminal model, TT.

Experiment: Data supplied by N. Vlannes, MIT, 1984.

line was fabricated in the central portion of a one inch diameter YIG film so that reflections from edges were minimized. Parameters used for the TT model program are listed in the figure. Input parameter H , for theoretical calculations, is the internal demagnetized field.

Similar agreement between theory and experiment, as represented by Figure 5-4, exists for the other two principal MSW modes.

Figure 5-5 also shows excellent agreement between theory and experiment for single element transducers, in this case MSSW. Here, however, the effects of changing the coupling between transducer and YIG is also shown. The upper left hand figure, $h = 0$, corresponds to a transducer touching the YIG surface. Parameter h gives the number of mils (thousandths of an inch) between transducer and YIG. The spacing was implemented with mylar spacers. Theory used is the TT model and the experimental data was provided by J. Parekh at the State University of New York at Stonybrook.

5.3.2 MULTIELEMENT TRANSDUCER DELAY LINES

Figure 5-6 shows reasonably good agreement between theory and experiment for a 2-element and an 8-element MSSW device. No loss was included in the theoretical curves. Experimental data was provided by H. Wu, from the University of Texas at Arlington. Clearly, the main features of the experiments are predicted by the theory. The fine structure and side lobe levels near the main response in the 8-element device are not adequately accounted for by the theory. The experimental response near the low end of the frequency band for the 8-element device shows significant deviation from theory. This deviation becomes more apparent as the number of elements increases, as shown dramatically in the next section.

5.3.3 LIMITS OF THE THEORY

As has been stated several times in this report, present MSW transducer theory works well for a small number of thin conducting strips. When the number of strips is large, 15 for example, and the strips are wide in comparison to interelectrode spacing, the theory breaks down catastrophically. This is shown in Figure 5-7.

Figure 5-7 shows the theoretical and experimental insertion loss for a 15-element grating transducer. Two of the transducers have been width weighted as indicated in the figure. Periodicity of all three transducers is the same so that the main transducer response occurs at the same frequency, 3 GHz, for all three transducers.

Near the main response, theory is breaking down primarily because the strips are wide. The theory should work well as long as the strips are narrow, and as long as overall transducer dimensions are small compared to electromagnetic wavelengths. The number of strips may actually be large while at the same time satisfying the preceding conditions. As for the weighting theory, it has been tested for narrow strips. It works well.

Near the low end of the passband, 2.5 GHz, theory and experiment do not agree. This is because several assumptions are violated here at the low frequency end of the MSSW passband. MSW wavelengths are comparable to transducer dimensions, and MSW beams spread out. They are not collimated as they are when MSW wavelengths are small compared to transducer aperture.

MSSW INSERTION LOSS VERSUS FREQUENCY THEORY AND EXPERIMENT

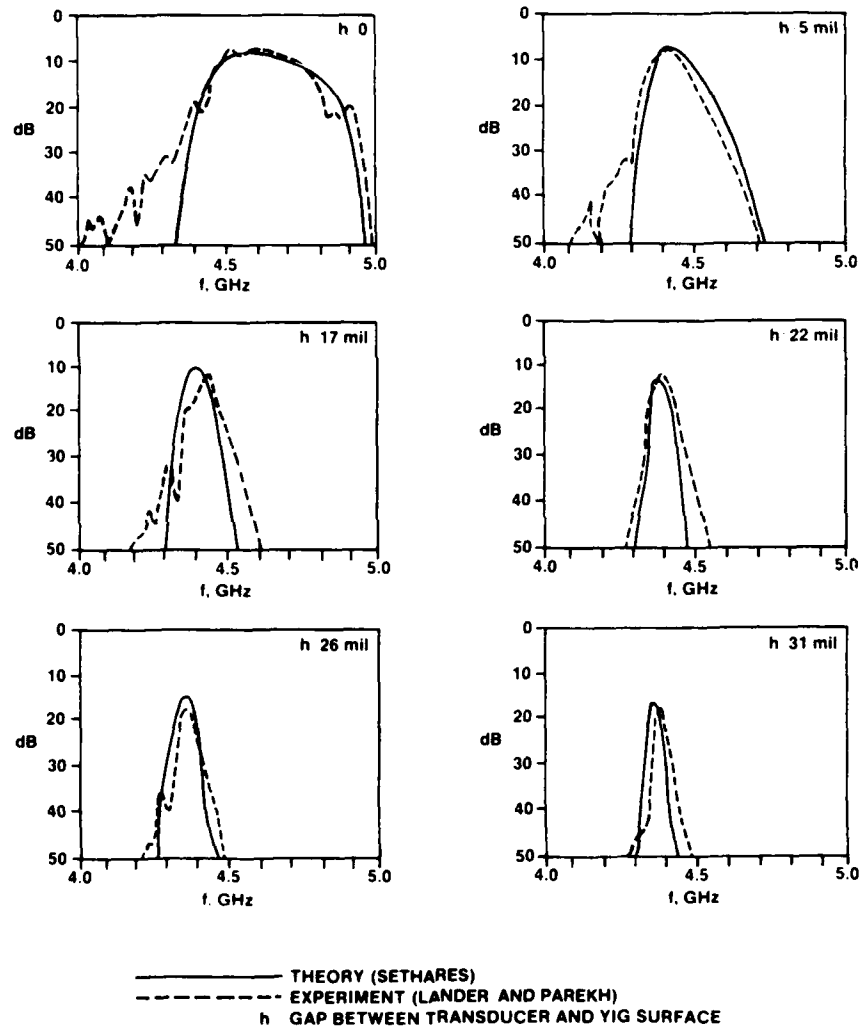


Figure 5-5. MSSW Passbands for Various Values of Liftoff; Theory and Experiment. Experimental data provided by J. Parekh, NYSU at Stonybrook.

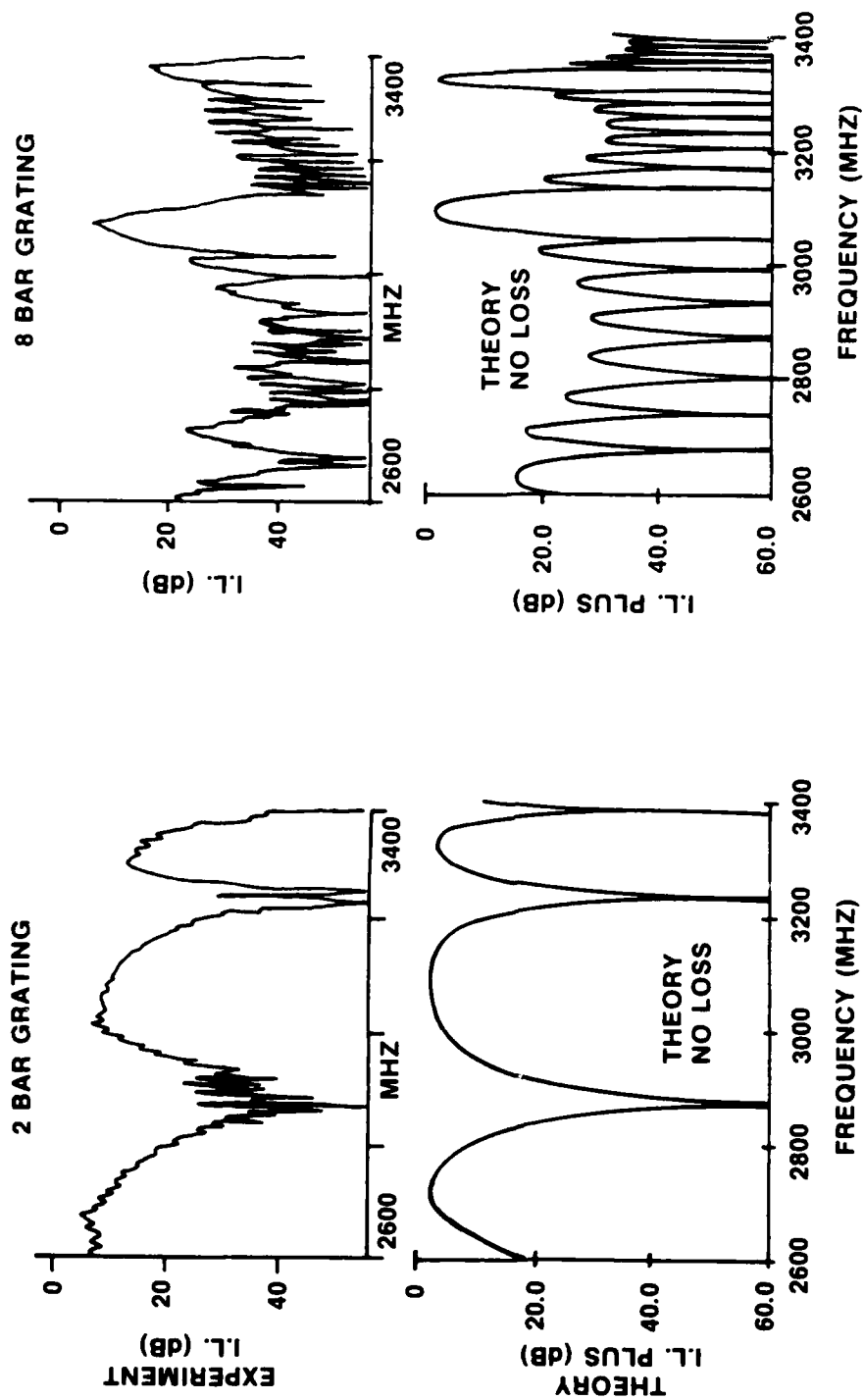


Figure 5-6. Comparison of Two Terminal, TT, Model With Experiment, for 2-Bar Transducer, and for 8-Bar Transducer, Delay Lines

MULTI-ELEMENT TRANSDUCER RESPONSES

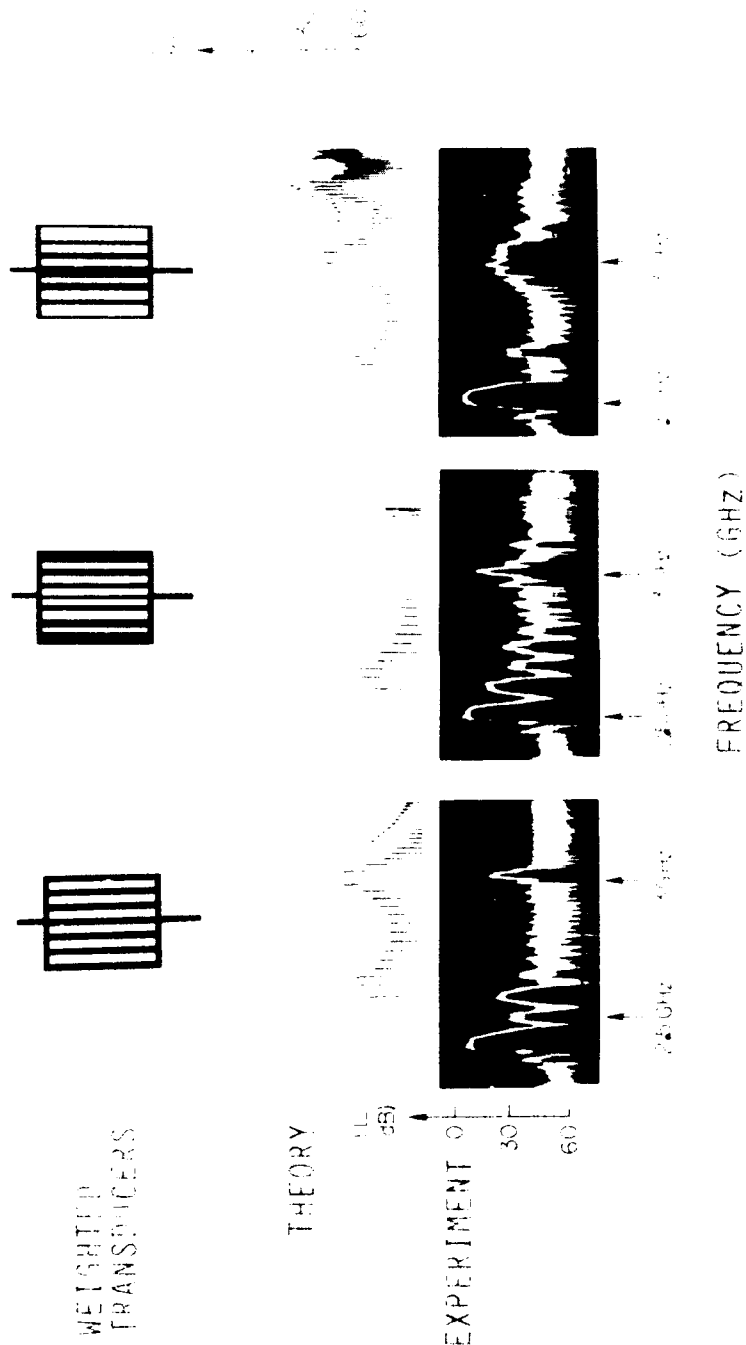


Figure 5-7. Width Apodized 15-Element Grating Transducer MSSW Delay Lines, Theory and Experiment

We note an interesting MSW characteristic depicted in Figure 5-7. The 2.5 GHz response near the low end of the passband is strongly dependent on transducer structure. In addition, the response for one of the width-weighted transducers, the one on the right, appears to make a good band pass filter. This leads us to the conclusion that there are two alternatives for designing MSW filters. One is based on the use of apodization of the fundamental transducer response using narrow strips; this is the analog of SAW filters; and the second is based on the use of long MSW wavelengths. The latter technique has the advantage of low loss, and the disadvantage of no adequate design theory. The first alternative has the advantage of a good theory, but, the disadvantage of large loss. These points need to be considered when attempting to design MSW filters.

5.4 Pulse Experiments

In general, for any of the three pure propagation modes, useful MSW pulse propagation times do not exceed about 1000 nsec. Larger time delays result in either excessive loss, pulse spreading, or both. These points are quantified somewhat in the following three sections.

5.4.1 SHORT PULSES AND ECHOES

Figures 5-8 and 5-9 summarize the results of experiments on 3 GHz MSFVW pulses over relatively short distances, less than about 250 nsec. Further important details of these experiments appear in Reference 1. Figure 5-8 shows the paths taken by four received pulses, and Figure 5-9 shows the received pulses and how they are reduced or enhanced, by properly concentrated magnetic biasing fields. That is, nonuniform fields are used near the sample ends for pulse control.

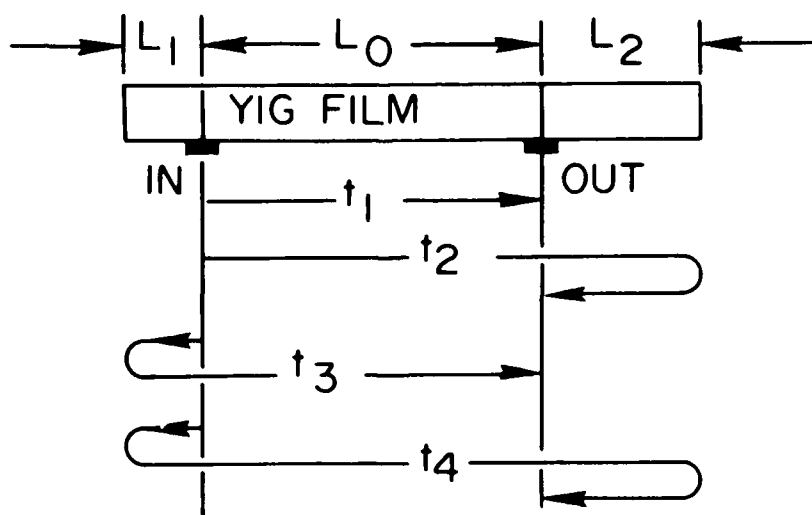


Figure 5-8. MSW Pulse Propagation and Reflections on a YIG Slab

1. Taylor, V.L., Sethares, J.C., and Smith, C.V. (1980) MSW Terminations, *IEEE Ultrasonics Symposium Proceedings*, 80CH1602 2.

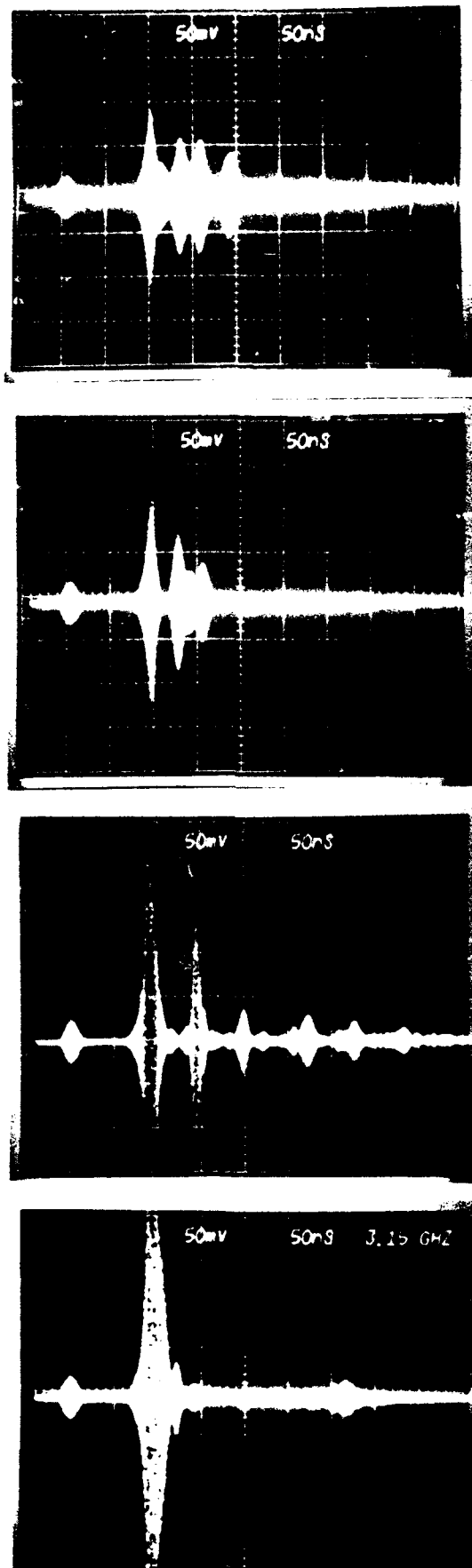


Figure 5-9. Oscilloscope Traces of Received MSW Pulses Following Paths Indicated in Figure 5-8

Figure 5-8 shows a rectangular YIG film upon which two MSW pulses are launched, one in each direction, at the input end. The pulse that travels directly from input to output transducer is detected first. Pulses that reflect off end faces are detected later, the exact time depending on specific paths taken and biasing fields encountered along the propagation path. By modifying the magnetic biasing field near the ends of the propagation paths, reflected waves are affected. For example, pulses t2 and t4 may be eliminated from the output, without affecting t1 and t3, by placing an absorber at the output end, or by making the region absorbing using bias field control.

In the top photo in Figure 5-9, the first small pulse at the extreme left is an RF leakage pulse detected at the output. Its time delay is negligible. Pulse width is about 20 nsec maximum. The second and largest pulse, with 100 nsec delay, is the direct MSW pulse t1. Pulses t2 and t3, with about equal amplitude, are next, and the final pulse, t4 at 200 nsec delay, has slightly lower amplitude. The extraneous pulse immediately following the direct pulse and before pulse t2, is not understood. The same pulse appears in the second photo between t2 and t3. The second photo shows elimination of pulse t4 and reduction of t3, without affecting t1 or t2. The third photo shows enhancement of t1 and t3, and a large reduction in t2 and t4. The final photo shows elimination of all except the direct pulse. At the same time the direct pulse is greatly enhanced. All of these results are understood in terms of a combination of absorption and enhancement of waves in the regions outside of the direct propagation path.¹ Note that the pulses maintain their shape quite well for these short delays. In particular, there is not much pulse spreading for delays less than 250 nsec. Note also that, amplitude of the leakage pulse has been maintained at a constant level, by adjustment of the input signal, for all four photos.

5.4.2 PULSE SPREADING FOR LONG DELAYS

Because of the dispersive nature of MSW, one would expect the pulse to spread out as time delay increased. At a given frequency, increased time delay is achieved through reduction of the biasing field, in the case considered in this section, MSSW. Figure 5-10 shows the output of a C Band MSSW delay line. Reflected pulses, similar to pulses t2, t3, and t4 in the previous figure, are suppressed by cutting the ends of the YIG films at an angle and by absorbing reflected signals on the bottom roughed-up YIG surface. Further details of this experiment are provided in Reference 2. The wave has no abrupt material discontinuities to reflect from. As the delay increases one can see both an increased loss and pulse spreading. Pulse width has almost doubled, for a delay of one μsec .

In the set of photos in Figure 5-10, the top single pulse is the direct leakage pulse. The RF pulse is at 4 GHz. In the 0.4 μsec delay photo, the input pulse level has been reduced from what it is in the first photo. It can be seen that the direct MSW pulse is much larger than the RF leakage pulse. In subsequent photos, which correspond to different biasing fields, the input pulse levels (with the exception of the last one) have been adjusted to maintain a relatively constant output level. Somewhere between a delay of 0.8 and 1.0 μsec the direct MSW signal and the RF leakage signal are equal. The leakage was measured to be about 40 dB down from the input signal level, so the MSW attenuation is excessive, greater than 30 dB, at 1 μsec delay. These results are typical for MSW;

2. Sethares, J.C. and Stiglitz, M.R. (1974) MSSW Delay Lines, *IEEE/MTT International Symposium Proceedings*, 74CH0838 3, pp 253-255.

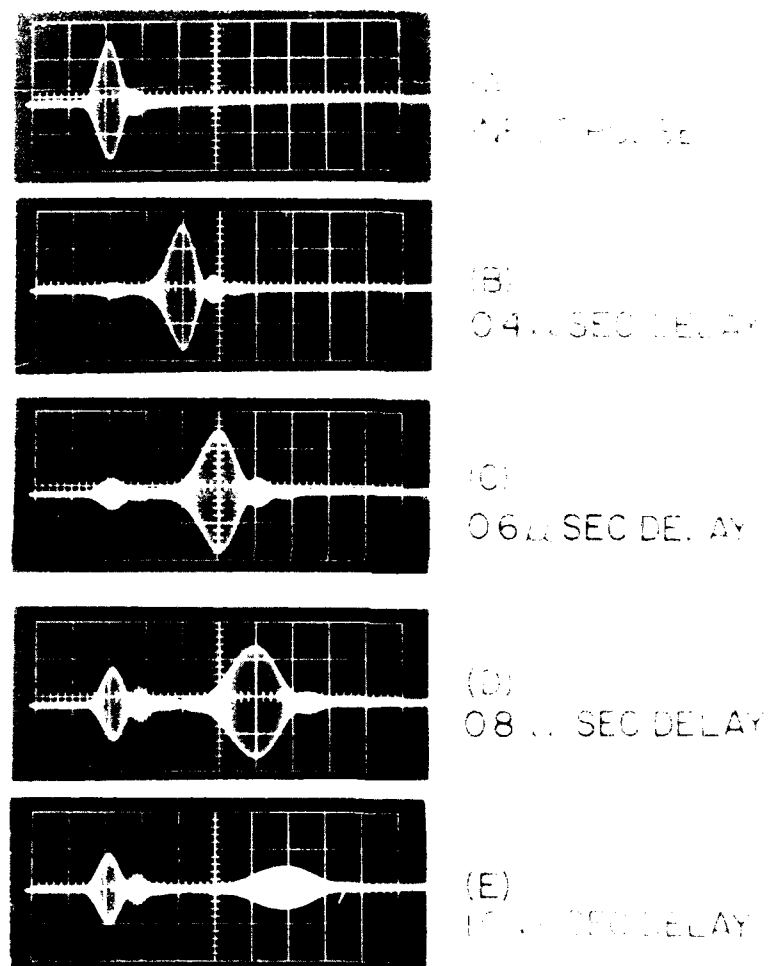


Figure 5-10. Oscilloscope Traces of MSSW Pulse Spreading as a Function of Delay Time

therefore, MSW technology will be most useful in those applications requiring delays below approximately 500 nsec.

A similar experiment was performed at X Band with a 120 nsec pulse width. Pulse width was measured as a function of delay time. Results are shown in Figure 5-11. Pulse spreading is seen to increase rapidly with increasing delay times.

5.4.3 PROPAGATION LOSS AND LINEWIDTH

YIG films are generally characterized by their resonance line width in oersteds. That is, as the magnetic field is tuned through ferromagnetic resonance, FMR, the field difference between half power points is the linewidth, ΔH . Good LPE/YIG films have linewidths of less than 1 Oe, by far the lowest linewidth material available today.

Experiments were conducted in an attempt to relate propagation loss with linewidth.³ The experiments led to the following quantitative relationship between propagation loss and linewidth. Loss in dB per microsecond equals 76.4 times the linewidth in oersteds. This relationship is used in the computer programs to calculate propagation loss.

Figure 5-12 shows experimental results for the loss measurements. An important point to note in this figure is that experimental propagation loss is linearly related to frequency above 3 GHz. The loss mechanism below 3 GHz is a complicated function of frequency dependent magnetic domain dynamics and anisotropy. It is beyond the scope of this report. The dashed lines in Figure 5-12 are theoretical and based on a phenomenological Gilbert magnetic damping parameter.³

Figure 5-13 shows the experimental setup used for most of the pulse experiments in Section 5.4. Field orientation is shown only for MSSW in this figure. For some of the experiments, the pulsed RF signal generator was replaced by a stabilized CW source and an external fast RF switch. This was done for experiments requiring short pulses, of about 20 nsec duration. A local oscillator CW signal was combined with the received pulse in a mixer/preamp for increased sensitivity.

5.5 MSW Oscillators

The basic experimental setup for oscillator experiments is shown in Figure 5-14. Depicted in the figure is a narrow band BVW delay line oscillator. When the gain of amplifier A is adjusted to compensate for MSW delay line loss and all circuit loss external to the line, and when the H field is adjusted so that the feedback signal at the input end of the delay line is of the proper phase, oscillations will occur. These conditions can be satisfied at several frequencies simultaneously depending on the magnitude of MSW dispersion and the passband loss versus frequency characteristics. Important oscillator parameters include the relative time delay of the MSW delay line and the electromagnetic delay in the rest of the oscillator feedback loop. Reference 4 provides further details of the work described in this section.

3. Sethares, J.C. and Stiglitz, M.R. (1974) Propagation Loss and MSSW Delay Lines, *IEEE Transactions on Magnetics*, **MAG 10**, (No. 3):787-790.

4. Sethares, J.C. and Stiglitz, M.R. (1981) Magnetostatic Wave Oscillator Frequencies, *J. Appl. Phys.* **52**, (No. 3), Part II:2273-2275.

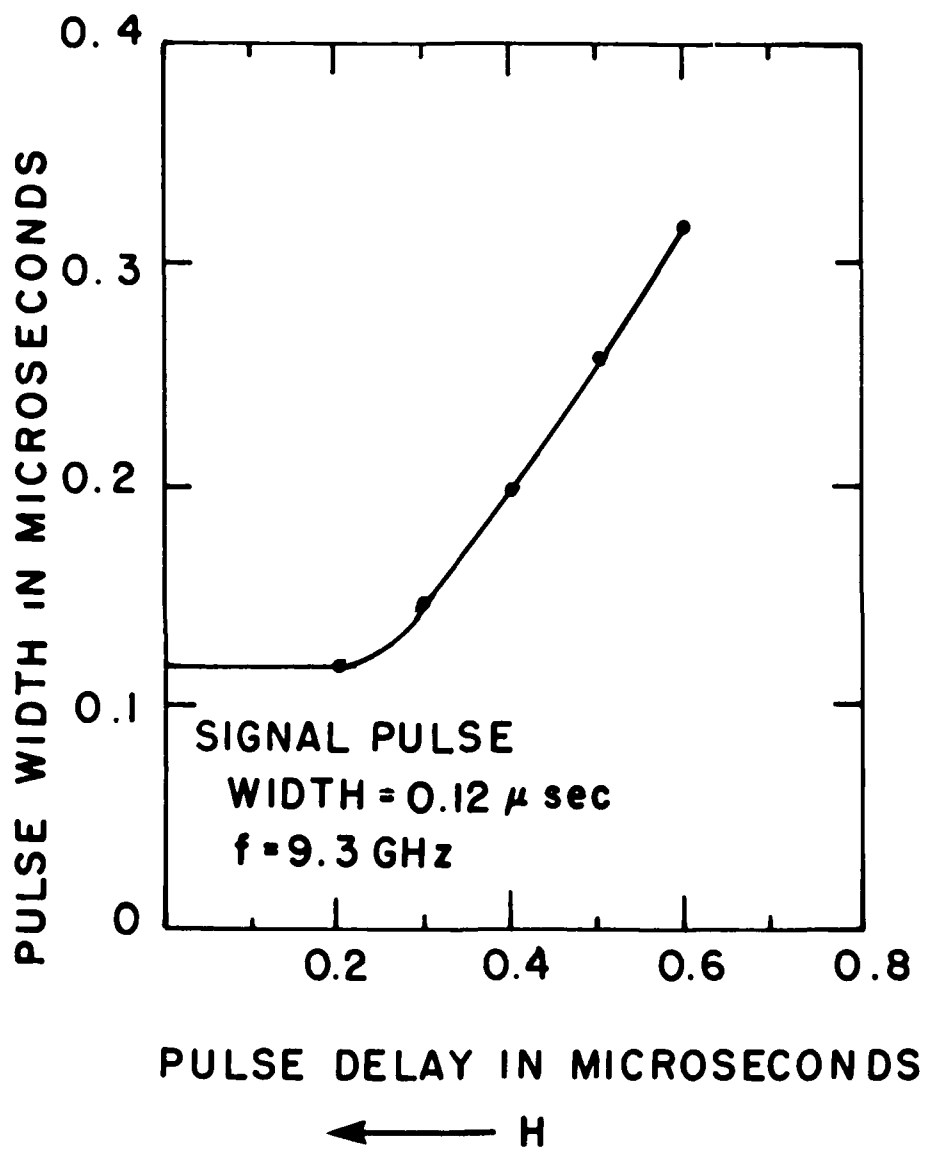


Figure 5-11. Pulse Width as a Function of Delay Time

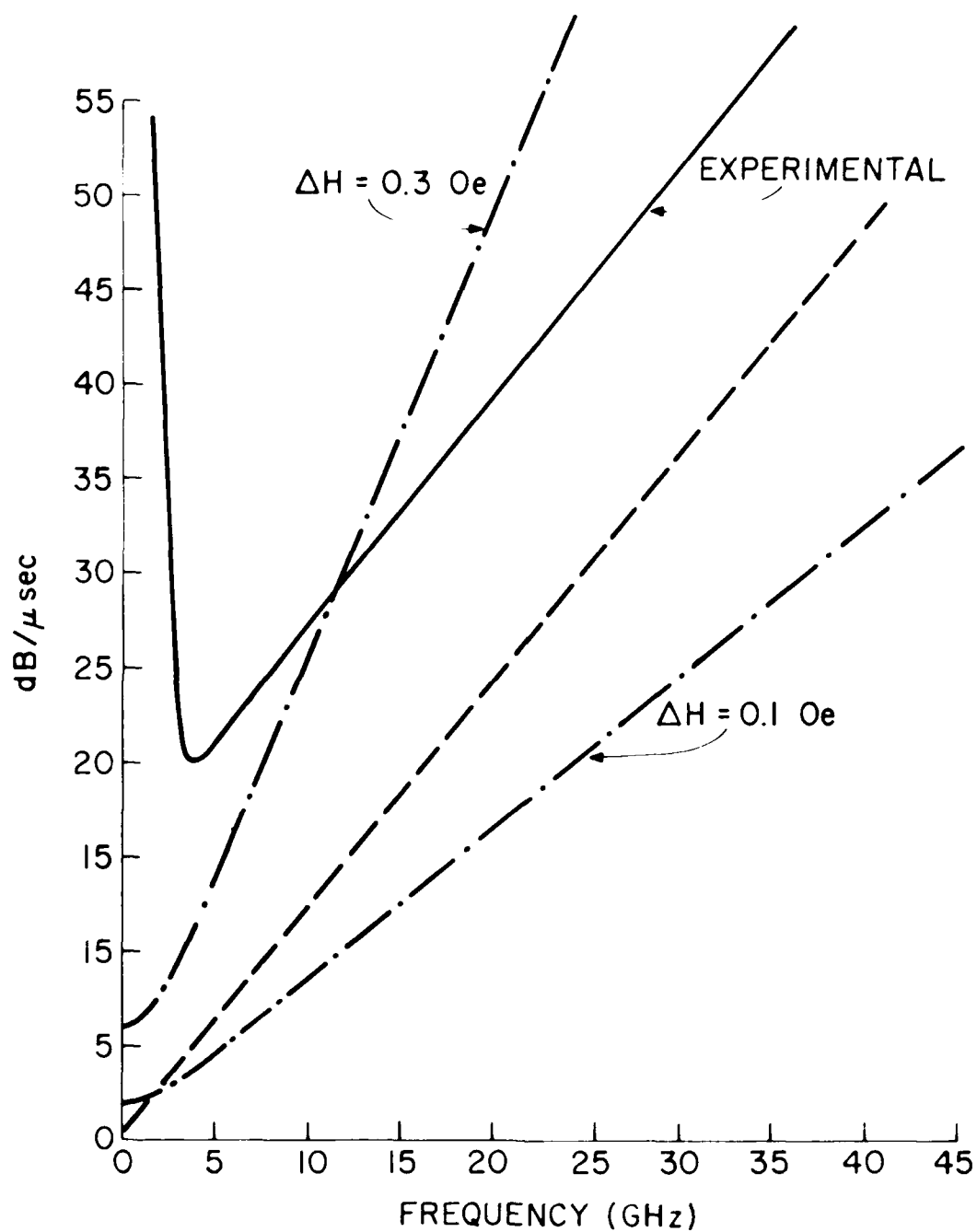


Figure 5-12. YIG Linewidth as a Function of Frequency, Theory and Experiment

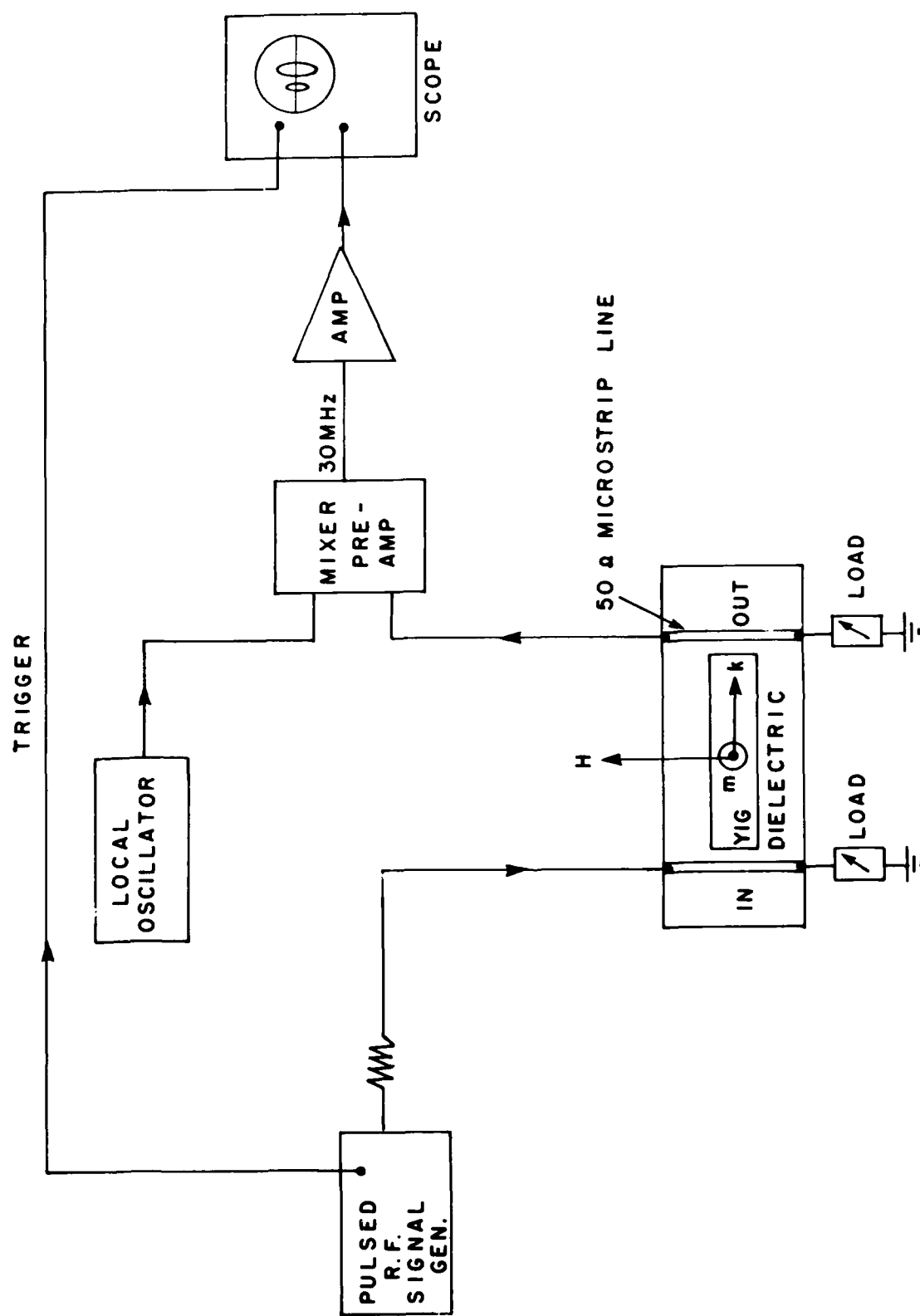
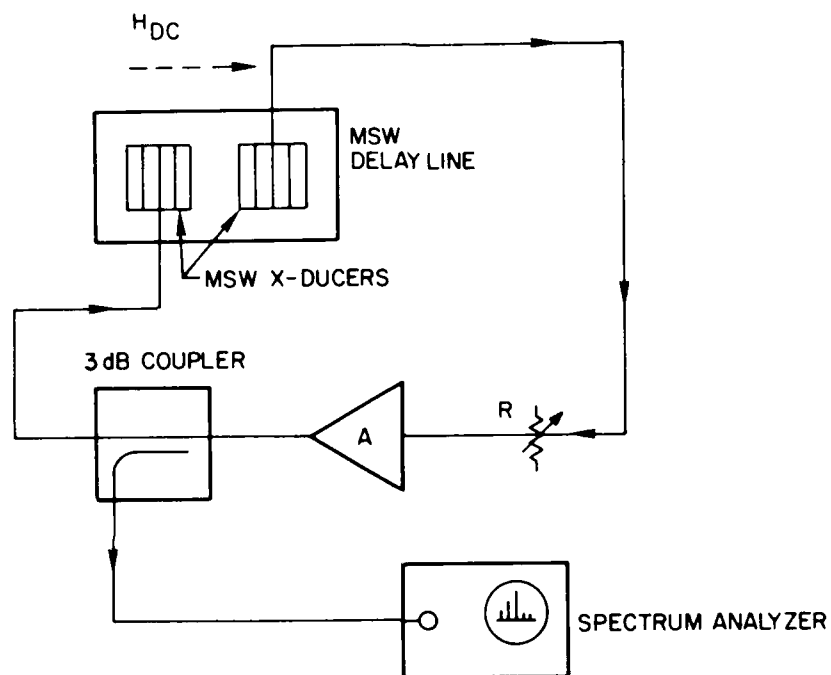


Figure 5-13. Experimental Arrangement for MSW Pulse Experiments



A, AVANTEK MODEL ABG-4005 AMPLIFIERS, 35dB GAIN

R, VARIABLE ATTENUATOR

H_{DC} DIRECTION OF DC BIAS FIELD

Figure 5-14. Block Diagram of MSW Oscillator

5.5.1 WIDE BAND DELAY LINE

Figure 5-15 shows a comb of simultaneous oscillator frequencies produced by an MSW delay line oscillator. For this oscillator the delay line has narrow single transducer strips at input and output, making it a wideband delay line. Note that all amplitudes are approximately equal. This is characteristic of such oscillators. The Q of these oscillators is on the order of 1000. All three pure MSW modes of propagation will produce a similar comb of frequencies under similar conditions. As the magnetic field is increased the comb of frequencies is shifted up or down in frequency depending on the particular mode used. In addition to this frequency shift, another phenomena, frequency hopping, may occur.

The cause of frequency hopping, the turning on and off of oscillator signals as H is changed, has been traced to the relative time delay difference between MSW delay and EM time delay external to the delay line. If the EM time delay is zero, frequency hopping does not occur. When EM time delay is not zero, frequency hopping occurs and it is more severe with larger EM delays.

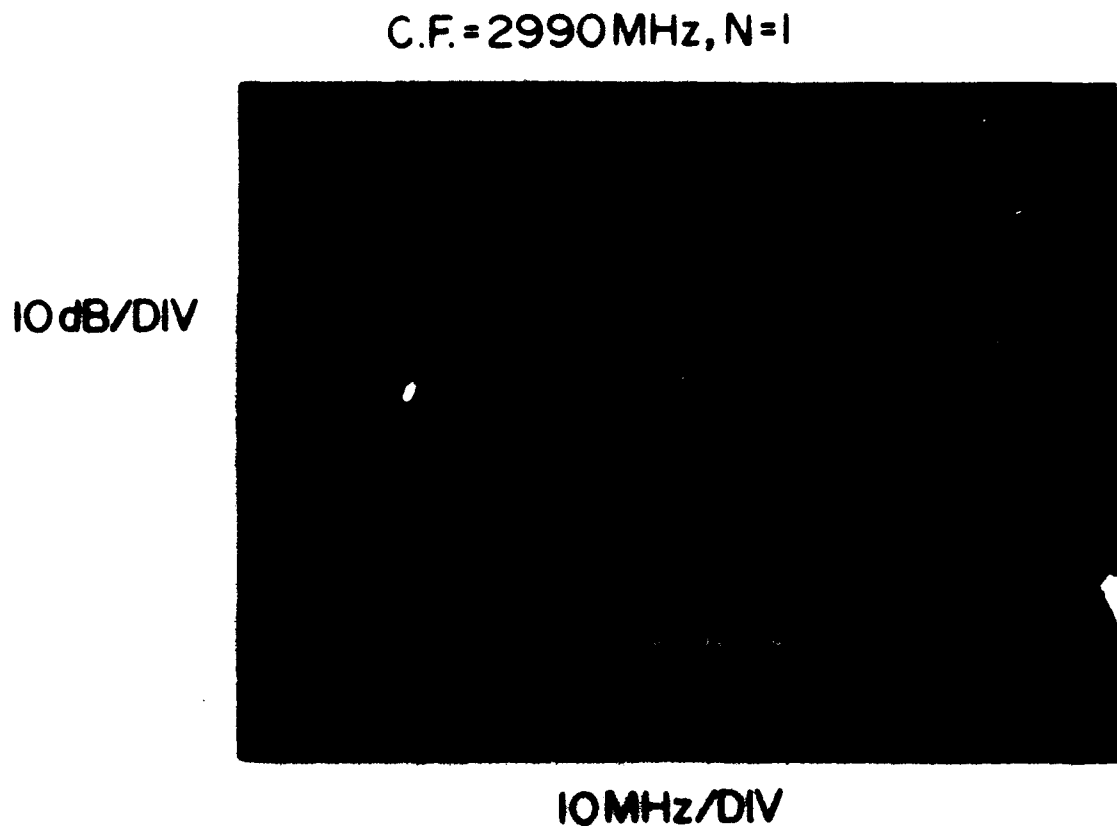


Figure 5-15. Spectrum Analyzer Display of a Wideband MSW Delay Line Oscillator, N=1

5.5.2 NARROWBAND TRANSDUCERS (N=15)

Figure 5-16 shows a single oscillator frequency produced by a narrow band delay line oscillator. In this case each transducer has 15 strips with 300 μm center-to-center spacing. The MSW wavelength therefore is 300 μm . Another oscillation may occur at 150 μm wavelength; however, the frequency corresponding to this wavelength is outside the frequency range of the spectrum analyzer display. Again, the signal may be tuned via the magnetic biasing field, and frequency hopping occurs because the EM external circuit delay is not negligible in comparison to MSW time delay.

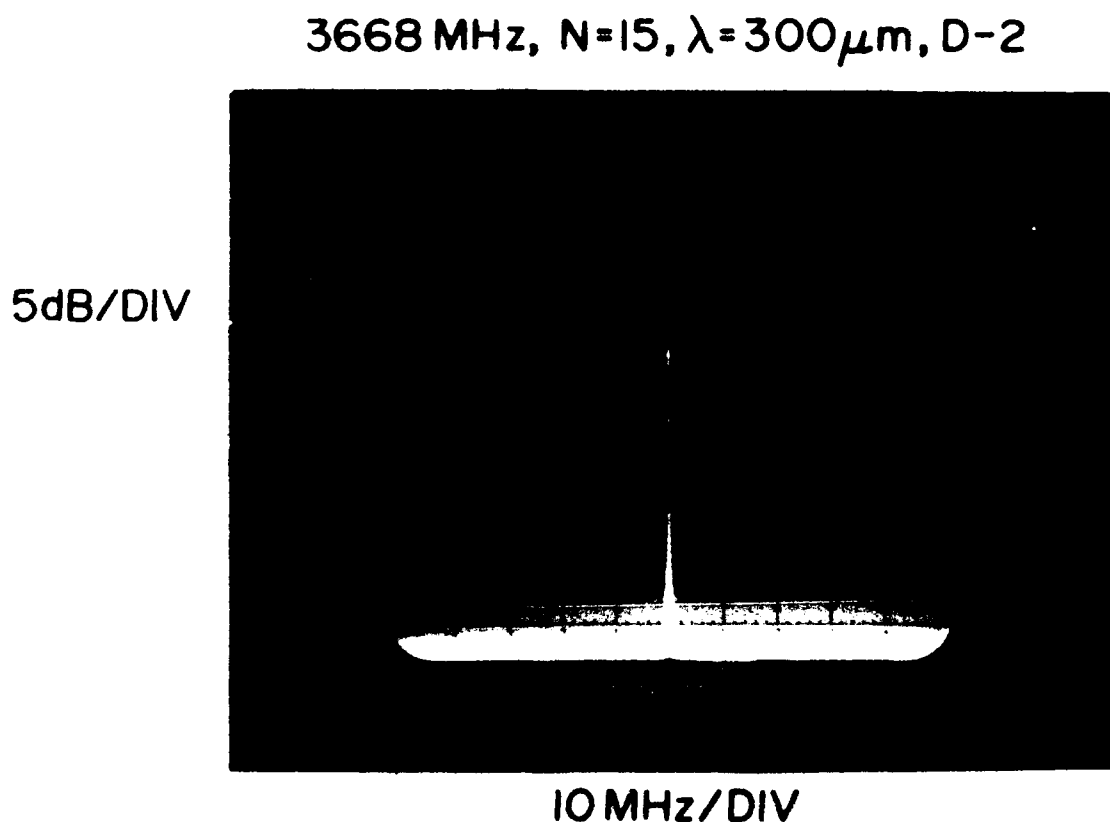
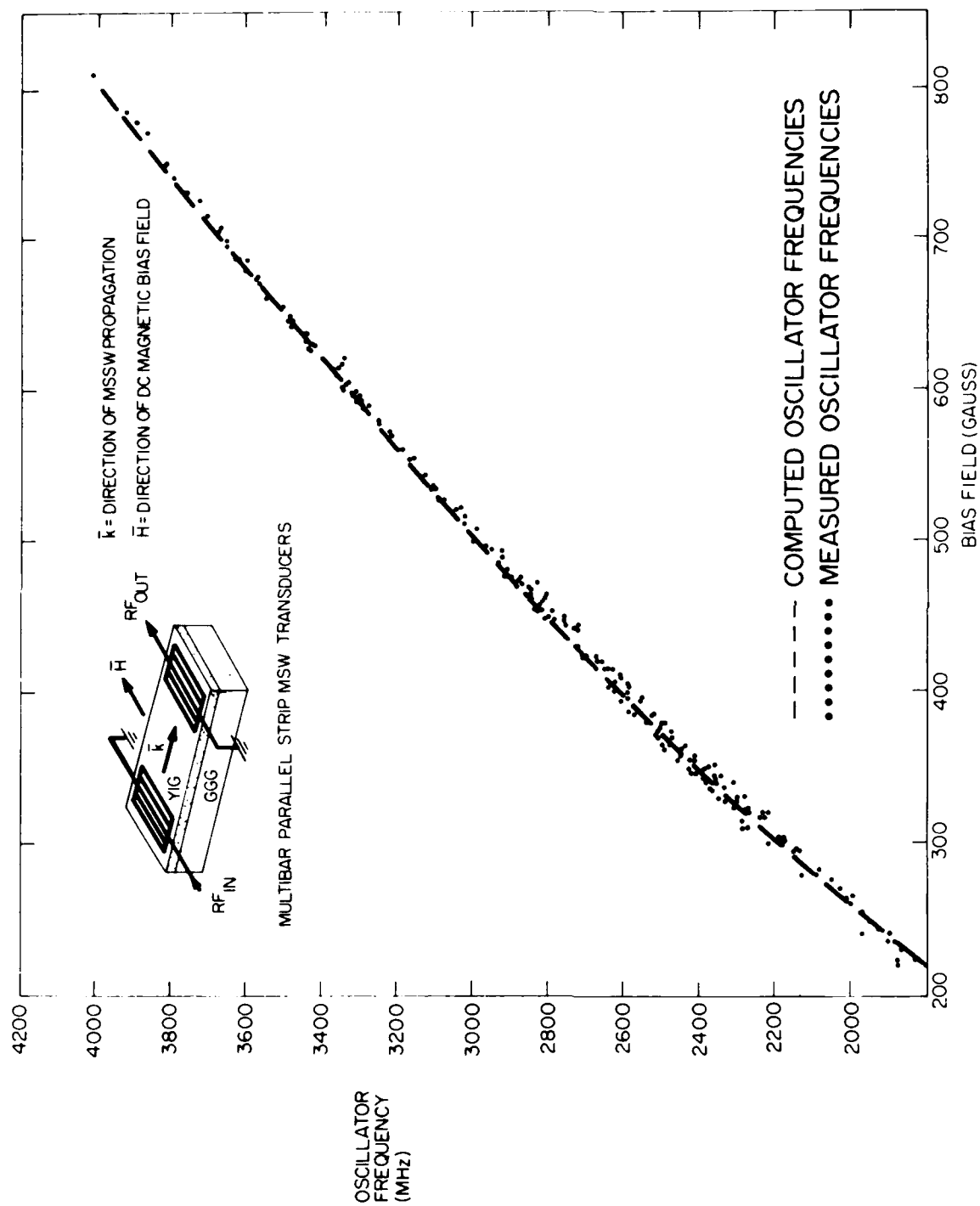


Figure 5-16. Spectrum Analyzer Display of a Narrow Band MSW Delay Line Oscillator, N=15

5.5.3 OSCILLATOR TUNING

Figure 5-17 shows an octave frequency range over which the narrow band delay line oscillator was tuned. Over this frequency range, hopping was present. Tuning sensitivity is seen to be on the order of 3 MHz/Gauss. The theoretical curve was obtained by assuming an MSW wavelength of 300 μm and calculating the frequency from the dispersion relation. The agreement between theory and experiment is seen to be excellent.



SURFACE WAVE OSCILLATIONS BETWEEN 2GHZ AND 4GHZ

Figure 5-17. MSSW Delay Line Oscillator Frequency versus Bias Field, Theory and Experiment

5.6 MSW Device Characteristics

In this section, we present experiments related to MSW passband ripple, electronic tuning, switching speed, and anisotropy.

5.6.1 AMPLITUDE RIPPLE

In Section 5.4, we discussed experiments in which MSW pulses were eliminated with nonuniform biasing fields. The mechanism for this effect is based on the fact that when MSSW or MSFVWs enter regions where the biasing field decreases with distance, MSW wavelength at a given frequency also decreases. Since shorter wavelengths experience higher loss, the wave attenuates as it propagates.

The rate of absorption can be large, the rate depending on the magnitude of field gradient. When pulses are absorbed, they do not reflect back onto the propagation path and cause interference and amplitude ripple. Nonuniform fields can therefore be used to reduce ripple in MSW devices. Such a reduction in amplitude ripple is shown in Figure 5-18. Also see Reference 1. Here, the biasing field near the end of a YIG slab was reduced by appropriately placed permalloy films. Ripple reduction, in this case, extends over almost the entire MSW passband.

Many other ripple reduction techniques have been used by us and others. These techniques include: cutting the ends of a YIG slab at an angle to reduce the amount of energy reflected straight back; strategically placing lossy ferrites, and other absorbers, in propagation regions; tapering the thickness of the propagation media; and roughing up YIG surfaces.

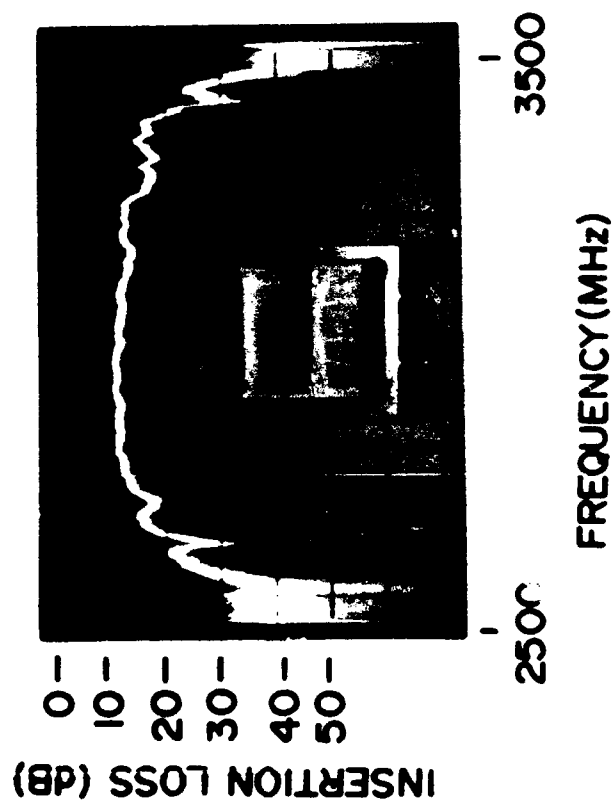
5.6.2 PHASE SHIFT RIPPLE

Figure 5-19 compares phase and time delay characteristics of coaxial cable and MSW as measured by a phase locked automatic network analyzer between 3000 and 3100 MHz. The first set of data, on the left, shows system accuracy. That is, input and output terminals of the analyzer are connected through a short low loss cable. Time delay is zero within 0.5 nsec error and phase deviation is zero with 0.5° error. In the second set of data, in the middle, a 3 foot coaxial cable has similar phase and time delay ripple. Absolute time delay is about 4.5 nsec. In the third set, on the right, phase ripple of the MSW device is about the same as that of the coaxial cable, and better than a 3 bit diode phase shifter; refer to Figure 5-20. Time delay is about 30 nsec at midband and the delay ripple about 1.5 nsec. This apparent delay ripple can be significantly reduced by averaging techniques.

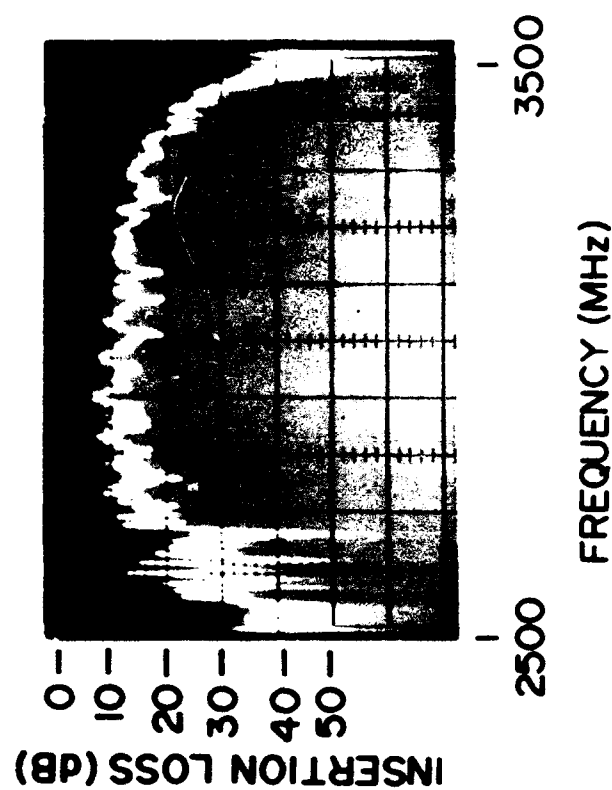
Figure 5-20 shows phase and time delay characteristics of a conventional 3 bit switched line phase shifter. These characteristics can be used for comparison with MSW delay lines. Note the ripple in insertion loss and phase. The group delay of this device is about 0.6 nsec, as can be verified from the slope of the phase versus frequency curve, S21 DEG, in the lower left portion of the figure. It would be difficult to obtain this information from the delay plots in the upper right portion of the figure. Group delay plots are very sensitive to the number of frequency data points used in the measurement. Group delay, which is equal to the derivative of phase with respect to frequency, is calculated from the phase data measured by the network analyzer. Two successive measurements are used to calculate differential phase and frequency to give group delay as in Eq. (5-5).

$$\text{Group Delay} = \frac{(\phi_2 - \phi_1)}{(\omega_2 - \omega_1)} \quad (5-5)$$

MSW TERMINATIONS WITH NON UNIFORM FIELDS INSERTION LOSS VS FREQUENCY



WITH PERMALLOY TERMINATIONS



NO TERMINATIONS

Figure 5-18. MSW Passband Ripple Reduction With Nonuniform Fields

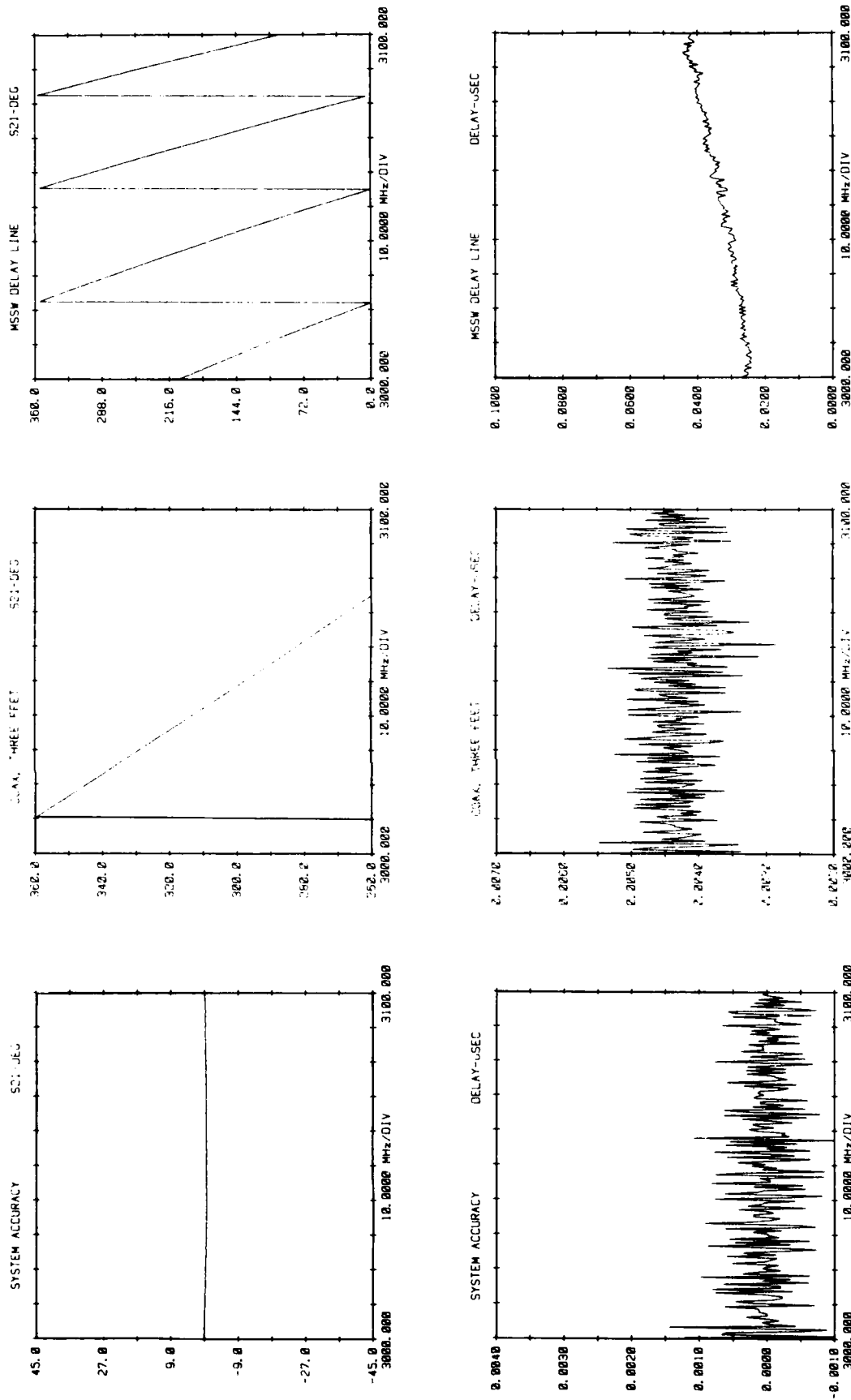


Figure 5-19. MSW Phase Ripple Compared With Coaxial Cable

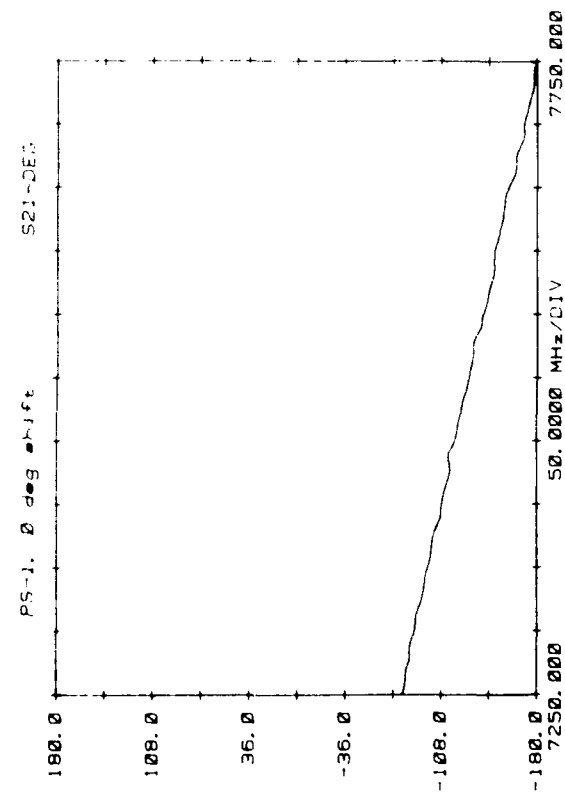
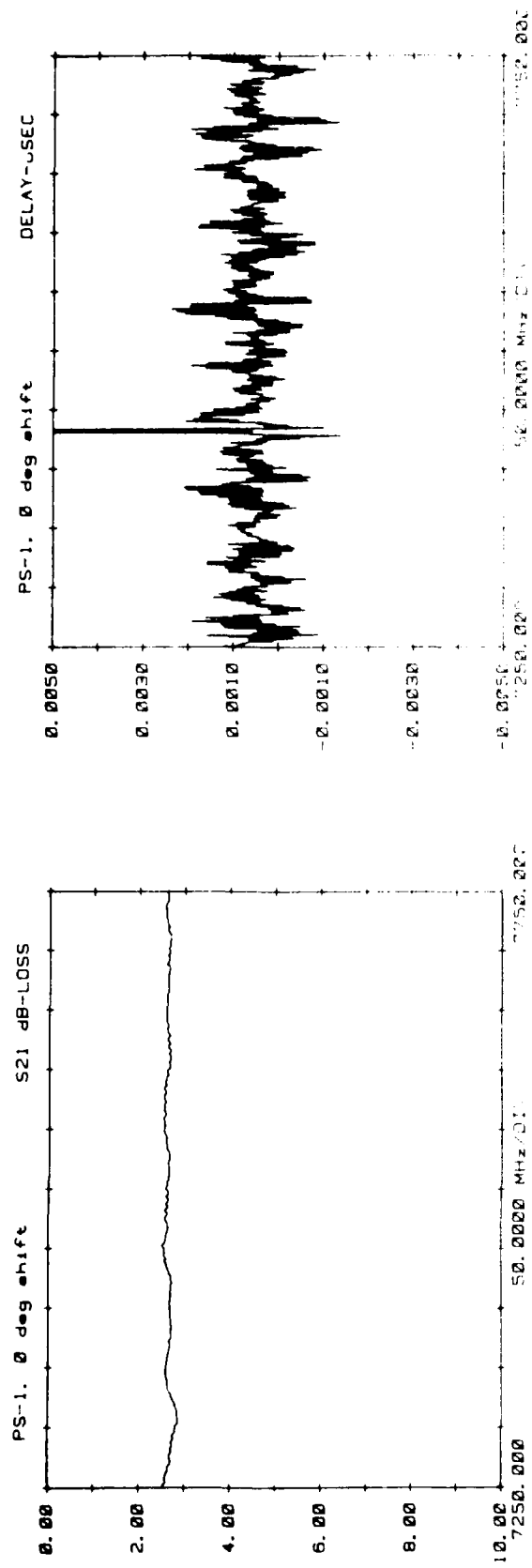


Figure 5-20. Phase Ripple in a 3-Bit Diode Switched Line Phase Shifter

Based on these comparison measurements, it is concluded that phase ripple, as opposed to time delay ripple, is a more realistic criteria for evaluating delay lines. In addition, phase ripple on MSW devices is about the same as it is on coaxial cable. Reference 5 provides further details.

To approximate actual group delay, closely spaced frequency points should be used; however, this results in rapid artificial fluctuations in group delay. The only way to obtain meaningful delay results is to use averaging techniques, but this can remove real delay variations. Again, phase measurements are a more meaningful way of evaluating phase shifters and time delay units than are group delays.

5.6.3 MAGNETIC FIELD TUNING

Experiments were performed to measure the amount of tuning possible using a flat current carrying strip.⁶ One experiment was implemented as indicated in Figure 5-21. The figure shows a microstrip line coupled to a thin YIG film disk which was grown on a GGG substrate. A current carrying tuning strip is perpendicular to a microstrip line. The magnetic field produced by current I adds (or subtracts when I is negative) to an applied biasing field H . This particular experimental configuration is a band stop filter when RF input and output signals are as shown in the figure. As the frequency is swept, maximum energy is absorbed by the YIG film at ferromagnetic resonance, FMR. At frequencies far from FMR, little energy is coupled into the YIG film.

In another experiment, two microstrip lines were coupled through a square YIG film resonator. At FMR, energy was coupled from one to the other, thus forming a band pass filter (see Appendix D). The response of such a filter is shown in Figure 5-22. Again, using a current carrying tuning strip, the FMR frequency can be shifted with current I . A plot of frequency shift versus current is shown in Figure 5-23. The theoretical curve is based on Eq. (5-6) from Reference 6,

$$\Delta\omega = \gamma \left(\frac{H + 2\pi M}{\sqrt{H(H + 4\pi M)}} \right) \left[\frac{1}{\pi A} \tan^{-1} \left(\frac{A}{2X} \right) \right] I, \quad (5-6)$$

where A is strip width, and X is the spacing between current strip and YIG film. Agreement between theory and experiment is excellent. For the structure shown in Figure 5-21 the tuning sensitivity is about 10 MHz/amp.

5.6.4 MAGNETIC FIELD SWITCHING SPEED

In a third experiment, current I was amplitude modulated with the results shown in Figure 5-24. In the figure, the horizontal scale is time and the vertical scale is frequency. Frequency was shifted from 3310 MHz to 3306 MHz in about four μ sec. Thus, the switching speed is about 1 MHz/ μ sec.

5.6.5 TEMPERATURE SENSITIVITY

Figure 5-25 shows how the phase near midband frequency of an MSW delay line varies with temperature over a 100°C range. As indicated in the figure, this temperature dependence is accurately

-
5. Sethares, J.C. and Floyd, R. (1985) MSW Applications for Phased Array Antennas, *Circuits Signals and Signal Processing*, Vol. 4, No. 1-2, pp 335/350.
 6. Tsai, T.L. and Sethares, J.C. (1977) Band Stop Filters, *IEEE/MTT-s International Microwave Symposium Digest*, Cat. No. 77/CH1219/S, pp 526, 7.

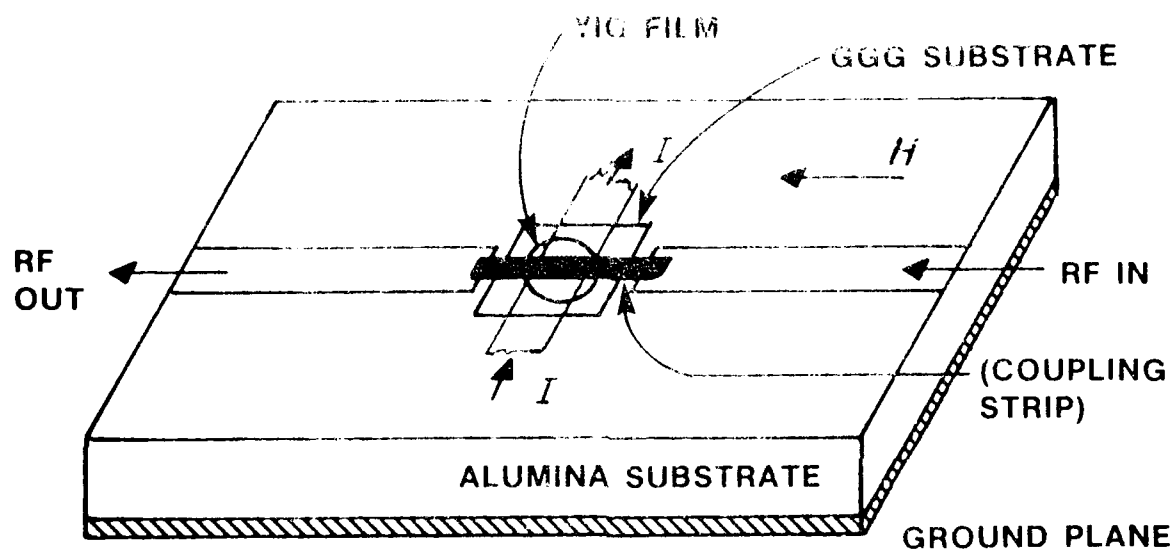


Figure 5-21. Figure Showing Construction of a Tunable Planar LPE/YIG Bandstop Filter Implemented in Microstrip

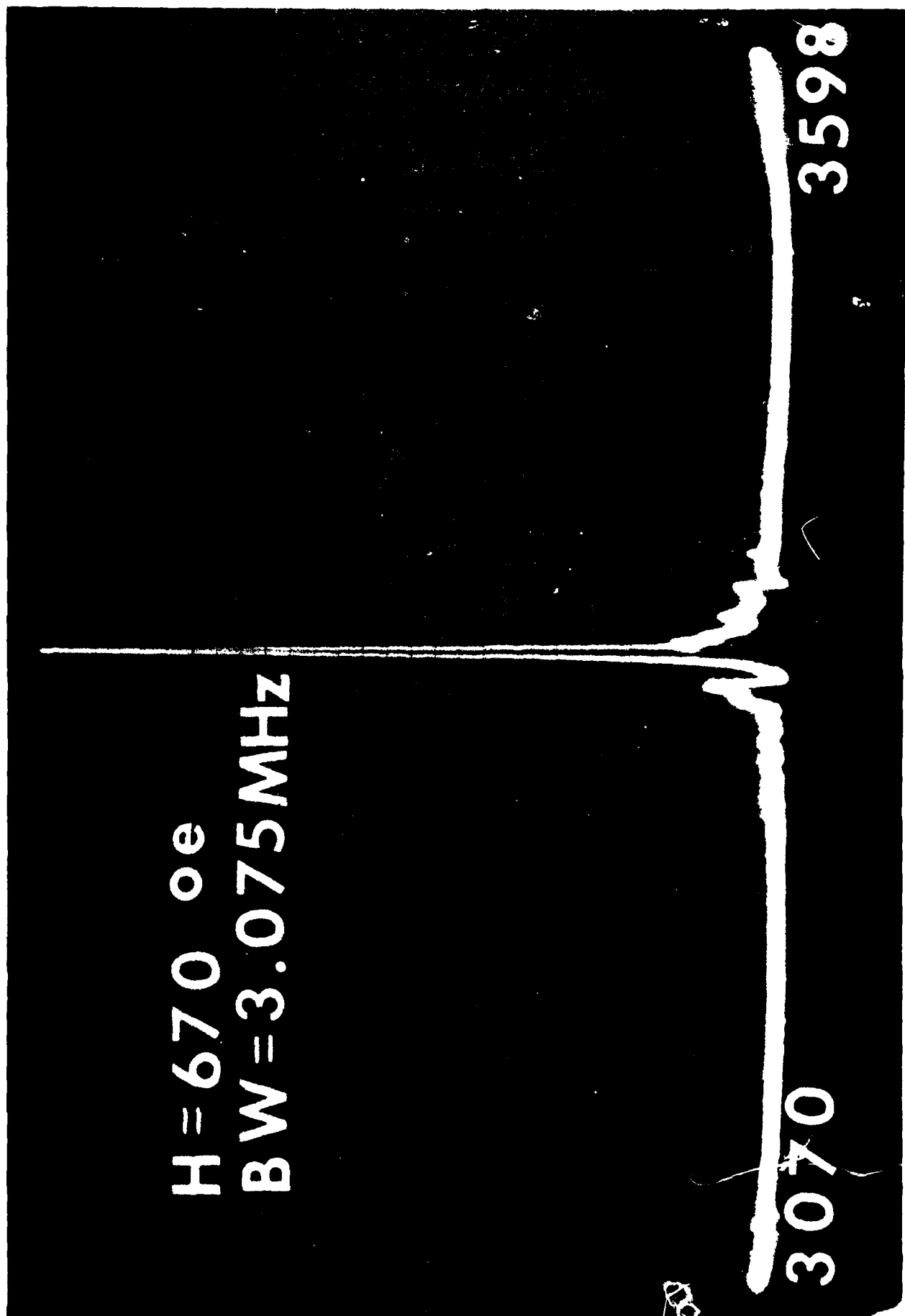
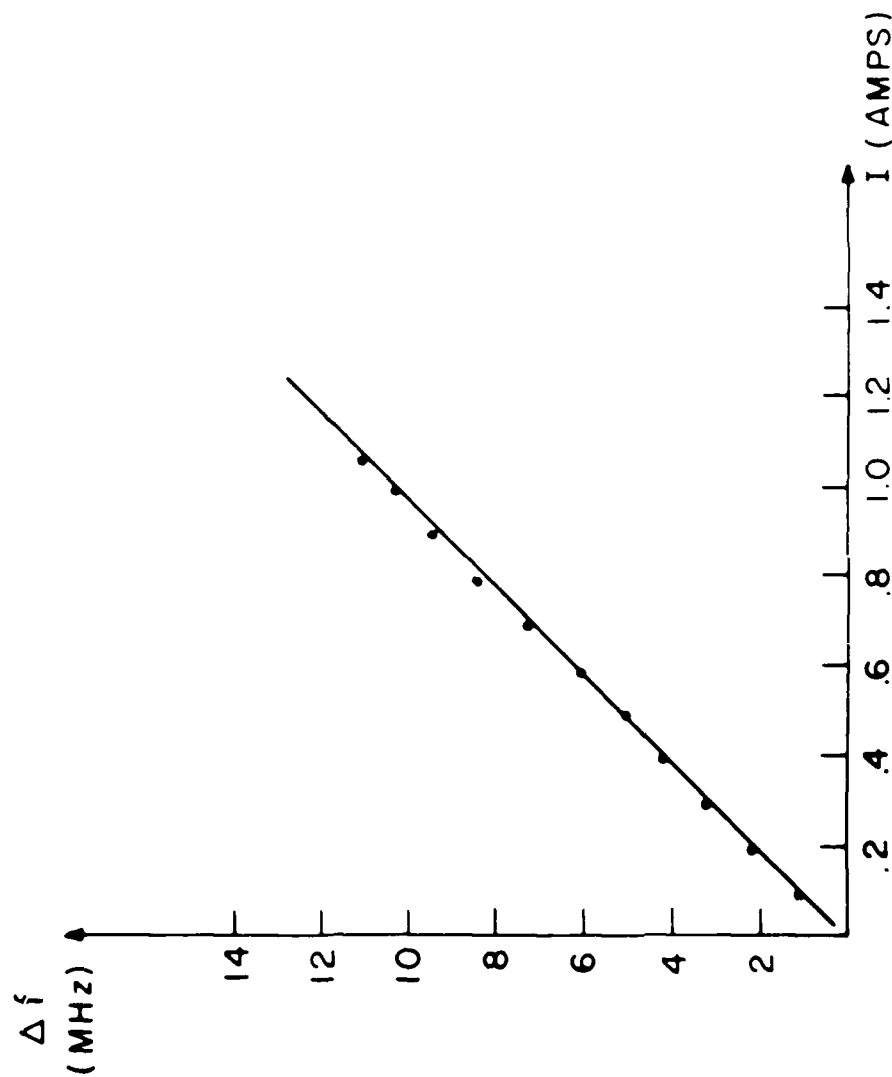


Figure 5-22. Oscilloscope Trace of the Output of a Tunable Planar LPE/YIG Bandstop Filter Implemented in Microstrip



Frequency shift against D-C current.
 ••• experimental results. _____ theoretical
 curve with $X = .13$ mm.

Figure 5-23. Tuning Sensitivity of Planar LPE/YIG Filters Implemented in Microstrip

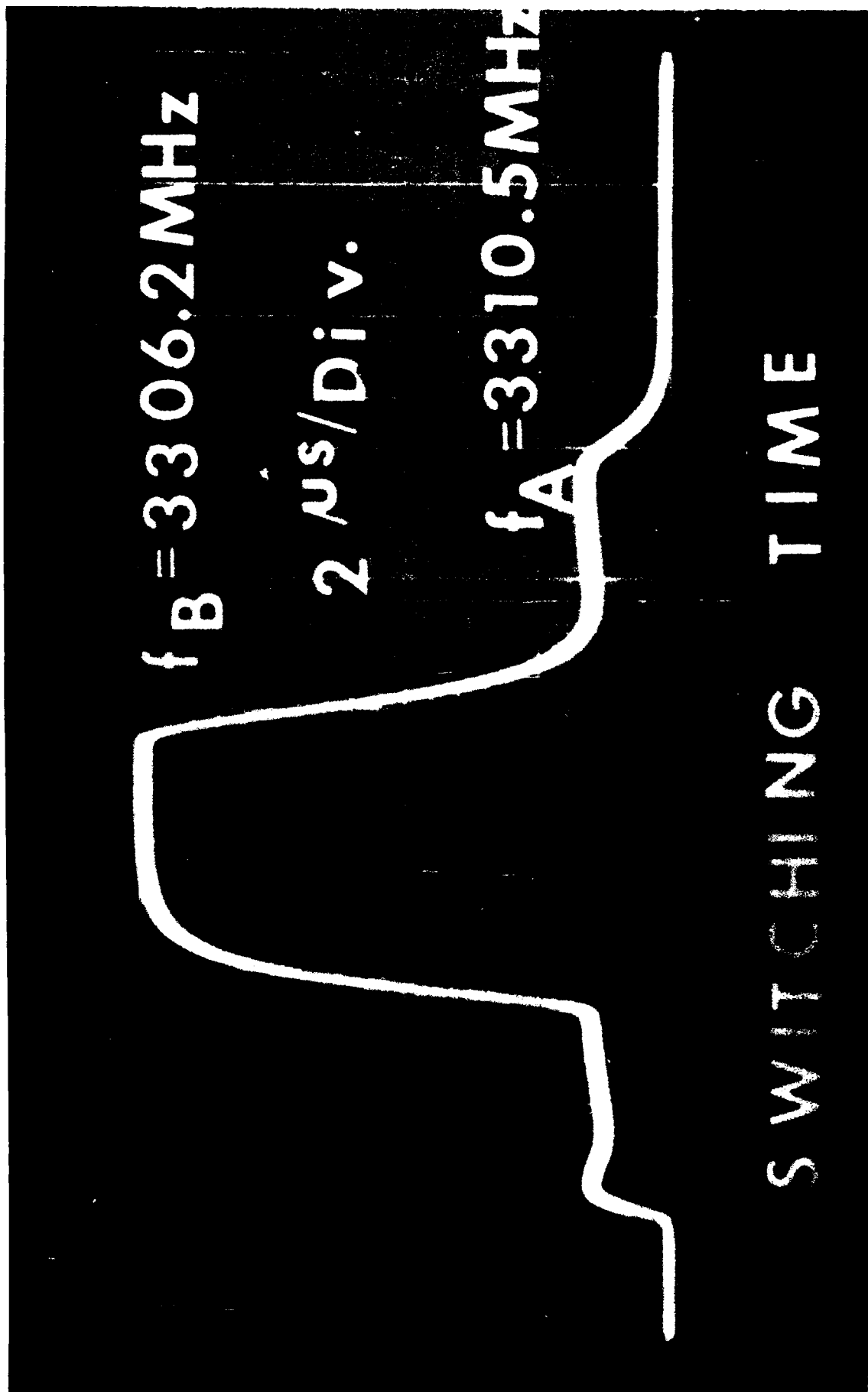


Figure 5-24. Rapid Switching Speed of Planar LPE/YIG Filter Implemented in Microstrip

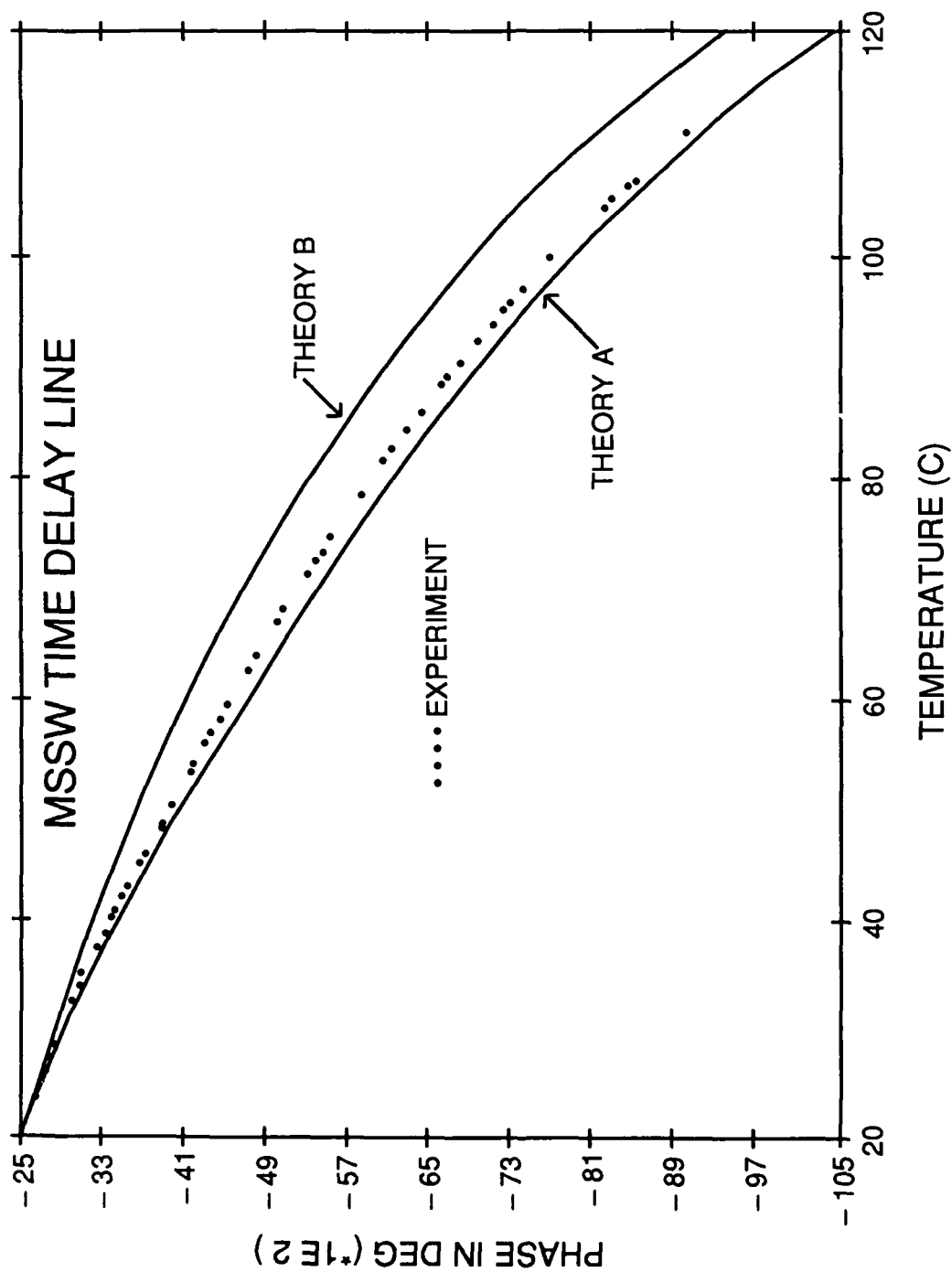


Figure 5-25. Phase Shift versus Frequency of an Uncompensated MSW Delay Line

predicted theoretically so that temperature compensation techniques can effectively be used within an enclosed structure protected from ambient temperature variations. Measurements were done on MSSW delay lines with temperature variation in the YIG only. The biasing magnet was held at a constant temperature. Theory B neglects ground plane effects in the dispersion relation. Theory A takes them into account.

5.6.6 MAGNETOCRYSTALLINE ANISOTROPY

All MSW device designs neglect the effects of magnetocrystalline anisotropy because it is small. Figure 5-26 shows how small the effect is in practice.⁷ Shown here is FMR frequency versus sample rotation. Thin circular LPE/YIG film disks were biased to resonance. As the film was rotated about an axis perpendicular to the film plane, the shift in FMR frequency was measured. As can be seen in the figure, the frequency shift is about 7 MHz out of 3895 MHz, which amounts to less than 0.2 percent. The sinusoidal frequency variation with orientation reflects the symmetry of the (III) YIG film plane.

This small frequency shift is the primary effect of crystalline anisotropy on MSW devices. A device passband will shift up or down in frequency by this amount. No other significant effects have yet been recorded for MSW devices.

Another altogether different type of experiment supports the notion that crystalline anisotropy does not play a vital role in MSW devices. Figure 5-27a shows a ring shaped GGG substrate 3/4 inch diameter and 1/4 inch thick, with an LPE/YIG ribbon film grown on the curved surface. Upon examination with a microscope, the YIG ribbon film exhibited faceting: flat crystal planes along the ring circumference.

MSSW were launched on this YIG film with fine wire couplers, and they were received with a second fine wire coupler placed half way around the ring. The measured pulse delay time was in agreement with theoretical calculations based on the assumption that MSSW wavelengths are small compared to curvature, but, large compared to facet size. Figure 5-27b shows that wavelengths on the order of 1/2 millimeter were detected in this experiment. The YIG film guides MSSW around the ring. It was not necessary to invoke magnetocrystalline parameters to explain the results of these experiments, with the exception of coupling variations due to faceting.

5.7 MSW Refraction and Simultaneous Pulse Separator

When MSWs propagate along the surface of a YIG film and encounter a metal region, on or near the surface, the wave speeds up. This effect was used to bend an MSW beam and to construct an MSW simultaneous pulse separator.

5.7.1 REFRACTION OF MAGNETOSTATIC WAVES

A triangular metal patch was placed in the propagation path; see Figure 5-28. A three inch diameter LPE/YIG film was placed on the microstrip circuit shown in the figure. A wideband MSW beam was launched at the input end. This beam was normally incident on the nearest metal boundary

7. Sethares, J.C. and Tsai, T.L. (1977) Magnetic Anisotropy of (III) LPE/YIG Films on GGG in Parallel Resonance, *IEEE Trans. on Magnetics*, **MAG13**, (No.5):1236.

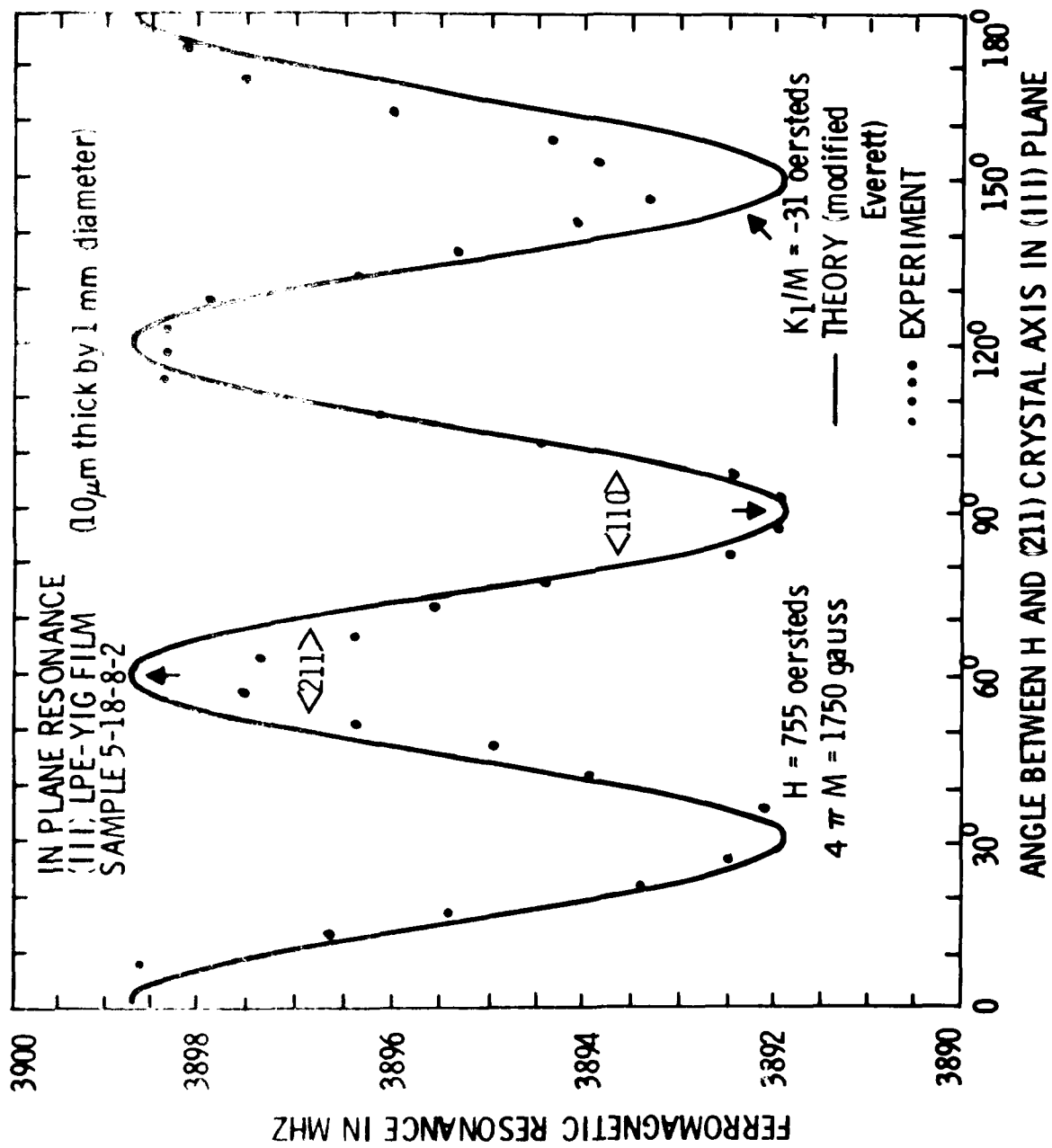


Figure 5-26. In-Plane Magnetocrystalline Anisotropy of a (111) LPE/YIG Film

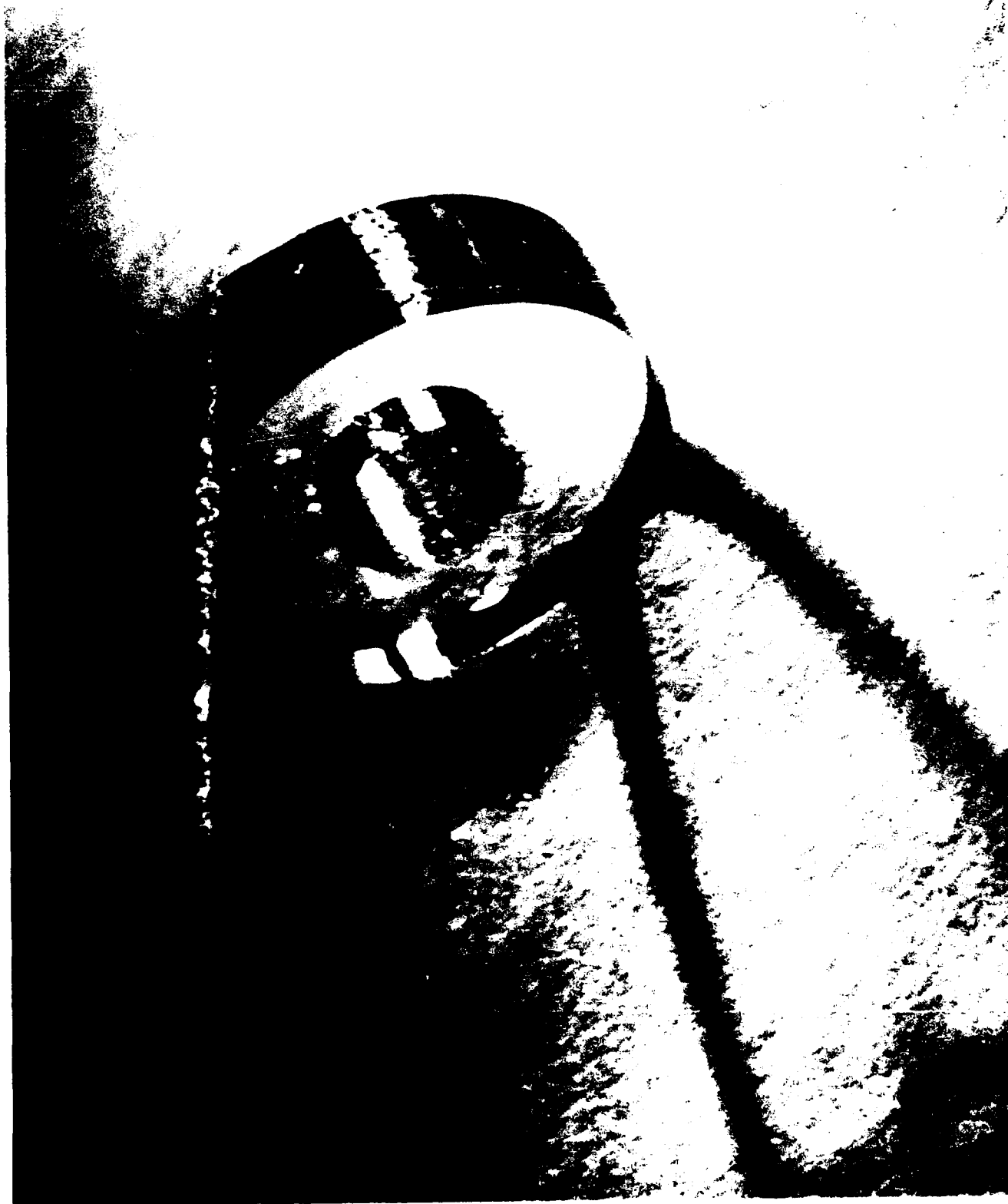


Figure 5-27a. MSW Propagation Along a Curved LPE/YIG Film. LPE/YIG film grown on a cylindrical surface. Ring has 3/4 inch outer diameter. YIG is on outer surface of ring.

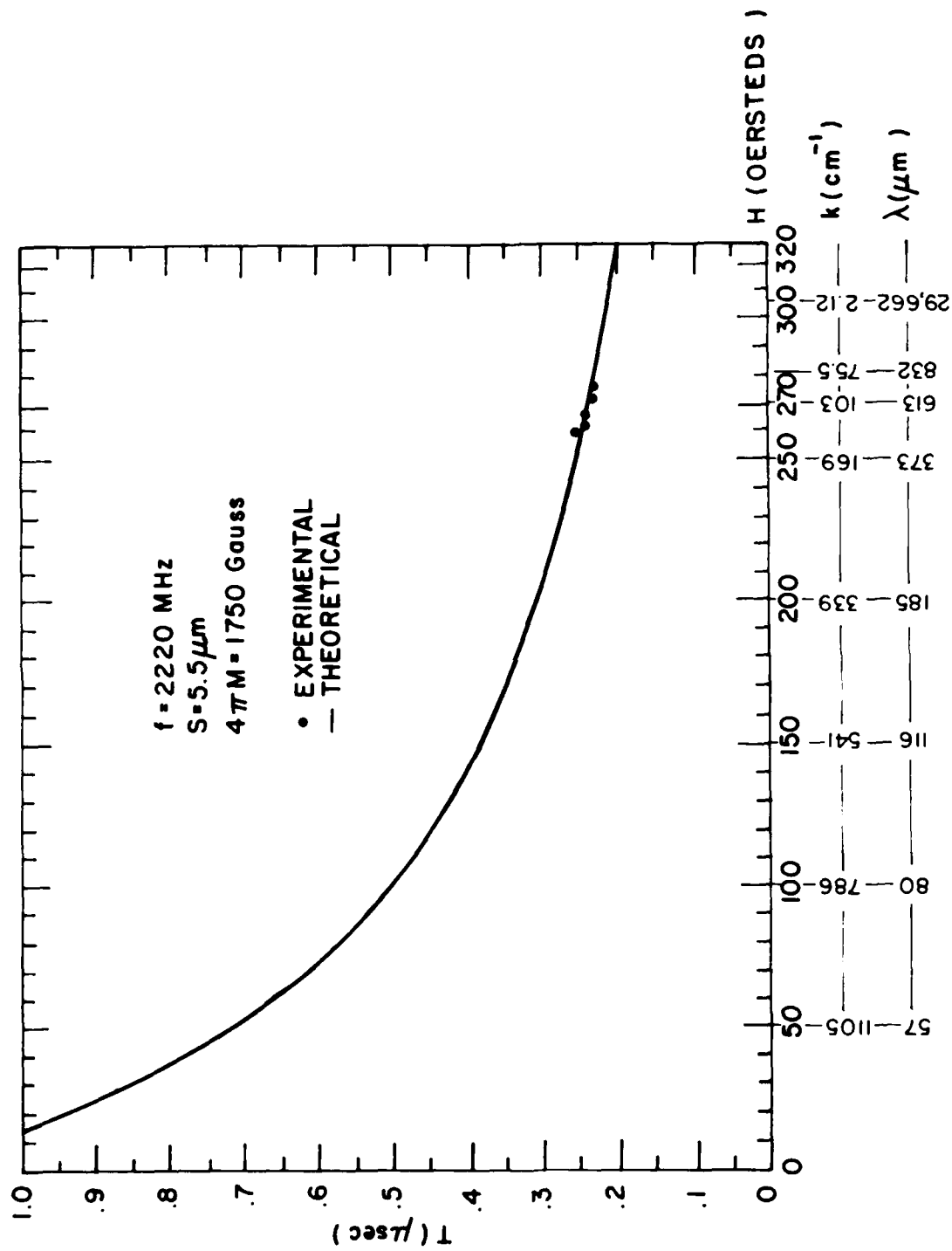


Figure 5-27b. MSW Propagation Along a Curved LPE/YIG Film. Pulse delay versus bias field, propagation constant and wavelength, on the curved YIG surface.

MSW MICROWAVE FREQUENCY ANALYZER

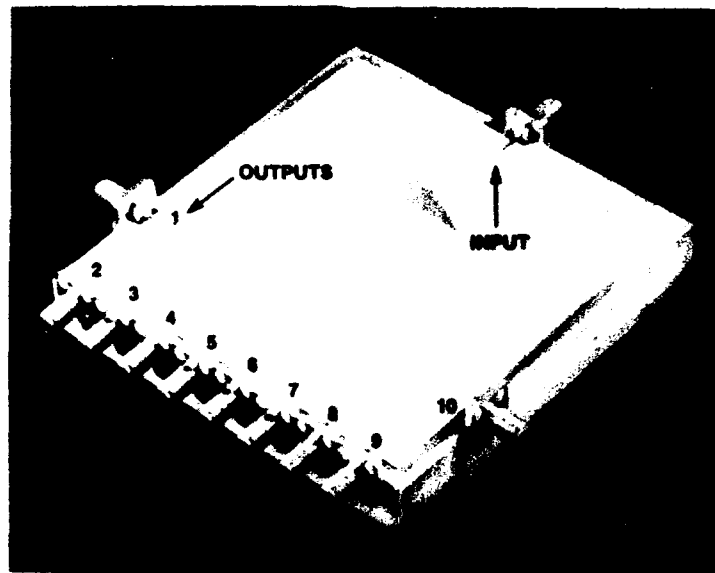


Figure 5-28. Device for Investigating MSW Refraction

of the triangular patch. The beam then traversed the metal region and exited at some angle to the original beam direction. Different frequencies within the beam were bent by different amounts. Output terminals 1 through 10, as indicated in the figure, were monitored. Results of this investigation are summarized in Reference 8.

Basically, when a wide band CW signal is input, the path taken by the shorter wavelength MSWs may be explained by bending of the beam through a triangular lens. Short wavelength means short with respect to beam aperture and lens dimensions. On the other hand, long wavelength MSWs were spread out due to the relatively small aperture. The long wavelength MSW beam spread to all outputs, with most of the energy traveling straight through the lens without being refracted.

Because different frequencies are bent by different amounts, this device can act as a simultaneous pulse separator. That is, when two RF pulses of different frequency are received simultaneously, the pulses can be spatially separated by refraction through a lens. They can also be separated in time, because of dispersion, even if path lengths are equal. This is demonstrated in the experimental results depicted in Figure 5-29.

5.7.2 SEPARATION OF SIMULTANEOUS RECEIVED PULSES

With reference to Figure 5-29, two 20 nsec RF pulses, one at 3.10 GHz and the other at 3.55 GHz, were applied to the input of the device shown in Figure 5-28. Output pulses were detected at Channels 3 and 4. The 3.55 GHz pulse appeared at Channel 3 and the 3.10 GHz pulse appeared at Channel 4. The two output transducers are spatially separated by 10° , as measured at the center of the input transducer. Not only are the signals spatially separated, but they are also separated in time because they have different velocities in the YIG. The 3.10 GHz pulse was received 250 nsec after application of the input signals, and the 3.55 GHz pulse was received at 380 nsec after application of the input pulse. Therefore, the signals are separated by 130 nsec. This translates to a time separation sensitivity of about 0.3 nsec/MHz. This type of device may prove useful because of the added flexibility of being tunable, through the biasing field.

-
8. Floyd, R.E. and Sethares, J.C. (1984) MSFVW Beam Steering and Spreading Over Large Path Lengths, *J. Appl. Phys.* **55**(No. 6), Part IIB: 2515-2517.

SEPARATION OF TWO SIMULTANEOUS CW PULSES

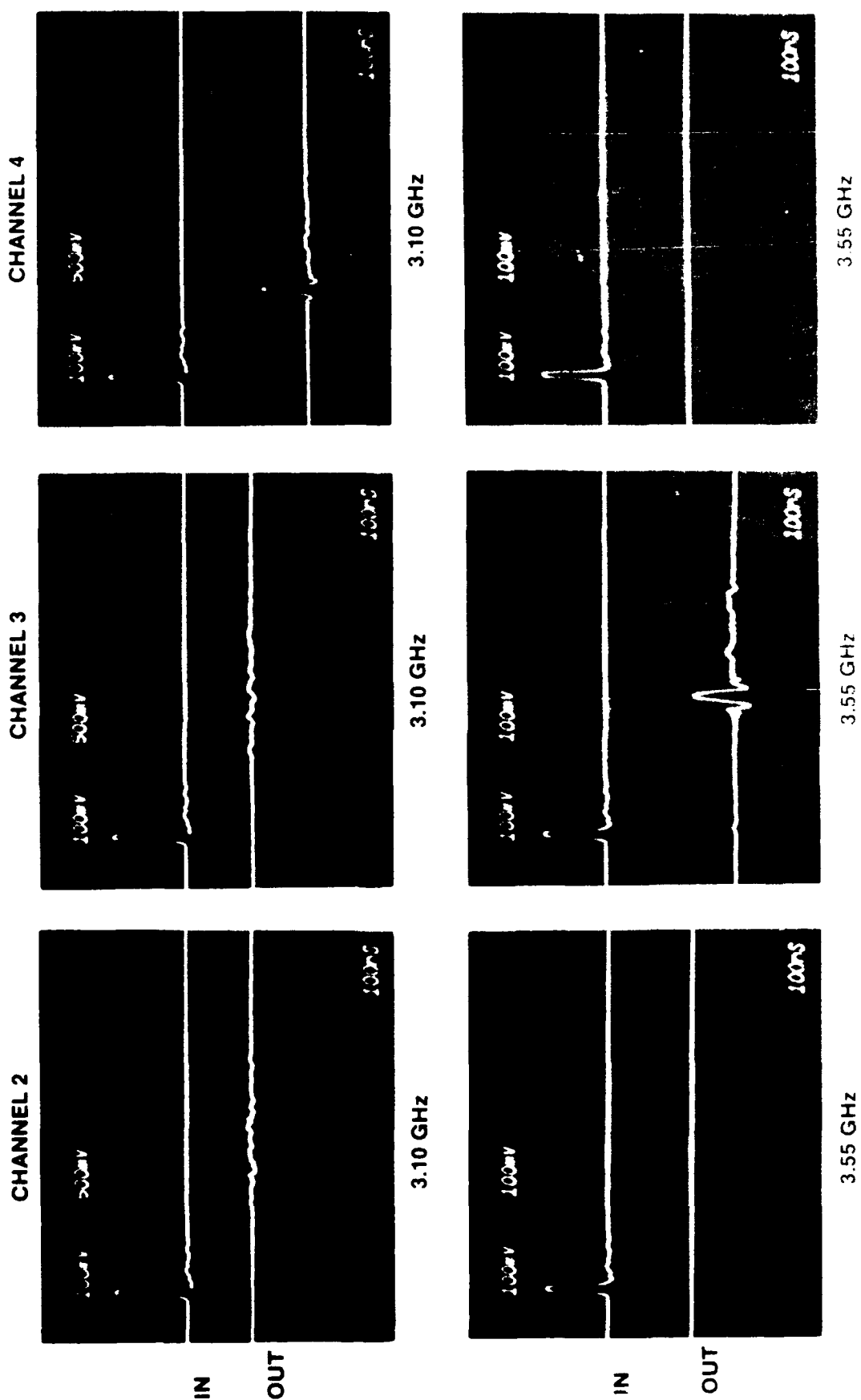


Figure 5-29. Separation of Simultaneously Received Pulses Using the Device Shown in Figure 5-28

References

1. Taylor, V.L., Sethares, J.C., and Smith, C.V. (1980) MSW Terminations, *IEEE Ultrasonics Symposium Proceedings*, 80CH1602 2.
2. Sethares, J.C. and Stiglitz, M.R. (1974) MSSW Delay Lines, *IEEE/MTT International Symposium Proceedings*, 74CH0838 3, pp 253-255.
3. Sethares, J.C. and Stiglitz, M.R. (1974) Propagation Loss and MSSW Delay Lines, *IEEE Transactions on Magnetics*, **MAG 10**, (No. 3):787-790.
4. Sethares, J.C. and Stiglitz, M.R. (1981) Magnetostatic Wave Oscillator Frequencies, *J. Appl. Phys.* **52**, (No. 3), Part II:2273-2275.
5. Sethares, J.C. and Floyd, R. (1985) MSW Applications for Phased Array Antennas, *Circuits Signals and Signal Processing*, Vol. 4, No. 1-2, pp 335/350.
6. Tsai, T.L. and Sethares, J.C. (1977) Band Stop Filters, *IEEE/MTTs-International Microwave Symposium Digest*, Cat. No. 77/CH1219/S, pp 526, 7.
7. Sethares, J.C. and Tsai, T.L. (1977) Magnetic Anisotropy of (III) LPE/YIG Films on GGG in Parallel Resonance, *IEEE Trans. on Magnetics*, **MAG13**, (No.5):1236.
8. Floyd, R.E. and Sethares, J.C. (1984) MSFVW Beam Steering and Spreading Over Large Path Lengths, *J. Appl. Phys.* **55**(No. 6), Part IIB: 2515-2517.

6. ADVANCED ANALYSIS AND DESIGN

In this chapter we present advanced concepts for MSW transducer models. Results may be used to improve predictions of the two basic models, TT and TL, that are discussed in this report.

6.1 Transducer Currents and Fields

In this section we consider current distribution along the strip width. Current along the strip length, the transducer aperture, is assumed uniform.

6.1.1 HYPERBOLIC CURRENT DISTRIBUTION

A hyperbolic current distribution is a better approximation to the actual distribution than is a flat current. The motivation for considering a hyperbolic current distribution is that it satisfies Maxwell's equations in a good conductor. A flat current distribution does not satisfy Maxwell's equations. Good conductors are of course desirable for current carrying MSW transducers to minimize loss. Moreover, hyperbolic current distributions result in a relatively simple closed form expression for the Fourier transform of the distribution.

Consider an isolated infinitely long, in the z direction, current carrying strip of width a , thickness t , and conductivity σ . Assume further that $t \ll a$ and $t \ll \delta$, the skin depth. Inside the conductor, Maxwell's equations, with $\exp(i\omega t)$ time dependence, require that

$$\nabla^2 J_y = i\omega\mu_0\sigma J_y. \quad (6-1)$$

Here J_y is the current in the z direction, per unit cross sectional area. Assuming uniform current distribution throughout the y direction, which is also the thickness direction, we have,

$$J = J_y t, \quad (6-2)$$

where J is now a surface current density. With all variations in the y and z directions identically zero, a valid solution to Eq. (6-1) is

$$J = A \sinh(kx) + B \cosh(kx) \quad (6-3)$$

where $k = (1 + i)/\delta$, and

$$\delta = 1/\sqrt{\pi\mu_0\sigma} \quad (6-4)$$

is the skin depth.

If we choose the coordinate system such that $x = 0$ is at the strip center and, if we assume J to be symmetric, because of physical symmetry, then $A = 0$. The total current I is given by Eq. (6-5).

$$I = \int_{-a/2}^{a/2} J dx \quad (6-5)$$

With the help of Eqs. (6-2) through (6-5), J , the current per unit width, becomes,

$$J(x) = \frac{(I/a) \cosh\{x/\bar{\delta}\}}{\sinh[a/(2\bar{\delta})]/[a/(2\bar{\delta})]} \quad (6-6)$$

where $-(a/2) < x < (a/2)$.

The quantity $\bar{\delta}$ is the complex skin depth, which for a good conductor is $\bar{\delta} = \delta/(1 + i)$

There are two limiting cases of importance here. When δ approaches infinity, $J(x) = I/a$ for $-a/2 < x < a/2$ and zero elsewhere, which is identical with a flat current distribution model. When δ approaches zero, $J(x)$ is a doublet; that is, $J[(+/-)a/2]$ equals infinity, and $J(x) = 0$ elsewhere. In particular, with δ approaching zero, Eq. (6-6) becomes

$$J(x) = [I/(2\bar{\delta})] \exp[(|x| - a/2)/\bar{\delta}]$$

Figure 6-1b shows theoretical plots of the current distribution magnitude across half of the strip width. For these curves, the calculations were simplified without loss of generality, by replacing $\bar{\delta}$ with δ in Eq. (6-6). The two limiting cases: a flat current, and a doublet current distribution, are evident. The curve labeled $\delta = 2.5$ mm, where $a/\delta = .2$, shows a nearly flat current distribution, while the curve labeled $\delta = .0025$ mm, where $a/\delta = 200$, shows an impulse of current near the strip edge.

Depending on the ratio of strip width to skin depth, one or the other of these two limiting cases may be useful. For example, for very narrow strips, where (a/δ) approaches zero, the flat current distribution will be better than the doublet model. For very wide strips, where (a/δ) approaches infinity, the doublet model will be more accurate. The above observations explain why flat current models have been successful even though a flat current distribution is unrealistic. Furthermore, use of a doublet model for wide strips should significantly reduce the complexity of analyzing wide strips. This has not been pursued to date.

It should be mentioned here that although the hyperbolic current distribution is a better approximation than a uniform current distribution, the distribution as given by Eq. (6-6) predicts that the phase, as well as the magnitude, of the current across the strip width is symmetric about the strip center. This symmetry was imposed here following Eq. (6-4). The more rigorous analysis for current distribution in Chapter 8 shows that current phase across a strip width is not symmetric; and, for narrow strips the phase is more nearly antisymmetric.

We have not attempted to generalize the hyperbolic analysis by removing the symmetry condition. It may be instructive to look at this generalization for wide strips because the magnitude and phase of J are neither symmetric nor antisymmetric in general, at least when a ferrite is present.

With reference to Figure 6-1a, we now obtain an expression for a hyperbolic current distribution in a multielement transducer. Three strips are shown in the figure. The magnitude of total integrated current across a strip width is assumed the same for all strips. Center-to-center strip spacing is p ; when $\eta = +1$, currents in adjacent strips have the same sign, and when $\eta = -1$, currents in adjacent strips have opposite signs.

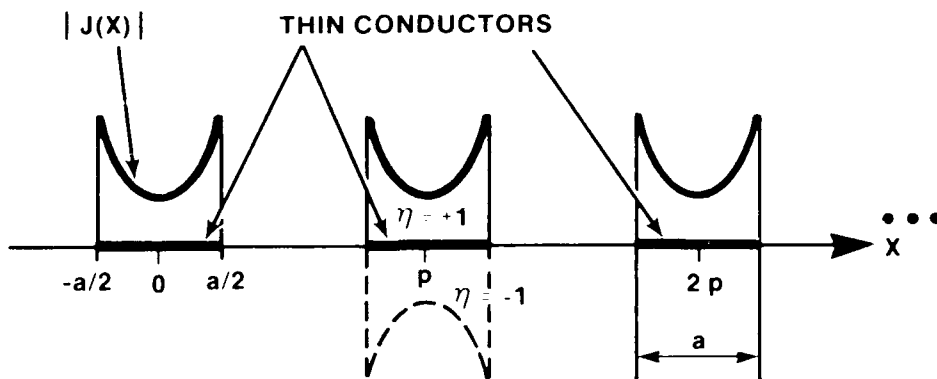


Figure 6-1a. Hyperbolic Current Distribution. Current distribution for grating, $\eta = 1$; and for meander line, $\eta = -1$.

6.1.2 HYPERBOLIC CURRENT DISTRIBUTION TRANSFORM

We can use the current distribution of Figure 6-1a in the computer programs of Chapter 3. It is required, however, to have the Fourier transform to incorporate it directly into the programs. One replaces $J(k)$ in the program with the new transform, derived below.

The appropriate normalization to use here for the Fourier transform is given by Eq. (6-7),

$$\tilde{J}_a(k) = \int_{-\infty}^{\infty} J(x) \exp(ikx) dx, \text{ (amps) .} \quad (6-7)$$

$\tilde{J}_a(k)$ has the units of current, and the subscript "a" means Eq. (6-7) is the transform of the entire array.

Using Eqs. (6-6) and (6-7), with the notation of Figure (6-1a), the integral across the n th strip is given by Eq. (6-8),

$$I(n) = \frac{(I/a)(\eta^{n-1})}{\left[\frac{\sinh(a/2\bar{\delta})}{(a/2\bar{\delta})} \right]} \int_{(n-1)p-a/2}^{(n-1)p+a/2} (\cosh [(x-(n-1)p)/\bar{\delta}]) e^{ikx} dx. \quad (6-8)$$

The total transform, $\tilde{J}_a(k)$, follows from Eq. (6-8) when we add up all the separate contributions. Here, I is the current in each strip.

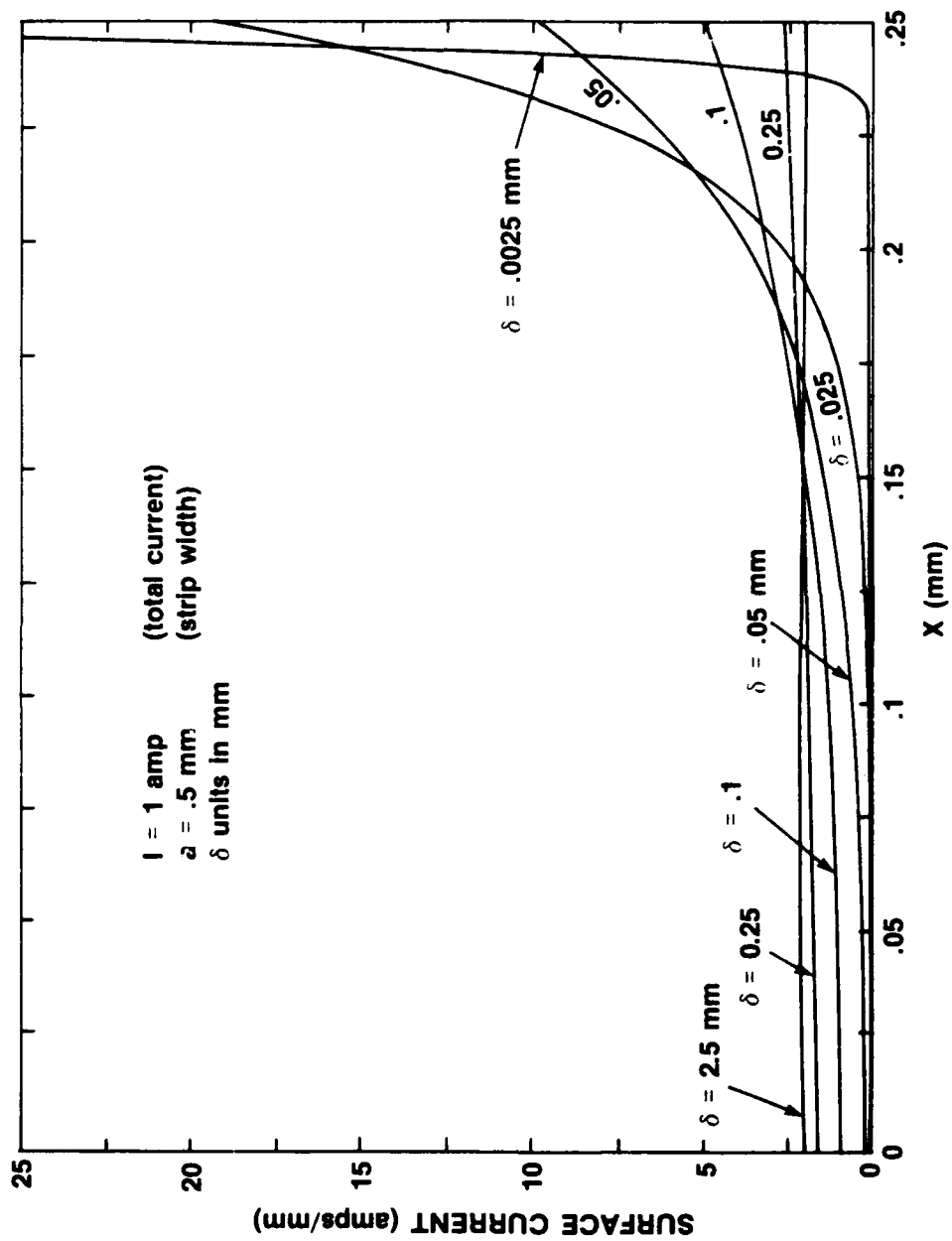


Figure 6-1b. Hyperbolic Current Distribution. Current distribution for parametric values of skin depth.

$$\tilde{J}_a(k) = \sum_{n=1}^N I(n) . \quad (6-9)$$

In Appendix B it is shown that Eq. (6-9) can be put into the form

$$\tilde{J}_a(k) = \frac{(I/a)}{\left[\frac{\sinh(a/2\bar{\delta})}{(a/2\bar{\delta})} \right]} \left(\frac{1 - \eta^N e^{ikpN}}{1 - \eta e^{ikp}} \right) F(a,k,\delta) , \quad (6-10)$$

where N is the total number of strips and

$$F(a,k,\delta) = \int_{-a/2}^{a/2} \cosh(x/\bar{\delta}) \exp(ikx) dx . \quad (6-11)$$

$F(a,k,\delta)$ is a normalized Fourier transform of the current distribution in one strip. For the hyperbolic distribution, it is derived in Appendix B. The complete expression, expressed explicitly in terms of a , k , and δ , is given below.

$$F(a,k,\delta) = \left[\frac{a}{(ak)^2 + 2(a/\delta)^2} \right] Q \quad (6-12)$$

where

$$Q = \exp[+(1+i)(a/2\delta)] [(a/\delta)(1+i) \cos(ak/2) + (ak) \sin(ak/2)] \\ + \exp[-(1+i)(a/2\delta)] [-(a/\delta)(1+i) \cos(ak/2) + (ak) \sin(ak/2)]$$

Note that when (a/δ) approaches zero, we retrieve expressions for the flat current model as expected. In particular,

$$F \equiv (2/k) \sin(ak/2) \quad (6-13)$$

$$\text{and } \tilde{J}_a(k) = I \left[\frac{[1 - \eta^N \exp(ikpN)]}{[1 - \eta \exp(ikp)]} \right] \left[\frac{\sin(ak/2)}{(ak/2)} \right] \quad (6-14)$$

where again, I is the current in each strip.

6.1.3 HYPERBOLIC CURRENT DISTRIBUTION INSERTION LOSS

Figure 6-2a shows how insertion loss varies when transducer skin depth is changed. Note that there is about a 10 dB insertion loss increase when the skin depth decreases from 25 μm to 20 μm . This is a substantial change. Since strip width is 50 μm , a/δ is approximately equal to 2. Inspection of Figure 6-1b shows that $a/\delta = 2$ represents a fairly uniform current distribution.

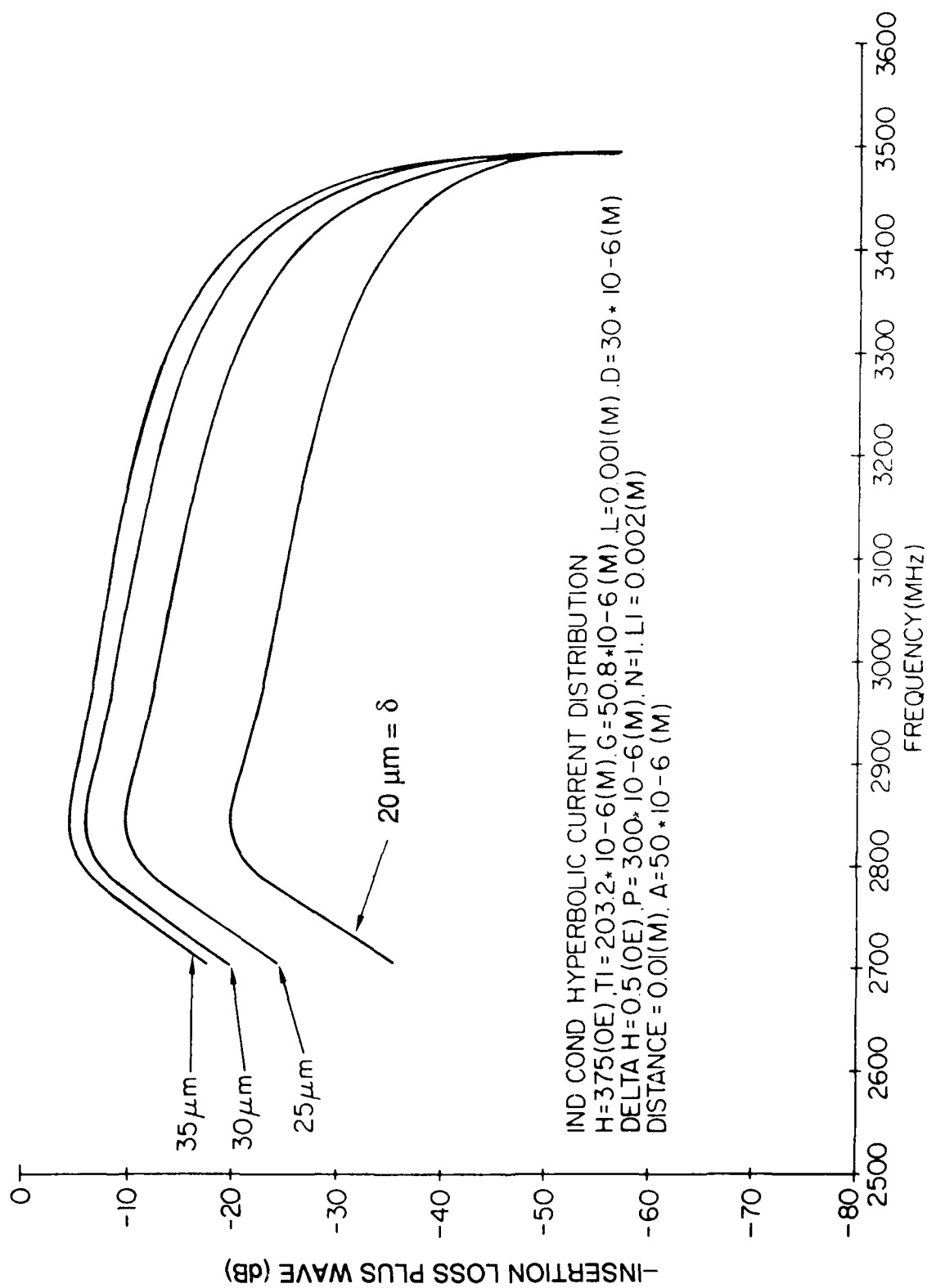


Figure 6-2a. Insertion Loss with Hyperbolic Current Distribution. IL versus f for parametric values of skin depth, $N = 1$.

IND. COND. HYPERBOLIC.

**H = 375 (oe), T1 = 228.6 microns, G = 25.4 microns, L = 1. mm,
D = 16 microns, $\Delta H = .3$ (oe), p = 300 microns, N = 15, ETA = 1, L1 = 3. mm,
DIST. = 1 cm, A = 150 microns, RL = 0**

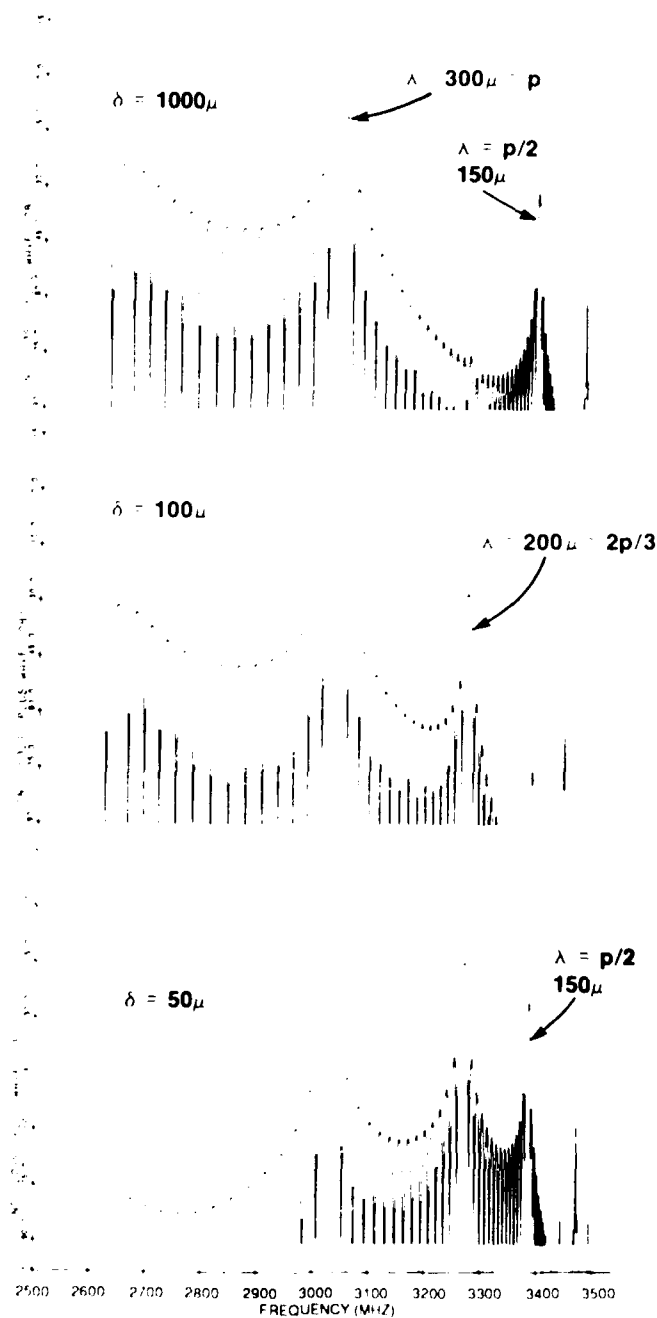


Figure 6-2b. Insertion Loss with Hyperbolic Current Distribution. IL versus f for parametric values of skin depth, N = 15

Computer generated insertion loss plots for a delay line made up of a pair of grating transducers is shown in Figure 6-2b. The top curve is for a relatively large skin depth, 1000 μm , and the bottom curve for a smaller skin depth, 50 μm . Strip width is 150 μm , and center-to-center spacing is 300 μm . The curves in Figure 6-2b can be understood in terms of the two limiting cases for (strip width)/(skin depth). As we saw in the previous section, where skin depth increases, current distribution becomes more uniform, and when skin depth approaches zero, current distribution approaches a doublet.

Figure 6-3 shows a uniform current distribution for a grating transducer. The figure also shows the fundamental response for a uniform current distribution, the 300 μm wavelength; and the fundamental response for the doublet current distribution, the 150 μm wavelength. Clearly, as the skin depth approaches infinity, the 300 μm wavelength is more efficiently excited.

Wavelengths at the individual peaks in Figure 6-2b, can be deduced from a normal mode analysis. As discussed later in Section 7.3.2 on normal modes, space harmonic amplitudes A_n are proportional to

$$A_n = \text{const}(1 + \eta \cos(n\pi)) \left\{ \frac{\sin[(k - n\pi/p) Np/2]}{[(k - n\pi/p) Np/2]} \right\} \quad (6-15)$$

For a grating transducer, $\eta=1$, and n is even for a nonzero A_n . The bracketed term in Eq. (6-15) is recognized as an array factor. It is maximum when $(k - n\pi/p) = 0$, or when MSW wavelength = $2p/n$. Since for a grating, n must be even, the first two space harmonics have wavelength p and $p/2$, or 300 and 150 μm , respectively. The response at 200 μm probably corresponds to $n = 3$, a space harmonic for a meander line excitation. This is physically reasonable because skin depth is not too much smaller than strip width.

In the limit when skin depth approaches zero, the 200 μm response should vanish. This would make a good test of the above interpretation for the $n = 3$ space harmonic.

6.1.4 TRANSDUCER FIELDS

MSW transducers are current driven circuit elements, as opposed to interdigital transducers, which are voltage driven circuit elements. IDTs are used for generating and receiving surface acoustic waves. Moreover, the coupling mechanism between MSW and electromagnetic signals, fed to or received from an MSW transducer, involves the RF magnetic fields set up by transducer currents. Studying current-induced RF magnetic fields surrounding an MSW transducer leads to insights into the coupling mechanism, which can be useful in MSW device design.

For example, a z directed transducer drive current sets up x and y RF magnetic field components, h_x and h_y . The same transducer is used for all three pure MSW modes of propagation. MSSW, with the DC magnetic bias field in the z direction, propagating perpendicular to the drive current, have x and y RF magnetization components, m_x and m_y . For MSSWs, both h_x and h_y applied RF magnetic fields drive both magnetization components, m_x and m_y . Consequently, MSSW excitation is generally a very efficient process. Volume waves, on the other hand, are generally less efficient. This is explained as follows.

Consider the same transducer as above, but with the DC magnetic bias field in the y direction, for generating MSFVWs propagating perpendicular to the drive current in the x direction. Now, RF magnetization components are in the x and z directions only. In this situation, the applied h_y field

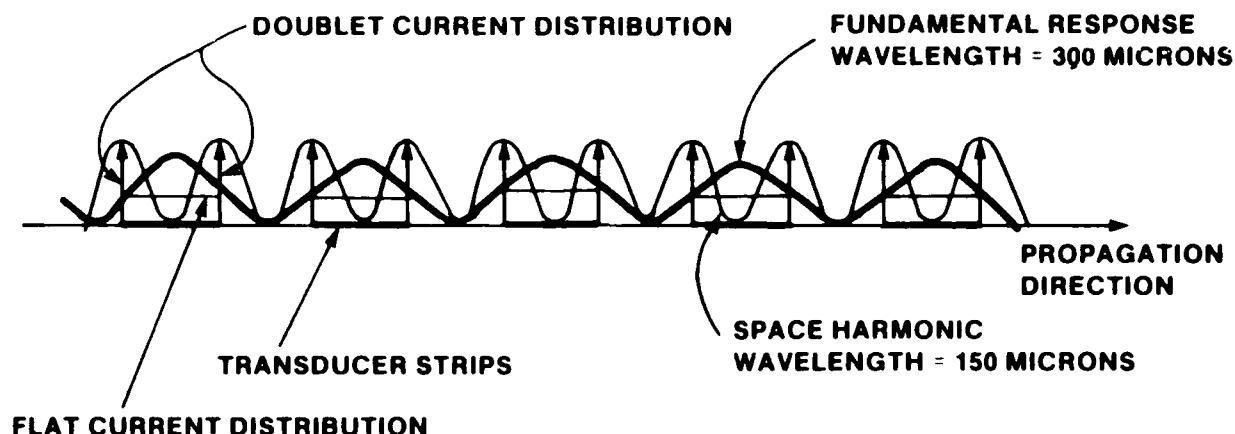


Figure 6-3. Limiting Cases for Hyperbolic Current Distribution. Uniform current; skin depth approaches infinity, favors generation of fundamental response. Doublet current; skin depth approaches zero, favors generation of first space harmonic response.

does not drive MSFVW; only the h_x component couples to MSFVW. A similar situation occurs for MSBVW, with the DC magnetic field in the x direction. Now, the h_x component does not couple to the RF magnetization; only h_y couples; and again, the excitation efficiency is low. The lower efficiency for volume waves is well established experimentally.

We have calculated RF magnetic fields set up by drive currents in an effort to better understand the generation and reception process. Figures 6-4 and 6-5 show examples of these calculations.

Figure 6-4a and 6-4b show typical plots for the x component of RF magnetic field near an MSW meander line transducer in the absence of a ferrite. Calculations are based on the theory developed in Chapter 2. With reference to the geometry in Figure 1-4b, set t_1 equal to infinity and $d = l = 0$. There remains an array of flat conducting strips, G units above a ground plane. Assume the array is periodic in x , and infinite in the x and z directions. It is composed of uniformly spaced strips of width a and center to center spacing p between strips.

Figure 6-4a shows h_x at the ground plane surface for various values of lift-off G . Note the rectangular function when G approaches zero, in agreement with a flat current distribution. As G increases, the RF driving field near the ground plane is sinusoidal with period equal to the meander line period of $2p$. For the same transducer array, Figure 6-4b shows the product (aH) near the ground plane, with a fixed value of lift-off G , for various values of strip width a .

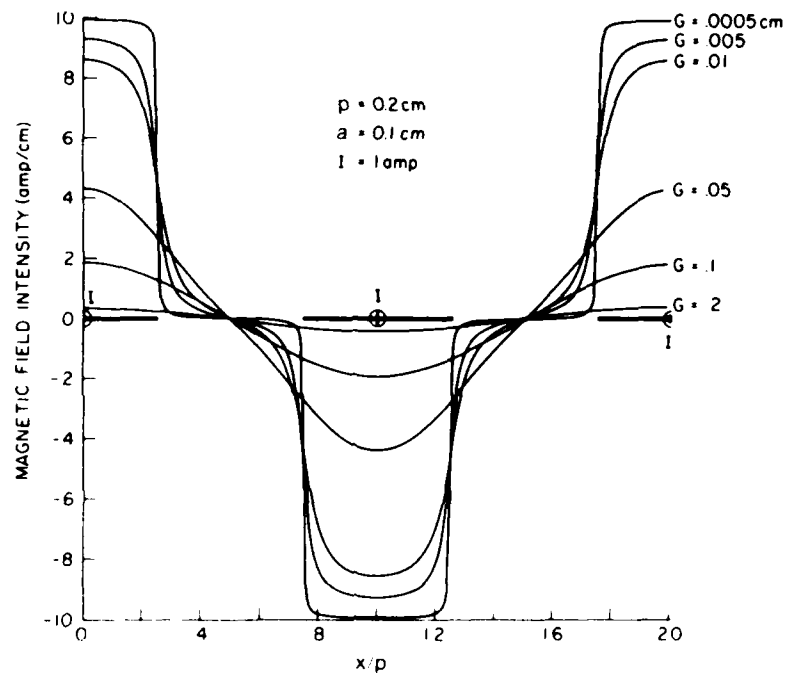


Figure 6-4a. RF Magnetic Field Component Using a Truncated Infinite Array Analysis. Horizontal RF magnetic field for parametric values of G .

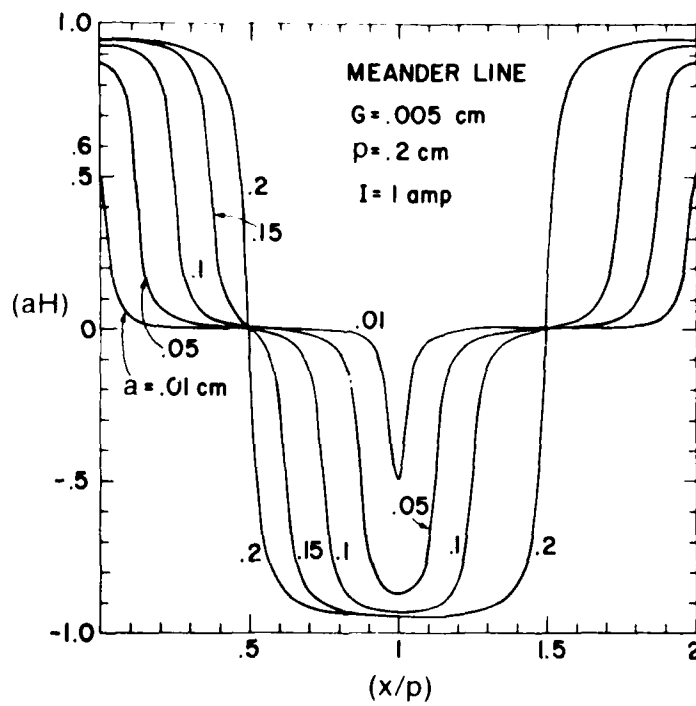


Figure 6-4b. RF Magnetic Field Component Using a Truncated Infinite Array Analysis. Horizontal RF magnetic field for parametric values of a .

Note that the fields depicted in these figures are symmetric about the center strip. Moreover, the fields surrounding every other strip are identical. These are the fields produced by an infinite array calculation. For a finite number of strips, the array is simply truncated without altering the fields. The theoretical expression for h_x is given in Eq. (6-16). (See also Eq. (7) in Reference 1 for the y component of h .)

$$h_x = (2I/a) \sum_{n=1}^{\infty} [1 - \cos(n\pi)] \frac{\sin(n\pi a/2p)}{n\pi} \exp[-n\pi G/p] \cos(n\pi x/p) \quad (6-16)$$

Figure 6-5 shows RF fields, again for a flat current distribution, but for a finite transducer with no ground plane, and for which end effects are taken into account. That is, magnetostatic fields surrounding an individual current strip depend on the strip's position within the array. The curves for this figure were obtained from Eq. (6-17).

$$h = \frac{I}{2\pi a} \sum_{n=1}^N \eta^{(n+1)} \left\{ \frac{\hat{y}}{2} \ln \left[\frac{(x - (n-1)p + a/2)^2 + y^2}{(x - (n-1)p - a/2)^2 + y^2} \right] \right. \\ \left. + \hat{x} \tan^{-1} \left[\frac{-ay}{y^2 + (x - (n-1)p)^2 - (a/2)^2} \right] \right\} \quad (6-17)$$

Eq. (6-17) was derived using superposition principles. That is, magnetostatic field contributions from N strips of width a , center to center spacing p , each carrying total current I , are summed.

For a single very narrow strip, width approaching zero, and $N = 1$, Eq. (6-17) reduces to

$$h = (I/2\pi) [\hat{y}x - \hat{x}y]/(x^2 + y^2) \quad (6-18)$$

Eq. (6-18) is recognized as the magnetostatic field surrounding a line current source. In reducing Eq. (6-17) to Eq. (6-18) use is made of the fact that $\ln(x)$ approximately equals $x - 1$ when x approaches unity. The magnitude of the field given by Eq. (6-18) is simply $(I/2\pi r)$ where $r = \sqrt{x^2 + y^2}$, as expected.

The field plots in Figure 6-5 are for the y component of the magnetic field in the plane of the transducer, $y = 0$. The top curve is for a grating, $\eta = 1$, and the bottom curve is for a meander line, $\eta = -1$. Note that h_y has peaks in the vicinity of strip edges, as expected. Also observe that zero field crossings do not pass through the strip centers. This only occurs in the infinite array calculation. Eq. (6-17) does not take into account the reaction of the ferrite back onto the transducer current distribution. Each strip carries total current I and the current distribution is spatially uniform.

6.2 Equivalent Circuit Models

In Chapter 2, an electromagnetic boundary value problem is solved for MSSW, MSBVW, and MSFVW modes of propagation. Power density carried by a propagating wave is related to transducer

1. Sethares, J.C., Frost, H.M., and Szabo, T.L. (1977) Fields of a Flat Conductor EM/SAW Transducer, *IEEE Trans. Sonics and Ultrason.* **SU/24**, (No. 2):88-94.

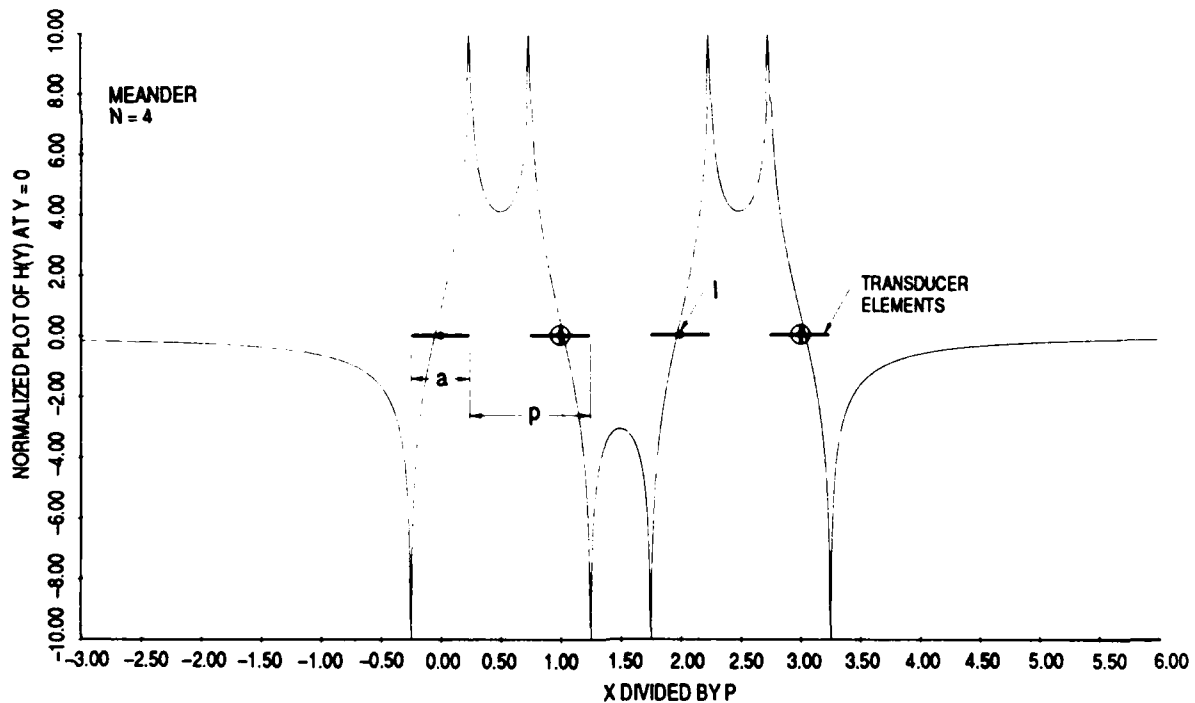
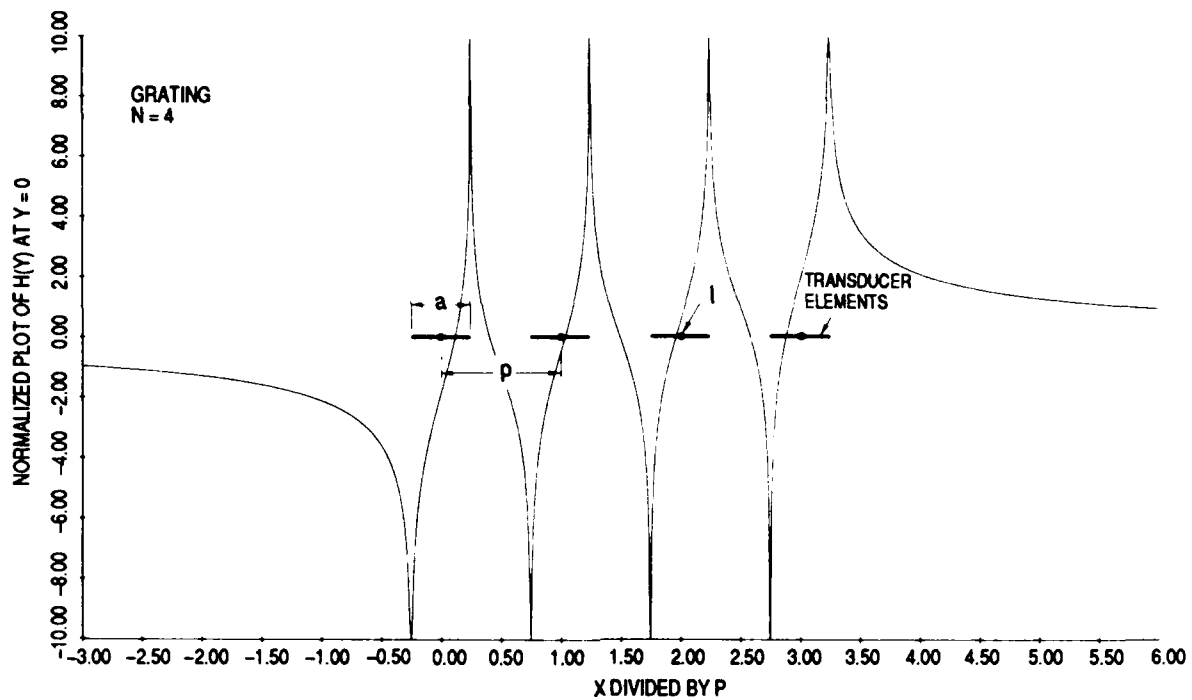


Figure 6-5. RF Magnetic Field Component Using Superposition for a Finite Array of Conducting Strips. Vertical RF magnetic field component.

Top: Four element grating transducer.

Bottom: Four element meander line transducer.

parameters and excitation current. From the resulting expressions, a radiation resistance, reactance, and dispersion relation are obtained for each propagating mode. Results become useful when design equations are developed relating material, transducer parameters, and controllable parameters such as frequency, magnetic biasing field, and ground plane spacing, to experimentally measurable device parameters. Important device parameters are insertion and return loss, time delay, and velocity versus frequency, that is, dispersion. Essentially, all scattering parameters are required.

Equations for a delay line configuration are presented in many of the references cited in this report. For completeness, the most important ones are tabulated in this section. They are also programmed into the Fortran programs described in Chapter 3. All Fortran programs are maintained on tape for a Cyber computer by RADC/EEA.

Electrical equivalent circuits are used as an analytical tool in the process of going from basic physical parameters to experimentally measurable parameters. The process is not repeated here because it is clearly presented in detail in Reference 2. This reference is important for understanding MSW computer programs of this report. Here, and in Reference 2, all assumptions are clearly spelled out.

In what follows and throughout this report, two names are used interchangeably for a single MSW model; namely, the two terminal, TT, and truncated array, TA, model. They are identical in every respect.

The basis for the TA model is that the transducer analysis is carried out assuming an infinite periodic array of flat current strips. Then the array is truncated to a finite array with the current induced RF magnetic fields surrounding individual strips the same for all strips. Regardless of where an individual strip is, at the center or at an array edge, the surrounding field patterns are identical. The entire truncated array transducer has one electrical input port; that is, two circuit theory terminals.

6.2.1 RADIATION RESISTANCE FOR TT MODEL

Radiation resistance is obtained from the power radiated from a transducer, given in Eq. (6-19).

$$P_{\text{tot}}(s) = (1/2)R_1(s) \{ l_1 |\tilde{J}(k)|^2 \} \quad (6-19)$$

This equation is identical with Eq. (12) of Reference 2. The "s" denotes propagation direction. $R_1(s)$ with units of resistance per unit width depends on YIG parameters and ground plane spacing only. The transducer aperture is l_1 , and $\tilde{J}(k)$ is a Fourier transform of the current distribution $J(x)$. $J(x)$ has units of current per unit width. The transform is defined throughout this report and in all our work, excluding the formulation in Chapter 8 where it is normalized differently, as:

$$\tilde{J}(k) = \int_{-\infty}^{\infty} J(x) \exp(ikx) dx \quad (6-20)$$

-
2. Sethares, J.C. and Weinberg, I.J. (1985) *Theory of MSW Transducers, Circuits, Systems and Signal Processing* 4, (No. 1, 2):41-62.

The quantity $R_1(s)$ is not radiation resistance. To define a proper transducer radiation resistance we need to equate $P_{\text{tot}}(s)$ to $(1/2) R_m(s) |I_{\text{tot}}|^2$ where now $R_m(s)$ is the radiation resistance of an entire transducer for any number of strips, and I_{tot} is the total current through the transducer terminals. For parallel strips $I_{\text{tot}} = NI_0$, for a meander line $I_{\text{tot}} = I_0$, and for parallel π transducers $I_{\text{tot}} = (N/2) I_0$, where N is the number of strips.

$$P_{\text{tot}}(s) = (1/2) R_m(s) |I_{\text{tot}}|^2 \quad (6-21)$$

Equating Eqs. (6-19) and (6-21) we find:

$$R_m(s) = [R_1(s) l_1 |\tilde{J}(k)/I_0|^2] / F_N^2 \quad (6-22)$$

where $F_N = N$ for parallel strips, 1 for a meander line and $N/2$ for parallel π transducers. Parallel π transducers are defined in Reference 3 and are made by connecting multiple two element meander lines in parallel.

For the flat current distribution the Fourier transform $J(k)$ in Eq. (6-22) is given by Eq. (6-14). Substitution of Eq. (6-14) into Eq. (6-22) yields Eq. (6-23). (We recognize that $I_0 = I$ and $J(k) = J_a(k)$.)

$$R_m(s) = \frac{R_1(s) l_1}{F_N^2} \left\{ \left| \frac{1 - \eta^N \exp(ikpn)}{1 - \eta \exp(ikp)} \right| \left[\frac{\sin(ak/2)}{(ak/2)} \right] \right\}^2 \quad (6-23)$$

where $\eta = +1$ for a grating and $\eta = -1$ for a meander line. We now relate Eq. (6-23) to the analysis in Chapter 2.

For MSSW, Eq. (2-55) gives $P_{\text{tot}}(s)/l_1$. Denoting the right hand side of Eq. (2-55) by RHS (55) we have,

$$P_{\text{tot}}(s) / l_1 = \text{RHS}(55) \quad (6-24)$$

where RHS (55) is what has been coded in the computer program. Since transducer current cancels out of the final expression for radiation resistance, as seen in Eq. (6-23), its value, I_0 , is arbitrary. Current has been set to unity in the program, wherever it appears in power expressions. Equating $P_{\text{tot}}(s)$ from Eqs. (6-21) and (6-24), noting that total transducer current I_{tot} may be written as,

$$I_{\text{tot}} = (1/2)[(1 - \eta) + (1 + \eta)N] I_0 \quad (6-25)$$

and setting I_0 to unity, yields

$$R_m(s) = \frac{4 l_1 \text{RHS}(55)}{(1 - \eta) + (1 + \eta)N^2} \quad (6-26)$$

which is identical with Eq. (2-99).

We now do a parallel development for MSFVW and MSBVW. For MSFVW, Eq. (2-74) gives

-
3. Wu, H.J., Smith, C.V. Jr., Collins, J.H., and Owens, J.M. (1977) Band Pass Filtering with Multibar MSSW Microstrip Transducers, *Electronics Letters* **13**, (No. 20).

$$P_{\text{tot}}(s) / l_1 = \text{RHS}(74) . \quad (6-27)$$

Equating $P_{\text{tot}}(s)$ from Eqs. (6-21) and (6-27) yields

$$R_m(s) = \frac{4l_1 \text{RHS}(74)}{(1 - \eta) + (1 + \eta)N^2} . \quad (6-28)$$

Similarly, for MSBVW,

$$R_m(s) = \frac{4l_1 \text{RHS}(93)}{(1 - \eta) + (1 + \eta)N^2} . \quad (6-29)$$

To summarize, Eqs. (6-26), (6-28), and (6-29) give the radiation resistance for the three modes of propagation.

For completeness, we relate $R_1(s)$ to Eq. (2-55) for MSSW. Equate $P_{\text{tot}}(s)$ in Eq. (6-19) to $P_{\text{tot}}(s)$ in Eq. (6-24). The result is,

$$R_1(s) = 2\text{RHS}(55) |\tilde{J}(k)|^2 . \quad (6-30)$$

Now,

$$\text{RHS}(55) = \frac{s\omega\mu_0 |G_S|^2}{4|k|^2} \times \left\{ \begin{array}{l} \text{unitless} \\ \text{bracketed term} \\ \text{of RHS}(55) \end{array} \right\} \quad (6-31)$$

where we have used the fact that $k = K_S = K$, and

$$G_S = [J(k) \exp(-|k|d)] / F_T'(k), \text{ from Eq. (2-38).}$$

Substituting G_S , from above, and Eq. (6-31) into Eq. (6-30) yields

$$R_1(s) = \frac{s\omega\mu_0 \exp(-2|k|d)}{2|k|^2 [F_T'(k)]^2} \times \left\{ \begin{array}{l} \text{unitless} \\ \text{bracketed term} \\ \text{of RHS}(55) \end{array} \right\} \quad (6-32)$$

Note that $F_T'(k)$ has units of length; see Eq. (2-40). Then it is easy to verify that $R_1(s)$ has units of ohms/m and it is independent of transducer parameters.

6.2.2 EM AND MSW POWER

Power carried by a magnetostatic wave can be calculated from Poynting's vector, $\mathbf{E} \times \mathbf{H}$. For the coordinate system in Figure 2-1, the average power density carried by an MSW, as calculated from Poynting's vector, is the real part of

$$p_x = (1/2)E_z H_y^* \quad (6-33)$$

Recall that $h_z = 0$ for all three pure MSW modes of propagation. Total power carried by an MSW is given by the integral of Eq. (6-33) over the cross section.

$$P_{\text{tot}} = (1/2) \int_{y=-(d+L)}^{t_1+g} \int_{z=0}^{l_1} E_z H_y^* dz dy \quad (6-34)$$

It is often easier to use an alternate form for power. The alternate form is derived from Maxwell's equations, using $\mathbf{H} = \text{grad}(\psi)$, where ψ is a magnetic potential. Thus,

$$\nabla \cdot (\mathbf{E} \times \mathbf{H}^*) = \mathbf{H}^* \cdot \nabla \times \mathbf{E} - \mathbf{E} \cdot \nabla \times \mathbf{H}^*$$

with $\nabla \times \mathbf{H} = 0$ and $\nabla \times \mathbf{E} = -i\omega \mathbf{B}$, we have,

$$\nabla \cdot (\mathbf{E} \times \mathbf{H}^*) = -i\omega \mathbf{H}^* \cdot \mathbf{B} = -i\omega (\nabla \psi^*) \cdot \mathbf{B}$$

using $\nabla \cdot (\psi^* \mathbf{B}) = \nabla \psi^* \cdot \mathbf{B} + \psi^* \nabla \cdot \mathbf{B}$

and $\nabla \cdot \mathbf{B} = 0$,

$$\nabla \cdot (\mathbf{E} \times \mathbf{H}^*) = -i\omega \nabla \cdot (\psi^* \mathbf{B})$$

$$\therefore \mathbf{E} \times \mathbf{H}^* = -i\omega \psi^* \mathbf{B}$$

$$\text{and } \mathbf{p} = \text{Re} \left[\frac{-i\omega}{2} \psi^* \mathbf{B} \right]. \quad (6-35)$$

6.3 MSW Delay Line Band Pass Filters

Results shown previously in Chapter 4, Sections 4.5 and 4.7 indicate that MSW delay line characteristics can be controlled to perform useful functions. In this section, two alternate techniques are described showing how MSW delay lines can be designed to perform band pass filtering.

6.3.1 LONG WAVELENGTH FILTERING

In the first technique, a pair of identical single strip transducers are spaced one centimeter apart. The transducer strip width and liftoff determine bandwidth, loss and sidelobe levels. Center frequency is dependent on the value of magnetic bias field.

Figure 6-6 shows the response of three such delay lines. In all three delay lines, the gap G , or liftoff, is 3 μm . This is much smaller than MSW wavelengths near the low end of the passband, near 2600 MHz, for all three cases. The ratio of strip width, a , to YIG film thickness, d , defines whether we have narrow, intermediate, or wide strips. Clearly, the main lobe bandwidth decreases as strip width increases, while insertion loss remains almost constant. Figure 6-7 shows how sidelobes are reduced by simply increasing G . With $G/d = 8.3$, the minimum insertion loss is about 2 dB, while the first sidelobe is >35 dB down. This represents respectable band pass filtering. The important tradeoffs are among insertion loss, bandwidth, and sidelobe suppression. This type of filter appears promising.

6.3.2 SPATIAL HARMONIC FILTERING

In the second bandpass filtering technique, a pair of multielement transducers are used in a delay line. The passbands of three delay lines are shown in Figure 6-8. Both transducers are eight-element gratings with a periodicity of 356 μm . MSW wavelength at the first main lobe is 356 μm .

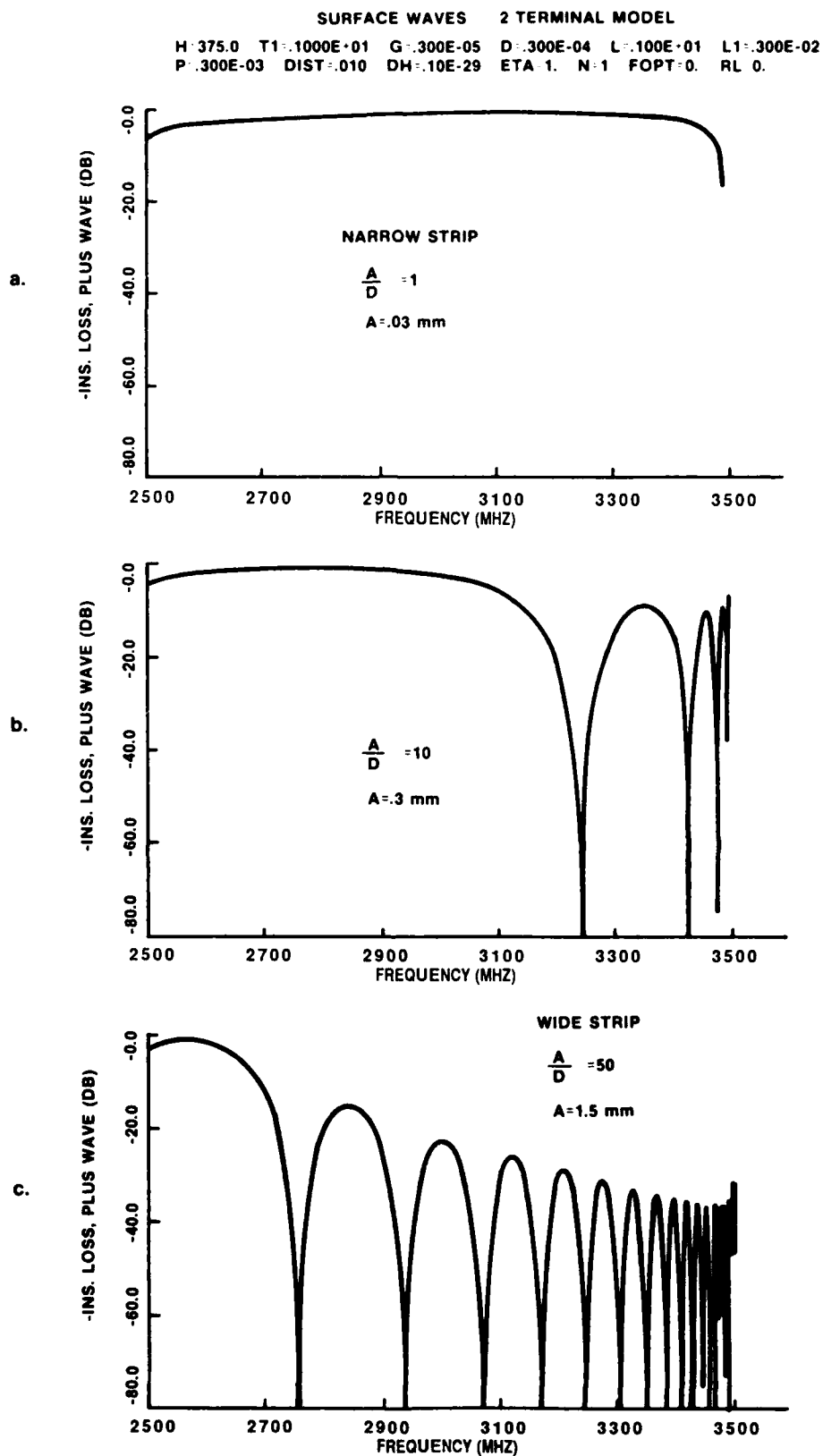


Figure 6-6. Passband Responses for a Pair of Narrow, Intermediate and Wide Single Element Transducers. $G/D = 1/10$ for all three cases.

a. Narrow strips, $A/D = 1$ b. Intermediate strips, $A/D = 10$ c. Wide strips, $A/D = 50$

SURFACE WAVES 2 TERMINAL MODEL

H=375.0 T1=.1000E+1 D=.300E-04 L=.100E+01 L1=.300E-02
A=.150E-02 P=.300E-03 DIST=.010 DH=.10E-29 ETA=1. N=1 FOPT=0.
RL=0.

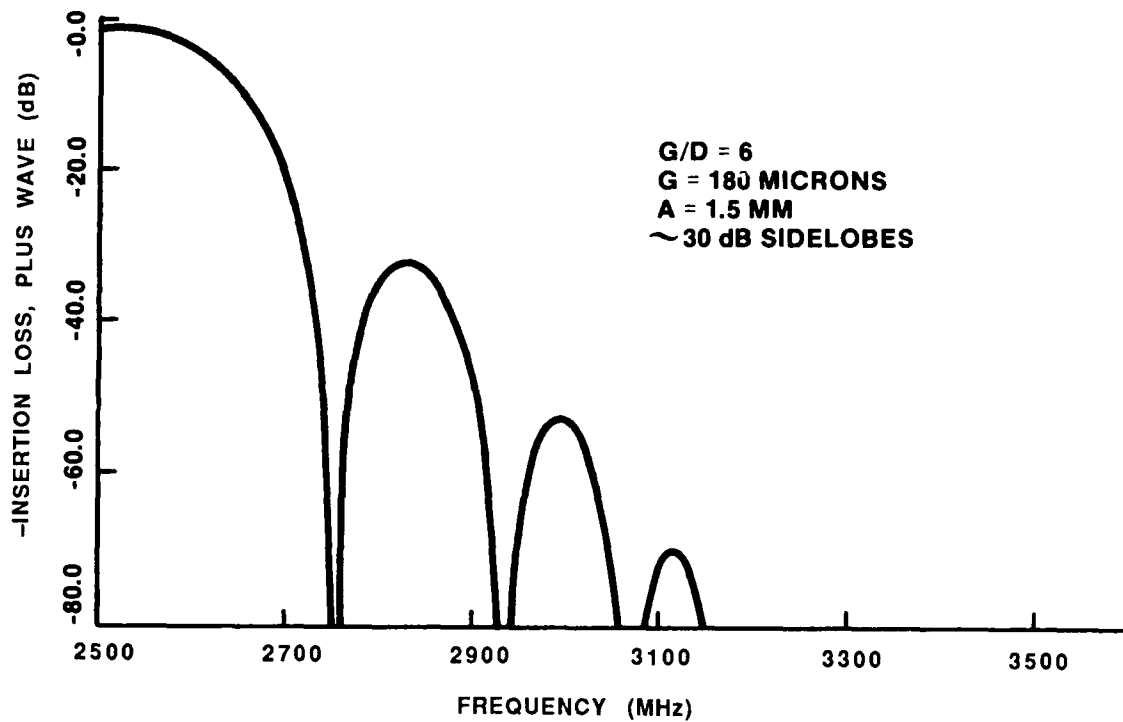


Figure 6-7a. Sidelobe Suppression for Bandpass Filtering Using One Wide Strip and Large G.
IL versus f with G = 180 μ m.

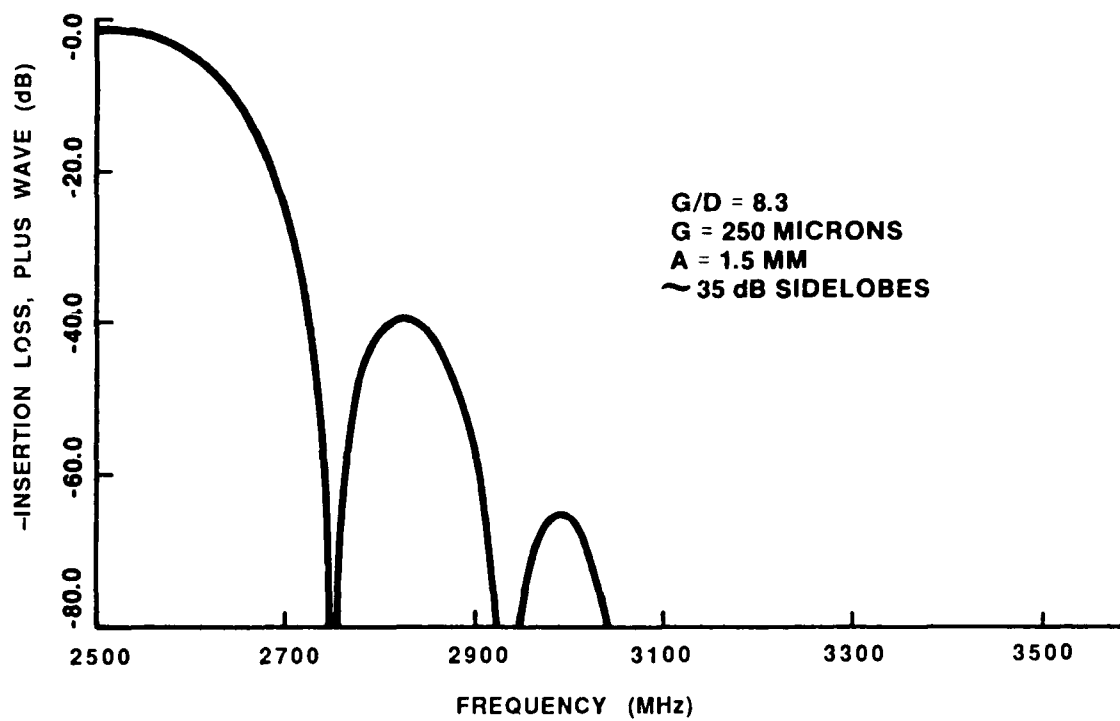


Figure 6-7b. Sidelobe Suppression for Bandpass Filtering Using One Wide Strip and Large G. IL versus f with $G = 250 \mu\text{m}$.

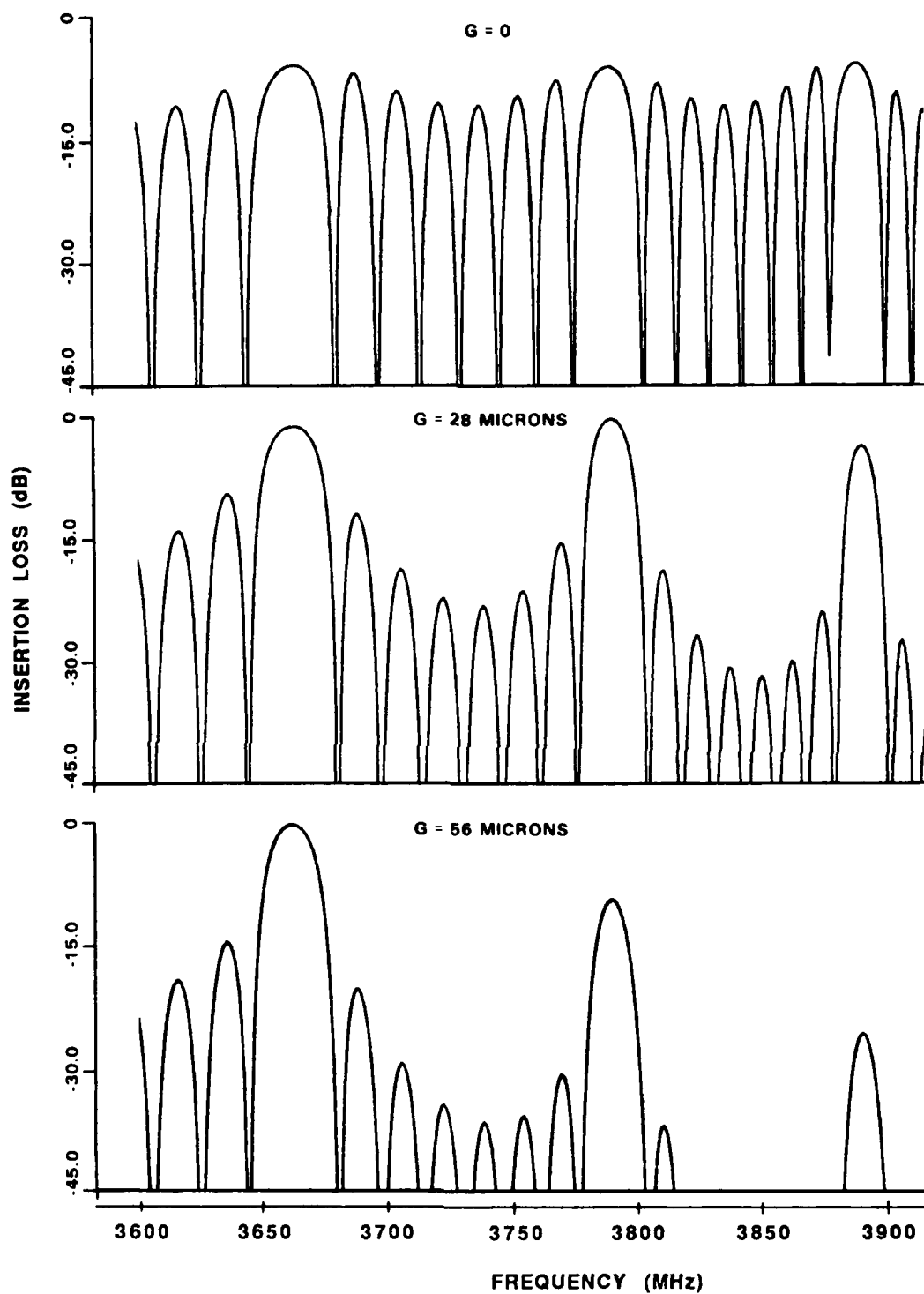


Figure 6-8. Sidelobe Suppression for Bandpass Filtering Using a Large Number of Narrow Strips and Large G . $H = 650$ oersteds, $D = 6.25$ mm, $T_1 = L = 254$ mm, $L_1 = 1$ cm, $P = 356$ mm, $a = 0.1P$, $\eta = 1$, and $N = 8$.

Clearly, as the transducers are lifted off the delay line surface, sidelobes are reduced more than the main lobe. This filtering technique involves spatial harmonics of the multielement transducers. This type of filter has more loss than the preceding one, because wavelengths within the passband are relatively short, and as such, experience more loss. They have the advantage that multipole filters are easier to fabricate.

6.4 Generalized MSW Transducer Model

In this section, we develop a procedure, or algorithm, whereby the TT MSW model is extended to account for arbitrary current variations along the coupling structure. The coupling structure may be a section of strip line such as microstrip, coplanar, or slot line. In this report, extensions of the TT model to spatially varying currents are developed for single element transducers. Further extension to multielement transducers is straightforward, following the procedure outlined here for a single element. The procedure utilizes some aspects of both the TT and TL models. Reference 2 is required for following the analysis presented here.

6.4.1 MSW POWER WITH SPATIALLY VARYING CURRENT

The first step in developing the algorithm to calculate MSW power when drive current is spatially varying along the length of the transducer, which is the same as the aperture, is to modify the MSW power expression given by Eq. (12) in Reference 2. It is given in this report by Eq. (7-23) or Eq. (6-19).

The real average power going into MSW is now a function of z . We can write,

$$P_{msw}(s) = (1/2)R_1(s) \int |J_z(k)|^2 dz , \quad (6-36)$$

where now $J_z(k)$ varies with z . $R_1(s)$ is, as before, dependent on parameters of the propagation medium and ground plane (if any) spacing, only. $J_z(k)$ is a function of strip current along z as well as transducer parameters. See also page 46 in Reference 2 for specific parameters.

In particular,

$$J_z(k) = I(z)W(a,k) , \quad (6-37)$$

where $I(z)$ is the current along the transducer coupling line, and $W(a,k)$ is a normalized Fourier transform, in the x direction, of the current distribution. For example, for a single strip carrying a flat current distribution along its width,

$$W(a,k) = [\sin(ak/2)]/(ak/2) .$$

Substitution of Eq. (6-37) into Eq. (6-36) leads to,

$$P_{msw}(s) = (1/2)R_1(s) |W(a,k)|^2 \int_{z_1}^{z_2} |I(z)|^2 dz \quad (6-38)$$

Eq. (6-38) is the average real power going into MSW, propagating in one direction, for a transducer length equal to $z_2 - z_1$.

The next step in the algorithm is to relate $I(z)$ to a generalized transmission line.

6.4.2 GENERAL TRANSMISSION LINE FOR TT/TL

Consider a transmission line with characteristic impedance Z_T and propagation constant, γ_T , connected through a lossless line to load Z_L . The circuit is driven by a voltage source V_S . See Figure 6-9. This figure represents an input transducer, with associated strip line circuit. The line between $z = -z_1$ and $-z_2$ represents the transducer coupling structure and YIG, while the line between $z = 0$ and $z = -z_1$ is an unloaded portion of strip line. A similar circuit with the source replaced by a load representing a receiver, would constitute an output transducer. Current $I(z)$ appearing in Eq. (6-38) is shown in the figure.

We need to relate $I(z)$ to voltage source V_S , along with all transmission line parameters, load and source impedance, R_o .

Using standard transmission line theory and the circuit shown in Figure 6-9, we can derive an expression for $I(z)$. See Appendix E for the derivation.

$$I(z) = I(-z_2)C(z) \quad (6-39)$$

where,

$$I(-z_2) = V_S / [R_o + Z(-z_2)] \quad (6-40)$$

and

$$C(z) = \{ \exp[-\gamma_T(z + l_1 + l_o)] \} \frac{1 - \Gamma_1 \exp[+2\gamma_T(z + l_o)]}{1 - \Gamma_1 \exp[-2\gamma_T(l_1)]} \quad (6-41)$$

INPUT TRANSDUCER AND STRIP LINE CIRCUIT

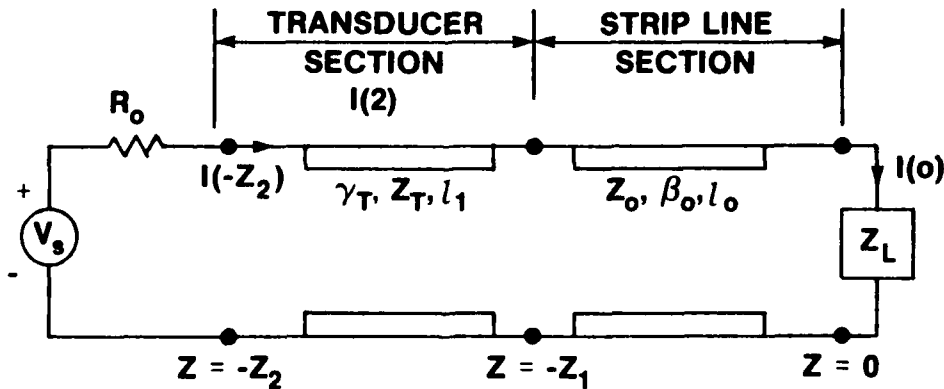


Figure 6-9. Equivalent Circuit for Combined TT/TL Model

where $z_2 = l_1 + l_0$

$$\left. \begin{aligned} Z(-z_2) &= Z_T \frac{[1 + \Gamma_1 \exp(-2\gamma_T l_1)]}{[1 - \Gamma_1 \exp(-2\gamma_T l_1)]} \\ Z(-z_1) &= Z_0 \frac{[1 + \Gamma_0 \exp(-j2\beta_0 l_0)]}{[1 - \Gamma_0 \exp(-j2\beta_0 l_0)]} \end{aligned} \right\} \quad (6-42)$$

and

$$\left. \begin{aligned} \Gamma_1 &= [Z(-z_1) - Z_T] / [Z(-z_1) + Z_T] \\ \Gamma_0 &= [Z_L - Z_0] / [Z_L + Z_0] \end{aligned} \right\} \quad (6-43)$$

We note that $C(-z_2) = 1$.

We can now define a new radiation resistance, $R_N(s)$, by following the development in Reference 2.

6.4.3 GENERALIZED RADIATION RESISTANCE

Following the development for radiation resistance for the TT model in Reference 2, we equate $P_{msw}(s)$ in Eq. (6-38) to $(1/2)R_N(s)|I(-z_2)|^2$, where $I(-z_2)$ is the current entering the transducer section, and $I(z)$ is given by Eq. (6-39). The result is

$$R_N(s) = R_1(s)[|W(a, k)|^2]Q \quad (6-44)$$

where

$$Q = \int_{z_1}^{z_2} |C(z)|^2 dz \quad (6-45)$$

$R_N(s)$ is the new radiation resistance for the TT model, which now handles current variations in the z direction. $R_N(s)$ replaces $R_m(s)$ in the TT model. Only the Q changes for different current variations.

Using the SUR program described in Chapter 3, a new version, SURN, of the program has been created to handle the case $l_0 = 0$, and Z_L real. Substitution of Eq. (6-41) into Eq. (6-45) with $l_0 = 0$, $Z_L = R_{load}$, $Z_T = Z_0$, $\gamma_T = \alpha + j\beta$ yields the following expression for Q .

$$Q = \frac{-\frac{1}{2\alpha}(1 - e^{2\alpha l_1}) + \frac{\Gamma_0^2}{2\alpha}(1 - e^{-2\alpha l_1}) - \frac{\Gamma_0}{\beta} \sin(2\beta l_1)}{e^{2\alpha l_1} + \Gamma_0^2 e^{-2\alpha l_1} - 2\Gamma_0 \cos(2\beta l_1)} \quad (6-46)$$

where

$$\Gamma_0 = [R_{load} - Z_0] / [R_{load} + Z_0]$$

The one remaining step in the algorithm is to relate the parameters α , β , and Z_0 to physical parameters of the strip lines. For example, in the SURN program, we let Z_0 equal the characteristic impedance of an unperturbed microstrip line, and equate $\gamma_T = \alpha + j\beta$ to the propagation constants of the microstrip model as derived in Reference 2. Then, the calculation of radiation resistance and insertion loss proceeds as in the TT model, exactly.

It has been found that the TT, TL, and the above hybrid TT/TL model are in excellent agreement with respect to calculation of insertion loss, over a wide range of parameters, with one exception. That is, passband frequencies, bandwidths, and occurrence of nulls in the passband, are consistent for the three models. When liftoff parameter G is varied, however, significant differences occur in the predictions of the models. This reflects the fact that the models differ fundamentally in how they model connections to generators and receivers. Liftoff experiments should prove useful for developing more sophisticated models.

References

1. Sethares, J.C., Frost, H.M., and Szabo, T.L. (1977) Fields of a Flat Conductor EM/SAW Transducer, *IEEE Trans. Sonics and Ultrason.* **SU/24**, (No. 2):88-94.
2. Sethares, J.C. and Weinberg, I.J. (1985) Theory of MSW Transducers, *Circuits, Systems and Signal Processing* **4**, (No. 1, 2):41-62.
3. Wu, H.J., Smith, C.V. Jr., Collins, J.H., and Owens, J.M. (1977) Band Pass Filtering with Multibar MSSW Microstrip Transducers, *Electronics Letters* **13**, (No. 20).

7. SUMMARY AND REVIEW OF SELECTED MSW PUBLICATIONS

From the late 1960s to the early 1970s when basic MSW phenomena were under investigation, fine wire couplers were often used for generating and detecting MSW. There was no theory then for predicting insertion loss as a function of frequency and transducer parameters, so the phenomena was unattractive from a device point of view, both because of practical problems associated with fine wire structures, and because of the lack of a suitable theory.

Then in 1975 Ganguly and Webb¹ derived an expression for radiation resistance of an MSW transducer made up of a length of microstrip line. This work provided a basis for extending the theory to more complicated transducers and developing more sophisticated transducer models.

Several extensions of the theory were then made.^{2,3,4} These extensions to transducer theory rely to a large extent on concepts and ideas generated in acoustic wave transducer theory. This has been both a help and a hindrance. It has been helpful because acoustic transducer theory with its MSW analog works well for predicting fundamental and space harmonic transducer responses. It has been a hindrance because theoretical problems peculiar to MSW transducer theory have been neglected, partially because of the success of acoustic analog theories in providing a first order theory adequate for many MSW investigations.

These problems include: MSW beam steering and focusing due to crystalline anisotropy; nonreciprocity; and especially the presence of long wavelengths in the MSW pass band. A transducer theory for long MSW wavelengths is particularly desirable because of the low insertion loss associated with this portion of the band.

Publications selected for review here are based on their relevance to the MSW computer programs described in Chapter 3. These publications provide the physical basis for understanding the MSW transducer models and computer programs developed by the authors.

7.1 Low Loss Magnetostatic Waves

Work on MSW at RADC intensified in 1973 after Merry and Sethares demonstrated, for the first time, low loss MSSW up to 15 GHz. This work is reported in

Low Loss Magnetostatic Surface Waves at Frequencies up to 15 GHz by Merry and Sethares.⁵

-
1. Ganguly, A.K. and Webb, D.C. (1975) Microstrip Excitation of Magnetostatic Surface Waves: Theory and Experiment, *IEEE Trans. on Microwave Theory and Techniques*, **MTT-23** (No. 12): 988-1006.
 2. Wu, H.J., Smith, C.V., and Collins, J.H. (1977, Sept.) Bandpass filtering with multibar MSW microstrip transducer, *Electron. Lett.* **13** (No. 20):610-611.
 3. Emtage, P.R. (1978, Aug.) Interaction of magnetostatic waves with a current, *J. Appl. Phys.* **49**:4475-4484.
 4. Sethares, J.C. (1979, Nov.) Magnetostatic Surface Wave Transducers, *IEEE Trans. on MTT*, **MTT-7** (No 11):902-909.
 5. Merry, J.B. and Sethares, J.C. (1973, Sept.) Low Loss Magnetostatic Surface Waves at Frequencies up to 15 GHz, *IEEE Trans. on Magnetics*, **9** (No. 3):527-529.

Merry and Sethares published data on the attenuation of MSSWs versus frequency from 4 to 15 GHz and the effect of surface polish upon that attenuation. Previous workers reported the observation of MSSWs on thick slabs of YIG at frequencies below 4 GHz and on thin films below 3 GHz.

For the thin films and most slabs the losses were about 100 dB/ μ sec; in one case lower losses (54 dB/ μ sec) in slabs at 4 GHz were obtained by chemically polishing the surfaces with hot phosphoric acid.⁶

Merry and Sethares employed a different polishing technique, using a silica gel, Syton, which reduced the losses by more than 20 dB, allowing 15 GHz MSSW to be observed. It was found that half the observed loss was due to removable volume pits, so that further significant reductions could be made. They also demonstrated that MSW losses increase linearly with frequency as opposed to SAW, whose losses increase as the square of frequency. This motivated several organizations to initiate MSW research efforts.

Over the next three years, at AFCRL and later RADC, several MSW investigations were completed in the area of delay lines^{7,8,9} interferometers^{10,11} magnetic anisotropy¹² and band stop and band pass filters^{13,14} using LPE/YIG. This led to an increased awareness of potential MSW applications. Publications that do not deal specifically with MSW transducers are not summarized or reviewed here.

7.2 Electromagnetic Transducers for Ultrasonic Waves

In parallel with the above MSW work, an unrelated effort was underway to study electromagnetic transducers (EMT). EMTs are used to generate and detect MHz ultrasonic waves in metals via a current-produced Lorentz force. It turned out that several concepts developed for EMT transducers were adaptable to MSW transducers.

-
6. Adam, J.D., Bennett, G.A., and Wilkinson, J. (1970) Experimental observation of magnetostatic modes in a YIG slab, *Electron Lett.* **6**:434.
 7. Sethares, J.C. and Merry, J.B. (1974, Feb.) *Magnetostatic Surface Waves in Ferrimagnets Above 4 GHz*, AFCRL-TR-74-0112, Physical Sciences Research Paper, No. 587, AD780640.
 8. Sethares, J.C. and Stiglitz, M.R. (1974, Sept.) Propagation Loss and MSSW Delay Lines, *IEEE Trans. on Magnetics*, **MAG-10** (No. 3):787-790.
 9. Sethares, J.C. and Stiglitz, M.R. (1974) Magnetostatic Surface Wave Delay Lines, IEEE Catalog No. 74CH0838-3 MTT, Lib. of Congress No. 72-75863, pp 253-255.
 10. Newburgh, R.G., Blacksmith, P., Budreau, A.J. and Sethares, J.C. (1974, Dec.) Acoustic and Magnetic Surface Wave Ring Interferometers for Rotation Rate Sensing, *Proc. of the IEEE*, **62** (No 12):1621-1628.
 11. Newburgh, R.G., Blacksmith, P., and Sethares, J.C. (1975, Sept.) United States Patent No. 3,909,710.
 12. Sethares, J.C. and Tsai, T. (1977, Sept.) Magnetic Anisotropy of (111) LPE/YIG Films on GGG in Parallel Resonance, *IEEE Trans. on Magnetics*, **MAG-13** (No. 5):1236-1237.
 13. Tsai, T.L. and Sethares, J.C. Bandpass Filter Using LPE/YIG Films, Appendix D, unpublished note.
 14. Tsai, T.L. and Sethares, J.C. (1977) Band Stop Filter Using LPE/YIG Films, *IEEE MTT-S*, Cat. No. 77CH1219 S, pp 526-527.

The EMT theory and concepts adaptable to MSW are described in References 15,16,17,18, and 19. Here we discuss those aspects of the papers that can be adapted to MSW.

The Flat Conductor Electromagnetic SAW Transducer: Theory and Experiment by Frost, Szabo and Sethares¹⁵

Flat conductor meander line and grating configurations were fabricated using photolithographic and thin film technologies and by multiconductor flexible cables. Thompson's model²⁰ for the wirewound EMT was adapted for this flat conductor model.

The magnetic field component in the plane of the flat conductor was calculated from magnetostatic theory. This field was then used in the Lorentz force calculation. The flat conductor model is based on equations for the magnetic fields from a flat ribbon conductor meander line above a ground plane.

Multiple conductor proximity effects, and the dependence of the fields on the strip/width spacing ratio and liftoff separation are included. Expressions are derived for Lorentz force transduction efficiency and for a circuit model including acoustic radiation resistance and reactance near resonance, and transducer inductance.

Experimental measurements of transducer characteristics for both wirewound and flat conductor types are presented. Meander line configurations are shown to have a $(\sin x/x)$ squared frequency response similar to the interdigital transducer.

This paper¹⁵ and the following¹⁶ are abbreviated versions of the analysis presented in References 17, 18 and 19. There are no analytical results included in References 15 or 16. Their main contribution was to show that theory and experiment are in good agreement. They also introduced the procedure for calculating radiation resistance, reactance, and transmission efficiency expressions for the flat conductor EMT.

Harmonic Operation of SAW Electromagnetic Transducers by Szabo and Sethares¹⁶

The main contribution of this paper is that a new equivalent circuit model, based on a description of dynamic RF fields surrounding transducer conductors in which current distributions

-
15. Frost, H.M., Szabo, T.L., and Sethares, J.C. (1975) The Flat Conductor Electromagnetic SAW Transducer: Theory and Experiment, IEEE Cat. No. 75CH0994-4SU, *Ultrasonics Symposium Proc.*, pp 601-603.
 16. Szabo, T.L. and Sethares, J.C. (1977) Harmonic Operation of SAW Electromagnetic Transducers, IEEE Cat No. 77 CH1264-1SU, *Ultrasonics Symposium Proc.*
 17. Sethares, J.C., Frost, H.M., and Szabo, T.L. (1977, Mar.) Fields of Flat Conductor Electromagnetic Surface Acoustic Wave Transducers, *IEEE Trans. on Sonics and Ultrasonics*, **SU-24** (No. 2):88-94.
 18. Szabo, T.L., Frost, H.M., and Sethares, J.C., (1977, Nov.) Periodic Surface Acoustic Wave Electromagnetic Transducers, *IEEE Trans. on Sonics and Ultrasonics*, **SU-24** (No. 6):393-406.
 19. Sethares, J.C. and Szabo, T.L. (1978, Mar.) A new model for the flat conductor electromagnetic SAW transducer, *Journal of Appl. Phys.* **49** (No. 3):1054-1060.
 20. Thompson, R.B. (1973) A Model for the Electromagnetic Generation and Detection of Rayleigh and Lamb Waves, *IEEE Trans. on Sonics & Ultrasonics*, **SU-20**:340-346.

are allowed to vary, is presented. The new results, while in agreement for fundamental frequency operation with earlier flat current theory, differ from earlier theory in harmonic prediction. Experiments were carried out to the seventh harmonic and experimental data favors the nonuniform current distribution model.

Previous models for SAW electromagnetic transducers, EMTs, were based on the assumption of a uniform current distribution of the form $K = I/S$ where I is total current and S is strip width. The flat current produced a flat field distribution of the field component parallel to the strip plane. The nonuniform current distribution model removes the uniformity requirement and requires only that the total integrated current over the strip width be equal to total current I , leaving the functional form of the surface current as an unknown to be determined.

Dynamic magnetic fields are calculated using magnetostatic theory with fields expressed in Legendre polynomials. Transducer current is found to peak at the strip edges, especially when the transducer is near a ground plane. As the transducer is moved away from the ground plane, the field distribution component parallel to the strip surface becomes sinusoidal. This is similar to the behavior of flat current theory. For weak coupling, the flat current distribution model is quite accurate, which also turns out to be true for MSW transducers.

The following three papers,^{17,18,19} contain all of the EMT theory and concepts that are later adapted to MSW. The first¹⁷ calculates the magnetic fields surrounding an array of parallel current carrying conductors in terms of spatial harmonics. It is, in essence, a spatial Fourier analysis.

Field of Flat Conductor Electromagnetic Surface Acoustic Wave Transducers by Sethares, Frost and Szabo¹⁷

Expressions for the dynamic, or RF, magnetic fields surrounding grating and meander line array EMTs are derived in terms of transducer dimensions, current, and liftoff from a ground plane. Current in the transducer strips is assumed to be spatially uniform. The analytical form of these field solutions permits a detailed quantitative evaluation of the harmonic content of the fields, a major factor in determining transducer efficiency.

Unlike interdigital transducers, the spatial harmonic amplitudes are shown to increase with decreasing s/b , strip width to center-to-center spacing, ratio. In addition, the solutions are used to calculate electrical inductance of the transducers from energy stored in the magnetic field, as a function of liftoff. Calculated inductance values are in excellent agreement with measured values.

This analytical description of the magnetic fields provides the fundamental information necessary for a comprehensive understanding of both the electrical and acoustical properties of these transducers.

Periodic Surface Acoustic Wave Electromagnetic Transducers by Szabo, Frost and Sethares¹⁸

In this paper, a normal mode model is presented for a meander line flat current transducer; from calculation of the dynamic magnetic fields to expressions of transducer efficiency. Also, the EMT acoustic radiation resistance and reactance are shown to be skewed somewhat differently from the unskewed characteristics previously published for interdigital transducers.

New measurements for transducer inductance and eddy current resistance and for the frequency dependence of transducer insertion loss are compared with both old and new theories. By accounting

for electrical EMT properties in an equivalent circuit, it is demonstrated, both theoretically and experimentally, that substantial reductions in insertion loss can be realized by matching techniques.

The transducer analyzed consists of an array of flat conductors of width S , spaced periodically at intervals p , and placed a distance G above a metal ground plane. A current I courses through conductors connected in series for the meander line. A second configuration, the grating geometry, consists of a similar array except that all conductors are connected in parallel.

The current I through these conductors causes dynamic magnetic fields to form around each conductor. These fields are affected by adjacent conductors and the metal ground plane. An expression for these fields was derived in Reference 17. It is reproduced here as Eq. (7-1), along with Eq. (7-2), which is an alternative form for the same expression.

$$H_{X\eta} = I \sum_{n=1}^{\infty} \frac{(1 + \eta \cos n\pi)}{p} \cos(n\pi X/p) \operatorname{sinc}(nS/2p) e^{-n\pi G/p} \quad (7-1)$$

$$H_X = \frac{I}{\pi S} \left\{ \arctan \left[\frac{2e^{-\pi G/p} \sin[(X + S/2)\pi/p]}{1 - e^{-2\pi G/p}} \right] + \arctan \left[\frac{2e^{-\pi G/p} \sin[(-X + S/2)\pi/p]}{1 - e^{-2\pi G/p}} \right] \right\} \quad (7-2)$$

These equations are included here because they also occur in MSW transducer theory. They represent one of the near field components of an MSW transducer. The expression is the most fundamental concept in this paper because it serves as the starting point for obtaining both the acoustical and electrical transducer characteristics.

Using the expression for H_X and the Lorentz force acting on a current element, one can arrive at a radiation resistance. This is done using a normal mode analysis. Then, using a Hilbert transform, the radiation reactance is obtained.

An equation for transducer inductance, as obtained in Reference 17 for infinite conductivity, is then modified as a result of conductor loss, and a new expression that correlates well with experiment is obtained for inductance.

Insertion loss expressions are also derived using an electrical equivalent circuit. EMT transducers are generally operated near synchronism so that the analysis is restricted to a normal mode approach.

The model developed is in excellent agreement with measurements over the transducer passband. The parallel between EMTs and IDTs became evident with this work. This led to borrowing, from IDT theory, apodization theory for EMTs. This apodization theory is based on a normal mode analysis valid near synchronism.

Characterization of the electrical properties of the transducer led to significant improvements in transducer efficiency through matching networks, and the ideas carry over into MSW theory, though the equations are quite different.

A New Model for the Flat Conductor Electromagnetic SAW Transducer by Sethares and Szabo¹⁹

Previous models assumed the current distribution in each transducer conductor is uniform. This paper presents solutions for the dynamic magnetic fields surrounding an array of flat conductors

above a ground plane in which the current distribution is allowed to vary.

Resulting solutions are used to calculate new space harmonic curves and to derive a new transducer model including electrical inductance, eddy current resistance, acoustic impedance, and transducer efficiency. A direct analogy to the interdigital transducer is established. For fundamental frequency operation the new model is nearly equivalent to previous flat field models, provided the conductor width/spacing ratio is 1/2 or less.

For harmonic transducer operation, the present analysis is substantially different from other models and it matches data more accurately. A method for measuring the individual insertion loss of dissimilar transducers in a lossy medium is presented.

Even though earlier models for surface acoustic wave electromagnetic transducers, EMTs, using uniform current distribution, work well for characterizing EMT operation at the fundamental frequency, synchronism, they are unable to predict transducer behavior accurately at harmonic frequencies.

The basic idea in the development of the new model was to obtain a solution for dynamic magnetic fields of a meander line without a priori assumptions about current distribution. The complete analysis, showing how magnetic field solutions are expressible in terms of Legendre polynomials, is presented. These solutions are similar in form to solutions for the potential and electric charge on an interdigital metal array on a dielectric. Results are shown to be analogous to Engan's²¹ solutions and that they are related to his solutions by a simple substitution.

A magnetic potential is defined, then boundary conditions are imposed and solutions are sought which satisfy all assumptions, equations of motion and boundaries. The solutions are then written in terms of spatial harmonics. Inductance is then calculated by calculating the energy stored in the magnetic field; and radiation resistance and reactance are then determined. Experiments were performed that showed that the nonuniform current distribution produced a more accurate model than the flat current distribution, for higher spatial harmonics. For fundamental frequency operation there is essentially no difference in the two models.

When it became evident that a good portion of EMT theory along with SAW IDT analysis could be adapted to MSW, an effort was initiated to develop a general MSW transducer theory including the analysis and development of computer programs. It was realized, at the outset, that there are fundamental differences that would have to be addressed, but that there were no fundamental stumbling blocks. It would be complicated by the dispersive nature of MSW, as opposed to SAW and EMT theory, which are based on nondispersive waves. In addition, the crystalline and DC magnetic field-induced anisotropies would significantly add to the complexity.

It was also realized that there are three pure MSW modes, where group and phase velocities are collinear, and that YIG is crystallographically a cubic crystal with relatively small anisotropy constants. These fortunate circumstances made the task possible within a reasonable amount of time.

21. Engan, H. (1969) Excitation of Elastic Surface Waves by Spatial Harmonics of Interdigital Transducers, *IEEE Trans. on Electron Devices*, **ED-16**:1014.

7.3 MSW Transducers

The following papers (References 4, 22 - 32) develop the basic MSW theory for the computer programs described in Chapter 3. Important formulas, which are programmed, are listed here and explained. The original references cited below should be consulted for further details.

Periodic Magnetostatic Surface Wave Transducers by Sethares, Tsai and Koltunov²²

Reference 22 is the basic report for the multielement MSW transducer modeling presented in the present report. Reference 22 extends the basic work of Ganguly and Webb,¹ who analyzed MSSW interactions with a single conducting strip carrying a uniform current above a YIG surface. They developed an expression for MSSW radiation resistance and microstrip input resistance, when the excitation current is the center conductor of an electrically short grounded microstrip line. This paper and a subsequent one of theirs³³ in which a radiation reactance is obtained from a Hilbert transform of radiation resistance, form the basic foundation for extensions to multielement transducers.

Here, the Ganguly and Webb theory is extended to multielement transducers. Included in the analysis are infinite and finite length, periodic and nonperiodic structures, and radiation resistance, for independent electrodes, as well as interacting electrodes when they are in an infinite array.

-
22. Sethares, J.C., Tsai, T., and Koltunov, I. (1978, Apr.) *Periodic Magnetostatic Surface Wave Transducers*, RADC-TR-78-78, ADA057214.
 23. Sethares, J.C. (1978, Jun.) Magnetostatic Surface Wave Transducer Design, IEEE International Microwave Theory and Techniques Symposium, Ottawa, Canada, published in *IEEE MTT Symposium Digest*.
 24. Sethares, J.C. and Weinberg, I.J. (1979, Mar.) Apodization of variable coupling MSSW transducers, *J. of Appl. Phys.* **50** (No. 3):2458-2460.
 25. Weinberg, I.J. and Sethares, J.C. (1978, Sept.) *Magnetostatic Wave Transducers With Variable Coupling*, RADC-TR-78-205, ADA063880.
 26. Sethares, J.C. and Weinberg, I.J. (1979, Jul.) Insertion Loss of Apodized/Weighted and Nonuniform Magnetostatic Surface Wave, MSSW, Transducers, 1979 International MMM Conference, New York City, Paper 6C-8.
 27. Sethares, J.C. (1983, Jan.) Magnetostatic Wave Transducers, 1981 RADC Microwave Magnetics Technology Workshop, June 10-11, 1981, published in RADC-TR-83-15, ADA126417, In House Report, *Proc. of the 1981 RADC Microwave Magnetics Technology Workshop*, pp 118-132.
 28. Sethares, J.C. and Cohen, E. (1982, Nov.) Current Distribution on Gratings and Meander Lines: with MSW Applications, ADA126042, *IEEE Trans. on Magnetics*, **MAG-18** (No. 6):1613-1615.
 29. Cohen, E. and Sethares, J.C. (1986) MSSW Back Reaction on a Generating Current Strip, *Journal of Magnetism and Magnetic Materials*, Elsevier Science Publishers B.V., **54-57**:1189-1190.
 30. Weinberg, I.J. and Sethares, J.C. (1983) Magnetostatic Volume Waves, *IEEE MTT-S Digest*, pp 253-255.
 31. Weinberg, I.J. and Sethares, J.C. (1984, April) Magnetostatic Forward Volume Wave Propagation - Finite Width, *IEEE Trans. on MTT*, **32** (No. 6):463-464.
 32. Sethares, J.C. and Weinberg, I.J. (1985) Theory of MSW Transducers, *Circuits, Systems and Signal Processing*, **4** (No 1-2):41-62.
 33. Ganguly, A.K., Webb, D.C., and Banks, C. (1978) Complex radiation impedance of microstrip excited magnetostatic surface waves, *IEEE Trans. on MTT*, pp 444-447.

MSSW, magnetostatic surface waves, have only three nonzero RF components. For propagation in the x direction and with biasing field in the z direction, MSSW amplitudes are functions of y. The waves are straight crested with the crests parallel to z; and phase and group velocities are parallel and in the same direction. The nonzero RF field components are E_z , H_x , and H_y . MSSW are pure TE modes, and have only the one E field component which is parallel to the transducer length, thus forcing current through the transducer strip. The Poynting's vector is given by $(1/2)E_z H_y^*$ which is x directed.

Boundary conditions are: continuity of tangential E and H across an interface; vanishing of normal B at a metal boundary; and discontinuity of H across a current sheet (transducer current).

The magnetostatic approximation sets limitations on possible MSW wavelengths. In the MSW limit, MSW wavelengths are much smaller than electromagnetic wavelengths in regions of dielectric constant ϵ . This statement is equivalent to Eq. (7-3).

$$K_s \gg 2\pi f \sqrt{\epsilon_r} / C \quad (7-3)$$

The right hand side of Eq. (7-3) is equal to the electromagnetic wavenumber in a region of dielectric constant ϵ . For a frequency of 3 GHz and $\epsilon_r = 10$, the EM wavelength is about π centimeters. This means MSW wavelengths of up to a few thousand microns satisfy the inequality of Eq. (7-3) very well. Practical MSW wavelengths are on the order of hundreds of microns and so the MSW approximation is well satisfied in practice.

Equations which are developed in this report²² and which appear in the MSW programs are described in the next few paragraphs.

Solutions for the RF field components and the dispersion relations are adequately described in Chapter 2 of the present report. They are the result of solving an electromagnetic boundary value problem in the presence of a material characterized by the Polder permeability tensor.

The dispersion relation is a transcendental equation and for its solution use is made of limiting values for making an initial guess. The frequency range of interest is first determined by letting K, the wavenumber, take on the values zero and infinity. These two limiting values determine the maximum theoretical bandwidth over which physically meaningful solutions will be found. For the dispersion relation calculation, frequency is incremented, and K calculated. An initial guess is first made assuming $K = 0$. Then a table is generated giving the calculated values of K for a given frequency. The $K = 0$ solution can be solved in closed form for any of the three pure MSW modes. It is important to use this fact because the frequency versus K equations have many other solutions, including complex ones, which have no practical utility, at least at the present time. Once the table of frequency and K number pairs is generated, all other quantities can be calculated.

The basic idea in developing transducer models proceeds as follows. The power carried by an MSW away from the excitation transducer is calculated from the Poynting vector. It is shown in the report²² that all field components are proportional to the Fourier transform of the transducer current distribution. Electromagnetic power is proportional to the magnitude of the Fourier transform squared. In all MSW equations and programs described in the present report, the Fourier Transform is normalized as in Eq. (7-4).

$$\tilde{J}(k) = \int_{-\infty}^{\infty} J(x) \exp(ikx) dx \quad (7-4)$$

$J(x)$ is the transducer surface current density, (amps/m). Current flows in the z direction along the strip length.

7.3.1 INDEPENDENT CONDUCTOR MODEL

Total power radiated from a transducer, as calculated from the Poynting's vector, can be equated to $(1/2)RI^2$ for use in an equivalent circuit model. The R is identified as a transducer radiation resistance, and I the total current through the transducer. The total current will also appear in the Poynting vector calculation and will cancel in the final expression for radiation resistance. Therefore, the radiation resistance is independent of excitation current, as it should be.

For a grating transducer, strips are connected in parallel. The radiation resistance per unit distance along the strip length is,

$$R_m^{(S)} = \frac{R_o^{(S)}}{N^2} \left[\frac{\sin(ak_s/2)}{(ak_s/2)} \right]^2 \left[\frac{\sin(k_s p N/2)}{\sin(k_s p/2)} \right]^2 .$$

Here, N is the number of strips; the middle term which involves strip width a is an element factor; and the last term involving center-to-center strip spacing is an array factor.

Eq. (7-5) is the radiation resistance of a truncated infinite array grating transducer; that is, the current in all strips is the same with end effects neglected. The transducer is a section cut out of an infinite array.

For a meander line transducer with an even number of strips connected in series, the radiation resistance is given by Eq. (7-6).

$$R_m^{(S)} = R_o^{(S)} \left[\frac{\sin(ak_s/2)}{(ak_s/2)} \right]^2 \left[\frac{\sin(k_s p N/2)}{\cos(k_s p/2)} \right]^2 .$$

Again, the two bracketed terms are element and array factors, respectively. Note that the radiation resistance of the grating transducer is divided by a factor of N squared. The factor $R_o^{(S)}$ contains all other information including ground plane spacings, material properties such as saturation magnetization, and magnetic biasing field, as well as the length of the transducer.

7.3.2 NORMAL MODE ANALYSIS

By expressing the current distribution in terms of space harmonics that match transducer periodicity, we can analyze harmonic operation of MSW transducers. This is equivalent to a normal mode analysis. Toward this end, $J(x)$ in the uniform current model is expressed as

$$J(x) = \frac{2I_o}{p} \sum_{l'=1}^{\infty} \text{sinc} \left(\frac{l' a}{2p} \right) \left[\frac{1 + \eta \cos l' \pi}{2} \right] \cos(l' \pi x/p) . \quad (7-7)$$

Eq. (7-7) is a rectangular function equal to I_o and ηI_o on alternate conducting strips, respectively, and extends over all x values. Its fundamental period is p for $\eta = 1$ and $2p$ for $\eta = -1$. For a transducer made up of a large number of conducting strips within a distance W in the x direction, W approaches

Np , where p is the center-to-center spacing of the conducting strips. Further, only two terms in the infinite sum contribute to the total Fourier transform $J(k)$, one for each direction of propagation.

For a wave in one direction,

$$R_m^{(S)} = \frac{R_0^{(S)} N^2 (1 + \eta \cos l' \pi)}{[(1 - \eta) + (1 + \eta)N^2]} \operatorname{sinc}^2 \left(\frac{l' a}{2p} \right) \operatorname{sinc}^2 \left[\left(k_s - \frac{l' \pi}{p} \right) \frac{Np}{2\pi} \right] \quad (7-8)$$

Equation (7-8) gives the radiation resistance for each normal mode, l' , of the system, $K_0 = l' \pi / p$. For a grating, $\eta = 1$, and for a meander line $\eta = -1$.

From previous work²², it is known that all field component amplitudes are proportional to $\tilde{J}(k)$. Further, at synchronism, K_s is approximately equal to $l' \pi / p$; consequently $\tilde{J}(k)$ reduces to

$$\tilde{J}(k) \equiv i N I_0 \left(\frac{1 + \eta \cos n \pi}{2} \right) \operatorname{sinc} \left(\frac{na}{2p} \right) \operatorname{sinc} \left[\left(k - \frac{n \pi}{p} \right) \frac{Np}{2\pi} \right] \quad (7-9)$$

for the uniform current distribution model. The normalized space harmonic amplitudes are simply the magnitude of the Fourier transform normalized to $I_0 N$.

Uniform current distributions are not realistic for good conductors. Considering only current distribution for interacting strips in an infinite array meander line, a more realistic current distribution that peaks at the strip edges is found. This nonuniform current distribution is expressible in terms of Legendre polynomials and complete elliptic integrals of the first kind. The resulting harmonic amplitudes are given in Eq. (7-10),

$$\bar{A}_{2m+1} = \frac{\pi}{2} \frac{P_m(\cos \pi a / p)}{K \left[\sin \left(\frac{\pi a}{2p} \right) \right]} \operatorname{sinc} \left[\left(k - (2m + 1) \pi / p \right) \frac{Np}{2\pi} \right] \quad (7-10)$$

Eq. (7-10) applies only to a meander line. Attempts to obtain an analogous expression for a grating transducer using Legendre polynomial and elliptic function solutions, to express a nonuniform current distribution, were unsuccessful. In Eq. (7-10), $P_m[\cos(\pi a / p)]$ are Legendre polynomials with argument $\cos(\pi a / p)$, and $K[\sin(\pi a / (2p))]$ complete elliptic integrals of the first kind with modulus $\sin(\pi a / (2p))$.

For fundamental frequency operation and $a/p < 1/2$, no significant differences exist between the two models. For harmonic operation, the two models are identical for a/p approaching zero; that is, very thin strips. When a/p approaches 1 there are considerable differences in the predictions of the two models.

To summarize this work, MSSW theory was extended to multiple and periodic conductors carrying more realistic nonuniform currents. In addition, a double ground plane structure is analyzed, and expressions are derived for radiation resistance and space harmonic amplitudes.

Magnetostatic Surface Wave Transducer Design by Sethares²³

In this paper further details are provided on the Fourier transform relation previously established between MSSW field amplitudes and transducer spatial current distribution, including: radiation resistance for periodic meander and grating transducers; spatial harmonic amplitudes; radiation resistance for uniform and nonuniform current distribution models; and radiation

resistance for apodized transducers. A quantitative relationship is established between radiation resistance for the independent conductor model and for the normal mode model.

7.3.3 GENERALIZED RADIATION RESISTANCE FOR UNIFORM CURRENT MODEL

With spatially uniform current I_0 flowing in each of N equally spaced transducer conducting strips, $\tilde{J}(k)$ can be evaluated in closed form and the radiation resistance, defined as

$$R_m^{(S)} = 2p^{(S)} / |I_t|^2 ,$$

can be put in the following form:

$$R_m^{(S)} = \left\{ \frac{2 R_1^{(S)} l_1}{(1 - \eta) + (1 + \eta)N^2} \right\} \left[\frac{\sin(ak_s/2)}{(ak_s/2)} \right]^2 \left| \frac{1 - \eta^N e^{ik_s p N}}{1 - \eta e^{ik_s p}} \right|^2 . \quad (7-11)$$

where $\eta = -1, +1$ for a meander and grating line transducer, respectively, and where $R_1^{(S)} l_1 = R_0^{(S)}$. For a grating, $I_t = NI_0$ and for a meander line $I_t = I_0$. Note that radiation resistance for meander and grating transducers differ by a factor of N^2 , as well as having different array factors. The two transducer types allow a wide impedance matching range capability for MSW transducers. Again, the second and third factors in Eq. (7-11) are element and array factors, respectively. For a given k number, or wavelength, the second term depends only on strip width and the last term on strip placement. $R_1^{(S)}$ is independent of transducer parameters and for $N = 1$ the single strip result is retrieved for either the meander or grating structures. Note that Eq. (7-11) will reduce to Eq. (7-5) when $\eta = 1$, and to Eq. (7-6) when $\eta = -1$ and N is even. Moreover, when $N = 1$ the array factor in Eq. (7-11) goes to 1 and $R_m^{(S)} = R_1^{(S)} l_1 [(\sin(ak/2))/(ak/2)]^2$ for either value of η as expected.

$R_0^{(S)}$ has been replaced by $R_1^{(S)} l_1$, where now $R_1^{(S)}$ is independent of transducer parameters and depends only on material properties of the propagation media and ground plane spacings.

7.3.4 GENERALIZED RADIATION RESISTANCE FOR NORMAL MODE MODEL

By expressing $J(x)$ in terms of space harmonics, again for the uniform current model, the integral for calculating the Fourier transform can be done in closed form to obtain a radiation resistance valid near any harmonic where K_s is near $n\pi/p$. The result of carrying out this integration is

$$R_m^{(S)} = \frac{R_1^{(S)} l_1 (1 + \eta \cos(n\pi)) N^2}{[(1 - \eta) + (1 + \eta) N^2]} \text{sinc}^2(na/2p) \text{sinc}^2 \left[(k_s - n\pi/p) \frac{pN}{2\pi} \right] . \quad (7-12)$$

If operation is at the fundamental, then Eqs. (7-11) and (7-12) give identical results. For the grating, $\eta = +1$, and $n = 2$, yielding $R_{mg} = R_1^{(S)} l_1 [\text{sinc}(a/p)]^2$. For the meander line, $\eta = -1$, and $n = 1$ and $R_{mm}^{(S)} = R_1^{(S)} l_1 N^2 [\text{sinc}(a/(2\pi))]^2$. Otherwise, for operation away from the fundamental, Eqs. (7-11) and (7-12) differ. Equation (7-11) is based on the superposition of field amplitudes generated by isolated, independent conducting strips. Eq. (7-12) is based on superposition of field amplitudes generated by identical but dependent strips of an infinite array.

7.3.5 SPACE HARMONICS FOR UNIFORM CURRENT DISTRIBUTION

With a uniform current distribution, spatial harmonic amplitude for the meander or grating transducer is given by Eq. (7-13). As noted previously, all field component amplitudes are proportional to $\tilde{J}(k)$. When $\tilde{J}(k)$ is evaluated near synchronism, $k = n\pi/p$, the normalized field amplitudes, defined as $A_n = |\tilde{J}(k)/(I_0 N)|$ is,

$$\bar{A}_n = \left(\frac{1 + \eta \cos n\pi}{2} \right) \text{sinc}(na/2p) \text{sinc} \left[(k - n\pi/p) \frac{Np}{2\pi} \right]. \quad (7-13)$$

A study of Eq. (7-13) shows that the fundamental is most efficiently generated or received with narrow transducers, with a/p approximately zero, but at the expense of high harmonic content.

Meander line transducers with wide conducting strips, with a/p close to unity, are slightly less efficient MSSW generators/receivers, but the harmonic content is lower than for narrow strips. Wide grating transducers are very inefficient for all harmonics. These conclusions are based on the uniform current model, which works well for narrow transducers. Narrow transducers have wide operating bandwidth, which is desirable for delay lines.

7.3.6 NONUNIFORM CURRENT DISTRIBUTION FOR A MEANDER LINE

Uniform current distribution is not realistic for good conductors, and moreover, the actual distribution is affected by current in adjacent strips. A more realistic current distribution is obtained by applying boundary conditions to perfect conductors, which results in current peaks at strip edges. It is shown in References 17 and 19 that current distribution in this case can be described by:

$$\frac{J_{LP}(x)}{J_{FF}} = \frac{\pi(a/p)}{\sqrt{2} \sqrt{\cos(2\pi x/p) - \cos(\pi a/p)} K \left[\sin \left(\frac{\pi a}{2p} \right) \right]}, \quad (7-14)$$

where $|x| < a/2$. Harmonic amplitudes for normal modes have already been given in Eq. (7-10), which can also be obtained from Eq. (7-13) by setting $\eta = -1$, replacing n by $2n + 1$ and using the substitution indicated in Eq. (7-15);

$\text{sinc}[(2n + 1)a/(2p)]$ is replaced by

$$(\pi/2) \{P_n[\cos(\pi a/p)]\} / K[\sin(\pi a/(2p))]. \quad (7-15)$$

These equations have not been programmed but are included here as they represent logical extensions and potential improvements to MSW models. In the above, subscript LP refers to Legendre Polynomial (nonuniform current distribution model) and FF to Flat Field (uniform current distribution model).

In general, space harmonic content is quite different for the two models, though for the fundamental the two do not differ significantly for $(a/p) < (1/2)$. At the strip center, $x = 0$, and for $(a/p) = (1/2)$, $J(LP)/J(FF) = 0.6$. This means that for $(a/p) < (1/2)$ fundamental strengths are of the same order of magnitude for both models. For a/p approximately zero, the two models are identical. The models differ significantly for $(a/p) > (1/2)$. For $(a/p) > (1/2)$ the models diverge for all harmonics. Again, the conclusion is that the uniform current model is accurate for narrow transducers.

For interdigital and electromagnetic acoustic transducers, LP theory is in better agreement with experiment than FF theory (References 19 and 16). It is not yet known if the same is true for MSW transducers, though it is expected that the nonuniform current is more accurate for MSW also.

7.3.7 GENERALIZED APODIZATION FOR RADIATION RESISTANCE FOR FF THEORY

By analogy with electromagnetic acoustic and interdigital transducer apodization theory,³⁴ the radiation resistance for normal mode apodized transducers with varying strip widths, separations, and lengths can be written:

$$R_m^{(S)} = R_1^{(S)} \left| \sum_{n=1}^N \text{sinc} \left[\frac{2a_n}{p_n(3-\eta)} \right] \text{sinc} \left[\left(\frac{k_s p_n}{2\pi} \right)^{-(3+\eta)/4} \right] \eta^n \sqrt{l_n} \exp(-i k_s n p_n) \right|^2. \quad (7-16)$$

In general there are N conducting strips each with different width a , center-to-center spacing p and length l . The relation between k_s and f , H , M , L and t_1 is given by the appropriate dispersion relation.

Apodization of Variable Coupling MSSW Transducers by Sethares and Weinberg²⁴

Here, apodization of radiation resistance is generalized to both normal mode and independent conductor models. In addition, a gap G is included in the equations to allow variable coupling between electromagnetic signals and MSW. Results are presented for three types of apodization: conducting strip length, width weighting, and variable periodicity. An independent strip and a truncated array model are considered. An application of the apodization is for tailored filters. Tailoring can be achieved by interaction of waves with apodized periodic structures placed in the propagation path, or with the transmitting or receiving transducers themselves. Here, the transducers are apodized.

The term apodization is used in a general sense to indicate any of three forms of transducer design. Length, width, and spacing apodization refer, respectively, to transducers whose electrodes have weighted length, width, and interelectrode spacing. Grating and meander lines are investigated. Transducers are allowed to be lifted off the surface by gap G . Each strip, or electrode, has width a , length l_1 , and center-to-center spacing between strips, p .

A general expression for radiation resistance of apodized transducers is given by Eq. (7-17). The previous apodization equation, Eq. (7-16) is a special case of Eq. (7-17)

$$R_m^{(S)} = \frac{R_1^{(S)}}{C(\eta, N)} \left| \sum_{n=1}^N U_n V_n \right|^2. \quad (7-17)$$

where

$$C(\eta, N) = ((1 - \eta) + (1 + \eta) N^2) / 2$$

34. Szabo, T.L. (1976) Advanced SAW electromagnetic transducer design, *Ultrasonics Symposium Proc. IEEE Cat 76 CH1120 5SU*.

and

$$U_n = \eta^n l_{1n}^{1/2} \exp(-iknp_n)$$

The parameter $\eta = +1$ for a grating and -1 for a meander line. The summation is from 1 to N , the number of individual conducting strips, $k(=2\pi/\lambda)$ is the magnetostatic wavenumber, l_{1n} the length of the n th strip and p_n the center-to-center spacing between conductors. For a transducer made up of non-interacting strips

$$V_n = \text{sinc}(a_n k / 2\pi) \quad (7-18)$$

with a_n the width of the n th conducting strip.

For the fundamental mode of a truncated infinite array transducer model,

$$V_n = \text{sinc}(2a_n/p_n(3 - \eta)) \text{sinc}(kp_n/2\pi - (3 + \eta)/4). \quad (7-19)$$

Eq. (7-17) has been experimentally verified by others for MSSW.³⁵ Although it was developed specifically for MSSW, it should apply equally well to MSFVWs and MSBVWs, but this has not been demonstrated experimentally. For a given k number, the quantities U_n and V_n are functions of transducer dimensions while $C(\eta, N)$ defines how individual strips are connected. The remaining term $R_1^{(S)}$, defined by Eq. (7-20), is a function of liftoff gap G , YIG parameters, and ground plane spacings t_1 and l . Its derivation is published in Reference 25.

$$R_1^{(S)} = \frac{\omega \mu_0 \exp(-2\beta k d)}{k^2 |F_T^{(1)}(k)|^2} |A_s| \quad (7-20)$$

where A_s and $F_T^{(1)}(k)$ are defined by Equations (106) and (76) in Reference 25. The quantity $\omega = 2\pi f$, is the radian frequency, μ_0 the permeability of free space, and d the YIG thickness.

Substituting A_s and $F_T^{(1)}$ into Eq. (7-20) and letting l and t_1 approach infinity yields the liftoff dependence when there are no ground planes.

$$R_1^{(S)} = |R_{10}^{(S)}| \exp(-2kG)$$

$$\text{where } R_{10}^{(S)} = \frac{\omega \mu_0 \mu_{22} T \exp(2\beta k d)}{2kd(\alpha_2 - 1)^2} \quad (7-21)$$

is independent of liftoff G . When $G = 0$, the radiation resistance for a single strip reduces to Ganguly and Webb's Eq. (45) in Reference 1. With no ground planes the functional dependence of radiation resistance on liftoff is seen to be $\exp(-2kG)$, or $\exp(-4\pi G/\text{wavelength})$, which is physically understandable from the way energy density decreases from the surface, and in agreement with Emtage, in Reference 3.

35. Ishak, W., Hewlett Packard, Palo Alto, CA, Private Communication.

7.3.8 VARIABLE COUPLING

Magnetostatic Wave Transducers with Variable Coupling by Weinberg and Sethares²⁵

The analysis presented in Reference 25 employs the magnetostatic approximation and introduces a magnetic potential at the outset. The procedure is useful for using the same analysis for MSFVWs and MSBVWs as well as MSSW. The physical geometry investigated consists of four regions with two of them separated by a thin periodic transducer that is lifted from a YIG slab by a gap, G . With $\text{curl } H = 0$ in all regions, including the YIG region, a magnetic potential function is defined such that the magnetic RF H field is the gradient of the potential function. All quantities of interest are assumed to be functionally constituted in the form,

$$f(x, y, t) = F(y) \exp(-iKx) \exp(i\omega t).$$

Suppressing the time dependence, t , the RF magnetic potential dependence in each region is assumed to be of the form,

$$\psi_j = [A_j \exp(a_j y) + B_j \exp(-a_j y)] \exp(-iKx),$$

where $j = 1, 2, 3, 4$. All a_j are positive real constants and all A_j and B_j are complex constants which are to be determined from the equations of motion and boundary conditions. RF H fields are expressed in terms of the magnetic potential. Following the analysis in Reference 22, while adding one new region between transducer and YIG surface, yields the sought-for solutions.

In this way variable coupling is analyzed. As in Reference 22, boundary conditions are applied which lead to a dispersion relation, followed by integration over all k to evaluate MSW fields. MSW power is calculated through the real part of the complex Poynting vector, and this is followed by integration of power density over the cross section. Total power is then equated to $(1/2)R|I|^2$ to yield a radiation resistance.

The report has a special section on reduced equations when there are no ground planes. This is useful for obtaining an understanding of the physics of the problem.

Radiation resistance, for the independent conductor and truncated array model, are then obtained. All equations reduce to those in Reference 22 when the gap is set equal to zero.

In summary, periodic magnetostatic surface wave transducer theory is extended to include variable coupling between MSSW and EM fields. Variable coupling was achieved by introducing a gap between YIG surface and transducer. The analysis is given in sufficient detail to allow one to follow the approach used and assumptions made, providing a basis for further extensions.

7.3.9 ASSUMPTIONS AND PHYSICAL BASIS FOR MULTIELEMENT TRANSDUCER MODELS

Magnetostatic Surface Wave Transducers by Sethares⁴

This was the first major publication on multielement MSW transducers. In this paper, a detailed quantitative relationship was established between the only two previous multielement MSW transducer publications, one a normal mode approach [Ertage] and the other a superposition of microstrip lines [Wu]. Reference 4 provided a solid base for future extensions of MSW transducer theory.

To summarize this paper: Magnetostatic surface wave transducer theory is extended and generalized. All important assumptions and restrictions are delineated. A Fourier transform relation is established between MSSW field amplitudes and transducer spatial current distribution. Expressions are developed for the radiation resistance of periodic meander and grating transducers, spatial harmonic amplitudes, and radiation resistance for uniform and nonuniform current distribution models. An expression is given for the radiation resistance of apodized transducers.

The transducer model presented here differs from others in that the present one does not contain microstrip parameters in the expression for radiation resistance. Ground planes are adequately accounted for through the dispersion relation.

All important restrictions and assumptions made in the analysis are listed below.

- 1) End effects caused by arrays of finite extent are neglected
- 2) MSW power is calculated in the far field region where the transducer has negligible effect on propagation modes.
- 3) The magnetostatic approximation $\text{curl } H = 0$ is employed.
- 4) Nonlinear effects are neglected.
- 5) A two dimensional problem with uniformity along the length of conduction strips is considered.
- 6) Good conductors are assumed and the thickness of conducting strips is assumed to be zero. A consequence of this assumption is discussed in Reference 4.

The dispersion relation with two ground planes, having one ground plane t_1 units above one YIG surface and the other l units below the other YIG surface is,

$$e^{-2\beta |k| d} = \frac{[\alpha_2 + \tanh(|k| l)] [\alpha_1 \coth(|k| t_1) + 1]}{[\alpha_1 + \tanh(|k| l)] [\alpha_1 \coth(|k| t_1) - 1]} \quad (7-22)$$

For a given frequency, the wavenumber is found from Eq. (7-22), which is the characteristic relationship between frequency and wavenumber for the unelectroded structure consisting of a YIG slab and two ground planes separated by dielectrics.

Eq. (7-22) must be solved numerically. When ground planes are removed, however, Eq. (7-22) can be solved for k exactly, for a given frequency and propagation direction. The computed k and corresponding frequency can then be used to calculate all field components. Field components are proportional to $J(k)$ which is the Fourier transform of an arbitrary impressed current distribution $J(x)$. This provides a general procedure for transducer analysis. For example, nonperiodic or periodic conducting strips may be driven with arbitrary current sources; then, an integration (that is, a Fourier transform) over the source distribution will yield transducer characteristics such as field components, radiation resistance and so forth.

Power is then calculated from the Poynting vector and it can be expressed in the form

$$P^{(S)} = (l_1/2) R_1^{(S)} |\tilde{J}(k)|^2 \quad (7-23)$$

The function $R_1^{(S)}$ is a function of YIG parameters and ground plane spacings, and it is independent of transducer parameters, while $\tilde{J}(k)$ is a spatial transform of transducer current distribution.

With spatially uniform current I_0 flowing in each of N equally spaced transducer conducting strips, $\tilde{J}(k)$ can be evaluated in closed form. Consider a transducer made up of N conducting strips each of width a carrying current I_0 . The Fourier transform of this current distribution is,

$$\tilde{J}(k) = (I_0/a) \sum_{n=1}^N (\eta)^{n+1} \int_{(n-1)p-a/2}^{(n-1)p+a/2} e^{ikx} dx \quad (7-24)$$

where the origin, $x = 0$, is placed at the center of the first strip. Eq. (7-24) can be reduced to the expression:

$$\tilde{J}(k) = I_0 \left[\frac{\sin(ka/2)}{(ak/2)} \right] \left\{ \frac{1 - \eta^N e^{ikpN}}{1 - \eta e^{ikp}} \right\} \quad (7-25)$$

Radiation resistance is defined by

$$R_m = 2P^{(S)} / |I_t|^2 \quad (7-26)$$

where

$$I_t = [(1 - \eta) + (1 + \eta)N] I_0 / 2 \quad (7-27)$$

Substitution of Eq. (7-23), (7-25), and (7-27) into (7-26) will yield Eq. (7-11). When ground planes are removed and Wu's Z_0 approaches zero and $[\sec(\beta l)]^2$ approaches unity, the two models are identical. This provides a connection between the two models, both of which agree well with experiment and differ only in second order effects. Radiation resistance reduces to Ganguly and Webb's results when $N = 1$, as it should.

By expressing the current distribution in terms of space harmonics that match transducer periodicity, space harmonic operation of MSSW transducers may be analyzed. See Eq. (7-7).

Because MSW spatial harmonics are closely spaced in frequency, the independent conductor model is more useful than the normal mode model for wide band, few strips, MSW transducers. When operation is away from the fundamental frequency the two radiation resistances are very different. One is based on the superposition of field amplitudes generated by isolated, independent conducting strips, and the other on the superposition of field amplitudes generated by identical but dependent strips of an infinite array. For operation near the fundamental, however, either is adequate. When the number of strips is large, the normal mode model is more accurate because it is based on an infinite array approximation.

This paper also provides a discussion of space harmonics for the normal mode model for both uniform and nonuniform current distributions and apodization for normal modes. Apodization for the independent conductor model is given in Reference 23.

7.3.10 INSERTION LOSS

The next paper²⁶ was the first reporting of our insertion loss expressions, and the first giving theoretical equations for apodized MSW transducers. We demonstrated that the predictions of our model and the microstrip model developed by Wu et al at the University of Texas were indistinguishable experimentally for practical MSW delay lines, even though they differed on a fundamental level. For example, the Wu model requires microstrip parameters to be incorporated

into the analysis. Our model does not require these additional input parameters. The reason for the agreement was eventually traced to the fact that the transducer frequency response is primarily dependent on geometrical parameters of the transducer which both models correctly account for. It is the variation of absolute value of insertion loss with coupling, between transducer and MSW, where significant differences in the two models are expected. Further work is still required on this problem, but it is a difficult one because the strong coupling case will have to be solved in order to adequately account for the coupling mechanism. This has not been done, at least it has not been published, as of December 1988.

Insertion Loss of Apodized Weighted and Nonuniform Magnetostatic Surface Wave (MSSW) Transducers by Sethares and Weinberg²⁶

An equivalent circuit model is presented from which insertion loss can be calculated. Included in the model are propagation loss, radiation resistance and reactance, transducer inductance, and variable coupling. Transducer fields are separated into near and far field components giving rise to transducer impedance and radiation impedance, respectively. Near fields are stationary in space and represent energy storage; while far fields represent energy radiated away from the transducer.

Previously, a general apodized equation for radiation resistance was obtained. Here an equivalent circuit model that can predict the insertion loss of apodized transducers is provided (see Figure 7-1). The model is made up of voltage source V , source resistance R_g , a two port electrical network that includes matching circuit elements and stray reactances, radiation resistances $R_m(+)$ and $R_m(-)$ for right and left going waves, and radiation reactance X_m , the Hilbert transform of $R_m = R_m(+) + R_m(-)$.

Radiation resistance is given by Eq. (7-17) which handles weighted transducers. The insertion loss for a pair of identical input and output transducers with series reactances X_e and X_o is

$$IL(+/-) = 20 \log\{[(R_g + R_m)^2 + (X_m + X_e + X_o)^2] / [4R_g R_m(+/-)]\} \quad (7-28)$$

This result is obtained from $-20 \log(TE)$ where TE is the transmission efficiency, defined as the ratio of power absorbed in $R_m(+/-)$ to the maximum power available from the voltage source of internal impedance R_g .

Reactance X_o , not shown in Figure 7-1, is found from transducer near fields. Reactance X_e includes series matching elements and stray inductances. The IL expression, Eq. (7-28), has the same form as the equation for IL obtained from the microstrip model. The two models differ in the way physical parameters enter the expression. In the microstrip model, for instance, radiation resistance and reactance contain a characteristic impedance and propagation constant of a microstrip line. These quantities do not appear in the radiation resistance and reactance of the present model. Ground planes are adequately accounted for in the dispersion relation.

Coupling between electromagnetic and magnetostatic waves is very strong and overcoupling can be a problem in band pass filtering where low sidelobes are required. Sidelobe levels can be reduced by decoupling electromagnetic and magnetostatic systems by lifting the transducer off the YIG surface; see for example Figure 4-9.

The effects of width weighting on insertion loss of a band pass filter are shown in Figure 7-2. Two weighting functions, in addition to no weighting, are illustrated in this figure. In Figure 7-2b the transducer has a wide element at its center and narrow ones at the ends. In Figure 7-2c the transducer

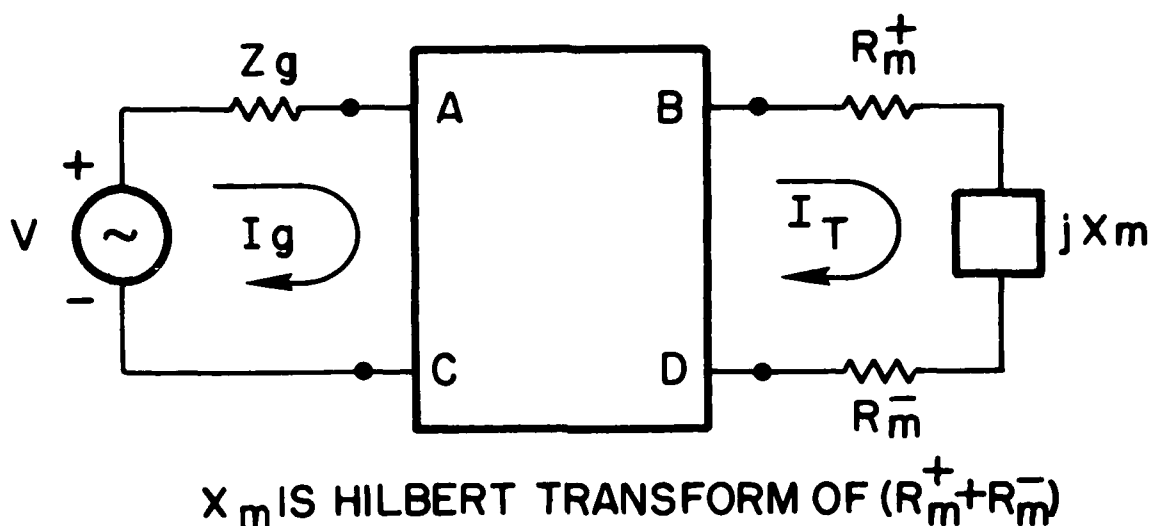


Figure 7-1. Equivalent Circuit Model for Two Terminal MSW Transducer Model

has wide elements at the ends and a narrow one at the center. Elements are not weighted in Figure 7-2a. The plots were obtained using Eq. (7-17) for the independent conducting strip model with $\eta = 1$ for a grating, $X_e = X_o = 0$, $R_g = 50$ ohms, $N = 15$, $p = 356 \mu\text{m}$, $H = 650$ oersteds, $t_1 = l = 254 \mu\text{m}$ and $l_1 = 1$ cm. For the uniform transducer, element width is $178 \mu\text{m}$. For the weighted transducers the widest element is $338 \mu\text{m}$ and the narrowest $58 \mu\text{m}$. Adjacent element widths differ by $40 \mu\text{m}$. Radiation resistance for this case reduces to:

$$R_m^{(\pm)} = \frac{R_1^{(\pm)} l_1}{N^2} \left| \sum_{n=1}^{15} e^{-i k n p} \frac{\sin(a_n k/2)}{(a_n k/2)} \right|^2 \quad (7-29)$$

which is used in Eq. (7-17) for calculating IL.

The weighting indicated in Figure 7-2b, a wide element in the center and narrow ones at the ends, produces a poor filter response. The width weighting indicated in Figure 7-2c produces near-in sidelobes about 35 dB down, thus showing promise as a weighting technique for multipole filters.

This work was reported at the MMM conference.²⁶ It was not published in the Proceedings of the Conference. The results are reported in subsequent papers.^{27,31}

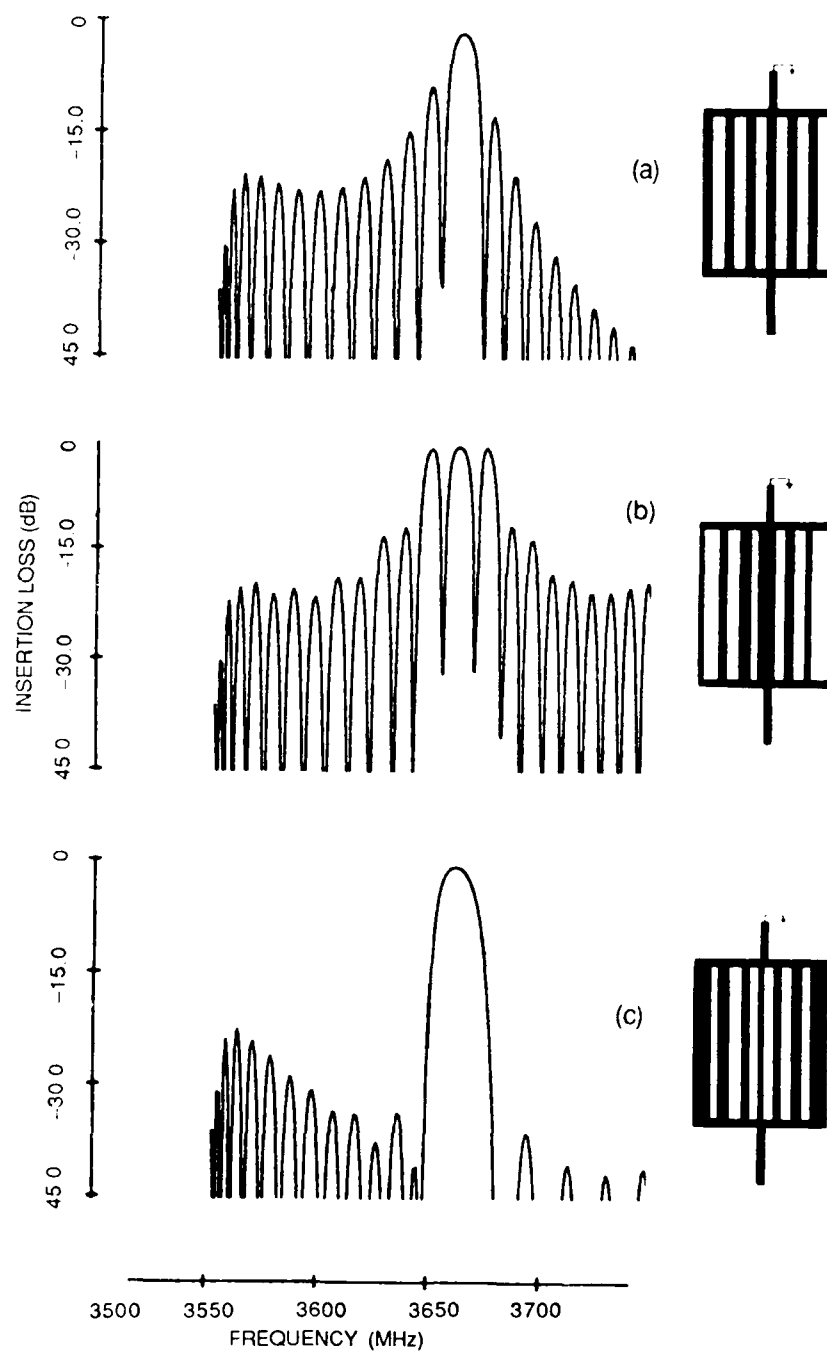


Figure 7-2. Width Weighting for a Pair of Identical MSSW Transducers in a Delay Line Configuration, Theoretical

7.3.11 GENERALIZED MSW ANALYSIS

Magnetostatic Wave Transducers by Sethares²⁷

This paper further develops IL theory, as well as a generalized approach to MSW transducer analysis which handles all three pure modes. A transducer theory for magnetostatic surface waves, MSSW, can be developed from a pure TE, transverse electric, mode analysis; however, the other two pure modes, magnetostatic forward and backward volume waves, are not TE or TM modes. Even so, the assumptions made still allow for considerable simplification.

Consider the coordinate system and geometry shown in Figure 1-4b. The assumptions of: uniformity in the z direction; the magnetostatic approximation; and transducer current flow only in the z direction; forces the z component of RF magnetic field over all space to vanish, that is $h_z = 0$, for all magnetostatic modes. This observation simplifies the analysis considerably; even though there are in general five nonzero electromagnetic field components. In addition, the power flow is proportional to $E_z H_y^*$ for all three modes.

Also, in solving the boundary value problem, electromagnetic field components can be separated into stationary near fields and radiating far fields. The near fields decay rapidly with distance in the x direction away from the transducer. All field components are known in terms of $J(k)$, which in our model is independent of YIG parameters. Fields are obtained by integrating over all k . And, all integrals have the same form, as follows: all complex field amplitudes are proportional to the integral over all k from minus to plus infinity of functions of the form $[J(k) Q(k, \omega)]/F(k, \omega)$, where $Q(k, \omega)$ only is different for each field component. $J(k)$ is the only term in the field expressions involving transducer geometry. It allows a variety of transducer structures to be handled by the same analysis. For instance, when current density, $J(x)$, is a uniform current sheet in a single strip of width a , that is, $J(x) = I_0/a$ for $(a/2) < |x|$, then $J(k) = I_0 [\sin(ak/2)]/(ak/2)$.

As shown by Ganguly and Webb,¹ the integration for field amplitudes splits naturally into two parts by writing $1/F(k, \omega) = [1 - F(k, \omega)/F(\infty, \omega)]/F(k, \omega) + 1/F(\infty, \omega)$. When this expression is put into the integral, there are two parts that must be integrated. The first part is integrated by contour integration to yield radiated fields. These radiated fields are guided waves that are attenuated by the material, as characterized by the magnetic line width, and by beam spreading. Integrating the second part directly, or numerically as is generally necessary, yields stationary fields that are concentrated near the transducer. The near fields give rise to an energy storage reactive element associated with the transducer structure. As a first approximation, this reactance may be neglected because it is small in comparison with radiation reactance. Inclusion of near field effects will give an improved but very complex model.

A Poynting vector is then formed from the far fields giving the power flow per unit width. From this, a radiation resistance per unit width is determined. Then, assuming causality, a Hilbert Transform of the total radiation resistance provides the radiation reactance. This reactance, associated with the far fields, is a significant portion of the radiation impedance and should not be neglected. The Hilbert transform, used for calculating X_m , is equal to $1/\pi$ times the integral over all ω' of the argument $R(\omega')/[\omega' - \omega]$. This is carried out numerically in the computer programs. No one has succeeded in deriving a closed form expression for MSW radiation reactance.

An equivalent circuit for a delay line, made up of an input and output transducer, and its insertion loss can now be obtained. In Figure 7-1, B and D are transducer terminals. A and C are output terminals of a microwave generator. All matching networks and connecting wire reactances

are included in network ABCD. Consider the case of no matching and short connecting leads. Then A and B terminals are connected as are C and D terminals. Insertion loss of a single transducer is defined as

$$IL = -10 \log(TE) \quad (7-30)$$

where TE is transmission efficiency given by Eq. (7-31).

$$TE = (\text{Power delivered to load})/(\text{Maximum power available}), \quad (7-31)$$

Power delivered to the load, in this case, is the total power carried by an MSW, say the positive wave, $(1/2)R_m(+)|I_t|^2$ where, from the circuit, $I_t = V/[R_m(+) + R_m(-) + R_g + iX_m]$. Maximum power available from the source V occurs when everything to the right of terminals A and C is replaced by a resistance R_g . The maximum available power is $(1/2)R_g|I|^2$ where $I = V/(2R_g)$.

When these expressions are substituted into Eqs. (7-30) and (7-31), insertion loss, IL, for one transducer is obtained. Assuming reciprocal coupling efficiency between electromagnetic system and MSW, the total IL for a pair of identical transducers is twice that given by Eq. (7-30). We find, for a transducer pair,

$$IL(+/-) = 20 \log\{[(R_g + R_m)^2 + X_m^2]/[4R_gR_m(+/-)]\} \quad (7-32)$$

This insertion loss is identical with S(21) in db, the transmission loss measured by commercial network analyzers. Propagation loss can be included by adding a term $76.4T_g \Delta H$ to Eq. (7-32) where T_g = group delay and ΔH is the full magnetic linewidth.

7.3.12 MODEL LIMITATIONS AND RANGE OF VALIDITY

In the following paragraphs we discuss certain aspects of single and multiple element transducers as they relate to experiment, and discuss the range of validity of the models. Figure 4-9 shows IL plots for two values of liftoff G. The frequency at the peak (minimum IL) near 3100 MHz corresponds to an MSW wavelength equal to the transducer periodicity, $p = 300 \mu\text{m}$; the second peak corresponds to the second spatial harmonic, and so forth. Insertion loss plots such as these are in reasonably good agreement with experiment. Minimum insertion loss for $G = 10 \mu\text{m}$ occurs at the fundamental frequency of the transducer, and a subsequent peak occurs at the next spatial harmonic. Both peaks occur within the MSW pass band, which extends from 2500 to 3400 MHz. Within this band a wide range of wavelengths are present. This is in marked contrast to acoustic wave transducers where spatial harmonics are widely separated in frequency. Moreover, in the MSW case, very long wavelengths are present at one end of the passband. As shown in the decoupled case, $G = 150 \mu\text{m}$, in Figure 4-9, the long wavelength limit response dominates the passband. It is this long wavelength limit where surface acoustic wave concepts are not applicable to MSW.

Figure 7-3 compares IL of three models for single strip transducer pair delay lines. Two of the curves use the theory presented here, with two different current distributions. The third is derived from a microstrip model.² Agreement between the models is seen to be quite good. The different current distributions are obtained from Eq. (7-33).

$$J(x) = \frac{(I_0/a)[\cosh(x/\bar{\delta})]}{[\sinh(a/2\bar{\delta})]/[a/(2\bar{\delta})]} \quad (7-33)$$

where $-(a/2) < x < (a/2)$, $x = 0$ is located at the conducting strip center, and $\bar{\delta} = \delta/(1 + i)$ with δ the strip skin depth defined by $\delta = 1/\sqrt{\pi f \mu \sigma}$. Eq. (7-33) represents a normalized current distribution where magnitude is minimum at the strip center and the strip edges at $x = (+/-)a/2$. In addition, the integral of current density over the strip width is equal to I_0 .

The two limiting cases of zero and infinite conductivity, σ , produce, respectively, a flat current distribution and a double impulse current distribution model. The flat current distribution is the one most commonly used. The curves in Figure 7-3 were obtained in the following way.

For the curve labeled "UNIFORM CURRENT DISTRIBUTION MODEL $R_{\text{loss}} = 35$ ohms", δ approaches infinity in Eq. (7-33) yielding $J(x) = I_0/a$ for $N = 1$. The transform $J(k) = I_0\{\sin(ka/2)\}/(ka/2)$ and $R_m^{(S)} = R_1^{(S)} \int_1^\infty \{[\sin(ka/2)]/[ka/2]\}^2$. This is the flat current radiation resistance using the TT model. R_{loss} was added to Eq. (7-32) by replacing $(R_g + R_m)$ with $[R_g + R_m + R_{\text{loss}}]$.

For the curve labeled "NONUNIFORM CURRENT DISTRIBUTION MODEL, $\delta = 27 \mu\text{m}$ ", ($\sigma = 1.2\text{E}5$ mhos/m at 3 GHz) Eq. (7-33) is substituted into Eq. (7-4) to obtain the Fourier transform. This transform can be integrated directly and substituted into the appropriate terms in Eq. (7-32).

For the microstrip model, and a uniform current, the theory given in Reference 2 is used, with conductivity $\sigma = 3,720$ mhos/m ($\delta = 0.15\text{E}-3$ meters at 3 GHz). Differences between the three models, as reflected in the curves, are not considered significant. Similar results pertain to multielement transducers, provided individual elements are narrow compared to center-to-center spacing and the number of strips is not too large; less than eight. See also Figure 4-2.

The solid lines in Figure 4-2 are obtained using the theory presented here, with no loss, and with a flat current distribution. Dashed curves are taken from Reference 2. Figure 4-2a is for an 8-element grating transducer and Figure 4-2b is for a two bar grating transducer. These results are also in good agreement with experiment.

The range of validity of MSW models has already been discussed in Section 7.3.12. Here, we consider further aspects of the assumptions and restrictions made in developing the transducer models. As before, in the magnetostatic limit, MSW wavelengths are much smaller than electromagnetic wavelengths in the propagation media. MSW wavelengths up to a few thousand microns satisfy the magnetostatic approximation very well. However, even though MSW wavelengths may be small compared to EM wavelengths, they may be too large in comparison with sample or transducer aperture dimensions. This would cause the theory to break down at shorter wavelengths than those satisfying the magnetostatic approximation. Some wavelengths within the MSW passband may approach physical dimensions of the propagation media or overall transducer dimensions. It is therefore not surprising, in view of the assumptions made, that the theory breaks down in the long wavelength limit. Breakdown of the theory for 15-element grating transducers is documented experimentally and theoretically in Reference 27.

Two important implications of these results are as follows. First, in time delay units utilizing single strip wide band transducers, mode suppression techniques will be needed to control the long wavelength region of the passband. Second, there are two alternate approaches to filter design. In one approach the long wavelength response is suppressed and the fundamental response apodized. Apodization of the fundamental response, near synchronism, using surface acoustic wave design techniques to produce desired filter characteristics, can be used. The other approach is to develop techniques for apodizing transducers in the long wavelength region. This is attractive because of the lower insertion loss at the longer wavelengths.

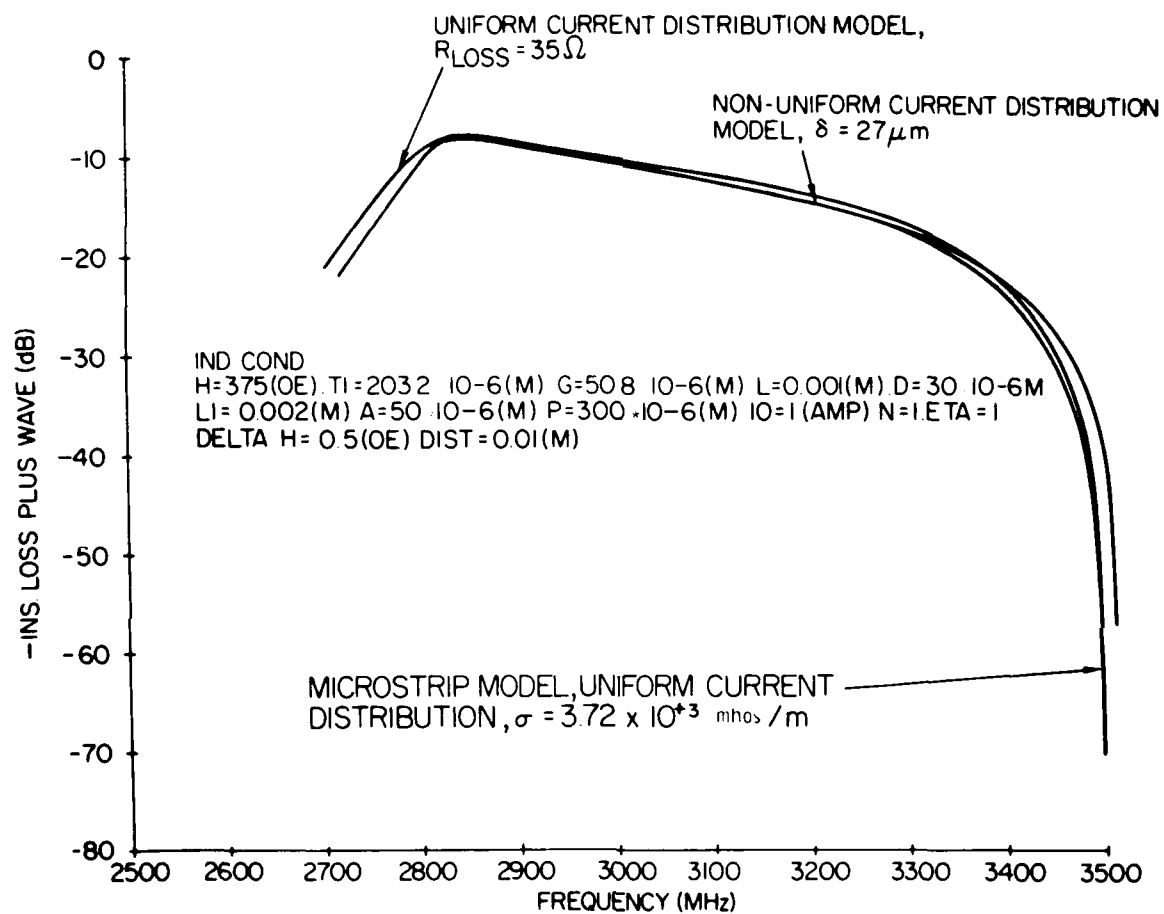


Figure 7-3. Comparison of Insertion Loss for Single Strip Transducers as Predicted by the Two Terminal, TT, and the Transmission Line, TL, Model

There is good agreement between theory and experiment over most of the MSW passband. It is in the MSW long wavelength region that theory breaks down. Work needs to be done on this problem because excellent filter responses in the long wavelength region are relatively easy to demonstrate experimentally.

To summarize this reference, an analysis is presented for developing a first order transducer theory for the three principal MSW modes of propagation. From expressions for radiation resistance and reactance, an equivalent circuit is defined from which insertion loss (or transmission loss, as measured by commercial network analyzers) is derived. A comparison is made between several models and between theory and experiment for single, multi-element, and apodized transducers. It is concluded that present MSW transducer theory provides a reasonably good first order theory, but that it fails in the long wavelength limit. Further improvements are crucial before the theory is useful for band pass filters employing long wavelength MSW.

Other theoretical problems requiring investigation are the inclusion of mutual coupling between transducer elements, and the inclusion of near fields. Significant progress has recently been made in the development of a three port transducer scattering matrix model by Owens et al at the University of Texas at Arlington.

7.3.13 STRONGLY COUPLED MSW

Current Distribution on Gratings and Meanderlines: With MSW Applications by Sethares and Cohen²⁸

One of the remaining theoretical problems in MSW technology is the development of an adequate analytical technique for predicting the frequency response of large multielement transducer arrays. Present models provide a good first order theory for a small number of narrow elements. However, the response of a 15-element array with interelement spacing equal to strip width, for example, is not adequately predicted by present theory. Theory does not take into account mutual coupling between elements or the reaction of the YIG back onto transducer current distribution for strong coupling. This work²⁸ and the next²⁹ represent a first step toward solving these problems. Reference 28 deals with mutual coupling and Reference 29 deals with strong coupling.

In this analysis,²⁸ currents distributed on parallel conducting strips of a planar array located near a ground plane are assumed to be mutually coupled by virtue of their magnetoquasistatic interaction. For MSW transducers operating at about 3 GHz, the quasistatic assumption is justified for sufficiently small arrays not too far from the ground plane, that is, when $L'/\text{wavelength} \ll 1$, where L' is the largest distance between current elements or image current elements and wavelength is the free space wavelength. An additional analytical simplification is exploited because the ratio of strip length/width is typically about 40:1, thereby permitting a two-dimensional analysis. The influence on the current distribution of finite conductivity and the presence of the YIG film are not considered.

For a line current varying harmonically with time above a lossless ground plane, the spatial portion of the vector potential reduces to

$$A = -(\mu_0 I / (2\pi)) \ln(r_1 / r_2) + (\text{higher order terms in } kr_1, kr_2) \quad (7-34)$$

when (kr_1) and $(kr_2) \ll 1$, r_1 and r_2 are the distances from the source and image currents to an observation point and k is the wave number in the medium surrounding the array. By superimposing fields due to strip current elements and their images, one is led to the following system of integral equations for the normalized vector potential, $a_k(w)$, in terms of the current density on all the strips.

$$a_k(w) = \sum_{j=1}^N \int_{-1}^1 dx K_j(x) \ln(|W|(W^2 + \beta)^{-1/2}) \quad (7-35)$$

where

$$W = 2(k - j)/\eta + w - x$$

and

$K_j(x)$ = current density over the j^{th} electrode

x, w = normalized spatial variables defined across each strip: $-1 < x, w < 1$

η = s/b = strip width/center-to-center strip separation

β = $16(G/s)^2$

G = lift-off distance

N = Number of strips in the array

$a_k = -A_k/(\mu_0/2\pi)$

= normalized vector potential of k^{th} strip.

Auxiliary conditions on vector potential and current depend on continuity conditions for the transducer configuration under consideration. For a grating the total current I entering and leaving (strips connected in parallel) equals the integrated current density over all strips.

$$I = \sum_{j=1}^N \int_{-1}^1 K_j(x) dx \quad (7-36)$$

and vector potential is the same for all strips, $a_k = a$. For a meander line the current is the same in all strips except for a sign change (strips connected in series) and equals the integrated current density over one strip,

$$I_j = (-1)^j \int_{-1}^1 K_j(x) dx \quad (7-37)$$

while the vector potential is different for each strip.

The problem is to solve the integral equation, Eq. (7-35), for all current densities, $K_j(x)$. A Galerkin procedure is used for the solution, and current density is expanded into Chebyshev polynomials of the first kind; namely,

$$K_j(x) = (1 - x^2)^{-1/2} \sum_{m=0}^{M-1} C_m(j) T_m(x) \quad (7-38)$$

The $T_m(x)$ are known polynomials, so the problem reduces to solving for expansion coefficients $C_m(j)$. Use is made of the orthogonality of Chebyshev polynomials. The a_k and $C_m(j)$ are determined numerically from a system of linear equations. Current density on outer elements is found to be

nonsymmetrical about the center of each strip. Current density in the center strip is symmetrical as expected from symmetry. Outer elements carry more current than inner ones also as expected.

After calculating current density, the Fourier transform of current density is calculated and inserted into the computer programs, and insertion loss is evaluated. Results are presented in Figure 7-4 for $N = 15$ element transducers with $s/b = 1/2$. This figure compares insertion loss for a uniform current distribution with the calculated current distribution $K_j(x)$ which includes mutual coupling. The most significant differences are in the increased sidelobes of the main response near 3 GHz, and the dropoff rate in sidelobe levels on either side of the main response.

Inductance of the transducer ground plane system was determined by equating energy stored in an inductor to energy stored in the magnetic field about the array, which is,

$$LI_0^2/2 = \int \bar{A} \cdot \bar{K} dv / 2 \quad (7-39)$$

all strips

where \bar{A} and \bar{K} are vector potential and current density, respectively, and I_0 is the total current entering the transducer.

The calculated inductance values are compared with previous inductance calculations based on uniform current distribution models. The results are entirely consistent in the appropriate limiting cases. Figure 7-5 summarizes the results.

Figure 7-5a, for a meander line, shows that mutual coupling has almost no effect on meander line inductance for a wide range of meander line parameters. For a grating, Figure 7-5b shows significant differences for large liftoff, $G/b > 1$; while for small liftoff, $G/b \ll 1$, and thin strips, there are no significant differences. This is consistent with the fact that current density becomes uniform when $G/b \ll 1$, and in addition, mutual coupling is weak for very narrow strips.

It was also found that when a magnetic medium with large permeability is present, circulating currents are possible for some transducer parameters; that is, self resonances occur in the transducer.

To summarize this reference: surface current density on an array of mutually coupled conducting strips near a ground plane is investigated in the quasistatic limit using the method of images. The nonuniform current distribution caused by mutual coupling and its effects on insertion loss and inductance are calculated. A comparison is made with previously published results obtained under the assumption of uniform current distributions. Emtage had previously calculated the exact complex current distribution on narrow strips assuming independent forward and reverse waves. Results reported here are valid for wide strips that simultaneously excite forward and reverse waves which are not independent. A Green's Function due to a line current is determined, then superposed assuming only a uniform potential on the strip. Then a Fredholm integral equation of the first kind is used to determine current density.

MSSW Back Reaction on a Generating Current Strip by Cohen and Sethares²⁹

RF current density is determined for a perfectly conducting, current carrying, strip which is strongly coupled to a YIG film and magnetically biased for magnetostatic surface waves. Both current amplitude and phase are found to be spatially nonsymmetrical for a single strip.

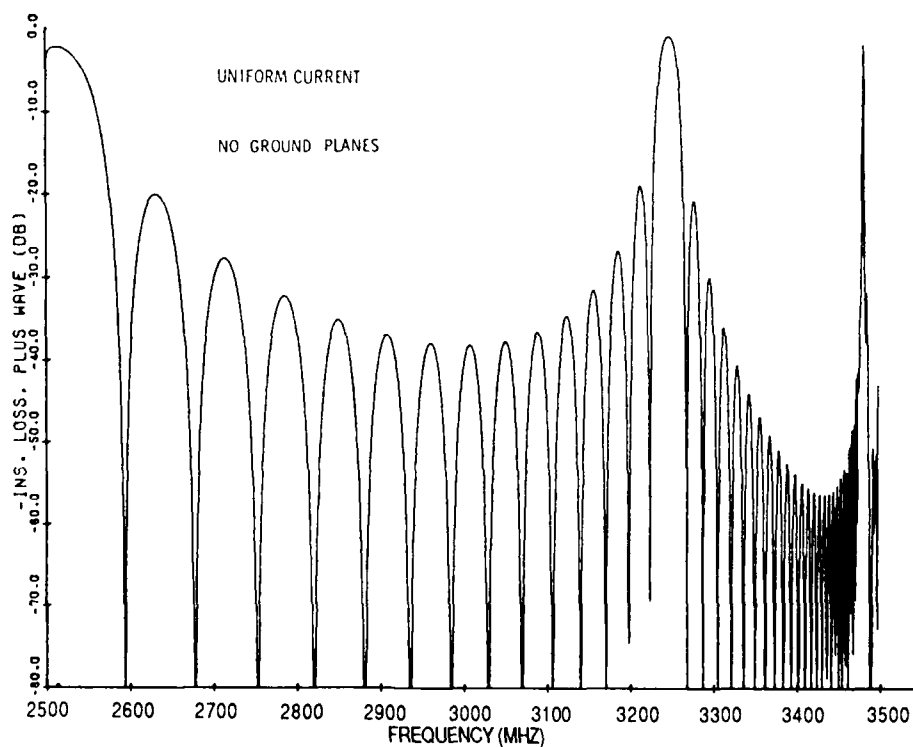
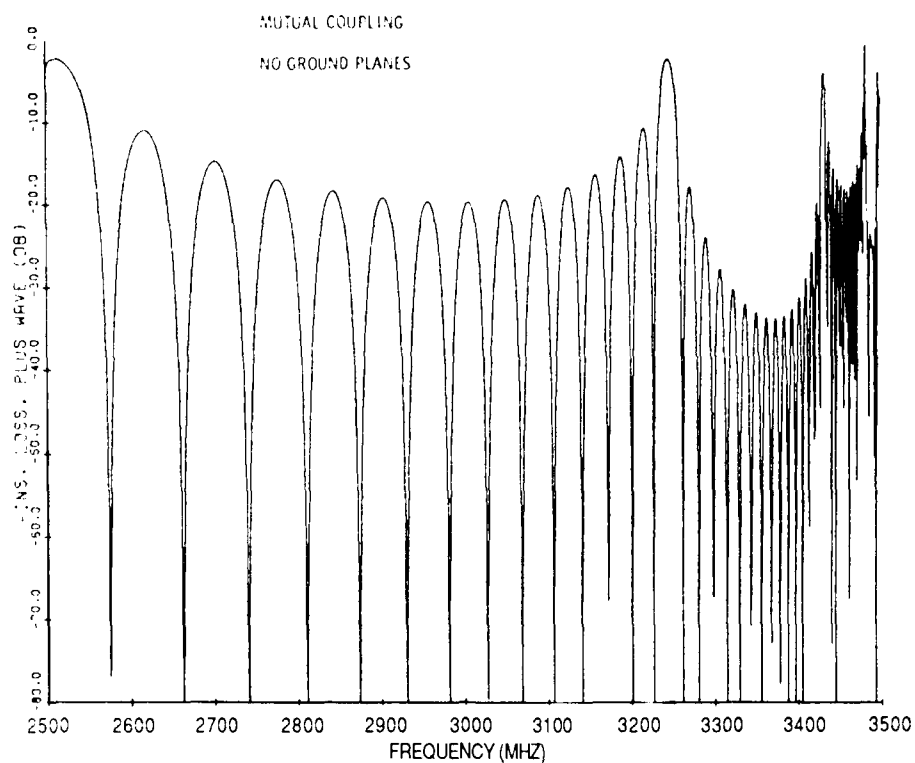


Figure 7-4. Comparison of Insertion Loss for a Uniform Current Distribution Analysis with That of a Mutual Coupling Analysis. $H = 375 \text{ Oe}$, $D = 30 \mu\text{m}$, $L1 = 2 \text{ mm}$, $a = 150 \mu\text{m}$, $N = 15$

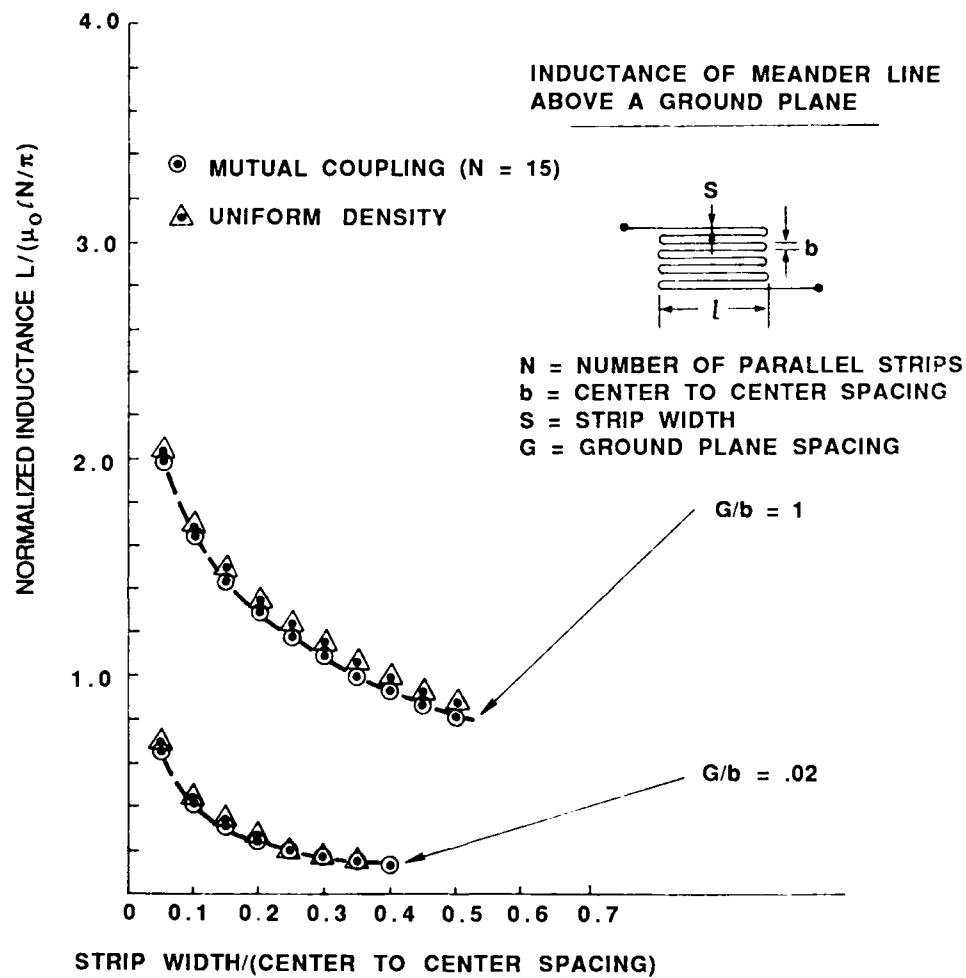


Figure 7-5a. Normalized Inductance for Mutual Coupling Analysis Compared with a Uniform Current Analysis. Meander line.

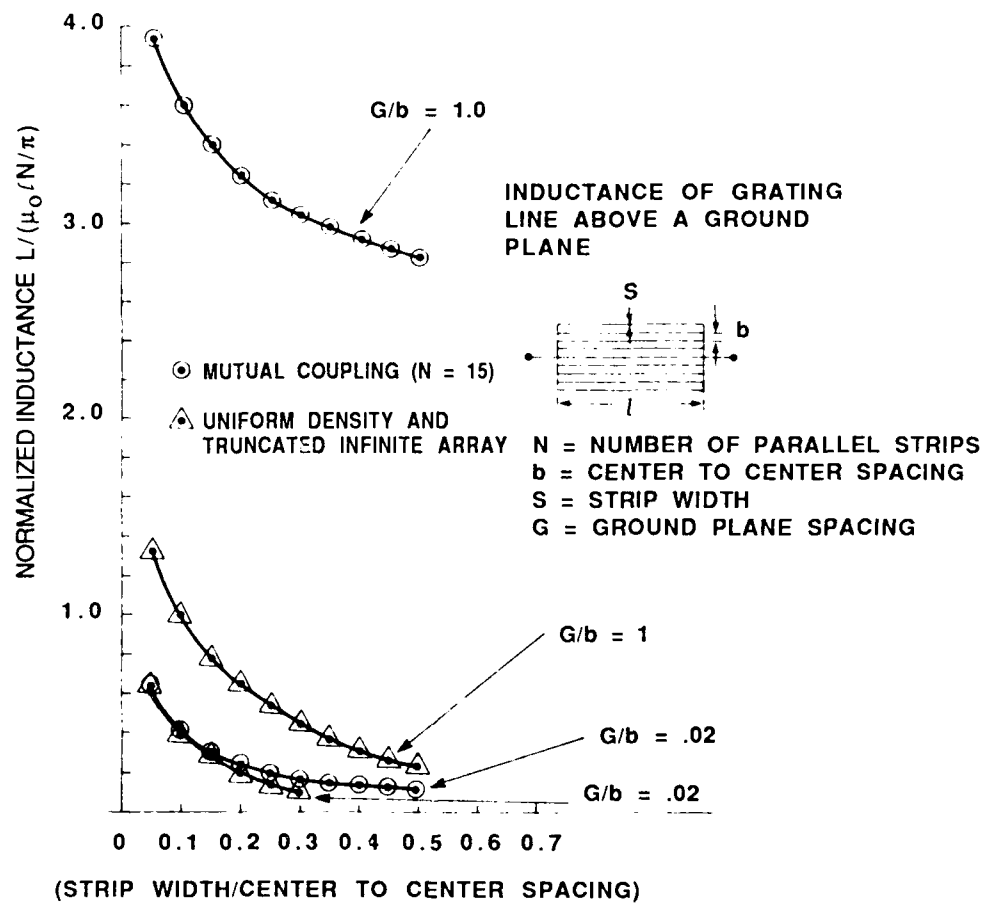


Figure 7-5b. Normalized Inductance for Mutual Coupling Analysis Compared with a Uniform Current Analysis. Grating.

This work is essentially an extension of Emtage's³⁶ analysis, which calculates the complex current distribution amplitude and phase on a narrow strip assuming independent plus and minus waves. Results reported here are for wide strips and interacting plus and minus waves. Our results reduce to those of Emtage in the appropriate limit.

A Green's function approach is used. A vector potential Green's Function, due to a line current, is derived. Then, for many strips, superposition is used. A uniform potential is assumed on the strips. A Fredholm integral equation of the first kind is then inverted, to obtain the current density.

In the quasimagnetostatic limit, which is employed, the permeability tensor of the YIG results in a large displacement current term in the region occupied by the YIG. Assuming Fourier integral solutions for the three regions, satisfaction of boundary conditions leads to explicit expressions for the potentials. By evaluating Fourier integrals at points on the strip, one arrives at a Green's function kernel of the form $g(w - u) = \ln |w - u| + G(+/-) (w - u)$, where w and u are normalized coordinates. By superposition, the total vector potential on the strip may be written as

$$A(w) = \int_{-1}^1 du J(u) [\ln |w - u| + G(+/-) (w - u)] .$$

$J(u)$ can be determined numerically by setting $A(w) = 1$ and solving by equispaced collocation. Inversion of the integral is aided by recognizing the Toeplitz structure of the matrix in the resulting system of equations.

Figure 7-6 shows the real (solid) and imaginary (dashed) parts of $G(+/-) (w - u)$ for a given parameter set. After one or more MSSW wavelengths the field resembles the usual MSSW. But very near the line current a spatially transient variation is observed that reacts on the strip and induces asymmetry in current density. Figure 7-7a and 7-7b show magnitude and phase, respectively, of current density across a wide, 150 μm , strip; and Figures 7-8a and 7-8b show magnitude and phase, respectively, across a narrow, 6 microns, strip. The results shown here are for several frequencies within the MSSW passband and for a transducer liftoff of one half the film thickness. As liftoff increases, the amplitude distribution tends towards that of an uncoupled strip, while the phase becomes linear across most of the strip width. The results can be incorporated into the MSW programs to determine insertion loss.

7.3.14 MAGNETOSTATIC VOLUME WAVES

Magnetostatic Volume Waves by Weinberg and Sethares³⁰

This paper presents a generalized expression for the dispersion relation, and another for the radiation resistance, of both FVWs and BVWs. With reference to Figure 2-1, the magnetic potential in the YIG region is expressed as

$$\psi = (A \cos \alpha |k| y + B \sin \alpha |k| y)(e^{-i k x}) e^{i \omega t}$$

where quantity alpha is defined by

36. Emtage, P.R. (1982) Generation of MSSW by a microstrip, *J. of Appl. Phys.* **53**:5122.

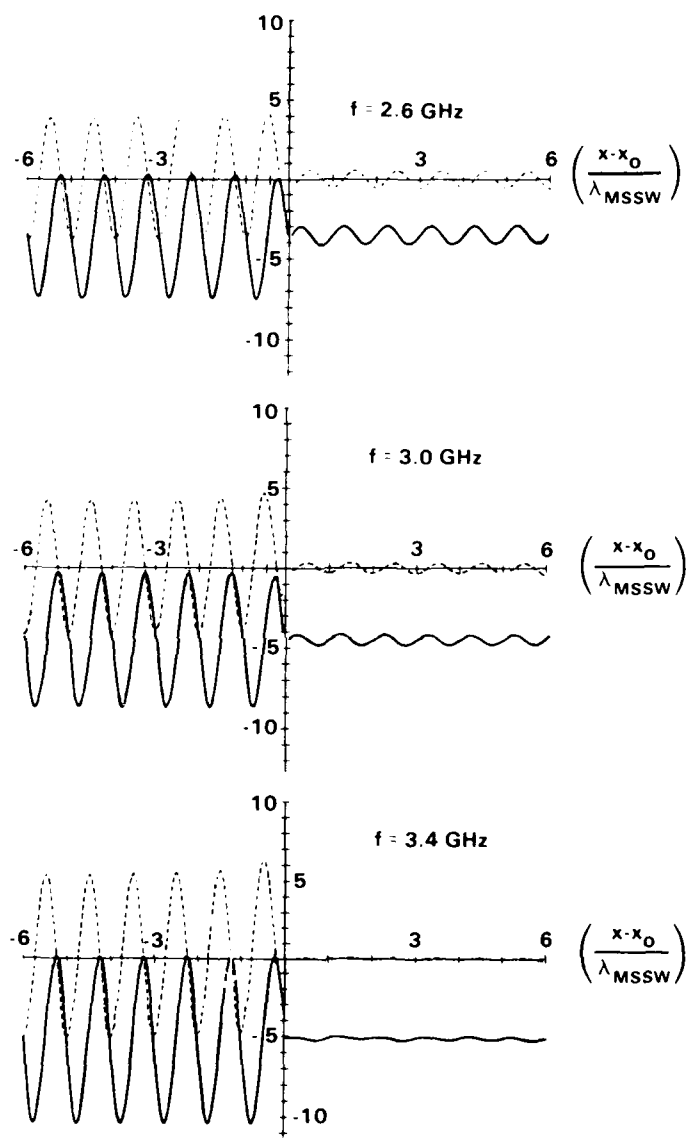


Figure 7-6. Green's Function in the Far Field, at Three Frequencies

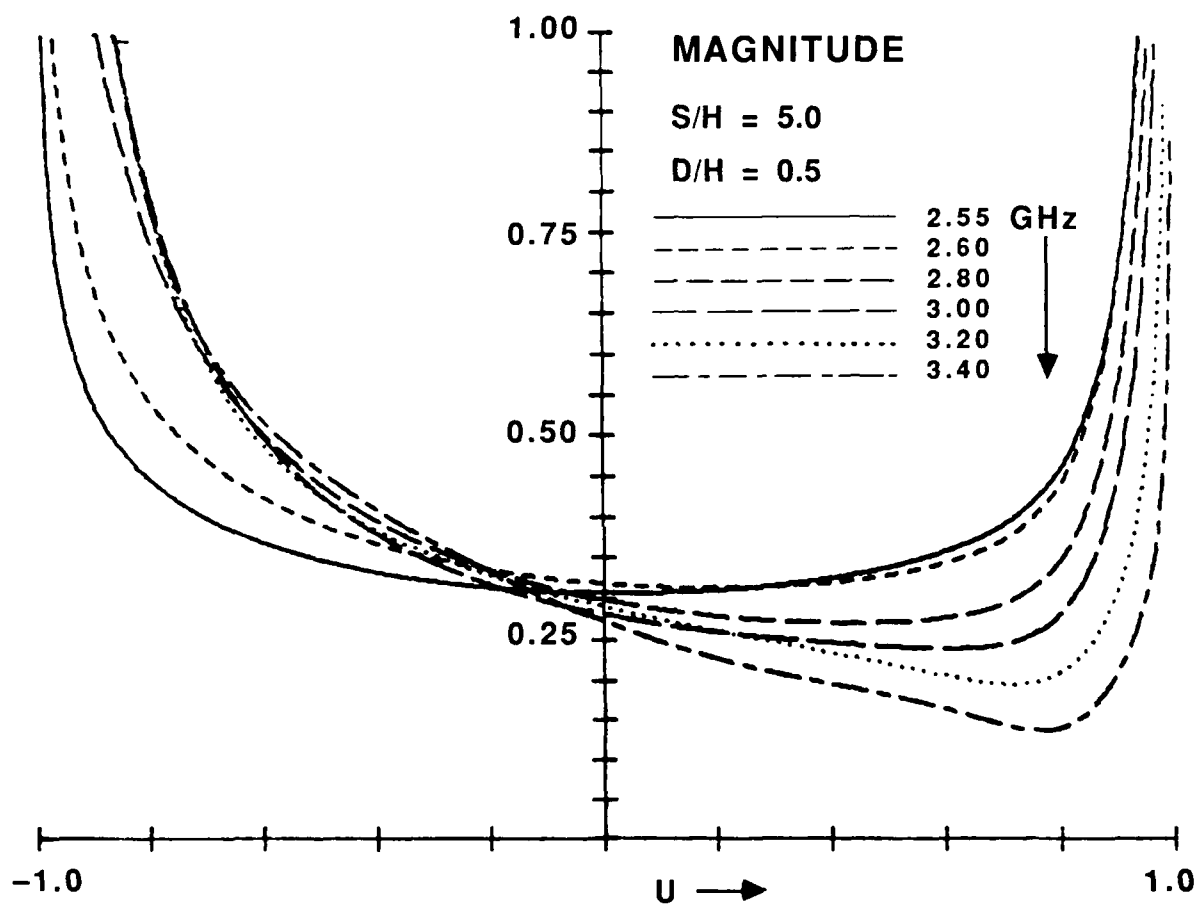


Figure 7-7a. Complex Current Distribution Across a Wide Strip. Magnitude of Current.

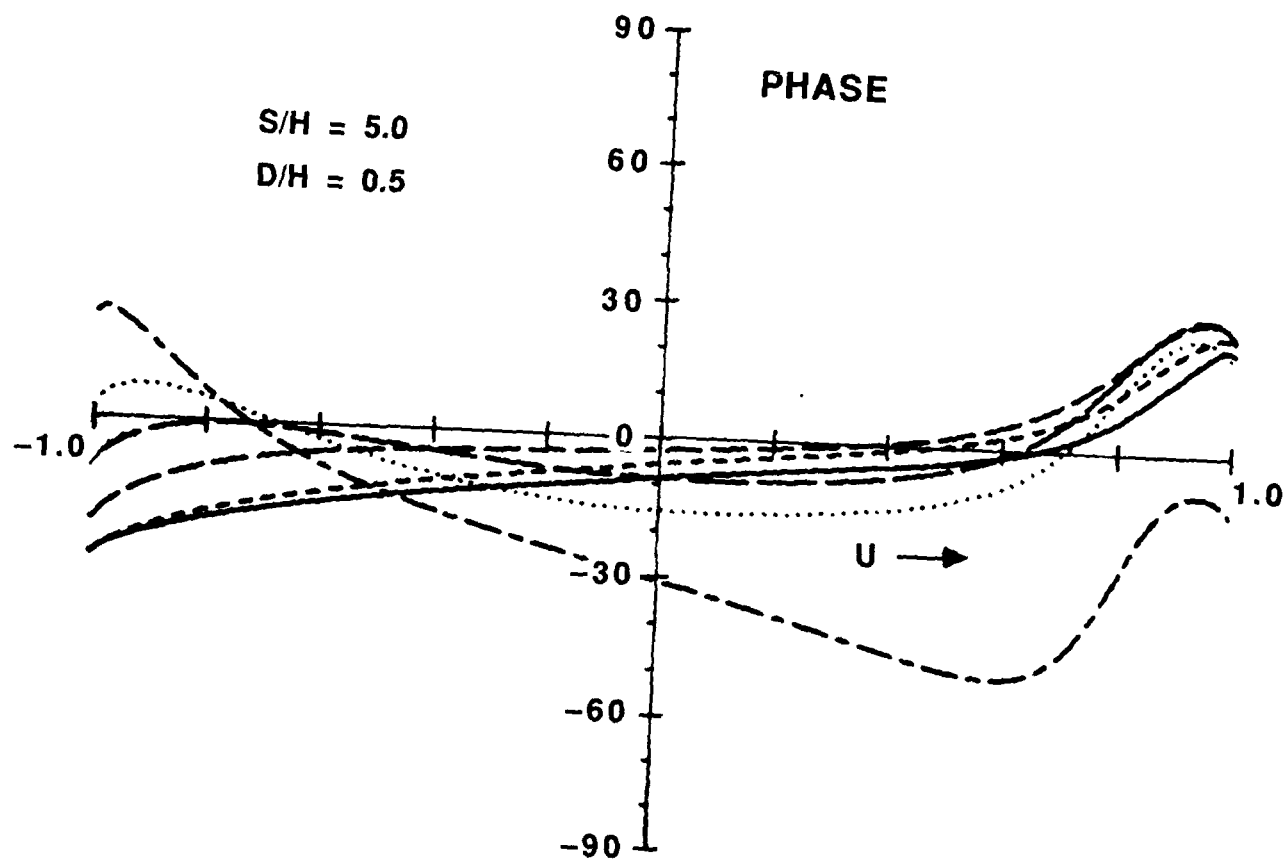


Figure 7-7b. Complex Current Distribution Across a Wide Strip. Phase of Current.

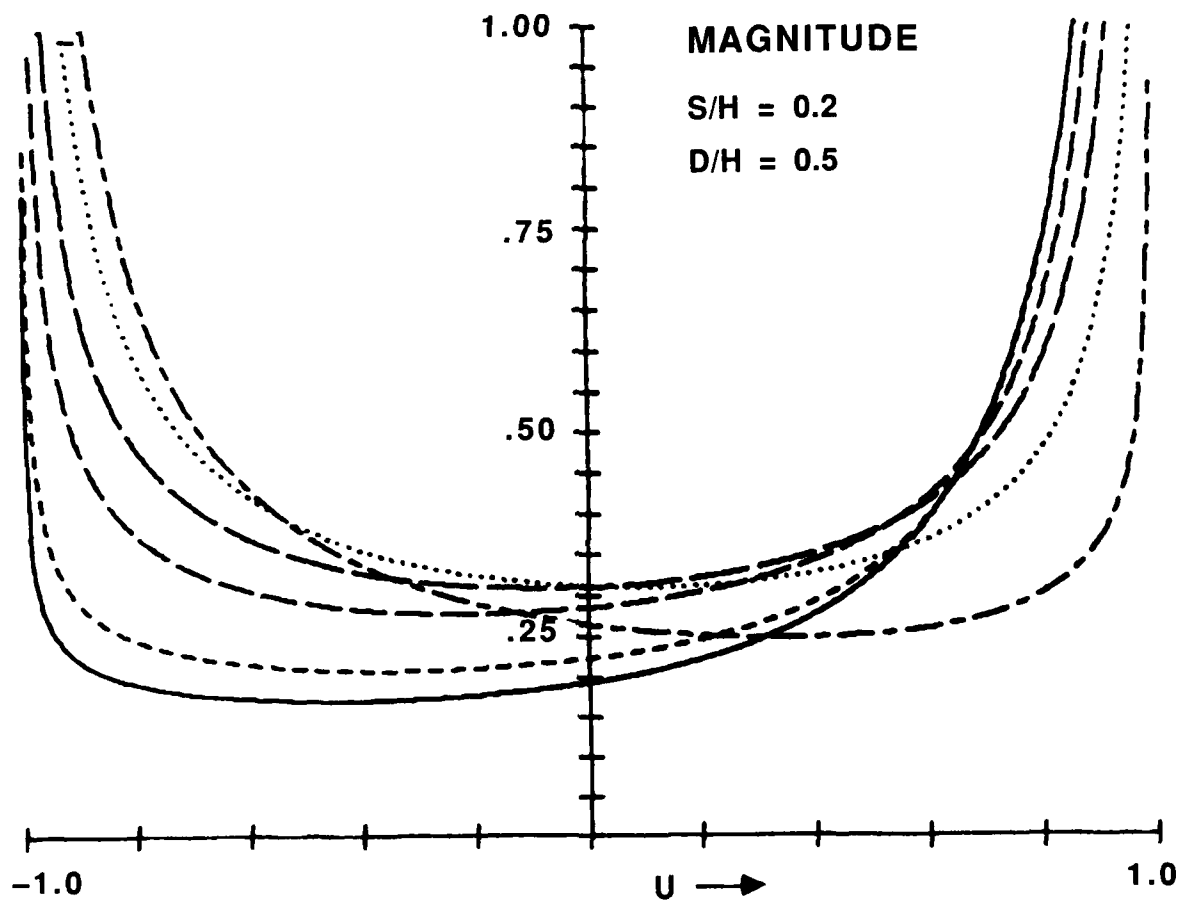


Figure 7-8a. Complex Current Distribution Across a Narrow Strip. Magnitude of Current.

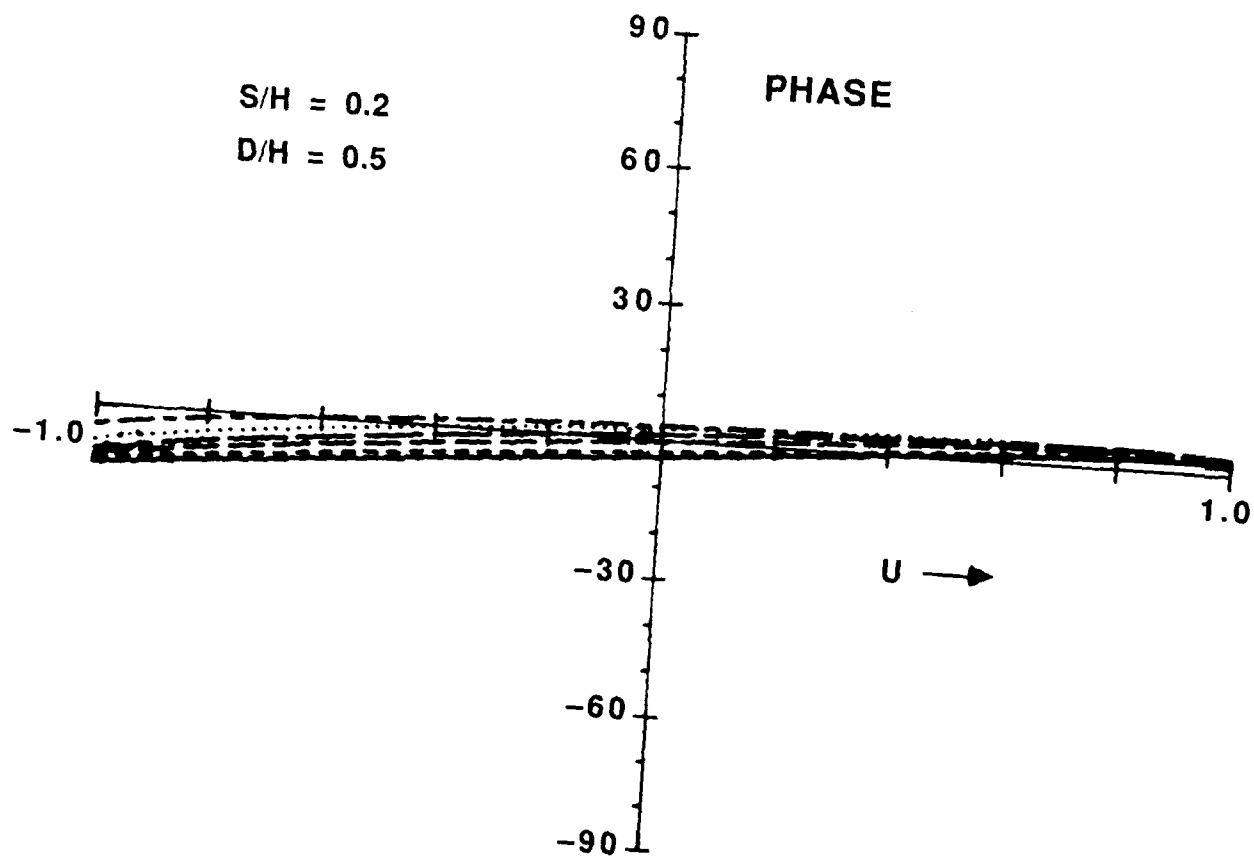


Figure 7-8b. Complex Current distribution Across a Narrow Strip. Phase of Current.

$$\alpha^2 = - \left(1 + \frac{\gamma^2 H_0 M_0}{\gamma^2 H_0^2 - f^2} \right)^* \quad (7-40)$$

The asterisk in the expression for α , Eq. (7-40), equals +1 for FVWs and -1 for BVWs.

The dispersion relation is given by

$$|k| = \frac{1}{\alpha d} \tan^{-1} \{ 2\alpha [e^{|k|l}(t_1 + g) - e^{-2|k|l} e^{-|k|l}(t_1 + g)] / \\ [(\alpha^2 - 1)e^{|k|l}(t_1 + g) + (-1)^*(\alpha^2 + 1)e^{-|k|l}(t_1 + g) \\ + (-1)^* e^{-2|k|l}(\alpha^2 + 1)e^{|k|l}(t_1 + g) + e^{-2|k|l}(\alpha^2 - 1)e^{-|k|l}(t_1 + g)] \}$$

The asterisk in the dispersion relation, Eq. (7-41), equals 0 for FVWs and +1 for BVWs. The dispersion relation is solved numerically by successive approximations. The principal value of the inverse tangent function is taken from 0 to π . An infinite number of solution modes can be found by considering the multiplicity of the inverse tangent function. Solution waves are the same for positive and negative k , for each solution mode. The fundamental mode contains most of the contribution to the power as is expected. The radiation resistance for positive and negative k are also identical and the total radiation resistance is twice the resistance from each wave for every mode. The total resistance for each mode is of the form

$$R_m = \left[\frac{2\omega\mu_0 |G|^2 l_1}{k^2[(1 - \eta) + (1 + \eta)N^2]} \right] C \quad (7-42)$$

where G is the same for both FVWs and BVWs and C is defined by Eq. (7-43). In the equation for parameter C the asterisk equals 0 for FVWs and +1 for BVWs.

$$C = 2e^{-2kl}(\sinh 2kl - 2kl) - 1 + (-1)^*(\alpha^2 + 1)kd - (-1)^*kg \\ \times \left(\frac{1 + \alpha^2}{\alpha} \sin 2\alpha kd + \frac{1 - \alpha^4}{2\alpha^2} - \frac{1 - \alpha^4}{2\alpha^2} \cos 2\alpha kd \right) \\ + (-1)^* \left(\frac{\sinh 2kt_1 - 2kt_1}{2 \sinh^2 kt_1} \right) \left(\frac{\alpha^4 - 1}{4\alpha^2} - \frac{\alpha^4 - 1}{4\alpha^2} \cos 2\alpha kd - \frac{\alpha^2 + 1}{2\alpha} \sin 2\alpha kd \right) \\ + e^{2kg} \left[\frac{(1 + \alpha^2)^2}{8\alpha^2} + \frac{4\alpha^2 - (1 - \alpha^2)^2}{8\alpha^2} \cos 2\alpha kd + \frac{1 - \alpha^2}{2\alpha} \sin 2\alpha kd \right] \\ \times \left(1 + \frac{\sinh 2kt_1 - 2kt_1}{2 \sinh^2 kt_1} \right)$$

$$\begin{aligned}
& + e^{-2kg} \left[\frac{(1 + \alpha^2)^2}{8\alpha^2} + \cos 2\alpha kd - \frac{(1 + \alpha^2)^2}{8\alpha^2} \right] \left(1 - \frac{\sinh 2kt_1 - 2kt_1}{2 \sinh^2 kt_1} \right) \\
& + e^{-2kl} \left\{ 2(\alpha^2 - 1)kd + kg \left[\frac{(1 - \alpha^2)^2}{\alpha^2} - \frac{(1 + \alpha^2)^2}{\alpha^2} \cos 2\alpha kd \right] \right. \\
& + \left(\frac{\sinh 2kt_1 - 2kt_1}{2 \sinh^2 kt_1} \right) \left[\frac{(1 - \alpha^2)^2}{2\alpha^2} - \frac{(1 + \alpha^2)^2}{2\alpha^2} \cos 2\alpha kd \right] \\
& + (-1)^* e^{2kg} \left[\frac{\alpha^4 - 1}{4\alpha^2} - \frac{\alpha^4 - 1}{4\alpha^2} \cos 2\alpha kd - \frac{\alpha^2 + 1}{2\alpha} \sin 2\alpha kd \right] \times \left(1 + \frac{\sinh 2kt_1 - 2kt_1}{2 \sinh^2 kt_1} \right) \\
& + (-1)^* e^{-2kg} \left[\frac{1 - \alpha^4}{4\alpha^2} - \frac{1 - \alpha^4}{4\alpha^2} \cos 2\alpha kd - \frac{\alpha^2 + 1}{2\alpha} \sin 2\alpha kd \right] \\
& \times \left(1 - \frac{\sinh 2kt_1 - 2kt_1}{2 \sinh^2 kt_1} \right) \Big\} \\
& + e^{-4kl} \left\{ 1 + (-1)^*(\alpha^2 + 1)kd + (-1)^* \frac{(\sinh 2kt_1 - 2kt_1)}{2 \sinh^2 kt_1} \right. \\
& \times \left(\frac{\alpha^2 + 1}{2\alpha} \sin 2\alpha kd + \frac{\alpha^4 - 1}{4\alpha^2} - \frac{\alpha^4 - 1}{4\alpha^2} \cos 2\alpha kd \right) \\
& + (-1)^* kg \left(\frac{1 + \alpha^2}{\alpha} \sin 2\alpha kd + \frac{1 - \alpha^4}{2\alpha^2} \cos 2\alpha kd - \frac{1 - \alpha^4}{2\alpha^2} \right) \\
& + e^{2kg} \left(1 + \frac{\sinh 2kt_1 - 2kt_1}{2 \sinh^2 kt_1} \right) \left[\frac{(1 + \alpha^2)^2}{8\alpha^2} - \frac{(1 + \alpha^2)^2}{8\alpha^2} \cos 2\alpha kd \right] \\
& + e^{-2kg} \left(1 - \frac{\sinh 2kt_1 - 2kt_1}{2 \sinh^2 kt_1} \right) \\
& \times \left[\frac{1 - \alpha^2}{2\alpha} \sin 2\alpha kd - \frac{(1 + \alpha^2)^2}{8\alpha^2} - \frac{4\alpha^2 - (1 - \alpha^2)^2}{8\alpha^2} \cos 2\alpha kd \right] \Big\} \quad (7-43)
\end{aligned}$$

The radiation reactance is then found by numerically evaluating a Hilbert transform.

Propagation loss can be included in the expression for insertion loss, [Eq. (7-32)], by adding a term $(-76.4\Delta HT_g)$, where T_g = group delay in microseconds and ΔH is the full magnetic linewidth in oersteds.

In Figure 7-9a, we obtain insertion loss for FVWs, using the two-terminal model, for both zero gap, and for a gap of $G = 25 \mu\text{m}$. In Figure 7-9b we obtain insertion loss for BVWs for a single element, using both the two terminal model and the microstrip model. In Figure 7-10a and b, insertion loss is presented for a 4-element parallel grating, using both the two-terminal model and the microstrip model, respectively.

• *Magnetostatic Forward Volume Wave Propagation: Finite Width by Weinberg and Sethares³¹*

• The infinite radiation resistance encountered at the low end of the magnetostatic forward volume wave frequency band³⁷ for a YIG layer of finite width is avoided by employing a physically justifiable low frequency cutoff value higher than that for which radiation resistance would be infinite. Radiation reactance and insertion loss can then be calculated. They are found to be insensitive to the choice of the cutoff frequency except for frequencies very close to cutoff. Beam spreading considerations determine the cutoff frequency. The infinite radiation resistance problem does not occur in the two-dimensional MSW transducer models.

For volume modes, finite width effects can be approximately taken into account by using potential functions of the form,

$$\psi = \int_{-\infty}^{\infty} e^{-l k x} \cos \left[\frac{n\pi}{l_1} Z \right] (A e^{\bar{k} y} + B e^{-\bar{k} y}) dk \quad (7-44a)$$

in non YIG regions, and

$$\psi = \int_{-\infty}^{\infty} e^{-l k x} \cos \left[\frac{n\pi}{l_1} Z \right] (A \cos \alpha \bar{k} y + B \sin \alpha \bar{k} y) dk \quad (7-44b)$$

in YIG regions, where k is the wave number in the x direction, l_1 is the strip width, n represents the width mode, and

$$\bar{k} = \sqrt{k^2 + (n\pi/l_1)^2} \quad n = 0, 1, 2, 3, \dots \quad (7-44c)$$

For $n = 0$, we have the infinite width case. For odd n , the potential vanishes at the strip ends $z = (+/-)l_1/2$. For no ground planes, application of boundary conditions yields the dispersion relation, Eq. (7-45).

$$[(\alpha^2 - 1) \sin \alpha \bar{k} d - 2\alpha \cos \alpha \bar{k} d] = 0$$

or

$$\bar{k} = \frac{1}{\alpha d} \tan^{-1} \frac{2\alpha}{\alpha^2 - 1} + \frac{m\pi}{\alpha d}, \quad m = 0, 1, 2, 3, \dots \quad (7-45)$$

• There are an infinite number of thickness solution modes, corresponding to the value of m , with $m = 0$ giving the fundamental mode. Using the boundary condition at $y = 0$, where the RF magnetic

37. Adam, J.D. and Bajpai, S.N. (1982, Nov.) Magnetostatic forward volume wave propagation in YIG strips, *IEEE Trans. on Magnetics*, **MAG-18** (No. 6):1598-1600.

FORWARD WAVES - FIRST MODE
 $H = 893(\text{OE})$ $D = 25(\text{UM})$ $T_1 = 250(\text{UM})$ $L = 1(\text{M})$ $L_1 = 3(\text{MM})$ $A = 50(\text{UM})$
 $\Delta H = 0.5$ $\text{DIST} = 0.01$ $R_{\text{LOSS}} = 0$ $N = 1$

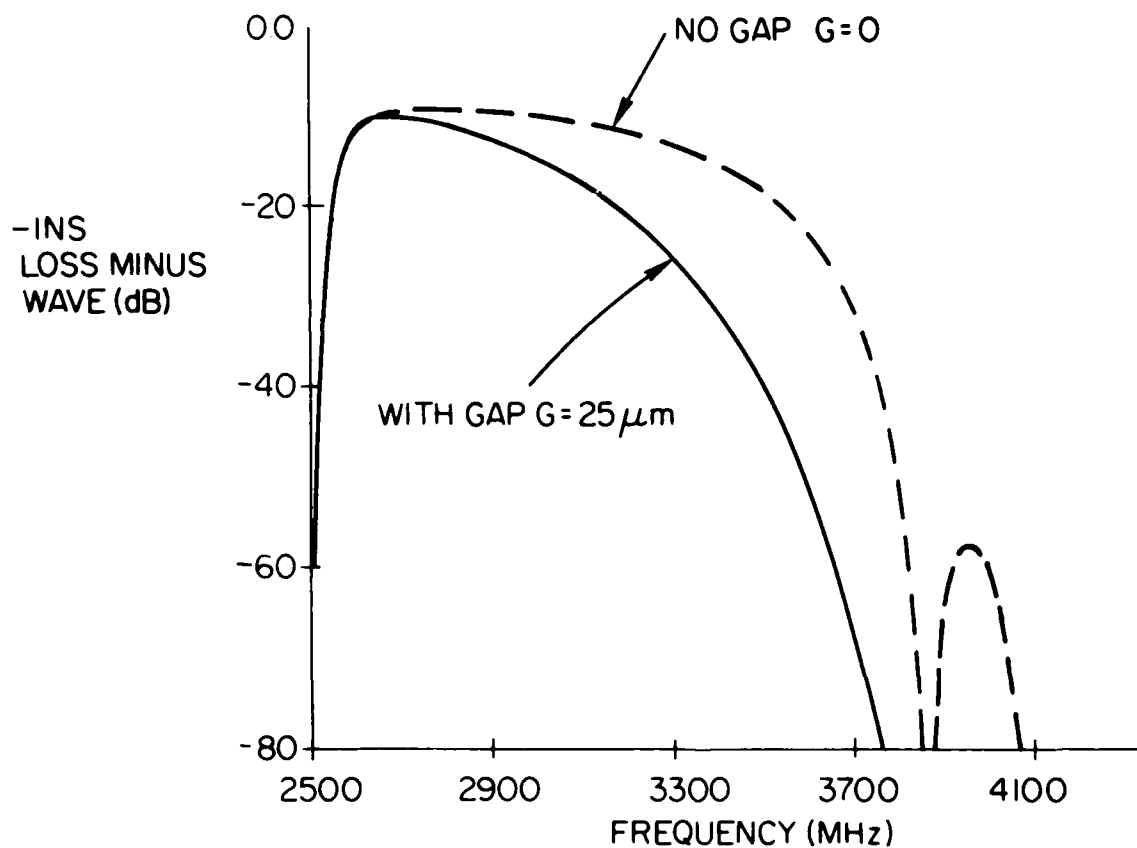


Figure 7-9a. Volume Wave Insertion Loss, $N = 1$. FVW with and without Gap.

BACKWARD WAVES—FIRST MODE
H=893(OE) D=25(UM) TI=250(UM) L=1(M) LI=3(MM) A=50(UM)
DELH=0.5(OE) DIST=0.01(M) N=1 G=25(UM)

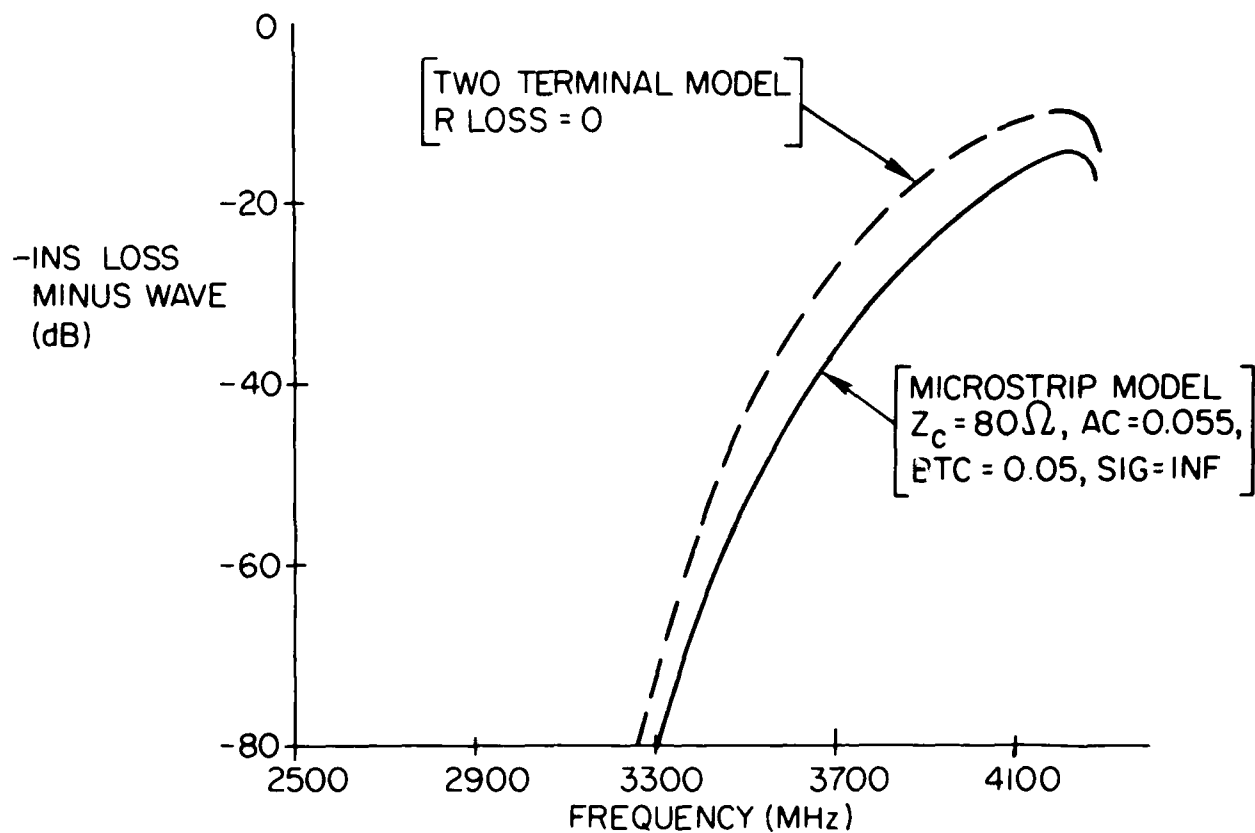
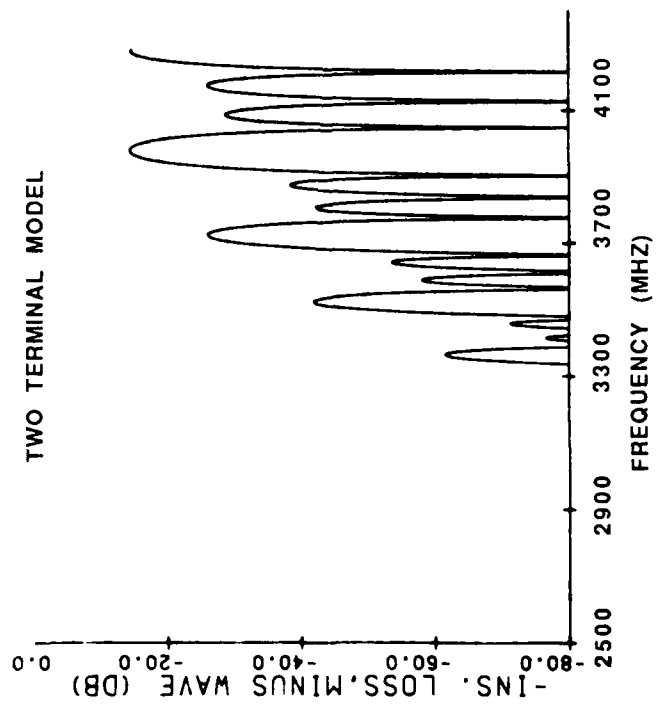


Figure 7-9b. Volume Wave Insertion Loss, N = 1. BVW Using TT and TL.

PARALLEL GRATING-BACKWARD WAVES-FIRST MODE

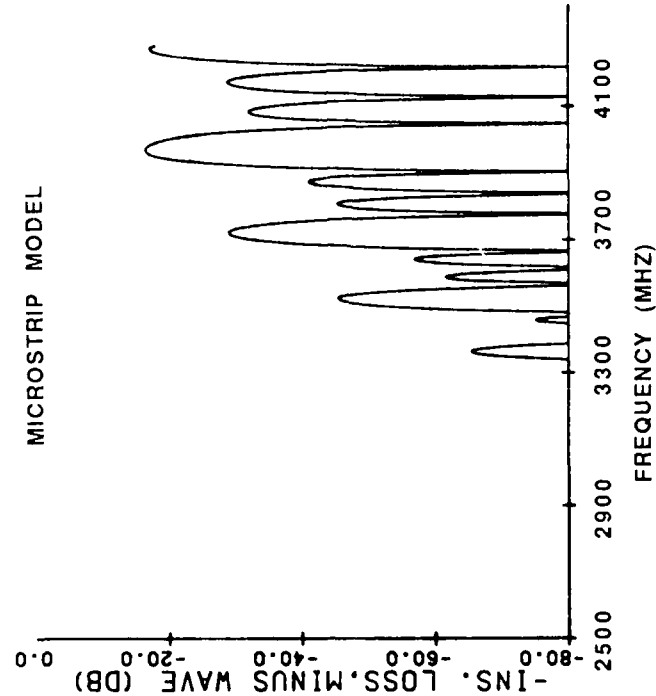
H=893 (OE) D=25(μ m) T1=250(μ m) L=1(M) L1=3(MM) A=50(μ m) P=300(μ m)
 DELTA H=5(OE) DIST=.01(M) R LOSS=0 N=4 G=25(μ m)



a. Two Terminal Model

PARALLEL GRATING-BACKGROUND WAVES-FIRST MODE-MICROSTRIP MODEL

H=893 (OE) D=25(μ m) L=1(M) L1=3(MM) A=50(μ m) P=300(μ m)
 DELTA H=5(OE) DIST=.01(M) N=4 G=25(μ m) ZC=80 AC=.055 BTC=.05 SIG=INF



b. Transmission Line Model

Figure 7-10. BVW Insertion Loss, N = 1

field is discontinuous by an amount equal to transducer surface current, and integrating in the x direction over all x , and in the z direction from $-l_1/2$ to $l_1/2$, we can then perform a contour integration to find the fields. Power can be obtained from the Poynting vector as before, or from Eq. (7-46),³⁷

$$P = \frac{1}{l_1} \int_{-l_1/2}^{-l_1/2} \left[\int_{-\infty}^{+\infty} -i \frac{\omega}{2} \psi^* b_x dy \right] dz \quad (7-46)$$

which leads to

$$P^s = \left(\frac{\bar{k}_s}{k_s} \right)^2 \frac{\mu_0 \omega \bar{J}^2(k_s)}{4 k_s d (\alpha^2 + 1)} \left\{ \begin{array}{ll} 1, & n = 0 \\ 0, & n = 2, 4, 6, \dots \\ \frac{1}{2} \left(\frac{4}{n\pi} \right)^2, & n = 1, 3, 5, \dots \end{array} \right\} \quad (7-47)$$

\bar{k}_s is obtained from the dispersion relation, Eq. (7-45), k_s is obtained from Eq. (7-44c), $J(k_s)$ is the Fourier transform of $J_z(x)$ and is obtained as before for a flat current distribution. Note that even n produces no solution modes.

The radiation resistance is proportional to power as given by Eq. (7-47). When $n = 0$, the infinite width case, the lower cutoff frequency is taken as γH ; where k_s vanishes and the power and radiation resistance are finite because of the infinite behavior of α . For $N > 0$, finite width case, the power and radiation resistance would become infinitely large at the lower cutoff frequency where k_s is zero since this frequency is greater than γH and α is not infinite there. However, we can justify taking the lower cutoff frequency to be larger than this value at which k_s is zero. When magnetostatic wavelengths are small compared to transducer aperture, a well collimated beam is formed and beam spreading is negligible. When magnetostatic wavelengths approach or exceed transducer aperture, beam width increases, thereby permitting a smaller portion of the total energy leaving the transducer to reach the output. This means a lower radiation resistance. In the limit as the ratio of transducer aperture to wavelength approaches zero, one would expect radiation resistance to vanish. Thus, instead of taking the lower cutoff frequency to be the value at which k_s is zero and power and radiation resistance are infinite, we take the lower cutoff frequency to be the value at which

$$k_{sc} = n_c (n\pi / l_1) \quad (7-48)$$

where n_c is a constant determined so that MSW wavelength \leq aperture. Appreciable beam spreading occurs when wavelength and aperture are approximately equal, or when Eq. (7-48) is satisfied for n_c approximately equal to two, when $n = 1$. When $n > 1$, n_c is found to be less than 2. Except at the very beginning of the bandwidth the results are the same for the three n_c values so that the lower cutoff frequency value is not critical, as long as it is sufficiently higher than that for which k vanishes. This means that it is physically justifiable to remove the end of the bandwidth where k_s is zero so that the radiation resistance is not infinite and the radiation reactance and insertion loss may be calculated.

Values of radiation resistance and insertion loss for the first width mode, $n = 1$, and for $n_c = 1, 2$, and 3 are shown in Figures 7-11a and 7-11b.

7.4 Theory of MSW Transducers

Theory of MSW Transducers by Sethares and Weinberg³²

This paper provides an overview and comprehensive analysis of the two MSW transducer models, TL and TT. The starting point for the analysis is the expression for MSW power radiated away from an MSW generating structure, the transducer, and into a YIG slab. Details of how the generating source couples to MSW, and, how the two models are similar and how they differ is clarified. A quantitative connection between the two models is provided. The paper is highly recommended as an overview for MSW transducer modeling.

The abstract for Reference 32 is as follows: this is a review of two electrical equivalent circuits for multielement magnetostatic wave transducers. The two circuit models are identified as a transmission line and a two terminal model. Both models have been extended to all three principal MSW modes of propagation to the point where computer programs have been written to plot phase and amplitude response as measured by commercial network analyzers. A review is provided of the basic assumptions used, similarities and differences, advantages and disadvantages, and limitations of the two models. The useful range of validity covers many cases of practical interest in the 1 to 12 GHz frequency range

Details of all the results presented in Reference 32 are included throughout the present report.

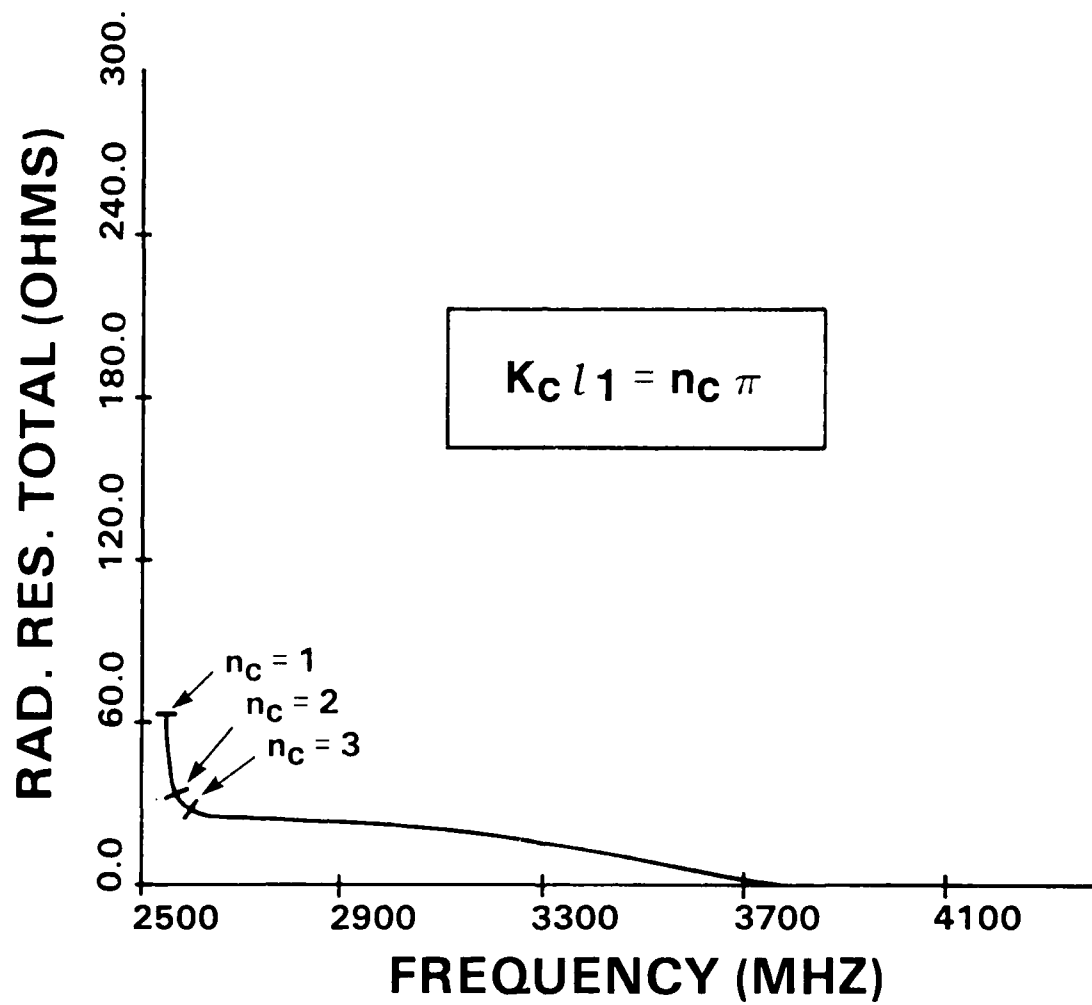


Figure 7-11a. FVW Width Mode. Radiation Resistance.

FORWARD VOLUME WAVES

2 TERMINAL MODEL

H= 893.0 T1= .1000E+01 G= .0

D=.250E-04 L= .100E+01 L1= .300E-02

A= .500E-04 P= .300E-03 DIST= .010 DH= .50E+00 ETA= 1. N= 1

RL= 0. WIDTH MODE= 1.

1ST (M=0) MODE

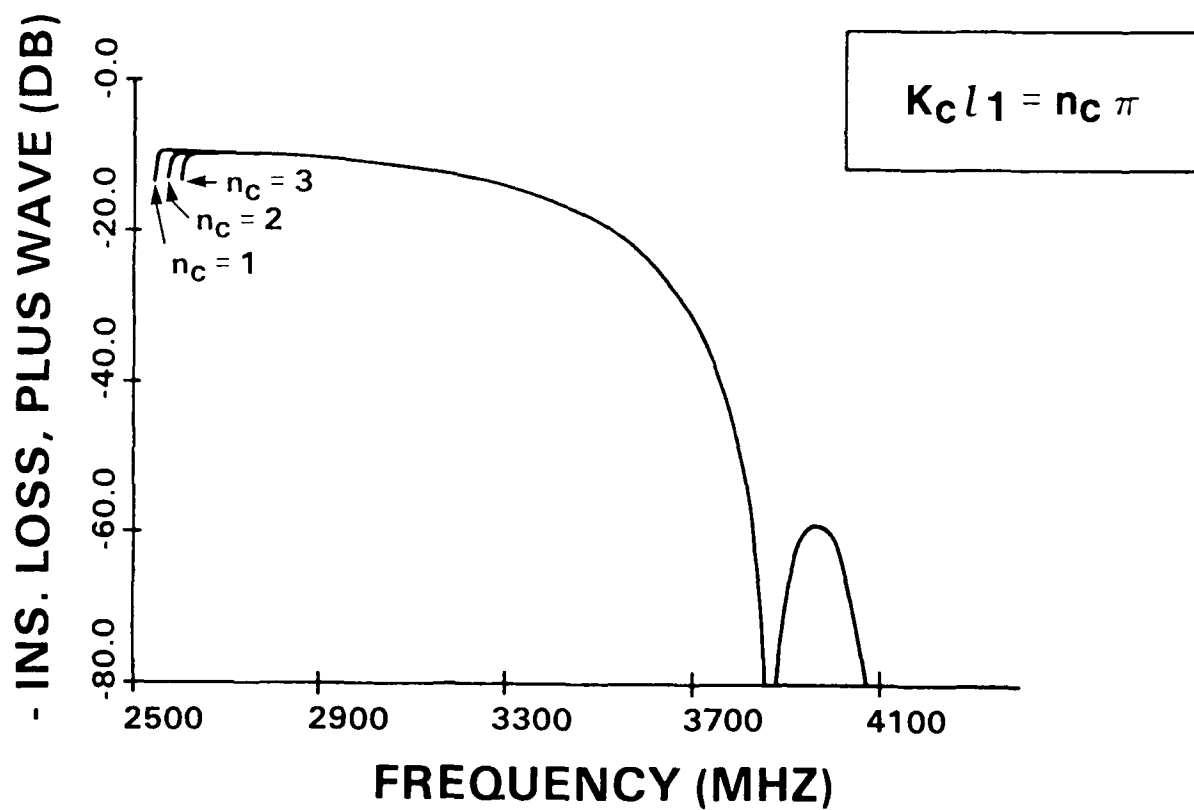


Figure 7-11b. FVW Width Mode. Insertion Loss.

References

1. Ganguly, A.K. and Webb, D.C. (1975) Microstrip Excitation of Magnetostatic Surface Waves: Theory and Experiment, *IEEE Trans. on Microwave Theory and Techniques*, **MTT-23** (No. 12): 988-1006.
2. Wu, H.J., Smith, C.V., and Collins, J.H. (1977, Sept.) Bandpass filtering with multibar MSW microstrip transducer, *Electron. Lett.* **13** (No. 20):610-611.
3. Emtage, P.R. (1978, Aug.) Interaction of magnetostatic waves with a current, *J. Appl. Phys.* **49**:4475-4484.
4. Sethares, J.C. (1979, Nov.) Magnetostatic Surface Wave Transducers, *IEEE Trans. on MTT*, **MTT-7** (No 11):902-909.
5. Merry, J.B. and Sethares, J.C. (1973, Sept.) Low Loss Magnetostatic Surface Waves at Frequencies up to 15 GHz, *IEEE Trans. on Magnetics*, **9** (No. 3):527-529.
6. Adam, J.D., Bennett, G.A., and Wilkinson, J. (1970) Experimental observation of magnetostatic modes in a YIG slab, *Electron Lett.* **6**:434.
7. Sethares, J.C. and Merry, J.B. (1974, Feb.) *Magnetostatic Surface Waves in Ferrimagnets Above 4 GHz*, AFCRL-TR-74-0112, Physical Sciences Research Paper, No. 587, AD780640.
8. Sethares, J.C. and Stiglitz, M.R. (1974, Sept.) Propagation Loss and MSSW Delay Lines, *IEEE Trans. on Magnetics*, **MAG-10** (No. 3):787-790.
9. Sethares, J.C. and Stiglitz, M.R. (1974) Magnetostatic Surface Wave Delay Lines, IEEE Catalog No. 74CH0838-3 MTT, Lib. of Congress No. 72-75863, pp 253-255.
10. Newburgh, R.G., Blacksmith, P., Budreau, A.J. and Sethares, J.C. (1974, Dec.) Acoustic and Magnetic Surface Wave Ring Interferometers for Rotation Rate Sensing, *Proc. of the IEEE*, **62** (No 12):1621-1628.
11. Newburgh, R.G., Blacksmith, P., and Sethares, J.C. (1975, Sept.) United States Patent No. 3,909,710.
12. Sethares, J.C. and Tsai, T. (1977, Sept.) Magnetic Anisotropy of (111) LPE/YIG Films on GGG in Parallel Resonance, *IEEE Trans. on Magnetics*, **MAG-13** (No. 5):1236-1237.
13. Tsai, T.L. and Sethares, J.C. Bandpass Filter Using LPE/YIG Films, Appendix D, unpublished note.

14. Tsai, T.L. and Sethares, J.C. (1977) Band Stop Filter Using LPE/YIG Films, *IEEE MTT-S*, Cat. No. 77CH1219 S, pp 526-527.
15. Frost, H.M., Szabo, T.L., and Sethares, J.C. (1975) The Flat Conductor Electromagnetic SAW Transducer: Theory and Experiment, IEEE Cat. No. 75CH0994-4SU, *Ultrasonics Symposium Proc.*, pp 601-603.
16. Szabo, T.L. and Sethares, J.C. (1977) Harmonic Operation of SAW Electromagnetic Transducers, IEEE Cat No. 77 CH1264-1SU, *Ultrasonics Symposium Proc.*
17. Sethares, J.C., Frost, H.M., and Szabo, T.L. (1977, Mar.) Fields of Flat Conductor Electromagnetic Surface Acoustic Wave Transducers, *IEEE Trans. on Sonics and Ultrasonics*, **SU-24** (No. 2):88-94.
18. Szabo, T.L., Frost, H.M., and Sethares, J.C., (1977, Nov.) Periodic Surface Acoustic Wave Electromagnetic Transducers, *IEEE Trans. on Sonics and Ultrasonics*, **SU-24** (No. 6):393-406.
19. Sethares, J.C. and Szabo, T.L. (1978, Mar.) A new model for the flat conductor electromagnetic SAW transducer, *Journal of Appl. Phys.* **49** (No. 3):1054-1060.
20. Thompson, R.B. (1973) A Model for the Electromagnetic Generation and Detection of Rayleigh and Lamb Waves, *IEEE Trans. on Sonics & Ultrasonics*, **SU-20**:340-346.
21. Engan, H. (1969) Excitation of Elastic Surface Waves by Spatial Harmonics of Interdigital Transducers, *IEEE Trans. on Electron Devices*, **ED-16**:1014.
22. Sethares, J.C., Tsai, T., and Koltunov, I. (1978, Apr.) *Periodic Magnetostatic Surface Wave Transducers*, RADC-TR-78-78, ADA057214.
23. Sethares, J.C. (1978, Jun.) Magnetostatic Surface Wave Transducer Design, IEEE International Microwave Theory and Techniques Symposium, Ottawa, Canada, published in *IEEE MTT Symposium Digest*.
24. Sethares, J.C. and Weinberg, I.J. (1979, Mar.) Apodization of variable coupling MSSW transducers, *J. of Appl. Phys.* **50** (No. 3):2458-2460.
25. Weinberg, I.J. and Sethares, J.C. (1978, Sept.) *Magnetostatic Wave Transducers With Variable Coupling*, RADC-TR-78-205, ADA063880.
26. Sethares, J.C. and Weinberg, I.J. (1979, Jul.) Insertion Loss of Apodized/Weighted and Nonuniform Magnetostatic Surface Wave, MSSW, Transducers, 1979 International MMM Conference, New York City, Paper 6C-8.
27. Sethares, J.C. (1983, Jan.) Magnetostatic Wave Transducers, 1981 RADC Microwave Magnetics Technology Workshop, June 10-11, 1981, published in RADC-TR-83-15, ADA126417, In House Report, *Proc. of the 1981 RADC Microwave Magnetics Technology Workshop*, pp 118-132.
28. Sethares, J.C. and Cohen, E. (1982, Nov.) Current Distribution on Gratings and Meander Lines: with MSW Applications, ADA126042, *IEEE Trans. on Magnetics*, **MAG-18** (No. 6):1613-1615.
29. Cohen, E. and Sethares, J.C. (1986) MSSW Back Reaction on a Generating Current Strip, *Journal of Magnetism and Magnetic Materials*, Elsevier Science Publishers B.V., **54-57**:1189-1190.
30. Weinberg, I.J. and Sethares, J.C. (1983) Magnetostatic Volume Waves, *IEEE MTT-S Digest*, pp 253-255.
31. Weinberg, I.J. and Sethares, J.C. (1984, April) Magnetostatic Forward Volume Wave Propagation - Finite Width, *IEEE Trans. on MTT*, **32** (No. 6):463-464.
32. Sethares, J.C. and Weinberg, I.J. (1985) Theory of MSW Transducers, *Circuits, Systems and Signal Processing*, **4** (No 1-2):41-62.
33. Ganguly, A.K., Webb, D.C., and Banks, C. (1978) Complex radiation impedance of microstrip excited magnetostatic surface waves, *IEEE Trans. on MTT*, pp 444-447.
34. Szabo, T.L. (1976) Advanced SAW electromagnetic transducer design, *Ultrasonics Symposium Proc.* IEEE Cat 76 CH1120 5SU.
35. Ishak, W., Hewlett Packard, Palo Alto, CA, Private Communication.
36. Emtage, P.R. (1982) Generation of MSSW by a microstrip, *J. of Appl. Phys.* **53**:5122.

37. Adam, J.D. and Bajpai, S.N. (1982, Nov.) Magnetostatic forward volume wave propagation in YIG strips, *IEEE Trans. on Magnetics*, **MAG-18** (No. 6):1598-1600.

8. TRANSDUCER CURRENT DENSITY AND RESPONSE

8.1 Introduction and Overview

Emtage¹ appears to have made the first serious attempt at determining the current profile across a strip residing on a YIG layer. He obtained a complex current density that exhibited even and odd spatial symmetry in magnitude and phase, respectively, about the strip center. Logarithmic phase singularities at the strip edges emerge from his study. Unfortunately, his analysis did not contend with finding $J(x)$ on one or more strips lifted off the YIG, with or without ground planes present, nor did it incorporate the YIG film thickness explicitly in the current density formula. In view of these limitations, and with an eye towards obtaining $J(x)$ on a receiving transducer as well as the generating element, we pursued an alternative formulation and solution technique.

Using the magnetic vector potential, an approximate quasimagnetostatic Green's function kernel was obtained for the integral equation governing $J(x)$ on a strip lifted off the YIG. In its present form, the Green's function is also relevant to the analysis of a transducer composed of several elements. The method used to get the Green's function can be applied to transducers with ground planes, although this was not pursued by us. It was found that despite the existence of a highly discontinuous, non-reciprocal component to the kernel, numerical inversion of the integral equation by collocation worked very well as evidenced by comparing Emtage's analytically derived $J(x)$ with our narrow strip results. Our numerical studies also predict oppositely flowing currents on the "wide" strips when a resonance condition involving the MSSW and the YIG-strip dimensions is satisfied. This chapter ends with a discussion of results, and includes plots of transducer response obtained using both the quasimagnetostatic analysis as well as a uniform current profile.

8.2 Statement of the Problem

We now consider a current-carrying strip near a YIG layer magnetically biased for surface wave propagation. The objective is to determine $J(x)$ on the strip and then its transform, $\tilde{J}(k)$. Figure 8-1 depicts the configuration of interest. $\tilde{J}(k)$ can then be incorporated into the Weinberg-Sethares code² for MSSW transducer response.

8.3 Field Equations

Maxwell's equations must be satisfied in the three regions, and boundary conditions enforced at $y = 0$, $y = -h$, and $y = \pm \infty$. The following field and permeability relationships are assumed in our model.

$$\mathbf{B}^{\oplus} = \mu_0 \mathbf{H}^{\oplus} = \nabla \times \mathbf{A}^{\oplus} ; \quad (8-1)$$

-
1. Emtage, P.R. (1982) Generation of magnetostatic surface waves by a microstrip, *J. Appl. Phys.* **53** (7):5122-5125.
 2. Weinberg, I.J. (1981, May) *Analysis and Concepts Studies for Magnetostatic Surface Wave Transducers*, RADC-TR-81-96, ADA102207.

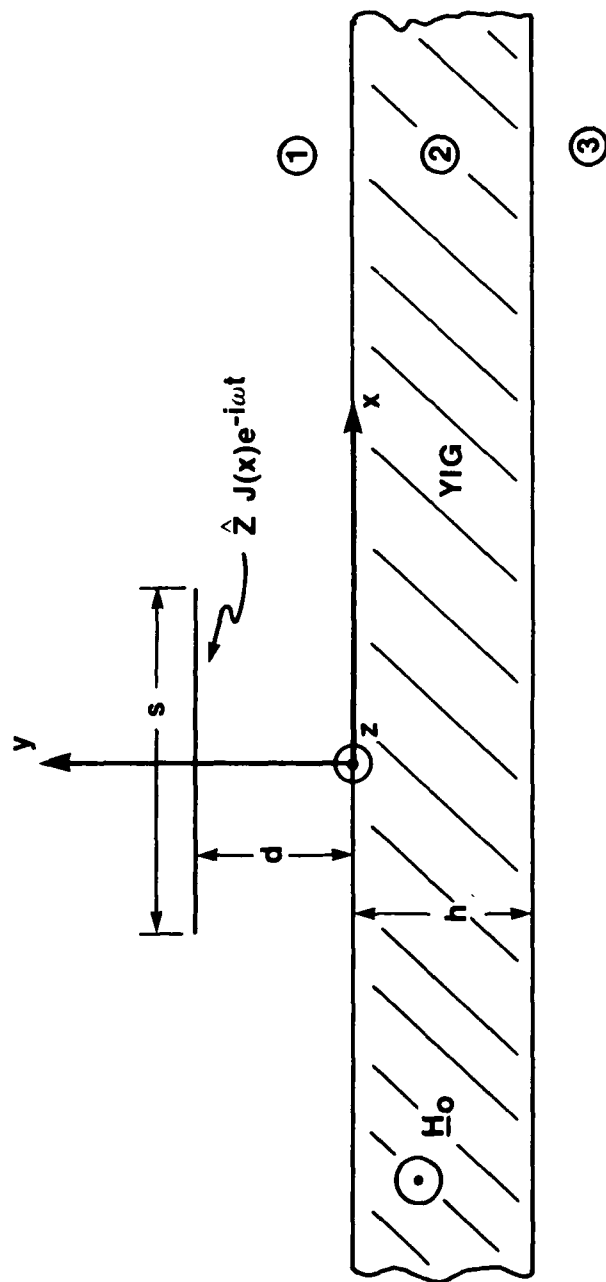


Figure 8-1. Transducer Geometry

$$\mathbf{B}^{(2)} = \mu_0 \underline{\underline{\mu}} \mathbf{H}^{(2)} = \nabla \times \mathbf{A}^{(2)} ; \quad (8-2)$$

$$\mathbf{B}^{(3)} = \mu_0 \mathbf{H}^{(3)} = \nabla \times \mathbf{A}^{(3)} ; \quad (8-3)$$

$$\nabla \cdot \mathbf{B}^{(1)} = \nabla \cdot \mathbf{B}^{(2)} = \nabla \cdot \mathbf{B}^{(3)} = 0 ; \quad (8-4)$$

$$\nabla \cdot \mathbf{D}^{(1)} = \nabla \cdot \mathbf{D}^{(2)} = \nabla \cdot \mathbf{D}^{(3)} = 0 ; \quad (8-5)$$

$$\underline{\underline{\mu}} = \begin{pmatrix} \mu_{11} & i\mu_{12} \\ -i\mu_{12} & \mu_{22} \end{pmatrix} ; \quad \underline{\underline{\mu}}^{-1} = \begin{pmatrix} b & -e \\ e & b \end{pmatrix} \quad (8-6)$$

(based on the linearized magnetization equation)

where

$$b = \frac{\mu_{11}}{\mu_{11}^2 - \mu_{12}^2} ; \quad (8-7)$$

$$\underline{\underline{\mu}} \underline{\underline{\mu}}^{-1} = \underline{\underline{I}} ; \quad (8-8)$$

and

$$e = \frac{i\mu_{12}}{\mu_{11}^2 - \mu_{12}^2} ; \quad (8-9)$$

for the surface wave case in which $\mu_{11} = \mu_{22}$. Maxwell's equations in the three regions take the following forms:

$$\nabla \times (\nabla \times \mathbf{A}^{(1)}) = \mu_0 \mathbf{J} + \mu_0 \frac{\partial \mathbf{D}^{(1)}}{\partial t} ; \quad (8-10)$$

$$\nabla \times \mathbf{E}^{(1)} = -\frac{\partial}{\partial t} (\nabla \times \mathbf{A}^{(1)}) ; \quad (8-11)$$

$$\nabla \times (\underline{\underline{\mu}}^{-1} \nabla \times \mathbf{A}^{(2)}) = \mu_0 \frac{\partial \mathbf{D}^{(2)}}{\partial t} ; \quad (8-12)$$

$$\nabla \times \mathbf{E}^{(2)} = -\frac{\partial}{\partial t} (\nabla \times \mathbf{A}^{(2)}) ; \quad (8-13)$$

$$\nabla \times (\nabla \times \mathbf{A}^{(3)}) = \mu_0 \frac{\partial \mathbf{D}^{(3)}}{\partial t} ; \quad (8-14)$$

$$\nabla \times \mathbf{E}^{(3)} = -\frac{\partial}{\partial t} (\nabla \times \mathbf{A}^{(3)}) . \quad (8-15)$$

Equation (8-11) yields

$$\mathbf{E}^{\textcircled{1}} = -\frac{\partial \mathbf{A}^{\textcircled{1}}}{\partial t} - \nabla \phi^{\textcircled{1}}, \quad (8-16)$$

and Eq. (8-10) becomes

$$\nabla (\nabla \cdot \mathbf{A}^{\textcircled{1}}) - \nabla^2 \mathbf{A}^{\textcircled{1}} = \mu_0 \mathbf{J} + \epsilon_1 \mu_0 \frac{\partial \mathbf{E}^{\textcircled{1}}}{\partial t}. \quad (8-17)$$

Inserting the expression for $\mathbf{E}^{\textcircled{1}}$ into the above gives

$$\nabla (\nabla \cdot \mathbf{A}^{\textcircled{1}}) - \nabla^2 \mathbf{A}^{\textcircled{1}} = \mu_0 \mathbf{J} - \epsilon_1 \mu_0 \left[\frac{\partial^2 \mathbf{A}^{\textcircled{1}}}{\partial t^2} + \nabla \left(\frac{\partial \phi^{\textcircled{1}}}{\partial t} \right) \right]. \quad (8-18)$$

Applying the Lorentz condition:

$$\nabla \cdot \mathbf{A}^{\textcircled{1}} + \epsilon_1 \mu_0 \frac{\partial \phi^{\textcircled{1}}}{\partial t} = 0 \quad (8-19)$$

leaves

$$\nabla^2 \mathbf{A}^{\textcircled{1}} - \epsilon_1 \mu_0 \frac{\partial^2 \mathbf{A}^{\textcircled{1}}}{\partial t^2} = -\mu_0 \mathbf{J}. \quad (8-20)$$

Similarly, for region ③:

$$\nabla^2 \mathbf{A}^{\textcircled{3}} - \epsilon_3 \mu_0 \frac{\partial^2 \mathbf{A}^{\textcircled{3}}}{\partial t^2} = 0 \quad (8-21)$$

when

$$\nabla \cdot \mathbf{A}^{\textcircled{3}} + \epsilon_3 \mu_0 \frac{\partial \phi^{\textcircled{3}}}{\partial t} = 0. \quad (8-22)$$

For region ②, since

$$\nabla \times (\underline{\underline{\mu}}^{-1} \nabla \times \mathbf{A}^{\textcircled{2}}) = \underline{\underline{\mu}}^{-1} \nabla (\nabla \cdot \mathbf{A}^{\textcircled{2}}) - (\nabla \cdot \underline{\underline{\mu}}^{-1} \nabla) \mathbf{A}^{\textcircled{2}} \quad (8-23)$$

we get

$$\underline{\underline{\mu}}^{-1} \nabla (\nabla \cdot \mathbf{A}^{\textcircled{2}}) - (\nabla \cdot \underline{\underline{\mu}}^{-1} \nabla) \mathbf{A}^{\textcircled{2}} = \mu_0 \epsilon_2 \left[-\frac{\partial \mathbf{A}^{\textcircled{2}}}{\partial t} - \nabla \phi^{\textcircled{2}} \right]. \quad (8-24)$$

The corresponding gauge requires imposing the condition

$$\underline{\underline{\mu}}^{-1} \nabla (\nabla \cdot \mathbf{A}^{\textcircled{2}}) + \mu_0 \epsilon_2 \frac{\partial}{\partial t} (\nabla \phi^{\textcircled{2}}) = 0, \quad (8-25)$$

leaving

$$(\nabla \cdot \underline{\underline{\mu}}^{-1} \nabla) \mathbf{A}^{\textcircled{2}} + \epsilon_2 \mu_0 \frac{\partial^2 \mathbf{A}^{\textcircled{2}}}{\partial t^2} = 0. \quad (8-26)$$

Assuming that

$$A_z = A e^{-i \omega t} \quad (8-27)$$

and

$$J_z = J e^{-i \omega t} \quad (8-28)$$

since the permeability tensor itself was also based on an $\exp(-i \omega t)$ assumption, the wave equations governing the z-component of the vector potential fields reduce to

$$\nabla^2 A^{(1)} + \mu_0 \epsilon_1 \omega^2 A^{(1)} = -\mu_0 J ; \quad (8-29)$$

$$\nabla \cdot (\underline{\underline{\mu}}^{-1} \nabla) A^{(2)} + \mu_0 \epsilon_2 \omega^2 A^{(2)} = 0 ; \quad (8-30)$$

and

$$\nabla^2 A^{(3)} + \mu_0 \epsilon_3 \omega^2 A^{(3)} = 0 . \quad (8-31)$$

For a line current source at \mathbf{r}_0 ,

$$J(x, y) = I \delta(\mathbf{r} - \mathbf{r}_0) . \quad (8-32)$$

and the vector potential becomes proportional to the Green's function of the system. With subscripts x, y denoting partial derivatives, the wave equations become the following:

$$A_{xx}^{(1)} + A_{yy}^{(1)} + \mu_0 \epsilon_1 \omega^2 A^{(1)} = -\mu_0 I \delta(\mathbf{r} - \mathbf{r}_0) ; \quad (8-33)$$

$$A_{xx}^{(2)} + A_{yy}^{(2)} + (\mu_0 \epsilon_2 \omega^2 / b) A^{(2)} = 0 ; \text{ and,} \quad (8-34)$$

$$A_{xx}^{(3)} + A_{yy}^{(3)} + \mu_0 \epsilon_3 \omega^2 A^{(3)} = 0 . \quad (8-35)$$

Representing the surface current on a perfectly conducting strip by a continuous density of line currents, it follows that the total vector potential field about the strip can be expressed as a superposition of potentials from a weighted density of line currents.

8.4 Boundary Conditions

Using the relationships governing \mathbf{B} , \mathbf{H} , and \mathbf{A} from Eqs. (8-1) - (8-3), one obtains the boundary conditions in terms of \mathbf{A} :

$$(i.) \text{ At } y = 0, \text{ (continuity of normal B):} \quad A_x^{(1)} = A_x^{(2)} \quad (8-36)$$

$$\text{(continuity of tangential H):} \quad A_y^{(1)} = b A_y^{(2)} + c A_x^{(2)} \quad (8-37)$$

$$(ii.) \text{ At } y = -h, \text{ (continuity of normal B):} \quad A_x^{(2)} = A_x^{(1)} \quad (8-38)$$

$$(\text{continuity of tangential H}): \quad A_y^{\textcircled{3}} = b A_y^{\textcircled{2}} + e A_x^{\textcircled{2}} . \quad (8-39)$$

$$(\text{iii.}) \text{ At } |y| = \infty, \quad A^{\textcircled{1}} = A^{\textcircled{3}} = 0 . \quad (8-40)$$

In the quasimagnetostatic limit, the wave equations reduce to

$$A_{xx}^{\textcircled{1}} + A_{yy}^{\textcircled{1}} \approx -\mu_0 I \delta(\mathbf{r} - \mathbf{r}_0) ; \quad (8-41)$$

$$A_{xx}^{\textcircled{2}} + A_{yy}^{\textcircled{2}} \approx 0 ; \quad (8-42)$$

$$A_{xx}^{\textcircled{3}} + A_{yy}^{\textcircled{3}} \approx 0 . \quad (8-43)$$

with

$$k_1^2 = \mu_0 \epsilon_1 \omega^2 , \quad (8-44)$$

$$k_2^2 \equiv -k_s^2 = \mu_0 \epsilon_2 \omega^2 / b , \quad (8-45)$$

and

$$k_3^2 = \mu_0 \epsilon_3 \omega^2 , \quad (8-46)$$

an examination of $|k_1|$, $|k_2|$, and $|k_3|$ at frequencies spanning the surface wave band shows that $|k_2|$ is significantly larger than the other two, especially over the lower portion of the band. For a lossless YIG layer sandwiched between GGG media, $\epsilon_1 \approx \epsilon_2 \approx \epsilon_3$, making the propagation constant in the YIG a factor of $|b|^{-1/2}$ larger in magnitude. Table 8-1 displays b^{-1} at several frequencies for a biasing field of $H_0 = 375$ oersteds.

Table 8-1. Frequency vs. $1/b$

$f = 2.5 \text{ Ghz}$	$1/b = -1166.$
2.6	-55.89
2.8	-17.31
3.0	-12.48
3.2	-6.302
3.4	-4.488

It was thus decided that the following extended quasimagnetostatic field equations would be used instead:

$$A_{xx}^{\textcircled{1}} + A_{yy}^{\textcircled{1}} \approx -\mu_0 I \delta(\mathbf{r} - \mathbf{r}_0) ; \quad (8-47)$$

$$A_{xx}^{\textcircled{2}} + A_{yy}^{\textcircled{2}} - k_s^2 A^{\textcircled{2}} = 0 \quad (8-48)$$

and

$$A_{xx}^{(3)} + A_{yy}^{(3)} \approx 0. \quad (8-49)$$

8.5 Fourier Integral Solutions

Fourier integral solutions of the form

$$bA^{(1)} = \ln[x^2 + (y-d)^2] + \int_{-\infty}^{\infty} dk e^{ikx} e^{-|k|y} B_1(k), \quad (8-50)$$

$$bA^{(2)} = \int_{-\infty}^{\infty} dk e^{ikx} \left[C_1(k) e^{y\sqrt{k^2 + k_s^2}} + C_2(k) e^{-y\sqrt{k^2 + k_s^2}} \right], \quad (8-51)$$

and

$$bA^{(3)} = \int_{-\infty}^{\infty} dk e^{ikx} D_1(k) e^{(y+h)|k|} \quad (8-52)$$

were assumed for the field equations (8-47) - (8-49), with the constant b given by

$$b = - \left(\frac{\mu_0 I}{4\pi} \right)^{-1} \quad (8-53)$$

since the vector potential near a line current goes as

$$A = - \frac{\mu_0 I}{2\pi} \ln \sqrt{x^2 + (y-d)^2} + \dots \quad (8-54)$$

It follows that the boundary condition at $y = +\infty$ is satisfied by the integral portion of $A^{(1)}$, while the condition at $y = -\infty$ is satisfied by $A^{(3)}$. The log portion of $A^{(1)}$ is actually the quasimagnetostatic limiting form of the free-space Green's function, that is,

$$-H_o^{(1)} \left[k_1 \sqrt{x^2 + (y-d)^2} \right] \quad (8-55)$$

which vanishes as $y \rightarrow +\infty$. Since uniform levels of potential have no influence on the shape of $J(x)$ in the generating strip problem, they can be dropped or ignored. The total current carried by the strip is eventually normalized to I_o . For the approximation being pursued, the line current is taken to be "close" to the YIG in the sense that $k_1 d \ll 1$.

8.6 Determination of $B_1(k)$

The procedure now is to substitute the assumed solutions into the boundary conditions at $y = 0$ and $y = -h$, take the inverse Fourier transform of the resulting equations, and obtain the amplitude $B_1(k)$. The boundary conditions at $y = -h$ yield

$$D_1(k) = C_1(k)e^{-h\sqrt{k^2 + k_s^2}} + C_2(k)e^{h\sqrt{k^2 + k_s^2}} \quad (8-56)$$

and

$$D_1(k)|k| = b\sqrt{k^2 + k_s^2} \left[C_1(k)e^{-h\sqrt{k^2 + k_s^2}} - C_2(k)e^{h\sqrt{k^2 + k_s^2}} \right] + iek \left[C_1(k)e^{-h\sqrt{k^2 + k_s^2}} + C_2(k)e^{h\sqrt{k^2 + k_s^2}} \right] \quad (8-57)$$

Applying the conditions at $y = 0$ leads to

$$-B_1(k) + C_1(k) + C_2(k) = h_1(k)/|k| \quad (8-58)$$

and

$$|k|B_1(h) + \left[b\sqrt{k^2 + k_s^2} + iek \right] C_1(k) + \left[-b\sqrt{k^2 + k_s^2} + iek \right] C_2(k) = h_2(k), \quad (8-59)$$

where

$$h_1(k) = \frac{1}{2\pi} \int_{-\infty}^{\infty} dx e^{-ikx} \frac{2x}{x^2 + d^2} = -i \operatorname{sgn}(k) e^{-|k|d} \quad (8-60)$$

and

$$h_2(k) = \frac{(-2d)}{2\pi} \int_{-\infty}^{\infty} dx \frac{e^{-ikx}}{x^2 + d^2} = -e^{-|k|d} \quad (8-61)$$

$D_1(k)$ can be eliminated from the $y = -h$ results; $C_2(k)$ is then a function of $C_1(k)$. Substituting into the $y = 0$ boundary condition results gives

$$-B_1(k) + C_2(k) \left\{ 1 + e^{2h\sqrt{k^2 + k_s^2}} \left[\frac{b\sqrt{k^2 + k_s^2} - iek + |k|}{b\sqrt{k^2 + k_s^2} + iek - |k|} \right] \right\} = (|k|)^{-1} h_1(k) \quad (8-62)$$

and

$$|k|B_1(k) + C_2(k) \left\{ \left[-b\sqrt{k^2 + k_s^2} + iek \right] + \left[b\sqrt{k^2 + k_s^2} + iek \right] \times e^{2h\sqrt{k^2 + k_s^2}} \left[\frac{b\sqrt{k^2 + k_s^2} - iek + |k|}{b\sqrt{k^2 + k_s^2} + iek - |k|} \right] \right\} = h_2(k) \quad (8-63)$$

Since the vector potential in region (1) gives the Green's function of interest, we need solve only for $B_1(k)$, which can be expressed as

$$B_1(k) = \frac{\text{numerator}}{\text{denominator}} \quad (8-64)$$

After some algebra one obtains

$$\text{num.} = \frac{2}{|k|} e^{-|k|d} \cdot e^{h\sqrt{k^2 + k_s^2}} \cdot \sinh h\sqrt{k^2 + k_s^2} [iek - |k| + b\sqrt{k^2 + k_s^2}] \quad (8-65)$$

and

$$\text{den.} = - \frac{2e^{h\sqrt{k^2 + k_s^2}} \cdot \sinh h\sqrt{k^2 + k_s^2}}{[b\sqrt{k^2 + k_s^2} + iek - |k|]} \quad (8-66)$$

$$\times \left\{ b^2(k^2 + k_s^2) + k^2 e^2 + |k|^2 + 2b|k|\sqrt{k^2 + k_s^2} \cdot \coth h\sqrt{k^2 + k_s^2} \right\}$$

Finally,

$$B_1(k) = \frac{e^{-|k|d}}{D(k)} \left\{ |k| q_{\pm}(k) + \frac{D(0)}{|k|} \right\} \quad (8-67)$$

where

$$D(k) = k_s^2 b^2 + k^2(1 + e^2 + b^2) + 2b|k|\sqrt{k^2 + k_s^2} \coth(h\sqrt{k^2 + k_s^2}) \quad (8-68)$$

$$q_{\pm}(k) = (b^2 - |e|^2 - 1) + 2|e|\text{sgn}(k) \quad (8-69)$$

and

$$\text{sgn}(k) = \begin{cases} 1 & k > 0 \\ -1 & k < 0 \end{cases} \quad (8-70)$$

For (b A⁰), the YIG-induced portion of the Green's function is denoted by

$$G_{\pm} = \int_{-\infty}^{\infty} dk e^{ikx} \cdot e^{-|k|y} \cdot B_1(k) \quad (8-71)$$

and must be calculated.

8.7 Evaluation of Green's Function

8.7.1 INTRODUCTION

The field generated by the presence of the YIG film near the line source is given by the Fourier integral of generalized functions:

$$G_{\pm} = \int_{-\infty}^{\infty} dk e^{ikx} \frac{e^{-|k|(y+d)}}{D(k)} \left\{ |k| q_{\pm}(k) + \frac{D(0)}{|k|} \right\} \quad (8-72)$$

Since

$$\frac{A^{(1)}}{(\mu_0 I / 4\pi)} = \ln[x^2 + (y - d)^2] + G_{\pm} \quad (8-73)$$

the total Green's function is thus taken to be

$$G = -\frac{1}{2} \left\{ \ln[x^2 + (y - d)^2] + G_{\pm} \right\}. \quad (8-74)$$

The tasks remaining are as follows:

1. Evaluate G_{\pm} for $y = d$ and x spanning the strip; and,
2. Using G_{\pm} , numerically invert the Fredholm integral equation of the first kind for the current density on the strip.

The first of the two is now addressed.

8.7.2 CALCULATION OF G_{\pm}

G_{\pm} may be re-written as

$$G_{\pm} = \int_{-\infty}^{\infty} dk e^{ikx} \cdot e^{-|k|(y+d)} \left\{ \frac{|k| q_{\pm}(k)}{D(k)} + \frac{\frac{D(0)}{D(k)} - 1}{|k|} \right\} + \int_{-\infty}^{\infty} dk e^{ikx} \frac{e^{-|k|(y+d)}}{|k|}. \quad (8-75)$$

The last integral is readily shown to correspond to the image field of the line source plus a term constant with respect to x variations:

$$-\ln[x^2 + (y + d)^2] + \ln(y + d)^2. \quad (8-76)$$

See Appendix to this chapter.

The remaining integrand can be shown to be non-singular and non-analytic at $k = 0$. The integration over k is, therefore, assumed to span two intervals: $(-\infty, 0^-)$ and $(0^+, +\infty)$. To within an additive constant, the total Green's function, G , takes the form

$$-2G = \ln \left[\frac{x^2 + (y - d)^2}{x^2 + (y + d)^2} \right] + \int_{-\infty}^{\infty} dk f(k). \quad (8-77)$$

where

$$f(k) = e^{ikx} \cdot e^{-|k|(y+d)} \left\{ \frac{|k| q_{\pm}(k)}{D(k)} + \frac{\frac{D(0)}{D(k)} - 1}{|k|} \right\}. \quad (8-78)$$

Assuming lossless media, the Fourier integral can be evaluated along the 2 semi-infinite, Real k -axis paths and around the poles of $D(k)$ as shown in Figure 8-2, in a manner consistent with outgoing fields for an $\exp(-i\omega t)$ time variation.

In Figure 8-2, the points 0^+ and 0^- actually correspond to the quasimagnetostatic limit positions of the branch points at $\pm k_1$, whose existence is revealed by a full-wave formulation. In our

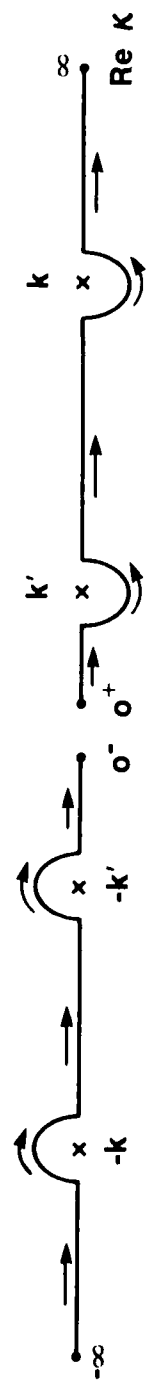


Figure 8-2. Effective Integration Paths in the Quasimagnetostatic Limit, Neglecting Uniform Potential Contributions

approximate analysis, contributions from integration paths around the (merging) branch points were ignored because they led to uniform potentials. Also, the interval $(-k_1, +k_1)$ itself vanishes.

The poles of the integrand are found to be well approximated by

$$K \approx \pm K_{\text{MSSW}} \quad (8-79)$$

and

$$K' \approx \pm \frac{1}{2} |\beta| k_s^2 h \quad (8-80)$$

where K' follows by considering k to be very small in $D(k) = 0$. Using these quantities for starting values, several iterations of a Newton-Raphson scheme gives excellent estimates of the roots. Unlike earlier MSSW formulations (with $k = 0$, identically), $D(k)$ is found to have 4 real roots instead of the 2 at $\pm K_{\text{MSSW}}$.

In the limit, as the radii of the semi-circular paths of the integration about K' and K vanish, the integrals around the poles lead to residue contributions R :

$$\pi i R = \pi i [\text{Res}(k = K') + \text{Res}(k = K) - \text{Res}(k = -K') - \text{Res}(k = -K)] , \quad (8-81)$$

while the real-axis integrations must be performed in the sense of Cauchy Principal-Value. One is left with

$$-2G = \ln \frac{x^2 + (y - d)^2}{x^2 + (y + d)^2} + \pi i R + \int_{-\infty}^{\infty} dk f(k) . \quad (8-82)$$

It remains to determine the residues of $f(k)$ at $k = \pm K'$ and $\pm K$, and to evaluate the Principal-Value integral of $f(k)$. (Note: a line across the integral sign means, as in the last term of Eq. (8-82), that the principal value is to be used.)

8.7.3 REAL-AXIS INTEGRATION

The evaluation of the Principal-Value integral will now be considered for $x > 0$. Negative values for x just require the complex conjugate.

$x > 0$:

$$\int_{-\infty}^{\infty} dk f(k) = \int_{0^+}^{\infty} dk [f(k) + f(-k)] . \quad (8-83)$$

Observe that

$$\begin{aligned} \int_{0^+}^{\infty} dk f(k) &= \int_{0^+}^{\infty} dk \frac{e^{-|k|(y+d)}}{D(k)} \left\{ |k| [\beta^2 - 1 - |e|^2] + \frac{D(0) - D(k)}{|k|} \right\} e^{ikx} \\ &+ \int_{0^+}^{\infty} dk \frac{e^{-|k|(y+d)}}{D(k)} \{ |k| \cdot 2 \cdot |e| \} e^{ikx} \\ &\equiv B(q_{\pm}) \end{aligned} \quad (8-84)$$

Similarly,

$$\begin{aligned} \int_{0^+}^{\infty} dk f(-k) &= \int_{0^+}^{\infty} dk \frac{e^{-|k|(y+d)}}{D(k)} \left\{ |k| [\epsilon^2 - 1 - |\epsilon|^2] + \frac{D(0) - D(k)}{|k|} \right\} e^{-ikx} \\ &+ \int_{0^+}^{\infty} dk \frac{e^{-|k|(y+d)}}{D(k)} \{-|k| \cdot 2|\epsilon|\} e^{-ikx} \\ &\equiv B^*(q_-) . \end{aligned} \quad (8-85)$$

Adding terms yields for $x > 0$,

$$\int_{-\infty}^{\infty} dk f(k) = B(q_+) + B^*(q_-) . \quad (8-86)$$

In a similar fashion it follows that for negative x , that is, $x = -|x|$,

$$\int_{-\infty}^{\infty} dk f(k) = [B^*(q_+) + B(q_-)] , \quad (8-87)$$

which is just the complex conjugate of the positive x result. The Principal-Value integrals thus require Real-axis integrations over the semi-infinite interval $(0^+, +\infty)$ involving the quantities $B(q_{\pm})$.

8.7.4 EVALUATION OF $B(q_{\pm})$

The task is to determine $B(q_{\pm})$ for $x > 0$.

$$B(q_{\pm}) = \int_{0^+}^{\infty} dk e^{ikx} e^{-|k|(y+d)} \left\{ \frac{|k| q_{\pm}}{D(k)} + \frac{\frac{D(0)}{D(k)} - 1}{|k|} \right\} \quad (8-88)$$

$$\equiv \int_0^{\infty} dk h_{\pm}(k) e^{-\gamma k} \quad (8-89)$$

with

$$\gamma = y + d - ix . \quad (8-90)$$

Since the poles of $D(k)$ satisfy the relationship

$$0 \leq |K'| \ll |K| , \quad (8-91)$$

it is useful to partition the semi-infinite range of integration into the two ranges $(0^+, 2K)$ and $(2K, +\infty)$. The finite range integration will be considered first.

8.7.4.1 Finite Range Integration

Observe that

$$\begin{aligned} \oint_{0^+}^{2K} dk e^{-\gamma k} h_{\pm}(k) &= \int_{0^+}^{2K} dk e^{-\gamma k} \left[h_{\pm}(k) - \frac{C_0^{\pm}}{k - K'} - \frac{C_1^{\pm}}{k - K} \right] \\ &+ \oint_{0^+}^{2K} dk e^{-\gamma k} \left[\frac{C_0^{\pm}}{k - K'} + \frac{C_1^{\pm}}{k - K} \right]. \end{aligned} \quad (8-92)$$

For the first integral to be non-singular, C_0^{\pm} and C_1^{\pm} must correspond to the residues of $h_{\pm}(k)$:

$$C_0^{\pm} = \lim_{k \rightarrow K'} (k - K') h_{\pm}(k) \quad (8-93)$$

and

$$C_1^{\pm} = \lim_{k \rightarrow K} (k - K) h_{\pm}(k). \quad (8-94)$$

With $h_{\pm}(k)$ expressed by

$$\frac{k q_{\pm}(k) + [D(0) - D(k)]/k}{D(k)} \equiv \frac{n(k)}{D(k)}, \quad (8-95)$$

it follows that

$$C_0^{\pm} = \left. \frac{n(k)}{D'(k)} \right|_{k=K'} \quad (8-96)$$

and

$$C_1^{\pm} = \left. \frac{n(k)}{D'(k)} \right|_{k=K} \quad (8-97)$$

where

$$\begin{aligned} D'(k) &= 2k(1 + e^2 + b^2) + 2b \left\{ \left[\sqrt{k^2 + k_s^2} + \frac{k^2}{\sqrt{k^2 + k_s^2}} \right] \coth \left(h \sqrt{k^2 + k_s^2} \right) \right. \\ &\quad \left. - k^2 h \operatorname{csch}^2 \left(h \sqrt{k^2 + k_s^2} \right) \right\}. \end{aligned} \quad (8-98)$$

Having obtained C_0^{\pm} and C_1^{\pm} , we can address the determination of the singular and non-singular integrals.

For the singular integrals, observe that

$$\int_{0^+}^{2K} dk \frac{e^{-\gamma k}}{k - K'} = \int_{0^+}^{2K'} dk \frac{e^{-\gamma k}}{k - K'} + \int_{2K'}^{2K} dk \frac{e^{-\gamma k}}{k - K'}. \quad (8-99)$$

For transducers, $|\gamma K'| \ll 1$. Substituting $w = (k - K')/K'$ gives the following excellent approximation for the first integral on the r.h.s.:

$$e^{-\gamma K'} (-2\gamma K') + \dots \quad (8-100)$$

For the second, inserting w yields

$$e^{-\gamma K'} \{E_1[\gamma K'] - E_1[\gamma(2K - K')]\}, \quad (8-101)$$

where $E_1[\cdot]$ denotes the Exponential integral. See Reference 3.

The singular integral involving C_1^\pm was put in the form

$$\int_{0^+}^{2K} dk \frac{e^{-\gamma k}}{k - K} = e^{-\gamma K} \int_{-1}^1 dw \frac{e^{-\gamma K w}}{w} \quad (8-102)$$

and accurately evaluated using an even-point Gauss quadrature. Finally, the non-singular contribution

$$\int_{0^+}^{2K} dk e^{-\gamma k} \left[h_\pm(k) - \frac{C_0^\pm}{k - K'} - \frac{C_1^\pm}{k - K'} \right] \quad (8-103)$$

was evaluated using 32-point Gauss quadrature and compared well with a 64-point Gauss quadrature scheme in the sense that discrepancies between the two appeared only in the 10th significant digit for the cases tested. This completes the integration over the range $(0^+, 2K)$.

The residues of $f(k)$, R , are simply the residues of $e^{-\gamma |k|} h_\pm(k)$; namely,

$$\text{Res}(k = \pm K') = C_0^\pm e^{-\gamma |K'|} \quad (8-104)$$

and

$$\text{Res}(k = \pm K) = C_1^\pm e^{-\gamma |K|}. \quad (8-105)$$

8.7.4.2 Semi-Infinite Range Integration

The integrand is non-singular over the range $(2K, +\infty)$; however, it can fall off as slowly as $1/k$ for large k . For the purposes of efficient and accurate computation, it is useful to "subtract off" the asymptotic behavior of the integrand and then to "add back" its effect into the final answer as shown:

-
3. Abramowitz and Stegun (1964) *Handbook of Math. Functions*, National Bureau of Standards, Applied Mathematics Series, No. 55, Government Printing Office, pp 228-229.

$$\int_{2K}^{\infty} dk e^{-\gamma k} h_{\pm}(k) = \int_{2K}^{\infty} dk e^{-\gamma k} \underbrace{\left[h_{\pm}(k) + \frac{1}{k} \right]}_{g(k)} - \int_{2K}^{\infty} dk \frac{e^{-\gamma k}}{k} \quad (8-106)$$

$$= \int_{2K}^{\infty} dk e^{-\gamma k} [g(k) - g_{\infty}(k)] + \int_{2K}^{\infty} dk e^{-\gamma k} g_{\infty}(k) - E_1[2K\gamma] . \quad (8-107)$$

$g_{\infty}(k)$ denotes the asymptotic form of $g(k)$ and results when

$$\coth\left(h \sqrt{k^2 + k_s^2}\right) \rightarrow 1 . \quad (8-108)$$

for $kh \gg 1$

After some algebra one obtains

$$g_{\infty}(k) = \frac{[k q_{\pm} + D(0)/k] D_{\infty}^{-1}}{k^2 - E_{\infty} D_{\infty}^{-1}} \quad (8-109)$$

where

$$E_{\infty} = (1 - |\beta|) |\beta| k_s^2 \quad (8-110)$$

and

$$D_{\infty} = 1 + e^2 + \beta^2 + 2\beta . \quad (8-111)$$

A partial fraction expansion of $g_{\infty}(k)$ yields:

$$g_{\infty}(k) = \frac{D_1}{k} + D_2 \left[\frac{1}{k - c} + \frac{1}{k + c} \right] , \quad (8-112)$$

where

$$D_1 = -D(0)/E_{\infty} . \quad (8-113)$$

$$D_2 = \frac{1}{2} [q_{\pm}/D_{\infty} + D(0)/E_{\infty}] . \quad (8-114)$$

and

$$c = \sqrt{E_{\infty}/D_{\infty}} . \quad (8-115)$$

Finally, substituting Eqs. (8-112) - (8-115) into

$$\int_{2K}^{\infty} dk e^{-\gamma k} g_{\infty}(k) \quad (8-116)$$

produces:

$$D_1 E_1 [2K\gamma] + D_2 \{ e^{-\gamma c} E_1 [\gamma(2K - c)] + e^{+\gamma c} E_1 [\gamma(2K + c)] \} . \quad (8-117)$$

The remaining integral to be evaluated takes the form

$$I = \int_{2K}^{\infty} dk e^{-\gamma k} Q(k) \quad (8-118)$$

where

$$Q(k) = g(k) - g_{\infty}(k) . \quad (8-119)$$

The exponential decay of the integrand helps the computation of I only when the source and field points are "far" from the YIG surface. But very important cases arise when they are even moderately close to the surface. The only analytical benchmark for J(x) available to us was for a current-carrying strip on the YIG surface. A method of integration appropriate for a wide range of strip-YIG separations is now discussed.

Let $k = v/x + 2K$, and substitute into I to get

$$I = \frac{e^{-2K\gamma}}{x} \int_0^{\infty} dv e^{-\left(\frac{y+d}{x}\right)v} \cdot e^{iv} \cdot Q\left[k = \frac{v}{x} + 2K\right] . \quad (8-120)$$

The procedure adopted for the evaluation of I was to integrate over N half-periods of the sine and cosine integrals, separately, to form 4 sets of partial sums as Bubenik⁴ did. Each sequence of partial sums was then extrapolated to $N \rightarrow \infty$ using a Shank's transformation.⁵ A modified Shank's transformation was implemented⁶ but did not perform better than the simpler version. $N = 60$ was found to be more than adequate for all cases investigated. Each half-period integral was calculated using 32-point Gauss quadrature.

In summary, for $x > 0$

$$B(q_{\pm}) = \int_{2K}^{\infty} dk \dots + \int_{2K}^{\infty} dk \dots \quad (8-121)$$

-
4. Bubenik, D.M. (1977, Nov.) A practical method for the numerical evaluation of Sommerfeld integrals, *IEEE Trans. Ant. and Prop.* **AP-25** (6):904-906.
 5. Hamming (1973) *Numerical Methods for Engineers*, McGraw Hill, New York, pp 205-207.
 6. Broeck and Schwartz (1979 May) A One-Parameter Family of Sequence Transformations, *SIAM J. Math. Analysis* **10** (3):658-666.

with

$$\begin{aligned} \int_{0^+}^{2K} dk \dots = & \int_{0^+}^{2K} dk e^{-\gamma k} \left[h_{\pm}(k) - \frac{C_0^{\pm}}{k - K'} - \frac{C_1^{\pm}}{k - K} \right] \\ & + C_0^{\pm} e^{-\gamma K'} \{ -2\gamma K' + E_1[\gamma K'] - E_1[\gamma(2K - K')] \} \\ & + C_1^{\pm} e^{-\gamma K} \cdot \int_{-1}^1 dw \frac{e^{-\gamma K w}}{w} \end{aligned} \quad (8-122)$$

and

$$\int_{2K}^{\infty} dk \dots = D_1 E_1 [2K\gamma] + D_2 \{ e^{-\gamma c} E_1[\gamma(2K - c)] + e^{+\gamma c} E_1[\gamma(2K + c)] \} + I \quad (N \rightarrow \infty) . \quad (8-123)$$

8.8 Numerical Inversion of the Integral Equation

A collocation method is now described for inverting the Fredholm integral equation of the first kind governing $J(x)$. It is convenient to use the dimensionless source and field point variables

$$u = 2x'/s \text{ and } w = 2x/s \quad (8-124)$$

for a strip of length s . The equation takes the form

$$A(w) = \int_{-1}^1 du J(u) G(w - u) . \quad (8-125)$$

To determine $J(u)$ at the uniformly spaced source points

$$u_j = (2j - 1 - M)/M \quad j = 1, 2, \dots, M, \quad (8-126)$$

we evaluate $A(w)$ on the strip at the collocated field points

$$w_k = (2k - 1 - M)/M \quad k = 1, 2, \dots, M, \quad (8-127)$$

and consider a rectangular integration scheme. It follows that $\Delta u = \Delta w = 2/M$ and that the endpoints of the strip are not sampled. A system of M linear equations in M unknowns results, namely:

$$A(w_k) = \sum_{\substack{j=1 \\ j \neq k}}^M \int_{u_j - 1/M}^{u_j + 1/M} du J(u) G(w_k - u) + \int_{w_k - 1/M}^{w_k + 1/M} du J(u) G(w_k - u) , \quad (8-128)$$

which can be approximated by

$$A(w_k) = \Delta w \sum_{\substack{j=1 \\ j \neq k}}^M \bar{G}(w_k - u_j) J(u_j) + O((\Delta w)^2) + \int_{w_k - 1/M}^{w_k + 1/M} du J(u) G(w_k - u) \quad (8-129)$$

where

$$\bar{G}(w_k - u_j) = \frac{1}{\Delta w} \int_{u_j - 1/M}^{u_j + 1/M} du G(w_k - u). \quad (8-130)$$

The latter corresponds to the average value of \bar{G} over a Δu interval. Noting that $(w_k - u_j)$ is a function of $k - j$, setting $J_j = \Delta w \cdot J(u_j)$, and $A_k = A(w_k)$, one is left with a set of linear algebraic equations characterized by a complex, non-hermitian matrix:

$$A_k \approx \sum_{j=1}^M \bar{G}_{k-j} \cdot J_j \quad k = 1, 2, \dots, M. \quad (8-131)$$

The $2M-2$ off-diagonal elements, which are non-singular and continuous, are readily determined: the log portion analytically; the G_{\pm} portion numerically using a low-order (e.g. 2-point Gauss) quadrature for each element. Since $J(u)$ is assumed to be continuous within the interval $(-1, 1)$ and is nearly uniform within $(u_j - 1/M, u_j + 1/M)$,

$$\int_{u_j - 1/M}^{u_j + 1/M} du J(u) \ln |w_k - u| \approx J(u_j) \cdot \int_{u_j - 1/M}^{u_j + 1/M} du \ln |w_k - u| \quad (8-132)$$

$$\begin{aligned} &= J(u_j) \Delta w \left\{ \left(\frac{w_k - u_j}{\Delta w} \right) \ln \left[\frac{w_k - u_j + 1/M}{w_k - u_j - 1/M} \right] \right. \\ &\quad \left. - 1 + \frac{1}{2} \ln \left[(w_k - u_j)^2 - \left(\frac{\Delta w}{2} \right)^2 \right] \right\} \end{aligned} \quad (8-133)$$

$$= J_j \cdot [\text{log portion of matrix element}]_{k-j}. \quad (8-134)$$

since $\Delta u = \Delta w = 2/M$. For $w_k \neq u_j$, one gets

$$\int_{u_j - 1/M}^{u_j + 1/M} du J(u) G_{\pm}(w_k - u) \approx J(u_j) \Delta w \cdot \frac{1}{\Delta w} \int_{u_j - 1/M}^{u_j + 1/M} du G_{\pm}(w_k - u) \quad (8-135)$$

$$= J_j \cdot [G_{\pm} \text{ portion of matrix element}]_{k-j}. \quad (8-136)$$

Adding the two portions we arrive at

$$\int_{u_j - 1/M}^{u_j + 1/M} du J(u) G(w_k - u) \approx \bar{G}_{k-j} \cdot J_j. \quad (8-137)$$

The diagonal matrix elements, \bar{G}_o , are evaluated in a similar fashion with special care being given to the discontinuous component. The log part approximates to

$$J(w_k) \int_{w_k - \Delta u/2}^{w_k + \Delta u/2} du \ln |w_k - u| = J_k \cdot \left[\ln \frac{\Delta w}{2} - 1 \right]. \quad (8-138)$$

Using $z = w_k - u$, the discontinuous integral can be expressed as

$$B = \int_{-\Delta w/2}^{\Delta w/2} dz J(w_k - z) G_{\pm}(z). \quad (8-139)$$

Expanding $J(w_k - z) = J(w_k) - z J'(w_k) + \dots$ and inserting into the integrand gives us

$$B = J_k \cdot \frac{1}{\Delta w} \int_{-\Delta w/2}^{\Delta w/2} dz G_{\pm}(z) - J'(w_k) \int_{-\Delta w/2}^{\Delta w/2} dz z G_{\pm}(z) + \dots \quad (8-140)$$

Retaining only the lowest-order term on the r.h.s.,

$$B \approx J_k \cdot \frac{1}{\Delta w} \left[\int_{-\Delta w/2}^{0-} dz G_{-}(z) + \int_{0+}^{\Delta w/2} dz G_{+}(z) \right] + O(\Delta w) \quad (8-141)$$

$$\equiv J_k \cdot G_o + O(\Delta w). \quad (8-142)$$

where G_o corresponds to the average value of $G_{\pm}(z)$ over $(-\Delta w/2, \Delta w/2)$. Each half-interval integral was accurately evaluated using 2-point Gauss quadrature for sufficiently small Δw .

In view of the approximations inherent in the basic physical model, terms of the order Δw and higher were dropped from the inversion process. Associated with such terms are derivatives of both J_k and $G_{\pm}(0^{\pm})$. This appears not to have affected the stability of the inversion for dimensions relevant to transducer applications. For example, with a YIG film 30 microns thick, there was no evidence of spurious oscillations in $\{J_j(M)\}$ for different values of M provided $M \geq 51$.

The actual numerical inversion of the matrix-vector equation was executed using a complex version of an efficient Toeplitz subroutine.⁷ All plots are based on $M = 201$.

8.9 Comparison With Emtage's Results

To test the inversion characteristics of our code, the G_{\pm} yielding Emtage's analytically derived profile was needed. Inserting the corresponding G_{\pm} into our code and comparing the numerically computed $J(u)$ against his formula would provide the needed check.

7. Carayannis, G. et al. (1982) Subroutine TOEPL, *IEEE Transactions on Acoustics, Speech, and Signal Processing*, **ASSP-30**.

In Emtage's analysis he derives the following Fredholm integral equation of the second kind:

$$J(u) - \frac{v}{\pi} \int_{-1}^1 du' \frac{J(u')}{u' - u} = 0 \quad -1 < u < 1. \quad (8-143)$$

Using his notation, the vector potential equation for $J(u)$ may be written as

$$A(u) = \int_{-1}^1 du' J(u') [\ln |u - u'| + G_{\pm}(u - u')]. \quad (8-144)$$

At the strip surface, $A(u) = \text{const.}$ or $B_n = 0$. Since

$$\mathbf{B}^{\textcircled{1}} = \nabla \times \mathbf{A}^{\textcircled{1}} \quad (8-145)$$

$$= \hat{i} A_y^{\textcircled{1}} - \hat{j} A_x^{\textcircled{1}}, \quad (8-146)$$

the boundary condition at the strip becomes

$$B_n^{\textcircled{1}} = B_y^{\textcircled{1}} = 0 = -\frac{\partial A^{\textcircled{1}}}{\partial x}, \quad (8-147)$$

which leads to

$$0 = \frac{\partial}{\partial u} \int_{-1}^1 du' J(u') [\ln |u - u'| + G_{\pm}(u - u')]. \quad (8-148)$$

The slope of the log term is positive for $u' > u$ and negative for $u' < u$ so that

$$0 = \int_{-1}^1 du' \frac{J(u')}{u' - u} + \frac{\partial}{\partial u} \int_{-1}^1 du' J(u') G_{\pm}(u - u'). \quad (8-149)$$

If we set

$$\begin{aligned} G_{\pm}(u - u') &= \gamma \operatorname{sgn}(u - u') \\ &= \gamma \quad u > u' \\ &= -\gamma \quad u < u' \end{aligned} \quad (8-150)$$

it follows that

$$\int_{-1}^1 du' J(u') \gamma \operatorname{sgn}(u - u') = \gamma \left\{ \int_{-1}^u du' J(u') - \int_u^1 du' J(u') \right\}. \quad (8-151)$$

$\frac{\partial}{\partial u}$ of the above yields

$$\gamma \{J(u_-) + J(u_+)\} \quad (8-152)$$

where

$$u_{\pm} = u \pm \delta, \quad \delta \rightarrow 0^+. \quad (8-153)$$

Because $J(u)$ is continuous within $(-1, 1)$, as $\delta \rightarrow 0^+$, one arrives at

$$\frac{\partial}{\partial u} \int_{-1}^1 du' J(u') G_{\pm}(u - u') = 2\gamma J(u). \quad (8-154)$$

The resulting integral equation becomes

$$0 = \int_{-1}^1 du' \frac{J(u')}{u' - u} + 2\gamma J(u). \quad (8-155)$$

To achieve correspondence with Emtage's equation, it is clear that one must set $\gamma = i \frac{\pi/2}{v}$. In effect, one finds that Emtage used the following non-reciprocal Green's function component

$$G_{\pm}^E(u - u') = i \frac{\pi/2}{v} \operatorname{sgn}(u - u'). \quad (8-156)$$

Substituting into our inversion code using $M = 201$ samples, excellent agreement was obtained between our numerically determined $J(u)$ and his analytically derived formula, namely,

$$J^E(u) = \frac{N^{-1}}{\sqrt{1 - u^2}} \left(\frac{1 - u}{1 + u} \right)^{i\varepsilon} \quad (8-157)$$

$$= \frac{N^{-1}}{\sqrt{1 - u^2}} e^{i\varepsilon \ln \left(\frac{1 - u}{1 + u} \right)} \quad (8-158)$$

where

$$\varepsilon = \frac{1}{2\pi} \ln \left| \frac{1 + v}{1 - v} \right| \quad (8-159)$$

and

$$N = \pi / \cosh \pi \varepsilon. \quad (8-160)$$

The only noticeable discrepancies occurred near the edges $u = \pm 1$, which were deemed unimportant. Having confirmed the convergence of the algorithm to a known result, the next step was to see how close the actual G_{\pm} , derived in Sections 8.2 - 8.8, brought the computed $J(u)$ to a known result. Using the case of a narrow strip placed very near (but not on) the YIG, a run was made and compared with

Emtage's current profile. The comparison is shown in Table 8-2. The agreement is seen to be quite good considering that

1. the strip is not quite on the YIG;
2. s/h is finite in our case;
3. the approximation of the integral equation by the algebraic system of equations ignores higher order terms; and,
4. the propagation term for the YIG region field equation is retained in our formulation and not in Emtage's.

8.10 Calculation of $\tilde{J}(k)$

Having obtained equispaced samples of $J(u)$ along the strip, the next task was to calculate $\tilde{J}(k)$ for use in the Weinberg-Sethares MSSW transducer response code. The known edge factor governing the current density on the strip led us to expand the $J(u)$ as the product of an edge factor and an expansion of Chebyshev polynomials.

$$J(u) = (1 - u^2)^{-1/2} \sum_{n=0}^{N-1} C_n T_n(u) \quad (8-161)$$

$$\equiv (1 - u^2)^{-1/2} g(u) . \quad (8-162)$$

At the equispaced u_j ,

$$g(u_j) = (1 - u_j^2)^{1/2} J(u_j) . \quad (8-163)$$

$g(u)$ was then obtained by a natural cubic spline interpolation of $g(u_j)$. Invoking orthogonality gives

$$C_n = \alpha_n \int_{-1}^1 du T_n(u) J_n(u) \quad (8-164)$$

$$= \alpha_n \int_{-1}^1 du \frac{T_n(u) g(u)}{\sqrt{1 - u^2}} \quad (8-165)$$

where

$$\begin{aligned} \alpha_n &= 1/\pi & n &= 0 \\ &= 2/\pi & n &= 1, 2, \dots \\ &\equiv \epsilon_n/\pi . \end{aligned} \quad (8-166)$$

Using Gauss-Chebyshev quadrature, it follows that

$$C_n = \alpha_n \frac{\pi}{N} \sum_{l=1}^N f_n \left[\cos \left(l - \frac{1}{2} \right) \frac{\pi}{N} \right] \quad (8-167)$$

Table 8-2. Comparison with Emtage's Results

U(I)	Our Magn.	Emtage's	Our Phase	Emtage's
-.9950	.453441E+01	.358362E+01	-68.66	-53.38
-.9851	.227931E+01	.207418E+01	-40.70	-43.55
-.9751	.165287E+01	.161070E+01	-38.70	-38.96
-.9652	.139718E+01	.136473E+01	-36.02	-35.92
-.9552	.122948E+01	.120664E+01	-33.73	-33.64
-.9453	.111123E+01	.109423E+01	-31.90	-31.80
-.9353	.102244E+01	.100913E+01	-30.36	-30.27
-.9254	.952664E+00	.941875E+00	-29.04	-28.95
-.9154	.896013E+00	.887032E+00	-27.87	-27.79
-.9055	.848868E+00	.841236E+00	-26.83	-26.75
-.8955	.808867E+00	.802273E+00	-25.88	-25.81
⋮	⋮	⋮	⋮	⋮
-.0498	.357984E+00	.357467E+00	-.89	-.89
-.0398	.357824E+00	.357308E+00	-.71	-.71
-.0299	.357699E+00	.357184E+00	-.53	-.53
-.0199	.357611E+00	.357095E+00	-.35	-.35
-.0100	.357557E+00	.357042E+00	-.18	-.18
-.0000	.357539E+00	.357025E+00	.00	.00
.0100	.357557E+00	.357042E+00	.18	.18
.0199	.357610E+00	.357095E+00	.35	.35
.0299	.357699E+00	.357184E+00	.53	.53
.0398	.357824E+00	.357308E+00	.71	.71
.0498	.357984E+00	.357467E+00	.89	.89
⋮	⋮	⋮	⋮	⋮
.8955	.808862E+00	.802273E+00	25.88	25.81
.9055	.848863E+00	.841236E+00	26.83	26.75
.9154	.896008E+00	.887032E+00	27.87	27.79
.9254	.952659E+00	.941875E+00	29.04	28.95
.9353	.102244E+01	.100913E+01	30.36	30.27
.9453	.111122E+01	.109423E+01	31.90	31.80
.9552	.122947E+01	.120664E+01	33.73	33.64
.9652	.139717E+01	.136473E+01	36.02	35.92
.9751	.165286E+01	.161070E+01	38.70	38.96
.9851	.227930E+01	.207418E+01	40.70	43.55
.9950	.453438E+01	.358362E+01	68.66	53.38

2600. MHz

D/H = .1000E-08

S/H = .1000E-03

201 J(U) Samples

N4 = 2-Point Gauss Quadrature

K-MSSW = 1487.8 [meter]⁻¹

where $f_n(u) = T_n(u) g(u)$ is sampled at the Gauss quadrature abscissas given by

$$u_l = \cos(l - 1/2) \frac{\pi}{N} . \quad (8-168)$$

The current transform is defined as

$$\tilde{J}(k) = \int_{-\infty}^{\infty} dx J(x) e^{ikx} \quad (8-169)$$

$$= \frac{s}{2} \int_{-1}^1 dx J(u) e^{ikus/2} . \quad (8-170)$$

Substituting the above expressions into $\tilde{J}(k)$, making use of the Fourier-Bessel expansion of a plane wave,⁸ setting $u = \cos \theta$, and evaluating the ensuing trigonometric integrals leads one to the expression

$$\tilde{J}(k) = \frac{\pi s}{2} \sum_{n=0}^{N-1} C_n i^n J\left(k \frac{s}{2}\right) . \quad (8-171)$$

Obtaining $\tilde{J}(k)$ and normalizing it in a fashion consistent with the total current normalization invoked in previous work, the resulting code was incorporated into the Weinberg-Sethares program. Representative examples of the resulting transducer response are shown in the figures.

8.11 Discussion of Results

Plots of the magnitude and phase of $J(u)$ are shown in Figures 8-3 - 8-24 for a variety of strip widths, s , and YIG-strip separations, d . The YIG film thickness, h , was taken to be 30 micrometers; the DC magnetic biasing field, H_0 , 375 Oersteds; and the saturation magnetization, $4\pi M_0$, 1750 Gauss. Each plot shows six curves corresponding to the current profiles obtained for the excitation frequencies $f = 2.55, 2.6, 2.8, 3.0, 3.2$, and 3.4 GHz for specified values of s/h and d/h .

In the absence of the ferrite, or under vanishingly weak coupling conditions, $J(u) \sim (1 - u^2)^{-1/2}$ for all frequencies, and $\arg(J(u))$ is zero in the limit of total decoupling. Figures 8-15 and 8-16 typify such cases. Even though $d = h$, the relative narrowness of the strip ($s = h/10$) makes the edge effect the dominating influence on the current shape relative to the back reaction.

At the other extreme, for $s/h = 10$ and $d/h = 0.1$, two conditions appear to be responsible for permitting a standing wave of current density across the strip width. See Figures 8-9 and 8-10. The requirements seem to be that the MSSW wavelength must be less than the strip width, and the coupling to the YIG, in some sense, balances the quasimagnetostatic edge effects of the strip. On the phase plot, the large excursions near $u = 0.1$ occur even in the absence of a metallic edge at that location. In

8. Stratton, J.A. (1941) *Electromagnetic Theory*, McGraw Hill, New York, pp 371,372.

Emtage's example (see Figure 8-14), the metallic strip edges are located where the phase variations are largest. As shown in Figures 8-7 and 8-8, increasing d/h to 0.1 weakens the coupling and detunes the system significantly. Other plots are included to show the effect of s/h , d/h , and frequency on $J(u)$.

For comparison, transducer response plots based on both uniform current density, and the theory presented above, are shown in Figures 8-25 through 8-31. Figure 8-31 shows a comparison of transducer responses, for narrow transducers, based on a flat current distribution, SUR program on the right. On the left of the figure are results for the more exact current distribution, calculated by the method of this chapter, the IL1 program. The notation used in Figure 8-31 is that defined in Chapter 3. In particular, the quantities A, D, and G in Figure 8-31, are the same as s , h , and d , in Figure 8-1, respectively. The largest difference in the results, is in the radiation resistance. Insertion loss plots are nearly identical except for the slightly flatter response of the exact current distribution.

All insertion loss plots in this report are based on the assumption that current profiles on generating and receiving strips are roughly the same. A rigorous assessment of this assumption was beyond the scope of this study and appears to require solution of a scattering problem using a full wave formulation because of the distances between input and output transducer strips.

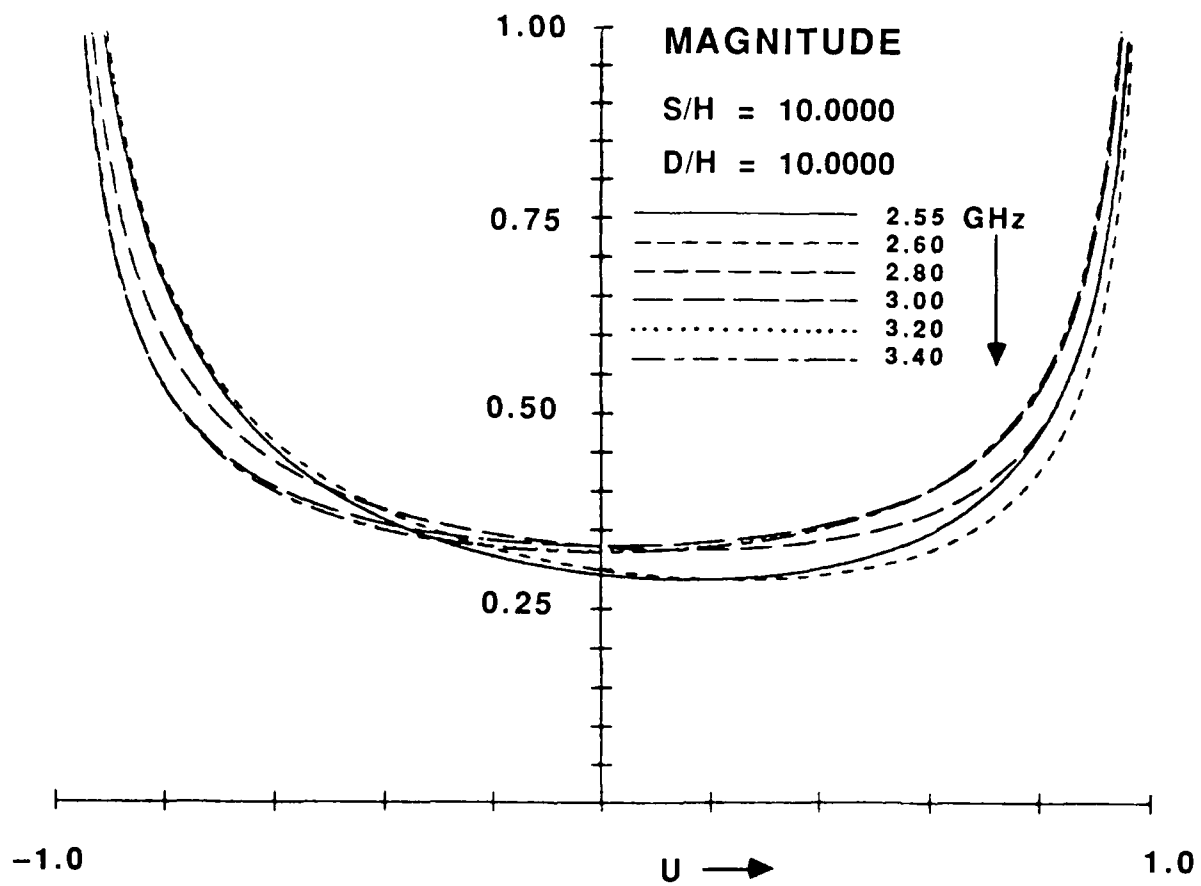


Figure 8-3. Magnitude of Current Density versus Normalized Position on Strip. $s/h = 10$; $d/h = 10$

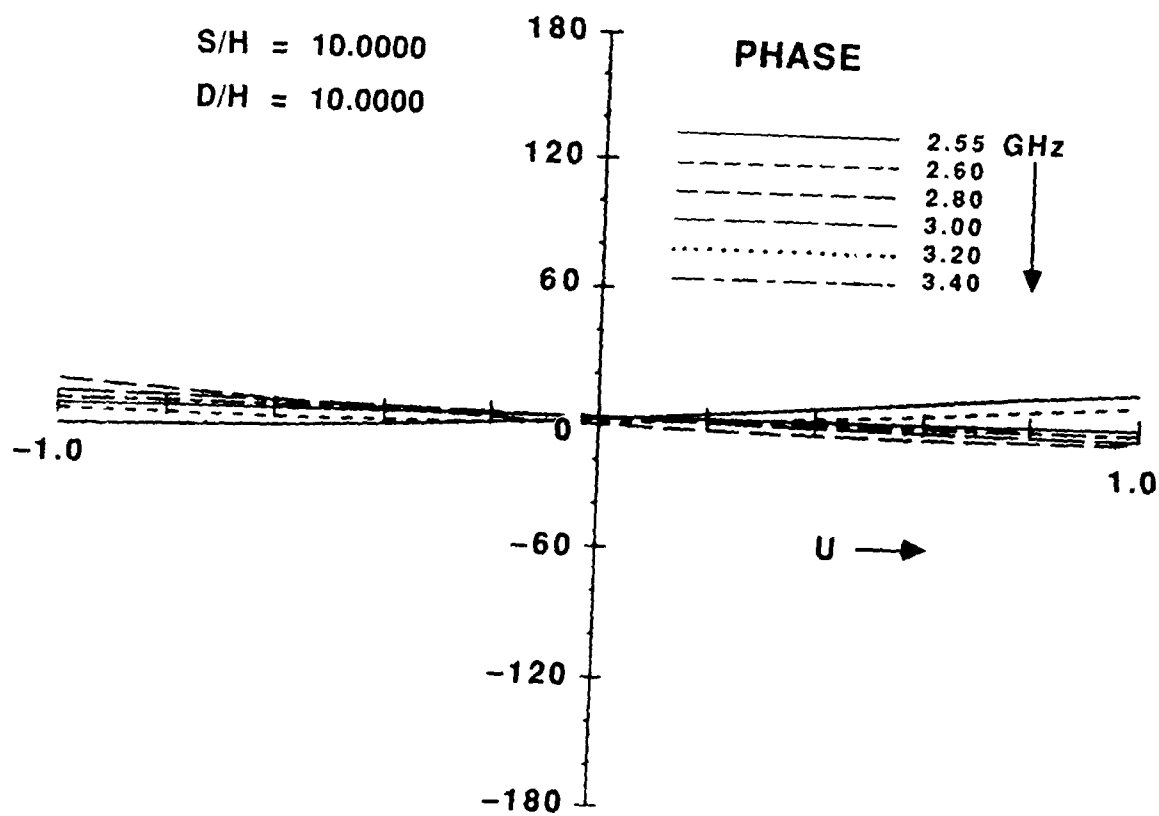


Figure 8-4. Phase of Current Density versus Normalized Position on Strip. $s/h = 10$; $d/h = 10$

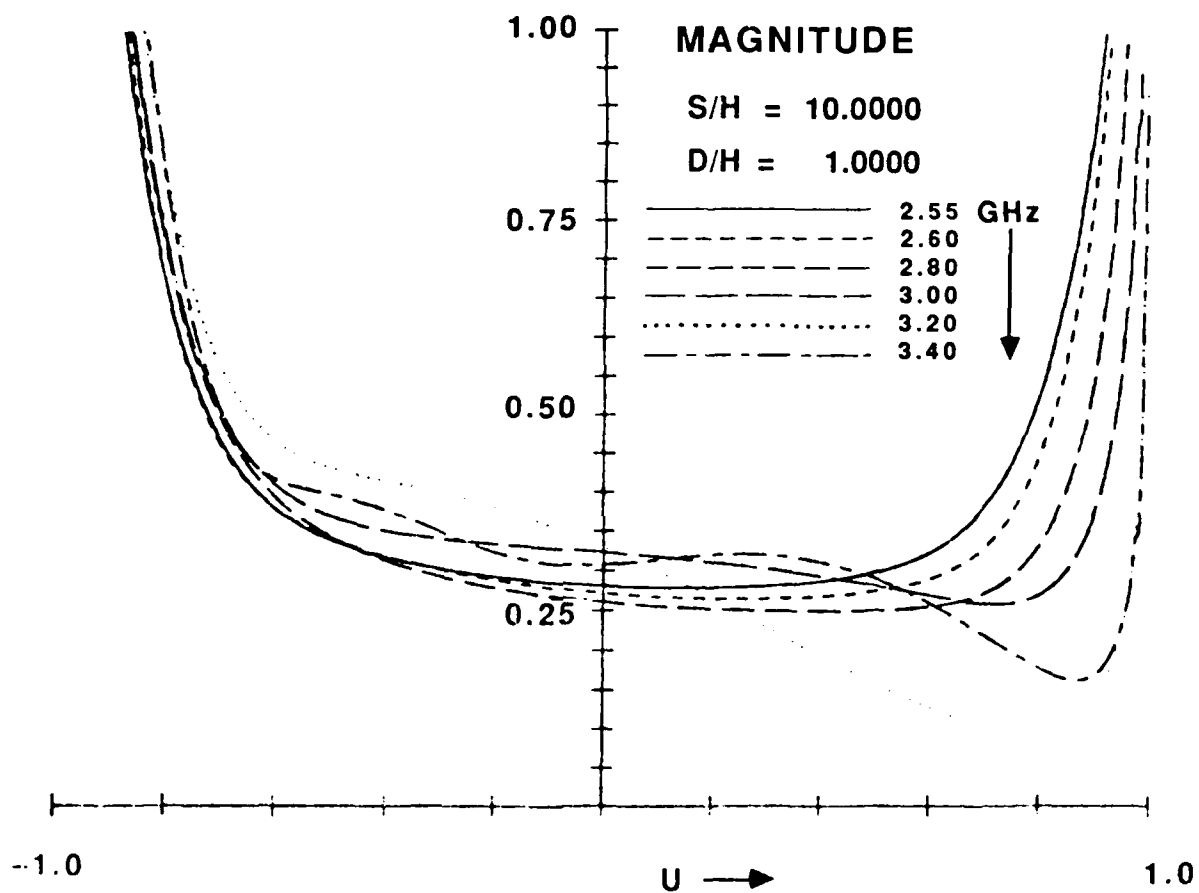


Figure 8-5. Magnitude of Current Density versus Normalized Position on Strip. $s/h = 10$; $d/h = 1.0$

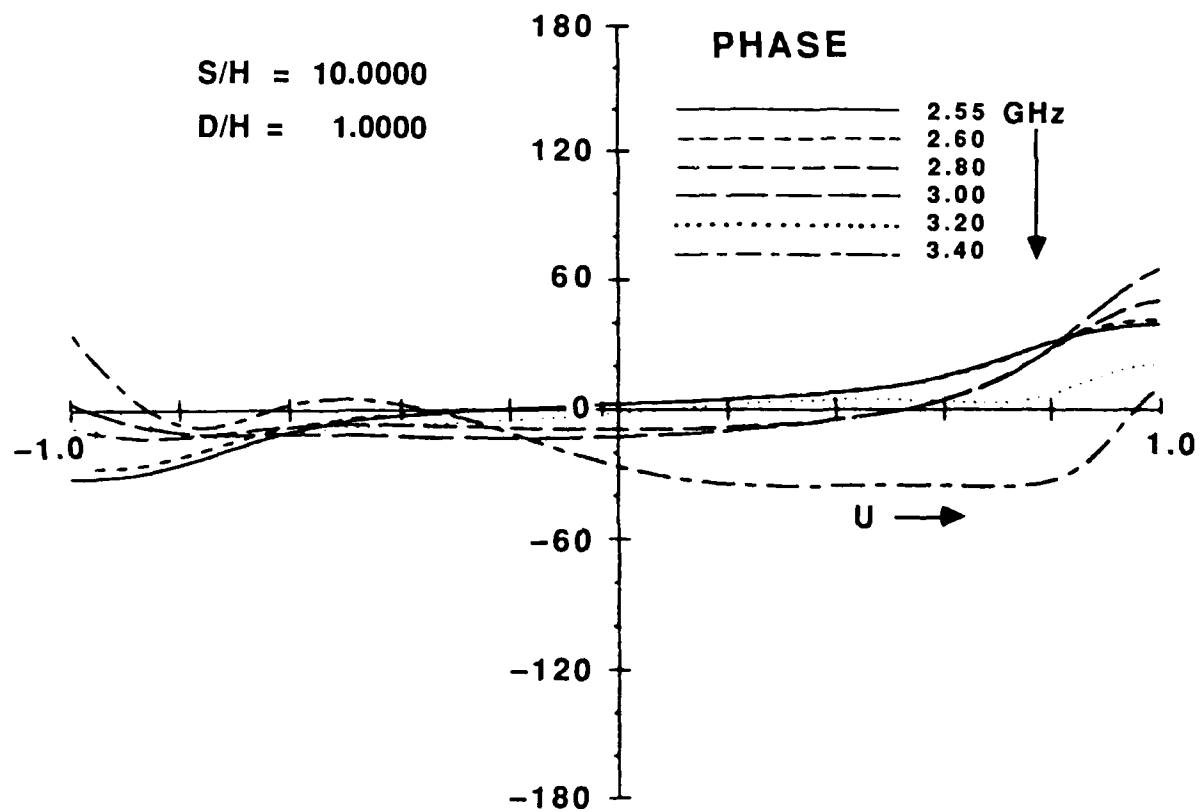


Figure 8-6. Phase of Current Density versus Normalized Position on Strip. $s/h = 10$; $d/h = 1.0$

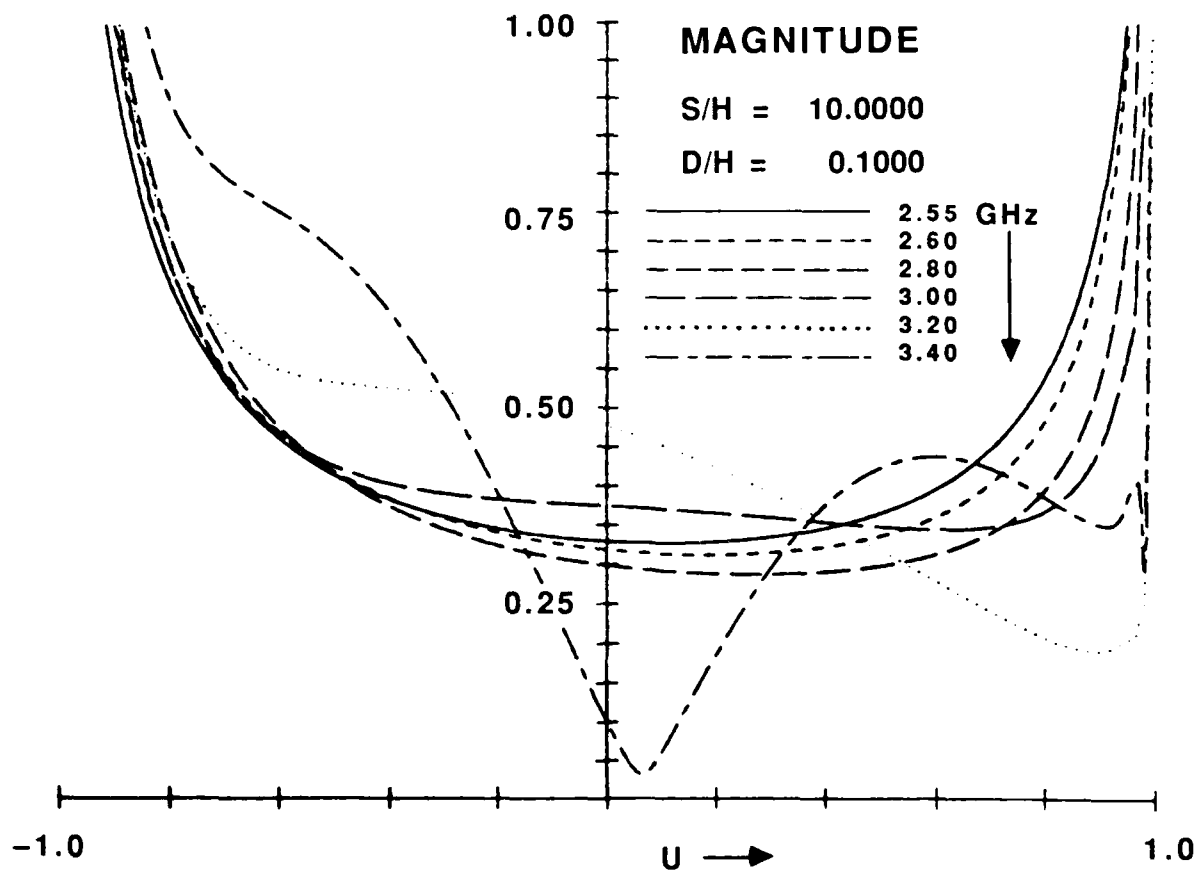


Figure 8-7. Magnitude of Current Density versus Normalized Position on Strip. $s/h = 10$; $d/h = 0.1$

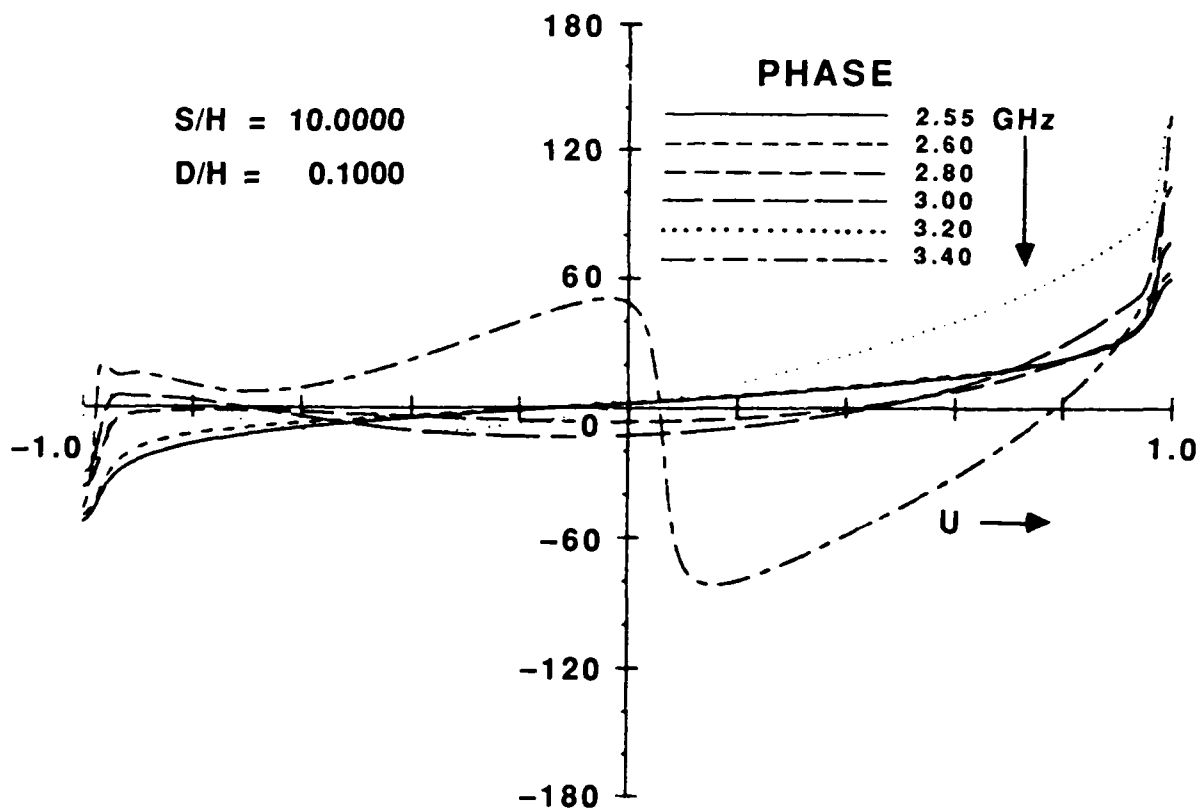


Figure 8-8. Phase of Current Density versus Normalized Position on Strip. $s/h = 10$; $d/h = 0.1$

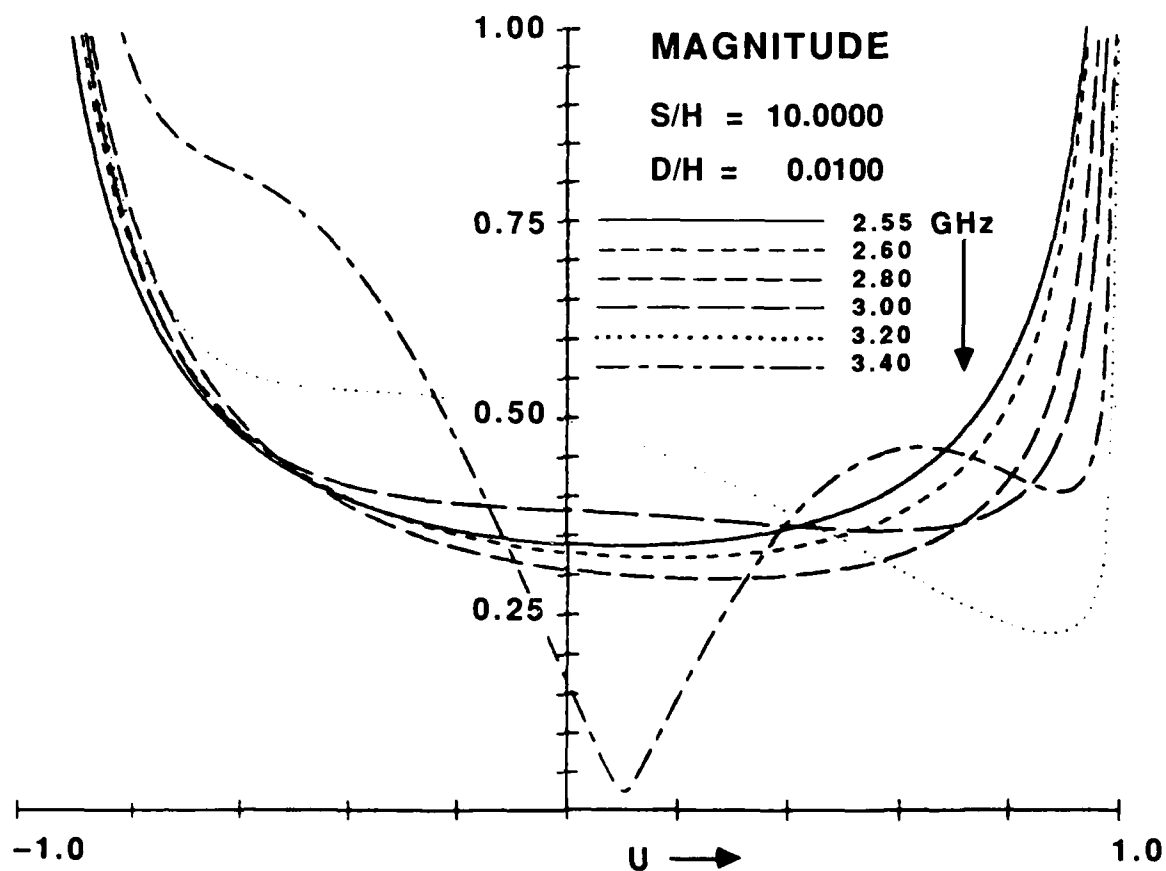


Figure 8-9. Magnitude of Current Density versus Normalized Position on Strip. $s/h = 10$; $d/h = 0.01$

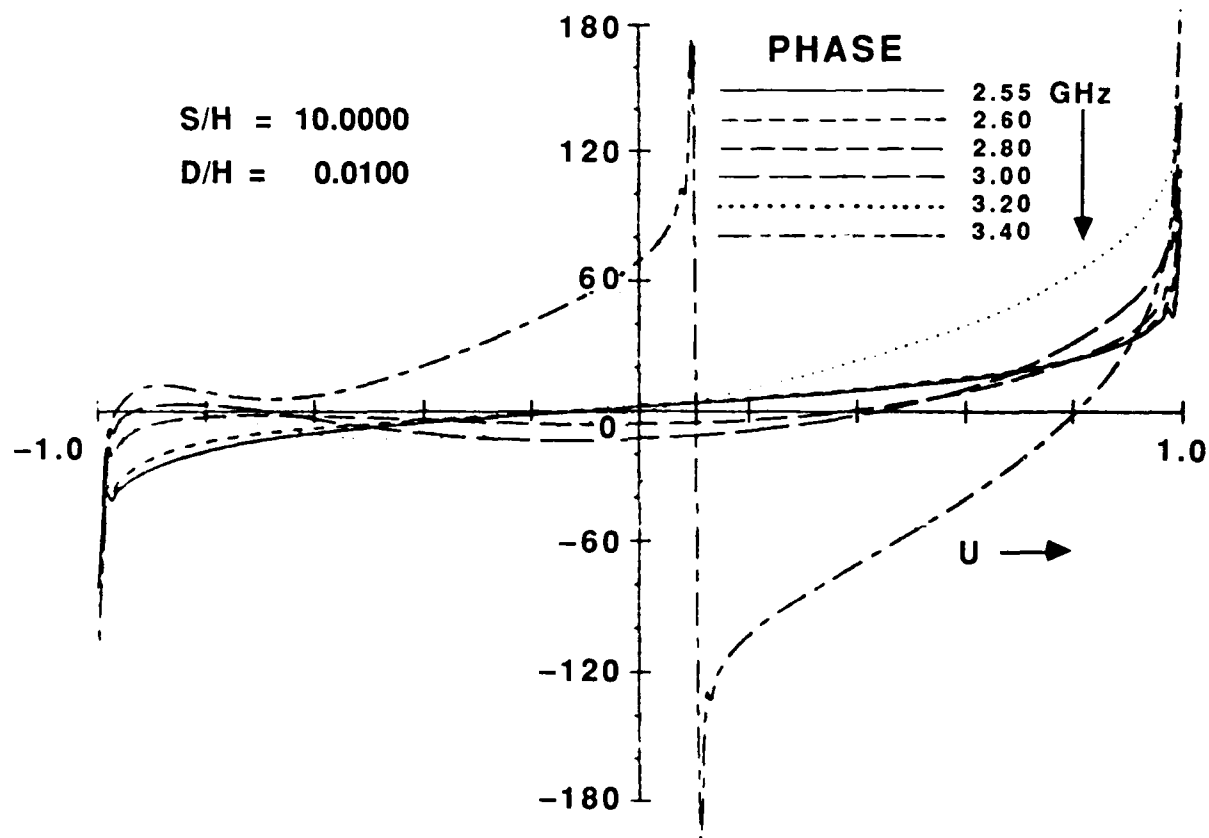


Figure 8-10. Phase of Current Density versus Normalized Position on Strip: MSSW Wavelength of 3.4 GHz Wave is 179 μm on Strip. $s/h = 10$; $d/h = 0.01$

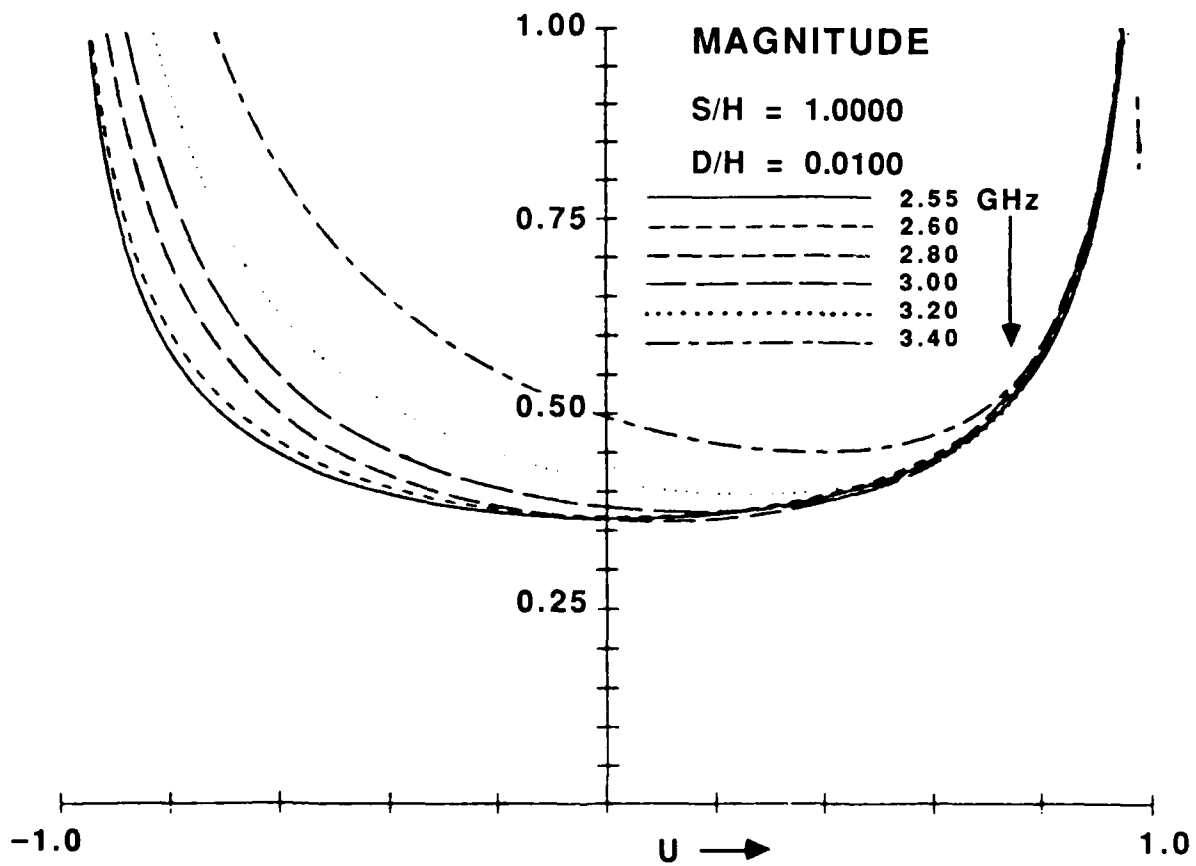


Figure 8-11. Magnitude of Current Density versus Normalized Position on Strip. $s/h = 1.0$; $d/h = 0.01$

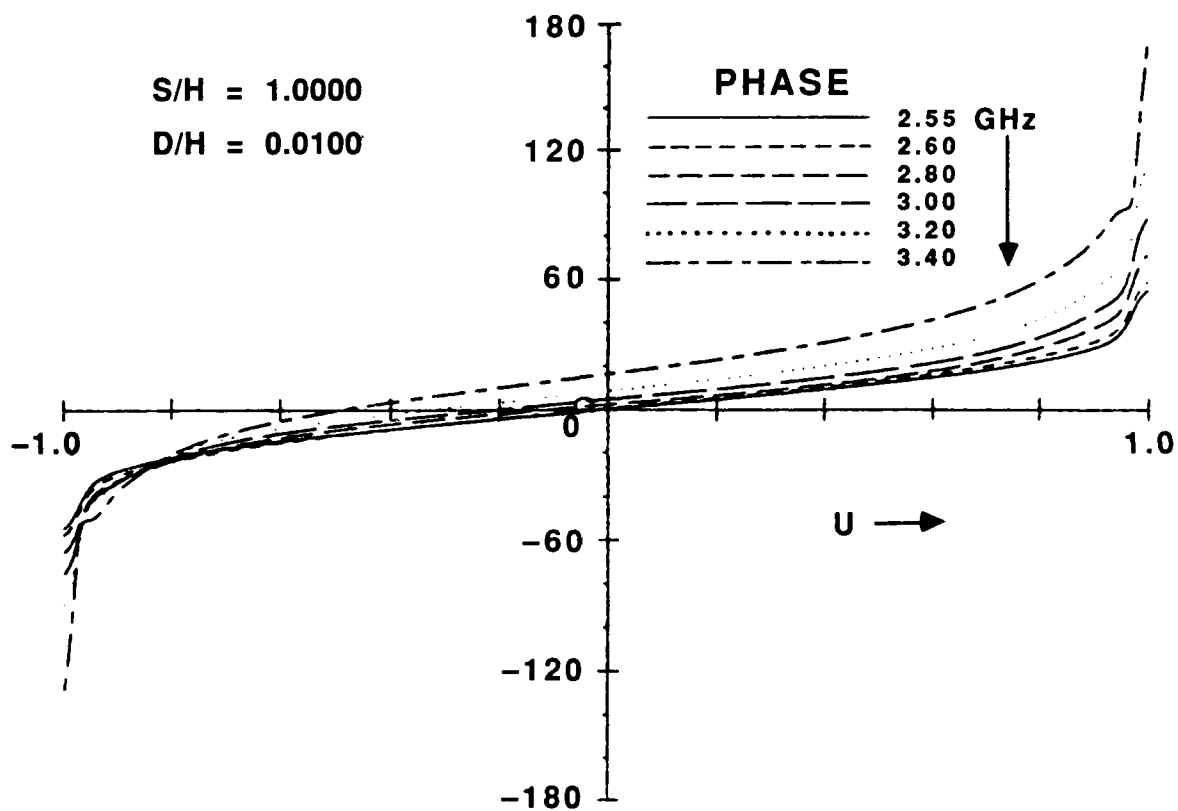


Figure 8-12. Phase of Current Density versus Normalized Position on Strip. $s/h = 1.0$; $d/h = 0.01$

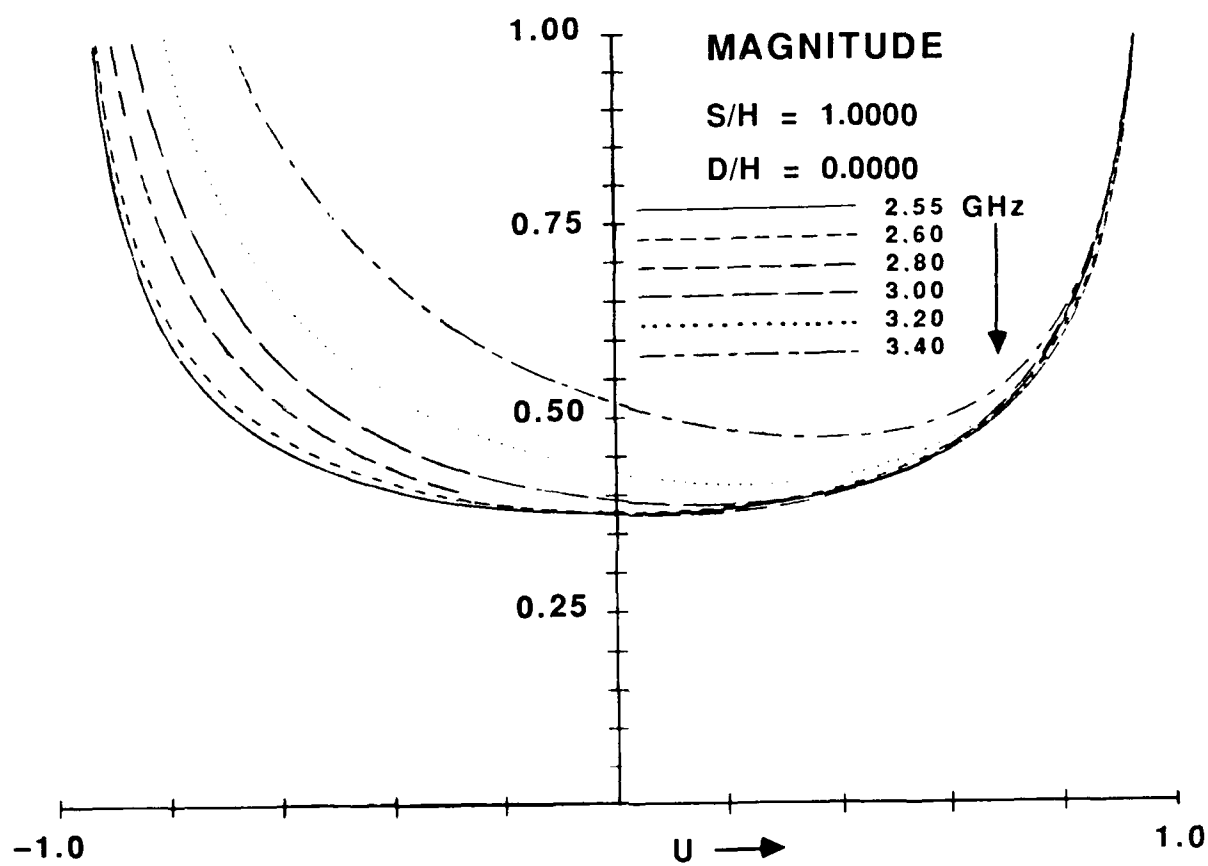


Figure 8-13. Magnitude of Current Density versus Normalized Position on Strip. $s/h = 1.0$; $d/h = 10^{-9}$

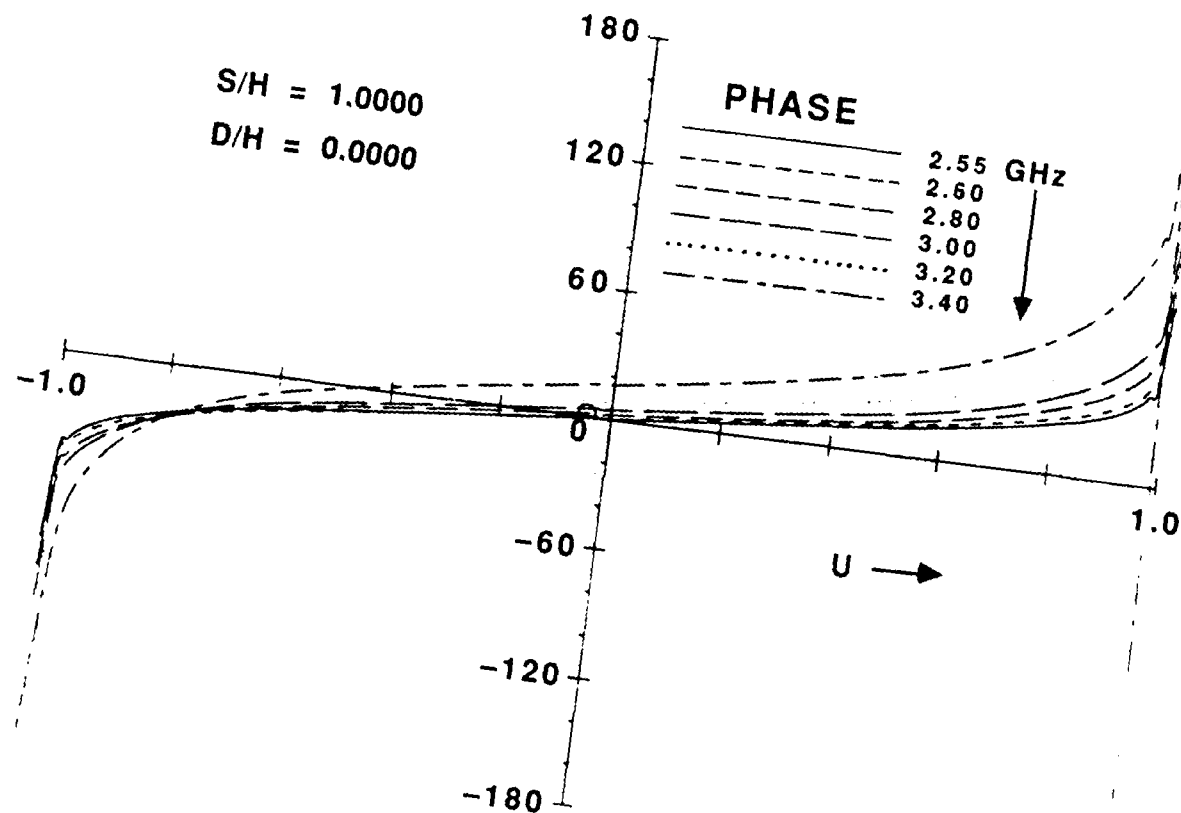


Figure 8-14. Phase of Current Density versus Normalized Position on Strip. $s/h = 1.0$; $d/h = 10^{-9}$

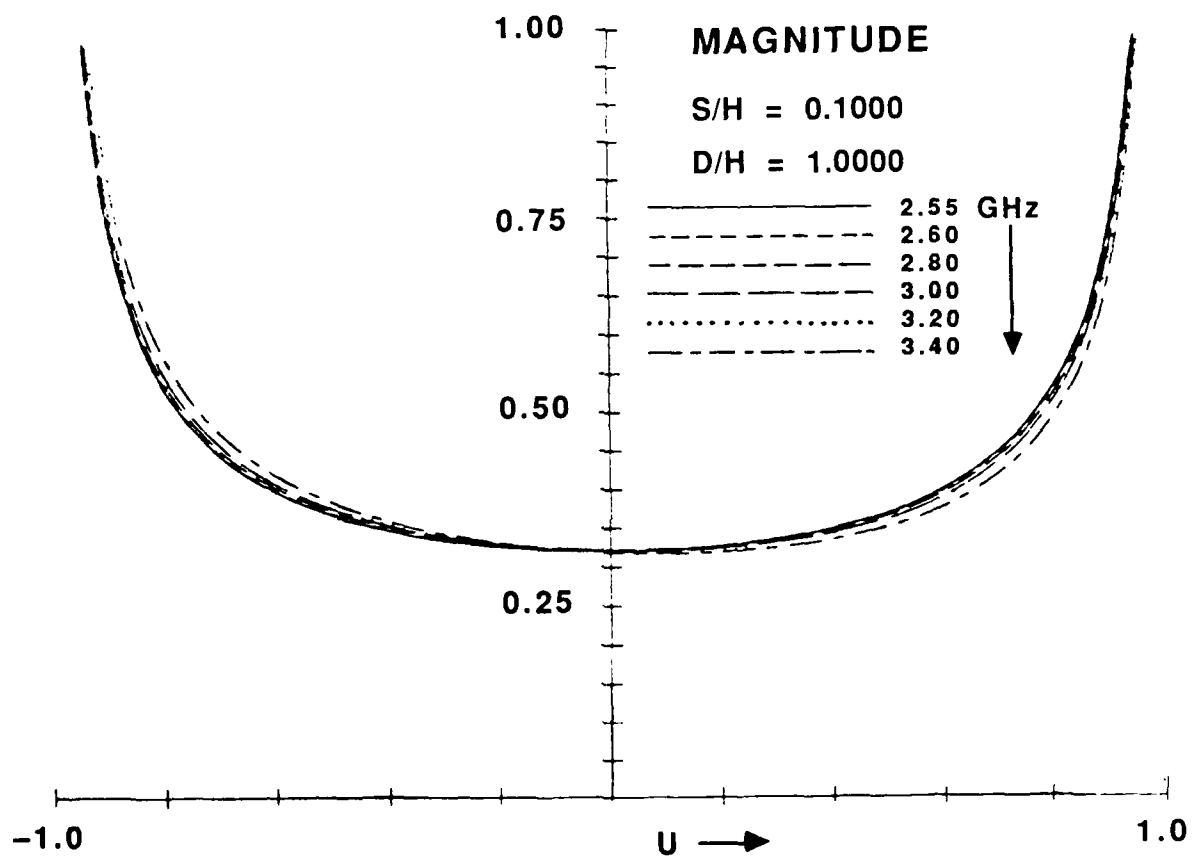


Figure 8-15. Magnitude of Current Density versus Normalized Position on Strip. $s/h \approx 0.1$; $d/h = 1.0$

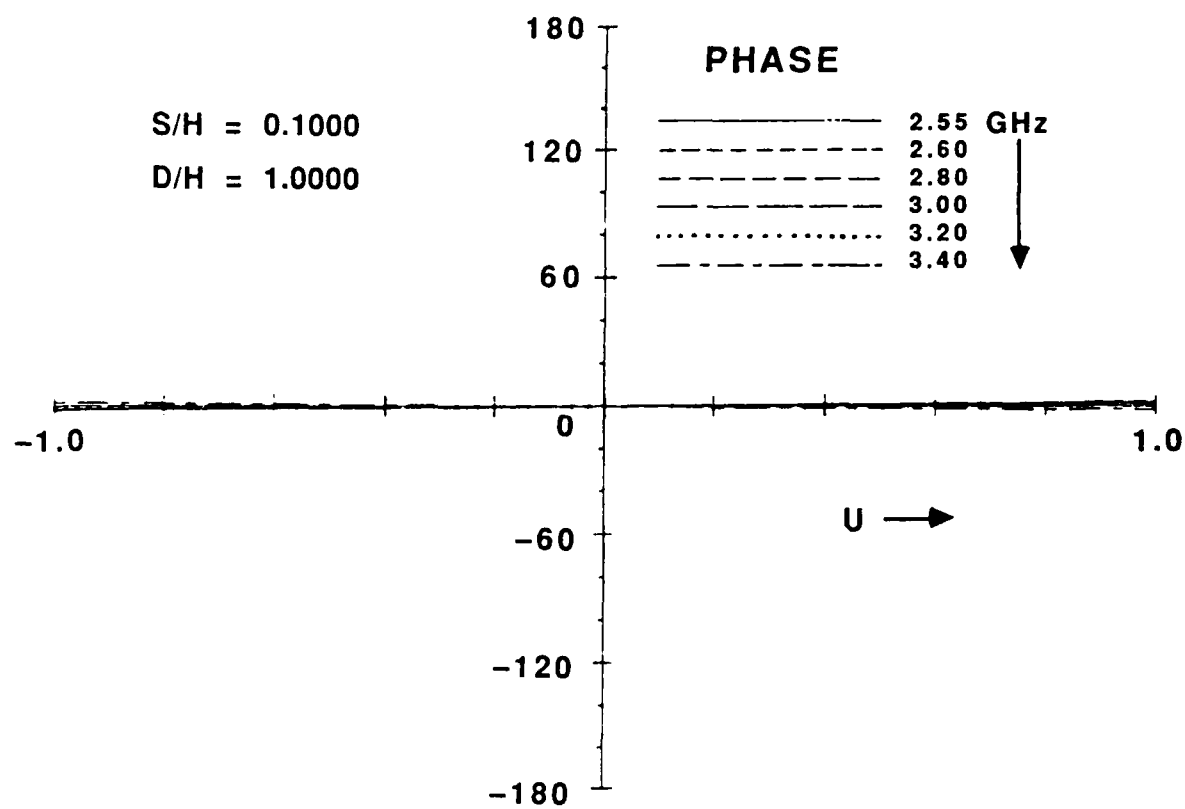


Figure 8-16. Phase of Current Density versus Normalized Position on Strip. $s/h = 0.1$; $d/h = 1.0$

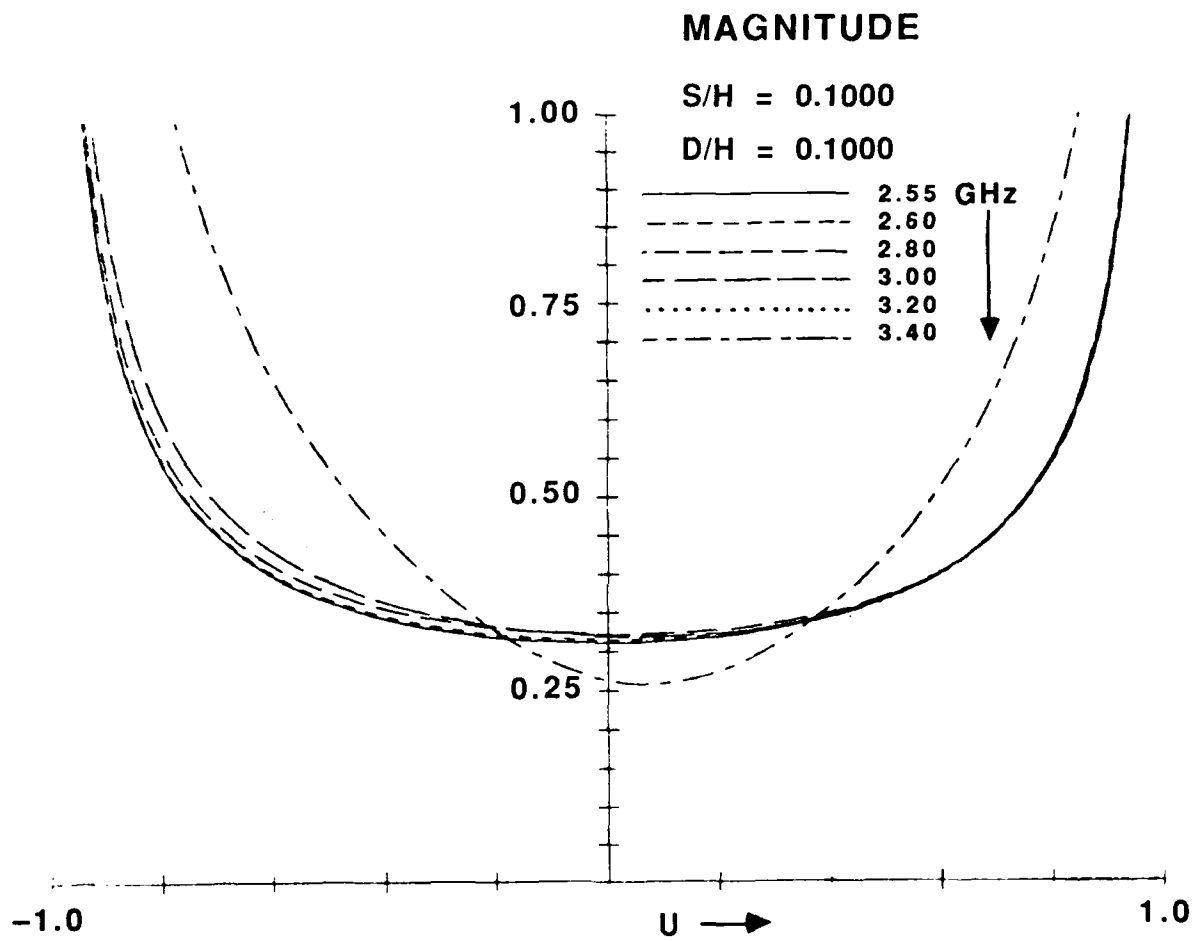


Figure 8-17. Magnitude of Current Density versus Normalized Position on Strip. $s/h = 0.1$; $d/h = 0.1$

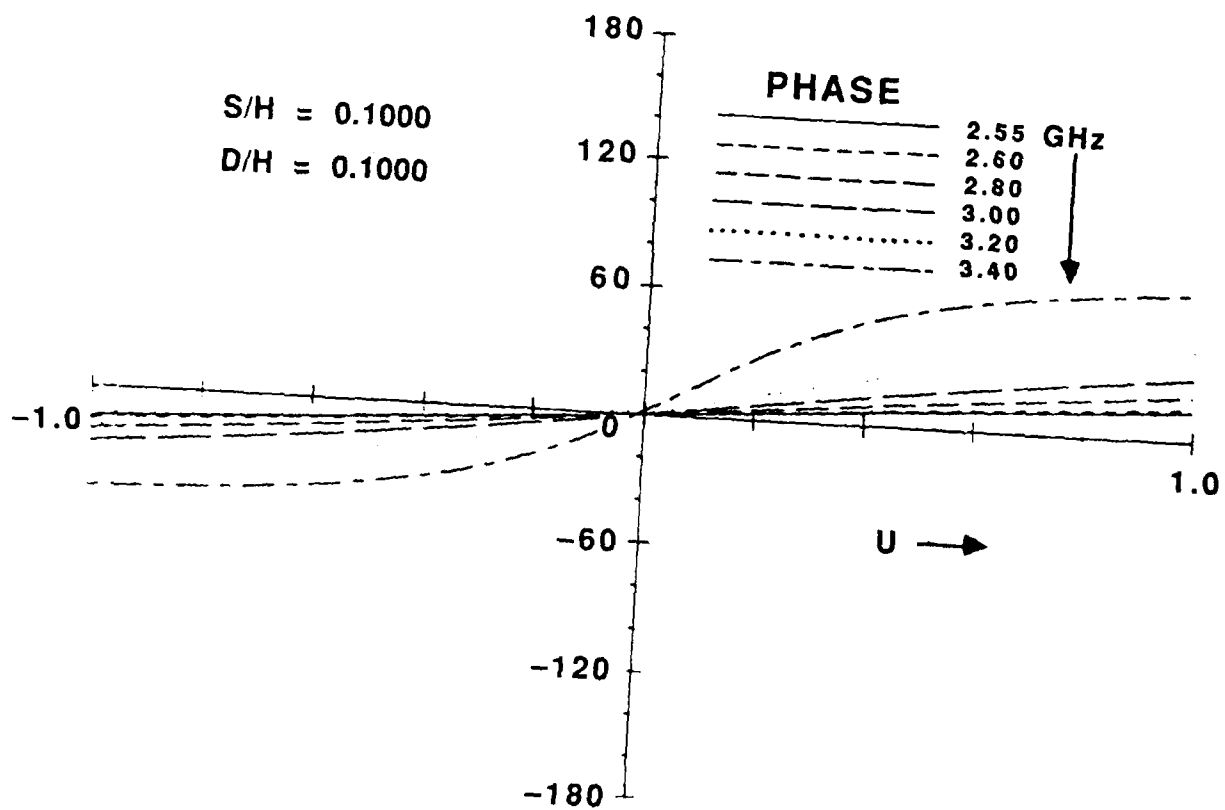


Figure 8-18. Phase of Current Density versus Normalized Position on Strip. $s/h = 0.1$; $d/h = 0.1$

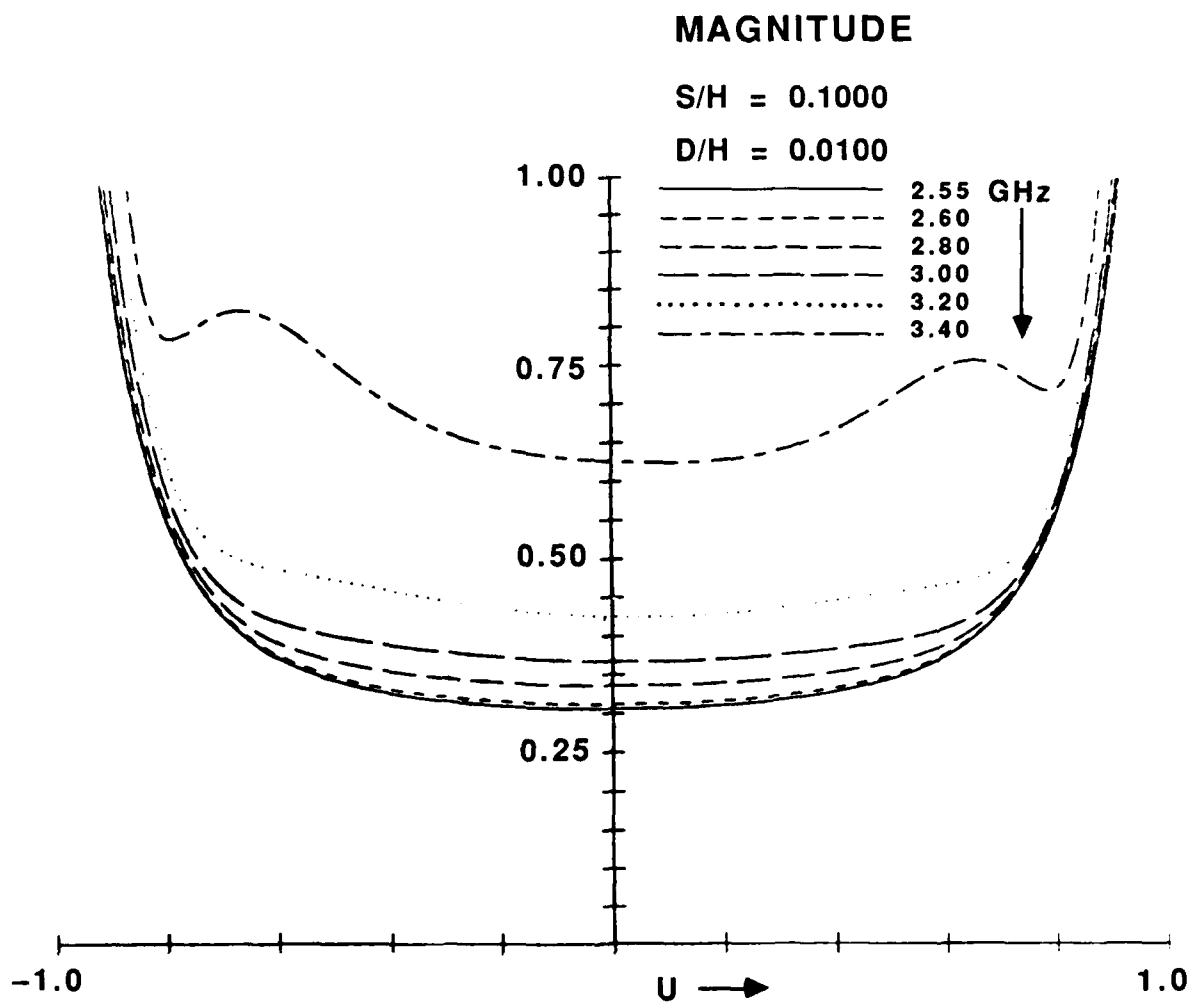


Figure 8-19. Magnitude of Current Density versus Normalized Position on Strip. $s/h = 0.1$; $d/h = 0.01$

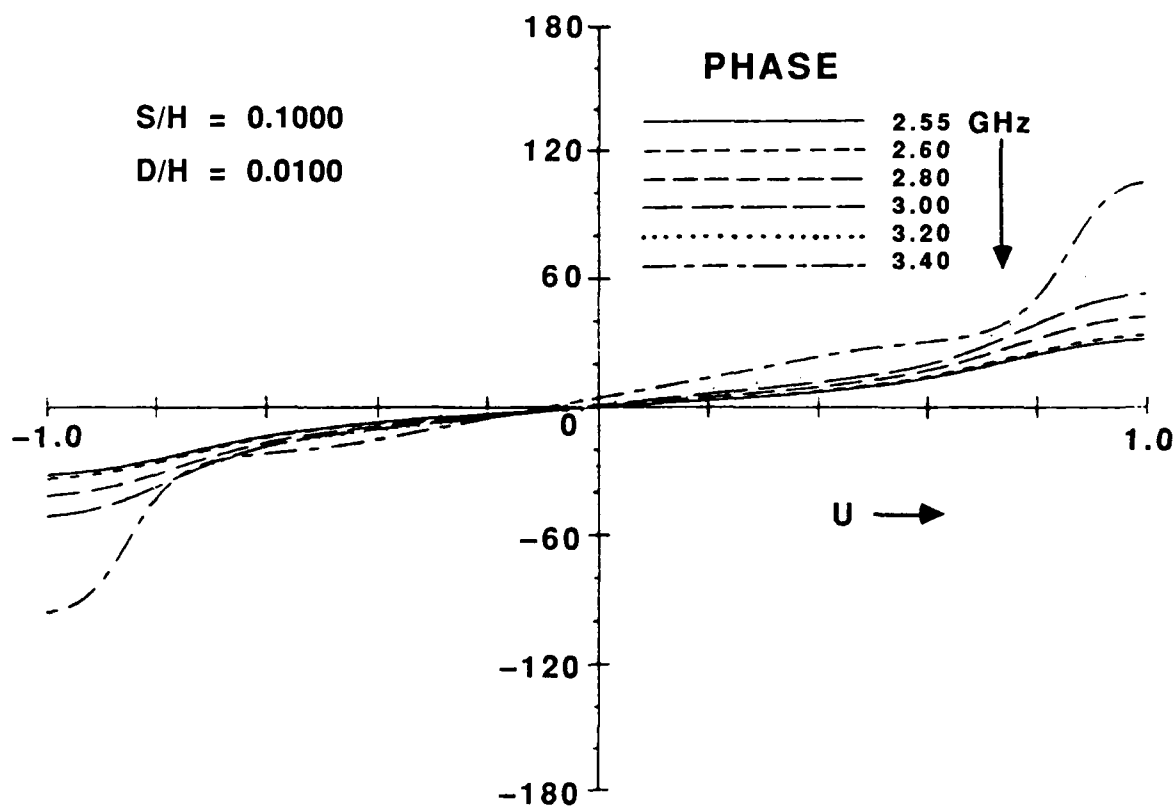


Figure 8-20. Phase of Current Density versus Normalized Position on Strip. $s/h = 0.1$; $d/h = 0.01$

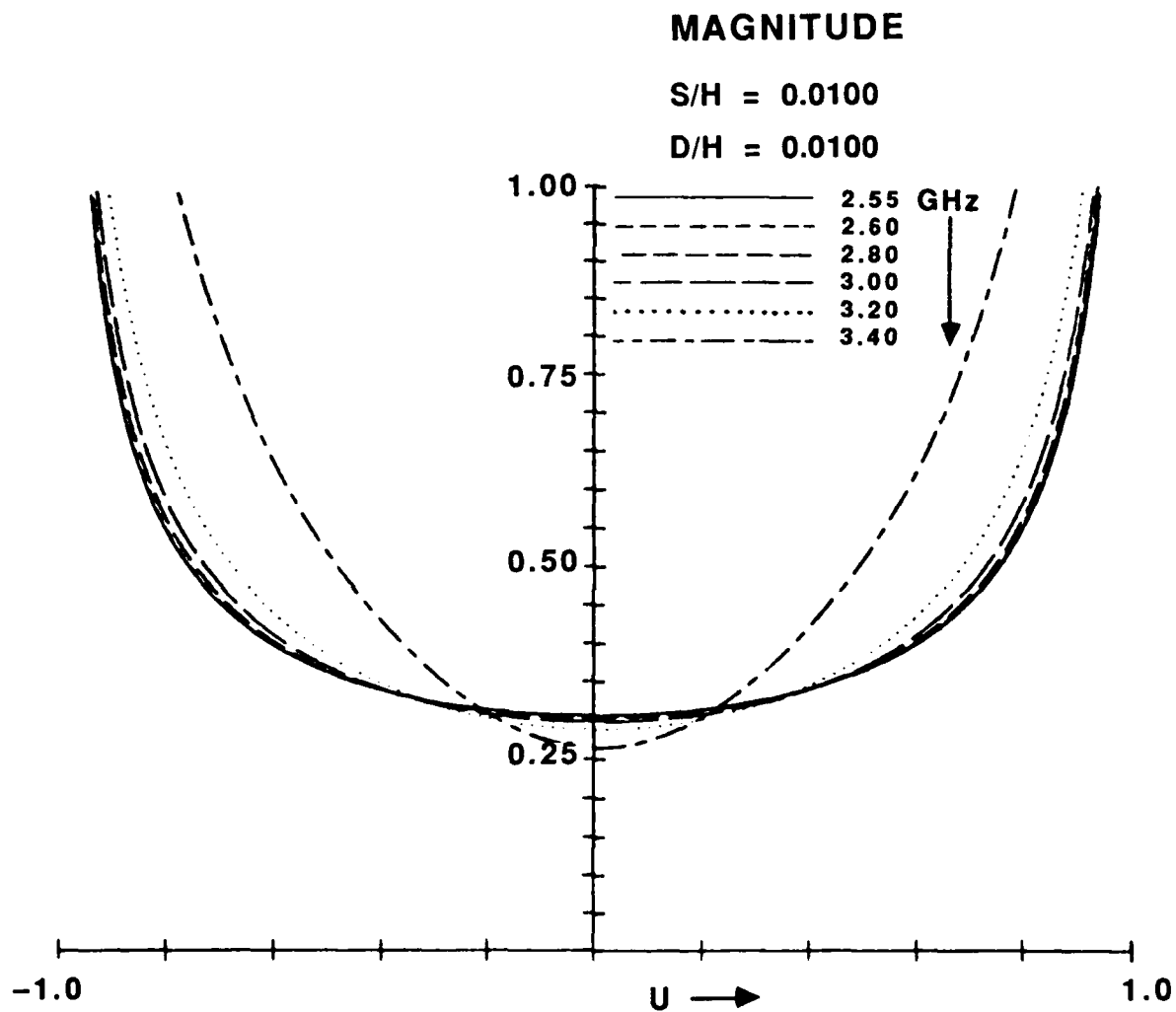


Figure 8-21. Magnitude of Current Density versus Normalized Position on Strip. $s/h = 0.01$; $d/h = 0.01$

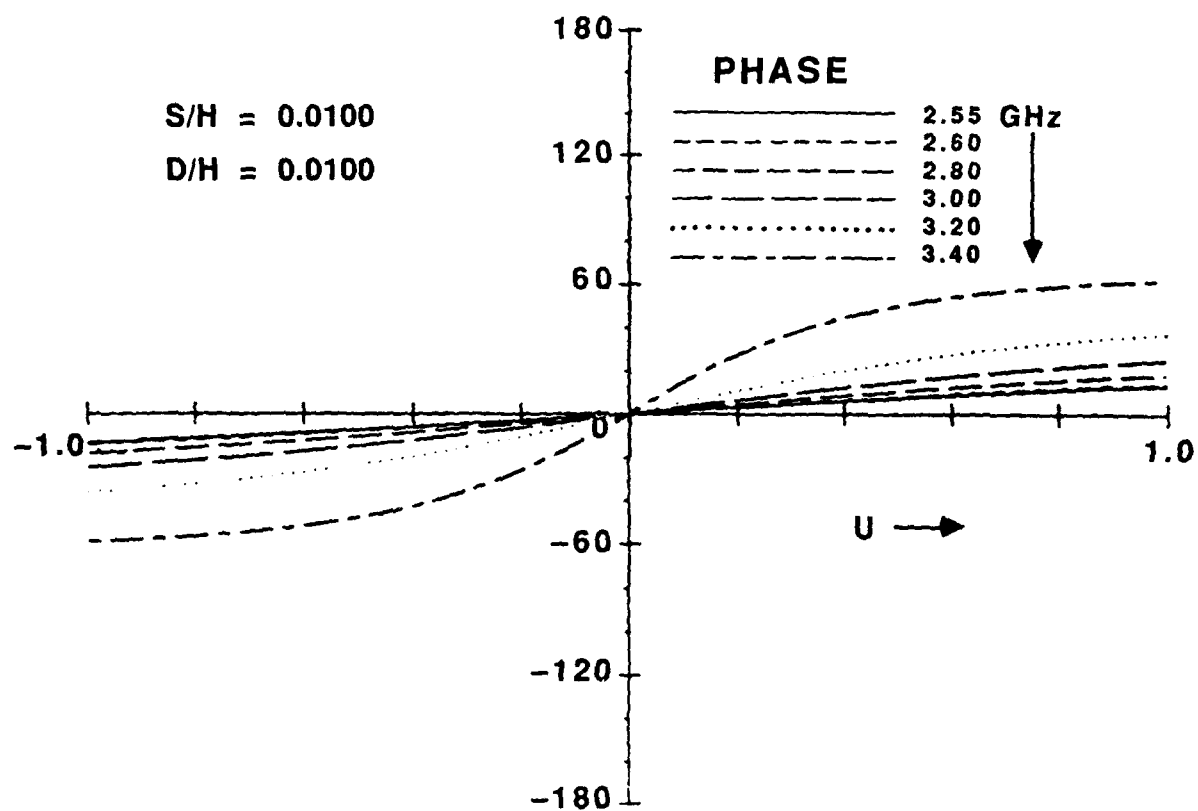


Figure 8-22. Phase of Current Density versus Normalized Position on Strip. $s/h = 0.01$; $d/h = 0.01$

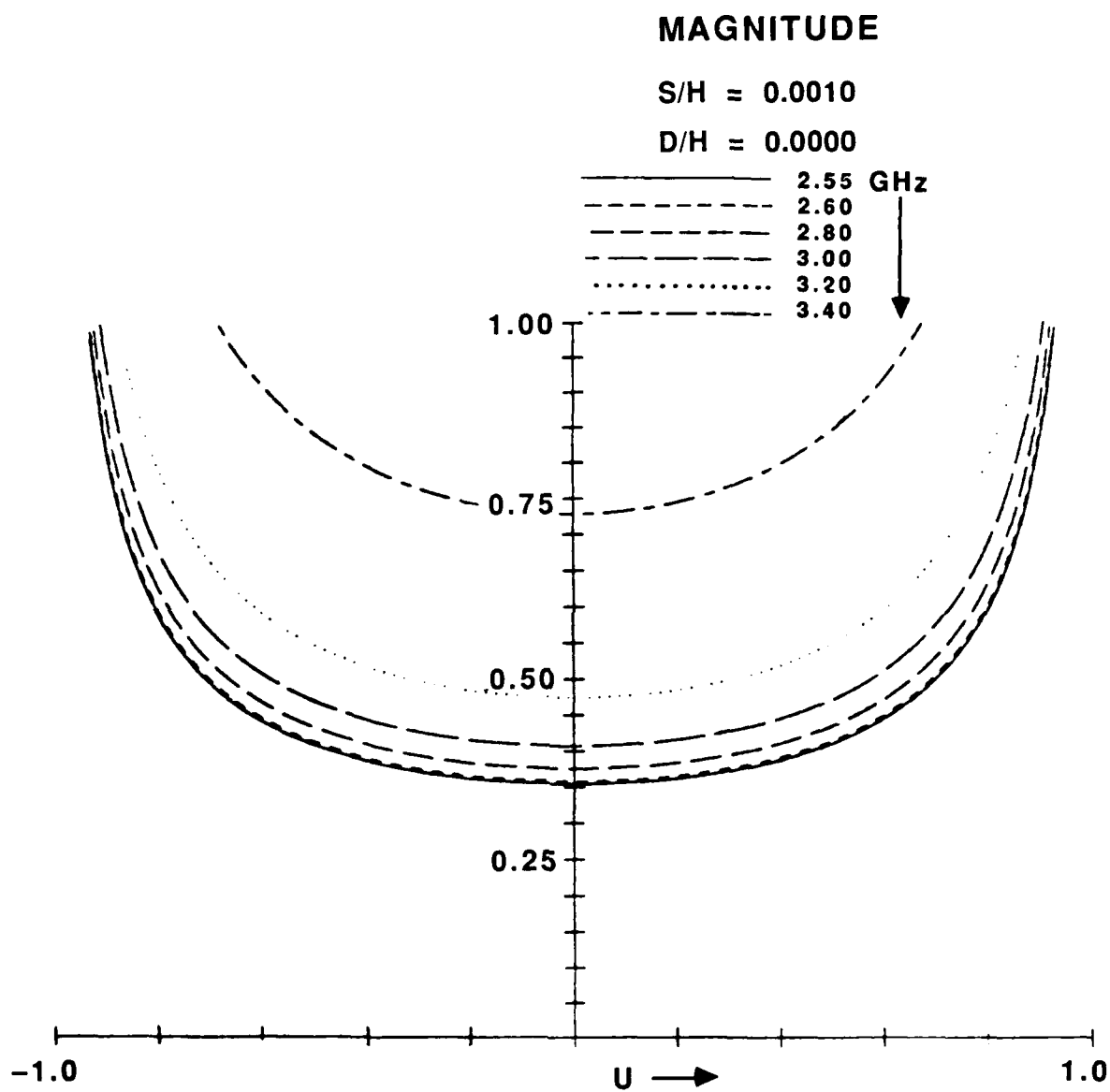


Figure 8-23. Magnitude of Current Density versus Normalized Position on Strip. $s/h = 0.001$; $d/h = 10^{-9}$

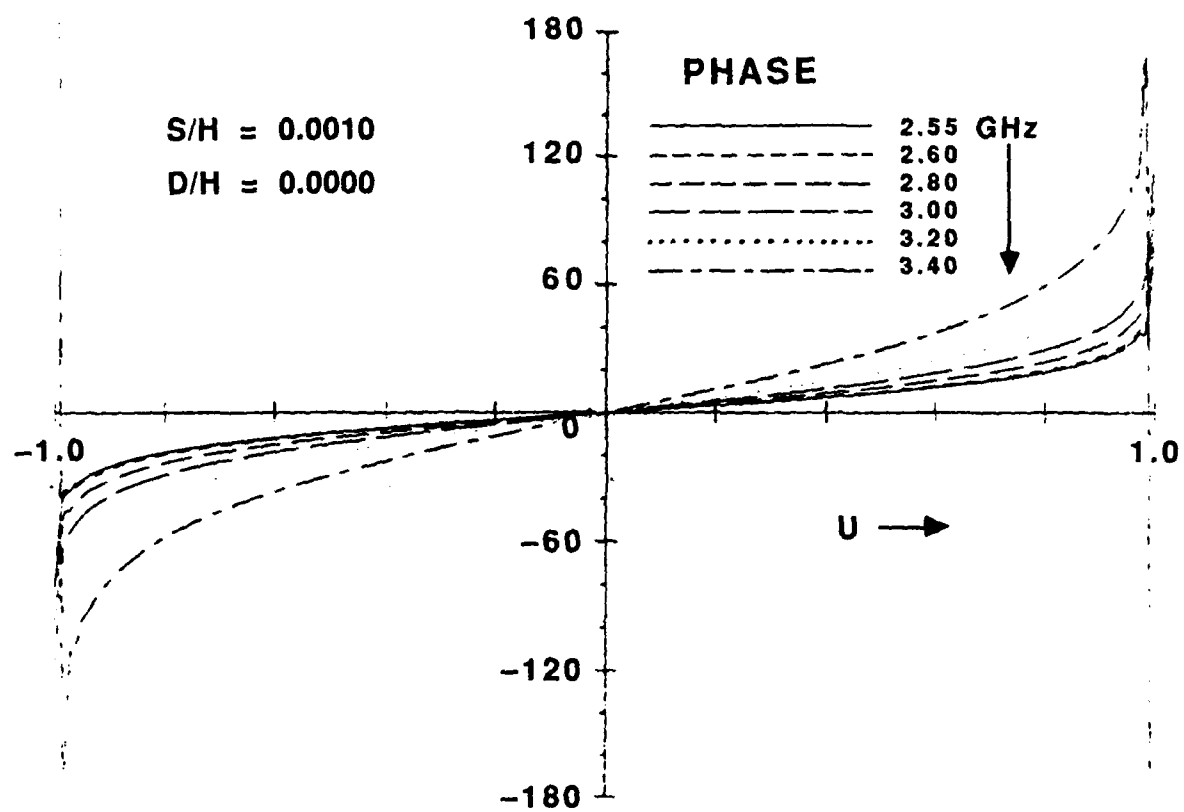
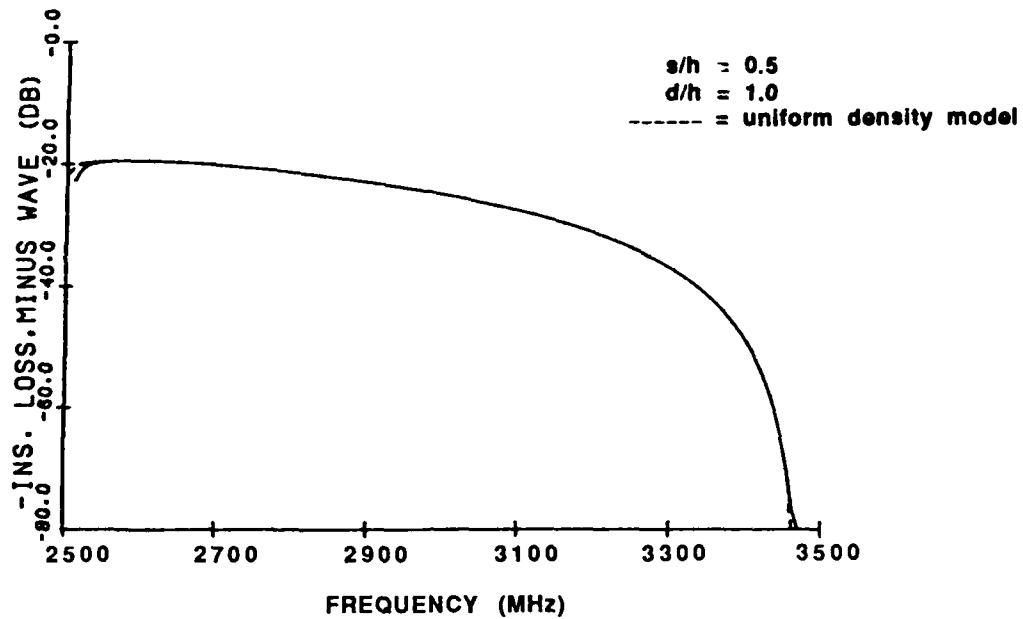


Figure 8-24. Phase of Current Density versus Normalized Position on Strip. $s/h = 0.001$; $d/h = 10^{-9}$

SURFACE WAVES 2 TERMINAL MODEL
H= 375.0 T1=.1000E+01 G=.300E-04 D=.300E-04 L=.100E+01 L1=.300E-02
A=.150E-04 P=.300E-03 DIST=.010 DH=.50E+00 ETA= 1. N= 1
RL= 0.



SURFACE WAVES 2 TERMINAL MODEL
H= 375.0 T1=.1000E+01 G=.300E-04 D=.300E-04 L=.100E+01 L1=.300E-02
A=.150E-04 P=.300E-03 DIST=.010 DH=.50E+00 ETA= 1. N= 1
RL= 0.

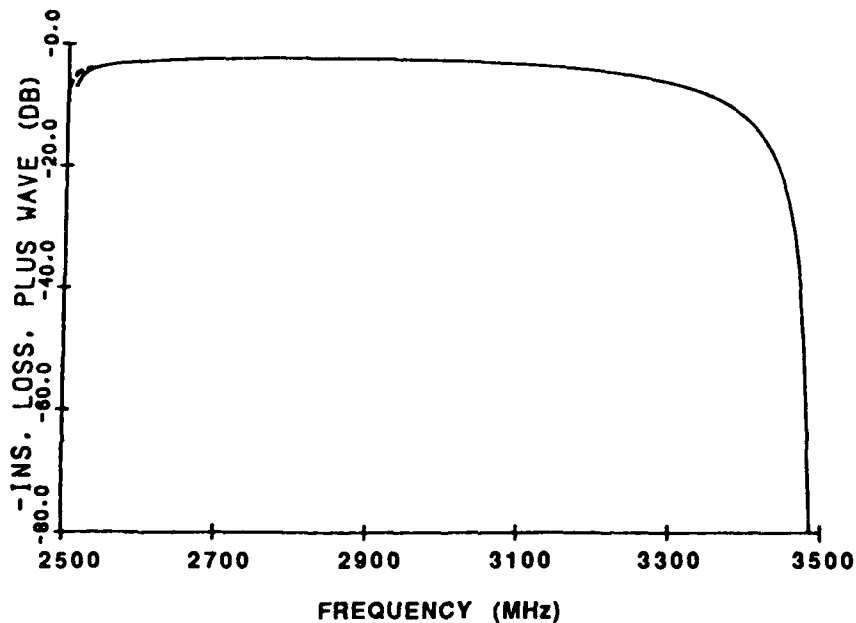


Figure 8-25. Insertion Loss versus Frequency. s/h = 0.5; d/h = 1.0

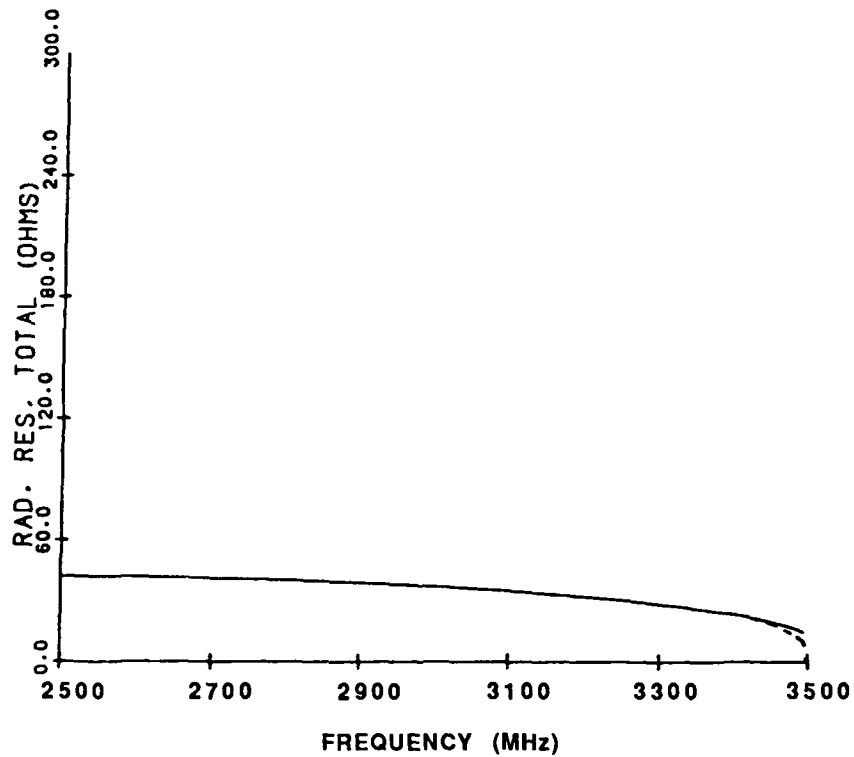
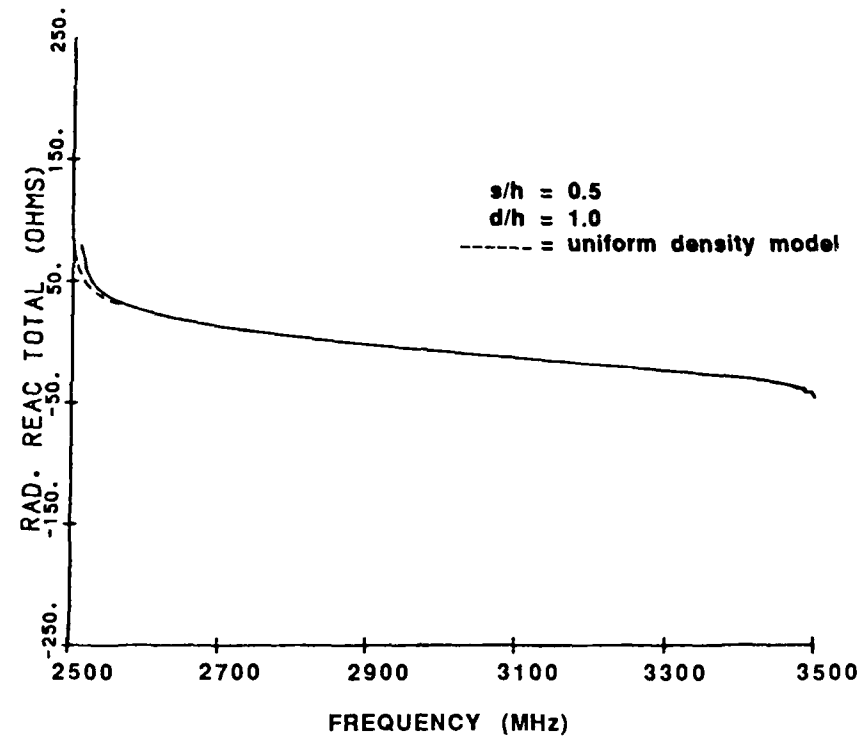
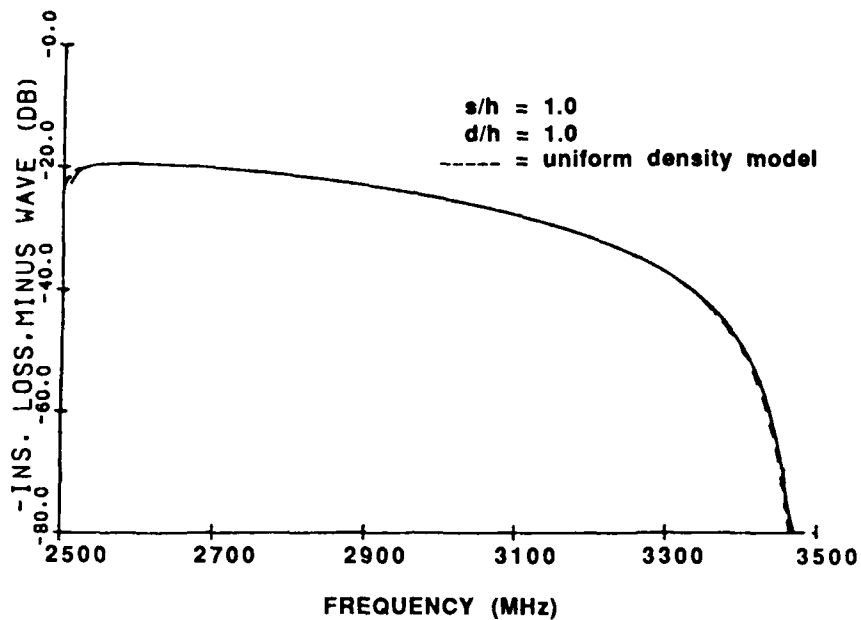


Figure 8-26. Radiation Impedance versus Frequency. $s/h = 0.5$; $d/h = 1.0$

SURFACE WAVES 2 TERMINAL MODEL
H= 375.0 T1=.1000E+01 G=.300E-04 D=.300E-04 L=.100E+01 L1=.300E-02
A=.300E-04 P=.300E-03 DIST=.010 DH=.50E+00 ETA= 1. N= 1
RL= 0.



SURFACE WAVES 2 TERMINAL MODEL
H= 375.0 T1=.1000E+01 G=.300E-04 D=.300E-04 L=.100E+01 L1=.300E-02
A=.300E-04 P=.300E-03 DIST=.010 DH=.50E+00 ETA= 1. N= 1
RL= 0.

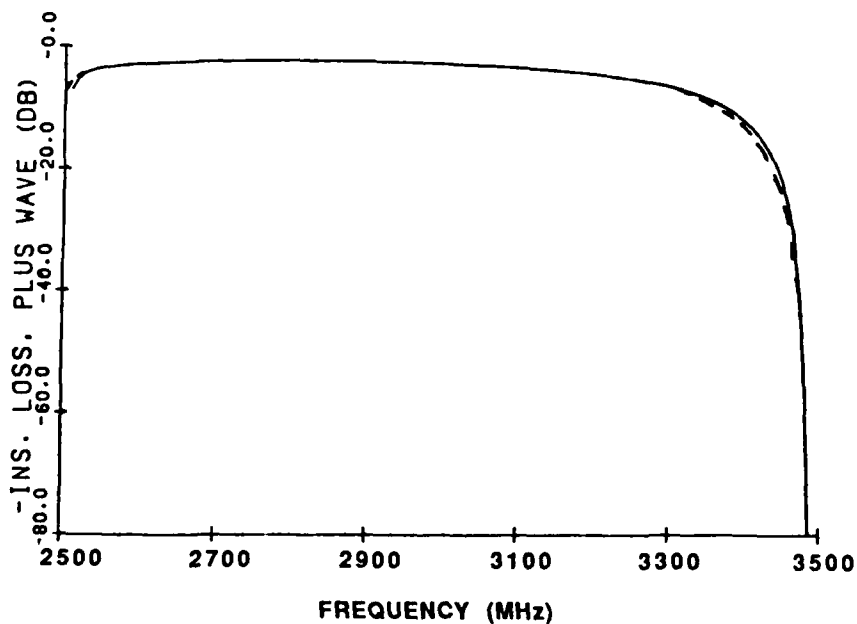


Figure 8-27. Insertion Loss versus Frequency. s/h = 1.0; d/h = 1.0

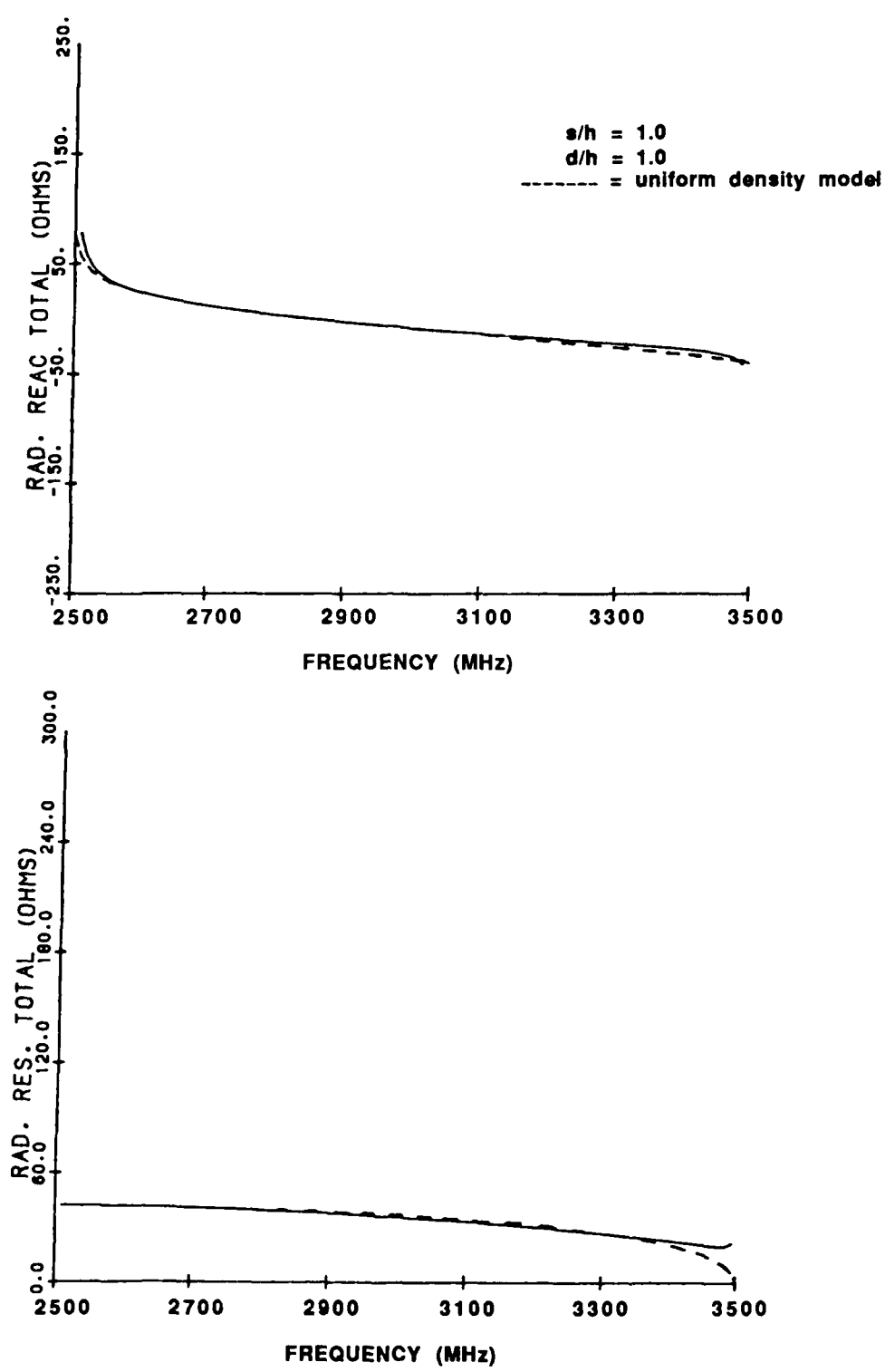
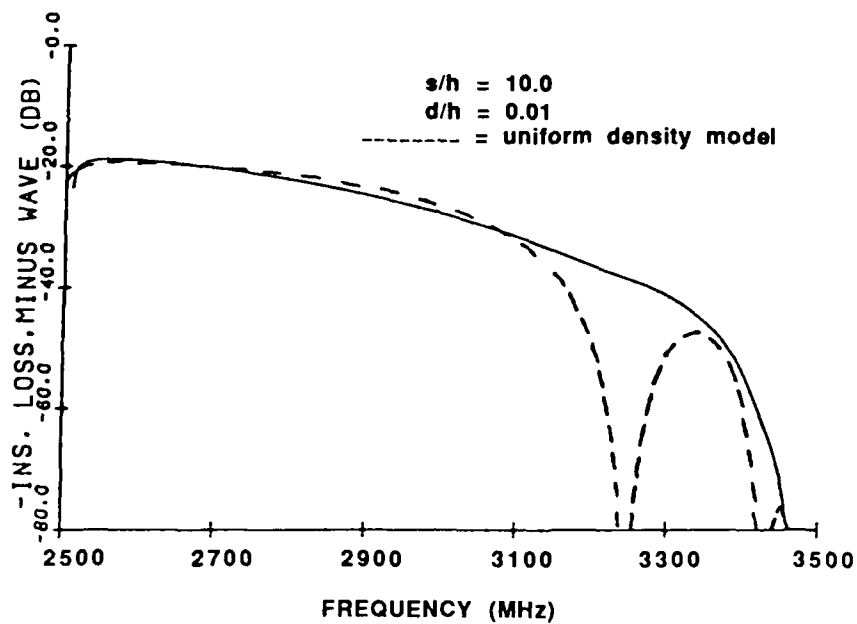


Figure 8-28. Radiation Impedance versus Frequency. $s/h = 1.0$; $d/h = 1.0$

SURFACE WAVES 2 TERMINAL MODEL
H= 375.0 T1=.1000E+01 G=.300E-06 D=.300E-04 L=.100E+01 L1=.300E-02
A=.300E-03 P=.300E-03 DIST=.010 DH=.50E+00 ETA= 1. N= 1
RL= 0.



SURFACE WAVES 2 TERMINAL MODEL
H= 375.0 T1=.1000E+01 G=.300E-06 D=.300E-04 L=.100E+01 L1=.300E-02
A=.300E-03 P=.300E-03 DIST=.010 DH=.50E+00 ETA= 1. N= 1
RL= 0.

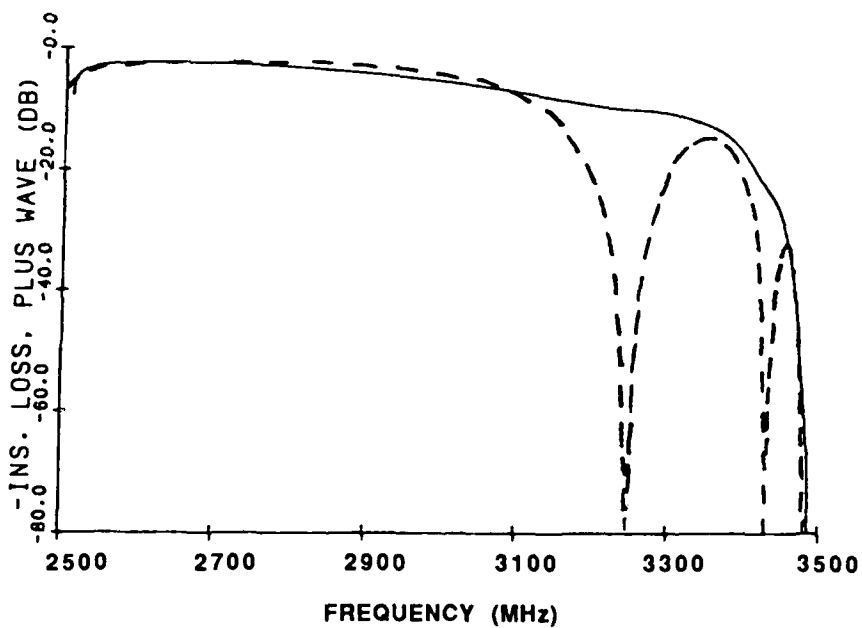


Figure 8-29. Insertion Loss versus Frequency. $s/h = 10.0$; $d/h = 0.01$

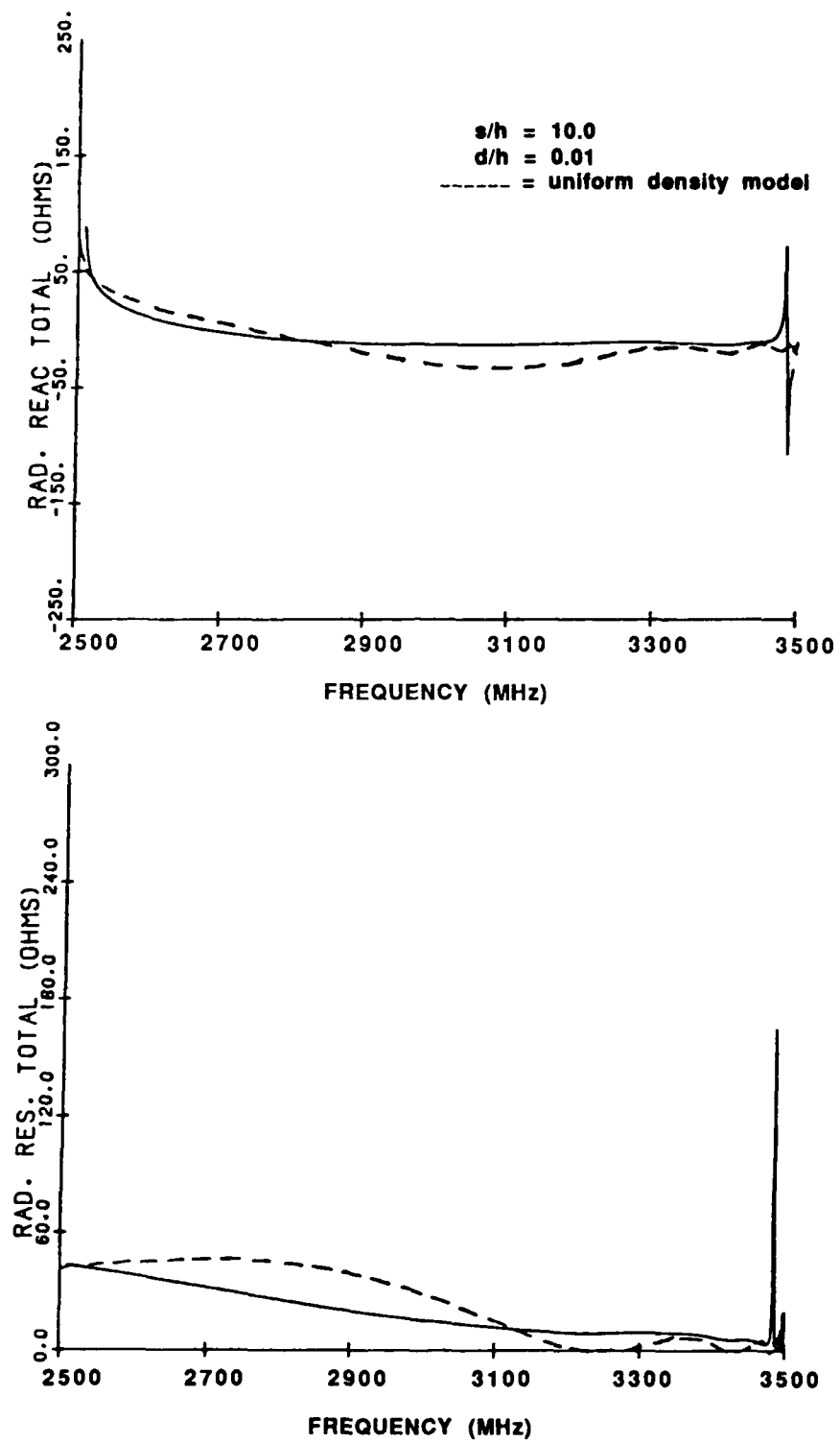


Figure 8-30. Radiation Impedance versus Frequency. $s/h = 10.0$; $d/h = 0.01$

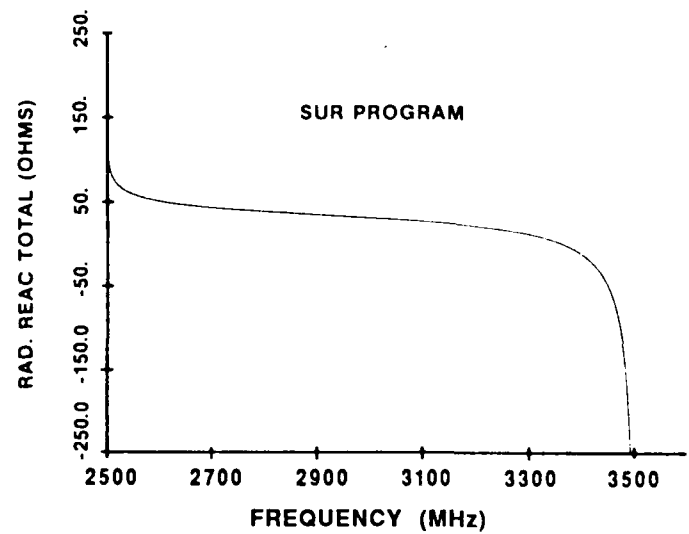
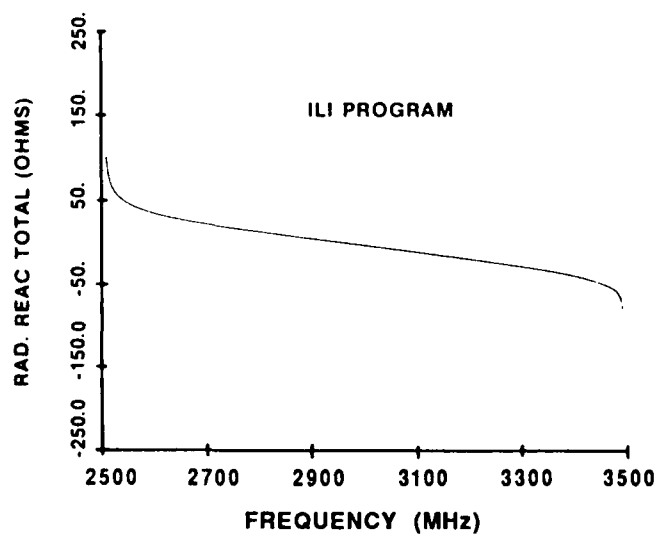
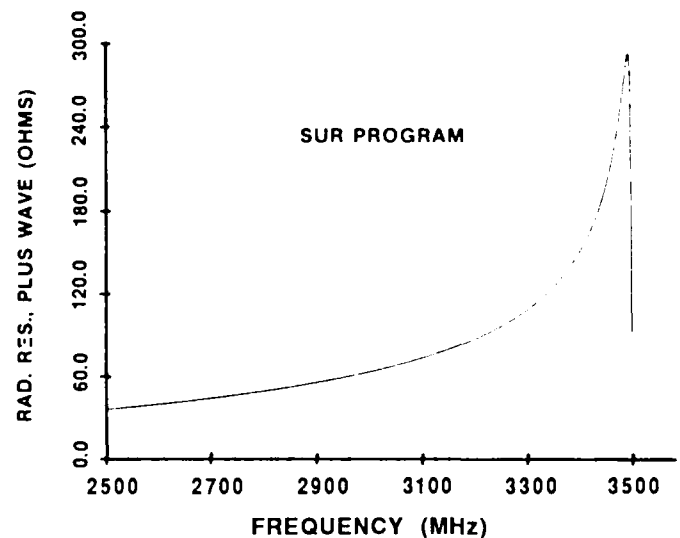
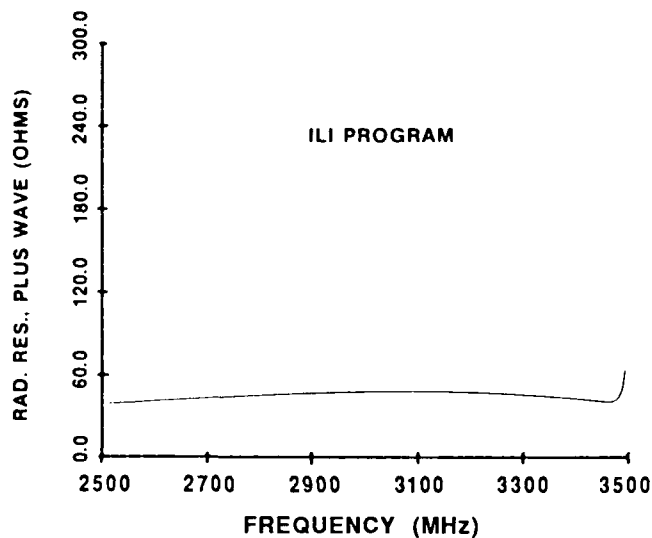
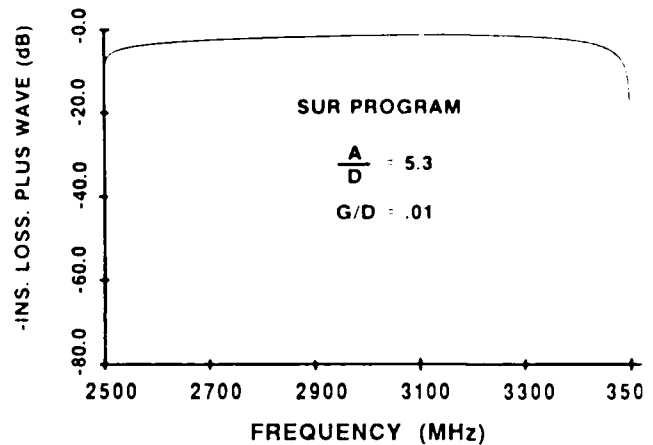
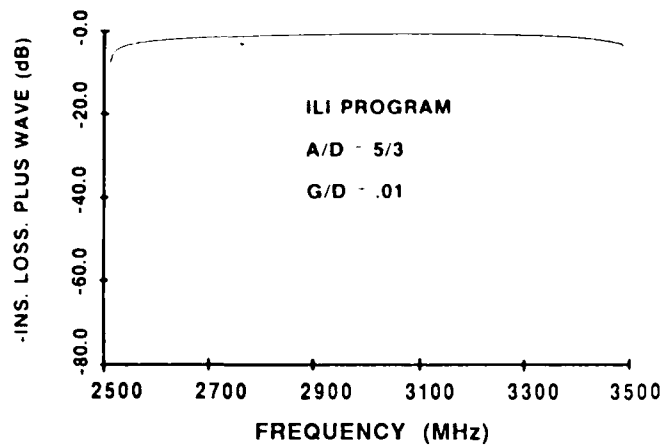


Figure 8-31. Insertion Loss Comparison: Flat Current versus Calculated Current Distribution
 $H = 375.0$ $T1 = .1000E+01$ $G = .300E-06$ $D = .300E-04$ $L = .100E+01$ $L1 = .300E-02$
 $A = .500E-04$ $P = .300E-03$ $DIST = .010$ $DH = 0.0$ $\eta = 1.$ $N = 1$ $RL = 0$

References

1. Emtage, P.R. (1982) Generation of magnetostatic surface waves by a microstrip, *J. Appl. Phys.* **53** (7):5122-5125.
2. Weinberg, I.J. (1981, May) *Analysis and Concepts Studies for Magnetostatic Surface Wave Transducers*, RADC-TR-81-96, ADA102207.
3. Abramowitz and Stegun (1964) *Handbook of Math. Functions*, National Bureau of Standards, Applied Mathematics Series, No. 55, Government Printing Office, pp 228-229.
4. Bubenik, D.M. (1977, Nov.) A practical method for the numerical evaluation of Sommerfeld integrals, *IEEE Trans. Ant. and Prop.* **AP-25** (6):904-906.
5. Hamming (1973) *Numerical Methods for Engineers*, McGraw Hill, New York, pp 205-207.
6. Broeck and Schwartz (1979 May) A One-Parameter Family of Sequence Transformations, *SIAM J. Math. Analysis* **10** (3):658-666.
7. Carayannis, G. et al. (1982) Subroutine TOEPL, *IEEE Transactions on Acoustics, Speech, and Signal Processing*, **ASSP-30**.
8. Stratton, J.A. (1941) *Electromagnetic Theory*, McGraw Hill, New York, pp 371,372.

Appendix to Chapter 8

Fourier Transform of a Generalized Function

Let $a = y + d$ and consider the evaluation of

$$H(a) = \int_{-\infty}^{\infty} dk e^{ikx} \frac{e^{-|k|a}}{|k|} \quad (8A-1)$$

$$= \int_{0+}^{\infty} dk \frac{[e^{-k(a+ix)} + e^{-k(a-ix)}]}{k} \quad (8A-2)$$

As a boundary condition, observe that

$$\lim_{a \rightarrow \infty} H(a) \rightarrow 0 \quad (8A-3)$$

Differentiating w.r.t. a gives

$$\frac{\partial H(a)}{\partial a} = - \int_{0+}^{\infty} dk [e^{-k(a+ix)} + e^{-k(a-ix)}] \quad (8A-4)$$

$$= - \frac{2a}{a^2 + x^2} \quad (8A-5)$$

Integrating this w.r.t. a gives

$$H(a) = -\ln(a^2 + x^2) + \text{Const.} \quad (8A-6)$$

Imposing (8A-3) leads to

$$H = \ln \frac{a^2}{a^2 + x^2} = \ln \frac{(y + d)^2}{x^2 + (y + d)^2} . \quad (8A-7)$$

9. DISCUSSION AND CONCLUSION

This report provides a review of all RADC in-house investigations related to the development of MSW transducer models. Results presented here, combined with a recent state-of-the-art review appearing in a Special Section of the Proceedings of the Institute of Electrical and Electronic Engineers, Feb, 1988, show clearly that MSW technology is in a developmental stage. Useful MSW devices are being developed, though commercial devices are highly specialized; and no large volume application has, as yet, surfaced.

This report discusses three MSW transducer models: Two Terminal (TT), Transmission Line (TL), and a combined TT/TL model. The new combined TT/TL generalized model provides an algorithm for extending the TT model to handle coupling between MSW and electromagnetic signals on any type of stripline structure. This report, however, concentrates on the TT model. Although TT and TL models have many features in common, they differ in several respects. Their common features include dispersion relations, and power carried by MSWs. That is, the MSW analysis portion of the models are identical, as they must be. Beginning with the definition of radiation resistance, however, the models differ. Each model, of course, must be and is internally consistent.

Radiation resistance, for the two models, is defined in different ways. Consequently, for a given frequency, and therefore wavelength as determined by the dispersion relation, radiation resistances are quantitatively and qualitatively different with respect to their dependence on transducer geometry, YIG parameters, and ground plane spacing. The most significant difference occurs with their dependence on liftoff, and this difference carries over into the combined TT/TL model. So far, the only significant difference found between the three models is in their predictions of insertion loss as a function of liftoff. Present experimental evidence supports one or the other of these models depending on the particular choice of input parameters. Liftoff experiments, using a wide range of input parameters, would be very useful in sorting out the range of validity of the various models.

Investigations described in this report have brought out several interesting or important aspects of the technology. First, in the past it has always been surprising how well MSW transducer models worked, considering the assumption that transducer currents, along the width of a transducer strip, are uniformly distributed. Based on the work presented in this report, it is clear why the uniform current assumption works so well; and over what range of parameters the uniform current assumption can be expected to be useful. Second, another aspect of MSW that has surfaced is the possibility of tunable filters using either resonant or nonresonant structures. This means utilizing long or short wavelength MSWs, respectively. Choosing one or the other represents a major decision point. There are tradeoffs between loss, available design theory, and bandwidth that must be considered. A third aspect of the technology relates to the choice of single crystal versus polycrystal materials. Important tradeoffs here include loss versus desired time delay. If large propagation times are involved, single crystals are required, otherwise loss is excessive.

Computer programs have been developed for investigating MSW characteristics and associated transducer models. There are approximately 40 programs, described in this report, which are available for analyzing MSW characteristics and their models. The programs are available on tape for a Cyber computer. They, the programs, are internally documented. Operating procedures for using the programs are described in this report.

The following general features of the analysis and models makes using and understanding the programs considerably easier. For the basic models, SUR and VOL, an EM boundary value problem is solved; and MSW power density is calculated in terms of an assumed generating current. Radiation resistance is then defined in terms of MSW power. Radiation reactance is then numerically calculated by a Hilbert transform of radiation resistance. All MSW RF fields are proportional to the spatial Fourier transform of the generating current distribution, whether assumed or calculated. RF fields surrounding the transducer are separated into near and far fields. Far fields contribute to radiation resistance. This means the dispersion relation, which must be used for MSW, is independent of transducer geometry. The wave is far from the influence of the transducer, and sees only the YIG and associated ground planes.

Work that remains to be done in the area of transducer modeling includes the development of new computer programs for the generalized TT/TL model, so that it handles multielement transducers; and the investigation of liftoff characteristics over a wide range of input parameters. From a broader perspective, an important problem to solve is the inclusion of magnetocrystalline anisotropy into the basic equations; and to search for crystal orientations where MSWs propagate over many hundreds of wavelengths without excessive loss or beam spreading. This would allow transversal filtering to be done directly at microwave frequencies.

Appendix A

MSW and Microwave Magnetics Publications

A1. REVIEW PAPERS AND RELATED PUBLICATIONS

1. Hogan, C.L. (1960, June) Ferrites, *Scientific American* **202**:92-104.
2. Sethares, J.C. (1965, July) Fonones De Microondas, INE, No. 31, Published in Spanish.
3. Dionne, G.F. (1975) A review of ferrites for microwave applications, *Proc. IEEE* **63**:777-789.
4. Adam, J.D. and Owens, J.M. (1975, Dec.) Microwave device applications of epitaxial magnetic garnets, *The Radio and Electronic Engineer* **45**(No. 12):738-748.
5. Adam, J.D. and Collins, J.H. (1976, May) Microwave magnetostatic delay devices based on epitaxial yttrium iron garnet, *Proc. IEEE* **64**:794-800.
6. Awai, I. and Ikenoue, J. (1977) Definition of Magnetic and Magnetostatic Waves and Their Characteristics, Institute of Electronics and Communication Engineers of Japan: Papers of the Technical Symposium on Microwaves (1977-1978 series), No. 11, pp 17-24. (This paper was translated by the Oriental Science Division of Emmanuel College, Boston Mass. for Air Force Geophysics Laboratory, Hanscom AFB.)
7. Collins, J.H., Owens, J.M., and Smith, C.V., Jr. (1977) Magnetostatic wave signal processing, 1977 *Ultrasonics Symposium Proc. IEEE* Cat. 77CH1264-1 SU, p541.
8. Vittoria, C. (1979, Jan.) *Feasibility Study of Ferrite Use at MM Waves*, Naval Research Laboratory Report, No. 3919.
9. Owens, J.M. and Smith, C.V., Jr. (1979, June) Beyond SAW Filters: Magnetostatics Show Promise, MSN, p44.
10. Adam, J.D., Daniel, M.R., and Schroder, D. K. (1980, May) Magnetostatic wave devices move microwave design into gigahertz realm, *Electronics*, p123.
11. Owens, J.M., Carter, R.L., Smith, C.V., Jr., and Collins, J.H. (1980) Magnetostatic waves, microwave SAW?, *Proc. IEEE Ultrasonics Symposium*, pp 506-513.

12. Nicholas, J. (1980) Microwave Ferrites, Chapter in *Ferromagnetic Materials*, Amsterdam, North Holland, E.P. Wohlfarth, Ed.
13. Stiglitz, M.R. and Sethares, J.C. (1982, Feb.) Magnetostatic waves take over where SAWs leave off, *Microwave Journal*, p18.
14. Sethares, J.C. (1982, Mar.) Magnetostatic wave devices and applications, *J. Appl. Phys.* **53**(No. 3) Part II:2646-2651.
15. Owens, J.M. and Carter, R.L. (1983, Mar.) Magnetostatics Advance: The Shape of Waves to Come, MSN, p103.
16. Castera, J.P. (1984, Mar.) State of the art in design and technology of MSW devices, *J. Appl. Phys.* **55**:2506-2511
17. Hatakeyama, K. and Inui, T. (1984) Electromagnetic Wave Absorber Using Ferrite Absorbing Material Dispensed with Short Metal Fibers, Digest of International Magnetics Conference, IEEE Cat. No. 84, CH1918 2, p491.
18. Ishak, W.S. and Chang, K.W. (1985, Feb.) Magnetostatic wave devices for microwave signal processing, *Hewlett Packard Journal*, pp10-20.
19. Ishak, W.S. (1985) Microwave Signal Processing Using Magnetostatic Wave Devices, *IEEE Ultrasonic Symposium Proceedings*.
20. Adam, J.D. (1988, Feb.) Analog Signal Processing with Microwave Magnetics, *Proc. IEEE*.
21. Ishak, W.S. (1988, Feb.) Magnetostatic Wave Technology: A Review, *Proc. IEEE*.
22. Sethares, J.C., Guest Ed. (1988, Feb.) Microwave Magnetics, Special Section, *Proc. IEEE*, pp 121-200.

A2. MICROWAVE MAGNETICS BIBLIOGRAPHY

1. *New Developments in Ferromagnetic Materials*, New York, Elsevier Publishing Co, 1947.
2. *Ferrites*, S. Smith and H.P.J. Wijn, John Wiley & Sons, New York, 1959.
3. *Physics of Magnetism*, S. Chikazumi, John Wiley & Sons, New York, 1961.
4. *Microwave Ferrites and Ferrimagnetics*, B. Lax and K.J. Button, McGraw Hill, New York, 1962.
5. *Ferromagnetic-Relaxation Theory*, M. Sparks, McGraw Hill, New York, 1964.
6. *Handbook of Microwave Ferrite Materials*, W. H. vonAulock, Academic Press, New York, 1965.
7. *Linear Ferrite Devices for Microwave Application*, W.H. vonAulock and C. Fay, Academic Press, New York, 1968.
8. *Ferrite Control Components*, Vol 1, Junction Circulators, YIG Filters and Limiters, Reprint Volume, L.R. Whicker, Artech House, Inc., 319 pgs, 1974.
9. *Ferrite Control Components*, Vol 2, Ferrite Phasers and Ferrite MIC Components, Reprint Volume, L.R. Whicker, Artech House, Inc., 325 pages, 1974.
10. *Microwave Propagation in Ferrimagnetics*, M.S. Sodha and N.C. Srivastava, Plenum Press, 1981.
11. *Microwave Magnetics*, R.F. Soohoo, Harper and Row, New York, 1985.
12. Magnetostatic waves and applications to Signal Processing, *Circuits, Systems and Signal Processing*, J.P. Parekh, Ed., Vol. 4, No's 1 and 2, 363 pages, 1985.

A3. AFCRL AND RADC REPORTS

1. Purnhagen, T.G. (1963, Oct.) *Automated Spin Wave Instability Threshold Measurement and Recording*, AFCRL-63-505, 26 pgs.
2. Sethares, J.C., Seavey, M.H. Jr., and Stiglitz, M.R. (1964, Jan.) *Spin Wave Anisotropy in Parallel Pumping Experiments on YIG*, Research Report, AFCRL-64-14, 65 pgs.
3. Sethares J.C. and Olson, F.A. (1965, Jan.) *Study of Ferrimagnetic Crystals by Parallel Pumping*, Special Reports No. 19, AFCRL-65-64, AD613321, 122 pgs.
4. Sethares, J.C. and Purnhagen, T.G. (1966, May) *Anisotropic Spin Wave Propagation in Ferrites*, Physical Sci. Res. Papers No. 222, AFCRL-66-306, AD635175, 4 pgs.
5. Sethares, J.C. (1966, Sep.) *Transmission Line Models of Magnon-Phonon Modes in Ferrites, Part I, Uncoupled Modes*, AFCRL-66-633 (I), AD641638, 17 pgs.
6. Sethares, J.C. (1967, May) *Transmission Line Models of Magnon-Phonon Modes in Ferrites, Part II, Coupled Modes*, AFCRL-67-0314, AD655777, 22 pgs.
7. Sethares, J.C. and Merry, J.B. (1974, Feb.) *Magnetostatic Surface Waves in Ferrimagnets Above 4 GHz*, AFCRL-TR-74-0112, AD780640, 26 pgs.
8. Sethares, J.C. (1975, July) *Magnetostatic Surface Waves on a Cylinder*, AFCRL-TR-75-0380, ADA017174, 48 pgs.
9. Sethares, J.C., Tsai, T.L., and Koltunov, I. (1978, Apr.) *Periodic Magnetostatic Surface Wave Transducers*, RADC-TR-78-78, ADA057214, 30 pgs.
10. Weinberg, I.J. and Sethares, J.C. (1978, Sep.) *Magnetostatic Wave Transducers with Variable Coupling*, RADC-TR-78-205, ADA063880, 41 pgs.
11. Weinberg, I.J. (1979, Jan) *Hilbert Transform by Numerical Integration*, RADC-TR-79-3, ADA068084, 19 pgs.
12. Weinberg, I.J. (1981, May) *Analysis and Computer Studies for Magnetostatic Surface Wave Transducers*, RADC-TR-81-96, Univ. of Lowell, ADA102207, 98 pgs.
13. Morgenthaler, F.R. (1982, Apr.) *Magnetic Field Synthesis for Microwave Magnetics*, RADC-TR-82-95, Mass. Institute of Technology, ADA115889, 170 pgs.
14. Adam, J.D., Daniel, M.R., Emtage, P.R., and Weinert, R.W. (1982, Jul.) *MSW Variable Time Delay Techniques*, RADC-TR-82-206, Westinghouse Electric Corp., ADA120648, 60 pgs.
15. Weinberg, I.J. (1982, Dec) *Analysis and Computer Studies of Magnetostatic Wave Transducers*, RADC-TR-82-307, Univ. of Lowell, ADA124530, 58 pgs.
16. Sethares, J.C. Ed. (1983, Jan.) *Proceedings of the 1981 RADC Microwave Magnetics Technology Workshop*, June 10-11, 1981, RADC-TR-83-15, ADA126417, 357 pgs.
17. Adam, J.D., et al. (1983, Sep.) *MSW Variable Time Delay Techniques*, RADC-TR-83-139, Westinghouse Electric Corp., ADA133770, 168 pgs.
18. Parekh, J.P. and Tuan, H.S. (1987, Dec.) *Studies of MSFVW to MSBVW Mode Conversion at a Region of Bias Field Discontinuity and of the Dispersion of an MSFVW Pulse*, RADC-TR-87-201, Univ. of New York at Stonybrook, ADA189343, 75 pgs.

Appendix B

Hyperbolic Current Distribution

Expressions for $\tilde{J}_a(k)$ and $F(a, k, \delta)$, which appear in Eqs. (6-10) and (6-12), are developed below. From Eqs. (6-8) and (6-9) we have, letting $I(n) = J_0 S_n$.

$$\tilde{J}_a(k) = J_0 \sum_{n=1}^N S_n \quad (B-1)$$

$$\text{where } J_0 = \frac{(I/a)}{\{[\sinh(a/2\tilde{\delta})]/(a/2\tilde{\delta})\}} \quad (B-2)$$

$$\text{and } S_n = \eta^{n-1} \int_{(n-1)p-a/2}^{(n-1)p+a/2} e^{ikx} \cosh[(x - (n-1)p)/\tilde{\delta}] dx . \quad (B-3)$$

Making a change of variables simplifies Eq. (B-3).

$$\text{Let } x - (n-1)p = z \quad (B-4)$$

$$\text{then } S_n = \eta^{n-1} \int_{-a/2}^{a/2} [\cosh(z/\tilde{\delta})] e^{ik[z+(n-1)p]} dz \quad (B-5)$$

$$\text{and, } S_n = [(\eta^{n-1} e^{ik(n-1)p}) \int_{-a/2}^{a/2} [\cosh(z/\delta)] e^{ikz} dz, \quad (\text{B-6})$$

From Eq. (6-11), the above integral is identified as $F(a, k, \delta)$. Therefore, Eq. (B-6) reduces to,

$$S_n = [(\eta e^{ikp})^{n-1}] F(a, k, \delta) \quad (\text{B-7})$$

Using Eq. (B-1),

$$\tilde{J}_a(k) = J_0 F(a, k, \delta) \sum_{n=1}^N (\eta e^{ikp})^{n-1} \quad (\text{B-8})$$

The summation can be expressed in closed form, using the identity

$$\sum_{k=1}^N q^{k-1} = \frac{1-q^N}{1-q}.$$

Eq. (B-8) has the desired form as given in Eq. (6-10). Setting $(\eta e^{ikp}) = q$ in Eq. (B-8) yields,

$$\tilde{J}_a(k) = J_0 F(a, k, \delta) \left[\frac{1 - \eta^N e^{ikpN}}{1 - \eta e^{ikp}} \right] \quad (\text{B-9})$$

We next give a closed form expression for $F(a, k, \delta)$ by performing the integration in Eq. (B-6). Performing the integration yields,

$$F(a, k, \delta) = \frac{a}{(a^2 k^2 + i2a^2/\delta^2)} [A_1' e^d + A_2' e^{-d} - i(A_3' e^d + A_4' e^{-d})], \quad (\text{B-10})$$

where $d = a/2\delta$

$$A_1' = d(\cos c + \cos f) + f \sin c + c \sin f$$

$$A_2' = -d(\cos c + \cos f) + f \sin c + c \sin f$$

$$A_3' = d(\sin f - \sin c) + f \cos c - c \cos f$$

$$A_4' = d(\sin f - \sin c) - f \cos c + c \cos f$$

$$c = \frac{a}{2}(k + 1/\delta)$$

$$\text{and } f = \frac{a}{2}(k - 1/\delta) \quad (\text{B-11})$$

Eq. (B-10) can be further simplified, we note that:

$$\cos c + \cos f = 2 \cos(ak/2) \cos(a/2\delta)$$

$$\sin f - \sin c = -2 \cos(ak/2) \sin(a/2\delta)$$

$$f \sin c + c \sin f = ak \sin(ak/2) \cos(a/2\delta) - (a/\delta) \cos(ak/2) \sin(a/2\delta)$$

$$f \cos c - c \cos f = -ak \sin(ak/2) \sin(a/2\delta) - (a/\delta) \cos(ak/2) \cos(a/2\delta) \quad (B-12)$$

With the help of Eqs. (B-11) and (B-12),

$$A_1' = (a/\delta) \cos(ak/2) [\cos(a/2\delta) - \sin(a/2\delta)] + (ak) \sin(ak/2) \cos(a/2\delta)$$

$$A_2' = -(a/\delta) \cos(ak/2) [\cos(a/2\delta) + \sin(a/2\delta)] + (ak) \sin(ak/2) \cos(a/2\delta)$$

$$A_3' = -(a/\delta) \cos(ak/2) [\sin(a/2\delta) + \cos(a/2\delta)] - (ak) \sin(ak/2) \sin(a/2\delta)$$

$$A_4' = (a/\delta) \cos(ak/2) [\cos(a/2\delta) - \sin(a/2\delta)] + (ak) \sin(ak/2) \sin(a/2\delta) \quad (B-13)$$

From Eq. (B-13) we have

$$A_1' - iA_3' = e^{ia/2\delta} [(a/\delta)(1+i) \cos(ak/2) + (ak) \sin(ak/2)]$$

$$A_2' - iA_4' = e^{-ia/2\delta} [-(a/\delta)(1+i) \cos(ak/2) + (ak) \sin(ak/2)] \quad (B-14)$$

Substitution of Eq. (B-14) into Eq. (B-10) gives, finally, an expression for $F(a, k, \delta)$ explicitly in terms of a, k , and δ .

$$F(a, k, \delta) = \frac{a}{(a^2 k^2 + i2a^2/\delta^2)}$$

$$\left\{ \begin{array}{l} e^{(1+i)(a/2\delta)} [(a/\delta)(1+i) \cos(ak/2) + (ak) \sin(ak/2)] \\ + e^{-(1+i)(a/2\delta)} [-(a/\delta)(1+i) \cos(ak/2) + (ak) \sin(ak/2)] \end{array} \right\} \quad (B-15)$$

Eq. (B-15) is the desired result for $F(a, k, \delta)$ appearing in Eq. (6-10).

Appendix C

List of Symbols and Notation

SYMBOL	DESCRIPTION
a, A	Transducer strip width
g, G	Transducer to YIG gap spacing (liftoff)
t_1 , T1	Transducer to upper ground plane spacing
l, L	YIG to lower ground plane spacing
d, D	YIG thickness
p, P	Center-to-center spacing between transducer strips
l_1 , L1	Transducer aperture length
k, K, k_s , K_s	MSW propagation constant
H	Internal demagnetized biasing field
$4\pi M$	Saturation magnetization
ΔH	FMR linewidth
σ	Electrical conductivity
Z_0 , Z_C , Z_c	Strip line characteristic impedance
ACC	Attenuation constant parameter
BTC	Propagation constant parameter
Dist, DelR	Propagation path length
N	Number of strips in transducer
Plus, (+) wave	Wave in $\vec{H} \times \hat{n}$ direction
Minus, (-) wave	Wave in $-\vec{H} \times \hat{n}$ direction

where \hat{n} is a unit vector
pointing out of YIG surface

GCG	Gadolinium Gallium Garnet
YIG	Yttrium Iron Garnet
WO	Wire over transducer configuration
FC	Flipped configuration. YIG on microstrip
ICFF	Independent conductor flat field
MSSW	Magnetostatic surface wave
MSFVW	Magnetostatic forward volume wave
MSBVW	Magnetostatic backward volume wave
TT, TA	Two terminal model
TL	Transmission line or microstrip model
TT/TL	Combined model
$\text{sinc}(x)$	$[\sin(\pi x)]/(\pi x)$
$R_1^{(s)} \equiv R_1(s)$	
$F_T^{(1)}(k) \equiv F'_T(k)$	

Appendix D

Band Pass Filter Using LPE-YIG Films

(Unpublished Paper)

by

Tung-Lin Tsai and J. Sethares

D1. INTRODUCTION

Liquid phase epitaxial-yttrium iron garnet (LPE-YIG) films are compatible with microstrip circuits and can form planar, rapidly tunable microwave filters. In recent years they have been the subject of great interest for microwave device applications. Potential applications of these devices have already been discussed.^{D1,D2,D3} In a previous report^{D3} on tunable band stop filters, we strengthened the potentiality of high speed frequency hopping devices by using current injection into flat ribbon strips placed adjacent to YIG films. In this section, YIG films constructed on microstrip circuits will be discussed. The possibility of multipole band pass filters incorporated with switching transistors to produce high speed switching of tunable microwave filters will also be commented on.

-
- D1. Adam, J., Collins, J., and Owens, J. (1975) Microwave device applications of epitaxial magnetic garnets, *The Radio and Electronic Engineer* **45**, (No. 12):738-748.
 - D2. Simpson, I., Morton, I., Owens, J., and Pringle, R. (1974) Tunable microwave filters using YIG grown by LPE, Proc. 4th European Microwave Conference, pp 590-594.
 - D3. Tsai, T.L. and Sethares, J. (1977, June) Band stop filter using LPE-YIG films, *IEEE-MTT Symposium Digest*, San Diego, CA.

D2. SINGLE POLE NARROW BAND FILTER

As shown in the insert of Figure D-1, square YIG films* with dimensions $4\text{ mm} \times 4\text{ mm} \times 10\text{ }\mu\text{m}$, grown on (111) GGG substrates, were used as resonator chips for this investigation. Microstrip lines with characteristic impedance of 50 ohms were used. The configuration used here provides a dual purpose filter- by choosing appropriate terminals for the output (that is, 1-2 for bandstop filter, 1-2' for bandpass filter). Characteristics of the bandstop filter were discussed in a previous report.^{D3} Here, the bandpass filter will be discussed.

Coupling between microstrip and film is enhanced by tapering the stripline, and spurious modes are greatly suppressed by separating YIG films from the striplines with GGG substrates by approximately 0.5 mm. A swept RF signal between $f_1 = 3.07\text{ GHz}$ and $f_2 = 3.6\text{ GHz}$ is fed to the microstrip line through an OSM connector at terminal 1 in Figure D-1. Resonant spikes are observed, through the coupling mechanism of the resonator chip, at a field intensity of around 600 Oe, applied parallel to the film surface. No attempt was made to match impedances. Insertion losses below 4.5 dB are easily obtained. Insertion loss could be further reduced at the sacrifice of decreasing the suppression of spurious modes. The 3 dB bandwidth was found to be 3.075 MHz at 3.335 GHz resonant frequency. The resonant spike can be tuned over a bandwidth of 5 percent without noticeable increase in insertion loss. Spurious modes are typically more than 12 dB down from the main resonant peak and out of band rejection is around 20 dB. The external Q , Q_e , calculated from Carter's formula^{D4}, is found to be around 1200. Overall, their characteristics are comparable to those of high quality bulk YIG devices.

D3. DISCUSSION

Using current injection into flat ribbon strips adjacent to YIG films as discussed in Reference D3, we can make a fast switching bandpass filter by using the present configuration. This has been done and our results have demonstrated the potential of this technique. Here a two-pole bandpass filter is used for the illustration. Figure D-2 is a two pole bandpass filter with MIC construction-shown at the upper right hand corner. Because the resonator chips were grown from different batches, they had different resonant frequencies. One chip was grown under compression, with lead added (less than 2 percent by weight) and the other was grown under zero misfit condition, that is, stress free. Both samples have linewidths of less than 0.5 Oe at 9 GHz and have around 3 MHz bandwidth for a single pole filter, tested as described in the previous section. With an appropriate current injected into current strips, insertion losses below 3 dB with 3 dB bandwidth of 3.68 MHz is easily obtained. No noticeable increase in the spurious mode suppression was observed. We believe that the narrow band resonant spike created from this tapered strip circuit is a magnetostatic mode, since the tapered strip line produces non-uniform RF fields in the neighborhood of the YIG films. We have achieved

* Films supplied by H.G. Glass, Rockwell International, through the efforts of Captain W. Steinbach, AFOSR.

D4. Carter, P.S., Jr. (1961) Magnetically tunable microwave filters using single crystal YIG resonators, *IRE Trans. on MTT*, **MTT-9**:252-260.

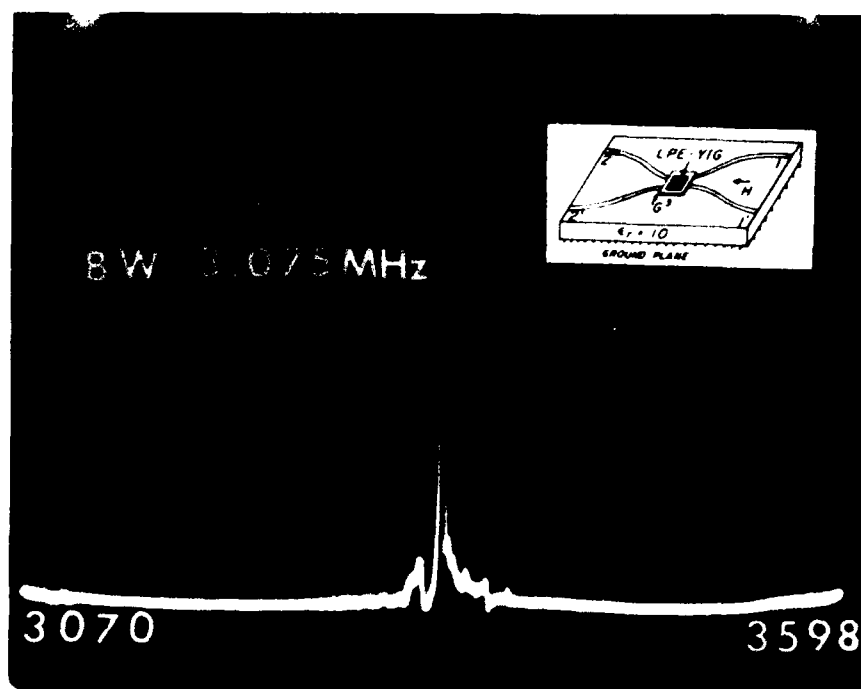


Figure D-1. Single Pole Filter with $H = 600$ Oe, with MSSW

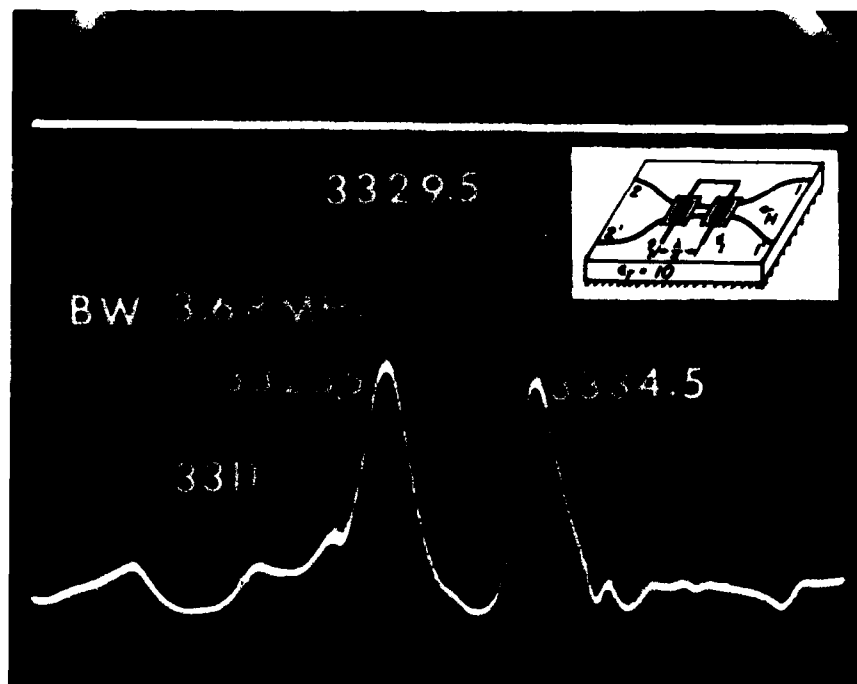


Figure D-2. Two Pole Filter: Solid Line Represents Two Individual Resonant Spikes Before Current Injection. Dashed line shows the result of current injection through flat ribbon strips.

10 MHz/ μ sec switching speeds and up to 100 MHz/ μ sec is expected (theoretical limit) if current passing through the flat ribbon strips is controlled by fast switching transistors. This will provide tunable narrow band filters, for high frequency hopping in communication applications.

References

- D1. Adam, J., Collins, J., and Owens, J. (1975) Microwave device applications of epitaxial magnetic garnets, *The Radio and Electronic Engineer* **45**, (No. 12):738-748.
- D2. Simpson, I., Morton, I., Owens, J., and Fringle, R. (1974) Tunable microwave filters using YIG grown by LPE, Proc. 4th European Microwave Conference, pp 590-594.
- D3. Tsai, T.L. and Sethares, J. (1977, June) Band stop filter using LPE-YIG films, *IEEE-MTT Symposium Digest*, San Diego, CA.
- D4. Carter, P.S., Jr. (1961) Magnetically tunable microwave filters using single crystal YIG resonators, *IRE Trans. on MTT*, **MTT-9**:252-260.

Appendix E

Transmission Line Analysis for TT Model Extension

With reference to Figure 6-9, the voltage and current along a generalized transmission line has the form,

$$V(z) = V_+ e^{-\gamma z} [1 + \Gamma(z)]$$

$$I(z) = \frac{V_+}{Z} e^{-\gamma z} [1 - \Gamma(z)] \quad (E-1)$$

where $\Gamma(z)$ is a generalized reflection coefficient defined as

$$\Gamma(z) = \Gamma_o e^{2\gamma_s z}, \text{ for strip section and } \gamma_s = j\beta_o.$$

$$\Gamma(z) = \Gamma_{oT} e^{2\gamma_T z}, \text{ for transducer section}$$

and Γ_o is the reflection coefficient at $z = 0$.

For the circuit in Figure 6-9,

$$\Gamma_o = \frac{Z_L - Z_o}{Z_L + Z_o} = \frac{Z_{LN} - 1}{Z_{LN} + 1}$$

For the stripline section, $Z = Z_o$ and $\gamma = j\beta_o$.

$$Z_{LN} \triangleq Z_L / Z_o, \text{ by definition.}$$

Also, for the stripline section,

$$V(z) = V_+ e^{-j\beta_0 z} [1 + \Gamma_0 e^{j\beta_0 z}]$$

$$I(z) = \frac{V_+}{Z_0} e^{-j\beta_0 z} [1 - \Gamma_0 e^{j2\beta_0 z}] \quad (\text{E-2})$$

The generalized reflection coefficient, looking to the right, at $z = -z_1$ can now be obtained from Eq. (E-2), as follows, (note that $z_1 = l_0$ and $z_2 = l_1 + l_0$)

$$Z(-z_1) = \frac{V(-z_1)}{I(-z_1)} = Z_0 \left[\frac{1 + \Gamma_0 e^{-j2\beta_0 l_0}}{1 - \Gamma_0 e^{-j2\beta_0 l_0}} \right] \quad (\text{E-3})$$

Now,

$$\Gamma_{0T} e^{-2\gamma_T l_0} = \frac{Z(-z_1) - Z_T}{Z(-z_1) + Z_T} \quad (\text{E-4})$$

When Z_T is the characteristic impedance of the transducer section, and Γ_{0T} is what goes into $\Gamma_T(z)$

$$\Gamma_T(z) = \Gamma_{0T} e^{2\gamma_T z}$$

The impedance at $z = -z_2$, looking to the right, is

$$Z(-z_2) = \frac{V(-z_2)}{I(-z_2)} = Z_T \frac{1 + \Gamma_T(-z_2)}{1 - \Gamma_T(-z_2)}, \quad (\text{E-5})$$

where $\Gamma_T(-z_2) = \Gamma_{0T} e^{-2\gamma_T z_2}$. Therefore,

$$\Gamma_T(-z_2) = \Gamma_{0T} e^{-2\gamma_T (l_1 + l_0)} \quad (\text{E-6})$$

Now, from Figure 6-9,

$$V_S = [R_0 + Z(-z_2)] I(-z_2) \quad (\text{E-7})$$

and from Eq. (E-1),

$$I(-z_2) = \frac{V_+}{Z_T} e^{\gamma_T z_2} [1 - \Gamma_T(-z_2)] \quad (\text{E-8})$$

where Z_T is the characteristic impedance of the transducer section.

Combine Eqs. (E-8) and (E-7) to get

$$\frac{[1 - \Gamma_T(-z_2)] V_+ e^{\gamma_T z_2}}{Z_T} = \frac{V_S}{R_0 + Z(-z_2)}$$

then,

$$V_+ = \frac{Z_T e^{-\gamma_T z_2} V_S}{[R_0 + Z(-z_2)] [1 - \Gamma_T(-z_2)]} \quad (\text{E-9})$$

The current $I(z)$ can now be expressed in terms of V_S , Z_L and transmission line parameters.

$$I(z) = \frac{V_S e^{-\gamma_T(l_1 + l_0)} e^{-\gamma_T Z}}{[R_0 + Z(-z_2)][1 - \Gamma_T(-z_2)]} [1 - \Gamma_{oT} e^{2\gamma_T Z}] , \quad (E-10)$$

where $Z(-z_2)$ is given by Eqs. (E-5) and (E-6), which yield,

$$Z(-z_2) = Z_T \left[\frac{1 + \Gamma_{oT} e^{-2\gamma_T(l_1 + l_0)}}{1 - \Gamma_{oT} e^{-2\gamma_T(l_1 + l_0)}} \right] \quad (E-11)$$

We can now put Eq. (E-10) into the form:

$$I(z) = \left[\frac{V_S}{R_0 + Z(-z_2)} \right] \left[\frac{1 - \Gamma_{oT} e^{2\gamma_T Z}}{1 - \Gamma_{oT} e^{-2\gamma_T Z_2}} \right] e^{-\gamma_T(z + l_1 + l_0)} . \quad (E-12)$$

We note that when $z = -z_2 = -(l_1 + l_0)$,

$$I(z = -z_2) = \left[\frac{V_S}{R_0 + Z(-z_2)} \right]$$

$$\text{Defining, } \Gamma_1 \equiv \frac{Z(-z_1) - Z_T}{Z(-z_1) + Z_T} = \Gamma_{oT} e^{-2\gamma_T l_0}$$

we have

$$\Gamma_{oT} = \Gamma_1 e^{2\gamma_T l_0} \text{ and, Eq. (E-12) becomes}$$

$$I(z) = \left[\frac{V_S}{R_0 + Z(-z_2)} \right] \left[\frac{1 - \Gamma_1 e^{2\gamma_T(z + l_0)}}{1 - \Gamma_1 e^{-2\gamma_T l_1}} \right] e^{-\gamma_T(z + l_1 + l_0)} , \quad (E-13)$$

Eq. (E-13) is now in the desired form [see Eqs. (6-39) and (6-41)].